FINAL REPORT

CONTRACT No. NAS5-9577

FEASIBILITY STUDY

SCANNING CELESTIAL ATTITUDE DETERMINATION SYSTEM

PREPARED FOR
GODDARD SPACE FLIGHT CENTER
NASA

RESEARCH DIVISION

CONTROL DATA
CORPORATION

Final Report:

FEASIBILITY STUDY FOR A SCANNING CELESTIAL ATTITUDE DETERMINATION SYSTEM (SCADS) FOR THREE AXIS ATTITUDE DETERMINATION AT A COMMAND AND DATA ACQUISITION (CDA) STATION

Contract No. NAS5-9577

Control Data Project No. 9560

RD-2001

September 22, 1965

Prepared for:

National Aeronautics and Space Administration
Goddard Space Flight Center
Greenbelt, Maryland

(Prepared by Control Data Corporation, Research Division, 8100 34th Avenue South, Minneapolis, Minnesota 55440. Authors: C. B. Grosch, Project Engineer; R. W. Peterson, R. C. Borden, D. F. Nickel, A. J. Mooers, B. D. Vannelli, E. J. Farrell, C. D. Zimmerman.)

ET AL continue with last

ABSTRACT

This is the final report for Contract NAS5-9577: Feasibility Study for a Scanning Celestial Attitude Determination System (SCADS). The attitude determination concept relies upon an instrument which consists of a scanning wide-angle camera with a slit positioned on its focal surface. Applications of such a concept for the Nimbus and Tiros spacecraft configurations are emphasized.

The effort during the study was devoted to the areas of optical, electrical, and mechanical design; optimum instrument design in view of the stellar background and detection limits of photodetectors; error analysis by means of computer simulation; and star identification.

Recommended designs are given. The design for the Tiros instrument is somewhat simpler than that of the Nimbus instrument.

TABLE OF CONTENTS

TABLE OF CONTENTS (Cont'd)

LIST OF FIGURES

LIST OF TABLES

FOREWORD

This final report represents a complete technical documentation of all efforts performed under Contract NAS5-9577, and does not require any supplementation from the various interim technical reports. The study was performed between May 10, 1965 and September 15, 1965, for NASA/Goddard Space Flight Center, Greenbelt, Maryland. It represents nine man-months of effort.

The study was performed by the Aerospace Research Group, Research Division, Control Data Corporation, Minneapolis, Minnesota. Mr. C. B. Grosch was project engineer. Other participants were B. D. Vannelli, R. W. Peterson, D. F. Nickel, R. C. Borden, E. J. Farrell, C. D. Zimmerman, and A. J. Mooers.

Control Data Corporation would like to acknowledge the assistance of Irving Lowen, the technical officer in charge of this study. Mr. Lowen defined the problem, and contributed to many of the results presented in this report.

GLOSSARY

Automated Design--An iterative computerized process by which the principal parameters of an instrument are optimized in view of criteria established by the designer. Primary constraints on the design in such a process are the required number of signal photons and the presence of unwanted dark current and background radiation.

Blur Circle--The image in which 80 percent of the energy of a point source of light is focussed; the focal surface being a plane which yields the minimum area of this image. Near the optical axis the image will be nearly a circle. As the image moves away from this axis, other shapes are formed.

Celestial Attitude--The orientation of a coordinate system as determined with respect to the celestial coordinate system. Three independent parameters are necessary to define this attitude.

Celestial Coordinate System--An inertial rectangular coordinate system. This coordinate system is Earth centered with two axes in the plane of the earth's equator, and the third axis in the direction of the earth's North Pole. One of the axes in the equator is in the direction of the First Point of Aries.

Dark Current--The anode current present at the photomultiplier output with voltage applied, but with no light energy incident upon the photomultiplier cathode. To measure dark current, the photomultiplier cathode is completely blacked out.

Declination--The elevation of a target with respect to the celestial coordinate system.

Diode Matrix--A multiple input-multiple output electronic switching circuit comprised of diodes and resistors which implements a number of Boolean logic functions.

Galactic Coordinate System--An inertial rectangular coordinate system which is defined with respect to the celestial coordinate system. The definition is such that the following equations are usable as first approximations.

$$m(\phi, \lambda) = m(-\phi, \lambda)$$

$$\frac{\partial\, m(\phi, \lambda)}{\partial\lambda} = 0$$

where ϕ = galactic latitude at a point

λ = galactic longitude at a point

$m(\phi, \lambda)$ = density of stars (number of stars per square degree) of magnitude m at (ϕ, λ).

The North Galactic Pole has a right ascension of 190° and a declination of 28°. The ascending node has a right ascension of 280°.

Gaussian Distribution (or Normal Distribution)--A continuous probability distribution given by the equation

$$p\left\{X \leq x\right\} = \frac{1}{\sqrt{2\pi}\,\sigma} e^{-\frac{1}{2}\left(\frac{x - \mu}{\sigma}\right)^2}$$

where $\mu = E(x)$ = mean of x

σ^2 = var (x)

Magnitude, Stellar--A number which indicates the relative intensity of a star. More precisely,

$$m = -2.5 \log \frac{I}{I_o}$$

where m = stellar magnitude

$$I = \int_0^{\infty} F(\lambda)\ K(\lambda)\ d\lambda$$

$$I_o = \int_0^{\infty} F_o(\lambda)\ K(\lambda)\ d\lambda$$

where $K(\lambda)$ = instrument response as a function of wavelength

$F(\lambda)$ = stellar intensity as a function of wavelength

$F_o(\lambda)$ = stellar intensity of reference star, i.e. a zero magnitude star

From this definition we see that the magnitude of a star depends on the instrument used to observe the star.

Nimbus--A horizon sensor-gyro stabilized meteorological satellite. More precisely defined in Section II.

Non-Stationary Poisson Distribution--A Poisson distribution in which the parameter of the distribution (mean) varies as a function of time.

Nutation, Torque Free--A variation of the elevation of the angular velocity vector of a rigid torque free body. This elevation is measured with respect to a plane perpendicular to the angular momentum vector of the body.

Poisson Distribution--A discrete probability distribution given by the equation

$$p\left\{ k \right\} = e^{-m} \frac{m^k}{k!}$$

where $E(k) = \text{var}(k) = m = \text{mean}$

Precession, Torque Free--A variation of the azimuth of the angular velocity vector of a rigid torque free body. This azimuth is measured with respect to a plane perpendicular to the angular momentum vector of the body.

Right Ascension--The azimuth of a target with respect to the celestial coordinate system.

SCADS--Scanning Celestial Attitude Determination System

Scanning Slit--A narrow opening which is located at the focal surface of the optical system and which is scanned across the sky.

Slit Width, Optical--The angle across the slit of the SCADS sensor as measured from the nodal point of the optical system. For the recommended wedged shaped slit, this angle is a function of distance along the slit.

Slit Width, Rotational--The dihedral angle between the two planes which define the projection of the recommended wedge shaped slit on the celestial sphere.

Tiros--A spin stabilized meteorological satellite; more precisely defined in Section II.

The following is the principal notation used in Section III. In particular, this notation appears in Table III-2, page 63, and Table III-3, pages 73-76.

D	optical aperture in inches
SW	optical slit width at optical axis in minutes of arc
M_L	photographic magnitude of weakest star in field of view for specified pointing direction
m_s	number of primary photoelectrons from limiting magnitude star during star transit time
m_b	number of primary photoelectrons from stellar background during star transit time
m_d	effective number of primary photoelectrons from dark current during star transit time
M_{noise}	equivalent photographic magnitude of noise
Tau	detection threshold
E_f	expected number of false star detections
E_w	expected number of weak star detections
DC	dark current in terms of equivalent photoelectron rate
QE	quantum efficiency

The following is the principal notation used in Sections IV and V. This notation is defined more precisely in the text. Other minor notation is also defined in the text.

S_1 = celestial reference system

S_3 = angular momentum system

S_6 = body fixed system along principal axes

α = right ascension of angular momentum vector (spin axis if body assumed to spin about a fixed axis)

δ = declination of angular momentum vector (spin axis if body assumed to spin about a fixed axis)

ξ = $90 + \alpha$

τ = $90 - \delta$

ϕ = precession angle, $\phi = \phi_0 + \dot{\phi}\, t$, $\dot{} = \frac{d}{dt}$

ψ = spin angle, $\psi = \psi_0 + \dot{\phi}\, t$

θ = cone angle or nutation angle

A,B = principal moments of inertia about axis perpendicular to transverse body axis ($\hat{k}_6$)

C = principal moments of inertia about transverse body axis ($\hat{k}_6$)

E = Euler matrix defined by ϕ, ψ and θ

H = Euler matrix defined by ξ and τ

η = elevation of a star with respect to slit

α_i = right ascension of the i^{th} star

δ_i = declination of i^{th} star

$\hat{S}$ = unit vector to star

μ_i = azimuth of i^{th} star measured from reference direction

β = azimuth of reference direction measured from North

r,p,y = roll, pitch and yaw, respectively

i = orbital inclination

I. GENERAL DESCRIPTION

It is the purpose of this first section to heuristicly describe the problem, methods of solution, and required instrumentation pertinent to this study. Details and more complete discussions are then to be found in later sections.

A. Purpose of Study

The purpose of the study is given by the following verbatum quote from the Statement of Work:

1. "Conduct an instrumental parameter and error analysis to establish the feasibility of using the Scanning Celestial Attitude Determination System (SCADS) for three axis attitude determination at a Command and Data Acquisition (CDA) station. The study shall be directed toward the utilization of SCADS for a stabilized platform type space probe where one axis coincides with the local vertical, and a spin stabilized probe."

2. "Establish the design parameters and estimate accuracies that will be obtained in actual practice. Consideration shall be given toward achieving minimum complexity and maximum reliability with a goal of three years life."

The study then involves three major topics:

(1) The attitude determination concept and analysis.

(2) The instrumentation.

(3) Error analysis.

Two distinct applications are to be considered. One is for a Tiros satellite which is a spin stabilized satellite. The other pertains to a Nimbus satellite which is horizon-sensor, gyro stabilized. These two applications necessitate two different analyses and instruments. A description of the two satellite operational modes is given by Tepper and Johnson [1].*

---

* Numbers enclosed in square brackets will be used to designate references.

From the point of view of instrument design, slightly greater emphasis is placed on the Nimbus Application because of the greater complication of this instrument. In contrast, from the point of view of spacecraft attitude determination, the Tiros application has required a more complex formulation.

We may note that this study was directed toward two specific spacecraft applications. However, the analysis is more general in that the Tiros satellite represents the problems encountered for a spin stabilized satellite, while the Nimbus configuration represents those for a local vertical stabilized satellite.

B. Overall Conclusion of Study

The general conclusion of this study is that the determination of stellar attitude by use of the SCADS sensor is indeed feasible. Moreover, the sensor for both the Nimbus and Tiros spacecrafts can be built with components which are within the present state-of-the-art. The accuracy requirement of 0.1° can readily be realized by the instrument.

1. Tiros

For the Tiros application, an accurate description of the precessional motion of the satellite can be given. Seven unknowns are present; a computer is required. If it is assumed that the motion is uniform rotation about a fixed axis, then an approximate manual solution is possible.

Weight, size, and power estimates for the SCADS sensor are as follows:

Weight--2.9 pounds

Size--4" x 6" x 3"

Power--(a) on board processing, digital transmission, 6 watts when in operation.

(b) signal recorded on tape, analog transmission, 2.5 watts when in operation.

2. Nimbus

For the Nimbus application, the rotational motion is not provided by the satellite but must be internal to the instrument. Also, an angle encoder must be provided.

Estimates of weight, size, and power are as follows:

Weight--7 pounds

Size--4" x 8" x 3.5"

Power (only when in operation)--20 watts.

C. Attitude Determination Concept

The basic problem we now consider is that of finding the attitude of a coordinate system, fixed in a satellite with respect to the celestial coordinate system, by optical sighting of stars and planets (other than the earth).

To explain the concepts involved, let us first assume that the satellite is not changing its attitude with respect to the celestial system, and the optical sightings are provided by a theodolite (Figure I-1A). The theodolite is capable of measuring the azimuth and elevation of stars with respect to the satellite system. If these stars have been identified, then the azimuth and elevation of the stars (right ascension and declination) with respect to the celestial coordinate system can be found from a catalog. Hence, we can obtain measured azimuths and elevations with respect to the satellite system and tabulated right ascensions and declinations with respect to the satellite system. Such information is sufficient to determine the orientation of the satellite system with respect to the celestial coordinate system. If the position of the satellite is known, the roll, pitch, and yaw of the satellite system may be found.

Conceptually, the process of determining attitude by use of a theodolite is excellent. However, to instrument such a system for a satellite would be extremely difficult and expensive because the instrument must be pointed at each star (or planet). To overcome this difficulty, SCADS relies on a scanning concept rather than a pointing concept. The earliest investigations of this concept seem to be in 1961 by Lillestrand and Carroll [2]. One difference between scanning and pointing is that scanning establishes targets along some curve on the celestial sphere rather than a point. (In Figure I-1B

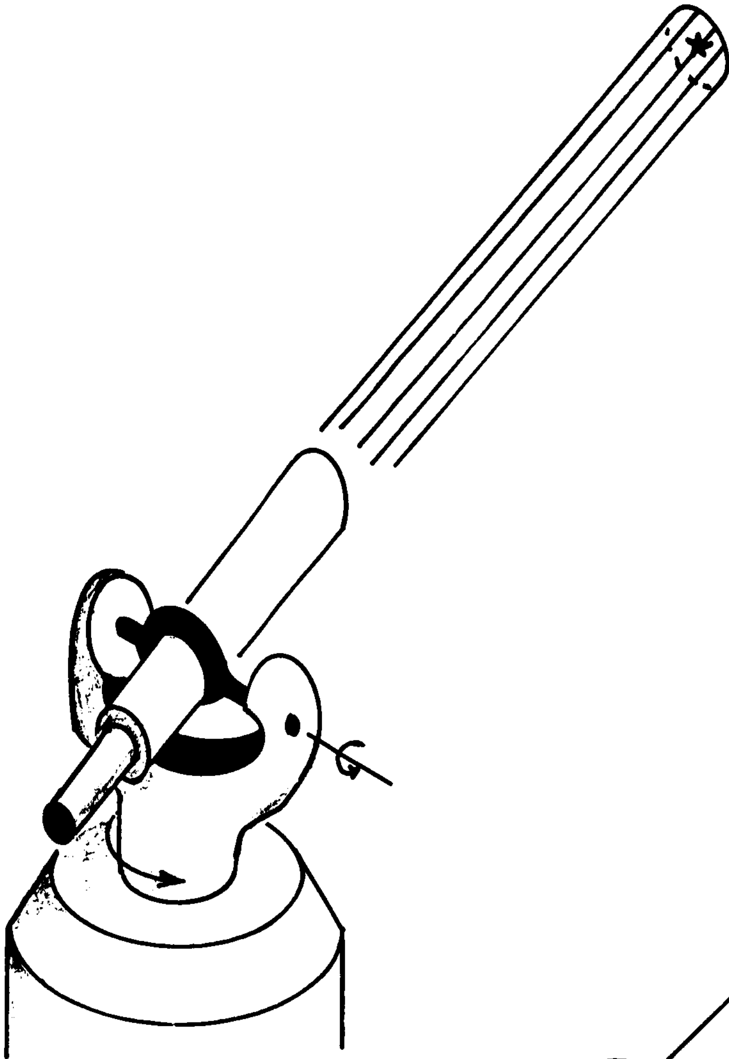

A. Measurements Provided by a Theodolite

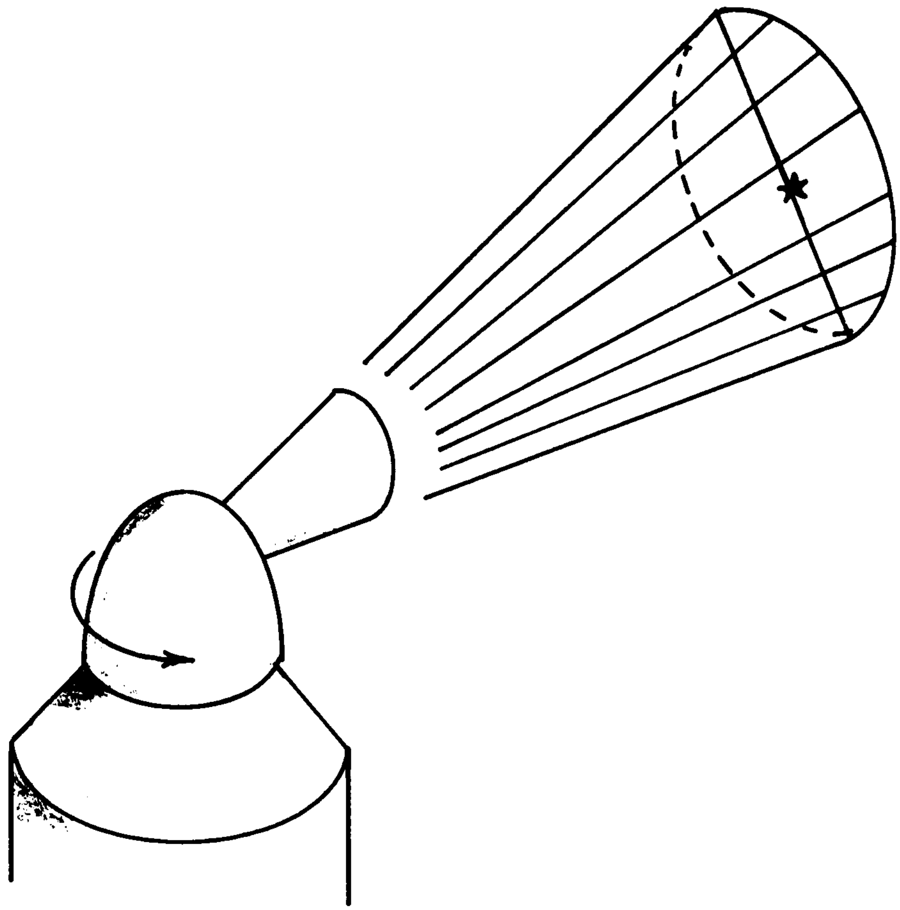

B. Measurements Provided by SCADS

Figure I-1: The Pointing and Scanning Concepts the target is established to lie on a great circle). This curve may then be rotated uniformly about some instrument axis, and at each instant a target appears on the curve (because of the instrumentation we generally speak of "appearing in the slit"), a measurement may be taken. A number of such measurements then establish the required orientation as before. Processing of the data, however, is slightly more difficult than that of the pointing system. The capability of handling a large number of targets with near simultaneity is the major advantage of the scanning system.

In our previous discussion, we assumed that the orientation of the satellite system was fixed with respect to the celestial coordinate system. This assumption is not necessary if the satellite is undergoing some known systematic change of orientation. One example of a systematic change of orientation is motion governed by the dynamics of a rigid torque-free body (as we will assume for the Tiros satellites). However, if the satellite is undergoing almost random changes in orientation (as we assume for the Nimbus), then pointing measurements taken at different times are virtually useless. This difficulty may be overcome by the scanning system, for the scanning motion may be made so rapidly that all measurements can be considered as simultaneous.

One important point should be made before we leave this section. If the orientation of the satellite system with respect to the celestial coordinate system is desired, then the position of the satellite need not be known. However, if the roll, pitch, and yaw are to be found, then the satellite's position must be given.

D. The Instrument

The basic scanning instrument consists of lens, slit, and photodetector and is illustrated in Figure I-2. The entire system rotates and consequently, the star images move across the slit. For the Tiros, this rotation is provided by the satellite, while for the Nimbus it is provided by a motor which rotates the instrument with respect to the satellite. The instrument is designed to: (1) detect stars crossing the slit(s), (2) measure their intensity, and (3) measure their crossing times. These measurements, together with a star map, provide the identification of the star and the desired orientation. The output of the photodetector is produced by the stars crossing the slit, plus (unfortunately), noise. A schematic of the electronic processing system internal to the instrument is given in Figure I-3. In this figure is shown the pulses produced by the photodetector as the star crosses the slit. The low pass filter smooths the pulse train from the photomultiplier. The resulting signal rises and falls smoothly as shown. If the filter output exceeds a fixed threshold, a star is "present".

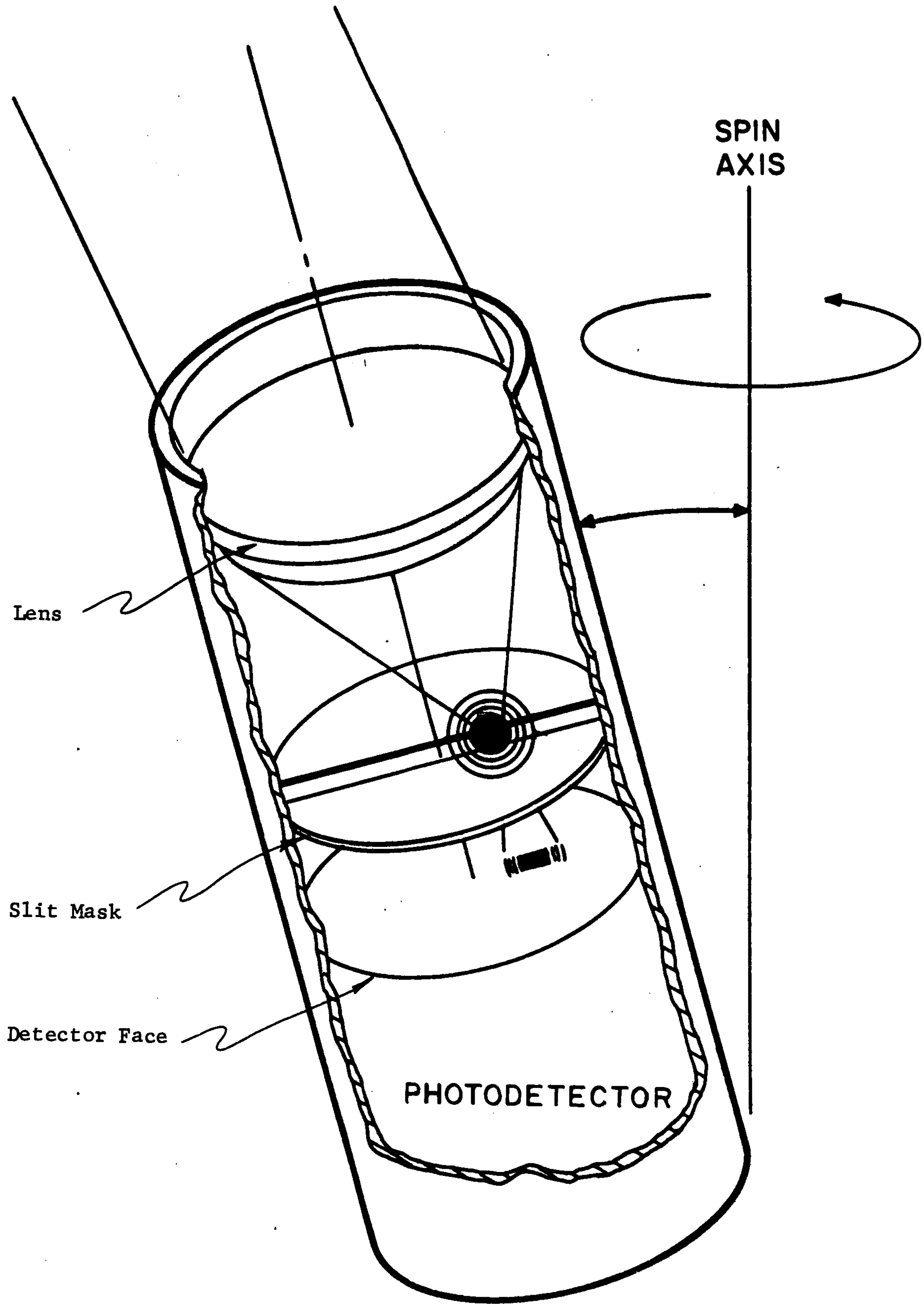

Figure I-2: Salient Features of SCADS Instrument

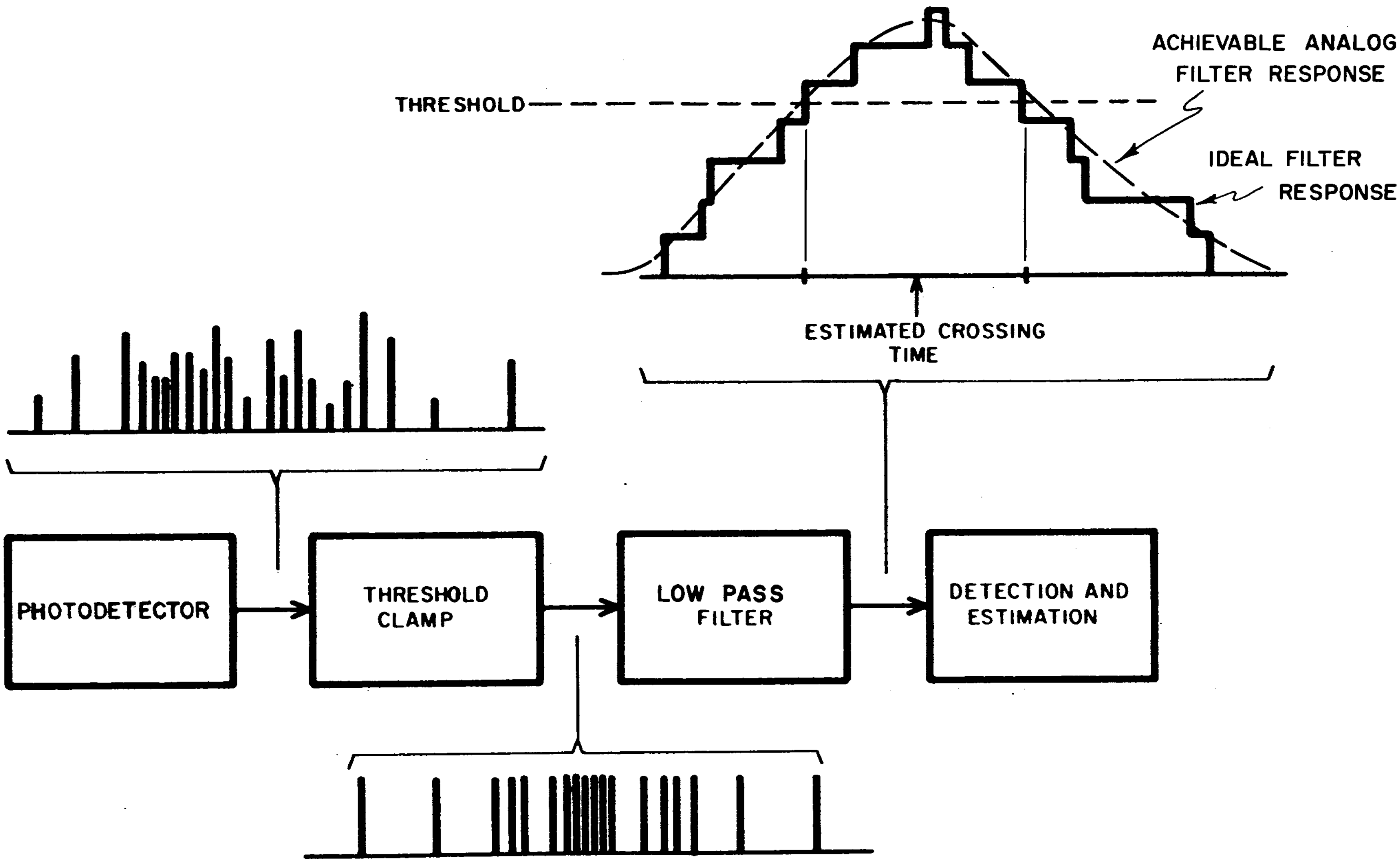

Figure I-3: Processing System

E. Data Reduction

The data reduction problem consists of two distinct phases:

(1) the problem of identifying the targets from the measured quantities, and

(2) the problem of calculating the orientation.

1. Target Identification

The target identification problem consists of establishing a pairing of a transit across the slit with the correct catalog number. The orientation problem cannot be solved without such a pairing.

Various levels of difficulty exist for the target identification problem. These levels depend upon the parameters selected for measurement. In the order of increasing difficulty which they produce for the target identification problem, the measured parameters considered in this report are as follows:

(1) azimuth, elevation, and magnitude,

(2) azimuth and elevation,

(3) azimuth and magnitude, and

(4) azimuth.

The measurement of magnitude cannot be made very accurately ($\pm$ 10 percent is optimistic). Hence, we have considered the problem without magnitude measurement at all. Solving the problem with azimuth only, (4), is a very difficult problem. In this case, four stars are required to be in the field of view (FOV).

It is worthwhile to note that the target identification problem is simpler in the SCADS application than in other applications, for the approximate pointing direction is fairly well known before hand. The total problem is discussed in Section VI.

2. Attitude Determination

The attitude determination problem also has levels of difficulties. These levels are dependent upon the physical assumptions of the problem. The most difficult problem considered here evolves from the assumption that the satellite is a torque-free rigid body with two equal moments of inertia. We apply this assumption to the Tiros. Seven unknowns are present and an iterative method of solution must be used. The problem is too complex to be solved without a computer. The running time on a CDC 924 is on the order of thirty-six seconds.

II. SPACECRAFT PARAMETERS

Before considering the more detailed phases of the study, it is necessary to define the problem in terms of the spacecraft parameters for the two systems.

A. The Tiros

The Tiros satellites are to be placed in a nominally circular orbit of altitude from 500 to 1000 nm. The orbit is to be sun-synchronous, which means that the plane of the orbit will always contain the sun. Strictly speaking, this condition cannot be met for the sun moves roughly uniformly along the ecliptic while the plane of a satellite rotates more or less uniformly about the earth's axis. For the orbits in question, the rotation about these different axes causes a maximum error in the sun-synchronous condition of only $2^{o}29'$. For our purposes this discrepancy is negligible.

At the three altitudes the orbital inclinations are as follows:

500 nm implies $i = 99.153^{o}$

750 nm implies $i = 101.378^{o}$

1000 nm implies $i = 103.980^{o}$

so the altitude has only a small effect on the inclination.

The satellite itself is approximately cylindrical with a diameter greater than the height. The moment of inertia about the axis of the cylinder is approximately 13.33 slug ft.^{2} while the moment of inertia about any axis perpendicular to this axis and through the center of mass is 9.331 slug ft.^{2}.

The spacecraft is to spin about the cylinder axis with a period of roughly six seconds. This axis is to be kept nominally perpendicular to the orbital plane by a low-torque magnetic attitude-control system. The relationship of the satellite to the orbit is pictured in Figure II-1. Useful satellite lifetime is expected to be three years.

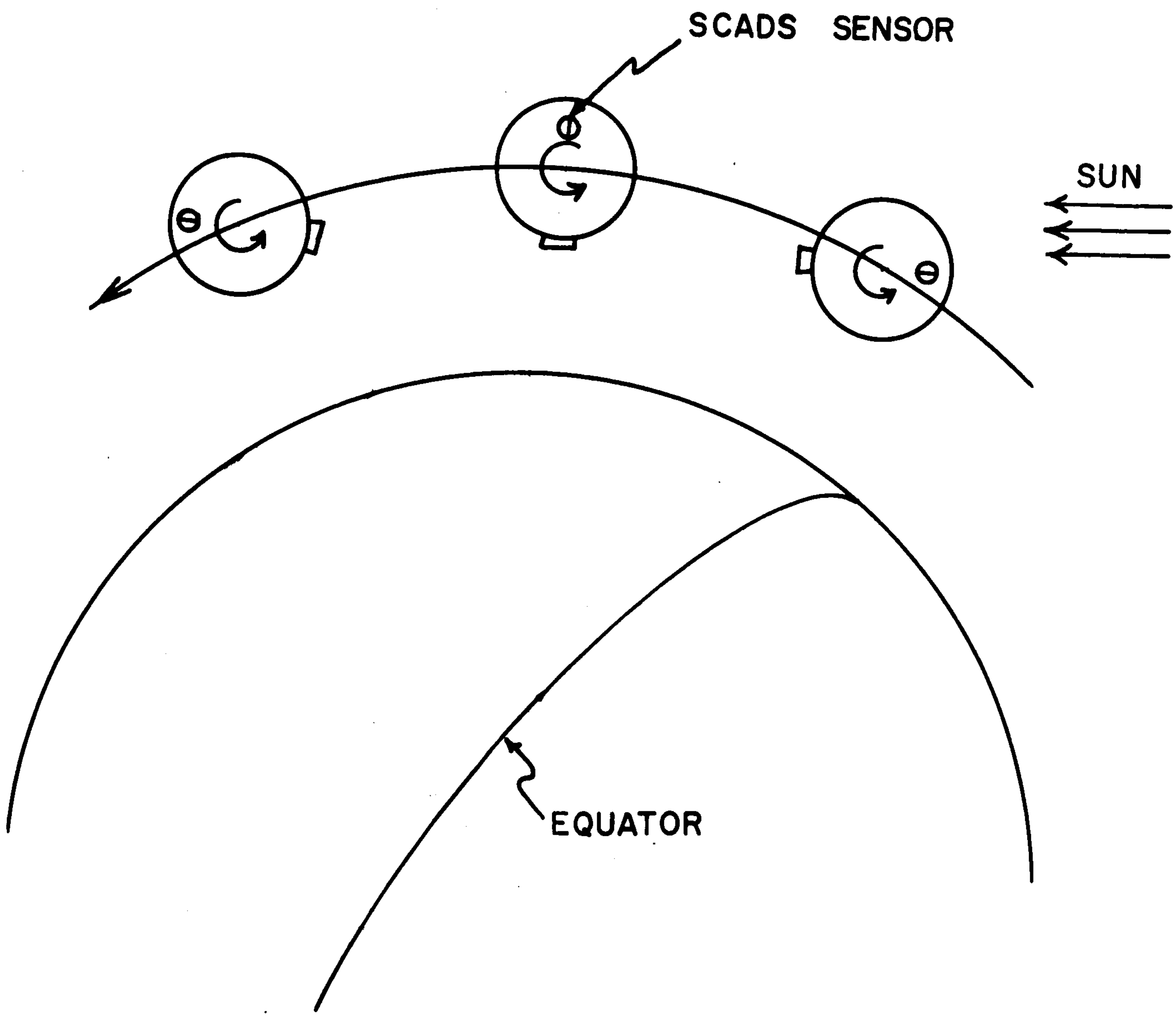

Figure II-1: Orientation of Tiros With Respect to Earth

B. The Nimbus

Orbital parameters for the Nimbus are planned to be about the same as those for the Tiros. For our purposes the principal differences between the two systems is that the Nimbus is horizon sensor-gyro stabilized while Tiros is spin stabilized.

The horizon sensor maintains the Nimbus oriented approximately along the satellite Earth-center line. In order to stabilize the Nimbus about this line, a gyro is employed. The gyro also stabilizes the satellite so that one axis (roll axis) is in the orbital plane.

A sketch of the system taken from Barcus [3] and modified to include SCADS is given in Figure II-2. The pitch axis is nominally perpendicular to the orbital plane. The SCADS sensor is to be mounted so that the sensor axis is parallel to the pitch axis. In this way, the satellite motion will provide one rotation of the SCADS sensor in approximately 115 minutes (orbital period). This rotational motion is far too slow so the sensor must be spun. We will show in Section VI.B.1 that it is necessary to spin the sensor so that a period of from two to three seconds is obtained.

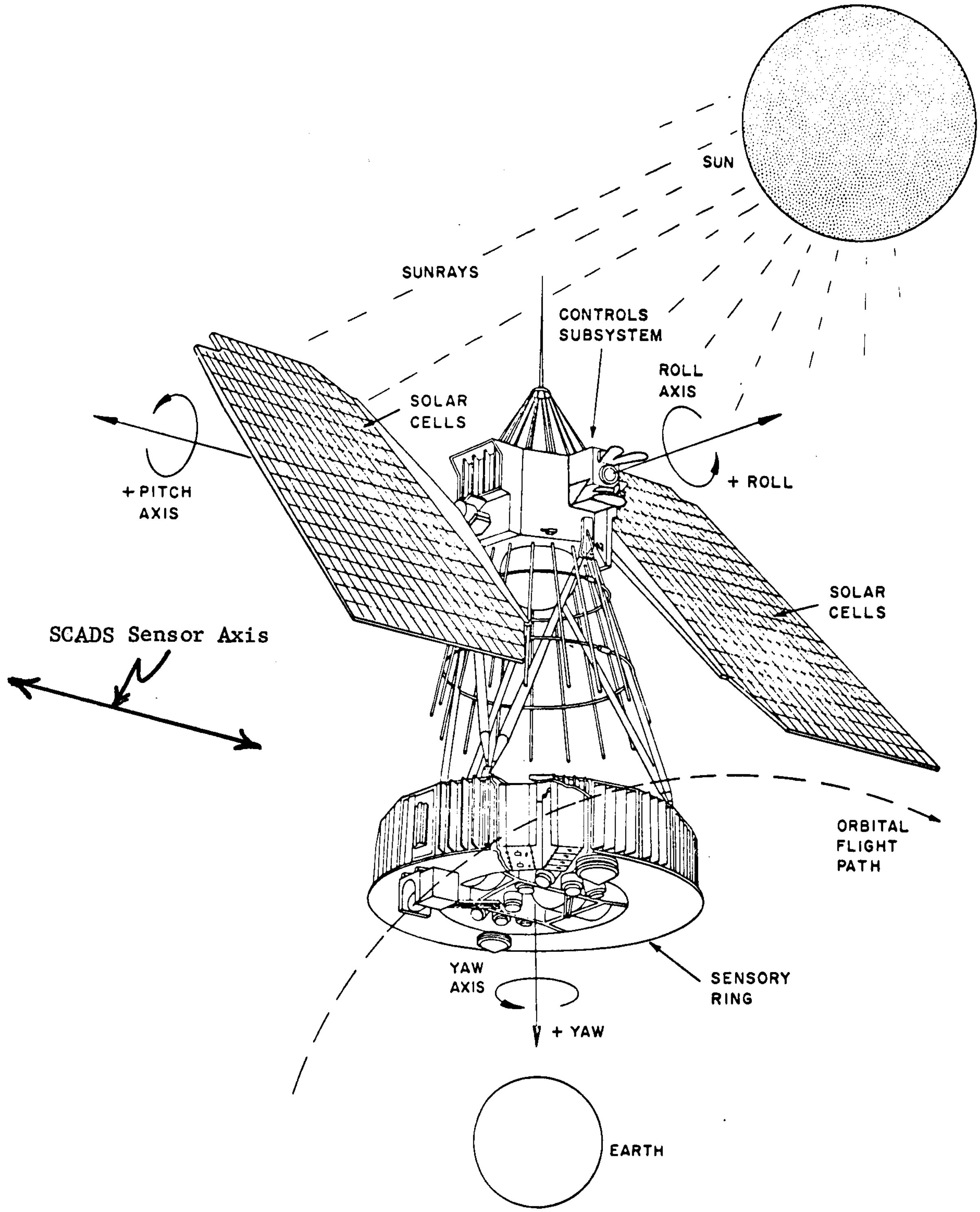

Figure II-2: Nimbus Spacecraft Configuration

III. INSTRUMENT DESIGN ANALYSIS

Two instruments are considered, one for Tiros and another, Nimbus. Both instruments, however, have many features in common so it is convenient to discuss the instruments together.

Before we consider the instruments themselves, we must approach the problem with a discussion of the underlying philosophy which motivates our choice of instrument design.

A. Optical Design

1. Field of View

One of the parameters which must be considered first in the optical design is the field of view. For both Tiros and Nimbus the viewing geometry is the same, and hence, the field of view considerations are the same. In this section, when we speak of field of view, we will mean effective field of view of the instrument. Another field of view which may be considered is the instantaneous field of view.

On one hand we would like a large field of view, for then we are more nearly assured that bright stars will lie in the field of view. On the other hand, a small field of view is desirable for then the optical design is simplified and the probability of the earth, moon, and sun entering the field of view is minimized.

For both satellites, the effective field of view of the instruments consists of two coaxial, common vertex cones. The outer cone gives the outer limits to the field of view, while the inner cone supplies the inner limit (see Figure III-1). The axis of the cones is the symmetric axis of the satellite for Tiros and is the pitch axis of the spacecraft for Nimbus.

The interior of the inner cone represents a dead zone in that targets interior to this zone will not be received by the instrument. We must include such a region for two reasons.

(1) The nominal spin axis of the instrument is the cone axis, so if a target fell close to the cone axis it would tend to always lie in the slit. Such a situation would saturate the instrument and must be avoided. Hence, the dead zone is included.

(2) Uniform image quality is desirable throughout the length of the slit. In order to achieve uniform quality, very severe requirements are necessary near the spin axis. These strict requirements are eliminated by including a dead zone.

However, from the error analysis, we see that the stars lying closer to the spin axis yield the more accurate attitude determination. Hence, as small a dead zone as possible seems desirable. Such considerations lead to an inner half cone angle of three degrees as defining the recommended dead zone (see Figure III-1).

We would like to have as large a field of view as possible without admitting extraneous background radiation from Earth reflected sunlight. Note that if the orbit is truly sun-synchronous, then the sun cannot be in the field of view if the earth is not in the field of view.

The earth's airglow generally occurs in the altitude range of 60 to 90 kilometers. If we were to completely avoid the airglow, then we must insist that the outer cone be no closer than 100 kilometers from the earth's surface. Under these conditions, in Figure III-2, the maximum half-cone angle, ρ, is plotted as a function of satellite attitude, h. For these results, we assume

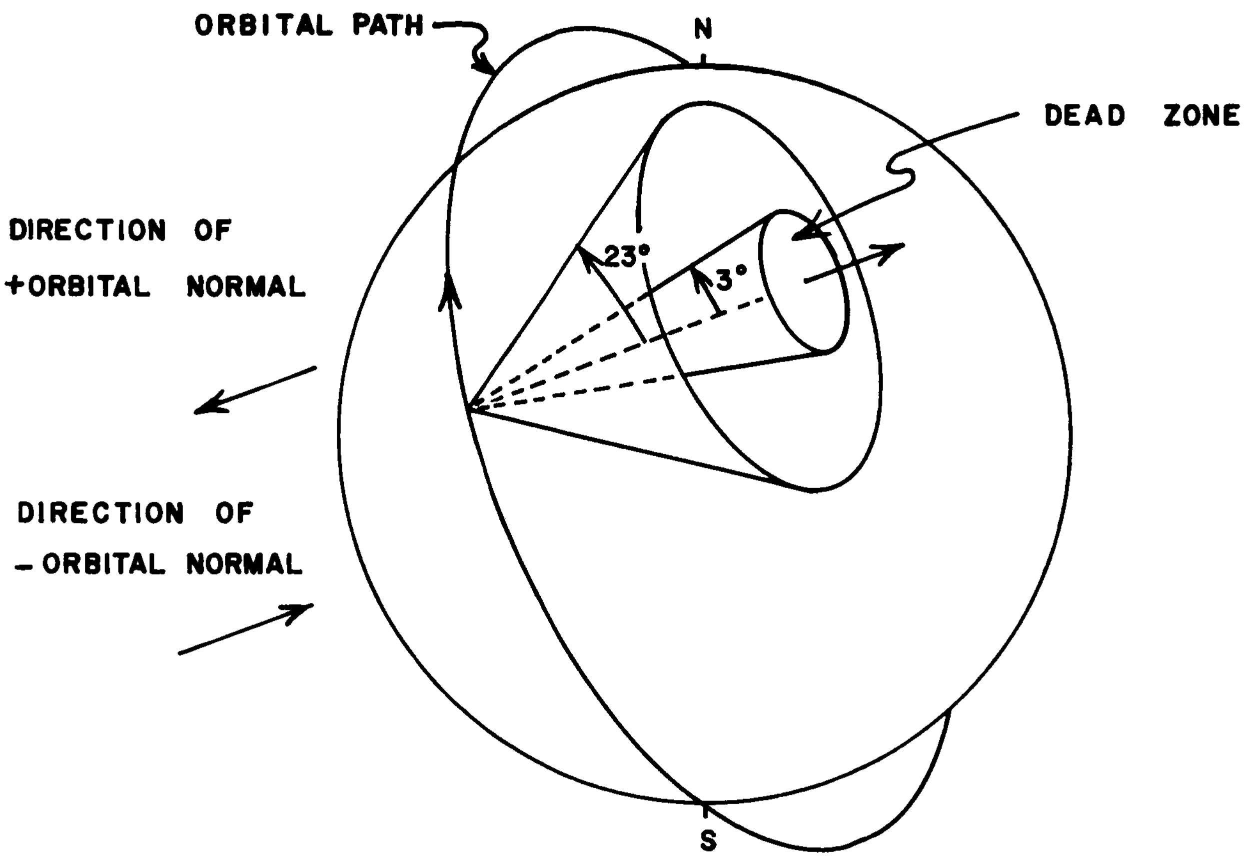

Figure III-1: Recommended Field of View for Tiros and Nimbus. (The field of view shown is centered around - orbital normal, but it may also be centered around + normal).

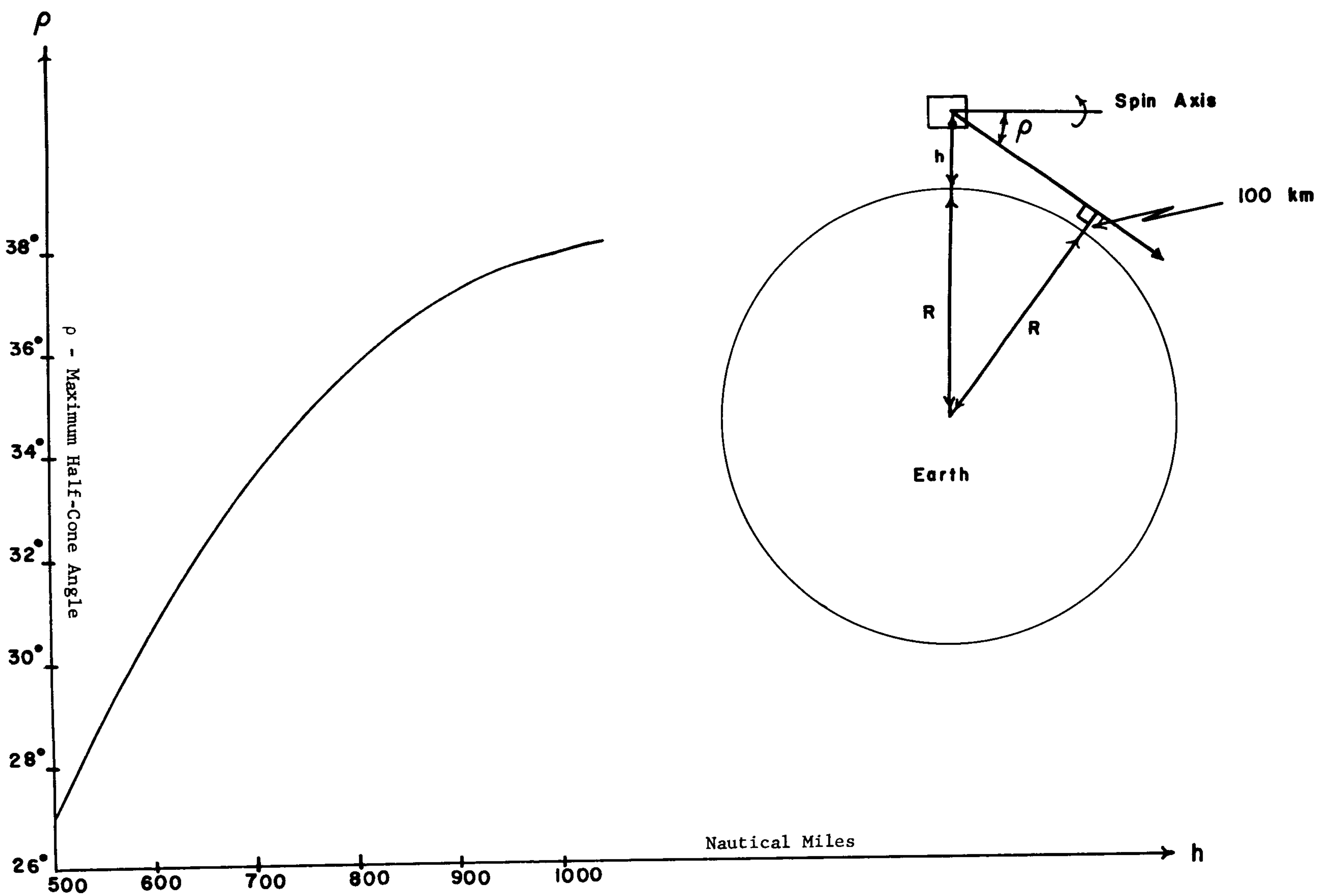

Figure III-2: Maximum Field of View as a Function of Satellite Altitude, h the spin axis is perpendicular to the orbital plane.

From Figure III-2, the maximum ρ for a 500nm orbit is 26.7°. However, calculations show that the airglow is no trouble to our instrument. Hence, the outer cone may come as close as 20 kilometers to the earth. Thus, ρ for a 500nm orbit may be 28.8°. Since a safety factor must be provided because the spin axis may not be the orbital normal, we recommend the outer cone angle to be 23° (see Figure III-1). A projection of the recommended field of view on the celestial sphere is shown in Figure III-3.

In Figure III-4, we plot the angle between the direction to the moon's center and the spin axis as a function of time for 1966. For this graph, we assume a sun-synchronous orbit and the spin axis along the positive orbit normal. Note that the moon will lie in the field of view for approximately forty days in the year 1966.

Finally, Figure III-5 is a plot of the number of stars in the recommended field of view as a function of the right ascension of the spin axis, α. Curves for limiting visual magnitudes of 3, 3.5, and 4 are plotted. Note that the number of stars in the field of view is a highly variable function of α if the magnitude of the dimmest star in the field of view is fixed. For this reason we recommend a "variable bias level" (see Section V.A.1.b for definition). Figure III-6 is a plot of the visual magnitude of the second, third, fourth, and fifth brightest stars in the field of view as a function of α.

2. Slit Configuration

There are a large variety of slit configurations which could be used to

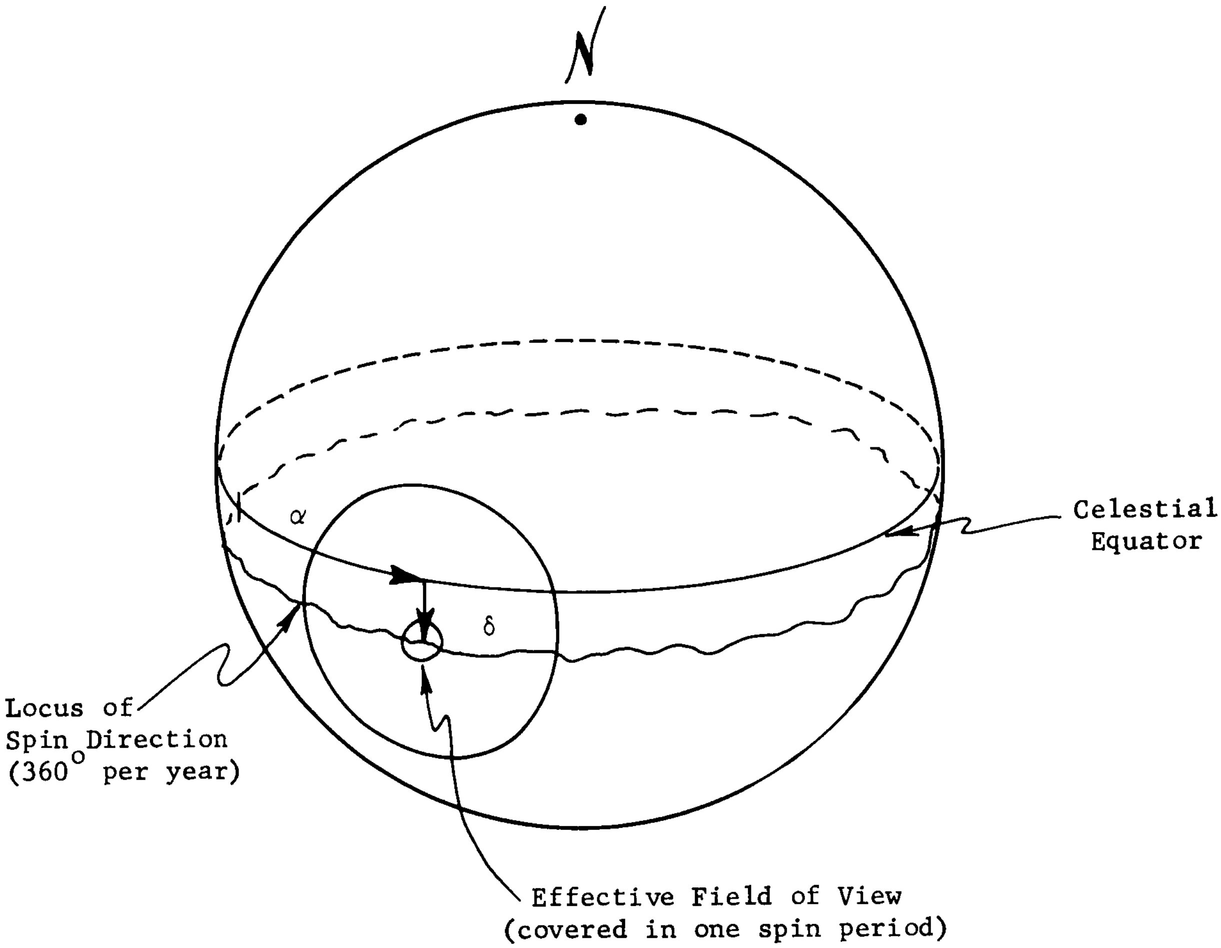

Note: α is measured from the First Point of Aries.
The δ shown is a negative angle.

α = right ascension of spin axis
δ = declination of spin axis

Figure III-3: Field of View With Respect to Celestial Sphere for Tiros and Nimbus

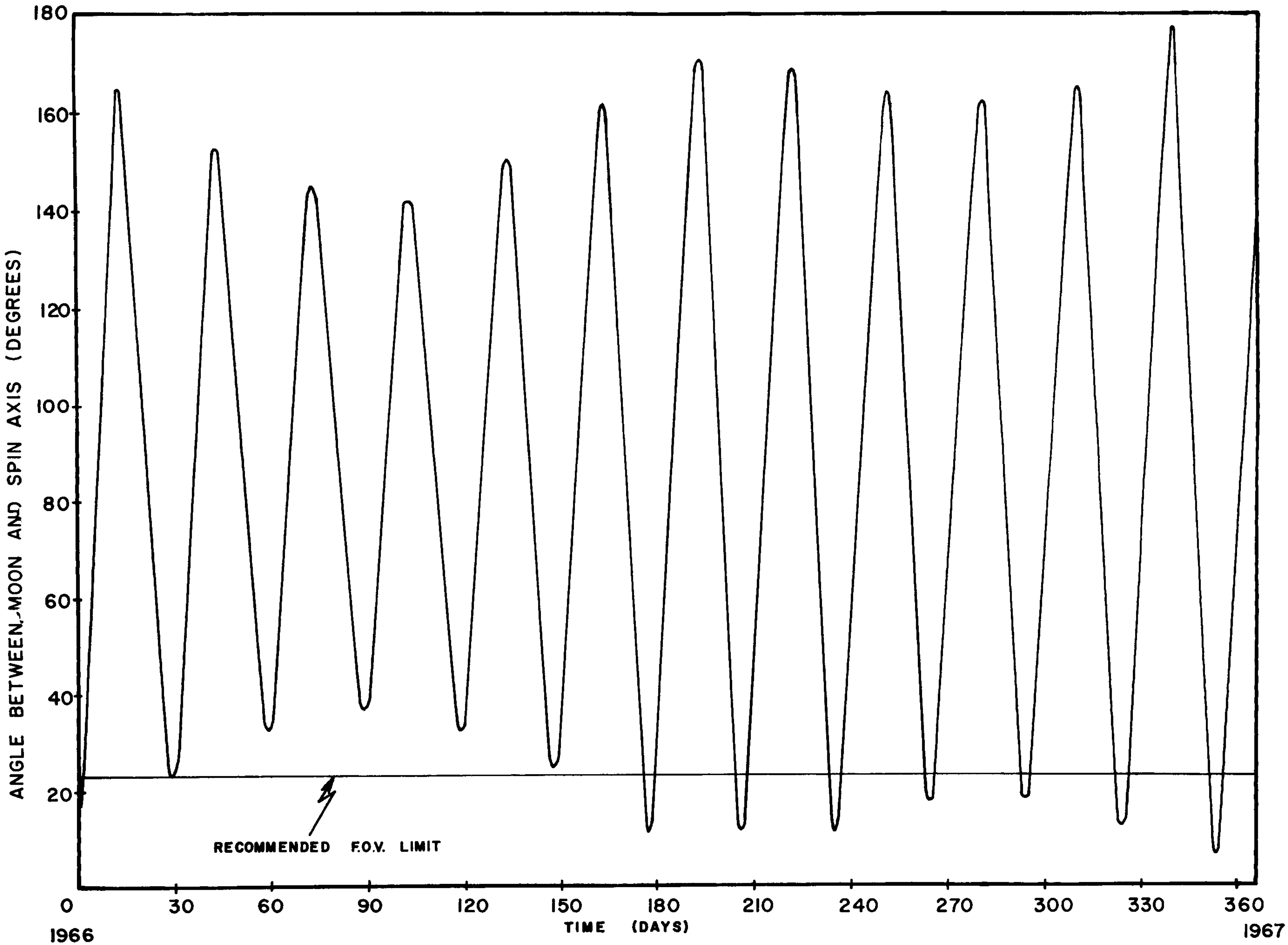

Figure III-4: Angle Between Moon and Spin Axis, β, as a Function of Time for 1966

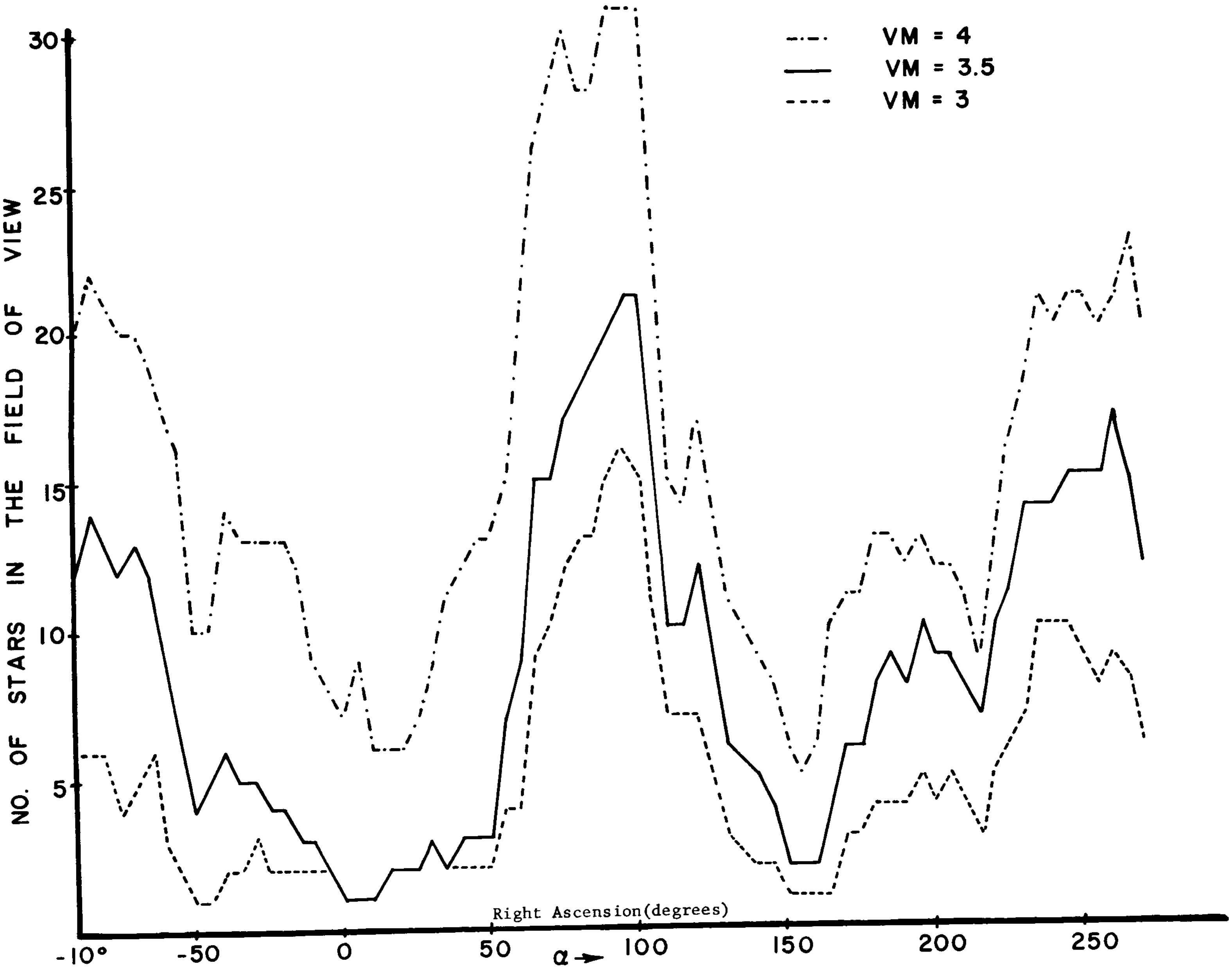

Figure III-5: Number of Stars in Recommended Field of View for Different Magnitude Limits

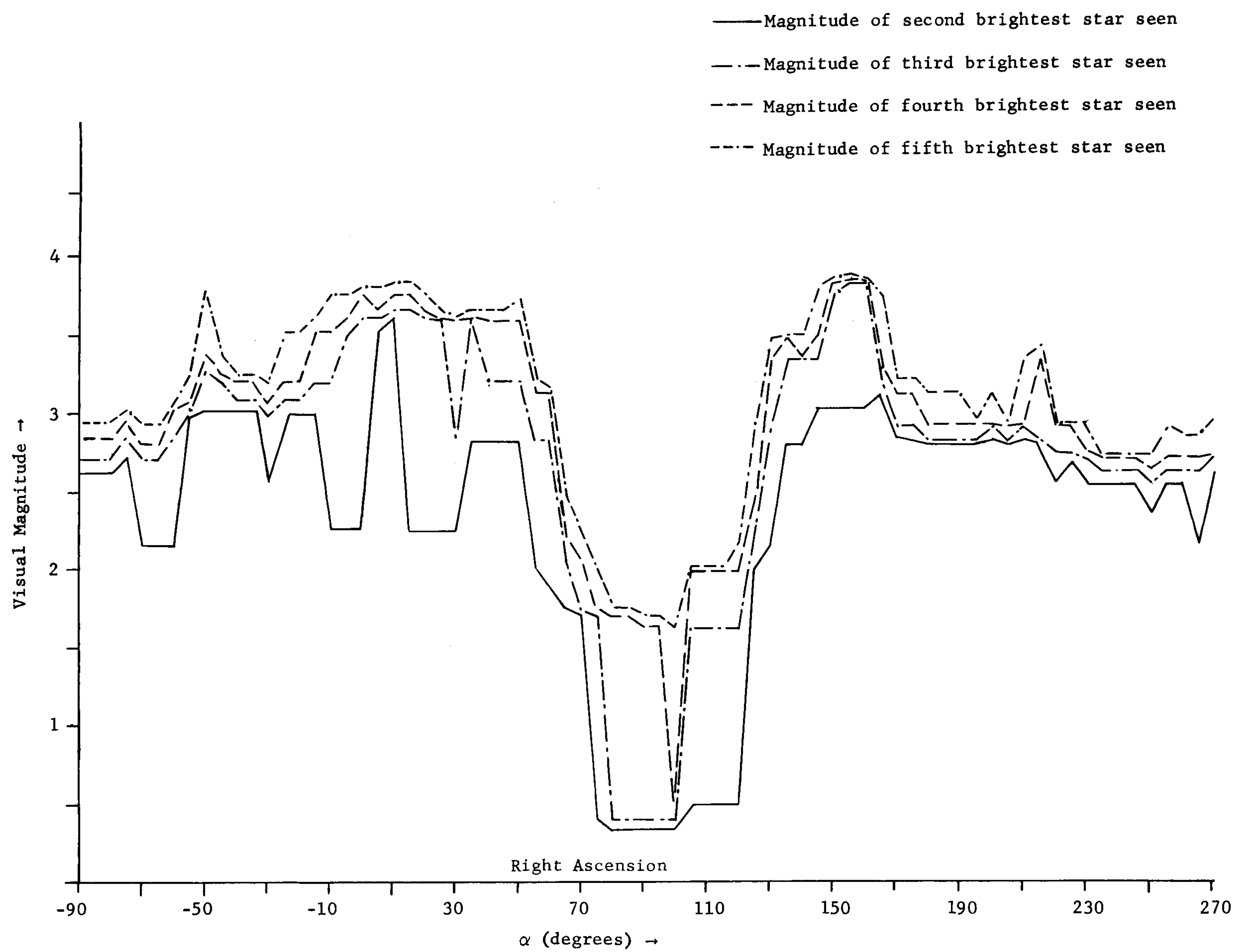

Figure III-6: Visual Magnitude of Second, Third, Fourth, and Fifth Brightest Stars in Field of View as a Function of α

yield information sufficient to solve the attitude determination problem. We might consider the focal surface apertures as follows:

(1) point(s),

(2) line(s) (more precisely, small surface area),

(3) surface(s).

For our particular application, the only configuration worth considering is the line(s) configuration. The point(s) slit configuration cannot measure positions of star targets because of the vanishingly small probability of the "point" detection element coinciding with a stellar target. Because of the very large exposed region, a surface configuration cannot be used except for signals from very strong (in intensity) targets.

During the course of the study, four line slit configurations were investigated; a single radial slit, a pair of parallel slits, a pair of logarithmic spirals, and a cross slit, as shown in Figure III-7. The advantages and disadvantages of each slit configuration are given in Table III-I.

The recommended slit configuration for the SCADS operation is the single radial slit. We feel the disadvantages 1 and 2, common to the multiple slits are strong enough to overcome advantages of multiple slits for the SCADS application.

The single radial slit and its projection on the celestial sphere are pictured in Figure III-8. Note that the slit is wedge-shaped. This shape is chosen so that the length of time any star is in the slit is independent of its position. This independence will ensure that the intensity will not be a function of the star's position. The dimensions shown for the slit width are

TABLE III-I

COMPARISON OF SLIT CONFIGURATIONS

Slit Configuration	Advantages	Disadvantages
Radial Slit	1. Simple to fabricate. 2. Minimizes any optical distortions caused by images near the edge of field. 3. Coma and many other aberrations of optical lenses will be symmetric about a radial line, thus eliminating radial effects. 4. No decision need be made as to which slit the star transits.	1. Three or more known stars are required for attitude determination. 2. Four or more stars are required for positive star identification (without magnitude). 3. Errors in computed attitudes are slightly greater than the other configurations.
Parallel Radial Slit	1. Can estimate coelevation angle as well as measuring relative azimuth. 2. Simple to fabricate. 3. Optical distortions are not too severe. 4. Only two stars are required; however, an accurate solution requires three stars.	1. Background problem more difficult with multiple stars. 2. Must know which slit the star transits. This fact requires an accurate intensity determination, or a coding on one of the slits.
Logarithmic Spirals	1. Equally good measure of relative azimuth and coelevation. 2. Only two stars are required.	1. Background problem more difficult with multiple slits. 2. Must know which slit the star transits. This fact requires an accurate intensity determination or a coding on one of the slits. 3. Difficult to fabricate. 4. Optical system must be uniformly good in all directions.
Crossed Slits	1. Good measure of relative azimuth and elevation. 2. Radical distortions of optical system cause no difficulties. 3. Only two stars required. 4. Easy to fabricate.	1. Background problem more difficult with multiple slits. 2. Must know which slit the star transits. This fact requires an accurate intensity determination or a coding on one of the slits.

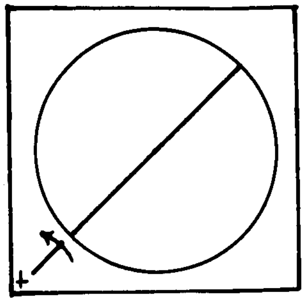

Single Radial

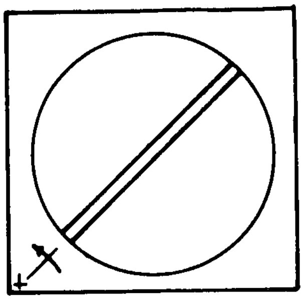

Parallel Radial

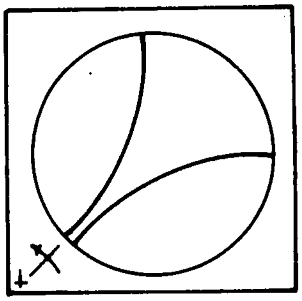

Logarithmic Spirals

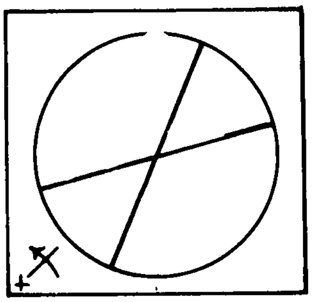

Crossed

Figure III-7: **Slit Configurations**

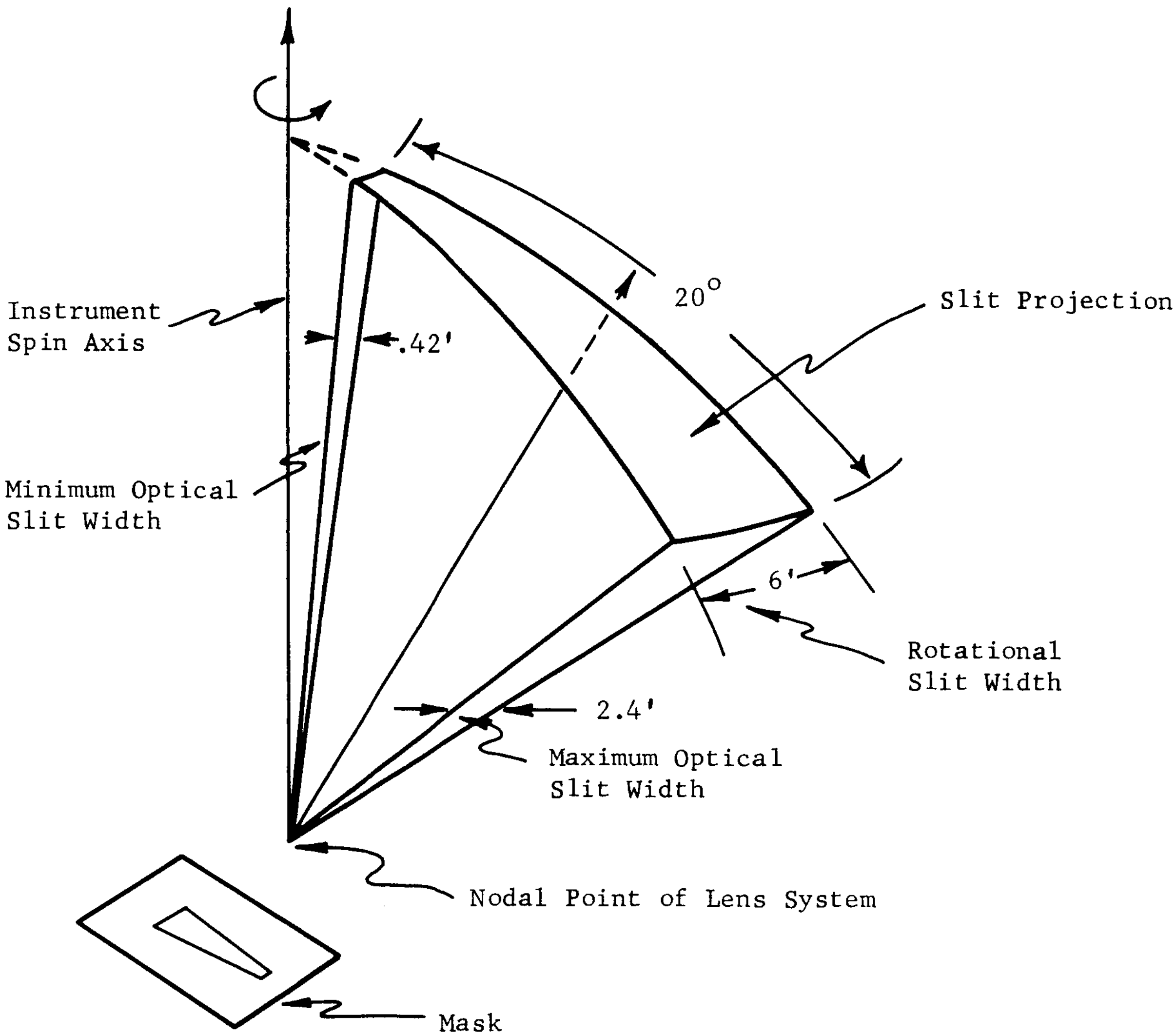

Figure III-8: Geometry of Single Radial Slit pertinent to a conservative design. These dimensions are obtained from analysis given in Section IV.

It is felt that the most attractive multiple slit is the crossed slit configuration shown in Figure III-9. Again, the slits are wedge-shaped so that the time duration of any star in the slit is independent of the stars position. In order for this dependence to be possible, the boundaries of the slits when projected on the celestial sphere must be great circles. In fact, it can be shown that the equation of the leading edge of the first slit expressed in S_6 (IV.B.2, page 168 for definition) is

$$\hat{s} = (S_1 \cos w - S_2 \sin w)\ \hat{i}_6 + (S_1 \sin w + S_2 \cos w)\ \hat{j}_6 + S_3\ \hat{k}_6$$

where $S_1 = \cos \gamma \cos \Gamma \cos \eta + \sin \gamma \sin \eta$

$S_2 = \sin \Gamma \cos \eta$

$S_3 = - \sin \gamma \cos \Gamma \cos \eta + \cos \gamma \sin \eta$

$2w$ = rotational slit width

2Γ = angle between center line of slits

η = parameter ($\hat{s}$ is a one parameter family)

σ = angle from spin axis to optical axis.

The mask which produces the projections shown in Figure III-9 is given in Figure III-10. In this figure,

$\beta_1 = \Gamma - w \cos \gamma$

$\beta_2 = \Gamma + w \cos \gamma$

$a = fw \sin \gamma$, for small w, f = focal length

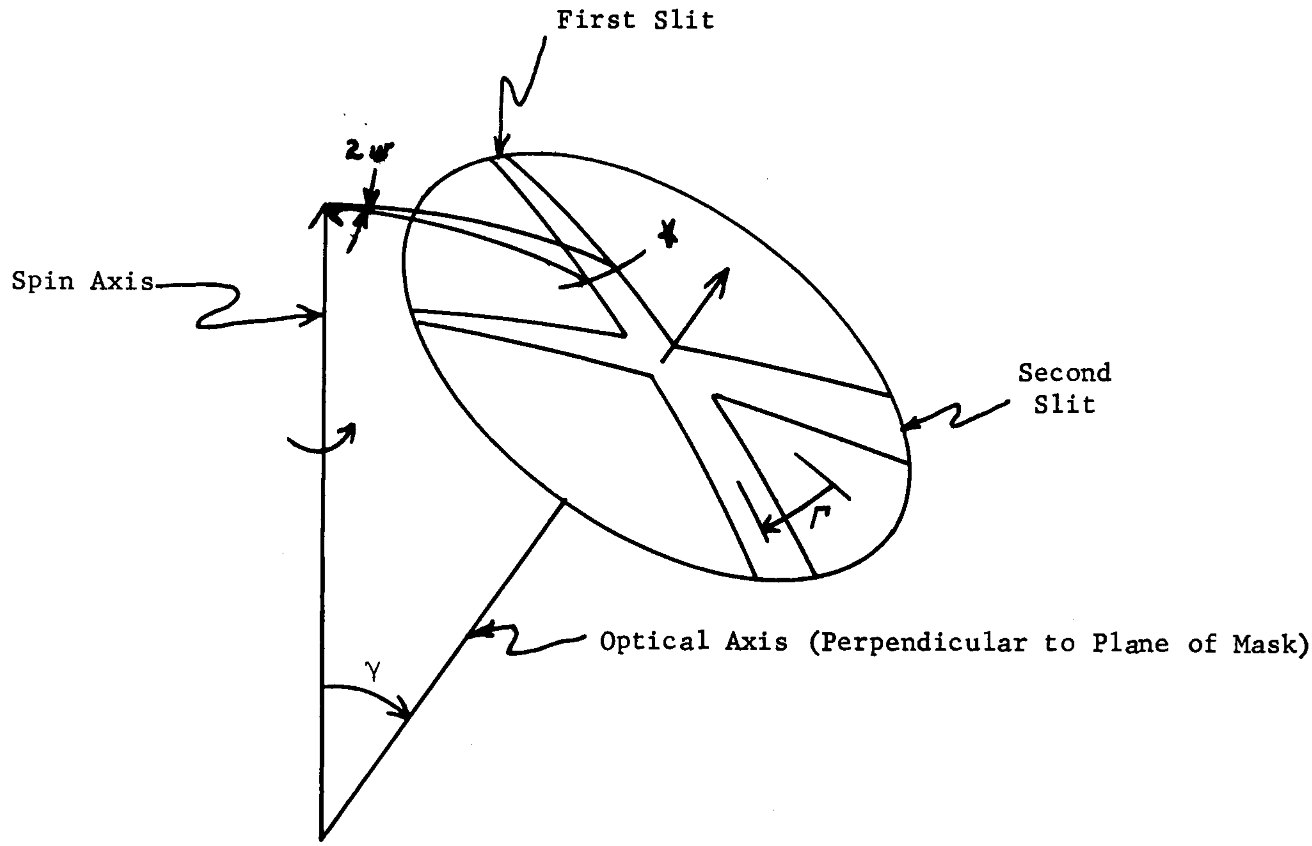

Figure III-9: Recommended Double Slit Configuration

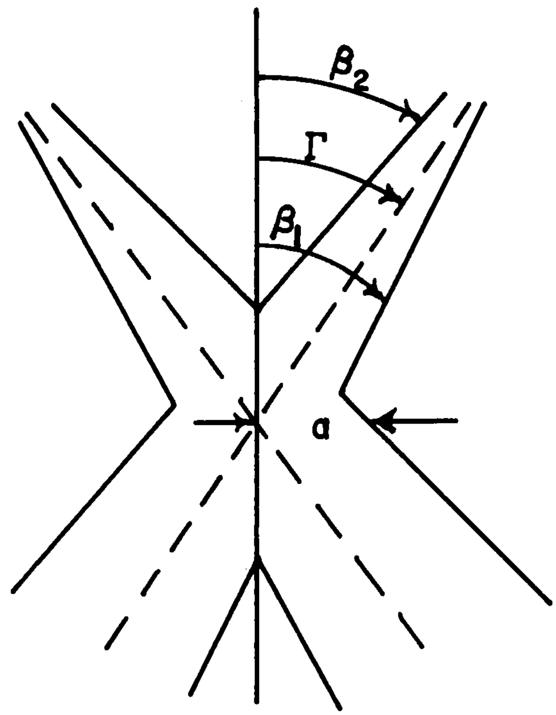

a = distance from optical axis intersection to edge

Figure III-10: Mask for Crossed Slits

With this configuration, for all stars crossing the slit, $\Delta t\ \omega = 2w$, where

Δt = time duration in slit, and

ω = spin rate.

The time, Δt, is independent of the star's position.

The advantages of this double slit configuration over other double slit configurations are:

(1) The slits are radially symmetric, hence, an optical system which produces a radial symmetric blur circle is ideal.

(2) All stars are in the slits in the same time interval.

(3) The mask contains only straight lines, hence, the fabrication is not unduly difficult.

A disadvantage of this configuration is that special attention must be taken to establish whether $0 \leq \rho < \gamma$ or $\rho > \gamma$, where ρ is the angle between the spin axis and the star. Hence, the identification may be difficult. However, a coding on one of the slits can be used to overcome this difficulty. Of course, such a coding produces other difficulties.

3. Basic Properties of Lens System

The primary parameters defining a lens system are focal length, aperture diameter, f/no, field of view, and image size. These parameters may be varied to suit the requirements of the system, but are not completely independent. Fundamental relationships exist, and factors of size, cost, and state-of-the-art limits must be considered. The primary equations showing the fundamental relationship are as follows:

$$d = 2 \tan \frac{FOV}{2} \times F.L.$$

$$f/no = \frac{F.L.}{D}$$

where d = the usable image diameter in inches

FOV = the field of view in degrees

F.L. = the focal length in inches

D = the clear aperture diameter in inches

f/no = dimensionless quantity representing comparative light gathering power or "speed" of the lens.

a. Tiros

In previous sections it was recommended that the Tiros optical system should have a field of view of 20 degrees, which defines one of the above parameters. Then, since the image is formed on the slit and read by the photomultiplier tube immediately behind, the active cathode diameter determines the maximum value of d, the image diameter. The first of the above equations then defines the maximum focal length that may be used in the system.

The minimum clear aperture diameter required is determined by many variables as discussed in the section on Automated Design. This analysis appears later in this section. With this minimum aperture established, the second of the above equations defines the maximum value that the f/no of the lens may be for satisfactory performance of the optical system.

Based on the results of the Automated Design program, the two best photomultipliers for this system would be the EMR 541B-03 or the EMR 541A-01. The 541A tube has an active cathode diameter of 1.0 inch and requires a clear optical aperture of 0.836 inch. The 541B tube has a cathode diameter of 0.4 inch, but requires a clear aperture of only 0.535 inch. The physical dimensions of both tubes are otherwise similar. The 541B tube appears to be the better, since it requires a smaller clear aperture. The available electronic data on this tube, however, is somewhat tentative and therefore the actual tube may not meet these specifications.

When calculating the actual optical parameters to be used for the recommended system, it is well to bear in mind the various limits and interrelated effects between these parameters. Maximum image size is, of course, dictated by the opening in the photomultiplier, and minimum size by the problems associated with manufacturing the slit to the proper geometry.

Focal length has a direct influence on the overall system dimensions which implies that it should be short. However, too short a focal length decreases the clear aperture or requires an extremely low f/no.

The clear aperture is directly related to the diameter of the objective lens (usually slightly smaller) and, therefore, effects the system size and weight, so usually the smallest aperture adequate for the requirements is desirable.

The f/no of a lens system is a relative "speed" index, or inverse square root measure of the amount of light falling on a unit area of the focal plane. Present optical design, however, places a lower limit of the f/no at about f/0.9 without serious distortion of the image qualities.

Other factors entering into the choice of the exact lens to use are such things as resolution or "blur circle", color correction, and the various types of aberration. These factors are best evaluated by actual testing of the particular lens to be used.

The Lens Calculation Nomograph shown in Figure III-11 was prepared to simplify solving the basic lens equations and to rapidly check catalog listings of lenses to determine whether they will meet the requirements. For the present case, a field of view of 20 degrees is required with a maximum image size for the EMR 541A-01 photomultiplier tube of 1.0 inch. Laying a straightedge on the nomograph at these values, the intersection point on the focal length scale shows that 2.8 inches is the maximum focal length that may be

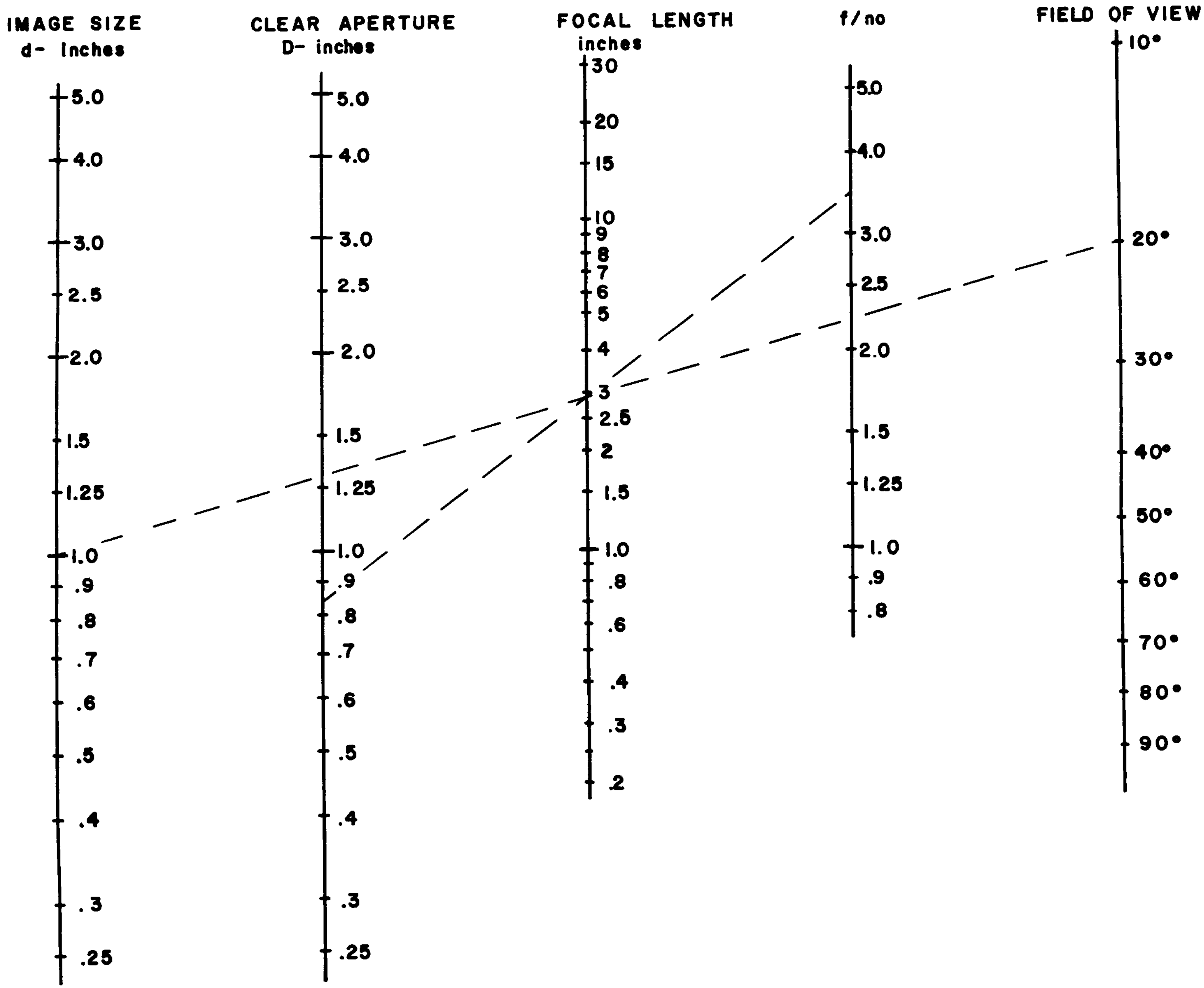

Figure III-11: Lens Calculation Nomograph D x f/no = F.L. = d/2 cot FOV/2 used. Then by pivoting the straight-edge about this point on the focal length scale until it intersects the clear aperture point of 0.84 inch, it is found that the maximum f/no the optical system may have is f/3.4.

The equivalent parameters are also found for the EMR 541B-03 photomultiplier tube and are tabulated below. Using these numbers as a guide, the nomograph was again used to determine the recommended optical system parameters which turn out to be a standard lens used for 8mm motion picture cameras. Note that this lens meets the requirements for either of the photomultiplier tubes.

	EMR 541A-01	EMR 541B-03	Recommended
Field of View (degrees)	20	20	20
Maximum Image Size (inches)	1.0	0.4	0.35
Minimum Clear Aperture (inches)	0.84	0.54	0.84
Maximum Focal Length (inches)	2.8	1.1	1.0
Maximum f/no	3.4	2.1	1.2

b. Nimbus

The Nimbus system configuration with its two second scan period rotating slit mode of operation requires a 46 degree field of view. The Automated Design program again recommends the EMR 541A-01 and the EMR 541B-03 photomultiplier tubes used with a clear optical aperture of 1.45 inch and 0.93 inch respectively.

Using the Lens Calculation Nomograph of Figure III-11 for the 541A tube with an image size of 1.0 inch and the field of view of 46 degrees indicates a lens system with a maximum focal length of 1.2 inches should be used. However, with this focal length and the required clear aperture of 1.45 inch, the f/no required would be f/0.8, which would be unreasonable in cost and probably would have relatively poor image quality. A similar calculation for the 541B tube with its required image size of 0.4 inch and clear aperture of 0.93 inch is even worse in this respect, since it would theoretically require a lens of f/0.6.

A possible solution for this problem would be to use a lens system with a larger image size from a longer focal length, which would allow a larger f/no. Then the rotating slit image could be offset and/or condensed so that the light passing through the slit would enter the smaller photomultiplier tube. This may be done in several ways, some of which are: single or multiple condensing lenses, Fresnel lens, prism, mirror, and optical fibers. Each of these methods have various undesirable characteristics such as transmission loss, size or weight increase, cost, or design complexity and for these reasons are not recommended for the present system.

With the system parameters fixed as they are, the best solution is to use a larger faced photomultiplier tube. However, it must also have characteristics similar to the EMR 541A-01 or else the clear aperture and image size would also increase and there would be no net gain.

It appears likely that the EMR 543A-01-14 or the EMR 543D-01-14 ruggedized tubes with an effective photocathode diameter of 1.7 inches would be satisfactory. The EMI 9514B tube, which unfortunately is not ruggedized, has an effective photocathode diameter of 1.75 inches and has Automated Design program data available. Using the Lens Calculation Nomograph for this photomultiplier tube, the following available recommended optical system is obtained.

	EMI 9514B
Field of View (degrees)	46
Maximum Image Size (inches)	1.75
Minimum Clear Aperture	1.6
Maximum Focal Length (inches)	2.0
Maximum f/no	1.25

B. Automated Design

The design of a scanning optical system is a complex problem in that there exist many complex non-linear relationships among the various system design and performance parameters. System design is basically the technique of determining the design parameters after the performance parameters are specified. The design parameters can be represented as a specific set of functions of the performance parameters. In many cases these are implicit functional relationships. In addition to performance specifications, design constraints may necessarily be imposed as not all solutions are acceptable.

The design problem thus reduces to solving a specified set of functions of the performance parameters within specified constraints. It is possible then to conceive of an automatic design program for a digital computer to determine the design. By its very nature, i.e., solution of mathematical functions, the problem becomes amenable to implementation on a computer system. System design would thus be achieved optimally and with much less time than by conventional methods.

The OPSCAN (OPtimum SCANner) program uses a number of specified performance parameters to design an optical scanning system that will operate according to the specified performance. In addition to the performance parameters, constraints on the calculated design parameters are specified.

Some of the supplied parameters are maximum RMS angle error, number of star detections required, probability of obtaining this many detections, the maximum number of false star detections, field of view, and scan period. Using these values the program designs a system with a minimum aperture for a specified number of primary photoelectrons. Many pointing directions are examined to determine the smallest aperture necessary to operate for any pointing angle. Note that the expected number of false star detections increases with slit width.

Different optimum designs can be determined with different fields of view and scan periods. The program does not attempt to find an optimum design among these because qualitative factors must be taken into consideration; such as, interception of bright objects in the field of view, vehicle motion, feasibility of optical design. Engineering judgment must be employed to select the appropriate final design. Thus, the program provides several optimum designs from which the evaluator may choose.

The program was developed from the analysis given in Appendix G. The notation used in discussing this program is the same as that of Appendix G. This notation is defined in the text, but for convenience a notation list is also given in the appendix. We will now discuss the main features and philosophy of this program.

1. Program Description

The general flow diagram of the OPSCAN program is shown in Figure III-12. The program is organized around nine basic functions which are:

(1) Determination of initial slit width,

(2) Identification of the bright stars in the scanned area,

(3) Determination of transit time,

(4) Determination of aperture,

(5) Determination of average number of background and dark current photoelectrons,

(6) Determination of detection threshold,

(7) Determination of expected number of false detections,

(8) Determination of final RMS transit error,

(9) Design evaluation.

a. Determination of Initial Slit Width (1)*

Given the average number of photoelectrons from the limiting magnitude star, the ratio of image diameter to slit width, and the maximum accuracy, the initial slit width can be determined. In the present program the initial slit width is simply set equal to a multiple of the maximum RMS transit error. In the most general case, however, a more complicated function of all three variables would be involved. In these computations the background and dark current are assumed to be zero. Consequently, the computed slit width is the initial slit width with the specified RMS transit error. Stellar background and dark current decrease the angle accuracy.

One such possible function is

$$SW_i = k\,\sigma_\theta \left[\frac{(2t+3)\ P_{2t+2}}{m_s^2\ P_t} - \frac{(t+2)\ P_{t+2}}{m_s^2\ P_t} + \frac{P_{t+1} - P_{2t+1}}{m_s\ P_t} \right]$$

where

*Numbers refer to box numbers in flow chart of Figure III-12.

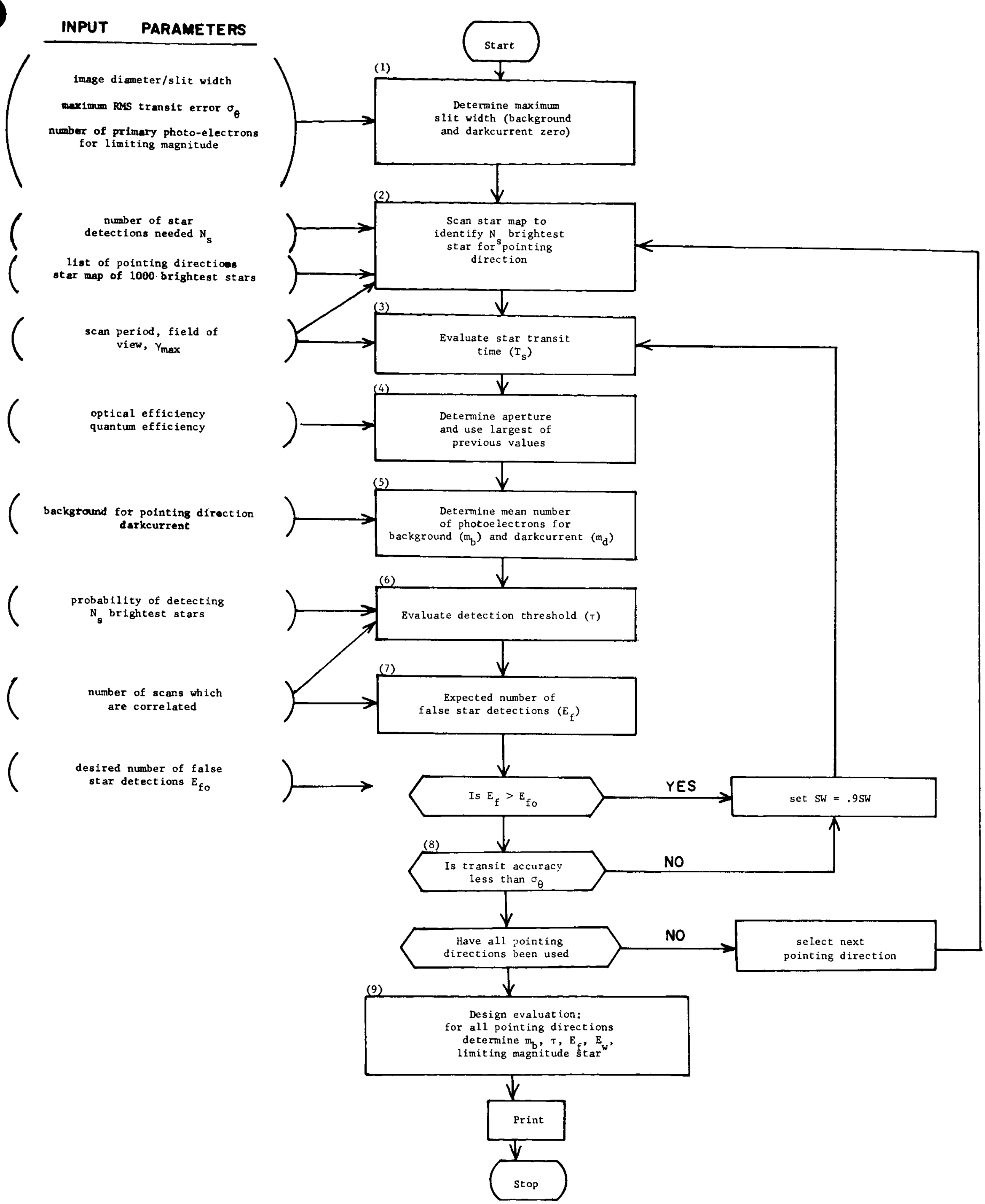

Figure III-12: OPSCAN Flow Diagram

SW_i = initial optical slit width in minutes of arc at optical axis

k = constant = $\sqrt{2}$

σ_θ = maximum RMS optical transit error in minutes of arc

t = largest value of t_1 for which

$$P_o \leq 1 - \sum_{j=0}^{t_1} \frac{m_s^{\,j}}{j!} e^{-m_s}$$

P_o = specified minimum probability of detection for the limiting magnitude star with no background or dark current

$$P_T = 1 - \sum_{j=0}^{T} \frac{m_s^{\,j}}{j!} e^{-m_s} \text{ where } T = t,\ t+1,\ t+2,\ 2t+1,\ 2t+2$$

m_s = average number of photoelectrons from limiting magnitude star

The optical slit width and RMS optical transit accuracy as angles are measured across the center of the field of view with the vertex at the intersection of the figure axis and optical axis. This is depicted in Figure III-13, where SW represents the optical slit width as measured by this technique and SW′ represents the rotational slit width measured in a plane orthogonal to the figure axis. The rotational slit width measurement is independent of this inclination, γ.

b. Identification of Bright Stars in Field of View (2)

To identify the N_s brightest stars in the scanned area a stored star

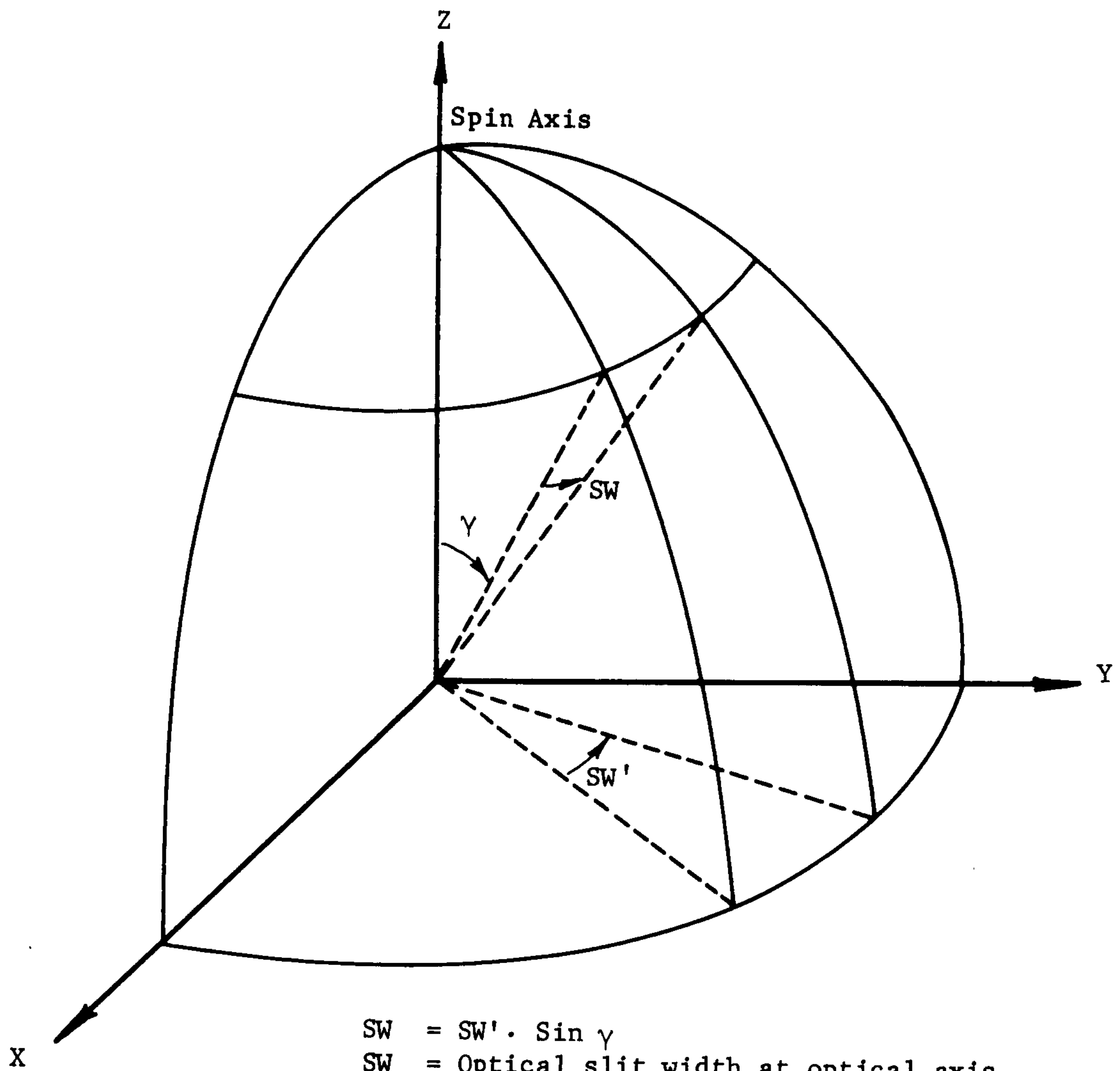

SW = SW'· Sin γ
SW = Optical slit width at optical axis
SW' = Rotational slit width

Figure III-13: Relation Between Optical Slit Width and Rotational Slit Width map is used. N is an input parameter. The scanned area is defined by the pointing direction ($\hat{P}$), inclination angle, i.e., the angle between the optical axis and spin axis, (γ), and the field of view, (FOV). The scanned area can be defined by the two angles $\gamma + \frac{FOV}{2}$ and $\gamma - \frac{FOV}{2}$.

To determine whether a star is in the scanned area, the direction cosines (p_x, p_y, p_z) of the pointing direction are expressed in galactic coordinates. The direction cosines of the star (s_x, s_y, s_z) are determined and the inner product $\hat{P} \cdot \hat{S}$ is calculated. The star is in the scanned area if the inner product is greater than $\cos(\gamma + \frac{FOV}{2})$ but less than $\cos(\gamma - \frac{FOV}{2})$. The procedure is depicted in Figure III-14. Summary of procedure,

(1) Calculate p_x, p_y, p_z.

(2) Calculate s_x, s_y, s_z.

(3) Calculate $\hat{P} \cdot \hat{S} = p_x s_x + p_y s_y + p_z s_z$.

(4) If $\cos(\gamma + \frac{FOV}{2}) < \hat{P} \cdot \hat{S} < \cos(\gamma - \frac{FOV}{2})$ go to 5; otherwise, go to next star, begin at Step 2.

(5) Ad 1 to N (N = number of stars located in scanned area).

(6) If $N \geq N_s$ terminate procedure; otherwise go to next star, begin at Step 2.

All stars in the scanned area are temporarily stored and the procedure is repeated until N_s stars are identified in the scanned area. The limiting magnitude is set equal to the highest magnitude of the N_s stars.

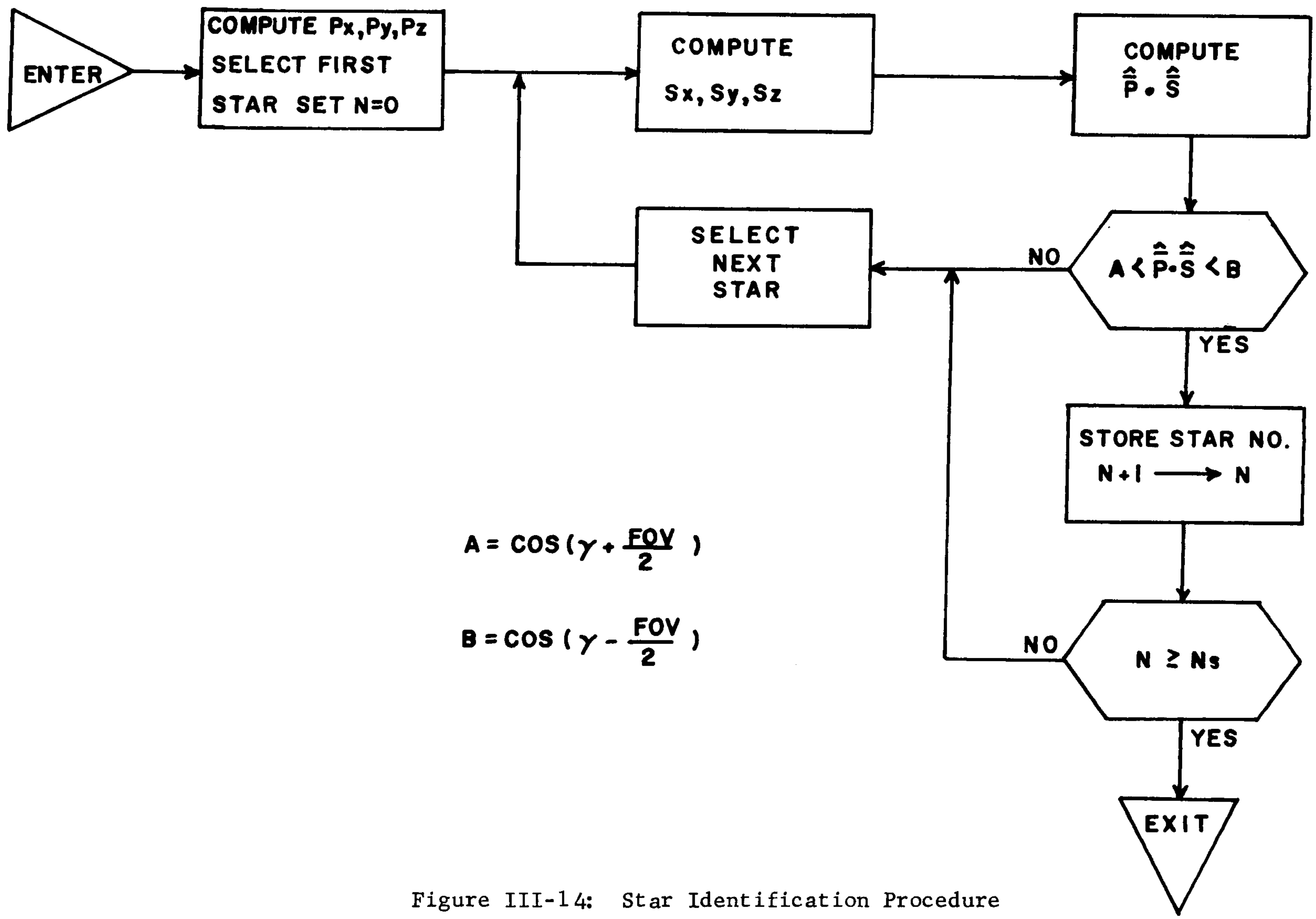

Figure III-14: Star Identification Procedure

c. Determination of Transit Time (3)

The star transit time is calculated using the following equations:

$$\gamma_{max} = \gamma + \frac{FOV}{2}$$

$$T_s = (SW)\ (T_{sp})/(21600)\ (\sin \gamma)$$

where T_s = length of time in slit (seconds)

SW = optical slit width measured at optical axis (Figure III-13)

γ = inclination angle in degrees of optical axis

T_{sp} = scan period in seconds (input parameter)

FOV = field of view in degrees (input parameter)

γ_{max} = maximum inclination in degrees (input parameter)

The angular relationships among the spin axis, the optical axis, and the field of view are depicted in Figure III-15.

d. Determination of aperture (4)

The basic equation by which the aperture diameter is determined is

$$m_s = \alpha\, \epsilon_q\, \epsilon_o C\, D^2\, T_s\, 10^{-.4M_L}$$

where m_s = average number of pulses from limiting magnitude star (input parameter). Pulses result from primary photoemissions; their amplitudes exceed the discriminator threshold.

D = aperture diameter (inches)

α = fraction of pulses allowed through threshold (input parameter)

ϵ_q = effective quantum efficiency relative to an S-4 response (input parameter)

ϵ_o = optical efficiency (input parameter)

C = constant = 1.2×10^7

M_L = limiting magnitude (photographic)

T_s = length of time in slit

This equation results from the fact that the average number of photons, λ_s, per second, striking an optical system with aperture, D, is proportional to $D^2\ 10^{-.4M_L}$ or (see Figure III-16)

$$\lambda_s = C\ D^2\ 10^{-.4M_L}$$

During the time of transit of the limiting magnitude star the average number of photons striking the system will be $T_s\ CD^2\ 10^{-.4M_L}$. The proportion of photons transmitted by the lens is the optical efficiency so the number of photons from the limiting magnitude star transmitted through the lens is

$$\epsilon_o\ T_s\ CD^2\ 10^{-.4M_L}$$

The proportion of photons converted to photoelectric pulses is the quantum efficiency. The photoelectric output of the limiting magnitude star is

$$\epsilon_q\ \epsilon_o\ T_s\ CD^2\ 10^{-.4M_L}$$

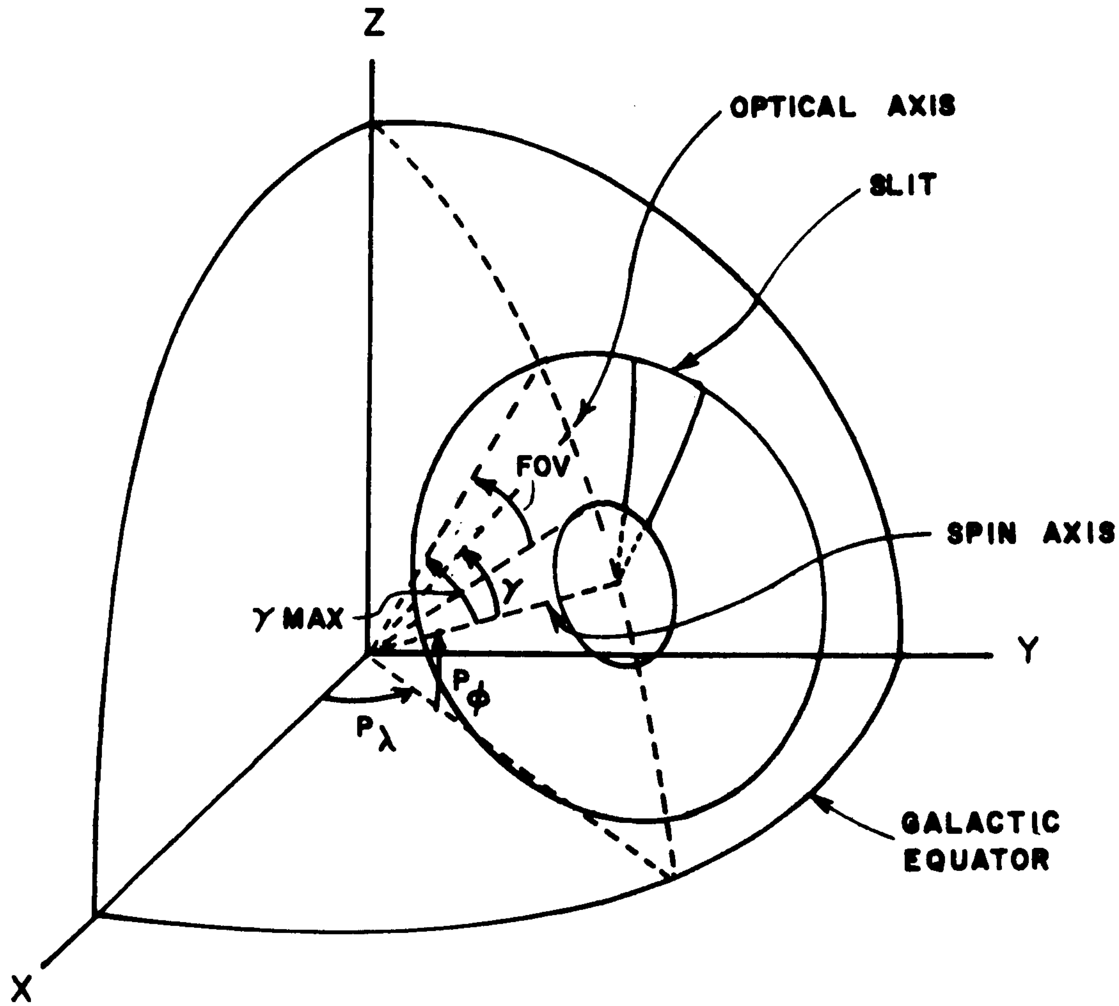

Figure III-15: Angular Relationships Among Spin Axis, Optical Axis, and the Field of View

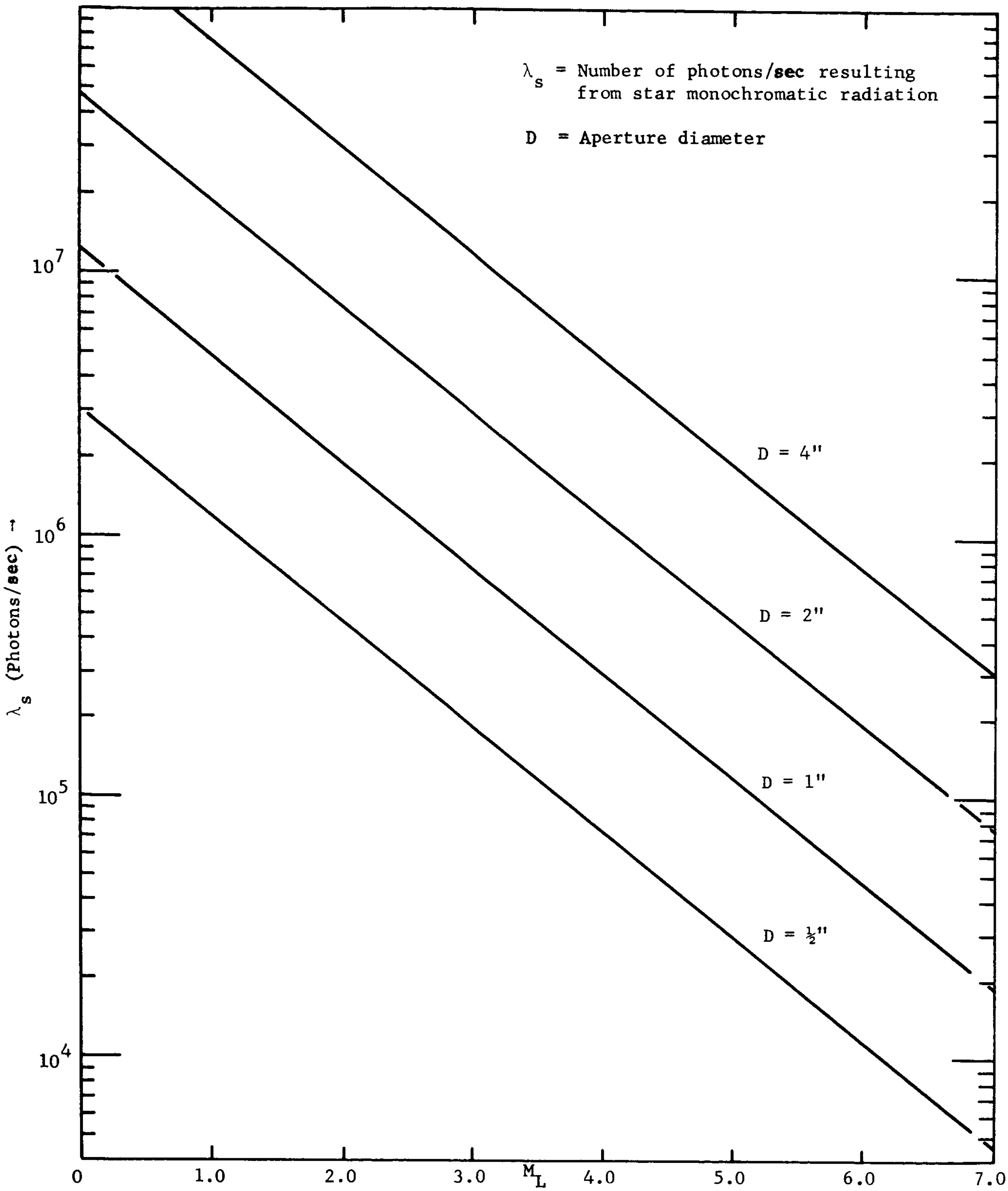

Figure III-16: Graph of $\lambda_s = (1.2 \times 10^7)\, D^2 10^{-.4M_L}$ as a Function of M_L for Various D

A lower limit threshold screens out the weakest α per cent of the photoelectric output. The average output of the threshold from the limiting magnitude star is thus

$$m_s = \alpha\, \epsilon_q\, \epsilon_o\, T_s\, CD^2\, 10^{-.4M_L}$$

The aperture diameter is

$$D = \left[m_s/\alpha\, \epsilon_q\, \epsilon_o\, C\, T_s\, 10^{-.4M_L}\right]^{\frac{1}{2}}$$

The newly calculated aperture diameter is compared against a previously stored value. If the new diameter is larger it will replace the previous value. Thus, the stored value represents the largest diameter determined up to that point.

If the newly calculated value is smaller than the previous value, the previous value will not be replaced and the average number of photoelectrons from the limiting magnitude star is recalculated as

$$m_s = m_{sp} \frac{D_p^2}{D^2}$$

where m_{sp} = previous value of average number of photoelectrons from limiting magnitude star

D_p = previous aperture diameter

D = calculated aperture diameter

e. Average Background and Dark Current Photoelectrons (5)

The average number of background photoelectrons is calculated by

$$m_b = 20\, N_{SL}\, \alpha\, \epsilon_q\, \epsilon_\circ\, T_s\, (FOV)\, (SW)\, (N_T)\, D^2$$

where m_b = average number of background photoelectrons during star transit

N_{SL} = number of slits

α = fraction of pulses allowed through threshold limits (input parameters)

ϵ_q = quantum efficiency (input parameter)

$\epsilon_\circ$ = optical efficiency (input parameter)

T_s = duration of time star is in slit

FOV = field of view (input parameter)

SW = optical slit width at optical axis

N_T = number of tenth magnitude stars per square degree

D = aperture diameter

The average number of dark current photoelectrons is calculated by

$$m_d = \lambda_d\, T_s$$

where m_d = average number of effective dark current photoelectrons

λ_d = effective dark current photoelectrons rate (input parameter)

T_s = duration of time star is in slit

f. Determination of Detection Threshold (6)

The detection threshold is determined from the inequality

$$p_o \leq \prod_{i=1}^{N_s} p_i \qquad p_i = 1 - \sum_{k=0}^{\tau_1} \frac{m_i^{\,k}}{k!} e^{-m_i} \quad \text{if } m_i < 50 \quad (m_i = m_{si} + m_{bi} + m_d)$$

$$p_i = \frac{1}{m_i\sqrt{2\pi}} \int_{\tau_1}^{\infty} \exp\left[-(x-m_i)^2/2m_i\right] dx \qquad \text{otherwise}$$

where p_o = specified minimum for the joint probability of detection of the N_s stars in the scanned area (input parameter)

p_i = probability of detection for the i^{th} star in the scanned area

τ_1 = initial estimate of detection threshold (photoelectrons)

N_s = number of stars needed in the scanned area (input parameter)

m_{si} = average number of photoelectrons from the i^{th} star in the scanned area

m_{bi} = average number of background photoelectrons from the stellar background near the i^{th} star

m_d = average number of dark current photoelectrons

The p_i represent probabilities of detection for each of the N_s stars in the scanned area and are evaluated by calculating the Poisson function or the normal approximation to the Poisson function. These probabilities are evaluated for various values of τ_1 and multiplied together to compare against p_o. The largest value of τ_1 that still results in the joint probability being less than p_o is set equal to τ, the detection threshold.

To reduce the amount of time required to calculate the detection threshold, τ, a starting value of

$$\tau_1 = m_i - K\sqrt{m_i}$$

is used, where

$$m_i = m_{si} + m_{bi} + m_d$$

$$K = \text{value for which} \quad \frac{1}{m_i\sqrt{2\pi}} \int_{-\infty}^{K} \exp\left[-(x-m_i)^2/2m_i\right] dx = p_o$$

By using this value and the fact that the calculated probability function is asymptotically normal, the time required to determine τ can be minimized.

g. Expected Number of False Star Detections Per Scan (7)

The expected number of false star detections, E_f, is calculated by determining the probability of detection of the background and dark current sources and multiplying this by the number of slit positions in the scanned area. The probability of detection of the background and dark current sources is

$$p(m_b + m_d, \tau) = 1 - \sum_{k=0}^{\tau} \frac{(m_b+m_d)^k}{k!} e^{-(m_b+m_d)}$$

where τ = detection threshold

The number of slit positions in the scanned area is

$$N_p = T_{sp}/T_s$$

where T_{sp} = scan period

T_s = duration in slit

The expected number of false star detections per scan is thus

$$E_f = p(m_b + m_d, \tau)\, N_p$$

h. Final Transit Accuracy (8)

The final transit accuracy is determined by forming

$$\sigma_o = c(SW_f)$$

where c = constant interpolation factor (c = 1/6 for all print given)

SW_f = final optical slit width at optical axis.

i. Program Logical Structure

The program begins by calculating the initial optical slit width based on the required angle accuracy, without background and dark current. Using this value of slit width, a stored star map is scanned to identify N_s stars in the scanned area, and the duration of star transit time and aperture are calculated. If the aperture is larger than the previously calculated aperture, it is stored. If not, the average number of photoelectrons from the limiting magnitude star is calculated using the previous aperture value.

The program then calculates the average number of background and dark current photoelectrons and evaluates the detection threshold. The expected number of false star detections is calculated and compared against a desired number of false star detections. If greater than the desired number, the slit width is reduced to 90 per cent of its previous value and processing is resumed at the evaluation of star transit time. The steps from the star transit time function (3) to the expected false star detection function (7) are repeated with the slit width being reduced 10 per cent each time until the expected number of false star detections becomes less than the desired number.

At this point, the RMS transit error is determined and compared against the maximum RMS transit error. The background and dark current are included in the calculation. If the computed error is larger than the maximum, the slit width is reduced once again by 10 per cent and control is returned to the star transit time evaluation. Reduction of the slit width and repetition of the steps from star transit time (3) to transit error (8) continues until the computed transit error becomes less than the maximum.

The above sequences are repeated using all pointing directions. The largest aperture and smallest slit width from any pointing direction are the final design values. With these values the design characteristics are evaluated for all pointing directions.

j. Design Evaluation (9)

When a design has been determined, several quantities that vary with the pointing direction are calculated and tabulated for all pointing directions. These values are the average number of background photoelectrons, the detection threshold, the expected number of false star detections, the limiting magnitude, and the expected number of weak star detections.

The expected number of weak star detections is determined by first calculating the scanned area as a proportion of the total surface. See Figure III-17.

The average number of photoelectrons is determined for stars of up to two magnitudes dimmer than the limiting magnitude. This is accomplished using the relationship

$$m_{s(i)} = .398\, m_{s(i-1)}$$

where $m_{s(i-1)}$ is initially m_s of limiting magnitude star.

The probabilities of detection for the stars of one and two magnitudes dimmer than the limiting magnitude are evaluated by calculating ρ_i according to Equation (3.1) using m_{si} and the detection threshold, τ.

The expected number of weak star detections is calculated by

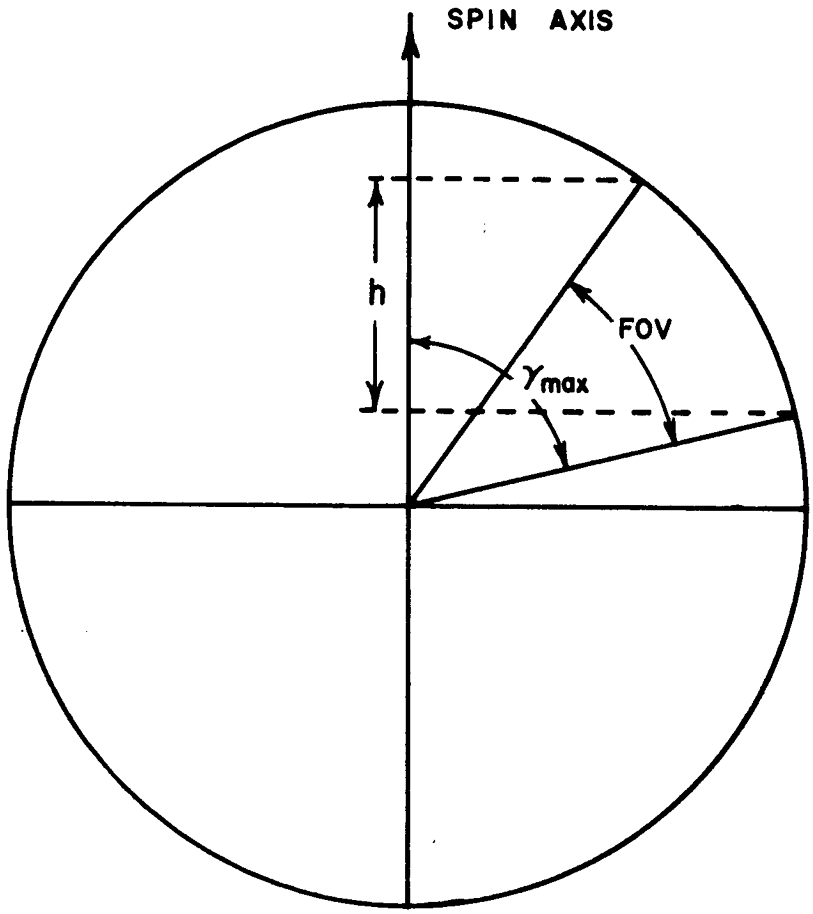

$$h = \cos(\gamma_{max} - FOV) - \cos(\gamma_{max})$$

SCANNED AREA = $h/2$

Figure III-17: Derivation of Scanned Area Calculation

$$E_f = SA \sum_{i=M_L+1}^{M_L+2} p_i N_i$$

where SA = scanned area

p_i = probability of detection for i^{th} magnitude star

N_i = number of i^{th} magnitude stars in scanned area

M_L = limiting magnitude (integral value)

A more elaborate model for the stellar background has been developed by Zimmerman [4], and this model will be incorporated in the OPSCAN program at a later time.

Following the design evaluation, the results are printed. At this point the program is terminated.

2. Numerical Example

The following is a numerical example where a design is calculated and evaluated for a specific set of input parameters. The data are taken from the computer printouts which follow and from Table III-2.

a. Maximum Slit Width (1)

An initial optical slit width at the optical axis of SW = 1.447 minutes of arc is computed. The rms optical transit accuracy at this point is σ_o = .241 minute of arc. The final value on SW is then found to be .506 minute of arc (see Table III-2).

TABLE III-2*

Multiple Pass Output Data

	(1)**	(3)	(4)	(5)	(5)	(6)	(7)
Pass No.	SW	T_s	D	M_b	M_d	τ	E_f
1	1.447	.00166	.916	1.21	50.66	67	64.4
2	1.306	.0015	.965	1.09	45.59	62	52.6
3	1.175	.00135	1.018	.98	41.03	58	34.2
4	1.058	.00121	1.073	.88	36.93	54	25.2
5	.952	.00109	1.131	.79	33.23	51	13.7
6	.857	.00098	1.192	.71	29.91	48	8.23
7	.771	.00088	1.257	.64	26.92	45	5.56
8	.694	.00080	1.325	.58	34.23	42	4.34
9	.624	.00072	1.396	.52	21.80	40	2.10
10	.562	.000641	1.472	.47	19.62	38	1.11
11	.506	.00058	1.552	.42	17.66	36	.65

* See Page xii for definition of notation.

** Numbers in parentheses refer to box numbers in Flow Chart on Page 45.

b. Identification of Bright Stars in the Scanned Area (2)

Using values of $N_s = 4$ for the required number of stars in the scanned area, a maximum inclination of 24 degrees, a pointing direction of 10 degrees right ascension and -10 degrees declination, and a field of view of 20 degrees, four stars are identified in the scanned area. The magnitude of the star with the least brightness is the limiting magnitude which was found to be $M_L = 4.3$.

c. Star Transit Time (3)

From a scan period of $T_{sp} = 6$ seconds a derivation of star transit time of $T_s = .00167$ second is calculated. The final value obtained by the program is $T_s = .00058$.

d. Aperture Diameter (4)

Given values of quantum efficiency of $\epsilon_q = .125$, optical efficiency of $\epsilon_o = .75$ and the average number of photoelectrons from the limiting magnitude star of $m_s = 30$, an aperture diameter of D = .916 inch is computed.

e. Average Number of Background and Dark Current Photoelectrons (5)

Given an average background photon rate of $\lambda_f = 16$ corresponding to the given pointing direction, an average number of background photoelectrons of $m_b = 1.21$ is computed.

Given an average dark current photon rate of $\lambda_d = 30{,}400$ an average number of dark current photoelectrons of $m_d = 50.66$ is determined.

f. Detection Threshold (6)

Using a specified maximum joint probability of detection of $P_o = .9$, a detection threshold of $\tau = 67$ is computed.

g. Expected Number of False Star Detections (7)

Given a maximum expected number of false star detections of $E_{f_o} = 1.0$, a computed number of expected false star detections of $E_f < 64.4$ is found to be too large.

As indicated by the flow diagram in Figure III-12, steps 3 through 7 are repeated with the slit width being reduced by 10 per cent at each repetition until the expected number of false star detections falls below the maximum specified. Table III-2 gives the values calculated for the variables involved in steps 3 through 7 or 11 repetitions. The last pass produced a value of $E_f = .65$ which was less than $E_{f_o} = 1.0$, and the repetition was terminated.

h. RMS Transit Accuracy (8)

An RMS transit accuracy of .084 minute of arc was computed and found to be less than the maximum of .241 minute of arc.

i. Evaluation and Printout

The design for the scanning optical system is printed out in detail. The design is evaluated for all pointing directions used and the evaluation is printed for each pointing direction. The following pages give the actual computer printout of the design and the design evaluation.

The OPSCAN program was used to design several systems based on the characteristics of various photomultipliers. These were done for two second and six second scan periods. The data resulting from these designs are found in Table III-3.

In Figure III-18, a scale of diameter cubed is drawn where one side represents a two second scan period and the other side represents a six second scan period. The photomultipliers are located on the scale according to the aperture determined for them. Because the weight is proportional to the aperture cubed the scale also represents the weight relationships.

* DESIGN FOR SCANNING OPTICAL SYSTEM * NO. 1-02

* OPTICAL SYSTEM

APERTURE DIAMETER	1.552 INCHES
FOCAL LENGTH (MIN.)	1.552 INCHES
IMAGE DIAMETER	0.506 ARC MINUTES
FIELD OF VIEW	20.000 DEGREES
FIELD OF VIEW SHAPE	CIRCULAR
OPTICAL EFFICIENCY	0.75
OPTICAL ARRANGEMENT	REFRACTING OPTICS
SPECTRAL FILTER	NONE

* RETICLE CONFIGURATION

WIDTH OF SLITS	0.506 ARC MIN	0.228 MILS
LENGTH OF SLITS	20.000 DEGREES	0.547 IN.
SLIT SHAPE	TRUNCATED SECTOR	
CODE PATTERN	000100000000000000000000 000000000000000000000000	
NUMBER OF CODE GROUPS	1	
COLOR CODE	NONE	
RELATIVE ORIENTATION OF CODE GROUPS	ONE RADIAL SLIT	

* DETECTOR

TYPE OF DETECTOR	PHOTOMULTIPLIER EMI 9514 B
DARK CURRENT	30400.00 PULSES PER SECOND
TIME RESPONSE	50.00 NANOSECONDS
QUANTUM EFFICIENCY	0.1250
DETECTION TECHNIQUE	HOLDING FILTER,THRESHOLD
RMS SPREAD OF PULSE AMPLITUDES TO MEAN	1.22
CATHODE SIZE	
CATHODE DIAMETER	1.75 IN.

* MOTION

SCAN PERIOD	6.00 SECONDS
ANGLE BETWEEN SPIN AXIS AND OPTICAL AXIS	14.00 DEGREES
STAR TRANSIT TIME (CENTRAL RAY)	581.08 MICROSECONDS
POINTING DIRECTIONS	
RIGHT ASCENSION	0.00 TO 360.00 DEGREES
DECLINATION	-10.00 TO -10.00 DEGREES

* DESIGN EVALUATION *

POINTING DIRECTION		
RIGHT ASCENSION	10.00	DEGREES
DECLINATION	-10.00	DEGREES

* TARGET CHARACTERISTICS

LIMITING STAR MAGNITUDE	4.30 PHOTOGRAPHIC
SPECTRAL CLASSES	ALL
PLANETS, SUN, OR EARTH IN FIELD OF VIEW	
SIGNIFICANCE OF EARTHS ATMOSPHERE	OUTSIDE ATMOSPHERE

* SIGNAL AND NOISE CHARACTERISTICS

MEAN NUMBER OF PULSES FROM LIMITING MAG STAR DURING STAR TRANSIT	30.00
MEAN NUMBER OF PULSES FROM STELLAR BACKGROUND DURING STAR TRANSIT	0.4249
MEAN NUMBER OF PULSES FROM DARK CURRENT DURING STAR TRANSIT	17.6648
PHOTOGRAPHIC MAG. OF NOISE	4.85
DETECTION THRESHOLD	36.00
MEAN VALUE OF OFF-PEAK MAXIMUM FOR CODE PATTERN	0.00

* STAR TRANSIT CHARACTERISTICS FOR LIMITING-MAGNITUDE STAR

POSITION ACCURACY	0.084 ARC MINUTES
RELATIVE INTENSITY ACCURACY	0.23
PROBABILITY OF DETECTION	0.96
EXPECTED NUMBER OF WEAK STARS DETECTED PER SCAN	7.9131
EXPECTED NUMBER OF FALSE STAR DETECTIONS PER SCAN	0.6553

* SYSTEM CHARACTERISTICS

MINIMUM NUMBER OF STARS IN FIELD OF VIEW WITH LIMITING MAGNITUDE AND BRIGHTER	4
ACCURACY OF ATTITUDE DETERMINATION	0.70 ARC MINUTES
PROBABILITY OF CORRECT STAR-PATTERN RECOGNITION	0.9
PATTERN RECOGNITION TECHNIQUE	
MEAN NUMBER OF STEPS FOR PATTERN RECOGNITION	

* DESIGN EVALUATION *

POINTING DIRECTION

RIGHT ASCENSION	90.00	DEGREES
DECLINATION	-10.00	DEGREES

* TARGET CHARACTERISTICS

LIMITING STAR MAGNITUDE	1.37 PHOTOGRAPHIC
SPECTRAL CLASSES	ALL
PLANETS, SUN, OR EARTH IN FIELD OF VIEW	
SIGNIFICANCE OF EARTHS ATMOSPHERE	OUTSIDE ATMOSPHERE

* STAR TRANSIT CHARACTERISTICS FOR LIMITING-MAGNITUDE STAR

POSITION ACCURACY	0.084 ARC MINUTES
RELATIVE INTENSITY ACCURACY	0.05
PROBABILITY OF DETECTION	0.91
EXPECTED NUMBER OF WEAK STARS DETECTED PER SCAN	0.0000
EXPECTED NUMBER OF FALSE STAR DETECTIONS PER SCAN	0.0000

* SIGNAL AND NOISE CHARACTERISTICS

MEAN NUMBER OF PULSES FROM LIMITING MAG STAR DURING STAR TRANSIT	445.78
MEAN NUMBER OF PULSES FROM STELLAR BACKGROUND DURING STAR TRANSIT	2.2575
MEAN NUMBER OF PULSES FROM DARK CURRENT DURING STAR TRANSIT	17.6648
PHOTOGRAPHIC MAG. OF NOISE	4.74
DETECTION THRESHOLD	437.00
MEAN VALUE OF OFF-PEAK MAXIMUM FOR CODE PATTERN	0.00

* SYSTEM CHARACTERISTICS

MINIMUM NUMBER OF STARS IN FIELD OF VIEW WITH LIMITING MAGNITUDE AND BRIGHTER	4
ACCURACY OF ATTITUDE DETERMINATION	0.70 ARC MINUTES
PROBABILITY OF CORRECT STAR-PATTERN RECOGNITION	0.9
PATTERN RECOGNITION TECHNIQUE	
MEAN NUMBER OF STEPS FOR PATTERN RECOGNITION	

* DESIGN EVALUATION *

POINTING DIRECTION

RIGHT ASCENSION	150.00	DEGREES
DECLINATION	-10.00	DEGREES

* TARGET CHARACTERISTICS

LIMITING STAR MAGNITUDE	3.70 PHOTOGRAPHIC
SPECTRAL CLASSES	ALL
PLANETS, SUN, OR EARTH IN FIELD OF VIEW	
SIGNIFICANCE OF EARTHS ATMOSPHERE	OUTSIDE ATMOSPHERE

* SIGNAL AND NOISE CHARACTERISTICS

MEAN NUMBER OF PULSES FROM LIMITING MAG STAR DURING STAR TRANSIT	52.13
MEAN NUMBER OF PULSES FROM STELLAR BACKGROUND DURING STAR TRANSIT	1.1288
MEAN NUMBER OF PULSES FROM DARK CURRENT DURING STAR TRANSIT	17.6648
PHOTOGRAPHIC MAG. OF NOISE	4.81
DETECTION THRESHOLD	59.00
MEAN VALUE OF OFF-PEAK MAXIMUM FOR CODE PATTERN	0.00

* STAR TRANSIT CHARACTERISTICS FOR LIMITING-MAGNITUDE STAR

POSITION ACCURACY	0.034 ARC MINUTES
RELATIVE INTENSITY ACCURACY	0.16
PROBABILITY OF DETECTION	0.92
EXPECTED NUMBER OF WEAK STARS DETECTED PER SCAN	0.0876
EXPECTED NUMBER OF FALSE STAR DETECTIONS PER SCAN	0.0000

* SYSTEM CHARACTERISTICS

MINIMUM NUMBER OF STARS IN FIELD OF VIEW WITH LIMITING MAGNITUDE AND BRIGHTER	4
ACCURACY OF ATTITUDE DETERMINATION	0.90 ARC MINUTES
PROBABILITY OF CORRECT STAR-PATTERN RECOGNITION	0.9
PATTERN RECOGNITION TECHNIQUE	
MEAN NUMBER OF STEPS FOR PATTERN RECOGNITION	

* DESIGN EVALUATION *

POINTING DIRECTION		
RIGHT ASCENSION	190.00	DEGREES
DECLINATION	-10.00	DEGREES

* TARGET CHARACTERISTICS

LIMITING STAR MAGNITUDE	3.07 PHOTOGRAPHIC
SPECTRAL CLASSES	ALL
PLANETS, SUN, OR EARTH IN FIELD OF VIEW	
SIGNIFICANCE OF EARTHS ATMOSPHERE	OUTSIDE ATMOSPHERE

* STAR TRANSIT CHARACTERISTICS FOR LIMITING-MAGNITUDE STAR

POSITION ACCURACY	0.084 ARC MINUTES
RELATIVE INTENSITY ACCURACY	0.11
PROBABILITY OF DETECTION	0.93
EXPECTED NUMBER OF WEAK STARS DETECTED PER SCAN	0.0000
EXPECTED NUMBER OF FALSE STAR DETECTIONS PER SCAN	0.0000

* SIGNAL AND NOISE CHARACTERISTICS

MEAN NUMBER OF PULSES FROM LIMITING MAG STAR DURING STAR TRANSIT	93.14
MEAN NUMBER OF PULSES FROM STELLAR BACKGROUND DURING STAR TRANSIT	0.5445
MEAN NUMBER OF PULSES FROM DARK CURRENT DURING STAR TRANSIT	17.6648
PHOTOGRAPHIC MAG. OF NOISE	4.84
DETECTION THRESHOLD	96.00
MEAN VALUE OF OFF-PEAK MAXIMUM FOR CODE PATTERN	0.00

* SYSTEM CHARACTERISTICS

MINIMUM NUMBER OF STARS IN FIELD OF VIEW WITH LIMITING MAGNITUDE AND BRIGHTER	4
ACCURACY OF ATTITUDE DETERMINATION	0.60 ARC MINUTES
PROBABILITY OF CORRECT STAR-PATTERN RECOGNITION	0.9
PATTERN RECOGNITION TECHNIQUE	
MEAN NUMBER OF STEPS FOR PATTERN RECOGNITION	

* DESIGN EVALUATION *

POINTING DIRECTION

RIGHT ASCENSION	270.00	DEGREES
DECLINATION	-10.00	DEGREES

* TARGET CHARACTERISTICS

LIMITING STAR MAGNITUDE	2.54 PHOTOGRAPHIC
SPECTRAL CLASSES	ALL
PLANETS, SUN, OR EARTH IN FIELD OF VIEW	
SIGNIFICANCE OF EARTHS ATMOSPHERE	OUTSIDE ATMOSPHERE

* STAR TRANSIT CHARACTERISTICS FOR LIMITING=MAGNITUDE STAR

POSITION ACCURACY	0.084 ARC MINUTES
RELATIVE INTENSITY ACCURACY	0.09
PROBABILITY OF DETECTION	0.91
EXPECTED NUMBER OF WEAK STARS DETECTED PER SCAN	0.0000
EXPECTED NUMBER OF FALSE STAR DETECTIONS PER SCAN	0.0000

* SIGNAL AND NOISE CHARACTERISTICS

MEAN NUMBER OF PULSES FROM LIMITING MAG STAR DURING STAR TRANSIT	151.75
MEAN NUMBER OF PULSES FROM STELLAR BACKGROUND DURING STAR TRANSIT	2.1247
MEAN NUMBER OF PULSES FROM DARK CURRENT DURING STAR TRANSIT	17.6648
PHOTOGRAPHIC MAG. OF NOISE	4.75
DETECTION THRESHOLD	154.00
MEAN VALUE OF OFF-PEAK MAXIMUM FOR CODE PATTERN	0.00

* SYSTEM CHARACTERISTICS

MINIMUM NUMBER OF STARS IN FIELD OF VIEW WITH LIMITING MAGNITUDE AND BRIGHTER	4
ACCURACY OF ATTITUDE DETERMINATION	1.40 ARC MINUTES
PROBABILITY OF CORRECT STAR-PATTERN RECOGNITION	0.9
PATTERN RECOGNITION TECHNIQUE	
MEAN NUMBER OF STEPS FOR PATTERN RECOGNITION	

TABLE III-3*

2 Second Scan Period

Photo-multiplier	D	SW	Right Ascension	M_L	m_s	m_b	m_d	M_{noise}	Tau	E_f	E_W
EMR	.928	1.451	10	4.3	30	1.22	2.70	6.51	24	0	1.23
541B-03			90	1.4	445.8	6.47	2.70	5.59	427	0	0
Ruggedized			150	3.7	52.1	3.24	2.70	6.06	48	0	0
DC = 4870/sec			190	3.1	93.1	1.56	2.70	6.42	83	0	0
QE = .37			270	2.5	151.7	6.09	2.70	5.63	144	0	0
EMR	1.449	1.451	10	4.3	30	1.22	1.41	6.94	23	0	.86
541A-01-14			90	1.4	445.8	6.47	1.41	5.75	426	0	0
Ruggedized			150	3.7	52.1	3.24	1.41	6.32	46	0	0
DC = 2540/sec			190	3.1	93.1	1.56	1.41	6.81	82	0	0
QE = .15			270	2.5	151.7	6.09	1.41	5.80	143	0	0
ITT	1.449	1.451	10	4.3	30	1.22	3.52	6.30	25	0	1.24
F 4027			90	1.4	445.8	6.47	3.52	5.49	428	0	0
Not Ruggedized			150	3.7	52.1	3.24	3.52	5.92	48	0	0
DC = 6340/sec			190	3.1	93.1	1.56	3.52	6.23	84	0	0
QE = .15			270	2.5	151.7	6.09	3.52	5.54	145	0	0
ITT	1.449	1.451	10	4.3	30	1.22	5.50	5.92	27	0	1.55
FW-130			90	1.4	445.8	6.47	5.50	5.30	430	0	0
Not Ruggedized			150	3.7	52.1	3.24	5.50	5.64	50	0	.01
DC = 9900/sec			190	3.1	93.1	1.56	5.50	5.87	86	0	0
QE = .15			270	2.5	151.7	6.09	5.50	5.33	146	0	0
EMI	1.587	1.451	10	4.3	30	1.22	16.89	4.85	36	.23	7.96
9514B			90	1.4	445.8	6.47	16.89	4.57	441	0	0
Not Ruggedized			150	3.7	52.1	3.24	16.89	4.73	61	0	.07
DC = 30400			190	3.1	93.1	1.56	16.89	4.83	97	0	0
QE = .125			270	2.5	151.7	6.09	16.89	4.59	157	0	0

* See Page xii for a definition of notation.

2 Second Scan Period

Photo-multiplier	D	SW	Right Ascension	M_L	m_s	m_b	m_d	M_{noise}	Tau	E_f	E_w
RCA 1P21	1.775	1.451	10	4.3	30	1.22	3.52	6.30	25	0	1.24
Standard			90	1.4	445.8	6.47	3.52	5.49	428	0	0
Not Ruggedized			150	3.7	52.1	3.24	3.52	5.92	48	0	.01
DC = 6330/sec			190	3.1	93.1	1.56	3.52	6.23	84	0	0
QE = .10			270	2.5	151.7	6.09	3.52	5.54	145	0	0
EMI	2.049	1.451	10	4.3	30	1.22	.17	7.64	22	0	.60
9514 S			90	1.4	445.8	6.47	.17	5.94	425	0	0
Not Ruggedized			150	3.7	52.1	3.24	.17	6.66	45	0	0
DC = 304/sec			190	3.1	93.1	1.56	.17	7.40	81	0	0
QE = .08			270	2.5	151.7	6.09	.17	6.00	141	0	0
RCA	3.213	.369	10	4.3	30	.31	18.1	4.83	37	.58	6.44
C70113A			90	1.4	445.8	1.65	18.1	4.76	437	0	0
Ruggedized			150	3.7	52.1	.82	18.1	4.80	59	0	.09
DC = 128000/sec			190	3.1	93.1	.40	18.1	4.83	97	0	0
QE = .12			270	2.5	151.7	1.55	18.1	4.76	154	0	0
EMR	3.354	1.451	10	4.3	30	1.22	.02	7.76	22	0	.53
541D-01-14			90	1.4	445.8	6.47	.02	5.96	424	0	0
Ruggedized			150	3.7	52.1	3.24	.02	6.71	45	0	0
DC = 35.6/sec			190	3.1	93.1	1.56	.02	7.50	81	0	0
QE = .03			270	2.5	151.7	6.09	.02	6.03	141	0	0
RCA	6.623	.104	10	4.3	30	.09	16.15	4.97	35	.80	5.56
1P21			90	1.4	445.8	.46	16.15	4.94	434	0	0
Ruggedized			150	3.7	52.1	.23	16.15	4.96	57	0	.05
DC = 405000/sec			190	3.1	93.1	.11	16.15	4.96	95	0	0
QE = .10			270	2.5	151.7	.43	16.15	4.94	151	0	0

6 Second Scan Period

Photo-multiplier	D	SW	Right Ascension	M_L	m_s	m_b	m_d	M_{noise}	Tau	E_f	E_W
EMR	.536	1.451	10	4.3	30	1.22	8.12	5.57	29	0	2.6
541B-03			90	1.4	445.8	6.47	8.12	5.08	432	0	0
Ruggedized			150	3.7	52.1	3.24	8.12	5.36	53	0	.02
DC = 4870/sec			190	3.1	93.1	1.56	8.12	5.53	88	0	0
QE = .37			270	2.5	151.7	6.09	8.12	5.11	149	0	0
EMR	.837	1.451	10	4.3	30	1.22	4.23	6.15	25	0	1.91
541A-01-14			90	1.4	445.8	6.47	4.23	5.42	428	0	0
Ruggedized			150	3.7	52.1	3.24	4.23	5.81	49	0	.01
DC = 2540/sec			190	3.1	93.1	1.56	4.23	6.09	85	0	0
QE = .15			270	2.5	151.7	6.09	4.23	5.46	145	0	0
ITT	.837	1.451	10	4.3	30	1.22	10.56	5.31	31	0	3.70
F 4027			90	1.4	445.8	6.47	10.56	4.91	435	0	0
Not Ruggedized			150	3.7	52.1	3.24	10.56	5.14	55	0	.03
DC = 6340/sec			190	3.1	93.1	1.56	10.56	5.28	91	0	0
QE = .15			270	2.5	151.7	6.09	10.56	4.94	151	0	0
ITT	.837	1.451	10	4.3	30	1.22	16.49	4.87	36	.15	6.94
FW-130			90	1.4	445.8	6.47	16.49	4.59	440	0	0
Not Ruggedized			150	3.7	52.1	3.24	16.49	4.75	60	0	.09
DC = 9900/sec			190	3.1	93.1	1.56	16.49	4.85	96	0	0
QE = .15			270	2.5	151.7	6.09	16.49	4.61	157	0	0
RCA	1.025	1.451	10	4.3	30	1.22	10.55	5.32	31	0	3.67
1P21 Standard			90	1.4	445.8	6.47	10.55	4.92	435	0	0
Not Ruggedized			150	3.7	52.1	3.24	10.55	5.14	55	0	.03
DC = 6330/sec			190	3.1	93.1	1.56	10.55	5.28	91	0	0
QE = .10			270	2.5	151.7	6.09	10.55	4.94	151	0	0

6 Second Scan Period

Photo-multiplier	D	SW	Right Ascension	M_L	m_s	m_b	m_d	M_{noise}	Tau	E_f	E_w
EMI	1.183	1.451	10	4.3	30	1.22	.51	7.40	22	0	.78
9514S			90	1.4	445.8	6.47	.51	5.88	425	0	0
Not Ruggedized			150	3.7	52.1	3.24	.51	6.56	46	0	0
DC = 304/sec			190	3.1	93.1	1.56	.51	7.20	81	0	0
QE = .08			270	2.5	151.7	6.09	.51	5.94	142	0	0
EMI	1.552	.506	10	4.3	30	.42	17.67	4.85	36	.66	7.9
9514B			90	1.4	445.8	2.26	17.67	4.74	437	0	0
Not Ruggedized			150	3.7	52.1	1.13	17.67	4.81	59	0	.09
DC = 30400/sec			190	3.1	93.1	.54	17.67	4.84	96	0	0
QE = .125			270	2.5	151.7	2.12	17.67	4.75	154	0	0
EMR	1.936	1.451	10	4.3	30	1.22	.06	7.73	22	0	.55
541D-01-14			90	1.4	445.8	6.47	.06	5.95	424	0	0
Ruggedized			150	3.7	52.1	3.24	.06	6.70	45	0	0
DC = 35.60/sec			190	3.1	93.1	1.56	.06	7.47	81	0	0
QE = .03			270	2.5	151.7	6.09	.06	6.02	141	0	0
RCA	3.491	.104	10	4.3	30	.09	15.31	5.02	34	.63	5.64
C70113A			90	1.4	445.8	.46	15.31	5.00	433	0	0
Ruggedized			150	3.7	52.1	.23	15.31	5.01	56	0	.05
DC = 128000/sec			190	3.1	93.1	.11	15.31	5.02	94	0	0
QE = .12			270	2.5	151.7	.43	15.31	5.00	150	0	0
RCA	7.195	.029	10	4.3	30	.02	13.68	5.15	33	.50	4.05
1P21			90	1.4	445.8	.13	13.68	5.14	431	0	0
Ruggedized			150	3.7	52.1	.07	13.68	5.15	55	0	.03
DC = 40500/sec			190	3.1	93.1	.03	13.68	5.15	92	0	0
QE = .10			270	2.5	151.7	.12	13.68	5.14	149	0	0

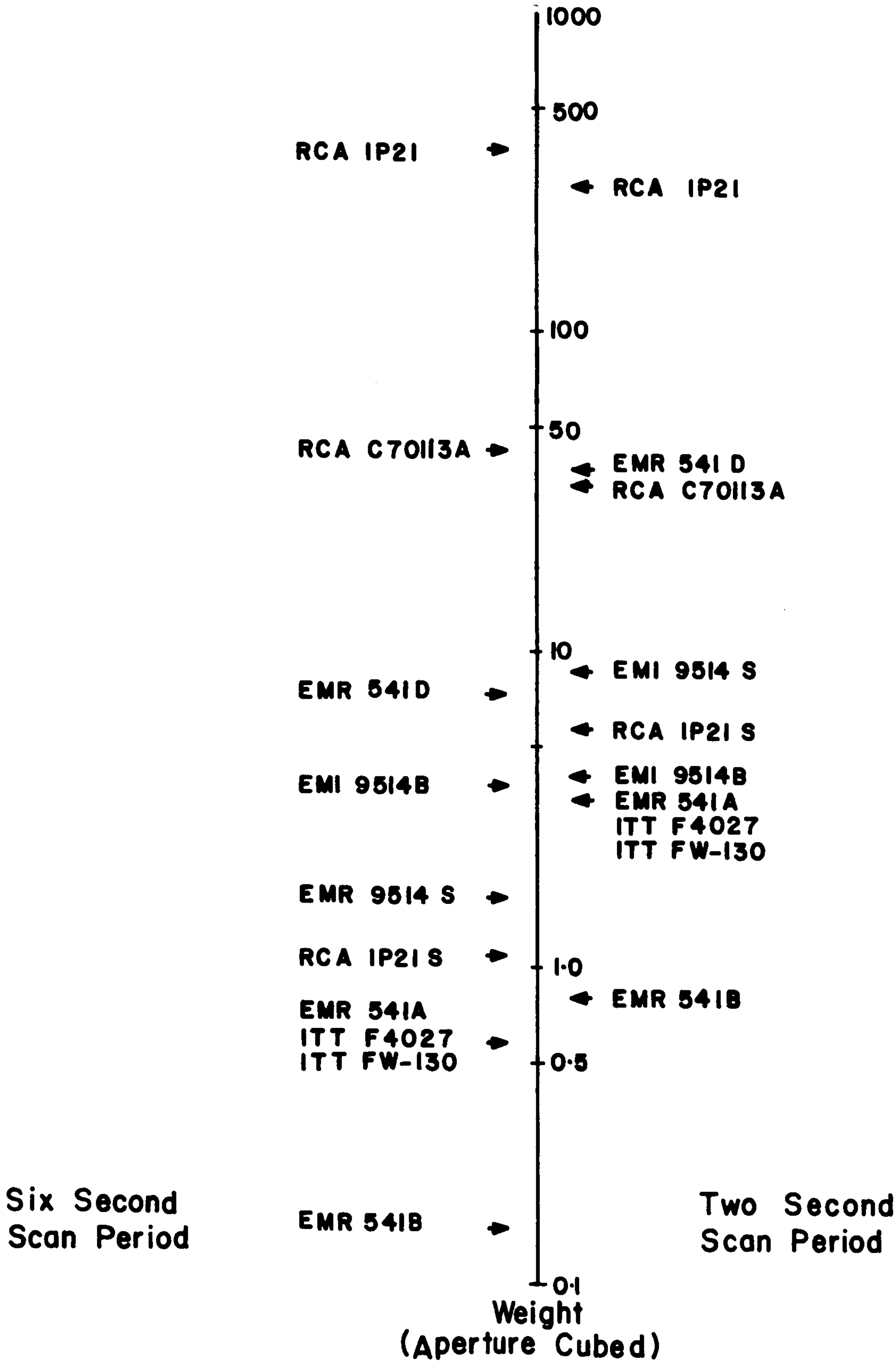

Figure III-18: Relative Merit of Various Photomultipliers

C. Electronic Design

1. Requirements and Functions of Electronic Components

The electronics of the SCADS instrument must be capable of gathering and storing star transit data (transit time or transit angle) and then relaying this data upon command to a ground tracking station via a telemetry data link. The process of gathering and storing star transit data requires the following basic functions.

(1) proportionally convert light energy passing a scanning slit into electrical energy,

(2) amplify the electrical impulse signals caused by stars passing the scanning slit,

(3) filter the signal from the noise and further amplify,

(4) detect all pulses caused by stars whose visual magnitudes are greater than or equal to 3.8,

(5) detect and store the time of occurrence (or the angle of occurrence) of the star pulse peak by gating the satellite digital clock (or an angle encoder), and

(6) convert available power from the satellite source into the regulated DC voltages required by the instrument electronics.

In addition, it may be required to convert the peak amplitude of each star pulse into a binary code which may be stored and forwarded via telemetry to the satellite ground tracking stations where star intensity data will assist in star identification.

The design goals of the SCADS electronics must be realized with maximum simplicity and mechanical rigidity to achieve maximum reliability and minimum size, weight, and power consumption. Consequently, these requirements are reflected in the discussion of the design considerations to follow.

All of the above functions are illustrated, with signal and data flow indicated by arrows, in the block diagrams shown in Figures III-19, III-20, III-21, and III-22.

2. Design Considerations of Associated Electronics

Figure III-19 shows a block diagram of the SCADS electronics for the Nimbus satellite. The rotating slit for the Nimbus satellite will be driven by a motor which also drives a 15 bit angle encoder (one part in 32,768) to insure transits accurate to one minute of arc. The angle encoder would not be needed if a sufficiently accurate constant ω motor could be designed to measure transit times between stars accurate to at least one part in 10^4. But since it is unlikely that this much accuracy can be achieved with a small rotating mass, a 15 bit angle encoder ($2^{15} = 32{,}768 > 60 \times 360 = 21{,}600$ minutes per revolution) would be necessary to directly measure angular separations between star transits accurate to one minute of arc.

Since the Tiros satellite will be rotating about its own axis, the slit can be mounted on the satellite base plate and scan the field of view as the satellite rotates. Therefore, the motor, motor drive, and angle encoder are not required for the Tiros system. Instead of measuring transit angles, transit times will be measured accurate to one part in 10^4. So a binary clock must be supplied.

The clock can consist of a stable oscillator driving a binary counter. Since the angular resolution must be one minute of arc, the time, t, to travel one minute of arc at constant ω and for a six second period of rotation is

$$t = \frac{6 \text{ sec/revolution}}{60 \times 360 \text{ min./revolution}} = \frac{6}{21{,}600 \text{ sec/minute of arc}}$$

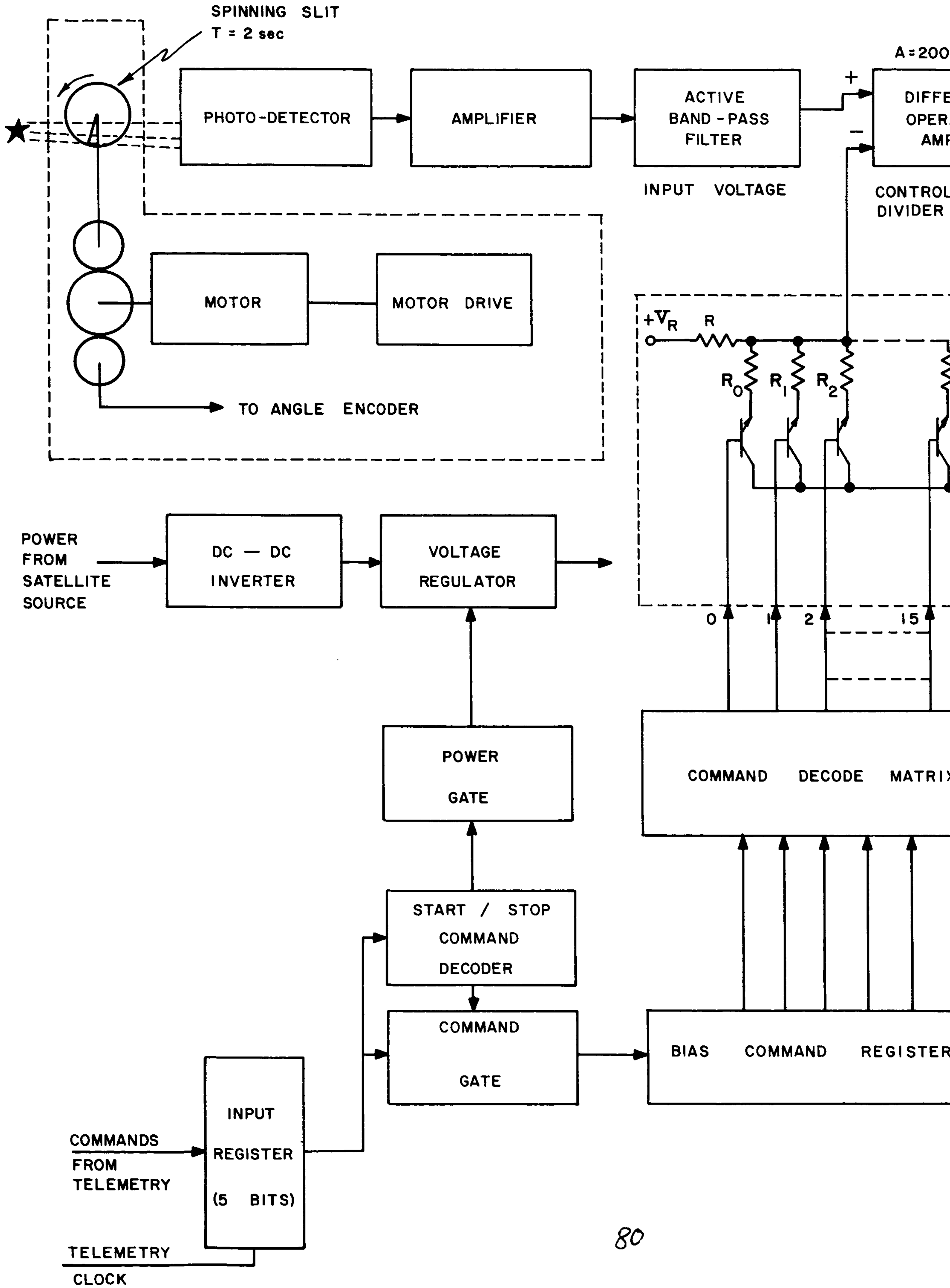
SPINNING SLIT
T = 2 sec
A=200
PHOTO-DETECTOR
AMPLIFIER
ACTIVE
BAND-PASS
FILTER
DIFFE
OPER
AMP
INPUT VOLTAGE
CONTROL
DIVIDER
MOTOR
MOTOR DRIVE
TO ANGLE ENCODER
+V_R
R
R_0
R_1
R_2
POWER
FROM
SATELLITE
SOURCE
DC — DC
INVERTER
VOLTAGE
REGULATOR
0
1
2
15
COMMAND DECODE MATRIX
POWER
GATE
START / STOP
COMMAND
DECODER
COMMAND
GATE
BIAS COMMAND REGISTER
INPUT
REGISTER
(5 BITS)
COMMANDS
FROM
TELEMETRY
TELEMETRY
CLOCK

80

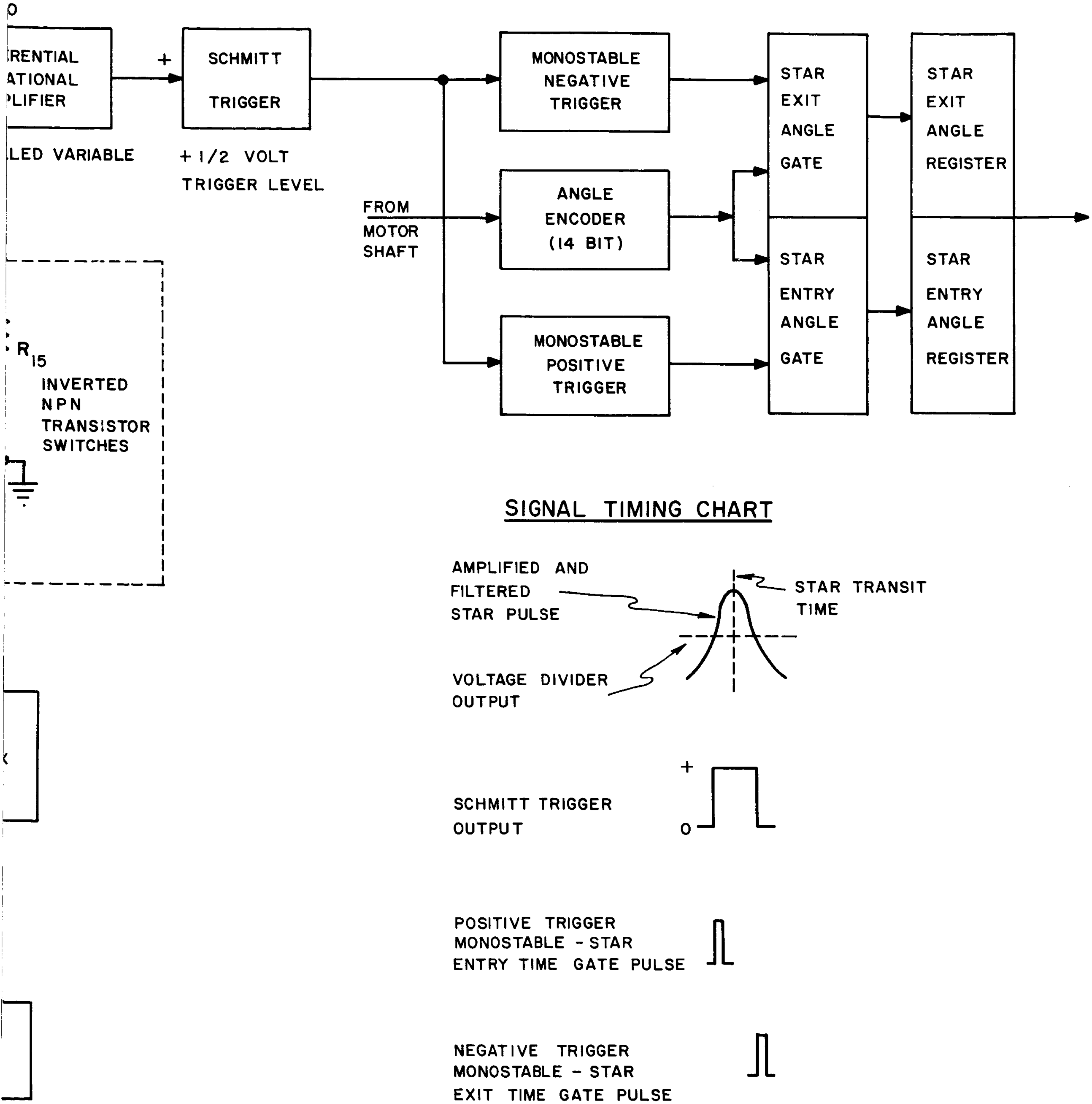

Figure III-19: Block Diagram Ground Controlled Star Transit Sensor for Nimbus Satellite

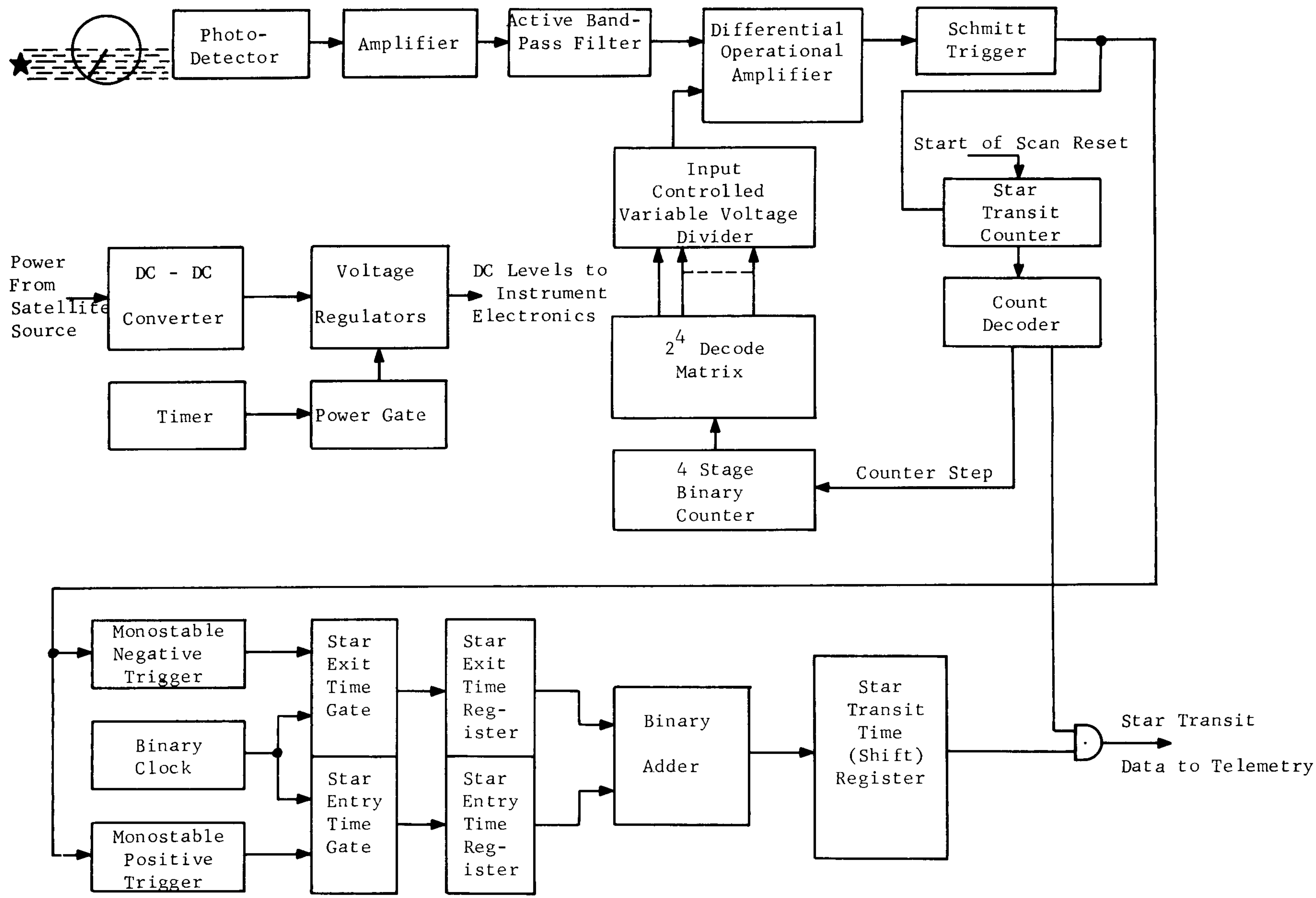

Figure III-20: Block Diagram of Automatic Controlled Bias Star Transit Time Sensor for Tiros Satellite

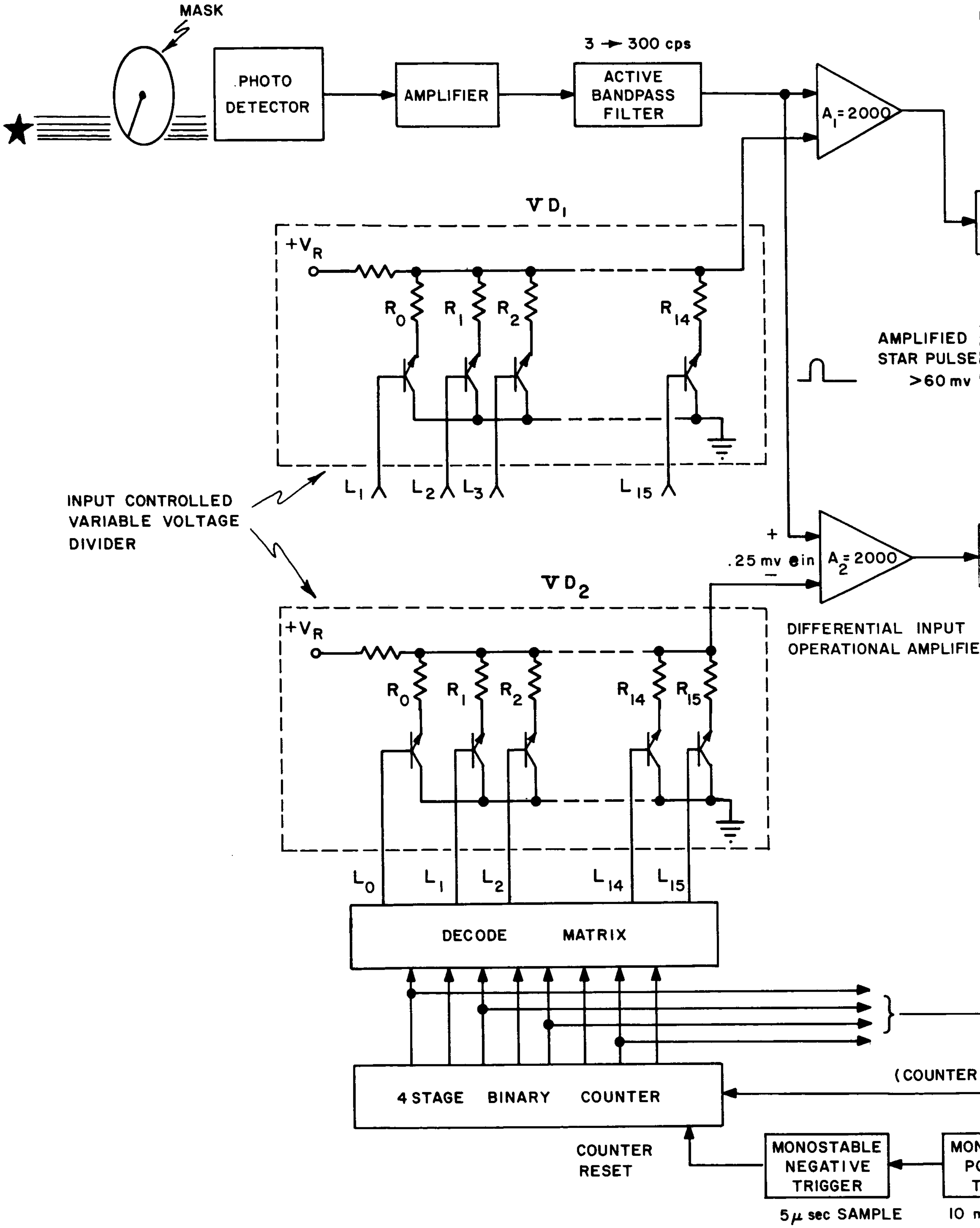
MASK
PHOTO DETECTOR
AMPLIFIER
3 → 300 cps
ACTIVE BANDPASS FILTER
A1 = 2000
VD1
+VR
R0 R1 R2 R14
L1 L2 L3 L15
AMPLIFIED STAR PULSE
>60 mv
INPUT CONTROLLED VARIABLE VOLTAGE DIVIDER
+
.25 mv ein
A2 = 2000
VD2
DIFFERENTIAL INPUT OPERATIONAL AMPLIFIE
R0 R1 R2 R14 R15
L0 L1 L2 L14 L15
DECODE MATRIX
4 STAGE BINARY COUNTER
(COUNTER
COUNTER RESET
MONOSTABLE NEGATIVE TRIGGER
5μ sec SAMPLE
MON
PC
T
10 m

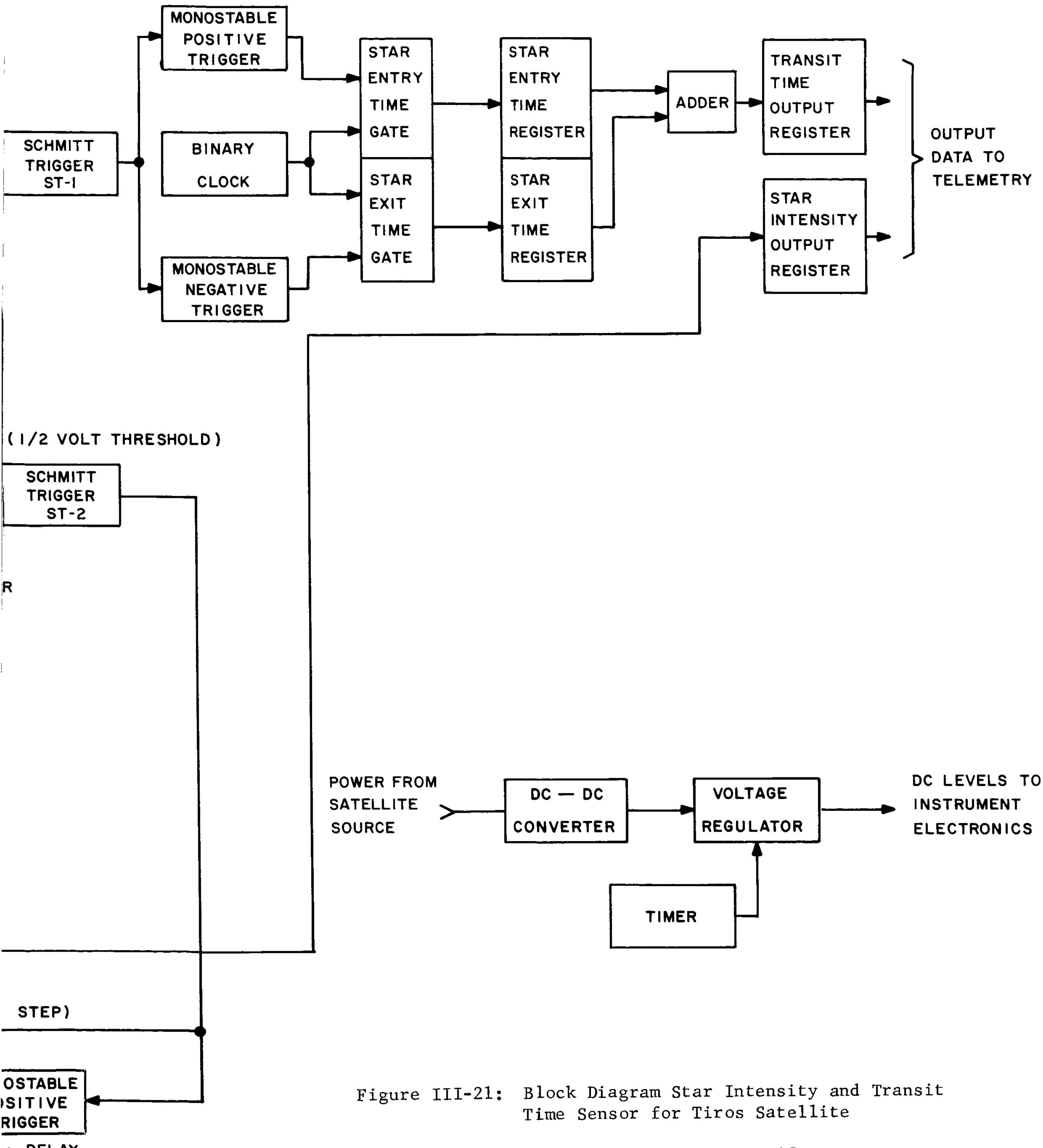

Figure III-21: Block Diagram Star Intensity and Transit Time Sensor for Tiros Satellite

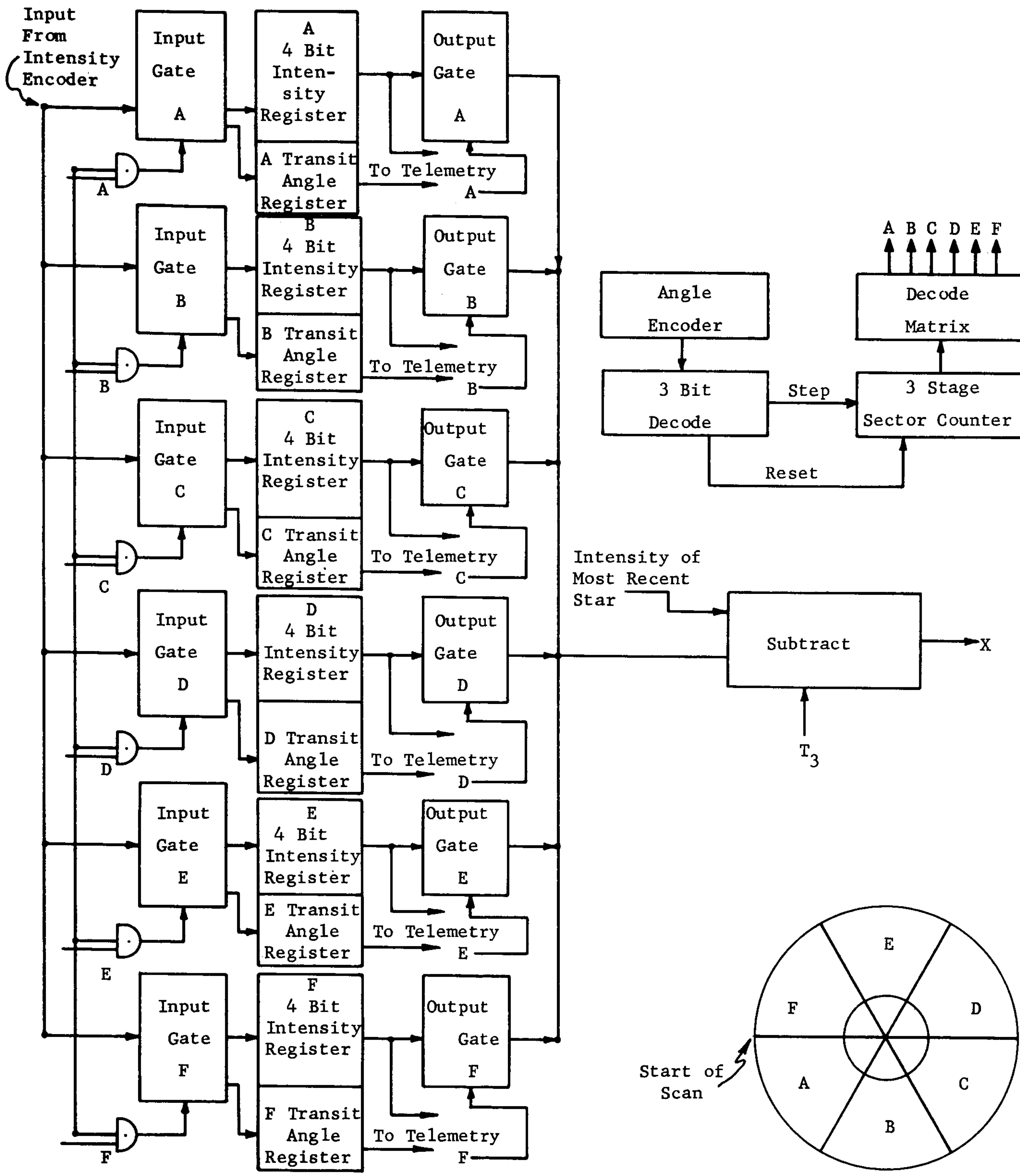

Figure III-22: Block Diagram Method for On-Board Detecting of Brightest Star per Field of View Sector

So one second must be divided into at least $\frac{21,600}{6} = 3600$ parts $\cong 4 \times 10^3$ parts. Therefore, the oscillator must have a repetition rate of 4×10^3 cycles per second. There are 4000 cycles per second x 6 seconds per scan = 24,000 cycles per scan, so the counter must have at least 15 stages ($2^{15} = 32,768 > 24,000$).

Although transit times are measured for the Tiros satellite, transit angles, i.e., azimuth angular differences between stars, are required. The angular differences must be calculated from $(\theta_2 - \theta_1) = \Delta\theta = \omega(t_2 - t_1)$, where θ_2 and θ_1 are the relative azimuths of the two stars, ω is the rotational velocity of the satellite and t_2 and t_1 are the transit times of the two stars. So to calculate $\Delta\theta$, ω must be known. By repeating several scans which always measure transit times for the same stars, the period of rotation can be calculated from the difference in time transits of the same star on successive scans. For example, assume star A transits at time $t_1 = t_a$ on scan number 1, at $t_2 = t_a + T$ on scan number 2, at $t_3 = t_a + 2T$ on scan number 3, etc. So by measuring $t_2 = t_1 = t_a + T - t_a = T$, we can calculate T and $\omega = 1/2\pi T$.

Based on the above discussion, the oscillator must not drift by more than one cycle over several (say ten) successive scan periods. So the oscillator must have a short term stability of about one part in 24,000 cycles per scan x 10 scans = 240,000 cycles or about four parts per million per minute.

a. Ground Controlled Star Transit Sensor for Nimbus Satellite

Figure III-19 shows a block diagram for a star transit angle sensor for the Nimbus satellite. This block diagram depicts a system consisting of a minimal number of functions for gathering star transit angle data. For this system the star magnitude threshold detection level (variable bias), which is adjusted so only the brightest stars are detected, can be controlled from the ground via telemetry command codes. As a star transit is detected, the angle of transit is gated from the angle encoder to the telemetry data link and transmitted real time to an earth tracking station. If too many stars are transitted per scan (at least four stars with good geometry are required), a command code can be sent to the sensor via telemetry which causes the threshold detection to be raised to a higher level. If less than four stars are transitted per scan, a command code can be sent to the sensor which causes the threshold detection level to be lowered a prescribed amount.

Amplifier and Bandpass Active Filter

Because of the relatively small amplitude of the star signal out of the photodetector and its presence in noise, it is necessary to amplify and filter the star signal. Assuming the photodetector is a photomultiplier, some calculations can be made with some typical numbers to show more clearly the need for amplification and filtering. For instance, if 37 photoelectrons are discharged at the cathode by a 3.8 magnitude star with a transit time of 10 milliseconds (typical Tiros conditions), the average cathode signal current

$$= \frac{37 \text{ electrons}}{10^{-2} \text{ seconds}} \times 1.6 \times 10^{-19} \frac{\text{coulomb}}{\text{electron}} = 59.2 \times 10^{-17} \text{ ampere.}$$

For a photomultiplier gain of 10^6, the average anode signal current is

$$59.2 \times 10^{-17} \times 10^6 \cong 60 \times 10^{-5} \text{ microampere.}$$

For a load resistance of 10×10^6 ohm, the average output signal voltage

$$= 10 \times 10^6 \times 60 \times 10^{-5}\ \mu\text{v} = 6 \text{ millivolts.}$$

But a photomultiplier has a typical average background (or dark current) of .005 microampere. So this means the 6 millivolt star pulse is superimposed on a $.005 \times 10^{-6}$ ampere $\times 10^{7}$ ohm = 50 millivolts DC level. Because of the relative magnitudes of the star pulse and the DC background, it is necessary to filter the star pulse from the DC background.

Also superimposed on the DC background level is a RMS fluctuation which occurs because the electron emissions from the cathode obey Poisson statistics. These RMS fluctuations are relatively small and can be approximated by the shot noise equation,

$$\frac{I_{RMS}}{(\Delta f)^{\frac{1}{2}}} = \sqrt{2e\ I_{dc}}$$

For a background current of 5×10^{-9} ampere, the RMS value equals

$$\frac{I_{RMS}}{\sqrt{\Delta f}} = \sqrt{2 \times 1.6 \times 10^{-19} \times 5 \times 10^{-9}} = 4 \times 10^{-14} \text{ ampere (second)}^{\frac{1}{2}}$$

This fluctuation is very small compared to the signal pulse amplitude, so filtering of the signal from the DC background is achievable.

Before filtering is attempted, it is desirable to amplify the signal pulse from the photomultiplier. Because the photomultiplier tube is a current source, it is necessary that the input impedance to the amplifier be as large as possible. The limiting factor on the input impedance is the RC time constant it forms with the output capacitance of the photomultiplier. This RC time constant limits the frequency response from the photomultiplier. If we assume the output and stray capacitance of the photomultiplier is typically

25×10^{-12} farad and the bandwidth of the star pulse is 425 cycles per second (see Section III.C.3.f) then the input impedance is limited to less than

$$R = \frac{1}{2\pi fC} = \frac{1}{2\pi \cdot 425 \cdot 25 \times 10^{-12}} \cong 15.2 \times 10^{6} \text{ ohm.}$$

The requirement of amplifying small signals with a large input impedance is a natural application for a field effect transistor amplifier. To reduce the sensitivity of the input amplifier to variations in the supply voltage, it is desirable that the input stage of the amplifier be a differential configuration. The voltage gain of the input amplifier should be about ten, so that the pulse amplitude from a 4^{th} magnitude star is about 60 millivolts. The gain must be limited to prevent circuit saturation due to a 0 magnitude star pulse which is about $(2.5)^4 = 39$ times greater than 60 millivolts, i.e., $60.0 \times 10^{-3} \times 39 = 2.34$ volts.

After the star pulse is amplified, it should be filtered from the DC background. Because each star signal is a unipolar pulse, its Fourier spectrum has significant DC and low frequency components. So when filtering the dark current DC background from the signal, it is desirable to remove the DC background of the star pulse without attenuating or delaying the low frequency components of the star pulse. It would be difficult to design a bandpass filter with a center frequency of 250 cps and a bandpass of 490 cps. Another approach is shown in Figure III-23. This requires an active low pass filter with as low a cut-off frequency as practical; let's say 2 cps. An active filter is required to prevent the capacitors from becoming prohibitively large.

Two stages of a probable low pass circuit configuration are shown in

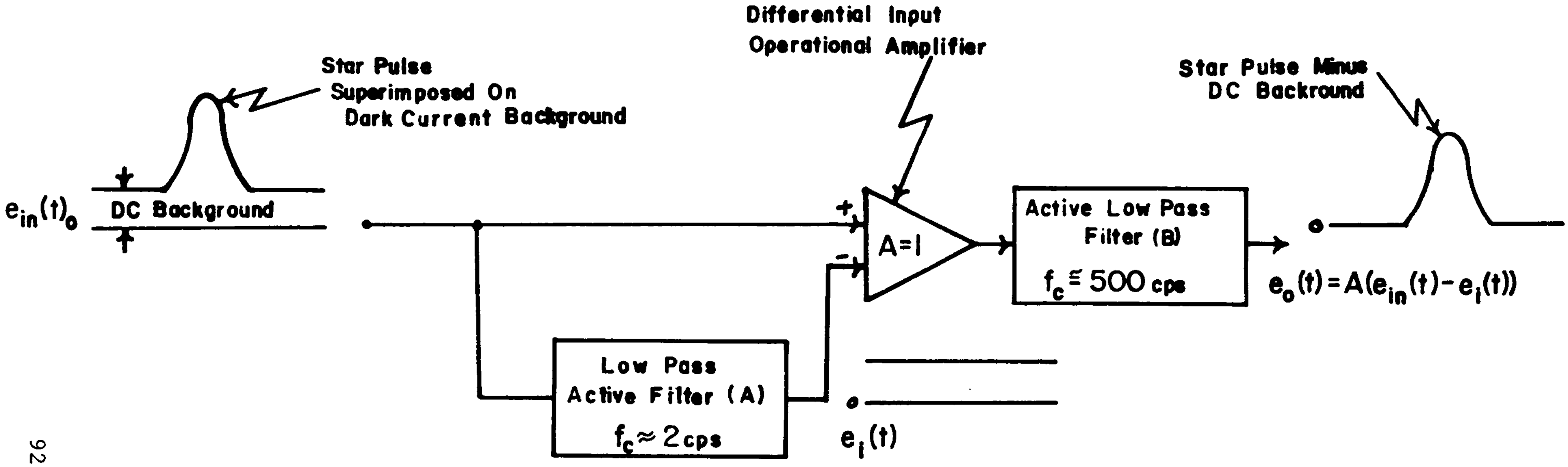

Figure III-23: Scheme for Filtering Star Pulse From DC Background

Figure III-24. Designing the filter involves matching the desired band pass characteristic with the poles of the transfer function. A critical design problem will involve the DC temperature stability of the unity gain amplifiers caused by the temperature coefficients of the transistor base-emitter voltage drops. This temperature variation can be minimized by designing the filter with an even number of stages as in Figure III-24. In Figure III-24, the variation in Vbe_1 of Q_1 (PNP) will nearly cancel the variation in Vbe_2 of Q_2 (NPN).

Figure III-23 shows a differential input operational amplifier with a gain of unity. Its purpose is to subtract the DC output of the low pass filter from the composite signal which includes the star pulse. Integrated circuit operational amplifiers suitable for this application are now available. As an example, Amelco Semiconductor type A13-251 amplifier has a typical DC open loop gain of 2×10^4, 10^6 ohm input impedance, and 25 $\frac{\mu Volt}{^oC}$ input offset voltage drift. Another suitable integrated operational amplifier presently available is the Westinghouse type WS161Q.

Figure III-23 shows another low pass filter (B) at the output of the unity gain operational amplifier. The purpose of this filter is to attenuate the high frequency noise in the frequency range above the star pulse spectrum. This filter can have the same circuit configuration as shown in Figure III-24; however, the cut-off frequency must be about 500 cps (assuming a 10 ms star pulse).

Bias Command Register

As already described in Figure III-19, the satellite ground station can

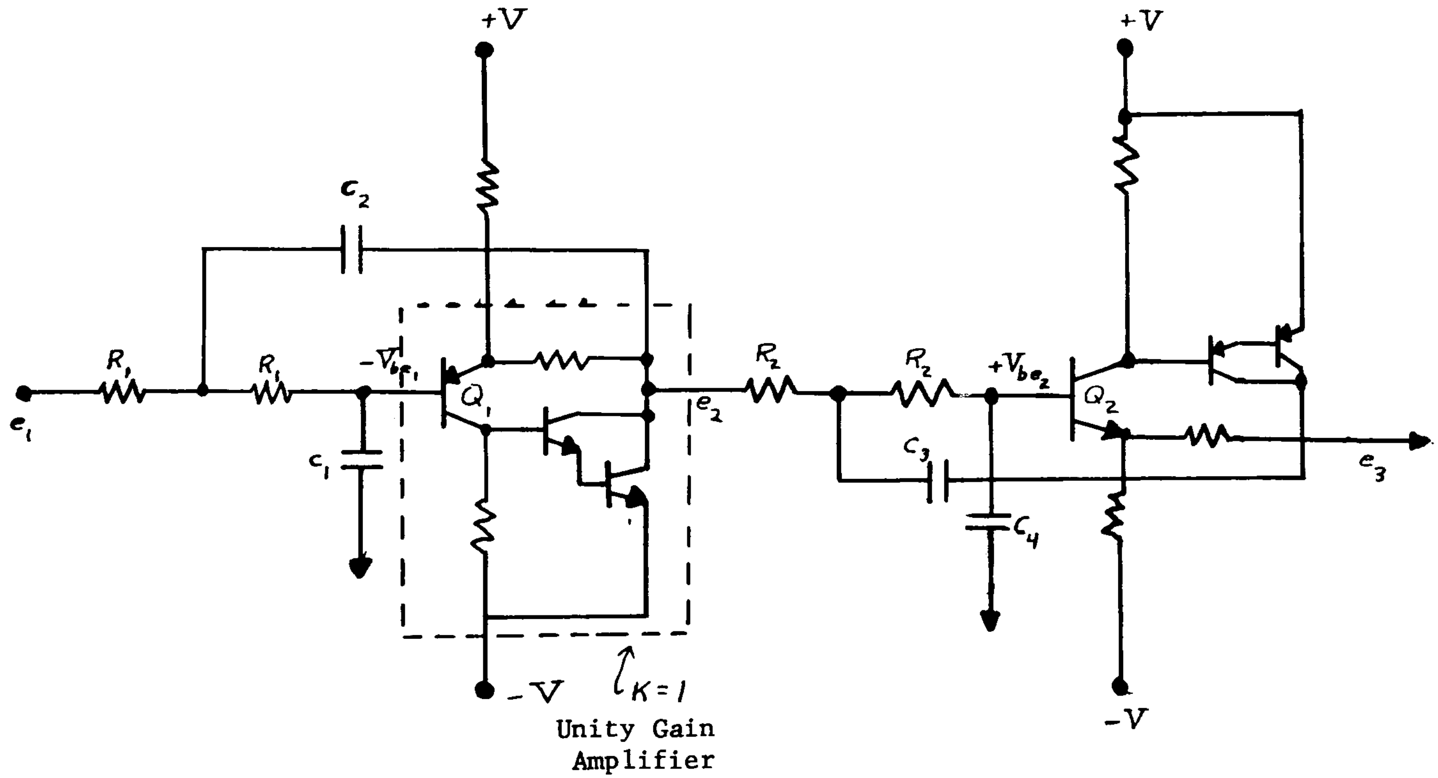

$$\text{Single State Transfer Function} = \frac{e_2(s)}{e_1(s)} = \frac{1}{[s^2\ C_1\ C_2\ R^2 + s\ R\ (C_1 + C_2\ [1 - K]) + 1]}$$

$$\left.\frac{e_2(s)}{e_1(s)}\right|_{\substack{K = 1 \\ s = 0}} = 1$$

Figure III-24: Low Pass Filter Circuit Configuration for Minimum DC Drift transmit bias command codes to the transit angle sensor electronics via telemetry. Each unique binary command code transmitted allows for establishing a new threshold (or bias) level for the detection of star pulses. The purpose of the register is to receive and store the binary command codes received from the telemetry.

Command Decode Matrix

Figure III-19 and Figure III-20 show a matrix for decoding the command codes stored in the command register. The matrix consists of an interconnection of logic gates which converts each combination of binary coded input signals into a unique signal at one of the matrix output terminals. The number of logic gates required to perform the decoding is fixed by the number of subdivisions of the star magnitude intervals.

Figure III-25 shows a possible distribution of $2^4 = 16$ subdivisions of the interval from star magnitude 0 to star magnitude 4. So the decoding matrix has $2^4 = 16$ outputs. Sixteen subdivisions were chosen because 16 is a power of 2 and also because 16 subdivisions appear to provide adequate resolution. More resolution could be obtained by assigning $2^5 = 32$ subintervals, but the decoding logic increases in complexity.

In Figure III-25, twice as many subdivisions were arbitrarily assigned between star magnitudes 3 and 4 than between star magnitudes 2 and 3 because the latter interval has approximately half as many stars in the celestial sphere as the interval between magnitudes 3 and 4. Figure III-25 also shows a binary code assignment for the bias commands which can be used for ground control of the star pulse detection threshold via the telemetry data link.

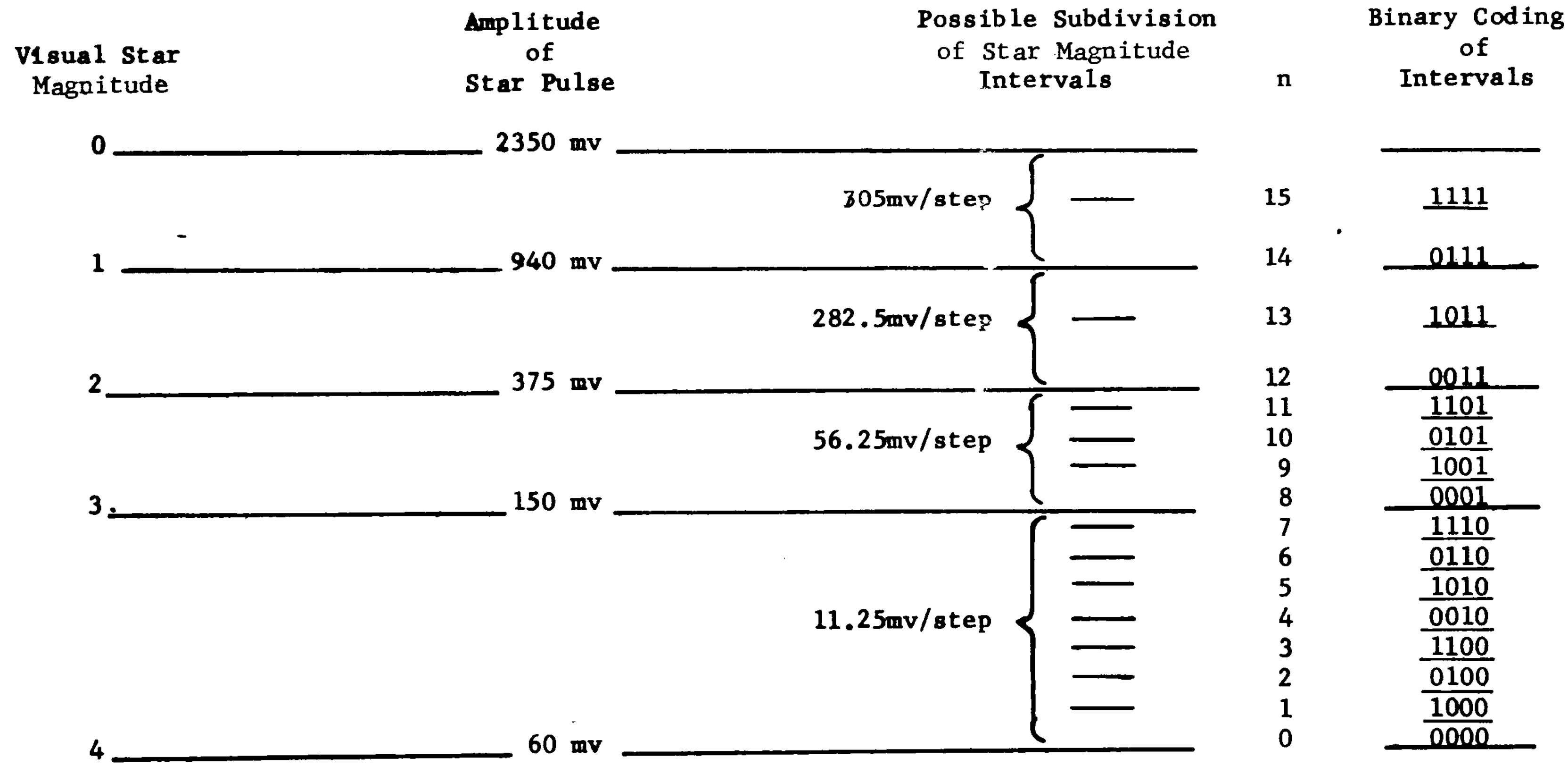

Figure III-26: A Possible Subdivision of the Star Magnitude Intervals for Establishment of Bias Levels

Each code defines a unique threshold level. Each star passing the slit whose amplified pulse exceeds the theshold level will result in the star's transit time being transmitted to the ground station via telemetry.

Input Controlled Variable Voltage Divider

This voltage divider, as shown in Figure III-19, consists of a reference voltage, V_R, a fixed resistor, R, and a set of multiple valued resistors (R_0, R_1, R_2, ..., R_{15}) which can be switched in or out of the divider with transistor switches. At any one instant, only one of the resistors is active in the divider, which means the transistor switch controlling that resistor is ON while all remaining transistor switches are OFF. The ON transistor is driven by the ON output from the command decode matrix, while the remaining switches are held OFF by corresponding decode matrix outputs.

The transistor switches must be operated in inverted connection (i.e., collector operated as emitter and vice versa) so the typical 1 to 3 millivolt inverted emitter-collector saturation voltage can be neglected.

Calculation of the values for the divider components is relatively simple. To prevent loading of the divider output, the amplifier input impedance must be much greater than the equivalent divider output resistance. With an amplifier input impedance of 10^5 ohms, suitable values would be $V_R = 12$ volts, $R = 5 \times 10^3$ ohms, $R_0 = 25$ ohms, $R_n = \frac{V_n \cdot 5000}{(12 - V_n)}$ where V_n can be determined from the schedule of desired bias levels shown in Figure III-25.

Differential Input Operational Amplifier and Schmitt Trigger

Figure III-19 shows a differential input amplifier whose output drives a Schmitt Trigger. The positive input to the differential amplifier is driven by the positive polarity star pulse signal from the bandpass filter while the negative input to the amplifier is driven by the output from the variable voltage divider. When the star pulse is less than the voltage divider output, the amplifier output is negative. Alternatively, when the star pulse is greater than the voltage divider output, the amplifier output is positive. If the threshold level of the Schmitt Trigger is set at + ½ volt and the gain of the differential amplifier is 2000, then the Schmitt Trigger will trigger ON when the rising portion of the star pulse input to the amplifier exceeds the voltage divider output by .5/2000 = .25 millivolt. Similarly, the Schmitt Trigger will be OFF when the star pulse input to the Schmitt Trigger does not exceed the voltage divider output by .25 millivolt.

The differential operational amplifier can be identical to the integrated amplifier described in the bandpass filter discussion, i.e., Amelco Semiconductor A13-251 or Westinghouse WS161Q. Schmitt Trigger level detector type circuits are also available in integrated form, for example, Westinghouse type WS113 or Fairchild μA710 would be suitable.

Monostable Positive Trigger, Monostable Negative Trigger, Angle Encoder Exit and Entry Angle Gates, and Register

Figure III-19 shows the output of the Schmitt Trigger driving both a positive trigger monostable and a negative trigger monostable. As the rising portion of the amplified star pulse exceeds the threshold level of the voltage divider, the Schmitt Trigger output goes from OFF to ON. Assuming the ON output level from the Schmitt Trigger is positive, then the positive trigger monostable will trigger causing the output of the angle encoder to be gated into the star entry angle register. When the falling portion of the amplified star pulse falls below the threshold level of the voltage divider, the Schmitt Trigger output goes from ON to OFF, which causes the negative trigger monostable to trigger. At that instant, the negative trigger monostable output gates the setting of the angle encoder into the star exit angle register. The star entry and exit angles are then available to the telemetry data link for real time transmission to the ground station.

Instead of an exit angle register, a star pulse duration counter and a pulse duration register can be employed. Initially, the duration counter would be reset. Immediately after the positive trigger monostable triggers, the duration counter will be stepped by the angle encoder until the negative trigger monostable output inhibits the counter stepping and gates the counter contents into the duration register. The duration count will give an indication of the star intensity.

DC-DC Converter, Voltage Regulators

The SCADS electronics will require power conversion circuits which can transform the power available from the satellite source into voltage supply levels which are compatible with the SCADS circuits. Both high and low voltage levels will be required.

High voltage levels will be required for the photomultiplier. Since the photomultiplier gain is strongly dependent on the voltages applied to the dynodes and anode, the high voltage supply should be regulated to within 0.1 percent. A typical photomultiplier requires 100 to 150 volts between dynodes, so a nine dynode photomultiplier such as the recommended EMR 541B-03 requires an anode voltage of 1000 to 1500 volts. A very practical means of supplying such large voltages in a small package without serious high voltage inverter transformer design problems is to design a regulated 100 volt source and then form a chain of 100 volt multiples with sucessive stages of voltage multiplier circuits, with each stage consisting of capacitors and extremely low leakage diodes. Figure III-26 shows a circuit configuration that can be employed. The high voltage multiplier stages should be positioned immediately adjacent to the photomultiplier tube in order to prevent high voltage arcing by reducing the high voltage lead lengths. Additional precautions against arcing can be taken by using special high voltage lead insulation. Photomultiplier tubes can be obtained in a package which also contains the high voltage supply such that high voltage arcing is no problem.

At least two low voltage levels will be required for the remainder of the SCADS electronics. Plus and minus 12 volts will probably be adequate for the analog and digital circuits. The regulation requirements need not be as critical as for the high voltage supply, so integrated circuit voltage regulators such as the General Instrument types NC/PC-511 and NC/PC-513 would be adequate.

Spinning Slit, Motor, Motor Drive, Angle Encoder

All the functions described for Figure III-19 can be similar for both the Nimbus and Tiros satellites except for the angle encoder, motor and motor drive circuit. These functions will be designed into the Nimbus satellite only.

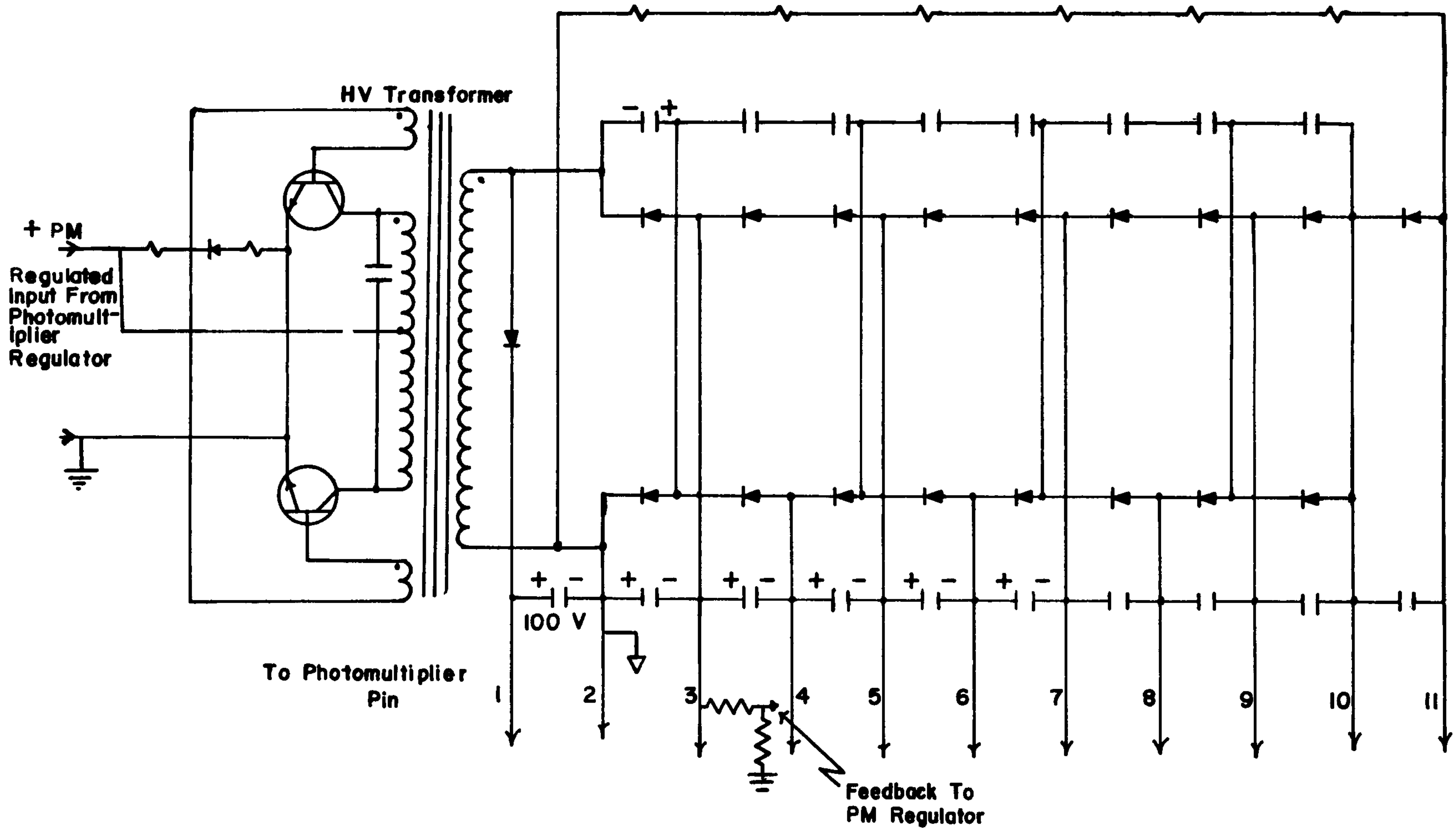

Figure III-26: Circuit Configuration for Photomultiplier Supply Voltages

The Tiros satellite will not have a spinning slit, instead the rotation of the satellite about its own axis will provide the scanning motion for the slit. As a star transiting the slit is detected, the entrance time of the star into the slit and the star exit time from the slit are gated into a holding register from a binary clock.

It will be assumed the oscillator for the binary clock, required for the Tiros SCADS system, is an integral part of the satellite system exclusive of the SCADS instrument. However, it is also assumed that the output of the clock will be available to the SCADS system for gathering of star transit time measurements.

Input Register, Start/Stop Command Decoder, Power Gate

All binary coded commands from Earth intended for the SCADS system are initially stored in an input register. The command repertoire would include as a minimum:

(1) a start command code which turns on power to the SCADS electronics exclusive of the photomultiplier, input register, start/stop command decoder and power gate.

(2) a stop command code which turns off power to the SCADS electronics exclusive of the photomultiplier, input register, etc., to reduce power drain on the satellite power source during SCADS idle portions of the orbit period.

(3) bias command codes to shift up or shift down the bias level of the star detection circuits. (16 bias commands are suggested in the discussion.)

A received command which is not a start or stop command must be a bias level command, so the start/stop decoder gates all bias commands into the bias command register.

The power gate, which is activated by the start/stop command decoder, gates the low voltage regulator outputs supplying DC power to the SCADS circuits other than the input register, start/stop command decoder, and power gate.

b. Automatic Controlled Bias Star Transit Time Sensor for Tiros

Figure III-20 shows a block diagram for a transit time sensor whose star threshold detection level is automatically controlled, thus reducing the communication channel requirements between the ground station and the satellite. Figure III-20 is merely a refinement of the ground controlled bias system described in Figure III-19. Because of the close similarities between the two systems, only the refinements will be described.

Star Transit Counter and Count Decoder

During each scan period, the star transit counter counts the number of stars which transit the slit whose pulse amplitudes are greater than the threshold level. If the number of star transits per scan is less than a preset number (e.g., four transits per scan) the count decoder steps backward a reversible counter which controls the variable voltage divider. Stepping the counter backward causes the threshold level to be lowered to a new threshold. If the number of star transits per scan is greater than a preset number (e.g., ten star transits per scan), the count decoder steps the reversible counter forward which causes the threshold level to be raised to a next higher level. Since the distribution of the brightest stars within the path of the field of view does not change abruptly, sufficient usable star transit time data should be available after only a few adjustment scans.

Binary Adder and Star Transit Time Register

As described for the system in Figure III-19, the star transit entry and exit times are transmitted to Earth via telemetry in real time. Figure III-20 shows a binary adder which can average the star entry time and star exit time to yield the transit time. Averaging the star entry and exit times aboard the vehicle can help to reduce the data transmission requirements on the telemetry system.

The block diagram of Figure III-20 can be made to apply to the Nimbus satellite with minor modifications. By omitting the binary clock and adding a rotating slit, motor, motor drive, and angle encoder interconnected as shown for Figure III-19, star transit angles can be measured.

Star Intensity and Transit Time Sensor for Tiros

By increasing the complexity of the electronics, it is possible to encode the intensity of any transiting star, as well as encoding its transit time (or its transit angle). Star intensity data is extremely valuable in star pattern recognition. Encoding of star intensity can be accomplished with variations of the techniques described in Figure III-19. In Figure III-20, an amplifier, A_2, a Schmitt Trigger, ST_2, a variable voltage divider, VD_2, a four stage counter and decode matrix are interconnected to encode the intensity of the star pulse. A similar arrangement involving variable divider, VD_1, an amplifier, A_1 and Schmitt Trigger, ST_2, is interconnected to record the star's entrance time into the slit and the exit time from the slit.

Star Intensity Encoding

A technique for star intensity encoding can be described by using A_2, ST_2, VD_2, the counter and decoder in Figure III-21. Initially, before a star pulse appears at the positive (+) input terminal of A_2, the four stage binary counter must be reset to state 0000, causing the decode matrix output to appear at terminal L_0. As a star pulse appears at the positive input of A_2, the output of A_2 will be negative because the star pulse initially is less than the threshold from the L_0 output of the voltage divider. As the star pulse increases and exceeds the threshold by .25 millivolt, the amplified output of A_2 becomes $.25 \times 10^{-3} \times 2 \times 10^{3} = .5$ volt. With the trigger level at ST_2 set at + 1/2 volt, the Schmitt Trigger will switch, which steps the four stage binary counter, causing the decode matrix output to appear at terminal L_1. This establishes a new threshold level which is greater than the previous level. This new level will occur before the star pulse can change substantially if the response time of each circuit is much less than the rise time of the star pulse. Typical circuit response time for integrated circuits is tens of nanoseconds compared to typical star pulse rise times of milliseconds. If the star pulse magnitude continues to increase, eventually it will again exceed the new threshold by .25 millivolt, thus causing ST_2 to switch again and step the counter to the next state. If the star pulse does not increase beyond the newest threshold set by the voltage divider, the Schmitt Trigger, ST_2, will not trigger and the counter will rest in the state which is the binary encoded equivalent of the star pulse amplitude. After a delay approximately equal to the duration of the star pulse and beginning with the leading edge of the star pulse, the counter contents are gated into a storage register followed by the resetting of the counter for encoding of the next star pulse.

The resolution of the encoded intensity is determined by the number of stages in the counter. Figure III-21 shows a four stage counter and $2^4 = 16$ levels of encoding. A typical encoding schedule for 16 levels is shown in Figure III-25. More resolution can be obtained by adding more counter states, i.e., adding more bits in the code. Increasing the resolution increases the complexity of the decoding matrix, but the resolution is ultimately limited by the noise superimposed on the star pulse and the temperature stability of the electronics.

Also shown in Figure III-21 is a voltage divider, VD_1, an amplifier, A_1, a Schmitt Trigger, ST_1, a positive trigger monostable, a negative trigger monostable and a binary clock interconnected as in Figure III-19 to record the entrance and exit times of the star passing the slit. Voltage divider VD_1 is similar to VD_2, except resistor R_n is active in VD_1 when resistor R_{n+1} is active in VD_2. If resistor R_n would be activated simultaneously in both voltage dividers, the star exit time would not be recorded because the star pulse may never exceed the newest threshold level; consequently, Schmitt Trigger ST_1 will not switch and the positive and negative trigger monostables will not gate respectively the entry and exit times into the holding register. Figure III-21 shows a binary adder for averaging the star entry and exit times and transmitting the result real time to the ground tracking station.

c. On-Board Satellite Data Processing and Storage

Instead of sending star transit data to Earth in real time, it may be desirable to perform a limited amount of data processing and storage on-board the satellite, followed by delayed transmission to an Earth receiving station. Figure III-22 shows a block diagram for dividing the field of view for a single scan into six equal sectors, and storing transit data for the brightest star in each sector. With this method, delayed transmission of transit data for only six stars is required, thus easing requirements on the telemetry data link and permitting the SCADS electronics system to share a telemetry channel with other satellite subsystems.

By choosing the brightest star in each of six sectors, at least three of the six stars will always have ideal geometry for the satellite attitude computation. The worst case occurs when the six brightest stars are grouped in three pairs with a sector boundary separating two adjacent stars. One star of each pair may be discarded, leaving three stars with ideal geometry for computing the satellite attitude.

d. Method for On-Board Detecting of Brightest Star per Field of View Sector

Logical implementation for on-board processing of the brightest star per field of view sector can be accomplished as shown in Figure III-22. A three stage counter and its associated decode matrix can be employed to divide the scan period in six equal time intervals. The method assumes that the magnitude of the star pulse is encoded as described in Figure III-21. For the Nimbus satellite, the counter can be stepped by the angle encoder output after each 60 degree rotation of the spinning slit. For the Tiros satellite, the slit is fixed to the rotating satellite, so since the approximate period of the satellite rotation is known, the satellite clock gated at equal time intervals can be used to step the sector counter.

During the initial interval after the beginning of each scan period, the decode matrix of Figure III-22 has an output on terminal A and no output signal on terminals B through F. During interval A, the encoded star intensity of the most recent transited star is compared with the stored encoded intensity for the brightest star previously detected during interval A. If the intensity of the latest star is greater than the stored intensity, the binary encoded transit angle (or transit time) and intensity of the latest star replaces the data of the previous brightest star in register A. If the intensity of the most recent star is less than the stored intensity, then the transit data of the most recent star is ignored and the transit data in register A is retained.

At the end of interval A, the three stage counter is stepped, causing the decode matrix to have an output at terminal B and no output at the remaining decode matrix terminals. During interval B, the intensity of the most recent star is compared with the brightest previous star of sector B, and the transit data of the brightest star is always stored in register B.

The comparison of two star intensities can be performed by parallel subtract logic. The sign of the remainder determines which of two stars is the brightest. The decode matrix controls the gating of the star data into the six data registers and also the gating of the intensity data into the subtract logic.

e. Detection of Four Brightest Stars per Scan

Another method for on-board processing of star data is to retain the transit data for the four brightest stars in the field of view. This method also requires encoding of the star pulse. A major disadvantage with this method is the logic required to continually determine which are the four brightest of five stars. As a new star transits, its magnitude may rank anywhere in an ordered set which includes the four previous brightest stars. It is required to determine which of the five stars has the smallest intensity and exclude it to form a new set of the four brightest stars. A method for determining the smallest of five binary numbers is shown in Figure III-27.

Whenever five binary numbers are complimented, the smallest uncomplimented number becomes the largest complimented number. Now, if each complimented number is stored in one of five counters, as in Figure III-27, and all five counters are stepped simultaneously by the gated output of a square wave clock, the counter initially containing the largest complimented number will be the first counter to reach the zero, or reset, state. As the counter reaches the zero state, the output of its associated zero state decoder can be employed to exclude the transit data of the weakest star from the set of

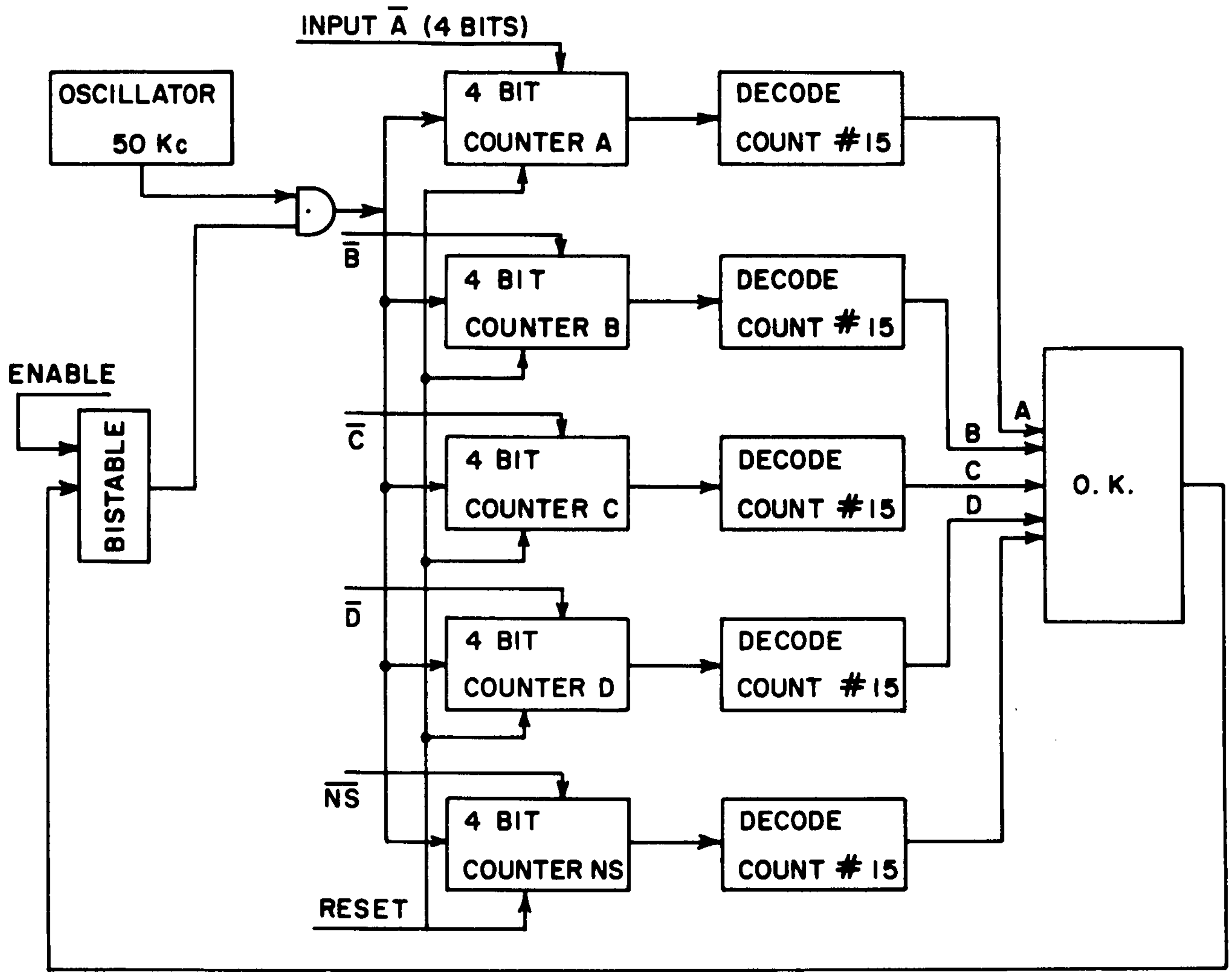

Figure III-27: Block Diagram Method for On-Board Detecting of Four Brightest Stars per Field of View five stars, thus leaving transit data for the four brightest stars. As each new star transits, this procedure can be repeated so that after a complete scan, only the transit data for the four brightest stars exists in storage. After the scan is completed, the transit data can be transmitted to Earth via telemetry.

f. Integration of SCADS Electronics with Tiros Satellite Tape Recorder

Because the Tiros satellite will have on board a magnetic tape recorder employed in other subsystems (Tiros I has two tape recorders to respectively store the video signals from a wide angle and a narrow angle television camera), there is a possibility that two adjacent tape channel tracks could be allocated to the SCADS system. Two adjacent tape tracks could be time shared with another system or assigned exclusively to the SCADS system. The reason for considering integration of the SCADS system with a tape recorder is to eliminate the need for on-board digital storage of star transit data. Instead, the star pulse or a reshaped form of the star pulse will be transmitted to the ground station where pulse shaping will be performed and star transit time will be determined.

It is undesirable to store and transmit the amplified star pulse because detectability of weak stars with low signal-to-noise ratios will be impossible at the ground station because of additional noise introduced by the tape recorder and the telemetry channel. An alternative to transmitting the star pulse directly is to generate a standard pulse (or pulses) which is the same for all stars and which contains enough significant information for determining the star transit time at the ground station. Since the bandwidth of the tape recorder channel and/or the telemetry channel may be less than the bandwidth of the actual star pulse, it may be necessary to restrict the star transit information transmitted. If it can be assumed that the star pulse is symmetrical, then the occurrence of the peak of the star pulse represents the minimum information required to determine the transit time. Hence, it is sufficient to transmit a pulse which is related in time to the occurrence of the star pulse peak. Figure III-28 shows a pulse of amplitude K and duration Ta which begins at the peak of the actual star pulse. The duration of the star pulse must be approximately equal to $1/f_b$ where f_b is the smallest bandwidth in the tape recorder-telemetry link.

Upon reception of the generated marker pulse at the ground station, it will be found that the rise time of the pulse has increased and the shape of the leading edge will have changed due to random noise, phase delays, etc. Consequently, at the ground station there is some uncertainty about when the marker pulse begins. It, therefore, seems reasonable to generate a pulse in the satellite with a controlled rise time, such as a sawtooth with an accurately known slope. At the ground station, a level detector will be set to trigger at some point on the sawtooth pulse slope. So, knowing the slope and the threshold level, it is easy to determine the start of the sawtooth. However, the sawtooth slope will also be distorted by noise, phase delays, amplitude stability, etc. Some improvement in system accuracy should be achievable by applying correlation techniques in comparing the expected sawtooth waveform with the received waveform. Further analysis to determine a suitable slope

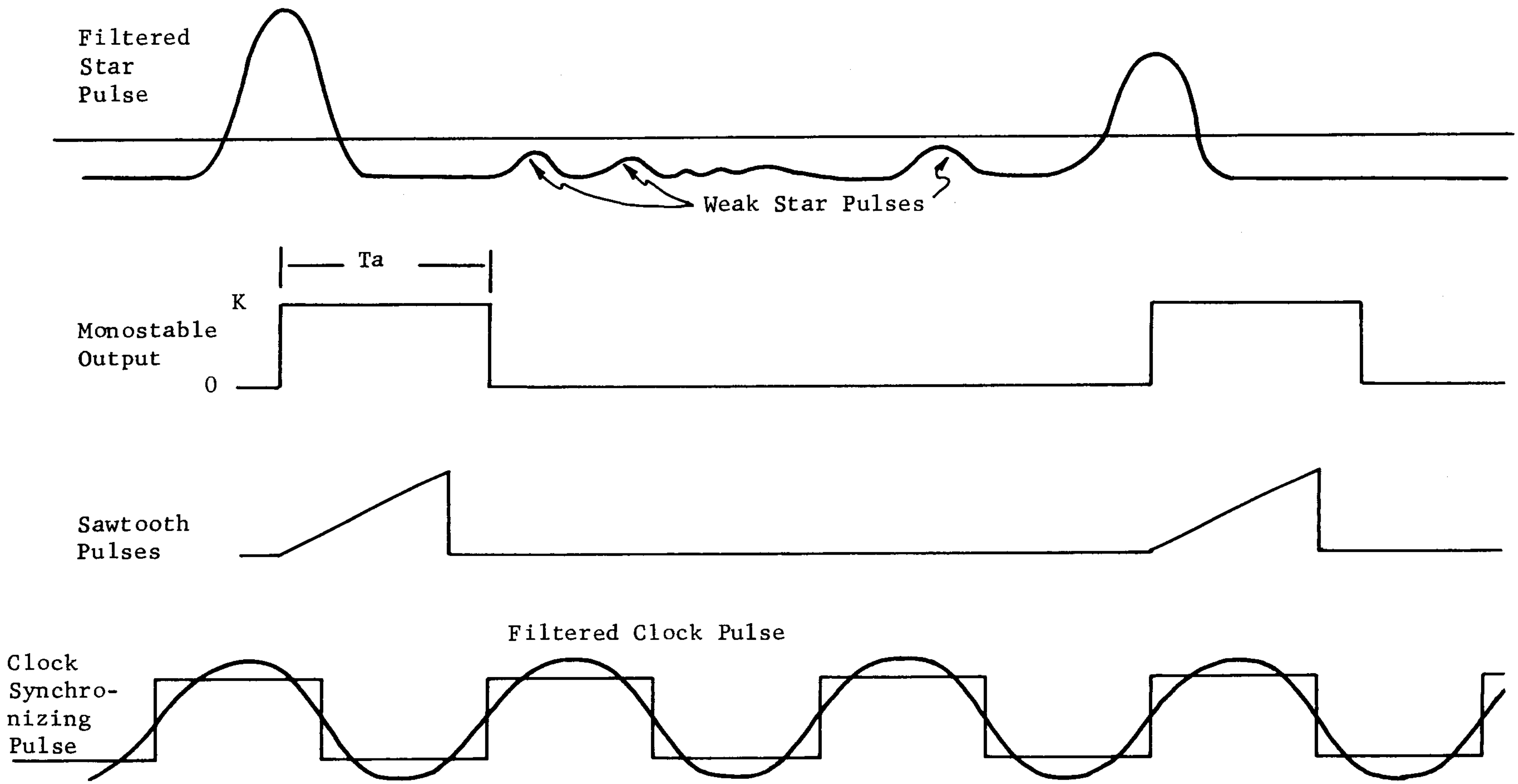

Figure III-28: Signal Shaping for SCADS Interface with Tiros Tape Recorder value can be performed when the characteristics of the tape recorder-telemetry channel are firmly established.

In order to realize any reasonable system accuracy, it will be necessary to transmit a clock synchronizing signal from the satellite to the ground receiving station. The clock synchronization signal will insure that the clock used to measure the transit time (instant of threshold crossing of the sawtooth slope) is in synchronism with the received star transit marker pulses. The frequency of the clock synchronizing signal will be limited by the bandwidth of the tape recorder-telemetry link. Therefore, the synchronizing signal may have to be less than the true clock frequency at the receiving station. It must, therefore, be assumed that between the synchronizing pulses, the clock at the receiving station is in step with the clock in the satellite SCADS electronics.

Figure III-29 shows a simplified block diagram for interfacing the SCADS electronics with the Tiros satellite tape recorder. When the filtered star pulse exceeds a certain bias level (which can be controlled from the ground as already described) a level detector activates an analog gate which passes the star signal to a differentiator operational amplifier. When the star pulse reaches its peak, the output of the differentiator should be near zero, and the output of the zero crossing detector (a high gain inverting amplifier) will trigger the monostable or sawtooth wave form generator. The output of the pulse generator will then pass through a low pass filter before entering the frequency modulation electronics of the tape recorder.

FM carrier recording will be necessary because of its ability to achieve

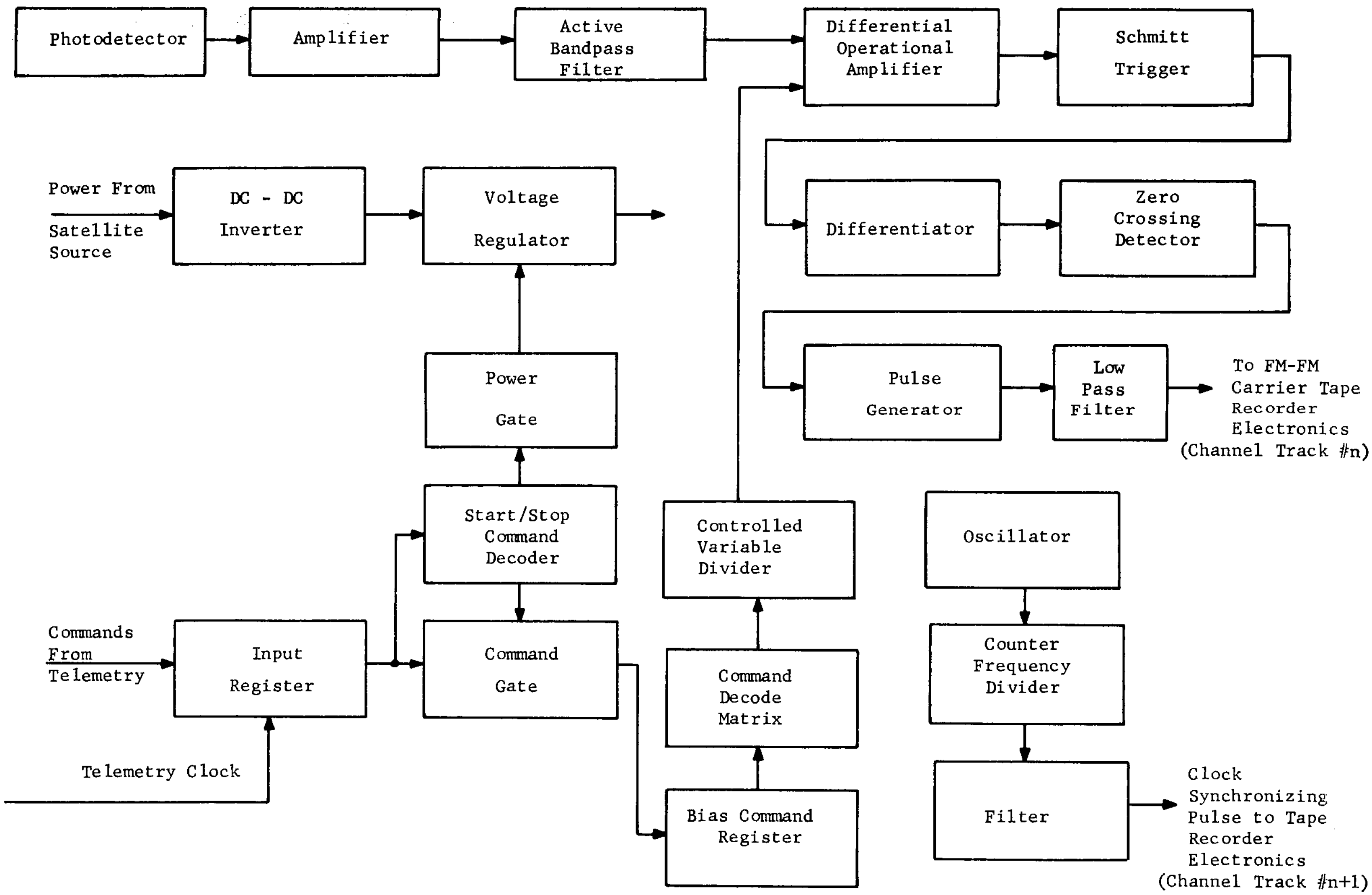

Figure III-29: Block Diagram SCADS Electronic Interface with Tiros Satellite Tape Recorder

DC response and give moderately high accuracy amplitude reproduction of data.

Operating the SCADS system in conjunction with the Tiros satellite tape recorder results in a reduction of the power required for the SCADS electronics if the tape recorder power is not included. This is valid since the tape recorder electronics will be operating anyway. It is estimated that at least 2.5 watts will be required for the SCADS electronics to operate with a tape recorder. These figures are based on the estimates of power tabulated in Figure III-33.

It is very unlikely that a SCADS system which depends on the transmission of analog pulses will be as accurate as any of the methods which encode the transit time in the satellite and transmit the digital code to the ground station. In transmitting analog pulses, amplitude and phase accuracy and stability are extremely critical, whereas in digital communication, it is only necessary to decide on the presence or absence of each signal bit pulse.

g. Electronic Design Recommendations

After evaluating the various electronic design concepts discussed in previous sections, it is apparent that the concept presented in Figure III-19 is the most satisfactory for the SCADS system. This judgment can be made because of several reasons.

(1) The concept of Figure III-19 presents the simplest functional system which requires fewer components to implement than the concepts presented in Figures III-20 and III-21.

(2) Because of reason (1), implementing the design of Figure III-19 should result in a smaller and slightly lighter overall package, plus greater reliability.

(3) The concept of ground controlled operation presented in Figure III-19 provides greater flexibility than the automatic operation concepts presented.

(4) The real time transmission of SCADS star transit data as presented in Figure III-19 appears to be acceptable, hence on-board satellite data processing, data storage, and data reduction are not worth the increased hardware complexity.

(5) Star intensity data for star identification is probably not needed since general pointing direction of sensor is approximately known.

(6) The system concept of Figure III-19 can be implemented with integrated and microminature components which are presently available without any need to develop new or special electronic components.

About the only disadvantage of the system concept presented in Figure III-19 is that simultaneous operation of the SCADS system and picture data transmission is impossible unless the SCADS system has its own telemetry transmission channel. However, the ground control makes it very simple for time sharing SCADS data transmission with picture data transmission. Whenever picture data is not being received at the ground station, a start command can be sent to the satellite to activate the SCADS system. However, it would probably be desirable for transmission of picture data to take priority and pre-empt transmission of SCADS data, since there should be ample picture idle time during each orbit to reschedule a complete SCADS data cycle.

3. The Photodetector

a. Energy Distribution of Navigational Stars

If the 100 brightest stars are considered and if the number of stars of a given spectral class are plotted against spectral class, the resulting graph is strongly peaked at class A_1 (df. reference [5]) with a lesser peak at class K_3. If the uniformly distributed standard navigational stars are treated in similar fashion, this peaking is even more pronounced.

It is, therefore, convenient to consider the response of photodetectors to either Type A or Type M stars. We consider Type A stars.

b. Peak Monochromatic Flux From Type A Star

Norton [6] has obtained a value for the peak monochromatic flux from Vega (Type A_0 V, visual magnitude m_v = .04) incident on the earth's atmosphere of,

$$f_{peak,\ Vega} = 6.16 \times 10^{-12}\ w/cm^2/\mu \tag{3.1}$$

If we consider third magnitude stars and an optical system of 1" aperture with 75 per cent efficiency, the peak monochromatic light which reaches the photodetector is,

$$f_{peak} = 6.16 \times 10^{-12} \times .75 \times \left(\frac{2.54}{2}\right)^2 \pi \times 10^{.04 - 1.2}$$

$$= 1.62 \times 10^{-12} \quad w/\mu$$

c. Effective Energy Flux Reaching Detector

We must next account for the spectral response of the photodetector, and do so by taking a flat response over the band of the detector. The Type A star is then approximated by a black body at 11,000°K. A detector bandwidth can thus be defined as

$$\frac{\int_{\lambda_1}^{\lambda_2} f_{bb}(\lambda, T)\, d\lambda}{f_{peak}} = \Delta\lambda \tag{3.2}$$

Here T is temperature in °K, and f_{bb} is the black body energy density distribution (watts/cubic meter)

$$f_{bb} = \frac{2\pi c^2 h}{\lambda^5 (e^{ch/k\lambda T} - 1)}, \quad f_{peak} = f_{bb}(\lambda_m, T)$$

where λ is wavelength and λ_m is the wavelength at which f_{bb} peaks.

c is velocity of light, k is Boltzmann's constant 1.38×10^{-16} ergs/°K, and h is the Planck constant 6.62×10^{-27} erg sec.

$$f_{peak} = 2\pi c^2 h \left(\frac{kT}{ch}\right)^5 \frac{x_m^5}{e^{x_m} - 1}$$

where

$$x_m = \frac{ch}{k \lambda_m T} = 4.965$$

(Reference [7]).

Equation (3.2) has been evaluated for s4, s5 Response, a Bolometer, and for the response of silicon and gallium arsenic photodiodes. The input data and results appear in Table III-4.

TABLE III-4

ENERGY INCIDENT ON THE SENSITIVE ELEMENT OF VARIOUS DETECTORS (1 INCH APERTURE)

Response	λ_1 Microns	λ_2 Microns	$\Delta\lambda$ Microns	f_{eff}, watts
s4	.3	.6	.1752	2.84×10^{-13}
s5	.2	.6	.2740	4.44×10^{-13}
Photo-Diode	.4	1.0	.1532	2.48×10^{-13}
Bolometer	0	∞	.4050	6.56×10^{-13}

$T = 11{,}000^\circ K$, Visual Magnitude 3

The last column of Table III- 4 gives the energy incident on the photodetector which is effective in producing an output signal when light from a third magnitude Type A star is collected with a one inch aperture optical system at 75 per cent efficiency.

Cd S is conspicuously absent from Table III- 4. Though it is competitive with a photomultiplier in its response to steady light, the response time to low light levels is of the order of seconds and thus could not be used in any system which used a rotating slit. If a platform which did not rotate were to be used, a mosaic of Cd S elements might be considered.

d. Sky Background

The sky background of faint stars [8]depends on galactic latitude and longitude, but averages 180 tenth magnitude stars per square degree. If these are assumed Vega type stars and a slit of $20^{\circ} \times 6'$ (Figure III-8) is used in the assumed optical system, the effective background reaching the detector is,

$$B_{eff} = 6.16 \times 10^{-12} \times .75 \times \left(\frac{2.54}{2}\right)^{2} \pi \times 10^{.04} \times 10^{-4} \times 2 \times 180$$

$$= 9.24 \times 10^{-13} \text{ watts.}$$

For s4 response,

$$B_{ave} = 16.3 \times 10^{-14} \text{ watts.}$$

For a given photodetector, the absolute minimum energy monochromatic signal which can be detected is that which causes a signal equal to the shot noise. This is (cf. [9]).

$$W_m^2 = 2\,\frac{(h\nu)^2}{q}\,\bar{n}\,\Delta f$$

where h is Planck's constant, ν is optical frequency, q is quantum efficiency, Δf is the electrical (as contrasted to optical) bandwidth, $\bar{n}$ is photon rate.

Of course,

$$\bar{n} = \frac{B_{ave}}{h\nu}$$

So that,

$$W_m^2 = \frac{2\,h\nu\,B_{ave}\,\Delta f}{q}$$

If we choose ν at the peak of the S_4 response, this becomes per cps.

$$W_{m1} = 30.2 \times 10^{-16}\ \text{watts/cps}^{\frac{1}{2}}$$

Since the device noise has not been included, it is conceivable that a photodetector could be limited by sky background, particularly for detection of stars weaker than third magnitude at fast scan rates.

e. Figure of Merit

A figure of merit often given for photodetectors is the "noise equivalent power per unit bandwidth" (N.E.P. or P_N) which is the input signal needed to give an output which is twice the noise, in a one cycle per second band. Since the noise contains contributions from both device and background, it is evident that measurement conditions must be specified in the evaluation of P_N. In addition, the noise from solid state detectors is frequency dependent. We shall use this figure of merit, and thus will need to find the required bandwidth of the associated electronics.

f. Electrical Bandwidth

The minimum signal which can be detected will depend on the electrical bandwidth of the detecting apparatus. This, in turn, will be set by the rise and fall times of the pulses due to star images traversed by the slit.

Let us assume that the stars "blur circle" is Gaussian and traverses the slit in three milliseconds. Recall that it was assumed that the arrival of photons formed a Poisson process. We now also assume that the optical envelop forms a blur circle whose intensity has a Gaussian distribution. This assumption is somewhat common in optical analysis, but, in truth, is difficult to justify. If the detecting system is not bandwidth limited, the signal in the time domain will be, for a narrow slit,

$$G(t) = \frac{1}{\sqrt{2\pi\sigma^2}} e^{-t^2/2\sigma^2} \tag{3.3}$$

The Fourier transform (spectrum) of (3.3) is

$$g(j\omega) = \sqrt{2}\, e^{-\sigma^2\omega^2/2}$$

The signal has fallen to 1/e in a time,

$$t = \pm\sqrt{2}\,\sigma \tag{3.4}$$

The response falls to 1/e at frequency,

$$\omega = \frac{\sqrt{2}}{\sigma} = \Delta\omega$$

From (3.4)

$$\Delta t = 2\sqrt{2}\,\sigma \tag{3.5}$$

and from (3.4)

$$\Delta\omega = 2\pi\ \Delta f = \frac{4}{\Delta t}$$

or the minimum necessary bandwidth is

$$\Delta f_{min} = \frac{2}{\pi\ \Delta t}$$

We double this to avoid any signal distortion and choose

$$\Delta f = \frac{4}{\pi\ \Delta t}$$

For $\Delta t = 3 \times 10^{-3}$ seconds, (typical duration in slit for Tiros and Nimbus)

$$\Delta f = 425 \text{ cps.}$$

g. Suitable Detectors

P_N is usually given in units of watts per cps½. We can now check whether a given device can be used simply by comparing the quantity.

$$p_N = P_N = \sqrt{425}\ P_N = 20.6\ P_N$$

with the f_{eff} in a table such as Table III- 4.

E.g., R. L. Williams [26] reports a silicon photodiode with

$$P_N = 1.8 \times 10^{-13} \text{ watts}$$

This diode using a 425 cps bandwidth can detect a signal of

$$p_N = 3.71 \times 10^{-12} \text{ watts}$$

and falls short by an order of magnitude in the required sensitivity.

It could just be used to detect a third magnitude Type A star if the aperture were increased to

$$D = \sqrt{\frac{37.1}{2.48}} = 3.87''$$

Here the signal to noise ratio would be unity.

There is no question that photomultipliers can be used. E.g., a 9502-S E.M.I. phototube with

$$P_N = 3.3 \times 10^{-17} \text{ watts/cps}^{\frac{1}{2}}$$

is available. Thus, in a 425 cycle band this can detect a signal of

$$p_N = 6.80 \times 10^{-16} \text{ watts}$$

With s4 response (see Table III-4) this power level with the assumed optical system corresponds to a 9.5 magnitude Type B star.

However, the necessary well regulated high voltage supply is a serious disadvantage of using the photomultiplier in space applications, and its elimination is desirable.

h. Use of Gas Phototube

G. Kron [27] has reported on the use of gas phototubes for infra-red photometry in the .8 micron region. (This region is at the peak of the s1 response.)

The principal sources of noise in a phototube will be the shot noise of the tube (which, in turn, depends on the convection current and the leakage conduction current) plus the Johnson noise of the load resistor.

If i_o be the tube current, σ be the gas multiplication factor and let the leakage current be neglected, (with care it can be made small), then R be the load resistor, the mean square fluctuation in the voltage to the first amplifier is,

$$\overline{v^2} = 2\ e\ i_o\ \sigma^2\ R^2\ \Delta f + 4\ k\ T\ R\ \Delta f$$

(see also reference [25]), where k is Boltzmann's constant, T is absolute temperature of the resistor, and e is the electronic charge.

The noise in the resistor exceeds the tube noise unless

$$R \geq \frac{2\ k\ T}{e\ \sigma^2\ i_o} \tag{3.6}$$

I.e., it is advantageous to have a large load resistor. E.g., if T is 300^oK, $i_o = 10^{-12}$ amp, and $\sigma = 1$ (vacuum photodiode) R must exceed 5000 megohms.

In our case, we will not want to make the time constant of the input circuit large enough to degrade the response. A 425 cycle three db. band in an RC filter implies a time constant

$$RC = \frac{1}{2\pi\ \Delta f} = 3.75 \times 10^{-4} \text{ sec.}$$

It is possible to reduce the input capacity, c, to about 5×10^{-12} fd. Thus, we can make R as large as

$$R = 75 \text{ megohms.}$$

If we take the f_{eff} from Table III-4 for an s4 response, the number of quanta incident on the photocell is

$$\bar{n} = \frac{f_{eff} \cdot \lambda}{hc} = 5.73 \times 10^{5}/\text{sec.}$$

At a quantum efficiency of 10 per cent, a signal current of,

$$i_s = e\, q\, \bar{n} = 9.18 \times 10^{-15} \text{ amps.}$$

results.

We temporarily neglect the gas amplification factor σ since it affects both signal and darkcurrent noise signal equally. The darkcurrent noise must not exceed the signal current. Thus,

$$i_s \gtrsim \sqrt{\overline{i^2}} = \sqrt{2\ e\ i_d\ \Delta f}$$

Or,

$$i_d \lesssim \frac{i_s^{\,2}}{2e\ \Delta f} = 6.20 \times 10^{-13} \text{ amp.}$$

This value can easily be obtained.

For efficient operation of the phototube we have by Equation (3.5)

$$\sigma^2 \gtrsim \frac{2k\ T}{e\ i_d\ R_L} = 1.111 \times 10^3$$

$$\sigma \gtrsim 33.3$$

Potassium hydride gas filled photocells have been successfully operated at gas multiplying factors of 50 without an increase in signal to noise ratio [28]. G. Kron [27] gives a design for a gas phototube which can be operated at gas multiplying factors up to 100.

Under the assumed conditions the signal voltage, due to a third magnitude Type A star, will be

$$i_s\ \sigma\ R = 9.18 \times 10^{-15} \times 33.3 \times 7.5 \times 10^7$$

$$= 22.9\ \mu\ \text{volts.}$$

At room temperature, the Johnson noise of the load resistor will amount to

$$\sqrt{\overline{v^2}} = \sqrt{4k\ T\ R\ \Delta f}$$

$$= \sqrt{4 \times 1.38 \times 10^{-23} \times 3 \times 10^2 \times 7.5 \times 10^7 \times 425}$$

$$= 23\ \mu\ \text{volts}$$

The following amplifier will add as much noise and the system is marginal. Indeed, shot noise = Johnson noise = "amplifier" noise = signal; S/N = 1/3!

However, improvement of signal to noise ratio by a factor 4 is possible by doubling the aperture. And further improvement can be had by cooling the load resistor. Indeed, the phototube and its associated circuitry may both be cooled to advantage [27]. This cooling might be simply done by insulating the detector from the rest of the vehicle and allowing the detector to radiate thermally to the 3.1°K space background. An additional factor of two increase in signal to noise can be had by using a photocathode with s5 response instead of s4 (see Table III-4).

It, thus, appears feasible to use gas phototubes as the light sensitive element. Internal sources of noise must be carefully suppressed. A 2" aperture at 75 per cent transmission may be necessary and it will be desirable to cool the load resistor and phototube.

The degradation of the cathode surface due to the cumulative effects of ion bombardment should also be considered. Use of the guard ring tubes of G. Kron [27] would greatly increase tube life besides allowing larger gas amplification factors.

i. Some Other Detectors

F. Low [29] has described a low temperature germanium bolometer, which appears "potentially competitive with phototubes". At a temperature of 7°K and if the conductivity to the surroundings was as low as 10^{-7} watts/°K this device has a noise equivalent power of

$$P_N = 3 \times 10^{-14} \text{ watts } /\text{cps}^{\frac{1}{2}}$$

Over a 425 cps band the minimum detectable energy flux into the 1" aperture system would be

$$p_N = 6.18 \times 10^{-13} \text{ watts}$$

Table III-IV gives for bolometers

$$f_{eff} = 6.56 \times 10^{-13} \text{ watts}$$

Thus this device would just suffice to detect a third magnitude star with the 1" aperture optical system visualized. It is true that Low calculates a time constant of .32 second for his device for these assumed conditions, but it is also likely that germanium bolometers with smaller time constants can be designed.

W. Franzen [30] describes a non-isothermal superconducting bolometer. A current passed through the sensitive element, which is an evaporated tin strip on a 1000 A^o thick Al_2O_3 substrate, heats the element enough to keep the center of the element above the superconducting transition. The ends are cooled below the transition. Incident radiation heating the element increases the length of element above the transition resulting in a resistance change. Franzen estimates that a noise equivalent power can be as low as

$$P_N = 2.8 \times 10^{-14} \text{ watts/cps}^{\frac{1}{2}}$$

The responsivity of this device is estimated to be of the order of

$$r \approx 10^3 \text{ volts/watt}$$

a very large value.

It is, however, yet but a laboratory device and to the authors knowledge has not yet been actually built.

The use of p-n junctions as both a photodetector and as a parametric amplifier has been suggested [31]. Modulated light falls on the diode as a pumping voltage is simultaneously applied. (cf. Figure III-30).

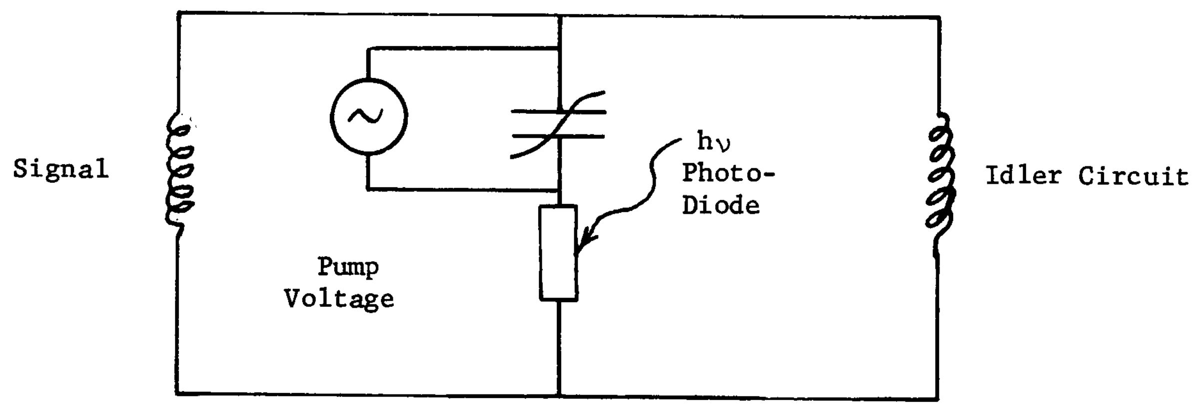

Figure III-30: Parametric Photo-Diode

The net gain here is that the noise contribution of the following amplifier is much reduced. Some discussion as to whether this arrangement is better than a photodiode followed by a parametric amplifier has occurred. [32], [33]. In any event, this does not improve the signal to noise ratio of the diode.

A more promising approach would seem to be the use of avalanche multiplication in a reverse biased photodiode. Current gains as large as a 1000 have been reported [34]. Di Domenico, et. al, [35] report a signal enhancement by 25 db when mixing modulated laser light with r.f. by means of a point contact Si photodiode operated near avalanche breakdown. They point out that this enhancement was obtained without an increase in the noise power and suggest the possibility of shot noise limited operation. Again, one should note that noiseless amplification does not improve the noise figure.

j. Detection of Type M_0 Stars

It may be recalled that the distribution of standard navigational stars in spectral class peaked at Type A_0 and Type M_0. We have discussed Type A_0, and now discuss Type M_0.

First, we need somehow to derive a value for f_{peak} watts/cm^2/μ for Type M_0 stars. This is conveniently done by means of the Planck distribution. We compare the value of the Planck function at wavelength 5550 Angstroms (the peak of the response of the eye) and 3600°K (Type M_0 star) to its value at 5550° and 11,000°K (Type A_0). The ratio of these values times the f_{peak} for Type A_0 gives an f_{peak} for Type M_0 stars.

I.e.,

$$\frac{f_{bb}\ (5550\overset{\circ}{A},\ 3,600^{\circ}K)}{f_{bb}(5550\overset{\circ}{A},\ 11,000^{\circ}K)}\ f_{peak}\ (A_{o}V,\ m_{v} = .04)$$

$$= f_{Peak}\ (M_{o},\ m_{v} = .04)$$

$$= \frac{7.58}{14.44} \times 6.16 \times 10^{-12}\ \text{watts/cm}^{2}/\mu$$

$$= 3.24 \times 10^{-12}\ \text{watts/cm}^{2}/\mu$$

For a bolometer, we have defined an effective optical bandwidth,

$$\Delta\lambda = \int_{0}^{\infty} f_{bb}\ (\lambda,\ T)\ d\lambda/f_{peak}$$

$$= \frac{\pi^{2}\ c\ h}{15\ k\ T}\ \frac{e^{x_{m}} - 1}{x_{m}^{5}}$$

If $T = 3600^{\circ}K$

$$\Delta\lambda = 1.253\ \mu\ \text{(microns)}$$

Thus, for a 1" aperture with 75 per cent transmission, a third magnitude star and a bolometer, the energy effective in producing an output is

$$f_{eff} = .75\left(\frac{2.54}{2}\right)^{2} \pi \times 10^{-.4(3.0\ -\ .04)} \times 3.24 \times 10^{-12} \times 1.253\ \text{watts}$$

$$= 1.068 \times 10^{-12}\ \text{watts}$$

If the electrical bandwidth is 425 cps. the noise equivalent power will be,

$$P_N = 5.18 \times 10^{-14} \text{ watts/cps}^{\frac{1}{2}}$$

The spectrum of Type M_0 stars peaks at about .80 micron, which is at about the peak of the PbS spectral response. We shall approximate the spectral response of PbS by a flat response between .5 and 3.3.

Allen [24] gives values of

$$\frac{\int_0^{\lambda} f_{bb}(\lambda, T)\, d\lambda}{\int_0^{\alpha} f_{bb}(\lambda, T)\, d\lambda} = \frac{F_o - \lambda}{F_o - \infty} = H(\lambda, T)$$

By means of which we find,

$$H(.5\ \mu, 3600^{\circ}K) = .0394$$

$$H(3.3\ \mu, 3600^{\circ}K) = .9142$$

Thus PbS is about 87.5 per cent as efficient as the bolometer for Type M_0 stars. The effective energy on the photoconductor (PbS) will be

$$f_{eff} = .875 \times 1.068 \times 10^{-12} \text{ watts}$$

$$= 9.33 \times 10^{-13} \text{ watts.}$$

Levy [36] has reported PbS operation at liquid N_2 temperature with a noise equivalent power of

$$P_n = 7.7 \times 10^{-14} \text{ watts/cps}^{\frac{1}{2}}$$

The noise power in a 425 cps band would be,

$$P_n = 1.59 \times 10^{-13} \text{ watts,}$$

a value which is somewhat less than f_{eff}. However, in PbS high sensitivity is usually obtained with a proportional increase in time constant.

k. Superiority of Photomultipliers Over Phototubes

Lallemand [37] has demonstrated the superiority of shot noise limited detectors to those limited by the input circuit to the electronics. The argument is specifically applied to photomultipliers versus phototubes, but will hold for any multiplying device as against its non-multiplying equivalent, e.g., gas phototube versus vacuum phototube, avalanche photodiode or parametric-amplifier photodiode as against simple photodiode.

The argument is worth repeating here. Let I_m be minimum signal detectable at signal to noise ratio S_n, for a photomultiplier and let I_p be the same quantity for a phototube. Then, if the photomultiplier is shot noise limited

$$I_m = S_n \sqrt{2\ e\ i_d\ \Delta f} \tag{3.7}$$

i_d = darkcurrent in amperes

$e = 1.602 \times 10^{-19}$ Coulombs = electronic charge

Δf = bandwidth, cps.

Assuming the phototube limited by the input circuitry,

$$I_p = S_n \sqrt{4\ k\ T\ \Delta f / R}$$

where T is in ^{o}K and R is the value of the input resistor in ohms.

Define a modulation factor by

$$\Gamma = \sqrt{2}\,\frac{I_m}{i_d} \tag{3.8}$$

Then (3.7) and (3.8) give

$$I_m = 2\sqrt{2}\; e\; S_n^{\;2}\; \Delta f/\Gamma$$

Then,

$$G = \frac{I_p}{I_m} = \frac{\Gamma}{S_n\; e}\sqrt{\frac{k\;T}{2R\;\Delta f}} \tag{3.9}$$

But R will inevitably be in shunt with some input capacity C which, indeed, sets the bandwidth as,

$$\Delta f = \frac{1}{2\pi\;R\;C} \tag{3.10}$$

The use of (3.9) in (3.10) leads to

$$G = \frac{\Gamma}{S_n\; e}\sqrt{\pi\;k\;T\;C}$$

which depends only on temperature T, capacity C, modulation factor Γ, and the signal to noise ratio S_n.

C can be as small as 5 pfd. Taking $T = 300^{o}K$, $S_n = 2$,

$G \approx 800\;\Gamma$

If $\Gamma = 1$, ($\sqrt{2}\, I_m = i_d$, a not unreasonable condition) G = 800. And the multiplier is almost three orders of magnitude better!

1. Conclusions

System should be based on detection of Type A and/or Type M stars. These are the most plentiful.

Of the available photodetectors, the photomultiplier is by far the best detector. Available cathode spectral response then limits us pretty well to Type A stars.

By careful design of the electronics, a gas phototube could probably be used, though it appears that detection of third magnitude stars with the detector at room temperature would require doubling the optical aperture (1" to 2"). Cooling the tube and input circuitry (by radiation into space), will increase the sensitivity. Considerations of photocathode life probably dictate a guard ring structure to protect the cathode as is done in thyratons. This would also provide a further gain in sensitivity by increasing the usable gas amplification factor.

If larger optical apertures (order of 4 to 6 inches) are not objectionable, Si or Ga As photodiodes may be used. Si back biased into an avalanche multiplying mode appears attractive, though the so-called "smooth" diodes must be used to avoid microplasma noise.

For detection of third magnitude Type M stars, PbS at liquid N_2 temperature is sufficiently sensitive, but this material probably has too long a time constant.

The general conclusion is that for the present and near future, the minimum aperture system demands a photomultiplier. Because of the severe weight and size limitations in the SCADS sensor, a minimum aperture system is essential.

For convenience, a list of the presently available better photomultipliers and their specifications is given in Table III-5. The SCADS application demands a ruggedized tube; non-ruggedized tubes are included in the list for the purposes of comparison. For various reasons indicated later in this section, the recommended tube (out of those presently available) for both the Tiros and Nimbus is 541A-01-14, manufactured by EMR.

TABLE III-5

SPECIFICATIONS OF THE BETTER PHOTOMULTIPLIERS AVAILABLE TODAY

EMI Photomultipliers

9514 S (not ruggedized)	
quantum efficiency (peak)	7.5%
darkcurrent equivalent photoelectron rate	304/sec.
spectral response	S
spectral correction factor	1
effective quantum efficiency	7.5%
photocathode size	
cathode diameter	1.75 inch
9514 B (not ruggedized)	
quantum efficiency (peak)	12.5 %
darkcurrent equivalent photoelectron rate	30400/sec.
spectral response	S-11
spectral correction factor	1
effective quantum efficiency	12.5%
photocathode size	
cathode diameter	1.75 inch

RCA Photomultipliers

1P21 (standard)	
quantum efficiency (peak)	10%
darkcurrent equivalent photoelectron rate	6330/sec.
spectral response	S-4
spectral correction factor	1
effective quantum efficiency	10%
photocathode size rectangular	.9375 x .3125 inch
1P21 (ruggedized)	
quantum efficiency (peak)	10%
darkcurrent equivalent photoelectron rate	405000/sec.
spectral response	S-4
spectral correction factor	1
effective quantum efficiency	10%
Photocathode size	
C70114 (ruggedized)	
quantum efficiency (peak)	12%
darkcurrent equivalent photoelectron rate	7,300,000/sec.
spectral response	S-11
spectral correction factor	1.00
effective quantum efficiency	12%
photocathode size minimum window diameter	1.24 inch
C70113A (ruggedized)	
quantum efficiency (peak)	12%
darkcurrent equivalent photoelectron rate	128000/sec.
spectral response	S-11
spectral correction factor	1.00
effective quantum efficiency	12%
photocathode size minimum window diameter	1.24 inch

EMR Photomultipliers

541D-01-14 (ruggedized)	
quantum efficiency (peak)	6%
darkcurrent equivalent photoelectron rate	35.6/sec.
spectral response	$.38\mu$ - $.52\mu$
spectral correction factor	.472
effective quantum efficiency	2.8%
photocathode size useful cathode diameter	1 inch
541A-01-14 (ruggedized)	
quantum efficiency (peak)	15%
darkcurrent equivalent photoelectron rate	2540/sec.
spectral response	S-4
spectral correction factor	1
effective quantum efficiency	15%
photocathode size useful cathode diameter	1 inch
541B-03	
quantum efficiency	23%
darkcurrent equivalent photoelectron rate	4870/sec.
spectral response	$.22\mu$ - $.68\mu$
spectral correction factor	1.59
effective quantum efficiency	36.6%
photocathode size active cathode diameter	.39 inch

ITT Photomultipliers

F4027	
quantum efficiency (peak)	12%
darkcurrent equivalent photoelectron rate	6340/sec.
spectral response	S-20
spectral correction factor	1.22
effective quantum efficiency	15%
photocathode size maximum usable diameter	.250 inch
FW-130	
quantum efficiency (peak)	12%
darkcurrent equivalent photoelectron rate	9900/sec.
spectral response	S-20
spectral correction factor	1.22
effective quantum efficiency	15%
photocathode size maximum usable diameter	.75 inch

D. Packaging Considerations

The SCADS electronics will be comprised of a mixture of integrated circuits and discrete components. A modular packaging concept should be employed with discrete components and integrated packages mounted on 1/32 inch thick epoxy-glass printed circuit boards. The printed circuit boards can then be joined by pin connectors to a printed circuit mother board which supports the electrical interconnections between individual circuit boards.

Printed circuit layouts must be performed to achieve as high a component packing density as is consistent with easy assembly considerations. Completed printed circuit boards should be individually mountable on the mother board to permit easy assembly and checkout. Some packaging concepts such as the cordwood concept (the mounting of components between two printed circuit boards) can cause excessive assembly and checkout time.

All circuit boards with mounted components should be conformal potted with epoxy after assembly and checkout to provide increased mechanical rigidity.

To insure optimum performance of the photomultiplier, it is essential that the tube be both magnetically and electrostatically shielded. It is recommended that the photomultiplier be shielded with two metal layers, each separated by a thin insulated layer. The inner metal layer should be a high mu metal while the outside layer should be a lower mu metal. The overall attenuation of two such insulated layers is known to be greater than the shielding possible with a single equivalent shield.

The preamplifier following the photomultiplier should be placed as close to the photomultiplier anode as is practical to reduce induced noise in the photomultiplier output signal lead. In addition, each low level amplifier and filter circuit module should be individually shielded to reduce induced noise due to radiation and coupling from high level circuits. Also, all low level signal interconnecting leads must be carefully isolated from high level and digital leads to reduce induced noise coupling into the low level signal leads.

The DC-DC inverter oscillator frequency should be picked high enough (30 kc to 60 kc) so the transformer size can be held to a minimum. The complete inverter module should be both magnetic and electrostatic shielded with RF chokes connected internally to all input-output leads to reduce radiated and induced noise in the low level circuits from the inverter square wave oscillator. Any components in the inverter (or elsewhere) dissipating relatively large amounts of heat must be positioned so the heat is dissipated to the case wall of the instrument.

Figure III-31 shows a three dimensional sketch of the packaging configuration for the Nimbus SCADS instrument. The layout for the various electronic functions is also illustrated. These functions were arranged with regard to the electronic packing considerations already discussed. The envelope dimensions of the package are 3.5" x 4" x 8". This amounts to a volume of 112 cubic inches with a small additional protrusion for the objective lens assembly which will fit into the outside panel of the satellite.

Since the Tiros instrument does not require a motor, motor drive and angle encoder, the volume of the Tiros instrument can be at least 20 $in.^3$ less than the volume of the Nimbus instrument. This could mean a reduction in one or all three of the envelope dimensions. For example, the 3.5 inch dimension might be reduced by 0.5 inch. Figure III-32 shows a three dimensional sketch

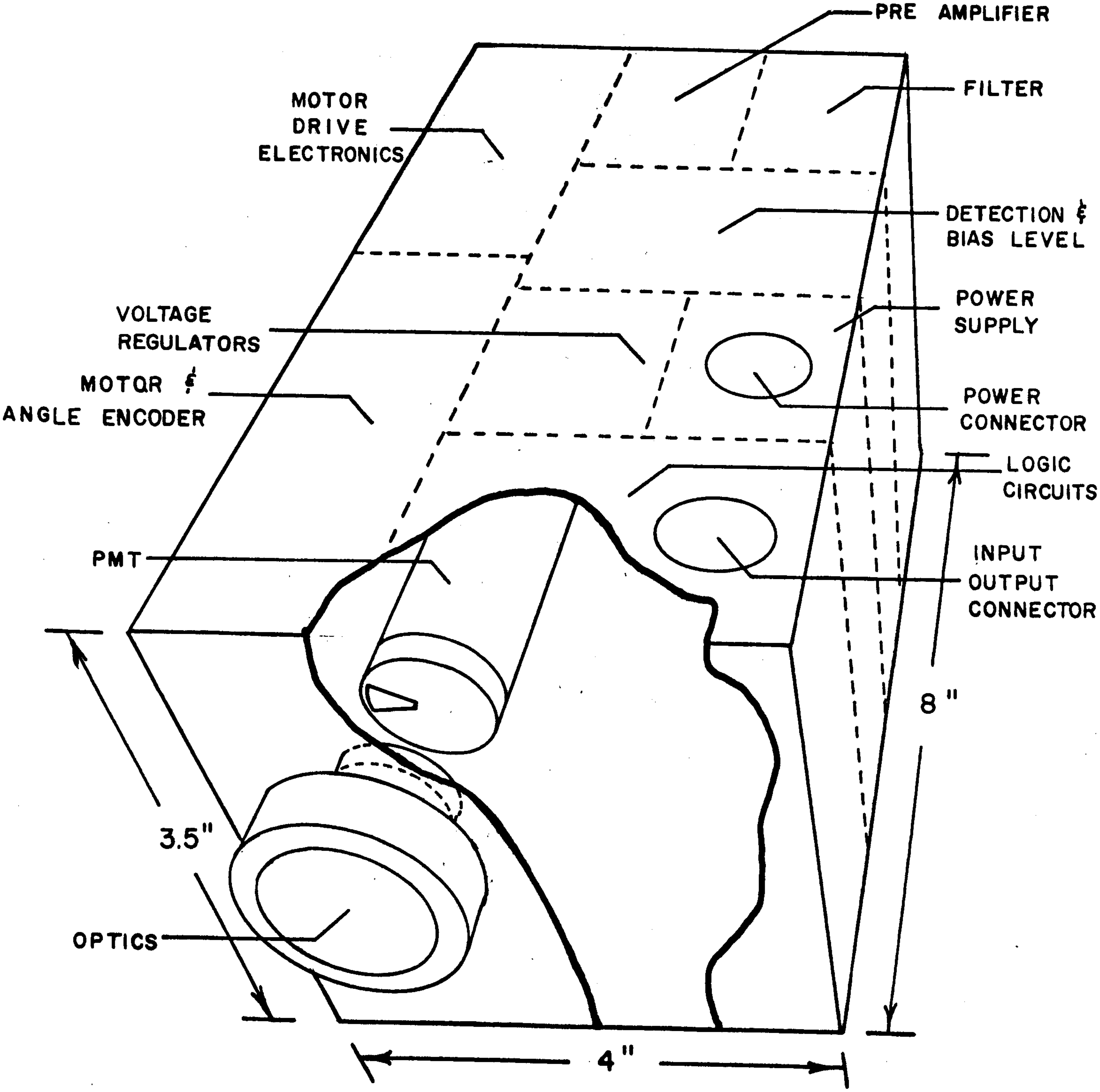

Figure III-31: Packaging Configuration for Nimbus

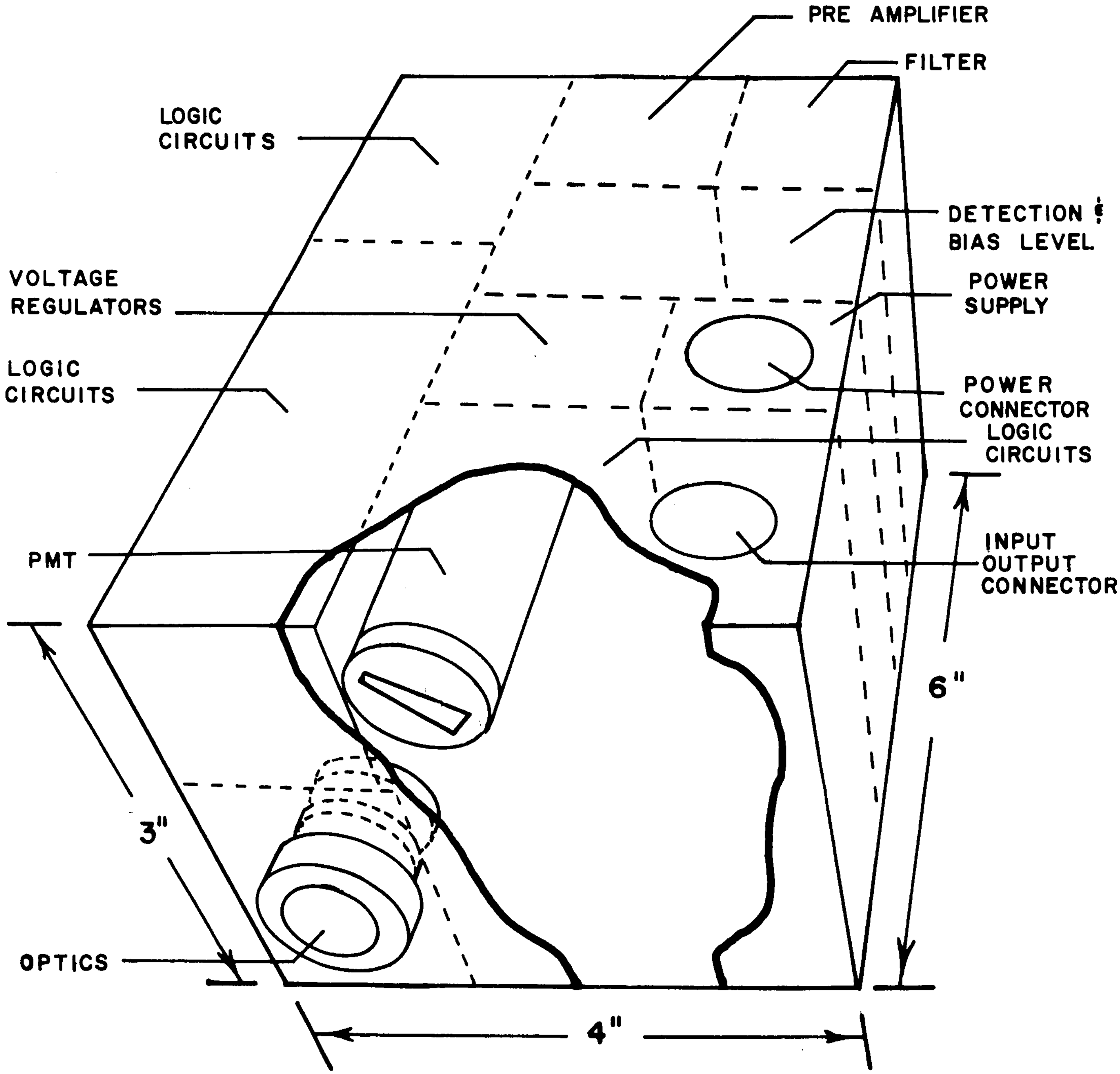

Figure III-32: Packaging Configuration for Tiros of the packaging configuration for the Tiros SCADS instrument.

The external case housing and framework should be constructed of sturdy lightweight material such as aluminum or an aluminum alloy. The thickness of the outside panels should be about .030 inch thick. There are approximately 150 in.^{2} of panel space, so the base case will weigh approximately

$$150 \times 3 \times 10^{-3} \text{ in.}^3 \times 168.5 \frac{\text{lbs.}}{\text{ft.}^3} \times \frac{\text{ft.}^3}{1728 \text{ in.}^3} = .439 \text{ lb.}$$

Figure III-33 shows a chart of estimated power, weight, and volume for the SCADS electronic functions. Total power, volume, and weight are given for both the Tiros and Nimbus electronics. The weight totals must be increased by the weight of the optics and the weight of the case. It is estimated that the optics will weigh approximately one pound, so approximately 1.0 + 0.5 lbs. must be added to the weight totals in Figure III-33.

Figure III-33 shows that the Nimbus electronics requires only 45 in.^{3}, while the case dimensions provide 8" x 4" x 3.5" = 112 in.^{3}. The remaining volume must contain the connectors, wiring harness, optics, and miscellaneous mounting hardware. A similar statement can be made for the Tiros instrument.

Summarizing the estimated power, dimensions, and weight for the SCADS instrument, we have:

Nimbus

Power	20 watts
Dimensions	3.5 x 4 x 8 inches
Weight	4.5 pounds

Tiros

Power	5.7 watts
Dimensions	3 x 4 x 6 inches
Weight	2.9 pounds

Figure III-33: Chart of Estimated Power, Weight, and Volume for SCADS Electronics

	Power	Volume	Weight
Operational Amplifier	120 mw	.03 in^3	1 gram
Signal Preamplifier	100 mw	.10 in^3	3 grams
Schmitt Trigger	30 mw	.01 in^3	1 gram
Monostable, Negative Trigger	50 mw	.03 in^3	1 gram
Monostable, Positive Trigger	50 mw	.03 in^3	1 gram
Bandpass Filter	250 mw	1. in^3	15 grams
Decode Matrix	120 mw	.5 in^3	15 grams
Bias Command Register	100 mw	.02 in^3	1 gram
Exit Angle Gate	70 mw	.5 in^3	15 grams
Entry Angle Gate	70 mw	.5 in^3	15 grams
Exit Angle Register Entry Angle Register	700 mw	.2 in^3	30 grams
Input Register	125 mw	.03 in^3	5 grams
Command Gate	20 mw	.2 in^3	4 grams
Start/Stop Command Decoder	25 mw	.15 in^3	5 grams
Power Gate	50 mw	.10 in^3	5 grams
Photomultiplier EMR 541A-10-14	10 mw	20 in^3	8 oz.
Tiros and Nimbus Sub-total	1890 mw	23.4 in^3	12 oz.
Motor and Motor Drive	5000 mw	1. in^3	8 oz.
Angle Encoder	5000 mw	18 in^3	8 oz.
Nimbus Sub-total	11890 mw	42.4 in^3	2.5 lbs.

	Power	Volume	Weight
DC-DC Inverter Inverter Voltage Regulators	Assume 60% efficiency	2.6 in^3	8 oz.
Nimbus Totals	$\frac{11.89}{.6} \cong 20$ watts	45 in^3	3 lbs.
Binary Clock (Counter)	1500 mwatts	.5 in^3	2 oz.
Tiros Sub-total	3390 mw	23.9 in^3	14 oz.
DC-DC Inverter Voltage Regulators	Assume 60% efficiency	2.6 in^3	8 oz.
Tiros Totals	$\frac{3390}{.6} = 5.7$ watts	26.5 in^3	$\frac{22}{16} \cong 1.4$ lbs.

Figure III- 34: SCADS Power Tabulation for Integration with Tiros Tape Recorder

	Power (milliwatts)
Operational Amplifier	120
Signal Preamplifier	100
Schmitt Trigger	30
Band Pass Filter	250
Decode Matrix	120
Input Register	125
Command Gate	20
Power Gate	25
Photomultiplier	10
Differentiator	120
Zero Crossing Detector	120
Pulse Generator	50
Analog Gate	20
Clock and Frequency Divider	+500
	1610 Sub-total
2.5 watts where power supply efficiency = 60% =	$\frac{1.610}{.6}$ Total

E. Environment Considerations

The environment which the SCADS sensor must withstand is rather severe. The most important environmental factors are acceleration, radiation, high vacuum, and meteoroid hazards. Each factor could represent a fairly complete study in itself. Our discussion here will be brief.

1. Acceleration and Vibration

The single most critical component of the sensor in its ability to withstand acceleration and vibration, is the photomultiplier. The launch environment necessitates the use of a ruggedized photomultiplier. These components have been tested and can withstand as much as 45 g's. Hence, the ruggedized component will operate even after a solid fuel launch.

For the rest of the sensor, the severe acceleration and vibration to which the instrument will be subjected represents a factor of primary importance to the designer. However, no problems are expected in this area, which cannot be solved by standard design practices and high quality workmanship.

2. Radiation

Hughes scientists [22] have conducted an extensive series of tests on the Canopus-Sun sensor of the Surveyor spacecraft. The effects of the Van Allen belts were simulated with a 120 milli-curie Sr^{90} source. Held against the sensor case, this provided a Beta ray source which was estimated to be several times as intense in its effects on the photomultiplier as the more energetic outer Van Allen belt. The effects were minimal. Though the background noise increased by 300 percent, it remained well below the level of the signal expected from Canopus.

It was concluded that an additional millimeter thickness of Al would reduce the net generated noise by a factor of three. Thus, the photomultiplier will probably not be seriously affected by the radiation due to electrons and ions trapped in the earth's magnetic field.

It remains to consider the rest of the circuitry. This will consist of evaluation of the effects of space radiation on the semiconductors of which the component transistors and diodes are made.

First of all, γ rays are weakly absorbed in Si and Ge. Thus, their effects will be minimal. Secondly, any degradation of the device must come from radiation induced changes in the electronic band structure of the semiconductors involved, which will come about by the creation of additional lattice defects. These defects must come about as the result of momentum exchange. The large mass difference between electrons and lattice stones means even M.E.V. electrons cannot create lattice defects. Conservation of mass and momentum cannot occur simultaneously in this case. Therefore, β rays will cause no permanent damage, though circuit operation may be disrupted momentarily.

However, energetic ions bombarding the circuitry can cause trouble. They are massive enough to exchange momentum with the lattice atoms and displace them.

The major source of energetic ions will be the high energy protons in the Van Allen belts. There appear to be two intensity peaks in the flux of

40 to 110 M.E.V. protons, associated with the Van Allen belts located roughly 1.5 and 2.2 earth radii above the magnetic equator [23]. The flux of protons observed has been as high as 1.5 x 10^4/cm^2/sec and has fallen to 2.3 x 10^3/cm^2/sec at 1/4 earth radii.

The Van Allen belts extend between about $\pm$ 30° magnetic latitude. If a satellite is in a 1000 mile polar orbit, it will then spend 1/6 of its time in a proton flux of about 2.3 x 10^3/cm^2/sec. Assuming each incident proton produces a lattice defect, (recombination center) the number of defects produced in four years will be about,

$$2.3 \times 10^3 \times 4 \times 1/6 \times 365 \times 24 \times 3600/\text{cm}^3 \approx 5 \times 10^{10}/\text{cm}^3.$$

Since the normal impurity doping densities are of the order of 10^{18}/cm^3, it is not expected that this amount of radiation will cause appreciable damage.

It is also worth while to note that the use of components with minimum junction size consistent with the application will minimize radiation damage from any source [24].

3. High Vacuum

Most metals and alloys are quite stable in space at normal operating temperatures. However, cadmium, zinc, and magnesium may cause trouble. Jaffe and Rittenhouse [25] feel these metals could sublime and redeposit on a cooler surface. This effect may cause shorts in the SCADS sensor. Hence, these metals should be avoided in the design. Glass causes no problem.

The Tiros application produces no lubrication problems, for there are no moving parts necessary in the SCADS sensor for this application. For the

Nimbus application a rotation mask must be provided. Gears must also be used. The torques required will be extremely small and the rate is not very great. For such applications, Clauss [26] highly recommends plastics. These materials can be machined quite accurately, and have a coefficient of friction lower than any other solid. No lubrication is required if plastics are used. Many other solutions of the problem are possible; these possibilities are discussed by Clauss.

4. Meteoroid Hazards

The lens of the SCADS sensor is of principal concern when the meteoroid hazard is considered. Micrometeoroid erosion in glass is very difficult to estimate, for no laboratory experience has been obtained with particles of this size impacting at escape-velocity speeds. Many theories exist predicting negligible to complete erosion, Beard [27].

Attempting to evaluate the effects of meteoroids on optical lenses is extremely difficult without making actual tests. Items that must be considered are abrading or pitting, chipping, and actual fracture. Small meteoroids would be responsible for the abrading, pitting, and chipping; depending upon the mass, velocity, and angle of impact with the lens causing a gradual deterioration of light transmission and optical resolution approximately proportional to the lens surface affected. Chipping would cause an additional effect of creating undesirable internal reflections and refractions whose magnitude would be dependent upon the exact shape, location, and orientation of the chipped surface. Fracture, of course, will generally destroy the lens.

Since some information is available on the penetration of aluminum sheets by meteorites, a first approximation of the probability of fracture of the lens may be made from this data. It is a characteristic of glass that it always breaks under a tensile stress which arises in the system, even though it fails under an applied compressive force. If it is assumed that aluminum fractures under impact in a similar manner, the ratio of their tensile strengths would give a measure to use for calculating the probability of fracture due to a meteoroid impact. This ratio gives the figure that glass is approximately 1/4 as resistant to penetration or fracture as is aluminum. If we use these estimates and the penetration curves for aluminum given in [28], and assume a lens of 10 in^2 area, then the expected number of penetrations of a 1/4 inch lens in three years is between 4×10^{-3} and .4.

It is possible to put a quartz window in front of the lens. Quartz is about twelve times harder than glass, and hence, the life of the lens will be prolonged.

We may also note that the SCADS sensor is less likely to sustain damage than the television cameras, for the SCADS lens will be smaller.

F. Protection for Sun, Earth, and Moon Radiation

If the sun or earth reflected sunlight were to enter the field of view of the SCADS, an excessive amount of current would be drawn from the photomultiplier. Permanent damage would undoubtedly result. However, the field of view was chosen so that the sun and earth would never fall within the field of view under normal operation of the instrument.

For a 500nm orbit, the earth with its clouds should never come closer than six degrees from the field of view, the safety factor is greater for higher altitude orbits (see Figure III-3). Since the orbit is sun-synchronous, the sun should never be closer than 65 degrees from the field of view. Hence, radiation from the sun and reflected radiation from the earth should present no problem during normal orbital operation. If the stated safety factors are not great enough, a shutter system could be provided, which will automatically block off high intensity radiation.

Even though direct sun and earth radiation should not enter the field of view during normal operation, a baffle system in front of the lens may be necessary. This system would protect the sensor from light reflected from other parts of the satellite. Also, a shutter may be necessary to protect the instrument during the launch. This shutter would be removed after the satellite was placed in orbit.

The moon will enter the field of view. From Figure III-4 we note that the moon will lie in the field of view for roughly 42 days per year. However, moon reflected radiation will not damage the instrument. If the moon does enter the field of view, the recovery time of the photomultiplier will probably be greater than the spin period. Hence, no data can be obtained, and the instrument will not operate during these 42 days. If this feature is objectionable, an electronic shutter could be provided to block the moon's reflected radiation during the part of the scan the moon is in the field of view.

Under the normal mode of operation the sun will not be in the scanned field of view. As a safety measure, however, we believe that a sun shutter may be justified. Such a shutter would take the form of that shown in Figure III-35. A panel of silicon solar cells is mounted interior to the optical system in front of the focal surface such that the sun's image is defocussed when it impinges on the solar cells.

In order to provide a fail-safe operational mode it is planned that the power generated by the sun will be used to actuate the shutter. This shutter is a long filament-like element which is spring mounted and electrostatically deflected. (A magnetic shutter actuator creates a danger of affecting the photomultiplier and, therefore, is not recommended.) By placing this filament immediately in front of the slit it can be made very small, typically about 1/20 inch wide. The physical translation necessary to place the shutter in front of the slit is about the same amount. The response of the deflection system need not be fast, since the field of view of the optical system is twenty degrees and the scan period is two to six seconds. Typically, a response time of 0.01 to 0.1 second will be adequate.

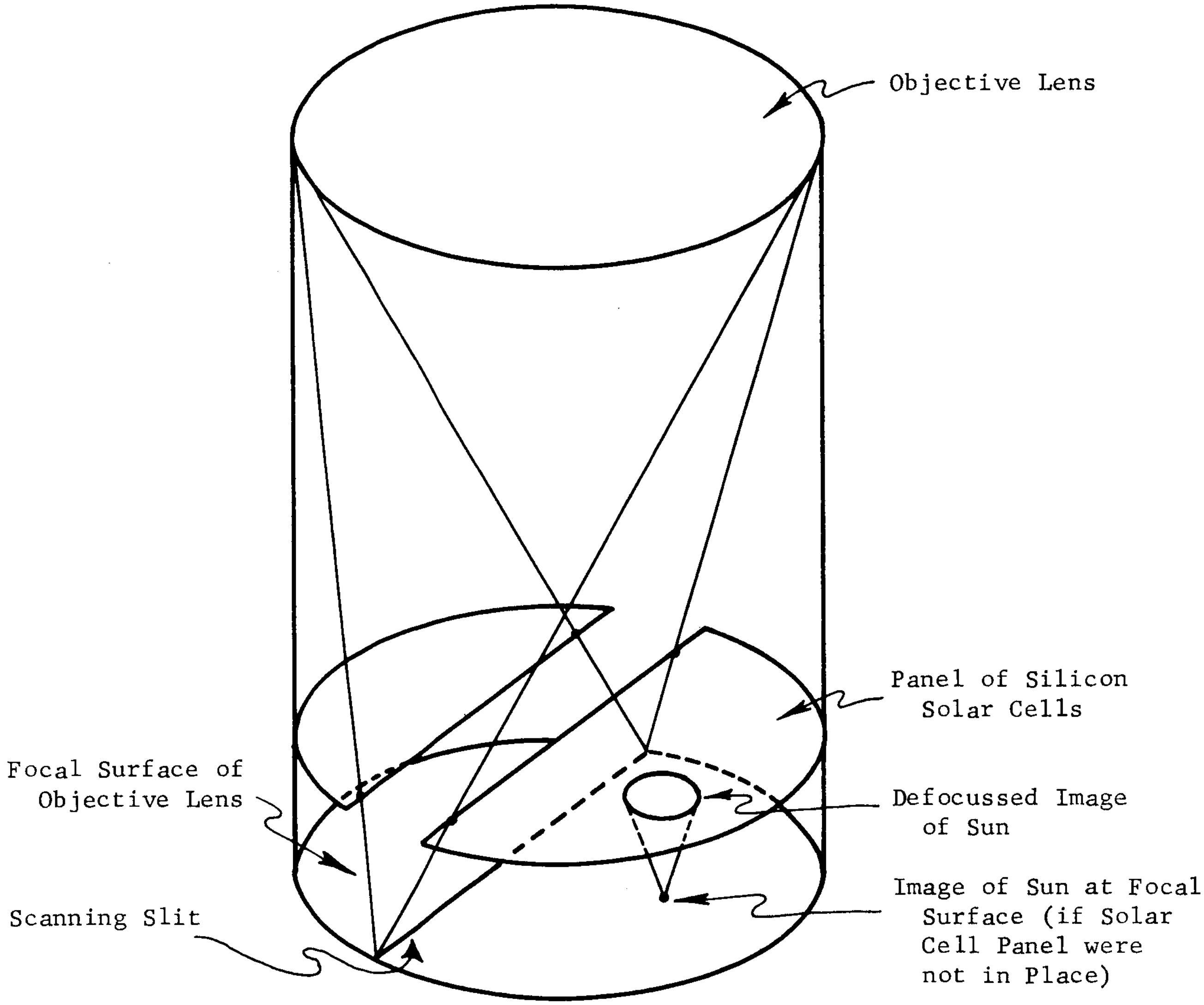

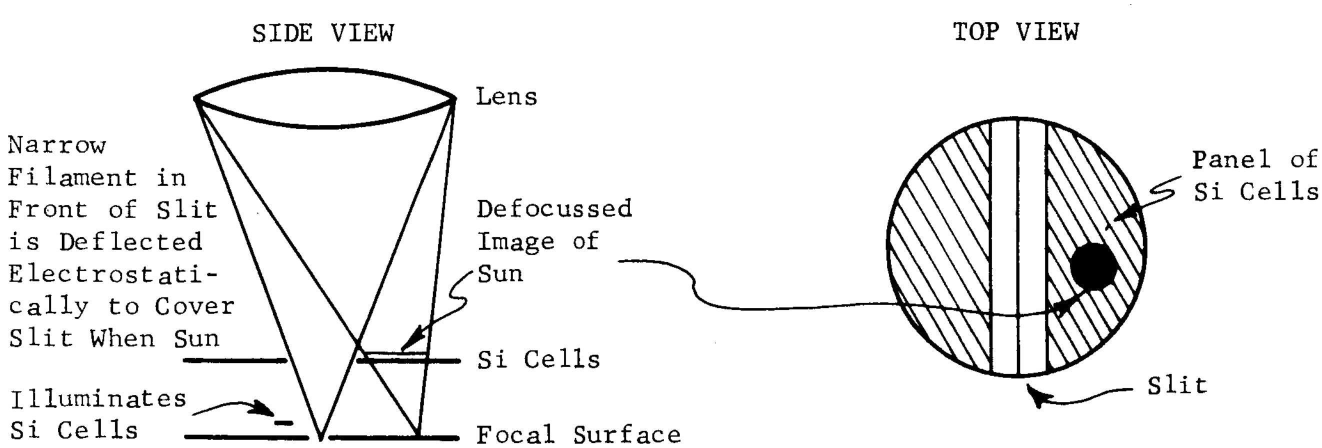

Figure III-35: Design of Electrostatically Actuated Sun Shutter

IV. MATHEMATICAL ANALYSIS

The purpose of this section is to obtain a workable solution to the problem of finding the orientation from the output of the SOADS Sensor. The analysis that follows is general in that no specific slit configuration is assumed. Before we attack the problem, let us consider the assumptions to be made as to the laws governing the orientation motion.

A. Physical Assumptions

1. Tiros

We assume that the Tiros satellite is a rigid body, torque-free, has two equal moments of inertia, and is spinning nearly about the third axis. In a qualitative manner, let us now consider the approximations implied by this assumption.

The satellite is not rigid. On board are tape records which move with respect to the rest of the satellite. Also on board is a liquid precession and nutation damper. However, during the period for which we intend to take measurements, this damper is expected to be more or less inactive.

Torque is incurred by the spacecraft due to the following sources:

(1) gravity gradient,

(2) magnetic field interaction with eddy current moments,

(3) magnetic field interaction with ferromagnetic materials,

(4) drag due to air, microscopic dust,

(5) solar radiation pressure.

Considerable analysis has been applied to the problem of predicting the long term effects of the torques (1), (2), and (3). Little, if any, results are available as to the effects of the torques (4) and (5).

The most general treatment of motion of a rigid satellite requires six second-order differential equations to describe the motion. It is usually assumed that these equations separate into three equations which describe the motion of the center of mass, and three which describe the orientation about the center of mass. The latter three equations have time variant parameters due to the position motion. This separation is only a good first approximation, for indeed the orientation motion of a satellite does perturbate the position motion of the center of mass for a non-spherical satellite.

Naumann [29] shows that the dominant torque-producing forces are (3), the magnetic field interaction with ferromagnetic materials. The gravity gradient torques, (1), are quite small in comparison. These results apply to Explorers IV, VII, VIII, and XI, which are spin stabilized satellites. Bandeen and Manger [30] arrive at similar results for the Tiros I satellite. In a theoretical study, Smith [31] showed that the effect of the magnetically induced eddy-current torques is primarily to reduce the spin rate. For the Tiros I, the observed effect [32] was a decrement from 10.0 rpm on April 1 to 9.4 rpm on May 27.

The general conclusion is that the torques (1), (2), and (3) produce a motion of the spin axis on the order of 3° to 5° per day. Most of this motion is due to magnetic effects.

For the Tiros, the effect (2) is reduced or eliminated by an attitude bias coil which is adjusted so as to neutralize the residual electric field of the spacecraft [1].

The general conclusion is that we assume Tiros is a rigid, torque-free body with two nearly equal moments. This assumption is only an approximation and no real analysis has been done by CDC to justify this assumption. Such analysis would constitute a complicated problem and could only be done if the satellite parameters were completely specified. It does appear that the errors in this assumption are small and it may be relied upon for time durations on the order of one or two hours.

2. Nimbus

The sensor is to be spun and the spin axis is perpendicular to the orbital plane (Figure V-1). The field of view of the sensor may be exactly the same as that of the Tiros. We will assume the sensor is spinning about a single fixed axis at a constant rate. We know that this assumption is only an approximation for the pitch rate will not be constant; also, roll and yaw motion will exist. The angular rates of orientation motion will be controlled to roughly $\pm .07^{\circ}$ per second for pitch, $\pm .1^{\circ}$ per second for yaw, and $\pm .06^{\circ}$ per second for roll. If the sensor is spun for a period of two to three seconds, these rates contribute negligible errors (see Section V-B-1).

3. Manual Solution

For both Tiros and Nimbus, the manual solution will rely upon the assumption of uniform spin motion about a single axis. Additional approximations will be made to reduce the problem to a planar one.

B. Orientation of a Torque-Free Body by Use of Star Transits (Tiros)

The general problem is to find the orientation as a function of time, t, of a system fixed in a spinning torque-free body. This orientation must be

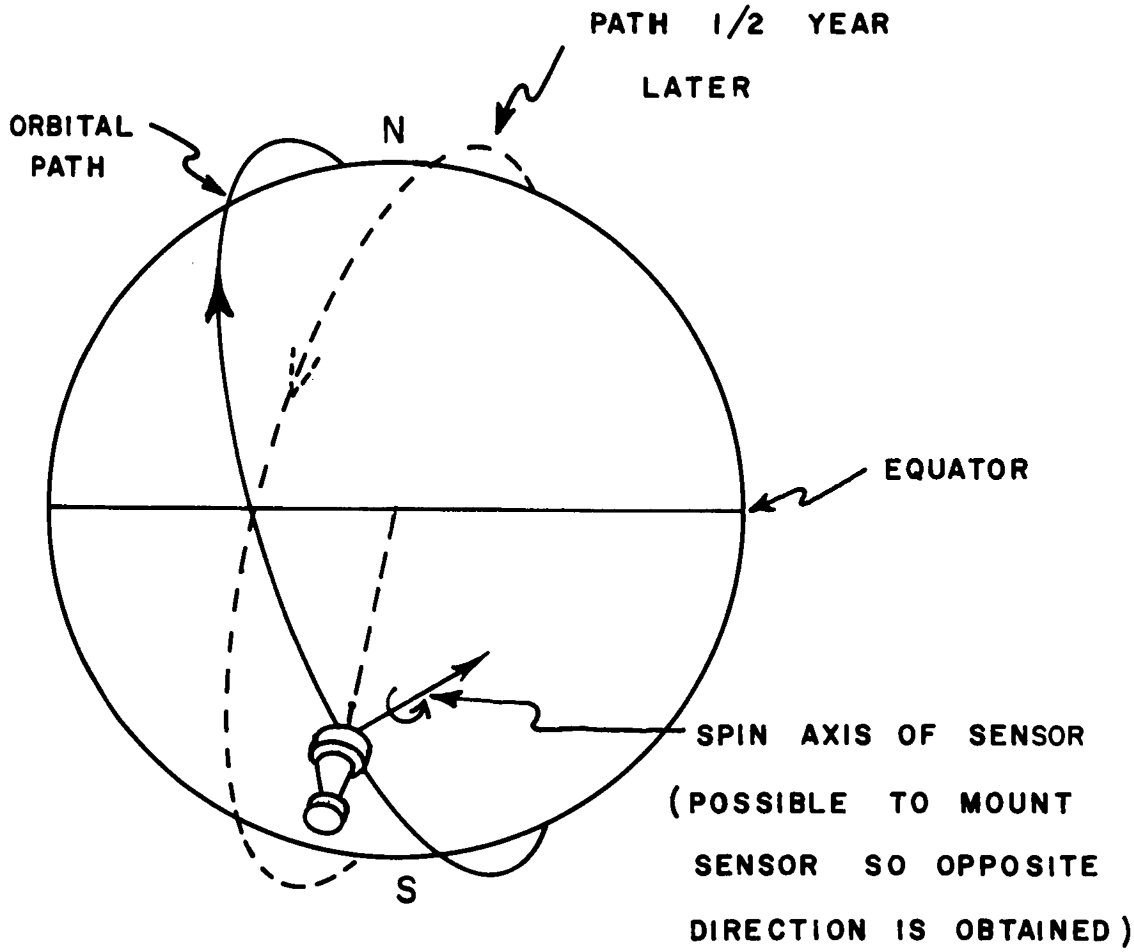

Figure IV-1: Relation of Sensor Spin Axis to Nimbus Orbit found with respect to the celestial system. The system fixed in the body, S_6, has axes parallel to the principal axes of the body.

The basic measurements which must be used to furnish this orientation are the times at which known stars lie in a plane(s) which contain the origin of S_6. This plane(s) is fixed with respect to S_6, and its equation(s) in S_6 is given. Physically, such a plane(s) (or portion of a plane(s)) is generated by an optical system which contains a slit(s), the optical system being fixed in the body. Because of the association of slits to the mechanization of the optical system, we will call these planes "slit-planes".

Before we attack the main problem, however, let us consider the salient features of the orientation motion of a rigid torque-free body. This is a classical problem in analytical dynamics (see e.g., Goldstein [33]); a discussion is included here for convenience.

1. Description of Motion

For a rigid torque-free body, the angular momentum vector is constant. Hence, an inertia system may be defined with one axis along the angular momentum vector and two other axes perpendicular to it. We will call this system S_3. Consider another coordinate system, S_6, oriented along the principal axes of the body. The orientation of these body fixed axes can be defined by three angles, θ, ϕ, and ψ. In general, these angles are functions of time (Figure IV-2). The angle θ may be called the cone angle (some authors use nutation angle) and is the angle from the angular momentum vector to the figure axis of the body. The angle ϕ is sometimes called the precession angle and measures the azimuth (see Figure IV-2) of the figure axis with

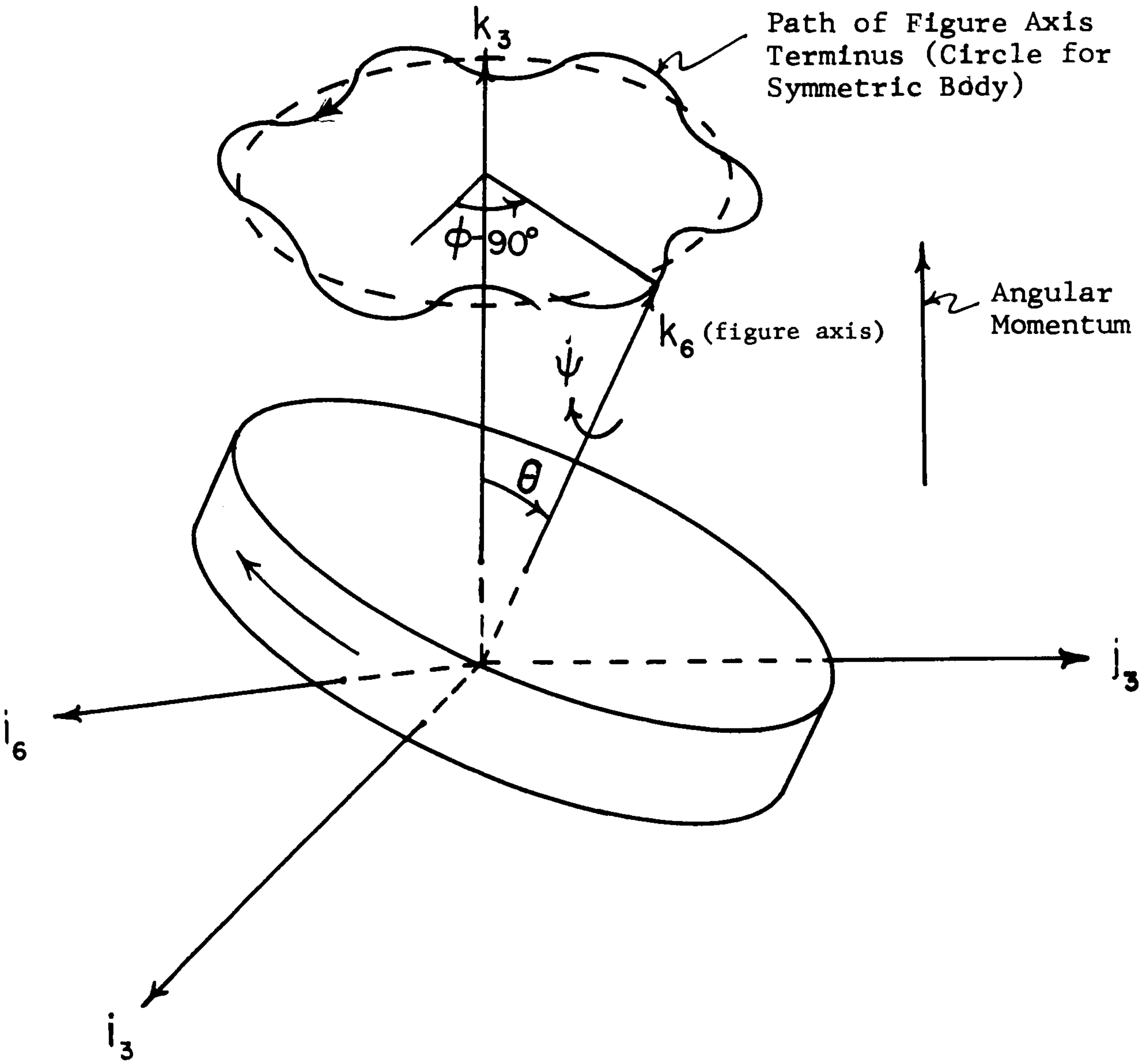

Figure IV-2: Motion of a Body Fixed System (Unsymmetric Body) with Respect to Momentum System (Inertial) respect to S_3 (the inertial system). Finally, ψ is called the spin angle and is a measure of the orientation of the body about its figure, or longitudinal, axis. The terms precession and nutation are often introduced into the discussion. A variation of ϕ is called precession while a variation of θ is called nutation.

We will now list some of the more important results for the general case.

(1) If the body is symmetric, or more precisely, has two equal moments of inertia, then θ = constant (i.e., no nutation), $\dot{\phi}$ = constant, and $\dot{\psi}$ = constant.

(2) If the body is rod-like, then $\dot{\psi}$ and $\dot{\phi}$ have the same sign. If it is disc-like (as is Tiros) then $\dot{\psi}$ and $\dot{\phi}$ have opposite signs.

(3) The only axes that the body can spin about, so that its angular velocity vector is constant, are the three principal axes.

(4) If the body has three unequal moments and is spinning about a principal axis, then this motion is unstable if this is an intermediate axis; otherwise, the motion is stable.

(5) The general problem of finding θ, ϕ, and ψ as a function of t and initial conditions can be solved in closed form. This solution is in terms of Jacobian elliptic functions.

(6) θ, ϕ, and ψ are periodic functions of t, but the periods can be incommensurable so the motion as a whole may be non-periodic.

Details of the motion of a nearly symmetric body are given in Appendix B. In Figure IV-3 is graphed the ratio $-\dot{\phi}/\dot{\psi}$ as a function of θ for the Tiros. From this graph we see that if $\dot{\psi}$ = 1 rad/sec, and $\theta = 30^{\circ}$ then $\dot{\phi}$ = - 2.9 rad/sec.

From Figure IV-4 we may note the effect of precession on the time between successive transits of the same star. Two cases are shown in this figure. One star is 4° from the angular momentum vector ($\rho = 4^{\circ}$) and the other is 21° ($\rho = 21^{\circ}$). For this figure, $\theta = .3^{\circ}$ and a radial slit is assumed. Note that if the Tiros satellite were to spin about a single axis ($\theta = 0^{\circ}$), then $t_{i+1} - t_i$ = constant, where t_i is the time of the i^{th} transit. In Figure IV-4,

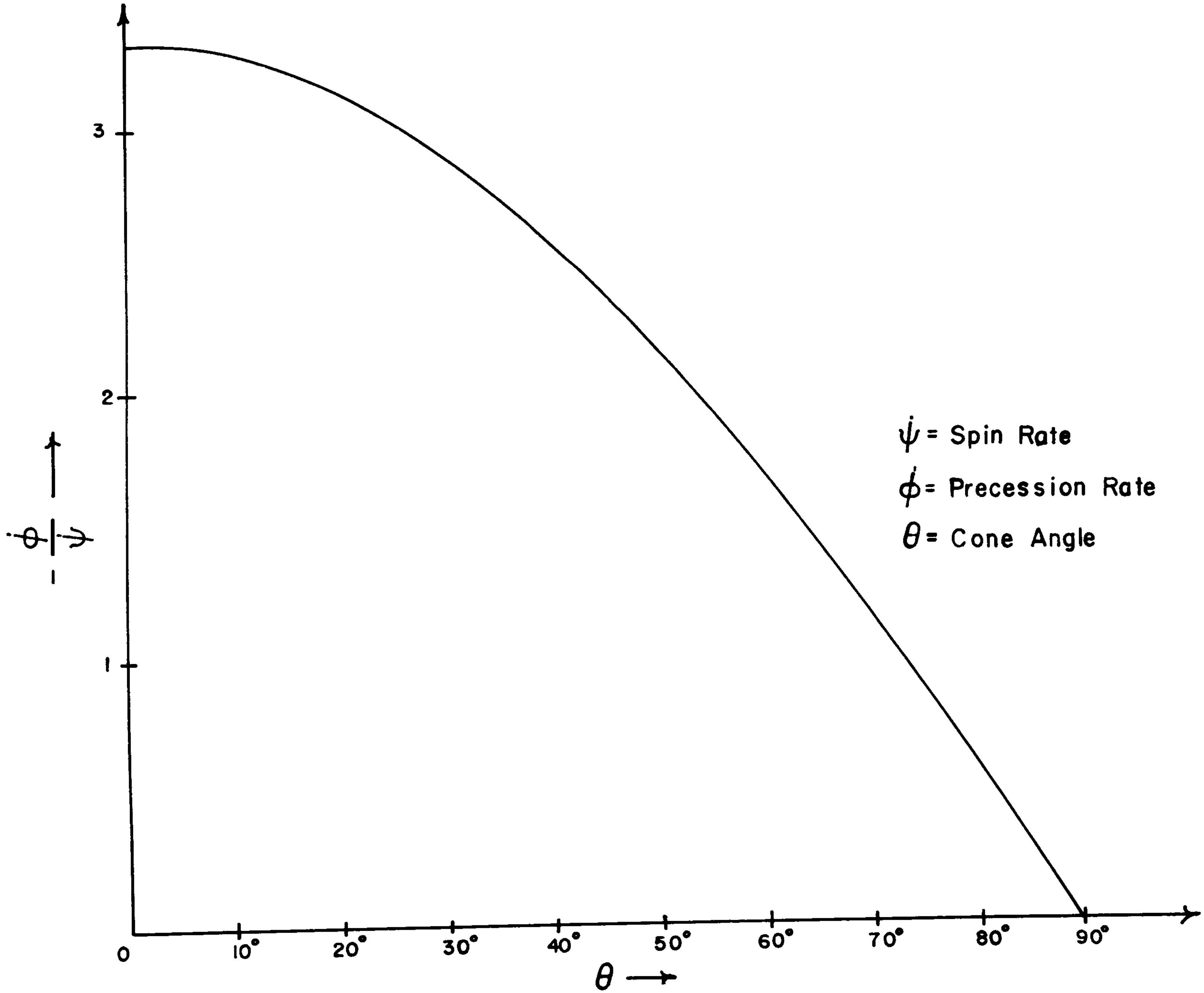

Figure IV-3: The Ratio - $\dot{\phi}/\dot{\psi}$ as a Function of θ for Tiros

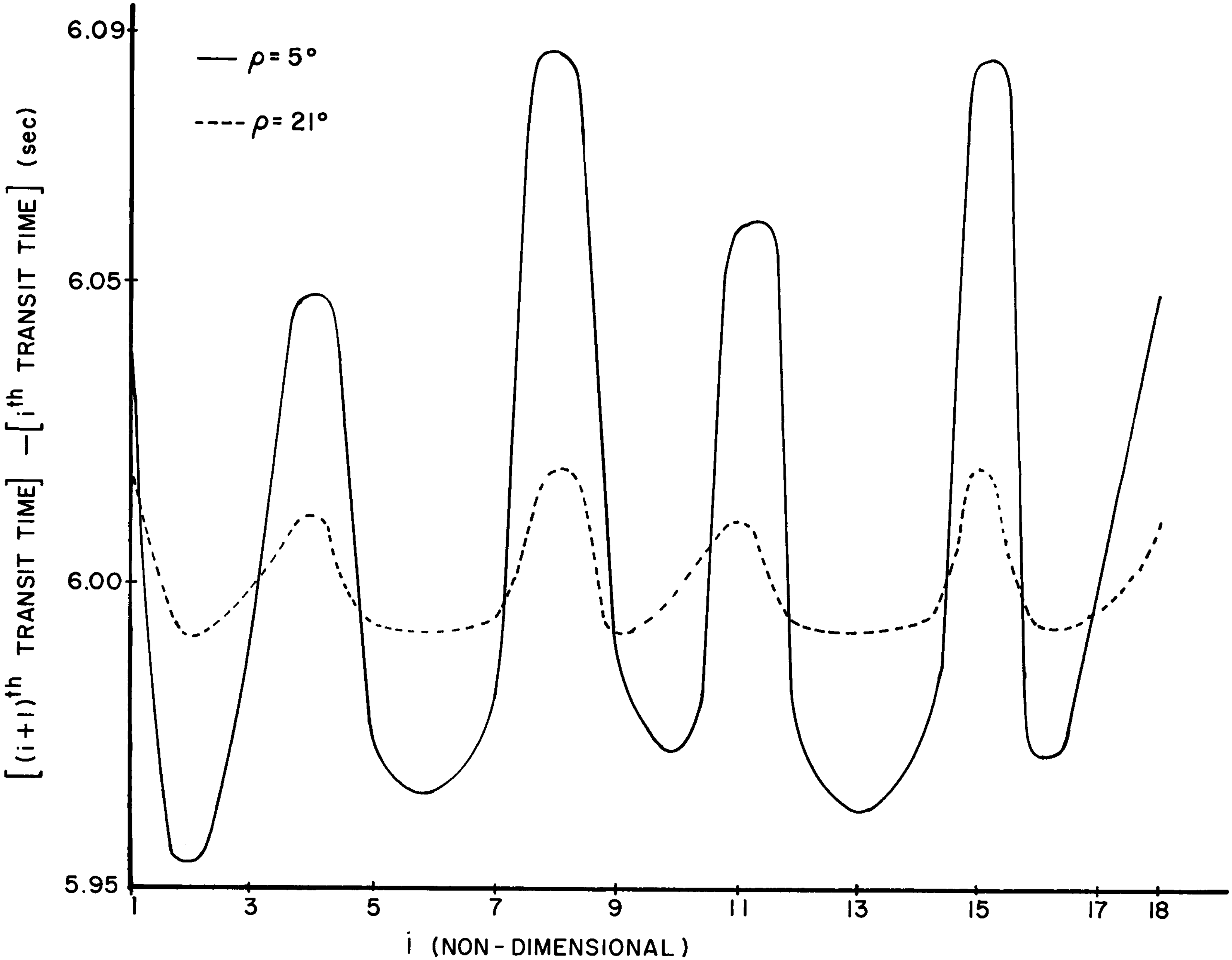

Figure IV-4: Time Between Successive Star Transits for Tiros Precessional Motion $\theta = .3^{\circ}$ (Two Cases) we see the $t_{i+1} - t_i$ is not a constant due to the precessional motion of the satellite.

We now attack the main problem. A method of solution as well as a computer program for obtaining the solution has been written by Control Data Corporation under a contract with NASA Langley (Contract No. NAS1-4646).

2. Coordinate System

In order to describe the orientation of a system fixed in the body with respect to the celestial system, three angles are sufficient. However, these three angles would be a somewhat complicated function of time. The classical method used to overcome this difficulty is to introduce five angles. Hence, six coordinate systems, S_i, are introduced with unit vectors $\hat{i}_i$, $\hat{j}_i$, and $\hat{k}_i$, $i = 1, 2, \ldots, 6$. Let, (Figures IV-5 and IV-6),

S_1 be the celestial system with associated unit vectors $\hat{i}_1$, $\hat{j}_1$, $\hat{k}_1$; $\hat{i}_1$ in the direction of the First Point of Aries, $\hat{j}_1$ in the equatorial plane, and $\hat{k}_1$ in the direction of the North celestial pole,

S_3 be an initial system defined with respect to S_1 by two angles, ξ and τ. $\hat{k}_3$ is parallel to the angular momentum vector of the body.

S_6 be a system fixed in the body with unit vectors $\hat{i}_6$, $\hat{j}_6$, and $\hat{k}_6$ parallel to the principal axis of the body. S_6 is defined with respect to S_3 by the angles ϕ, θ, and ψ.

The angles ξ, τ, ϕ, ψ, and ψ will be defined as follows:

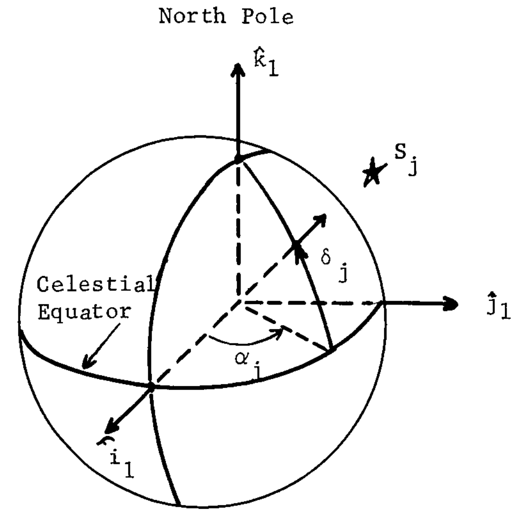

(a) The Coordinate System S_1

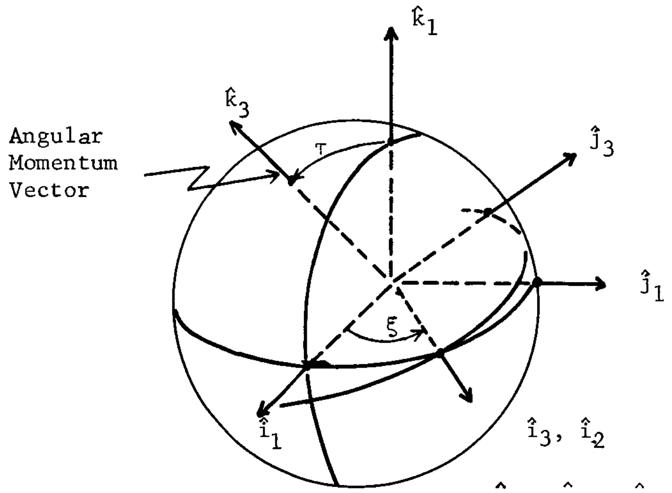

(b) The Systems S_2 and S_3 ($\hat{k}_2 = \hat{k}_1$), $\hat{j}_2$ not shown

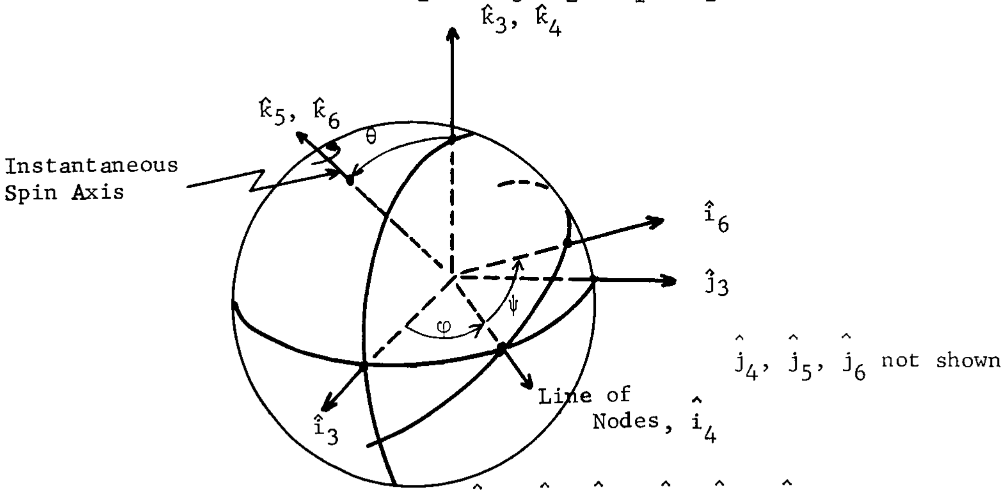

(c) The Systems S_4, S_5, and S_6 ($\hat{k}_4 = \hat{k}_3$, $\hat{i}_5 = \hat{i}_4$, $\hat{k}_6 = \hat{k}_5$)

Figure IV-5: Relations Between Various Coordinate Systems

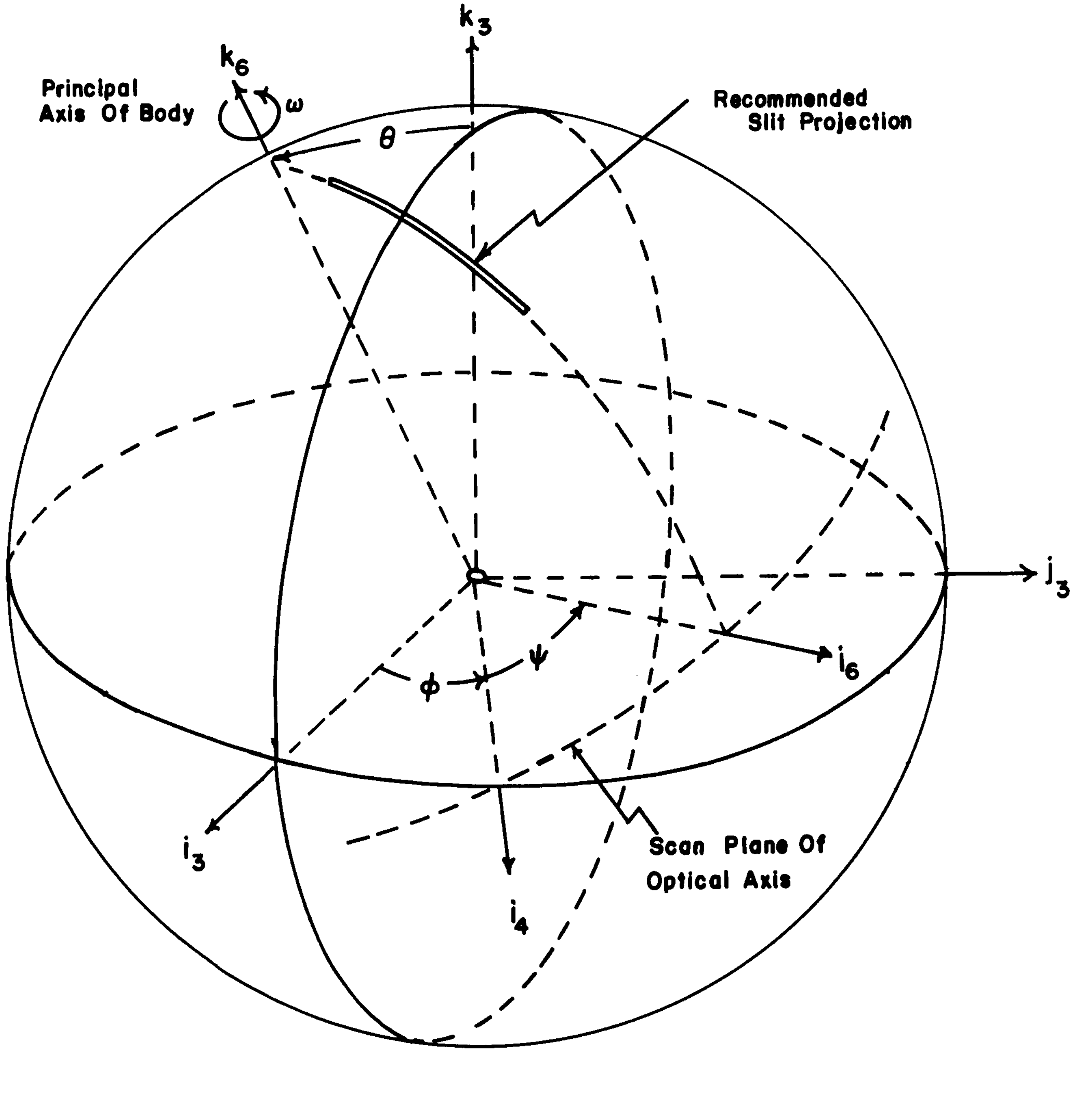

Figure IV-6: Relationship of Body Fixed Reference System to Angular Momentum Frame

$\hat{i}_1 \to \hat{i}_2$ rotation ξ about $\hat{k}_1, \hat{k}_2$
$\hat{k}_2 \to \hat{k}_3$ rotation τ about $\hat{i}_2, \hat{i}_3$
$\hat{i}_3 \to \hat{i}_4$ rotation ϕ about $\hat{i}_3, \hat{i}_4$
$\hat{k}_4 \to \hat{k}_5$ rotation θ about $\hat{i}_4, \hat{i}_5$
$\hat{i}_5 \to \hat{i}_6$ rotation ψ about $\hat{k}_5, \hat{k}_6$

Hence, ξ = constant

τ = constant

and if the moments of inertia about the principal axis parallel to $\hat{i}_6$ and $\hat{j}_6$ are equal (A = B), then

$\phi = \phi_o + \dot{\phi}t$, $\dot{\phi}$ constant

θ = constant

$\psi = \psi_o + \dot{\psi}t$, $\dot{\psi}$ constant

where

$\dot{\phi} = d/A$

$\dot{\psi} = d\,\frac{A-C}{AC}\cos\theta$

d = magnitude of the angular momentum

A = B = moments of inertia about the principal axis parallel to $\hat{i}_6$ and $\hat{j}_6$

C = moment of inertia about the third principal axis.

For the main part of our discussion, we assume A = B. Later, we will show the errors caused by this assumption if $C \neq A \doteq B \neq C$, and small θ.

3. Constraint Equations

If we consider the moments of inertia, A and C to be known, then the problem may be formulated as that of seeking the six unknowns, ξ, τ, ϕ_o, θ, ψ_o, and d.

However, if A and C are unknown, or poorly known, then the problem may be formulated in terms of the seven unknowns, θ, ξ, τ, ϕ_o, $\dot{\phi}$, ψ_o, and $\dot{\psi}$. We will concentrate on the second formulation; the change to the first will then be obvious.

We will now develop an equation which is satisfied the instant a known star is in a slit. This equation is an algebraic equation in the seven unknowns of the problem.

First of all, the transformation from S_1 to S_6 may be written

$$\begin{pmatrix} \hat{i}_6 \\ \hat{j}_6 \\ \hat{k}_6 \end{pmatrix} = E\ H \begin{pmatrix} \hat{i}_1 \\ \hat{j}_1 \\ \hat{k}_1 \end{pmatrix}$$

Where E is the Euler matrix

$$E = \begin{pmatrix} \cos\psi\cos\phi - \cos\theta\sin\phi\sin\psi & \cos\psi\sin\phi + \cos\theta\cos\phi\sin\psi & \sin\psi\sin\theta \\ -\sin\psi\cos\phi - \cos\theta\sin\phi\cos\psi & -\sin\psi\sin\phi + \cos\theta\cos\phi\cos\psi & \cos\psi\sin\theta \\ \sin\theta\sin\phi & -\sin\theta\cos\phi & \cos\theta \end{pmatrix}$$

and

$$H = \begin{pmatrix} \cos\xi & \sin\xi & o \\ -\cos\tau\sin\xi & \cos\tau\cos\xi & \sin\tau \\ \sin\tau\sin\xi & -\sin\tau\cos\xi & \cos\tau \end{pmatrix}$$

The slit-plane may be defined with respect to S_6 by two angles γ' and β' (Figure IV-7). Let $\hat{i}_7$ be in the $(\hat{i}_6, \hat{j}_6)$ plane and also in the slit-plane. Let $\hat{j}_7$ be perpendicular to the slit-plane. Then,

$$\begin{pmatrix} \hat{i}_7 \\ \hat{j}_7 \\ \hat{k}_7 \end{pmatrix} = A \begin{pmatrix} \hat{i}_6 \\ \hat{j}_6 \\ \hat{k}_6 \end{pmatrix}$$

where

$$A = \begin{pmatrix} \cos\gamma' & \sin\gamma' & o \\ -\sin\gamma'\cos\beta' & \cos\gamma'\cos\beta' & \sin\beta' \\ \sin\gamma'\sin\beta' & -\cos\gamma'\sin\beta' & \cos\beta' \end{pmatrix}$$

γ' and β' are known quantities.

Now, the instant a star lies in the slit-plane (which is moving with respect to S_1) its position with respect to S_7 may be determined by a single parameter η, hence,

$$\hat{S} = \cos\eta\,\hat{i}_7 + o + \sin\eta\,\hat{k}_7$$

where $\hat{S}$ is a unit vector in the direction of the star. Moreover, $\hat{S}$ may be defined with respect to S_1 in terms of the declination and right ascension of the star. Hence,

$$\hat{S} = \cos\delta_j\cos\alpha_j\hat{i}_1 + \cos\delta_j\sin\alpha_j\hat{j}_1 + \sin\delta_j\hat{k}_1 \qquad (4.1)$$

where δ_j = declination of the j^{th} star (given)

α_j = right ascension of the j^{th} star (given).

Thus, the instant a star is in the slit-plane,

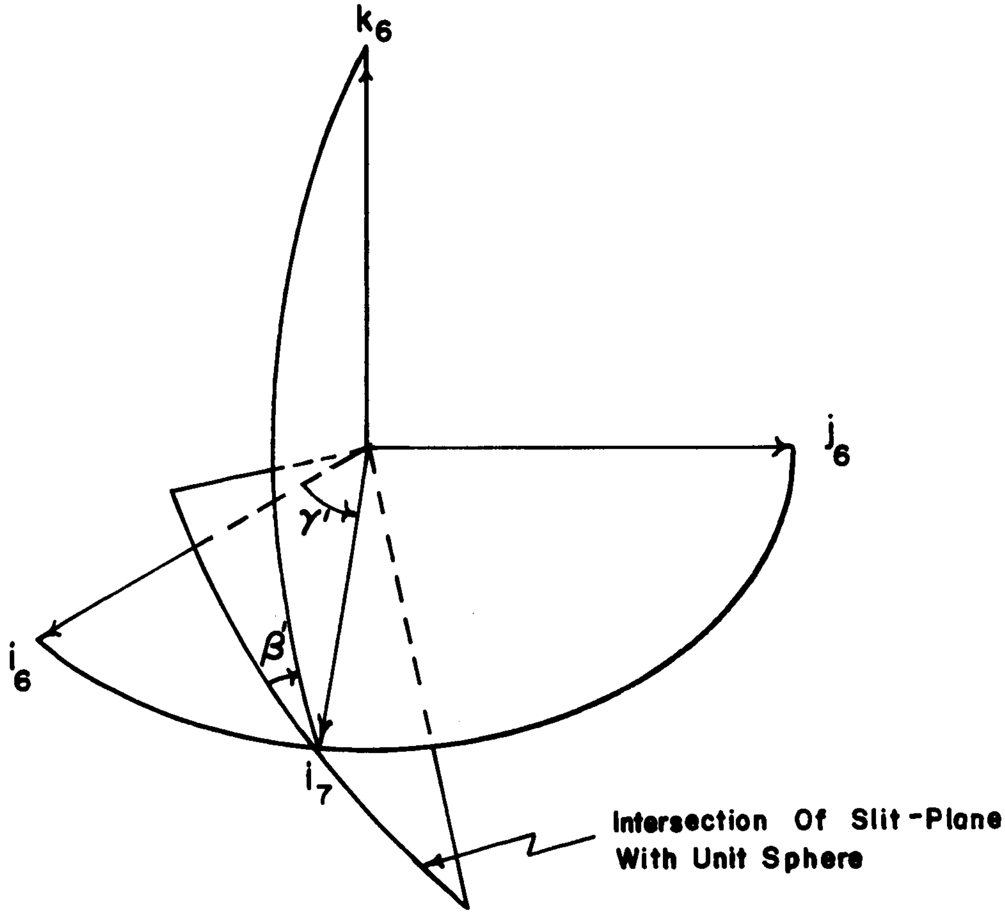

Figure IV-7: Orientation of Slit-Plane With Respect to S_6 (General)

$$\begin{pmatrix} \cos\eta \\ o \\ \sin\eta \end{pmatrix} = A\,E\,H\,\hat{S} \qquad (4.2)$$

where $\hat{S}$ has components in S_1 as given by (4.1). We may eliminate the parameter η from (4.2) to obtain

$$0 = A_2\,E\,H\,\hat{S} \qquad (43)$$

where A_2 is the second row of A.

Equation (4.3) is thus the basic constraint equation which must be satisfied the instant a star is in the slit-plane. Each time measurement thus supplies one equation in seven unknowns of the form (4.3).

4. Method of Solution

Each transit time of a known star across a slit-plane furnishes a trans-endental Equation (4.3) in the seven unknowns

$$\bar{X} = \begin{pmatrix} x_1 \\ x_2 \\ \cdot \\ \cdot \\ \cdot \\ x_7 \end{pmatrix} = \begin{pmatrix} \theta \\ \psi_o \\ \dot{\psi} \\ \phi_o \\ \dot{\phi} \\ \xi \\ \tau \end{pmatrix}$$

One method of attempting to solve such a system is the Newton-Raphson method.

To this end, let

$$\bar{X} = \bar{X}_o + \Delta\bar{X}$$

where $\bar{X}_o$ is a guess as to $\bar{X}$, then an approximate equation for $\Delta\bar{X}$ is

$$0 = A_2 \; E \; H \; \hat{S} + \nabla(A_2 \; E \; H \; \hat{S})\Delta\bar{X} \tag{4.4}$$

In (4.4) ∇ is the seventh dimensional gradient operator, also E and H are evaluated at $\bar{X}_o$. Since (4.4) is only an approximate equation for $\Delta\bar{X}$, an iterative method of solution must be used. If more equations than unknowns are present, a least squared solution may be used.

Solution for Small θ

If the initial guess is such that $\theta_o \equiv \chi_1^{(0)} = 0$, then the matrix coefficient of $\Delta\bar{X}$ has rand five, and thus $\Delta\bar{X}$ can not be determined from a system of equations of the type (4.4). For small θ, this system of equations can not accurately be solved for $\Delta\bar{X}$ without special attention. The physical reason for this fact is that for small θ the intersection of the plane determined by $(\hat{i}_6, \hat{j}_6)$ with $(\hat{i}_3, \hat{j}_3)$ is poorly defined. Analytically, this difficulty appears since we may write

$$E\;(\phi,\;\theta,\;\psi) = R\;(\phi + \psi) + \sin\theta\; S\;(\phi,\;\psi) + (1 - \cos\theta)\; T\;(\phi,\;\psi)$$

where

$$R = \begin{vmatrix} \cos(\psi+\phi) & \sin(\psi+\phi) & o \\ -\sin(\psi+\phi) & \cos(\psi+\phi) & o \\ o & o & 1 \end{vmatrix}$$

$$S = \begin{pmatrix} 0 & 0 & \sin\psi \\ 0 & 0 & \cos\psi \\ \sin\phi & -\cos\phi & 0 \end{pmatrix}$$

$$T = \begin{pmatrix} \sin\phi\sin\psi & -\cos\phi\sin\psi & 0 \\ \sin\phi\cos\psi & -\cos\phi\cos\psi & 0 \\ 0 & 0 & -1 \end{pmatrix}$$

So,

$$\frac{\partial E}{\partial \psi_o} = E_{\psi_o} = R_{\psi} + \sin\theta\, S_{\psi} + (1 - \cos\theta)\, T_{\psi}$$

$$E_{\psi} = t\, E_{\psi_o}$$

$$E_{\phi_o} = R_{\psi} + \sin\theta\, S_{\phi} + (1 - \cos\theta)\, T_{\phi}$$

$$\doteq E_{\psi_o}, \text{ small } \theta$$

$$E_{\phi} = t\, E_{\phi_o} \doteq E_{\psi}, \ \theta \text{ small}$$

Thus the matrix coefficient of $\Delta\overline{X}$ has two pairs of columns approximately equal (θ small).

To overcome this difficulty we may solve for a new variable, $\Delta\overline{Y}$, instead of $\Delta\overline{X}$. We choose

$$\Delta\overline{Y} = \begin{pmatrix} \Delta\theta \\ \Delta\phi_o + \Delta\psi_o \\ \Delta\dot{\phi} + \Delta\dot{\psi} \\ \Delta\xi \\ \Delta\tau \\ 2 \sin\frac{\theta}{2}\,\Delta\phi_o \\ 2 \sin\frac{\theta}{2}\,\Delta\dot{\phi} \end{pmatrix}$$

In terms of this new variable, (4.4) becomes

$$0 = A_2 \; E \; H \; \hat{S} + \overline{V}' \; \Delta\overline{Y} \qquad (\text{' represents transpose}) \tag{4.5}$$

where

$$\overline{V} = \begin{pmatrix} A_2 \; (\cos\theta_o \; S + \sin\theta_o \; T) \; H \; \hat{S} \\ A_2 \; (R_\psi + \sin\theta_o \; S_\psi + (1 - \cos\theta_o) \; T_\psi) \; H \; \hat{S} \\ t \; A_2 \; (R_\psi + \sin\theta_o \; S_\psi + (1 - \cos\theta_o) \; T_\psi) \; H \; \hat{S} \\ A_2 \; E \; H_\xi \; \hat{S} \\ A_2 \; E \; H_\tau \; \hat{S} \\ A_2 \; (\cos\frac{\theta}{2} \; (S_\phi - S_\psi) + \sin\frac{\theta}{2} \; (T_\phi - T_\psi)) \; H \; \hat{S} \\ t \; A_2 \; (\cos\frac{\theta}{2} \; (S_\phi - S_\psi) + \sin\frac{\theta}{2} \; (T_\phi - T_\psi)) \; H \; \hat{S} \end{pmatrix}$$

Each observation then furnishes an equation in $\Delta\overline{Y}$. This system of equations does not possess a singularity for small θ_o. After finding $\Delta\overline{Y}$, $\overline{X}$ is found by

$$\overline{X} = \overline{X}_o + \begin{vmatrix} \Delta y_1 \\ \Delta y_2 - \dfrac{\Delta y_6}{2 \sin \frac{\theta_o}{2}} \\ \Delta y_3 - \dfrac{\Delta y_7}{2 \sin \frac{\theta_o}{2}} \\ \dfrac{\Delta y_6}{2 \sin \frac{\theta_o}{2}} \\ \dfrac{\Delta y_7}{2 \sin \frac{\theta_o}{2}} \\ \Delta y_4 \\ \Delta y_5 \end{vmatrix} , \quad | \theta_o | \geq \epsilon$$

$$= \overline{X}_o + \begin{vmatrix} \Delta y_1 \\ \Delta y_2 \\ \Delta y_3 \\ 0 \\ 0 \\ \Delta y_4 \\ \Delta y_5 \end{vmatrix} , \quad | \theta_o | < \epsilon$$

Note that for very small θ_o, ϕ_o, and ψ_o as well as $\dot{\phi}$ and $\dot{\psi}$ can not be determined separately. In this case only $\phi_o + \psi_o$ and $\dot{\phi} + \dot{\psi}$ can be determined.

The total problem has been programmed on the CDC 3600 computer. The average running time is about seven seconds. Flow charts are given in Appendix B.

5. Appropriateness of Solution For an Asymmetric Body

All of the previous discussion assumed that the two moments of inertia were equal, A = B. Let us now examine the errors produced by this assumption for the case $C \neq A \doteq B \neq C$, and θ small.

From Appendix A such a body moves so that

$$\psi = \psi_0 + \mu t + \frac{\epsilon}{4}(1 + r)(2 + \tan^2 \theta_0) \sin 2\mu t$$

$$\left[\frac{\epsilon}{8}(1 + r)(2 + \tan^2 \theta_0)\left(2 \cos 2\mu t - \left(\frac{\sin \theta_0}{1+\cos^2 \theta_0}\right)^2\right)\right] + ---$$

$$\phi = \phi_0 + \Omega t - \frac{\epsilon(1 + r)}{2 \cos \theta_0} \sin 2\mu t \left[1 + \frac{\epsilon}{4}(1 + r)(2 + \tan^2\theta_0) \cos 2\mu t\right] + ---$$

$$\theta = \theta_0 - \frac{\epsilon}{2} \tan \theta_0 (1 + r)\left[\cos 2\mu t + \frac{\epsilon}{8} \sec^2 \theta_0 (1 + r)(\cos 4\mu t - \cos^2\theta_0)\right] + --- \tag{4.6}$$

where ψ_0, ϕ_0, θ_0, μ, and Ω are constant and

$$\epsilon = \frac{A - B}{A + B}$$

$$1 + r = \frac{2C}{2C - (A + B)}$$

Now, consider a system, S_{6s}, which moves with respect to S_3 so as to satisfy (4.6) with $\epsilon \equiv 0$ (A = B). This is the system considered earlier in this section. Next, consider another system, S_{6a}, which moves with respect to S_3 so as to satisfy (4.6) with $\epsilon \neq 0$ $(A \neq B)$. Now we would like to predict the misorientation of S_{6a} with respect to S_{6s} as a function of t.

In general, there always exists an axis such that a rotation about this axis will cause S_{6a} to coincide with S_{6s}. Let the amount of this rotation be Φ. Then it can be shown that

$$\cos \Phi/2 = \cos \Delta\theta/2 \cos \frac{\Delta\psi + \Delta\phi}{2}$$

So for small $\Delta\theta$, $\Delta\psi + \Delta\phi$ we may write

$$\Phi = \sqrt{(\Delta\theta)^2 + (\Delta\psi + \Delta\phi)^2}$$

If we neglact terms $0(\epsilon^2)$ and $0(\theta_o^2)$, we may write

$$\Phi = \epsilon/2\ \theta_o\ (1 + r) \cos 2\ \mu t$$

A graph of Φ_{max} for Tiros is given in Figure IV-8, as a function of θ_o. We assume ϵ_{max} = .-5 (which implies B = 1.1A), 1 + r = 3.33.

The precession and nutation damper in Tiros is expected to perform so that $0 \leq .3^o \leq \theta_o$, so from Figure IV-8 we see that the unequal moment problem is negligible.

C. <u>Computer Solution for Nimbus</u>

In order to obtain an accurate solution to the orientation problem, the

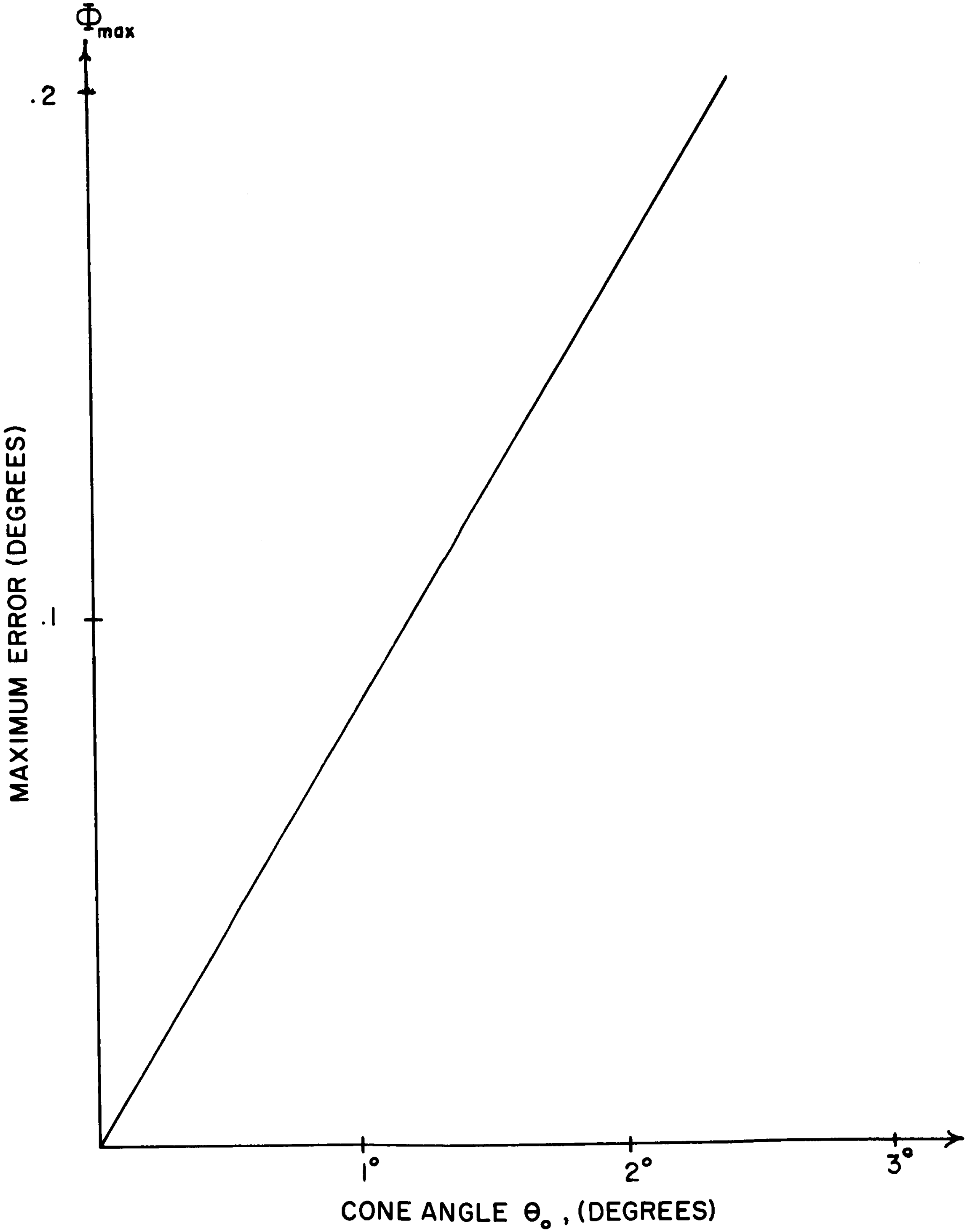

Figure IV-8: Maximum Misorientation Due to Asymmetry (in degrees) as a Function of θ_o

laws governing the orientation motion of the satellite must be known. That is, if the orientation is a random function of time, then we are forced to submit to the problem and call the measurements useless. For the Tiros, the laws governing the orientation motion are known via analytical dynamics. For the case of Nimbus, these laws are governed by the control system.

The SCADS instrument does not take all measurements simultaneously. To exaggerate the problem, suppose the measurements are taken with a long time duration between each measurement. The only way to solve the problem would then be to utilize the outputs of the control system together with the dynamics of the Nimbus. The mathematical problem then takes the form of seeking a solution to a system of differential equations given nonlinear constraints implied by the measurements. Such a formulation would produce a mathematically interesting and challenging problem. However, such a solution is probably not acceptable for it relies on outputs from other sensors. Hence, we must assume that we are spinning the sensor fast enough so that the sensor motion is essentially a uniform rotation about a fixed direction.

We may use the results of the analysis of Section B and our assumption of the sensor motion to reduce the orientation determination for Nimbus to a trivial problem. Hence, for Nimbus we may set $\theta \equiv \psi \equiv 0$. For Nimbus, the system S_4 is then fixed in the sensor. The system S_3 is fixed in the body. Thus, E in Equation (4.4) becomes

$$E = \begin{pmatrix} \cos\phi & \sin\phi & 0 \\ -\sin\phi & \cos\phi & 0 \\ 0 & 0 & 1 \end{pmatrix} \qquad (4.7)$$

$$\phi = \phi_0 + \dot{\phi}\, t$$

Equation (4.4) where E is given by (4.7) is the basic constraint equation which must be satisfied in the instant a star is in the slit. In particular, we recommend (see Figures IV-6 and IV-7) one slit with $\gamma' = \beta' = 0$. Hence, A_2 in (4.3) becomes

$$A_2 = (0,\ 1,\ 0),\ \text{for}\ \gamma' = \beta' = 0$$

Hence, for this special case (4.4) becomes

$$-\tan\phi\cos(\alpha_i - \xi) + \cos\tau\sin(\alpha_i - \xi)$$

$$+\tan\delta_i\sin\tau = 0 \tag{4.8}$$

In (4.8), $\phi = \phi_o + \mu_i$. μ_i is the measured angle, α_i and δ_i are the right ascension and declination of the star (known). ϕ_o, ξ, and τ are the unknowns of the problem.

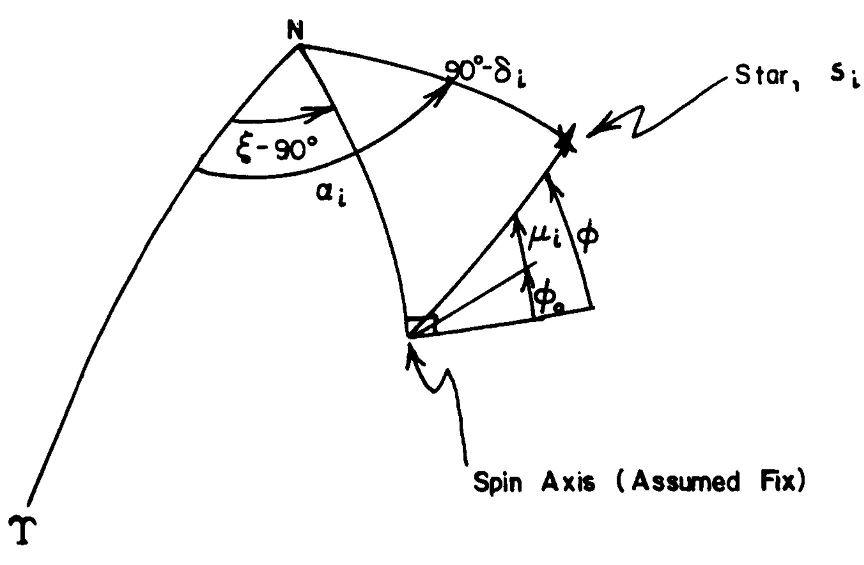

Figure IV-9: The Angles ϕ, ξ, τ, α_i, and δ_i

The above method of arriving at the principal Equation (4.8), started from a rather complex problem and these results were applied to a special case. To give more insight into the process, we can rederive (4.8) by simply using Figure IV-9 and spherical trigonometry.

For convenience, let us use δ , α , and β instead of τ, ξ, and ψ_o. These angles are pictured in Figure IV-10. $\xi - 90^o = \alpha$, $90 - \tau = \delta$, $\phi_o + 270^o = \beta$.

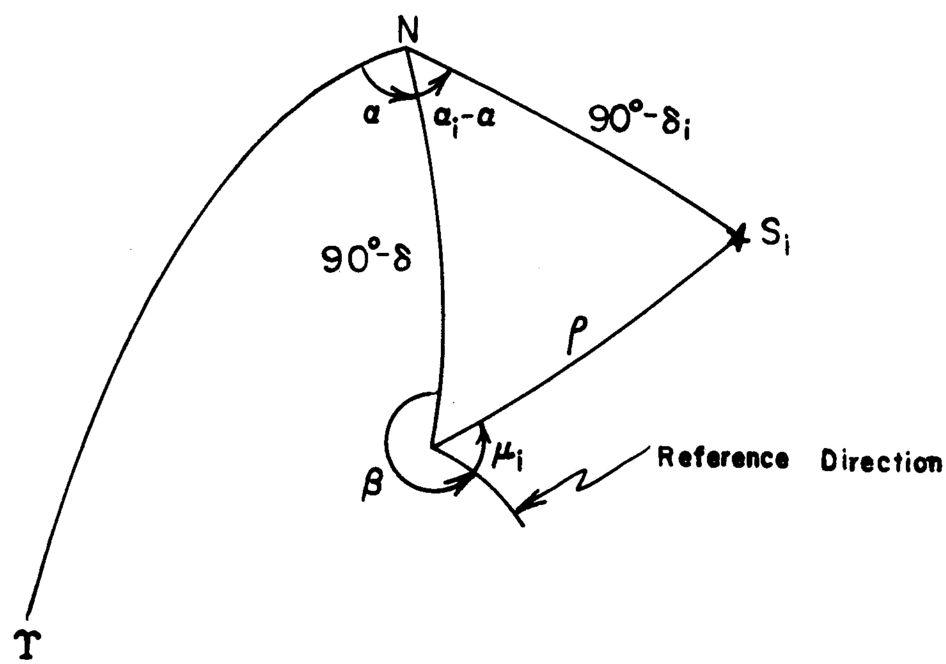

Figure IV-10: The Angles α, δ, α_i, δ_i, β, and μ_i

So (4.8) becomes

$$\tan(\beta + \mu_i) = \frac{\sin(\alpha - \alpha_i)\cos\delta_i}{\sin\delta_i\cos\delta - \cos\delta_i\sin\delta\cos(\alpha - \alpha_i)} \qquad (4.9)$$

where α = right ascension of instrument pointing direction (to be found).

δ = declination of instrument pointing direction (to be found).

α_i = right ascension of i^{th} star (known).

δ_i = declination of i^{th} star (known).

β = azimuth angle from North to reference direction, positive counter-clockwise (to be found).

μ_i = azimuth angle from reference direction to star (measured).

The unknowns in the problem are now α, δ, and β. These angles determine the three axis celestial attitude of the Nimbus. Three measurements are then necessary to complete the solution. This solution may be found by Newton's method.

Newton's method is an iterative scheme which requires an initial guess and the method then improves this guess. For this particular problem, the region of convergence is quite large. Experience has shown that 30 degree errors in the initial guess for each variable yield convergence. A flow chart of the solution is given in Appendix A.

D. Manual Solution

For both the Tiros and Nimbus the manual solution must rely upon the assumption of uniform motion about a fixed axis. We now discuss four methods of manual solution, two of which are not recommended.

1. Desk Calculator

One method of manual solution is to simply utilize a desk calculator to carry out the solution suggested in Section C. Such a method, however, is tedious and can not be recommended with enthusiasm. A list of the operations required for each iteration is given in Table IV-I. A minimum of two hours is required to perform these operations.

A desk calculator method which can be recommended is one in which much of the calculations are done by a computer. We note that the method of computation requires an initial guess. If this initial guess is close enough (roughly 5 degrees) then a computer can be used to perform the tedious precalculation (see flow chart Appendix A). After these precalculations are performed the only part of the calculation needed to be completed on the desk calculator is the solution of a system of linear equations in three unknowns. If the exact stars to be sighted were known before hand, then a matrix of the linear system could be inverted by the computer. Hence, the task to be completed on the desk is reduced to a matrix times a column vector. However, it seems that the SCADS instrumentation is such that preselected stars can not be furnished with certainty.

This method of utilizing a computer to do the precalculations is accurate and convenient. A central computer may be used to publish the calculations. These calculations must be updated periodically to compensate for the changing orientation of the satellites. An updating of once a week seems feasible.

We now will discuss purely graphic methods. These methods require no precalculation.

2. Spherical Graphic Methods

In Section C it was noted that the problem was described by geometry on a sphere. This fact suggests that a spherical graphical solution be utilized.

TABLE IV-1

OPERATIONS/ITERATION FOR THE MANUAL SOLUTION

Operation	Number	Word Length (Dec.)
sin	16	5
cos	16	5
x	102	5
÷	12	5
+	62	5

A description of the spherical graphical method is given by Lowen and Maxwell [49]. We now quote directly from their description.

"Manual data reduction can be carried out on an ordinary celestial globe fifteen inches in diameter which will contain all the stars that the sensor can reliably detect. The procedure would require the operator to determine the star-to-star measured angular separation from the telemetry data. With a cap-shaped cursor containing adjustable great circle arcs and representative of the SCADS field of view the operator adjusts the longitudinal angles to match the measured angular separation. The cursor is positioned manually on the globe while centering it on the predicted scan axis center. Minor adjustments are performed until the arcs are positioned through the stars within the scanning annulus. The coordinate of the cap center read from the celestial globe will determine the celestial intercept of the spin axis to within 0.5 degree (0.06 inch on surface of the sphere)."

3. Plane Graphic Methods

A well known result of differential geometry tells us that a sphere of finite radius cannot be isometrically mapped into a plane. Any mapping of a sphere onto a plane must produce some distortions and tearing. However, if a small portion of a sphere is mapped, the distortion can be made small. Any number of mappings may be used. Good mappings, for our purposes, are conformal. Examples are the Mercator and the stereographic projections. There is no "best" mapping for our purposes. All mappings produce some error. We now discuss a mapping which we have used to obtain a plane graphical solution to the orientation problem.

We may write (4.9) in the form

$$\tan(\beta + \mu_i) = \frac{\sin(\alpha - \alpha_i)}{\sec\delta_i \sin(\delta_i - \delta) + (1 - \cos(\alpha - \alpha_i))\sin\delta}$$

Now, if $(\alpha_i - \alpha)$ and $(\delta_i - \delta)$ are small, and we neglect second order terms, then (4.9) becomes

$$\tan(\beta + \mu_i) \doteq \frac{\alpha - \alpha_i}{\sec\delta_i(\delta_i - \delta)} \doteq \frac{\alpha - \alpha_i}{\delta_i \sec\delta_i - \delta\sec\delta} \qquad (4.10)$$

The Equation (4.10) now suggests a planar problem (Figure IV-11).

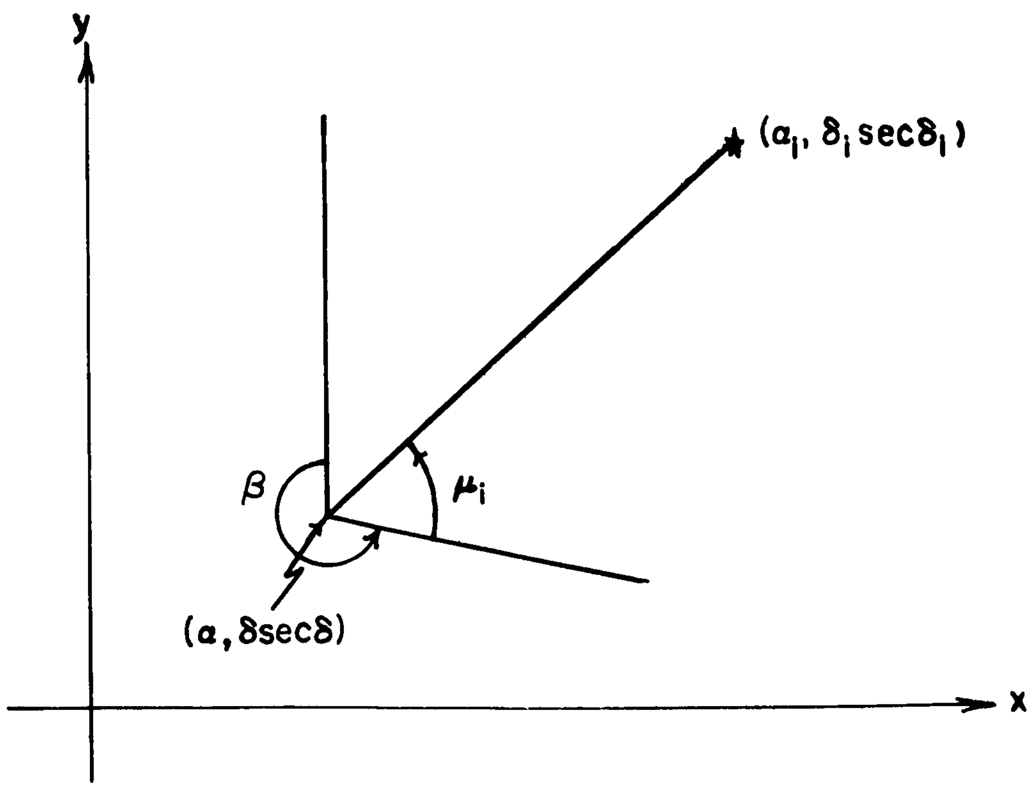

Figure IV-11: Plane Geometry Approximation

On a x, y coordinate system, we lay off the right ascension, α_i, of each star along the x axis, and $\delta_i \sec \delta_i$ along the y axis. The angle $\theta_2 - \theta_1$ may then be used to construct an arc of a circle on which $(\alpha, \delta \sec \delta)$ must lie. Then $\theta_3 - \theta_2$ (or $\theta_3 - \theta_1$) may be used to construct another such arc. The intersection of such arcs yields $(\alpha, \delta \sec \delta)$, and hence β may be measured.

An example on the necessary construction is given in Figure IV-12. From this figure,

$$\tau = -9.25^{o}$$

$$\alpha = 45.0^{o}$$

$$\beta = 341.0^{o}$$

While the correct answer is,

$$\tau = -9.15^{o}$$

$$\alpha = 45.0^{o}$$

$$\beta = 340.5^{o}$$

Hence, for this example, the plane geometry construction was quite accurate. Other examples were tried with similar results.

Appendix C gives the stars of magnitude four and brighter on our projection. These figures can then be used to obtain a graphical solution.

4. Nomographic Solution

A serious attempt at a nomographic solution was made. It was concluded that such methods are useless as a solution or aid in the solution to the problem.

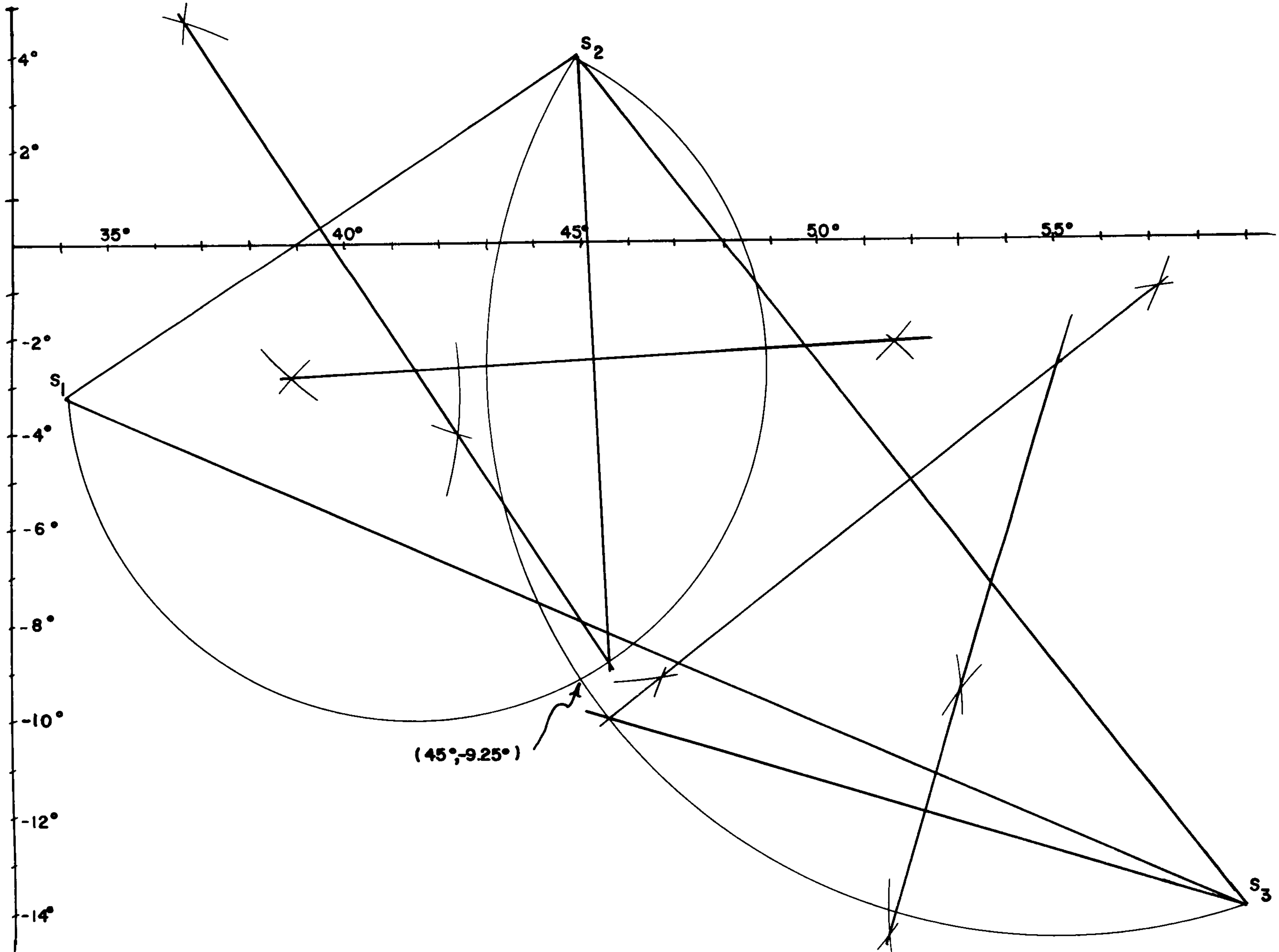

Figure IV-12: Manual Solution

E. Final Parameters

Thus far, we have only considered the problem of finding the orientation, as a function of time, of a system fixed in the satellite, S_6, with respect to a celestial system, S_1. We have found a solution to this problem which depends only on the output of theSCADS sensor. The position of the spece-craft need not be known. The solution we have found may be just an inter-mediate answer, the final parameter may depend upon the satellite's position.

1. Roll, Pitch, and Yaw

The parameters roll, pitch, and yaw are not well defined unless the order of rotation is given. These parameters could be used for the Tiros, but are probably of little significance in this application. However, the Nimbus is stabilized so that the roll, pitch, and yaw are nominally zero, so these parameters are of interest.

Recall the S_4 for Nimbus was defined so as to rotate with theSCADS sensor. Up to now, the orientation of S_4 at t = 0, $S_4(0)$, was arbitrary. Let us now define $S_4(0)$ so the $\hat{i}_4(0)$ is along the vertical axis of Nimbus and $\hat{j}_4(0)$ is along a horizontal axis (Figure IV-13). Physically, this definition implies an alignment of the sensor with respect to the satellite.

Let us now define a system S_7 which is a system associated with the satellite's orbit (Figure IV-14). Let $\overline{R}_s$ be the position vector of the satellite, and let S_7 move with $\overline{R}_s$. Let $\hat{i}_7 = \overline{R}_s/|\overline{R}_s|$, $\hat{j}_7$ is in the plane of motion of $\overline{R}_s$ such that $\dot{\overline{R}}_s \cdot \hat{j}_7 > 0$ (Figure IV-14), $\hat{k}_7$ is perpendicular to the orbit and completes the right handed system.

Now the orientation of S_7 with respect to the celestial system S_1 depends only on the position of Nimbus and not its attitude. In fact,

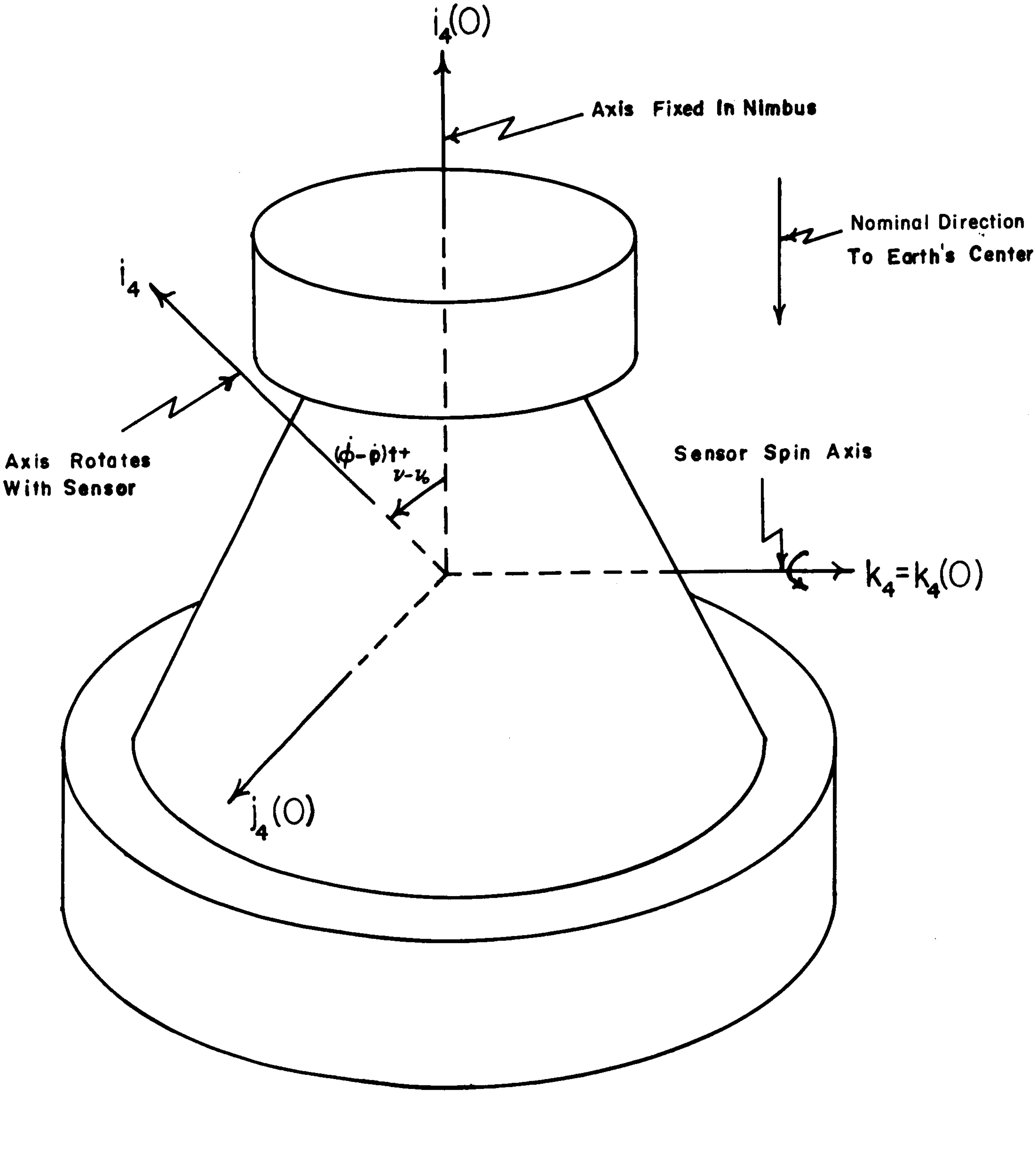

Figure IV-13: The Orientation of S_4 and $S_4(0)$ for Nimbus

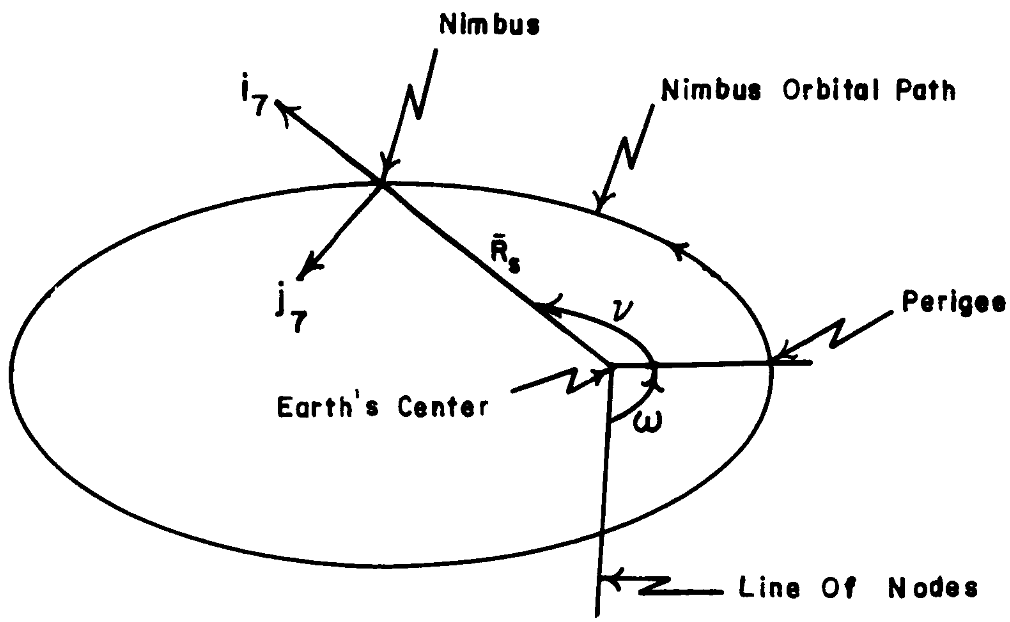

Figure IV-14: The System S_7

$$B(t) \begin{pmatrix} \hat{i}_1 \\ \hat{j}_1 \\ \hat{k}_1 \end{pmatrix} = \begin{pmatrix} i_7 \\ j_7 \\ k_7 \end{pmatrix} \text{, where}$$

$$B^T(t) = \begin{pmatrix} \cos\Omega\cos(\omega+\nu) - \sin\Omega\cos i\sin(\omega+\nu) & -\cos\Omega\sin(\omega+\nu) - \sin\Omega\cos i\cos(\omega+\nu) & \sin\Omega\sin i \\ \sin\Omega\cos(\omega+\nu) + \cos\Omega\cos i\sin(\omega+\nu) & -\sin\Omega\sin(\omega+\nu) + \cos\Omega\cos i\cos(\omega+\nu) & -\cos\Omega\sin i \\ \sin i\sin(\omega+\nu) & \sin i\cos(\omega+\nu) & \cos i \end{pmatrix}$$

where Ω = longitude of ascending node

ω = angle from ascending node to line joining Earth's center and perigee

ν = true anomaly (a function of t)

i = orbital inclination

We now define roll, pitch, and yaw.

$\hat{j}_7 \rightarrow \hat{j}'_7$ rotation y about $\hat{i}_7$ (yaw)

$\hat{j}'_7 \rightarrow \hat{j}''_7 = \hat{j}_4(0)$ rotation p about $\hat{k}'_7$ (pitch)

$\hat{i}''_7 \rightarrow \hat{i}_4(0)$ rotation r about $\hat{j}_4(0)$ (roll)

Hence,

$$\begin{pmatrix} \hat{i}_7 \\ \hat{j}_7 \\ \hat{k}_7 \end{pmatrix} = A \begin{pmatrix} \hat{i}_4(0) \\ \hat{j}_4(0) \\ \hat{k}_4(0) \end{pmatrix}$$

where

$$A = \begin{pmatrix} \cos p \cos r & -\sin p & \cos p \sin r \\ \cos y \sin p \cos r + \sin y \sin r & \cos y \cos p & \cos y \sin p \sin r - \sin y \cos r \\ \sin y \sin p \cos r - \cos y \sin r & \sin y \cos p & \sin y \sin p \sin r - \cos y \cos r \end{pmatrix}$$

But,

$$\begin{pmatrix} \hat{i}_1 \\ \hat{j}_1 \\ \hat{k}_1 \end{pmatrix} = E(\phi_o + \dot{p}t + \nu - \nu_o)\ H \begin{pmatrix} \hat{i}_4(0) \\ \hat{j}_4(0) \\ \hat{k}_4(0) \end{pmatrix}$$

where $\phi_o = \phi$ at $t = 0$

$$\dot{p} = \frac{dp}{dt}$$

$\nu_o = \nu$ at $t = 0$

Hence,

$$A = B\ (t)\ E(\phi_o + \dot{p}t + \nu - \nu_o)\ H$$

So,

$$\sin p = B_1\ (t)\ E\ H^2$$

$$\tan y = \frac{B_2\ (t)\ E\ H^2}{B_3\ (t)\ E\ H^2}$$

$$\tan r = \frac{B_1(t)\ E\ H^3}{B_1(t)\ E\ H^1} \tag{4.11}$$

where $B_i(t)$ is a row vector formed from the i^{th} row of $B(t)$

H^j is a column vector formed from the j^{th} column of H

E is evaluated at $\phi + \dot{p}t + \nu - \nu_0$

Equation (4.11) then determines the roll, pitch, and yaw as functions of t. In these equations E and H are given by the SCADS sensor, and B is given from the orbital parameters of the satellite.

Note that nominal values imply,

$\tau = i$

$\psi_0 = \nu_0 + \omega$

$\xi = \Omega$

2. Camera Pointing Parameters

Parameters associated with the pointing direction of the camera may also be computed from the orientation supplied by SCADS and positional information.

For Nimbus the system $S_4(0)$ may be chosen to be aligned with the plane of the camera image, while S_6 is aligned with the Tiros camera image (Figure IV-15). These considerations call for a prealignment of the camera system and the body fixed system.

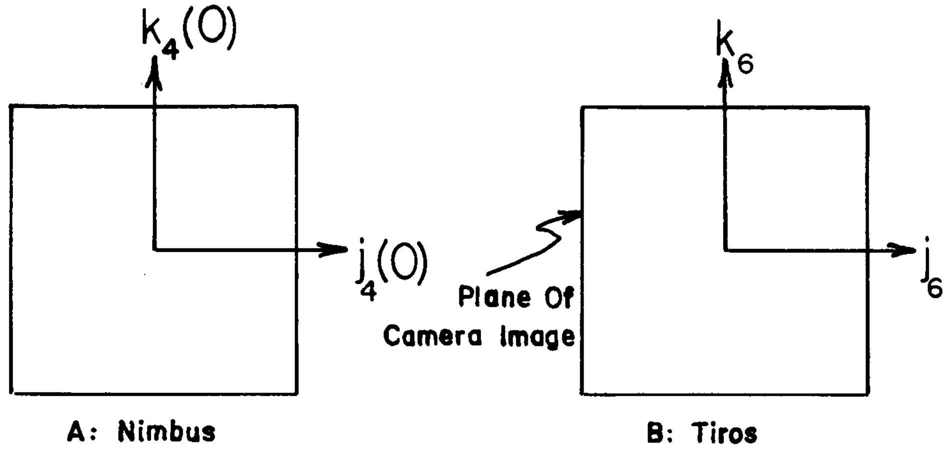

Figure IV-15: Orientation of $S_4(0)$ and S_6 with respect to Camera Image (Nimbus and Tiros)

Let us concentrate on the Tiros geometry. The desired parameters may be the point (latitude and longitude) at which $\hat{i}_6$ extended pierces the Earth (Figure IV-16), and the orientation of the picture vertical, $\hat{k}_6$ with respect to the local vertical at the terminus of $\overline{R}_e$ (see Figure IV-16).

$$\overline{R}_e = \overline{R}_s - \lambda \hat{i}_6 \quad \text{(determine latitude and longitude)}$$

$$\tan \mu = \frac{\hat{j}_6 \cdot \overline{R}_e}{\hat{k}_6 \cdot \overline{R}_e} = \frac{\hat{j}_6 \cdot \overline{R}_s}{\hat{k}_6 \cdot \overline{R}_s} \quad \text{(determines picture vertical orientation)}$$

Hence, to obtain these parameters we must know the satellite position, $\overline{R}_s$, and the time (GST).

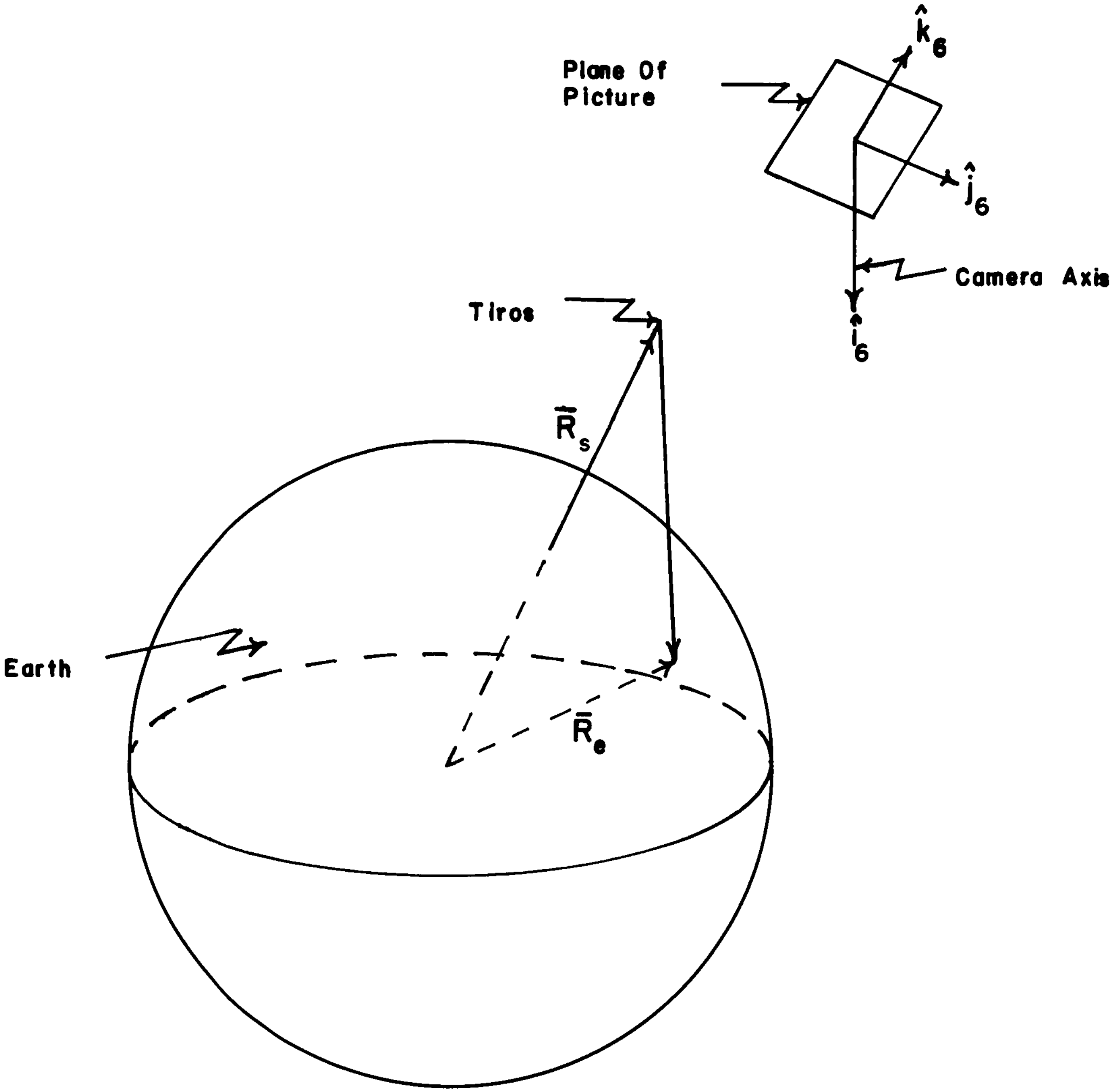

Figure IV-16: Camera Pointing Parameters

V. ERROR ANALYSIS

The error analysis which follows will rest on several assumptions. They are as follows:

(a) Stars are point targets.

(b) Planets are not used.

(c) The SCADS sensor rotates at a constant rate about a spin axis fixed in inertial space.

(d) Only stars brighter than fourth magnitude are used. They have already been identified.

Not taken into account are such sophistications as (1) corrections for target positions due to aberration, proper motion, target size, etc., (2) general rigid body torque free motion, and (3) a more physical simulation of the SCADS detection. It was felt that in order to facilitate immediate progress on the program, and also to obtain a 'first order' picture of the error patterns to be expected in the more complex cases, such steps were warranted. We do not feel that any essential features were omitted or that a future more correct error analysis will significantly alter the present conclusions.

The main purpose of this section is to predict the effects of relative geometry and errors in the measured quantities upon the computed celestial attitude.

A. Errors in the Orientation With Respect to S_1

We note that our assumptions are such that the error analysis pertinent to finding the orientation with respect to S_1 is the same for Tiros and Nimbus.

1. Single Slit Configuration

The first section will assume a single slit with $\beta' = \gamma' = 0$ (see Figures IV-6 and IV-7). Hence, the measured quantities are the relative azimuth μ_i of stars. These angles are pictured in Figure IV-10.

a. Artificial Stars

Before we consider real stars, much insight into the significance at the relative geometry of the stars and the spin axis is gained by considerations of artificial stars. Hence, we will first perform a numerical experiment to test the accuracy and sensitivity of the systems by use of artificial stars.

Three stars were chosen all at the same co-elevation, ρ, with respect to the spin axis. For the first and second stars, we chose to fix (see Figure V-1).

$$\phi_1 = -30^\circ$$

$$\phi_2 = 30^\circ$$

$\alpha = \delta = 0$ (spin axis at First Point of Aries)

We then will study the effect of the geometry of the problem as ϕ_3 and ρ take on various values. The standard deviation in determining the relative azimuth of a star is fixed at

$$\sigma(\mu_i) = \text{one minute of arc},\ i = 1, 2, 3$$

We assume that the errors in the measured quantities are independent, and each has a standard deviation of one minute of arc.

With these assumptions we can obtain $\sigma(\alpha)$, $\sigma(\delta)$, and $\sigma(\beta)$, (see Figure IV-10) as functions of ρ and ϕ_3. Results are plotted in Figures V-2,

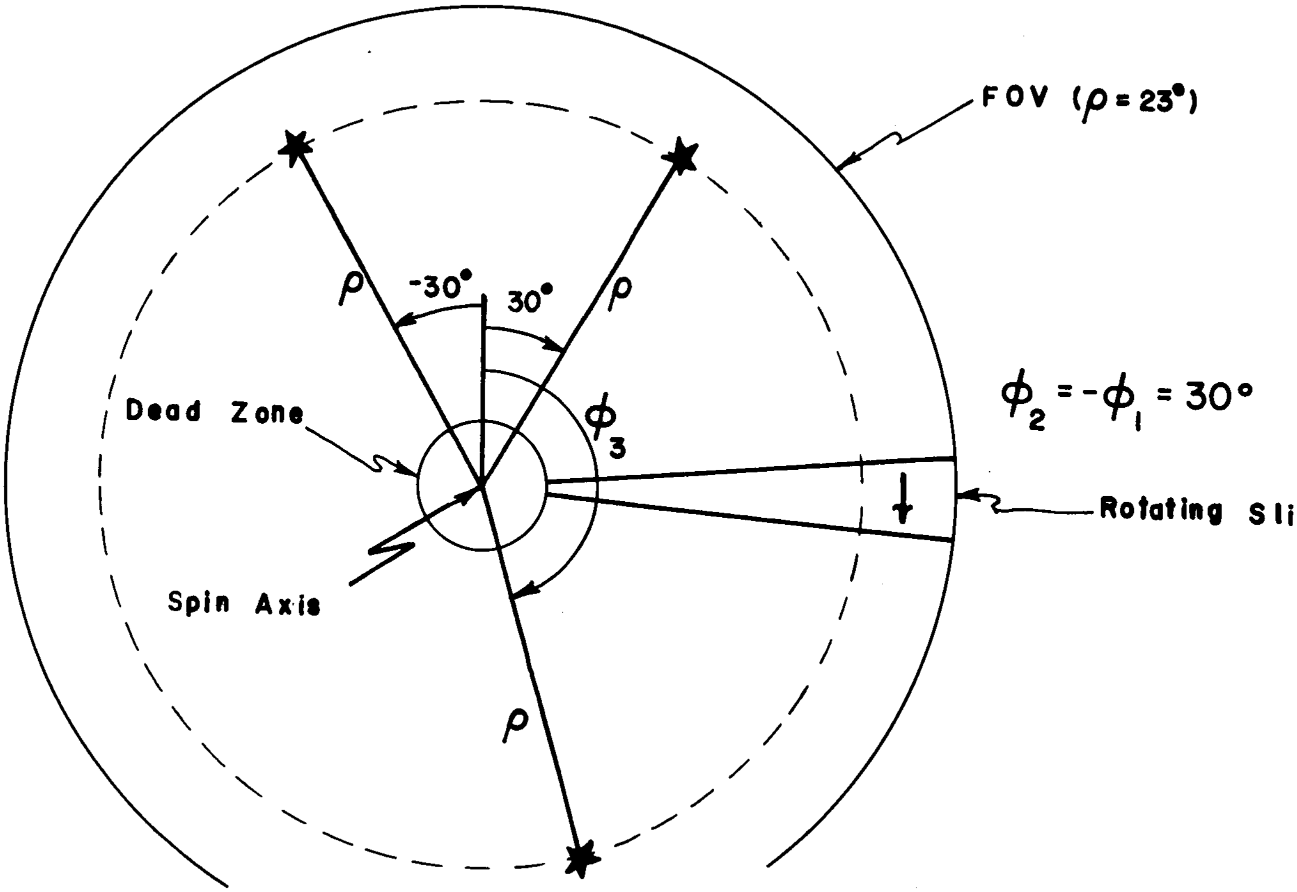

Figure V-1: The Position of the Three Artificial Stars

V-3 , and V-4 as constant error contours. These plots are on polar graph paper, the radial coordinate is the common co-elevation of the stars ρ (in degrees) while the angular coordinate is the azimuth of the third star ϕ_3.

From Figure V-2 we see that $\sigma(\alpha)$ (error in right ascension of spin axis) is independent of ϕ_3 (the azimuth of the third star). However, as the angle between the spin axis and each of the three stars, ρ, becomes larger and larger, the errors grow.

From Figure V-3 , $\sigma(\delta)$ (error in declination) is a strong function of ϕ_3. Indeed, as ϕ_3 becomes closer to 30° and - 30°, the errors in δ become extremely large. We also see that $\sigma(\delta)$ becomes small as ρ becomes small.

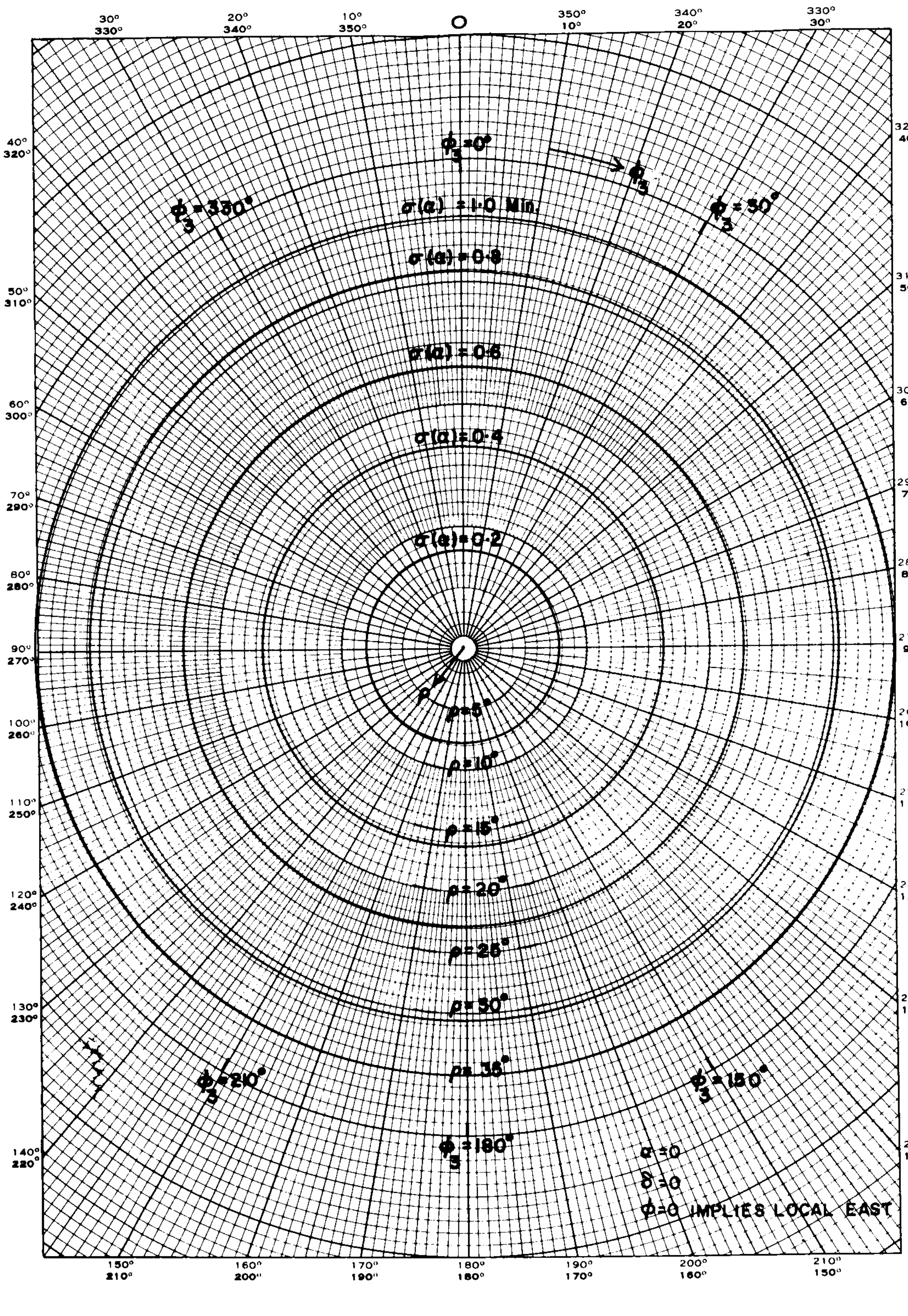

Figure V-2: $\sigma(\alpha)$, Error in Right Ascension as a Function of Common Co-elevation of the Three Artificial Stars, ρ

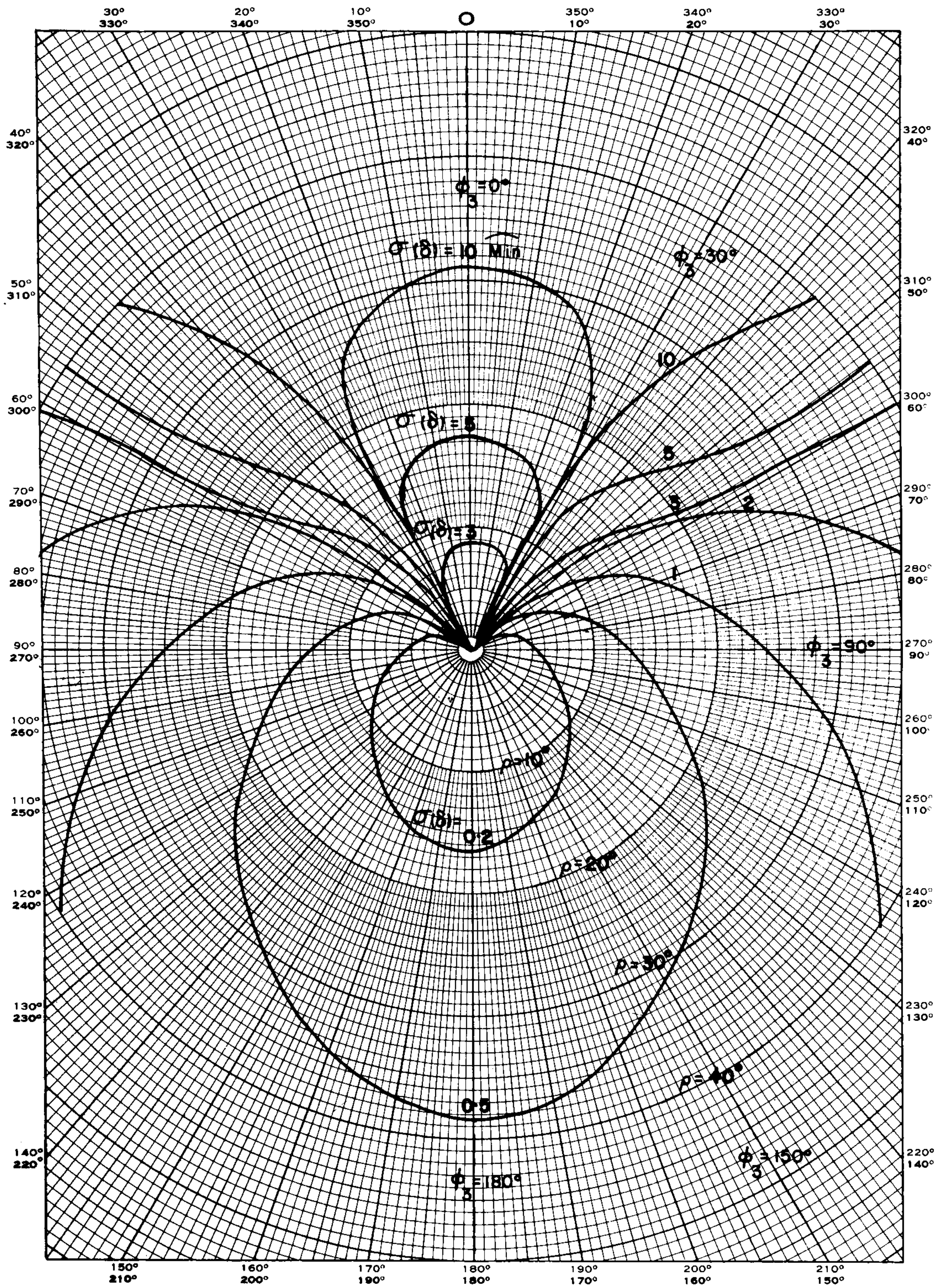

Figure V-3: $\sigma(\delta)$, Error in Declination as a Function of the Common Co-elevation, ρ, and the Azimuth of the Third Star, ϕ_3

Figure V-4 shows that $\sigma(\beta)$ for this case depends only on ϕ_3. Note that the errors become very great as $\phi_3 \rightarrow \phi_2$ or ϕ_1. The smallest errors occur (.6 minute) for $\phi_3 = 180^\circ$.

The general conclusion from this study of attitude determination by use of three stars is that the errors grow as the stars become further (in angle) from the spin axis, and as the distribution in azimuth becomes less uniform (i.e., $\phi_3 \rightarrow \phi_2$ or ϕ_1 see Figure V-1). This is the reason we choose a small dead zone (3°). It is true that few stars will lie close to the spin axis (in angle), but any such star is important for attitude determination.

b. Real Stars

The next problem considered is that obtained by using the geometry produced by the stars and field of view recommended for Tiros and Nimbus (Section III-A-1).

We note that the nominal spin direction is perpendicular to the orbital plane (for both Tiros and Nimbus). Hence, we may choose two directions for the field of view's center. One direction along the orbit's position normal, and another along the negative normal (see Figure III-1). The useful stars and the stellar background were found to be quite similar for the two directions. Results in this section are given for only the positive normal direction (see Figure III-1). The spin axis is then assumed to be along the positive normal of a sun synchronous orbit. Three circular orbits were assumed with altitudes 500 nm, 750 nm, and 1000 nm. Then we obtain the inclinations:

500 nm implies $i = 99.153^\circ$

750 nm implies $i = 101.378^\circ$

1000 nm implies $i = 103.980^\circ$

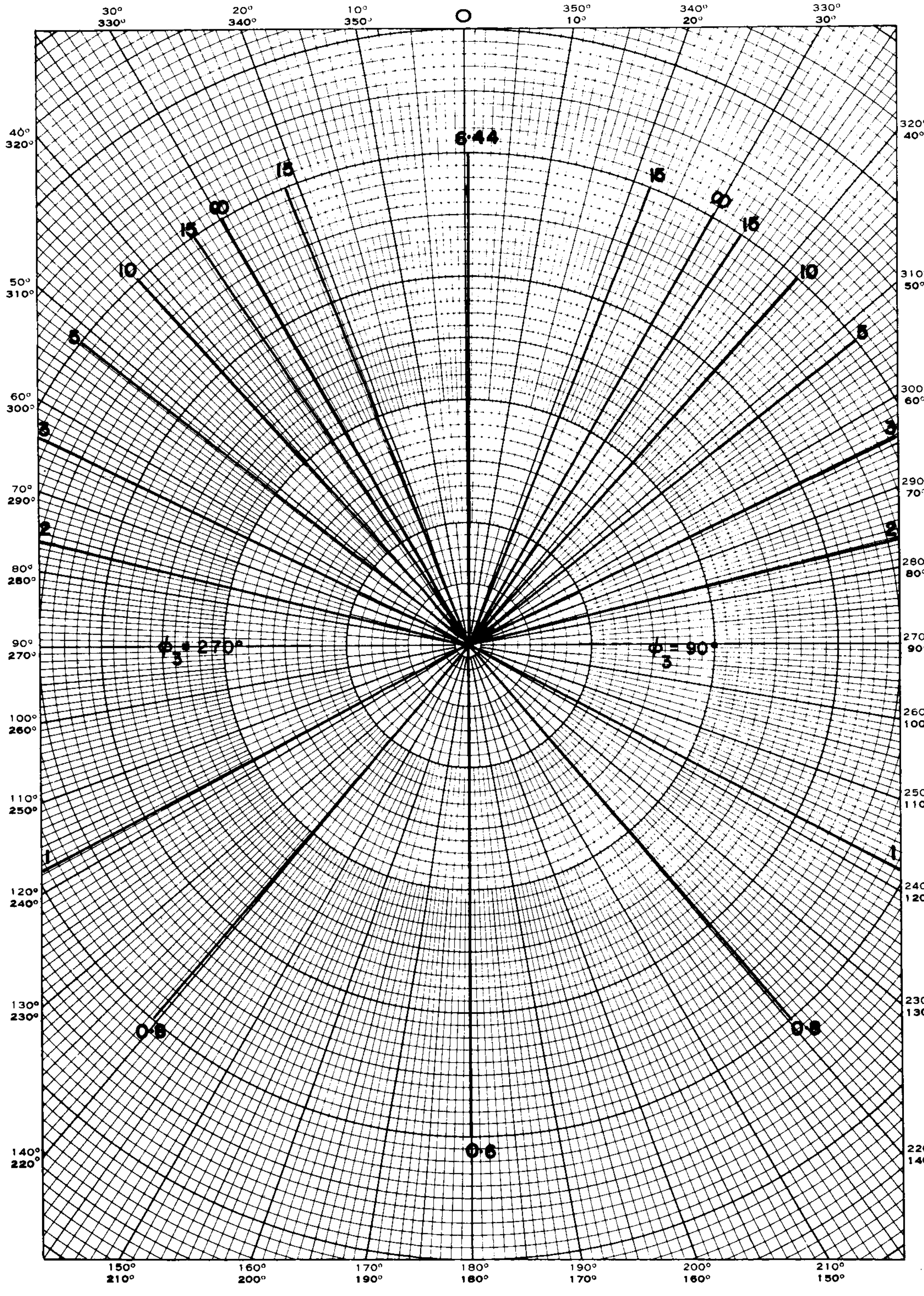

Figure V-4: $\sigma(\beta)$, Error in Direction of Local North as a Function of the Azimuth of the Third Star, ϕ_3

A field of view was chosen with an outer half cone angle of 23°, and an inner half cone angle of 3°. The inner cone is a dead zone.

In Figure V-5, we see plotted the total error as a function of the right ascension of the spin axis, α. Three altitudes are indicated. These altitudes determine the declination of the spin axis. In this case, only stars of visual magnitude of + 3 and brighter were chosen. Note that for some right ascensions, fewer than three stars are in the field of view so that a determination is not possible. For this graph, and all other graphs given in this section, we assume the standard deviation of the measured azimuth angles is one minute of arc, i.e.,

$$\sigma(\mu_i) = \text{one minute of arc}$$

This assumption corresponds to time errors of

$$\sigma(t_i) = 2.78 \times 10^{-4} \text{ seconds (for Tiros)}$$

$$\sigma(t_i) = .93 \times 10^{-4} \text{ seconds (for Nimbus)}$$

The time errors must be smaller for Nimbus because we are obligated to spin the Nimbus sensor for a period of about two seconds (see Section V-B). By the term total error, we mean the sum of the squares of the three orientation errors, i.e.,

$$\sqrt{\sigma^2(\alpha) + \sigma^2(\delta) + \sigma^2(\beta)}$$

We see from Figure V-5 that the results are about the same for all three altitudes. In the rest of the work of this section, we will use an altitude

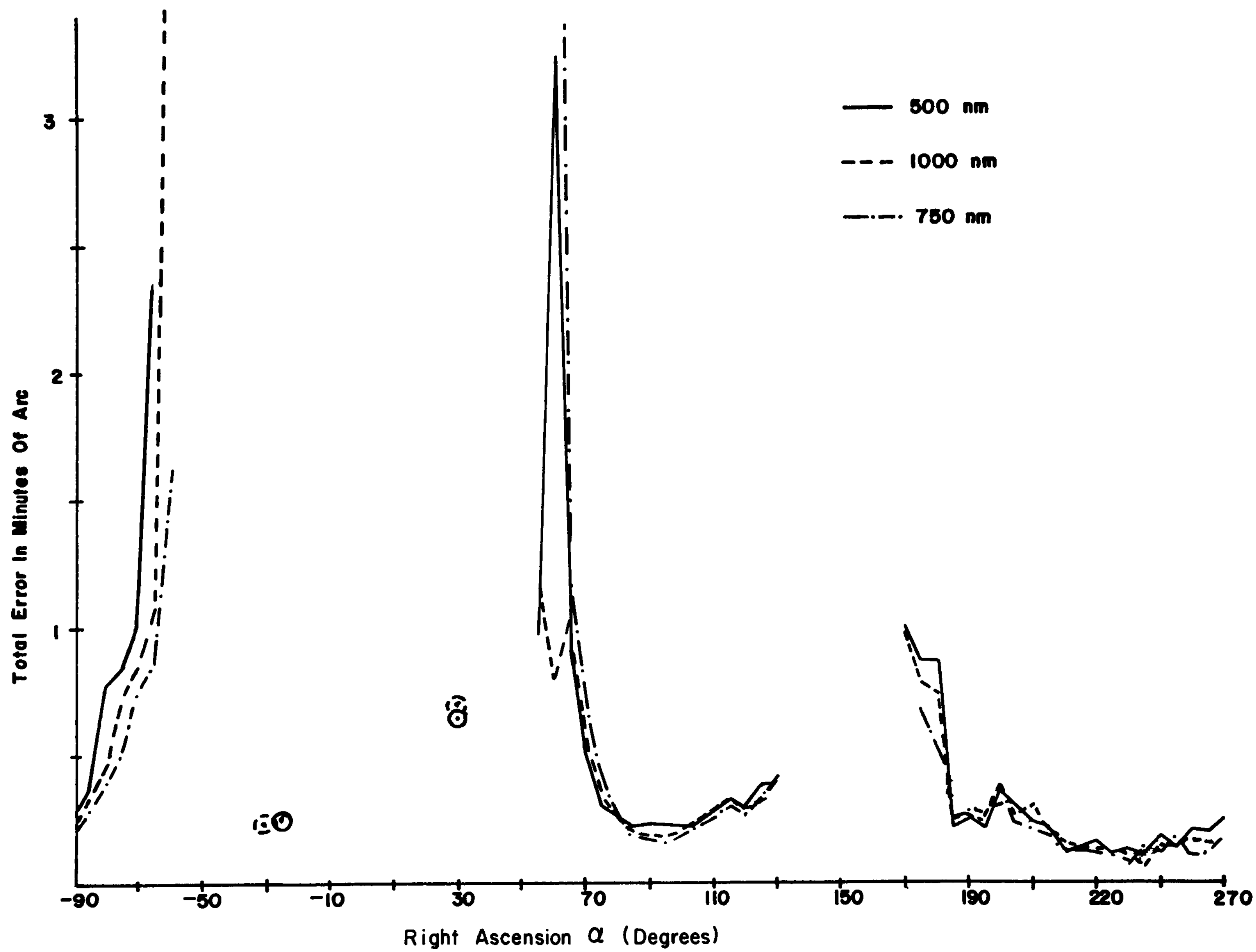

Figure V-5: Total Orientation Error as a Function of α for Three Satellite Altitudes of 750 nm.

In Figure V -6 we set the altitude at 750 nm and see the effect of including dimmer stars in the field of view. Again

$$\sqrt{\sigma^2(\alpha) + \sigma^2(\delta) + \sigma^2(\beta)}$$

is the dependent variable. The limiting magnitudes are + 3, + 3.5, and + 4. The coverage is 62.5%, 84.7%, and 100%. Note that the errors are quite small as more stars are utilized.

As explained in Section III-A-1, (Field of View), we favor a variable bias level rather than utilizing all stars brighter than a fixed magnitude. Results for a fixed magnitude are given in Figures V-5 and V-6. By a variable bias level, we mean the sensitivity of the instrument will be changed so as to respond to a given number of the brightest stars in the field of view. For example, if it is desired to have three stars in the field of view, then the sensitivity of the instrument will be so adjusted that the instrument will respond to the three brightest stars in the field of view.

Figure V -7 is a graph of

$$\sqrt{\sigma^2(\delta) + \sigma^2(\tau) + \sigma^2(\beta)}$$

as a function of α for three, four, and five of the brightest stars in the field of view. Again we assume $\sigma(\mu_i)$ = one minute of arc.

Note that for three stars within the field of view, there are many α's such that this error is too large (> 6 minutes of arc). However, for four stars within the field of view, the errors are excessive only for $\alpha = 235^\circ$. At this point five stars are required to drop the error.

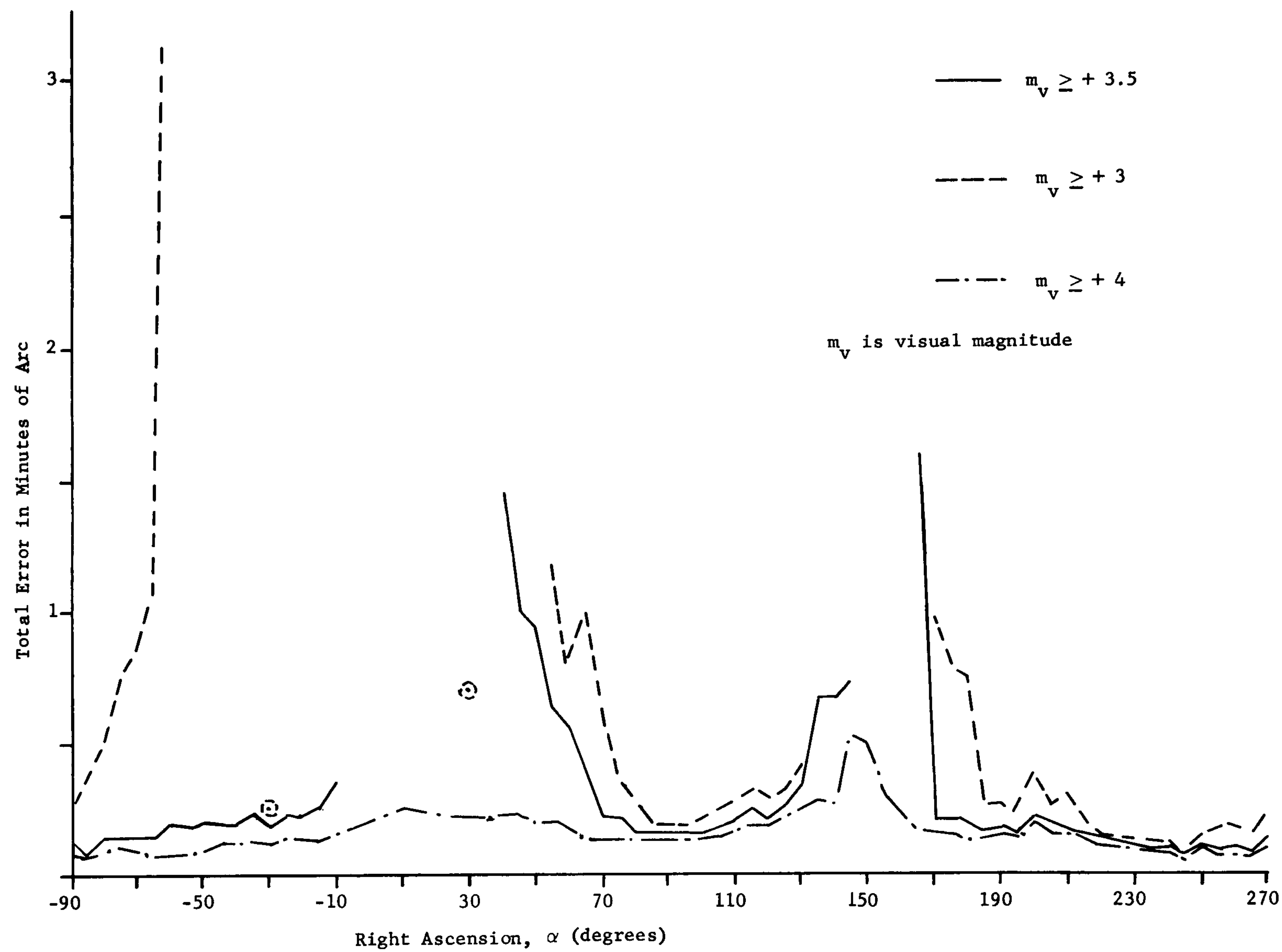

Figure V-6: Total Error for 750 nm Altitude Orbit and Various Magnitude Limits

2. Double Slit Configuration

We will now consider the error propagation studies for the double slit configuration discussed in Section III.A.2. Again, we first consider artificial stars.

a. Artificial Stars

For the double slit configuration, only two stars are required to lie in the field of view. Let us then study the effect of geometry on the errors for the double slit configuration and two stars in the field of view. Recall that in Section V.A.1.a. we studied the geometry effect for a single slit, and three stars (minimal number) in the field of view. The present analysis parallels that of Section V.A.1.a.

Let us choose $\phi_1 = 0$ and $\rho_1 = \rho_2 = \rho$ (see Figure V-1). We then vary ϕ_2 and ρ, and obtain equal error contours plotted in polar coordinates as before. The radial coordinate is the common coelevation of the stars, ρ, while the angular coordinate is the azimuth of the second star, ϕ_2. Results are plotted in Figures V-8, V-9, V-10, and V-11. These graphs are similar to Figures V-2, V-3, and V-4, except that we now add a plot of the total error,

$$\sqrt{\sigma^2(\alpha) + \sigma^2(\delta) + \sigma^2(\beta)}$$

in Figure V-11.

We also choose

$$\alpha = \delta = 0$$

$\sigma(\phi_i)$ = one minute of arc, i = 1, 2 as before. However, for the two slit configuration, we have the capability of measuring ρ as well as ϕ. We assume errors in ρ given by

$$\sigma(\rho_i) = \text{one minute of arc, } i = 1, 2.$$

Note that Figure V-8 is quite similar to Figure V-2. However, $\sigma(\alpha)$ now becomes a weak function of ϕ_2 and is numerically greater at any given point in the polar coordinate system than before. Similar comments are true for Figures V-9 and V-10.

b. Real Stars

Figure V-12 yields $\sqrt{\sigma^2(\alpha) + \sigma^2(\delta) + \sigma^2(\beta)}$ as a function of α for real stars. This figure is similar to Figure V-7 except the double slit configuration was used. The double slit configuration utilized is shown in Figure III-7.

$$\sigma = 13^\circ$$

$$\Gamma = 10^\circ$$

We also assume the same input errors as for the single slit configuration. This assumption may not be realistic, for the addition of another slit may produce effects which produce greater errors.

Figure V-13 then gives the necessary visual magnitude so that the total error

$$\sqrt{\sigma^2(\alpha) + \sigma^2(\delta) + \sigma^2(\beta)}$$

be less than six minutes of arc. Results are given for one and two slits.

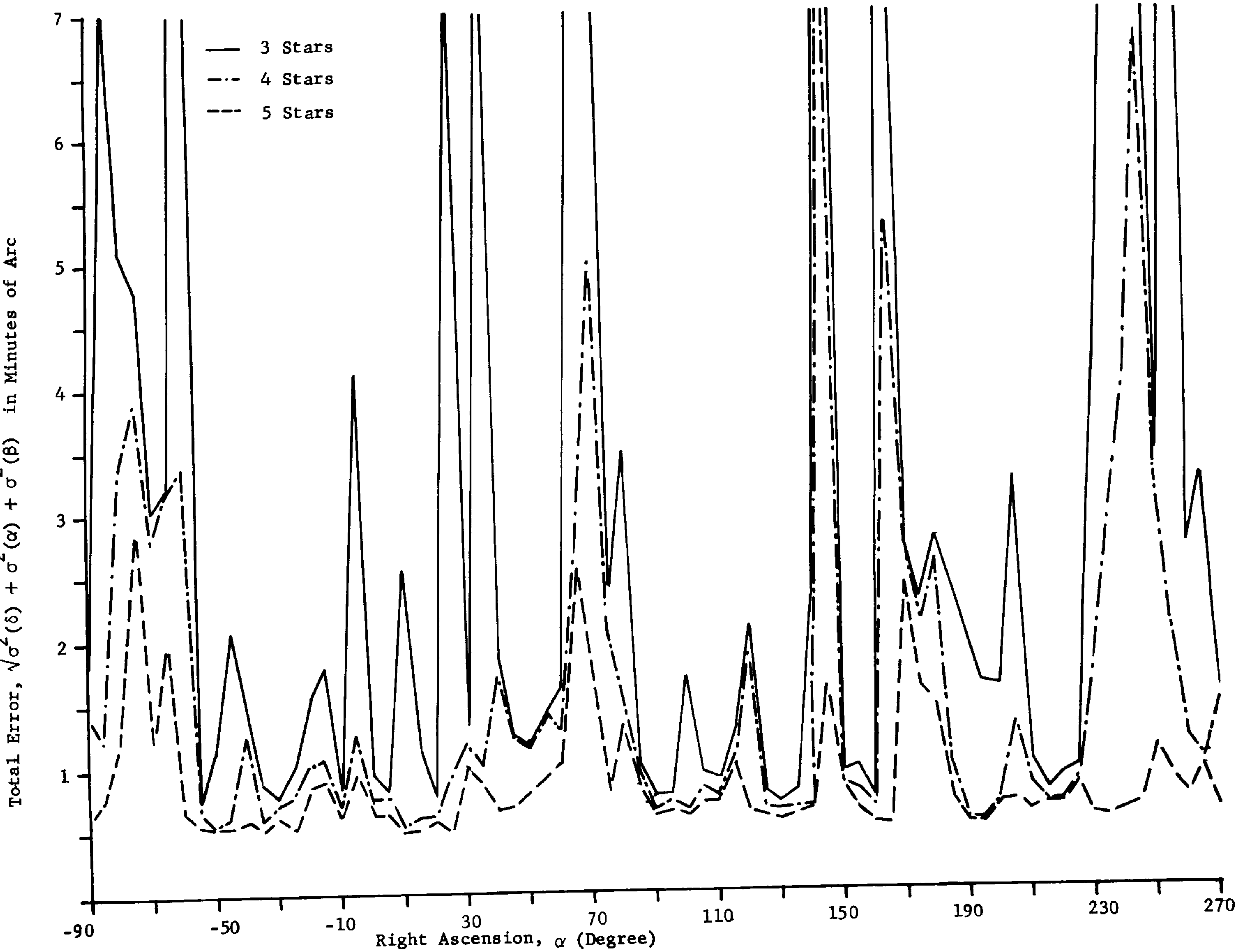

Figure V-7: Total Error as a Function of α for 3, 4, and 5 Stars in Field of View

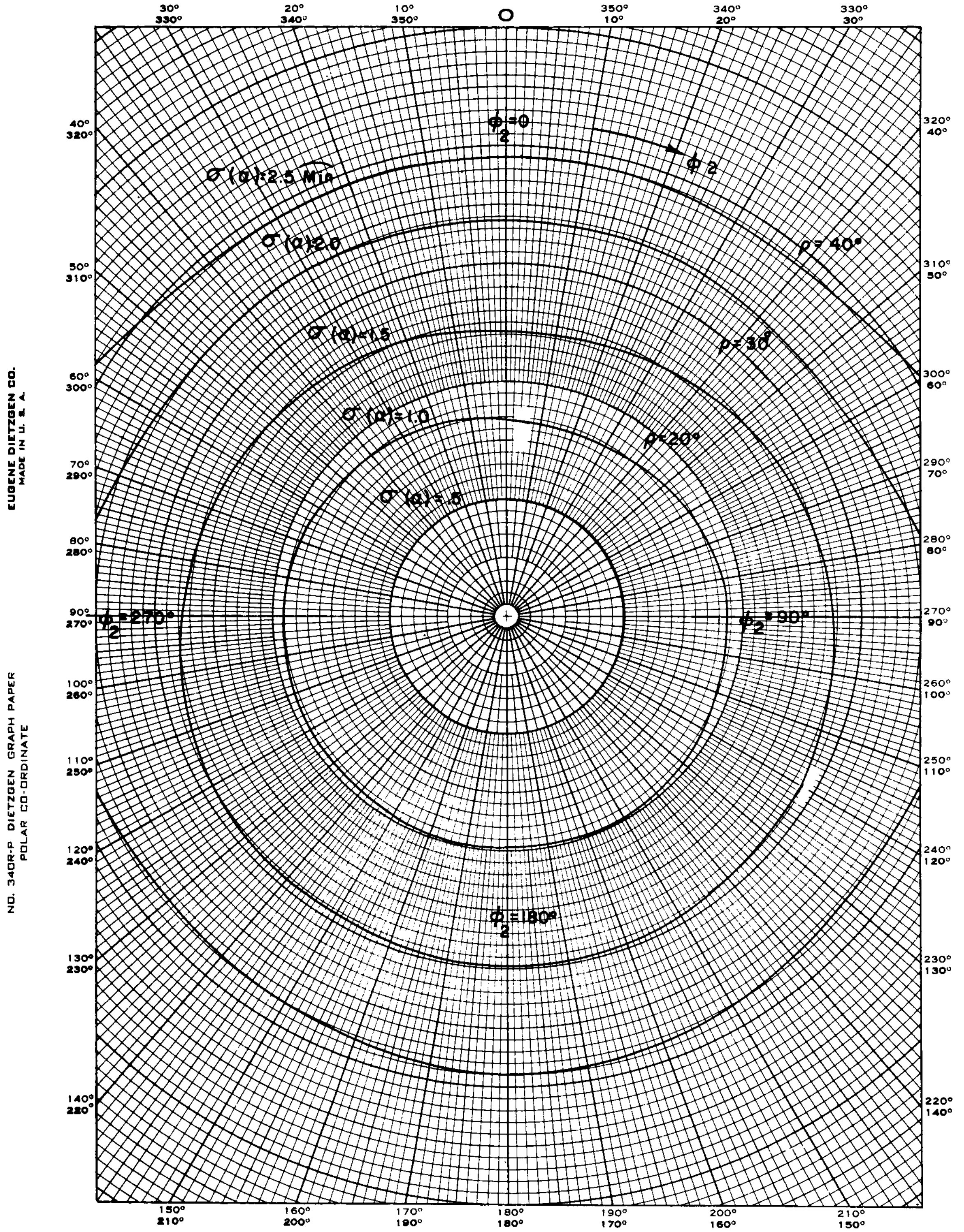

Figure V-8: $\sigma(\alpha)$, Error in Right Ascension (Minutes of Arc) as a Function of Common Coelevation of the Two Artificial Stars, ρ, and the Azimuth of the Second Star, ϕ_2

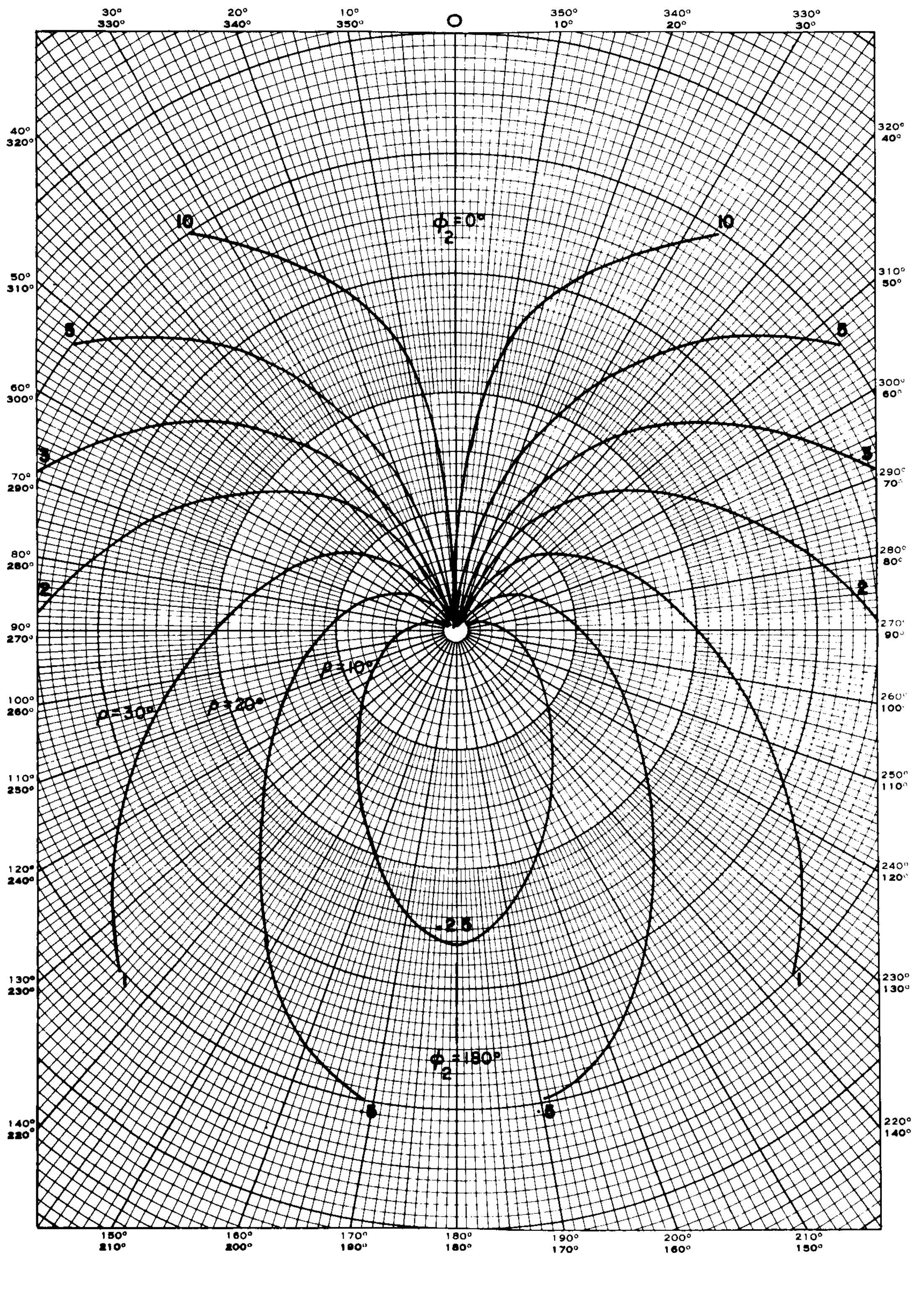

Figure V-9: $\sigma(\delta)$, Error in Declination (Minutes of Arc) as a Function of Common Coelevation of the Two Artificial Stars, ρ, and the Azimuth of the Second Star, ϕ_2

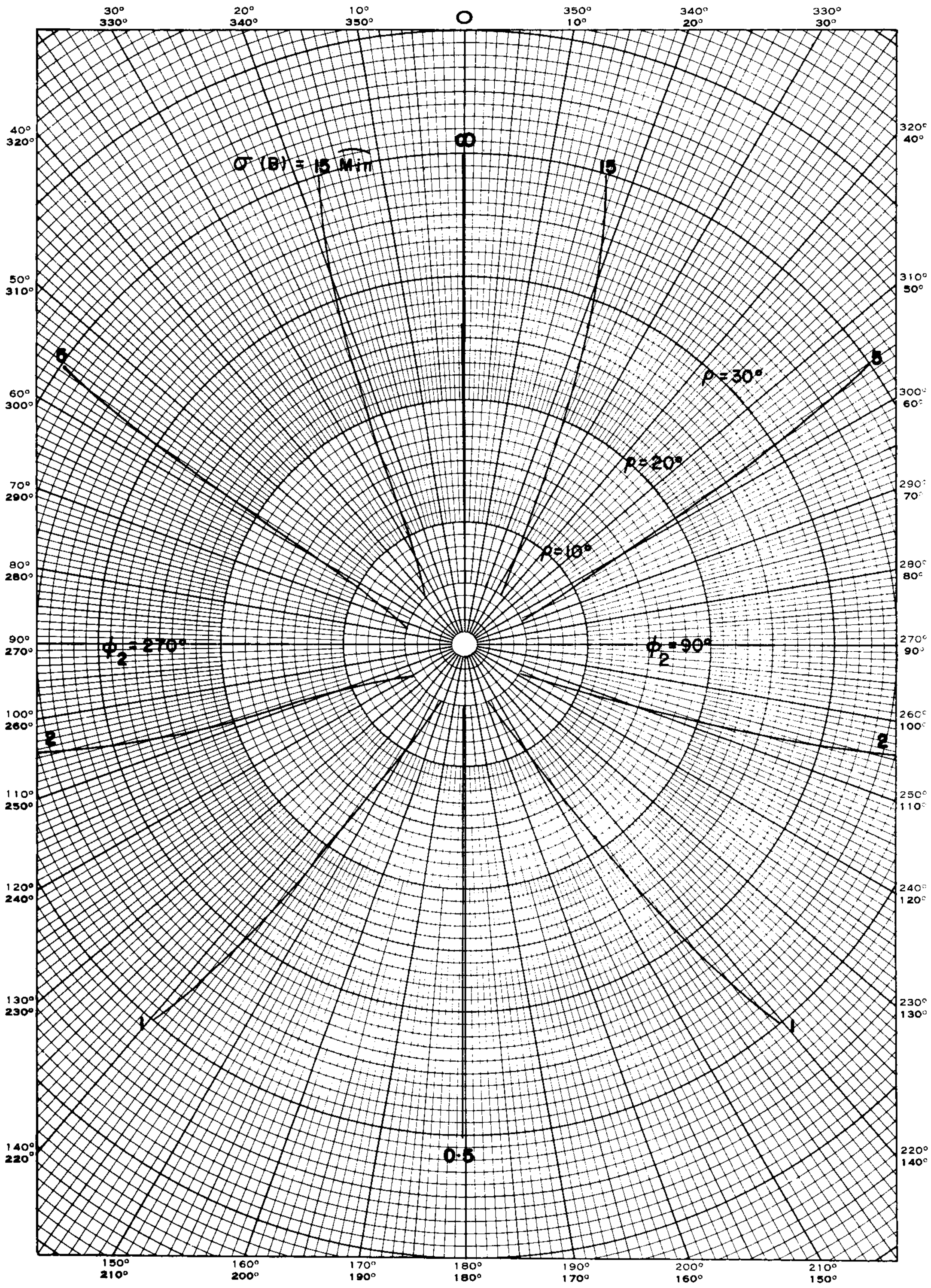

Figure V-10: $\sigma(\beta)$, Error in Direction of North (Minutes of Arc) as a Function of Common Coelevation of the Two Artificial Stars, ρ, and the Azimuth of the Second Star, ϕ_2

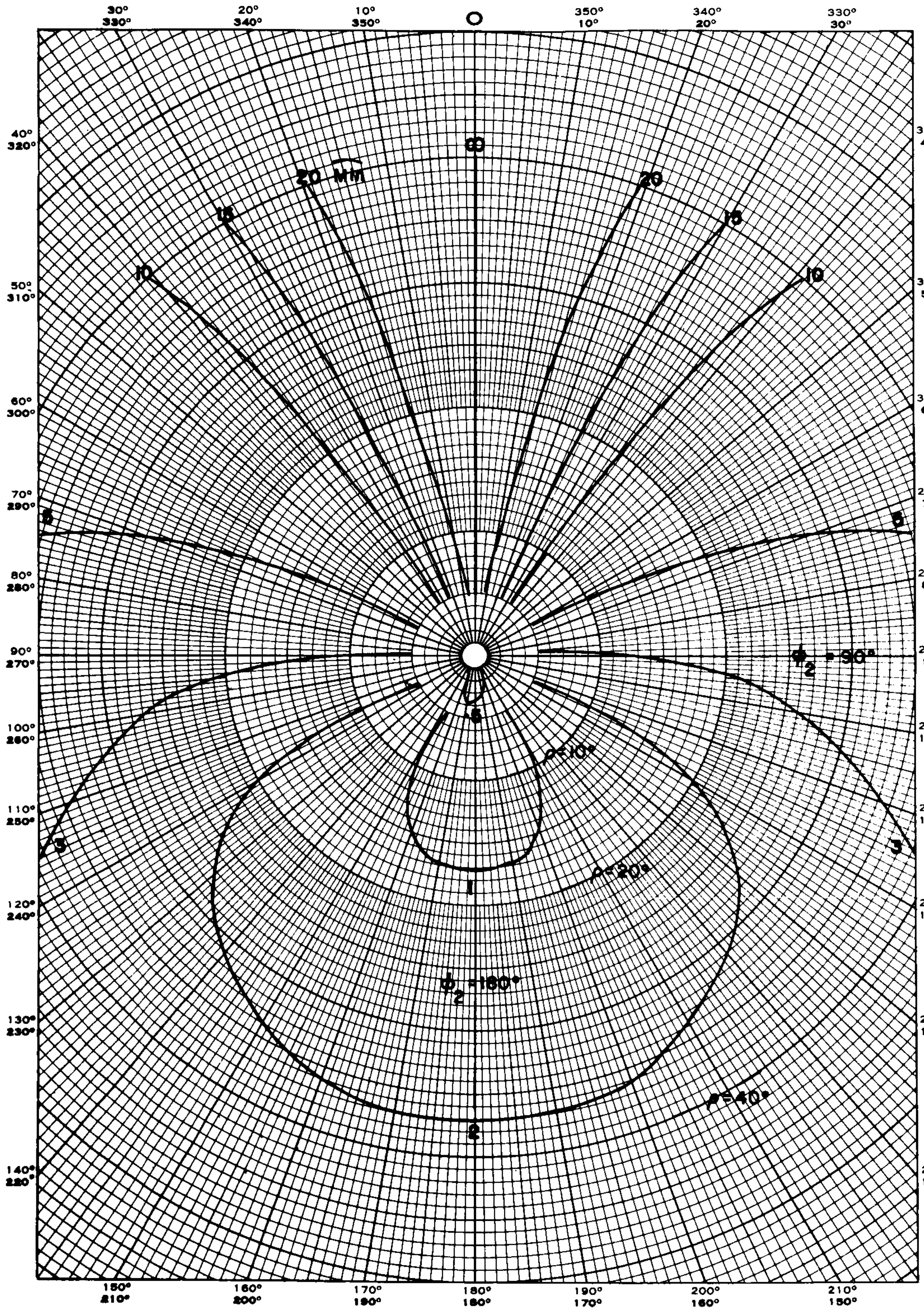

Figure V-11: $\sqrt{\sigma^2(\alpha) + \sigma^2(\delta) + \sigma^2(\beta)}$, Total Error as a Function of Common Coelevation of Two Artificial Stars, ρ, and the Azimuth of the Second Star, ϕ_2

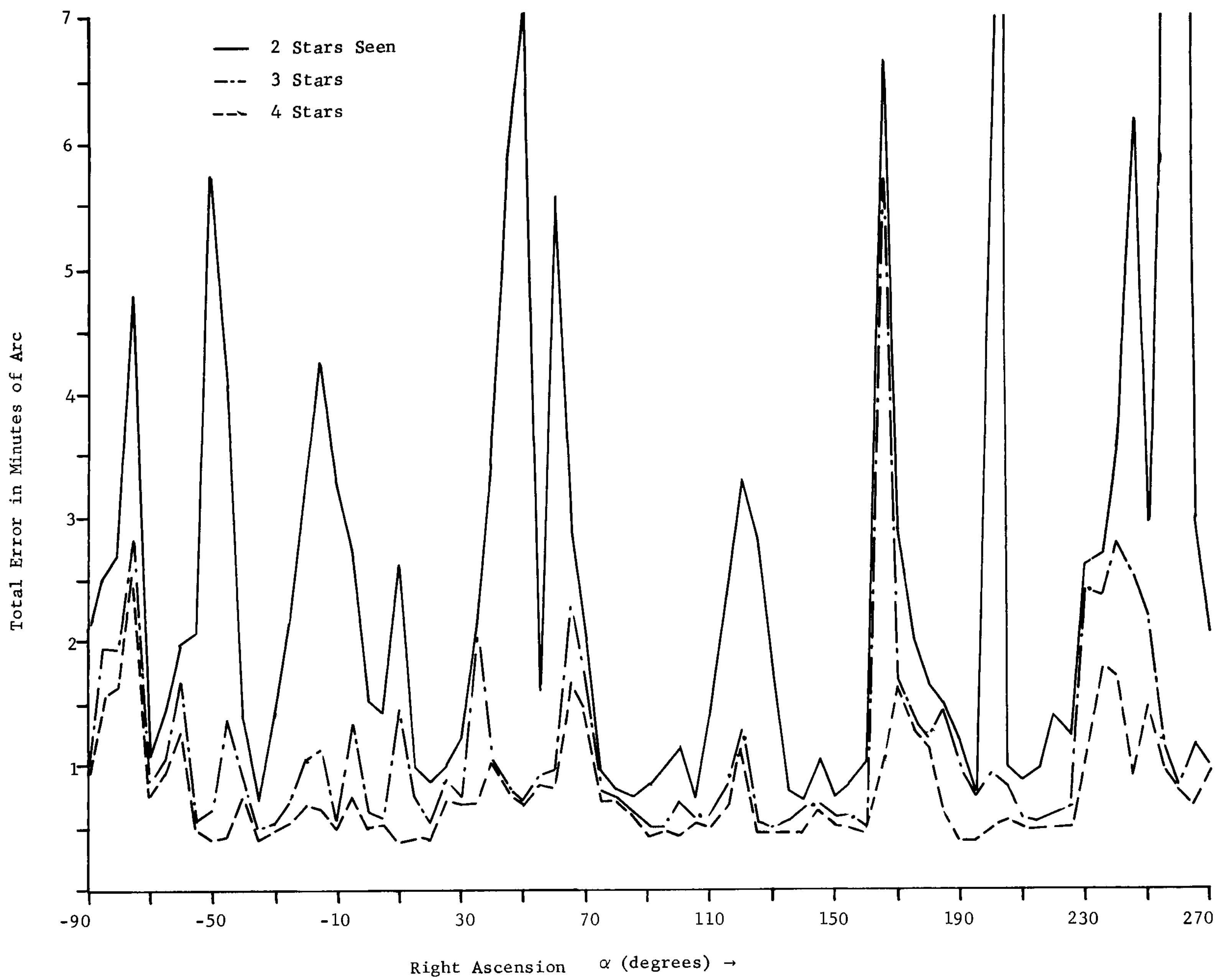

Figure V-12: Total Error as a Function of α for Two, Three, and Four Stars in Field of View (Double Slit)

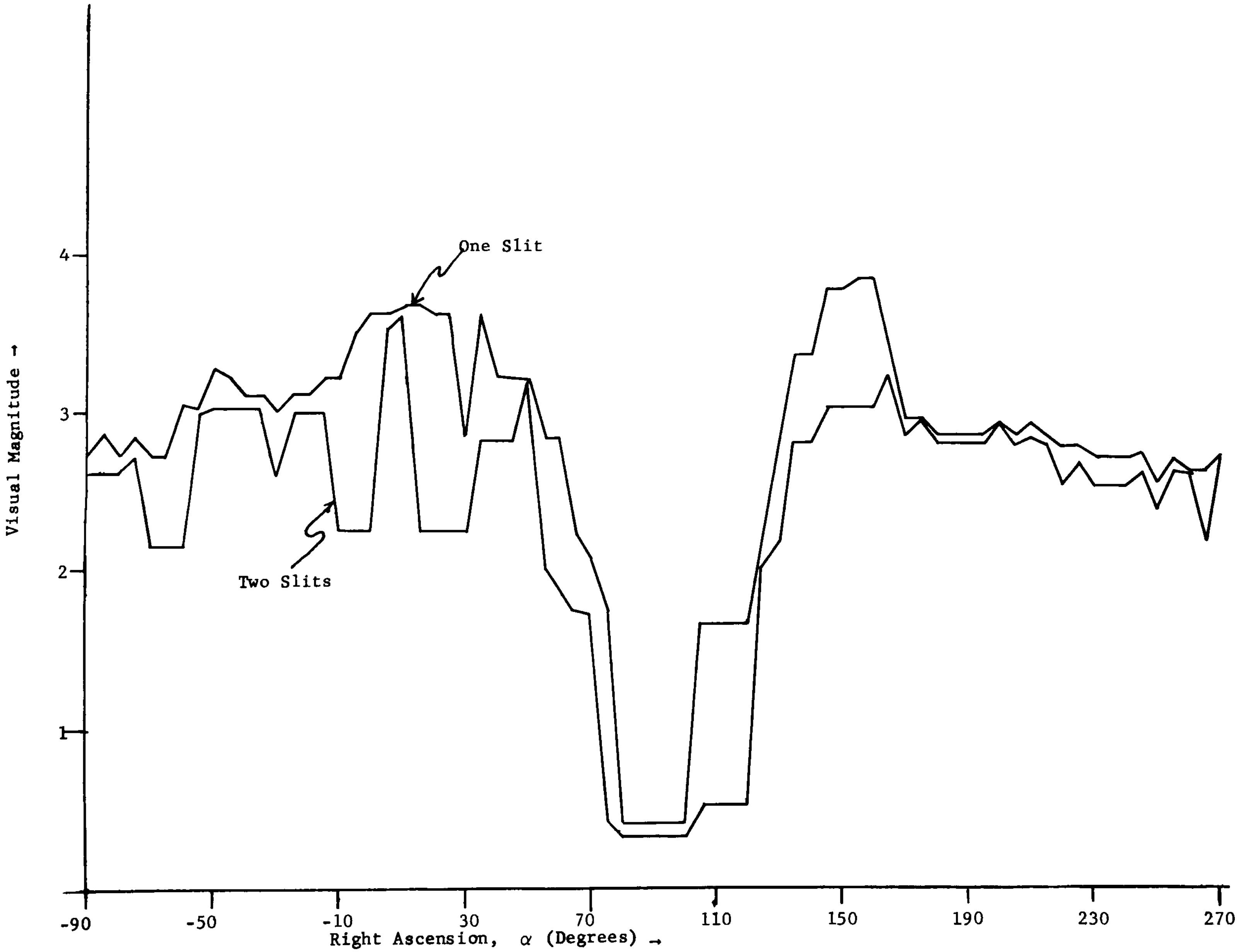

Figure V-13: Visual Magnitude Necessary so that Error < 6 Minutes (One Slit and Two Slits)

B. Error Due to Small Secondary Rate

Thus far, we have assumed that the sensor was spinning about a single fixed axis. We know that this assumption is only an approximation. For the Tiros, the main rate is approximately 360 degrees per six seconds. A secondary rate exists about the earth's axis of nominally one degree per day. Figure V-14 shows the errors which would result in α, δ, and β if this secondary rate exists, but is ignored in the data reduction. Note that for a rate of fifty degrees per day, which is fifty times the nominal value, the errors are still negligible.

A graph similar to Figure V-14, but pertinent to Nimbus, is given in Figure V-15. Here we have graphed the errors as a function of the spin period of the instrument. We assume a secondary rate of .1 degree per second, about the pitch axis (a maximum value). Note that this graph indicates we require a spin rate of two to three seconds or less.

To obtain the results indicated in these two graphs, we assumed no errors in the measurements.

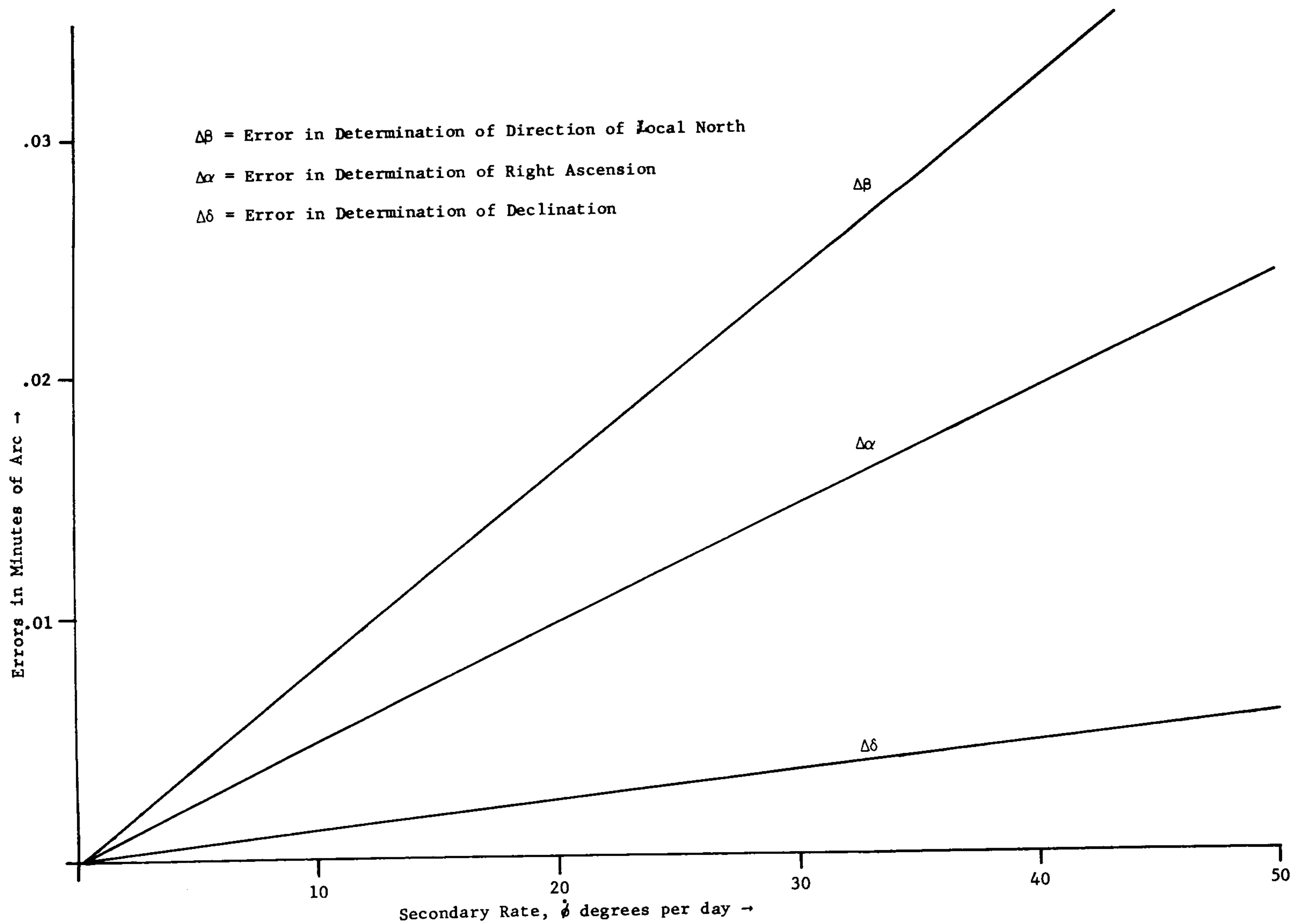

Figure V- 14: Error Due to Small Secondary Rate (Tiros)

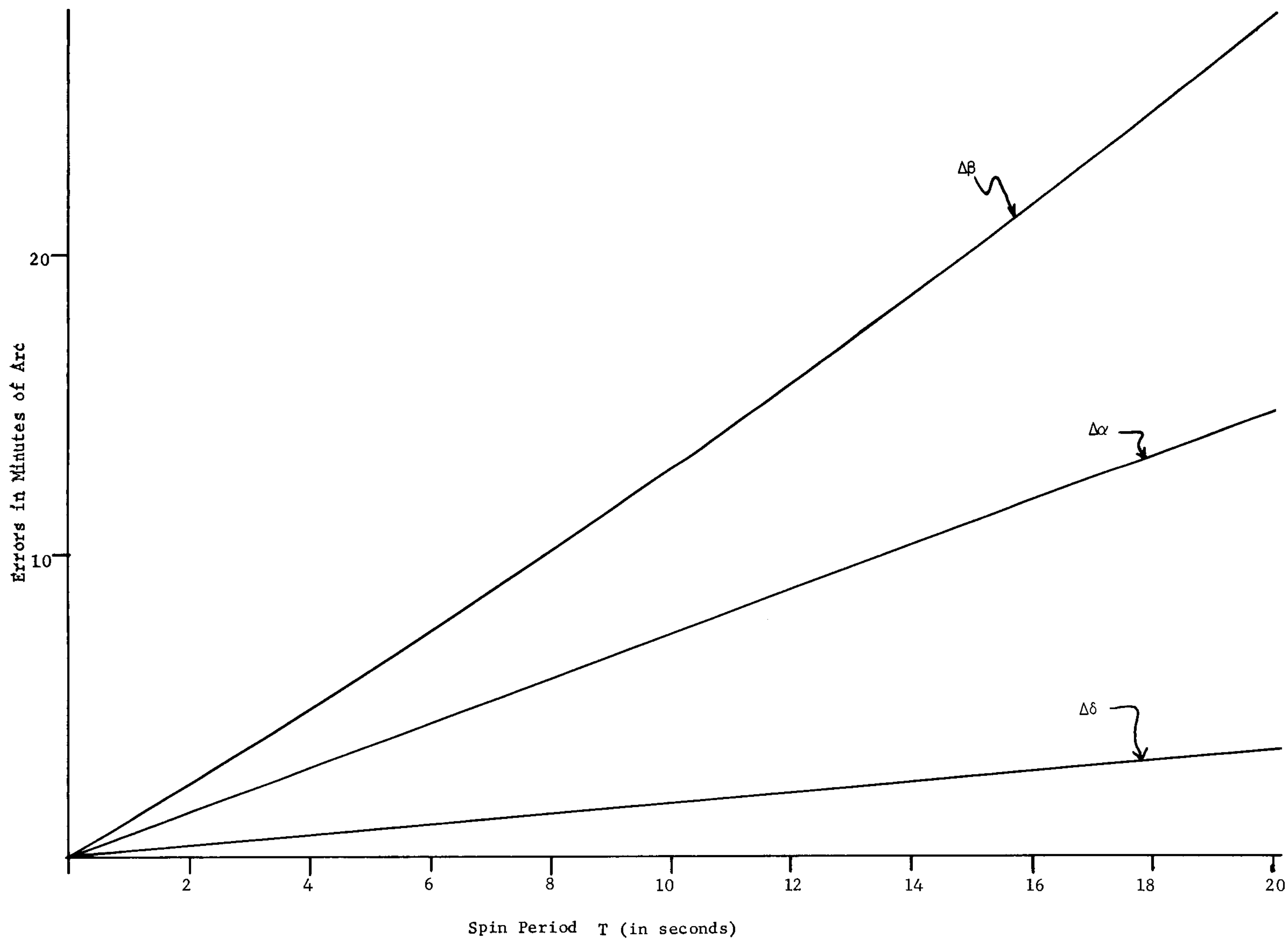

Figure V-15: Pitch Rate of + .1° per Second (Nimbus) Errors Due to Pitch Rate as a Function of Spin Period

VI. STAR IDENTIFICATION

The star identification problem consists of establishing a pairing of a transit time with the name (number) of the star which furnishes that transit. We now direct ourselves to this problem as presented by the single slit configuration. Since stellar magnitudes can not be measured accurately by the sensor, we describe a method which does not utilize magnitude measurements for the identification process.

The problem of identifying stars when only the relative azimuth of a set of targets is measured (angle as measured from some arbitrary reference about an unknown spin axis) is a very difficult task. Only if the approximate pointing direction of the instrument were known (to within five degrees, say) can the method described here assure us of a high probability of identification. If magnitudes are also measured accurately, this task becomes somewhat simpler, but certainly not trivial.

A. Modes of Operation

The method of identifying stars using relative azimuth angles will be illustrated. The explanation should follow the outline or block diagram as shown in Figure VI-1. Two modes of operation will be considered; normal and search mode.

Search mode is to be used during startup procedures and whenever the normal mode operation breaks down. In this mode, an attempt at identification is made using the given approximate pointing direction and a relatively large tolerance angle is used in defining the approximate field of view. If no quadruple can be identified, the pointing direction is changed systematically

Figure VI-1: SCADS Star Identification

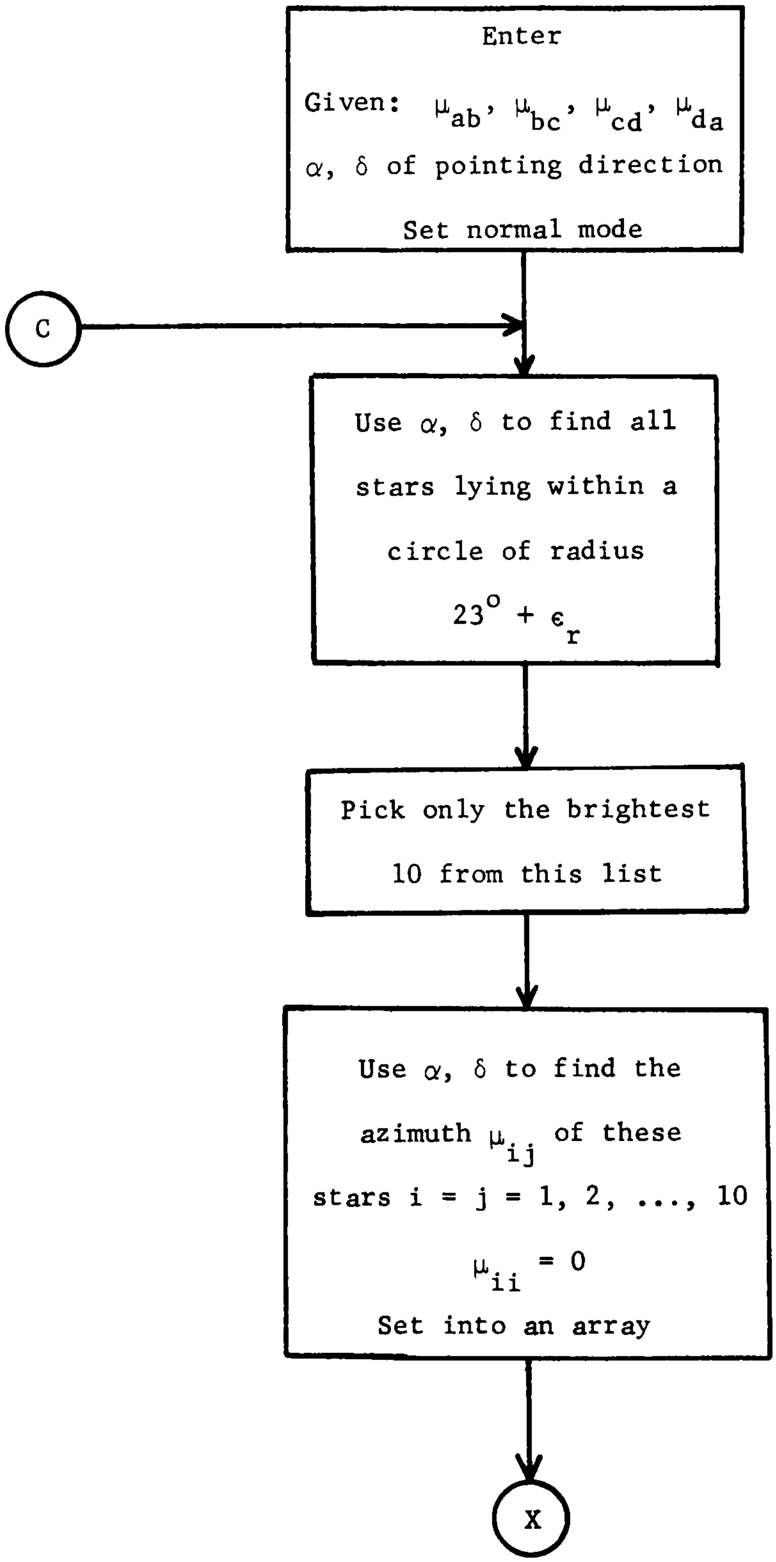

Figure VI-1 (Cont.)

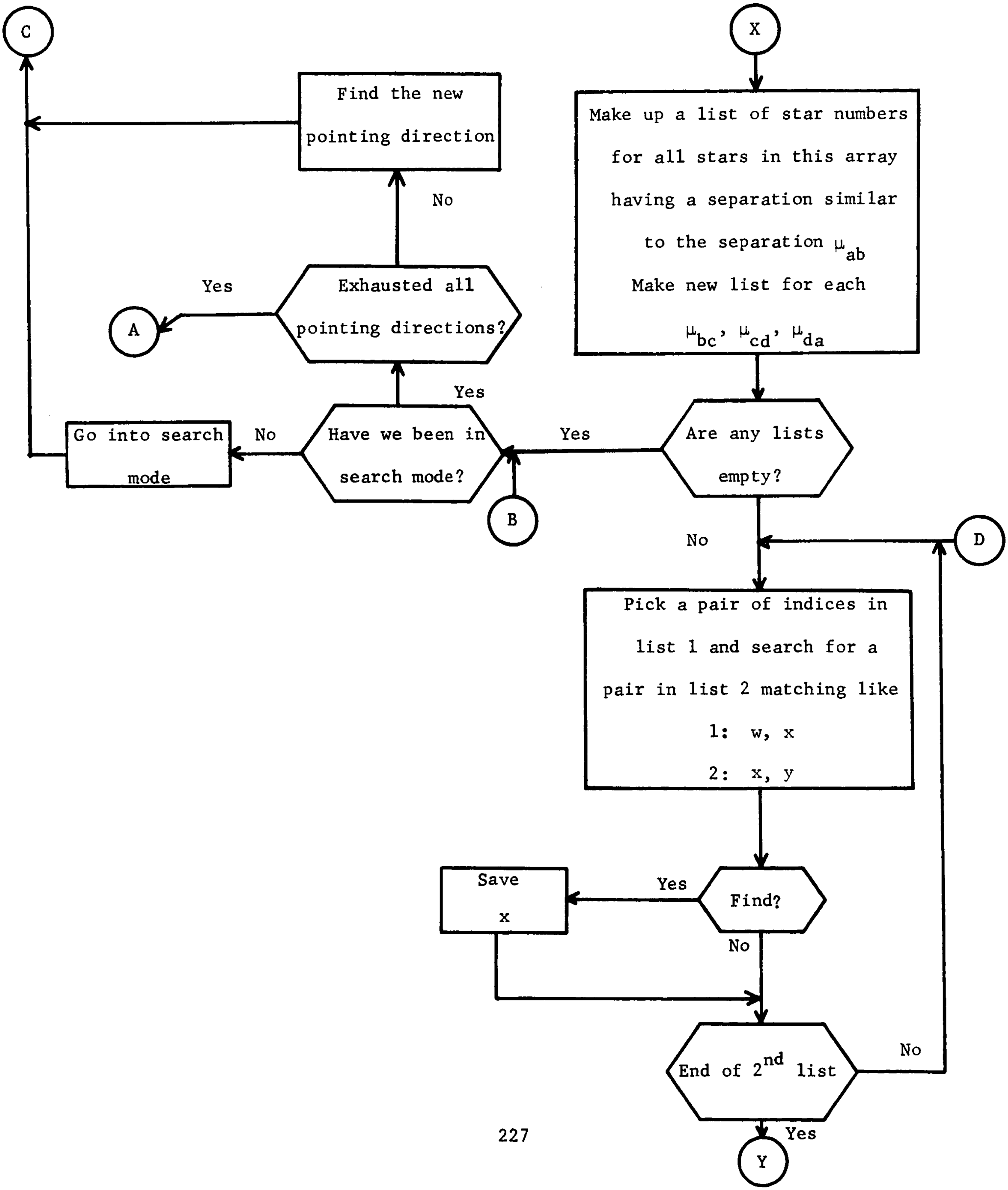

Figure VI-1 (Cont.)

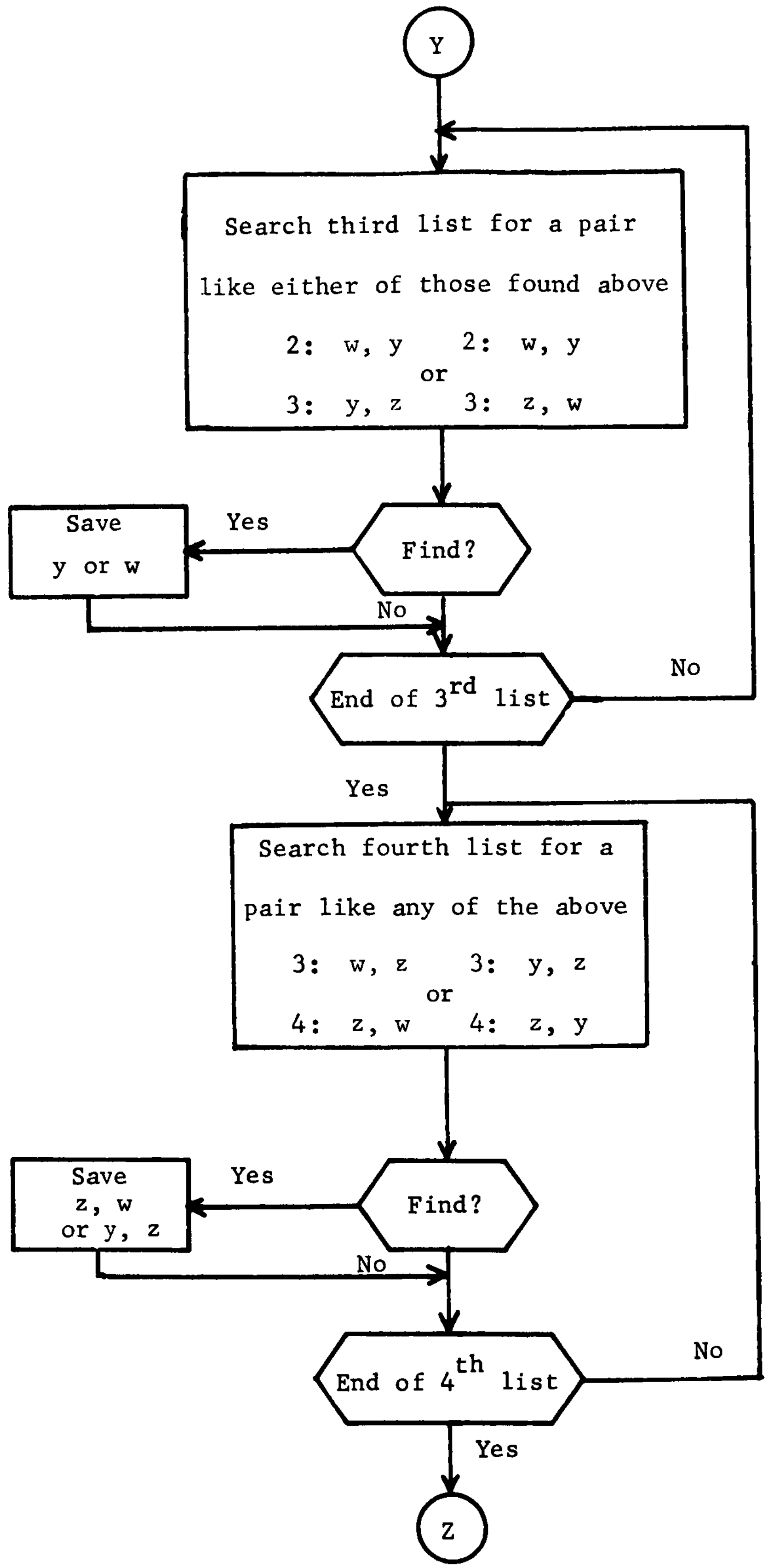

Figure VI-1 (Cont.)

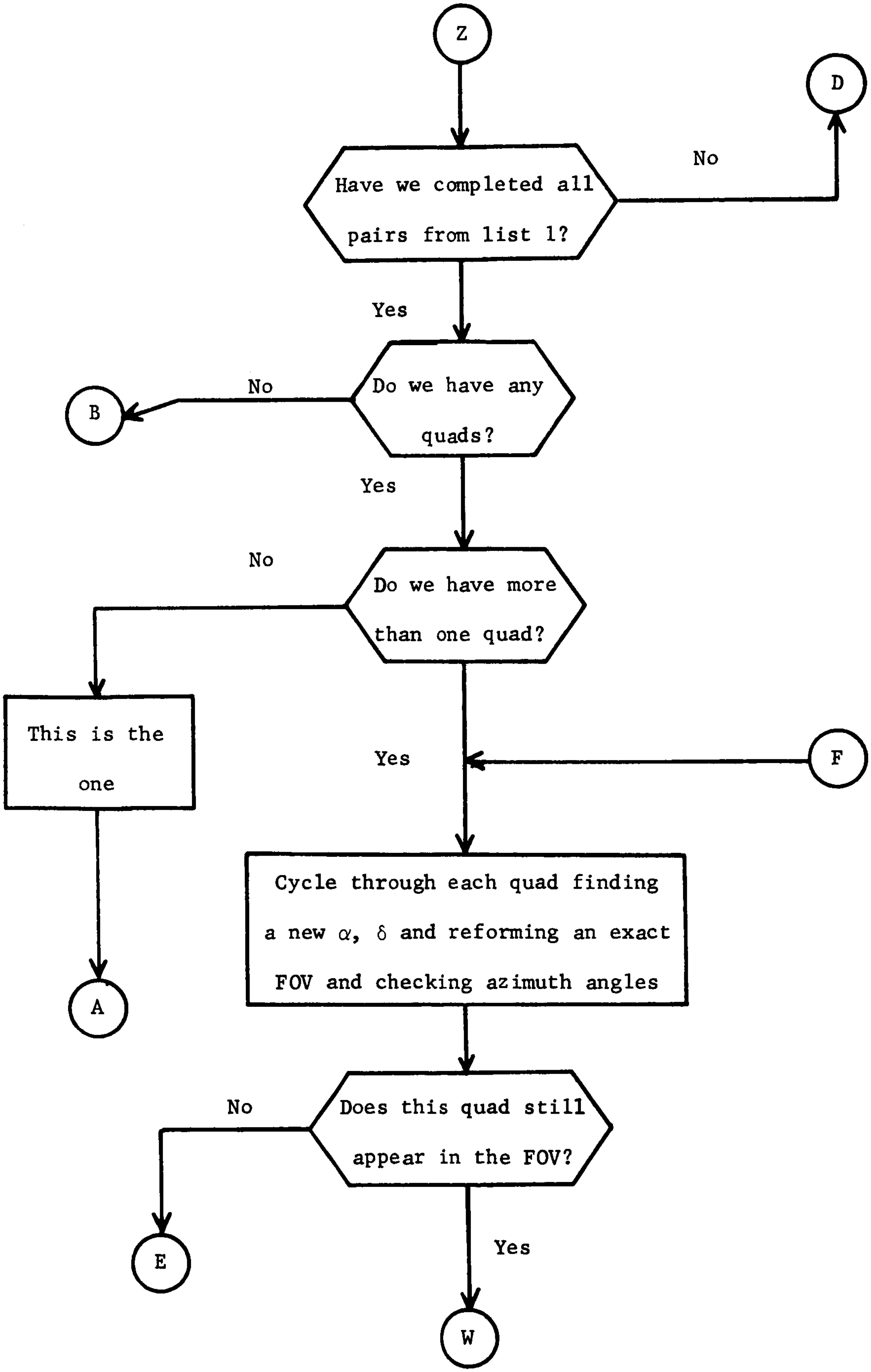

Figure VI-1 (Cont.)

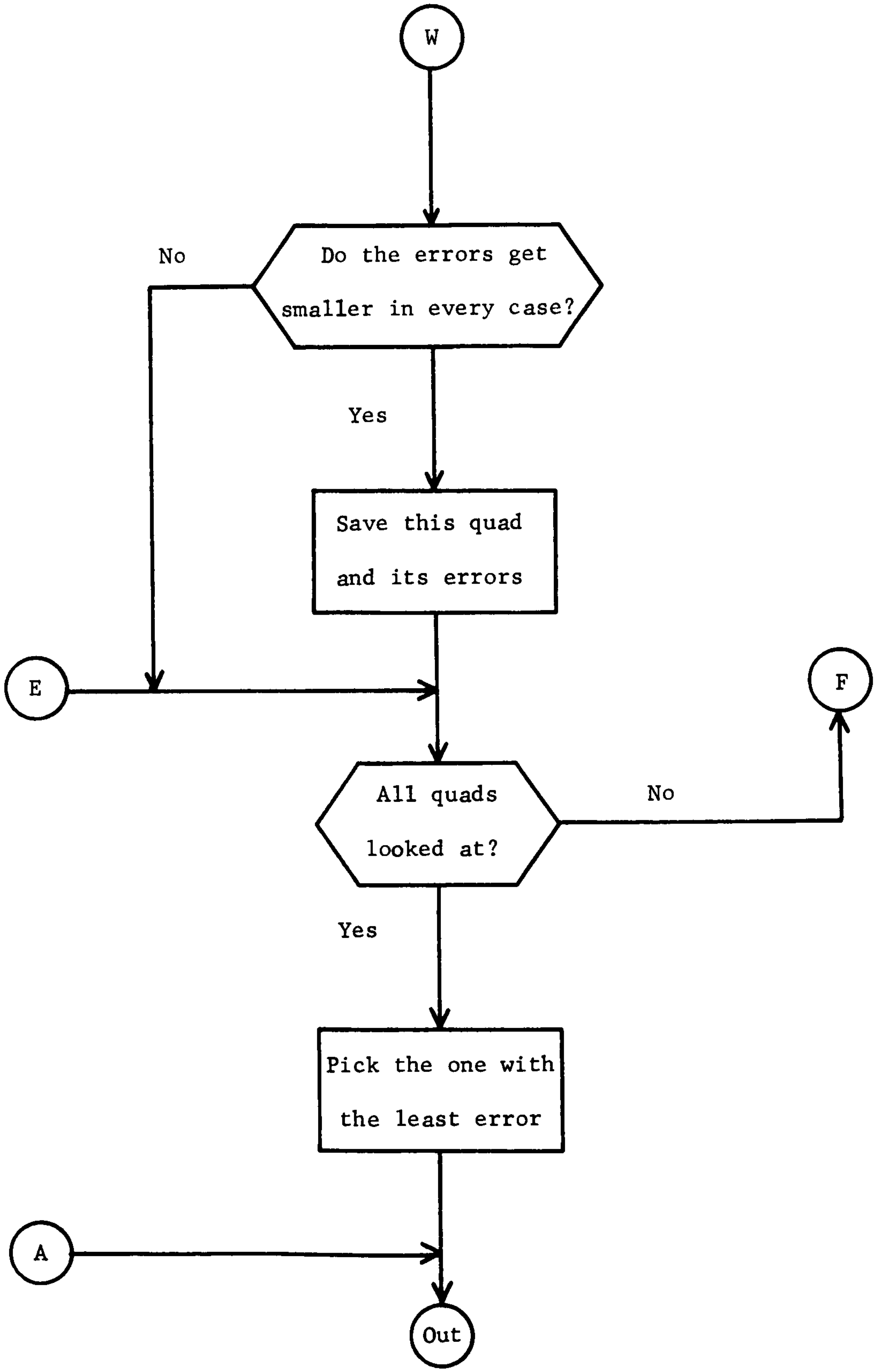

until the targets are identified. Once an accurate pointing direction has been found, the mode of operation switches from search to normal.

In the normal mode only a small tolerance angle is added to the optical field of view in order to find stars to be considered as candidates for the observed ones. This eliminates more stars (reduces the number of candidates) and simplifies the testing involved. If, at any time, the current position can not produce an identified quad, the next pointing direction position is taken, as indicated by Figure VI- 2.

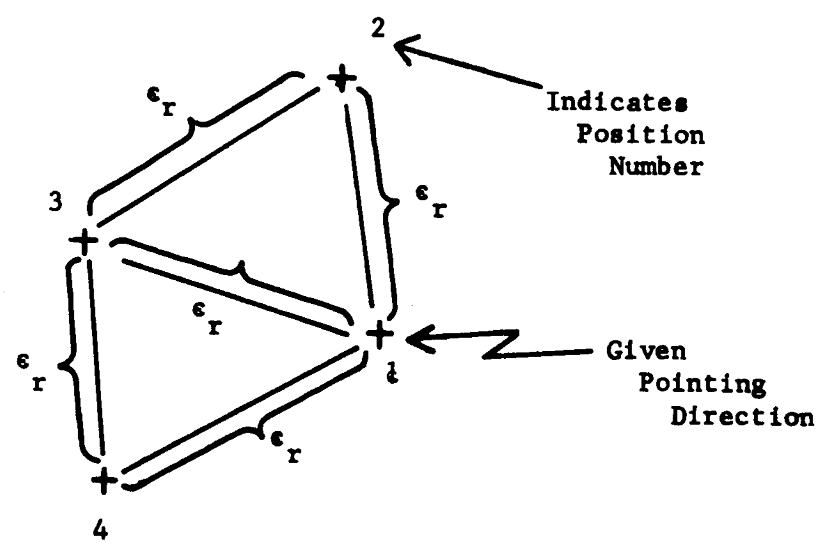

Figure VI- 2: Method of Searching

B. Identification Using Azimuth Angles

The actual method of matching stars with measured angles is relatively simple. The scanning instrument measures the angles $\beta + \mu_a$, $\beta + \mu_b$, $\beta + \mu_c$, and $\beta + \mu_d$ (β is unknown). A simple subtraction produces the angles μ_{ab}, μ_{bc}, μ_{cd}, and μ_{da}, as shown in Figure VI-3.

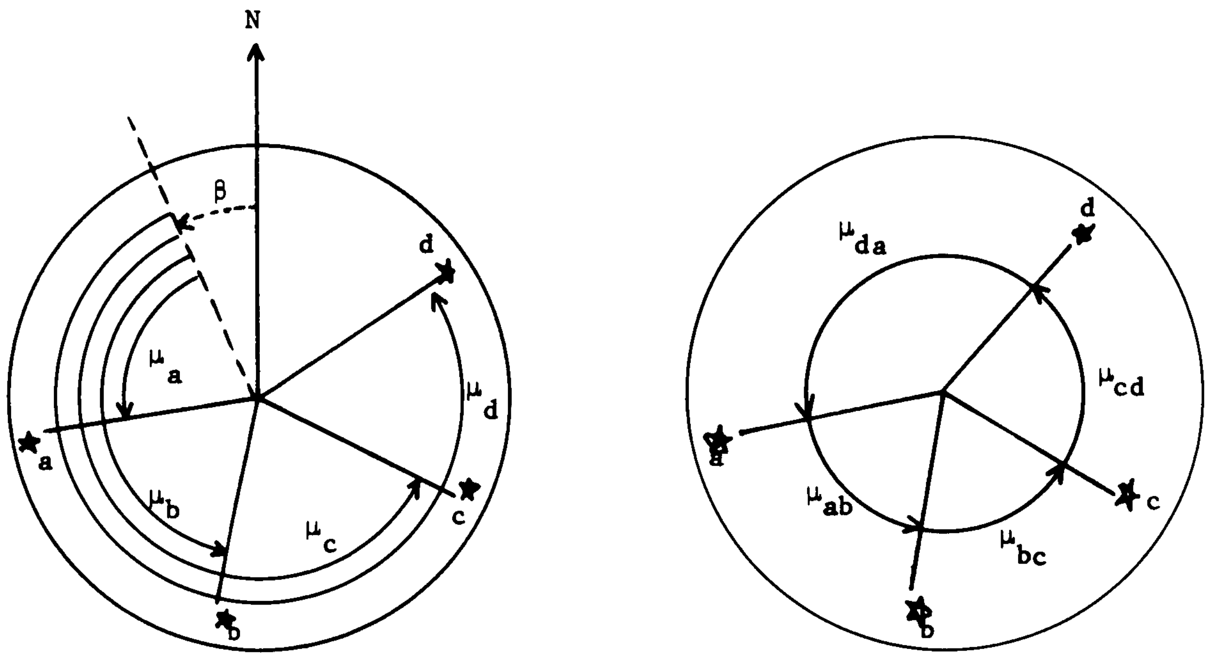

Figure VI-3: The Measured Azimuth Angles

An approximate star field is described using the current pointing direction and appropriate tolerance angle (both these quantities depend on the mode of operation). A list of all stars falling inside this field is set up. Next, all but the 10 brightest of these are eliminated from further consideration because of the method of detection involved (only the brightest 6 stars in the actual field of view are ever detected). A matrix is then made of relative azimuths of these 10 (or perhaps fewer) stars using the current pointing direction. Note that $\mu_{ij} = 360 - \mu_{ji}$ (the azimuth between star i and j is 360° - the azimuth between j and i).

Next, we take each of the four measured azimuth angles and search through the separation matrix seeking an angle μ_{ij} agreeing to within some relatively large tolerance angle μ_{ϵ} (about 5 degrees or so) with μ_{ab}, μ_{bc}, etc.

The indices i and j are saved for any angle found in this manner and searching continues until all tabulated angles have been checked. After considering all four measured azimuths we will have four lists of indices.

μ_{ab}	μ_{bc}	μ_{cd}	μ_{da}
1 - 3	1 - 4	1 - 2	1 - 10
1 - 10	3 - 5	2 - 4	4 - 5
3 - 7	3 - 6	3 - 9	4 - 9
3 - 8	3 - 10	5 - 6	6 - 3
3 - 9	6 - 2	8 - 2	
5 - 1	7 - 2	10 - 4	
5 - 2	8 - 5	10 - 5	
8 - 6	10 - 2		
8 - 10			

The actual identification process then is simply to scan across the four lists looking for sets of indices of the form

a - b   b - c   c - d   d - a

The underlined indices exhibit this form. We must conclude then that the four observed stars are 3, 8, 5, and 6 respectively. However, it may be very possible to find other sets of four stars which also are of this form. In this case, each quadruple must be further examined. Suppose there are several quadruples satisfying this condition. Each set is used to establish the pointing direction right ascension and declination according to these four stars. Using the actual camera field of view (23 degrees), stars are picked from the catalog which fall within this field. A test is made to determine whether the four stars of the set are among these possibilities. If not, we are probably working with the wrong set and we choose the next one. If these four stars are among the possibilities, their azimuths are recomputed, using the most recently calculated pointing direction. This direction could be tested to see if it falls near the assumed direction and the set discarded if not. A check then is made to determine if all four of the angles agree better than before with the measured azimuths. If not, we discard this quadruple and take the next one. If the angles do agree better than before, we record the errors and the star numbers and consider the next set. If many sets agree better than before (each set produces its own pointing direction), all possible identifications will be considered as correct; however, the set which produces the smallest azimuth angle deviations will be suggested as the most likely candidate.

VII. CONCLUSIONS AND RECOMMENDATIONS

The most general conclusion for this study is that the SCADS sensor is indeed feasible and can be designed to be a highly convenient instrument for satellite application in that the requirements of weight, volume, and power are not excessive. The mechanical and electronic designs do not necessitate an advance in the state-of-the-art.

Let us now enumerate the most salient conclusions of this study.

Instrumentation

(1) The Tiros instrument may be contained in the dimensions 3" x 4" x 6". The weight will be about 2.9 pounds. The required operating power will be about 5.7 watts if a system which digitizes the stellar signal is utilized. If the satellite tape recorder is utilized, or the analog signal is telemetered directly, then 2.5 watts are required.

(2) The Tiros optics require a 1" clear aperture, whereas, the Nimbus requires about 1.5" diameter optical system.

(3) For the Nimbus instrument, the dimensions are 3.5" x 4" x 8", will weigh about 4.5 pounds, and will require 20 watts of power while in operation. Three watts may be saved if the signal is not digitized on-board.

(4) The Tiros instrument will have no moving parts, but the slit in the Nimbus instrument must be rotated with about a two second period.

(5) An angle encoder must be provided with the Nimbus configuration.

(6) For both instruments, a single wedge-shaped slit is recommended.

(7) The recommended photodetector is a photomultiplier.

(8) An electronic design which features a ground controlled variable bias level is recommended rather than a design which automatically changes the bias level. A fixed bias level cannot be recommended.

(9) For the Tiros instrument, a saving in power can be achieved by integrating the SCADS instrument with the satellite tape recorder. It is estimated the SCADS instrument will require only 2.5 watts.

Analysis

(1) The accuracy of the instruments in determining celestial attitude is highly dependent on the portion of the sky observed, but is always better than 0.1 degree.

(2) The Tiros sensor is capable of determining the precessional motion of the satellite.

(3) A manual solution is possible for both Tiros and Nimbus, but this solution must assume uniform rotation about a fixed axis.

Stellar Targets and Background

(1) The earth and sun should never be within the field of view of the instruments.

(2) Three stars are required to be within the field of view for the mathematical solution of the problem, but four stars are required so that an identification can positively be guaranteed.

(3) The moon will be in the field of view for roughly 42 days per year. It is possible to design the instrument so that it operates during this period.

REFERENCES

1 Tepper, Morris and David S. Johnson, "Toward Operational Weather Satellite Systems," Astronautics and Aeronautics, Vol. 3, No. 6 (June 1965).

2 Lillestrand, R. L. and J. E. Carroll, "Self-Contained System for Interplanetary Navigation," American Astronautical Society Meeting, August 1961.

3 Barcus, R., "A Functional Description of the Stabilization and Control Subsystem for the Nimbus Satellite (Flight Vehicle)," General Electric Doc. No. 635D4295, August 1964.

4 Zimmerman, C. D., "Star Background Model," Control Data Memorandum TM 9558-4, Research Division, Control Data Corporation, Minneapolis, Minnesota, September 1965.

5 Final Report "Special Techniques for Space Navigation," Vol. 2: Physical Phenomena. Submitted to M.I.T. Instrumentation Laboratory. Subcontract 247 of Prime Contract NAS9-153, July 1964. Research Division, Control Data Corporation.

6 Norton, R. H., "The Absolute Spectral-Energy Distribution of Canopus," Jet Propulsion Laboratory Technical Report No. 32-641, California Institute of Technology, Pasadena, California, August 15, 1964.

7 Richtnyer, F. K. and E. H. Kennard, Introduction to Modern Physics, McGraw-Hill Book Company, New York, Third Edition, 1942.

8 Allen, C. W., Astrophysical Quantities, Athlone Press, Second Edition, 1963.

9 Smith, R. A., F. E. Jones and R. P. Chasmar, The Detection and Measurement of Infra-Red Radiation, Oxford at the Clarendon Press, 1957.

10 Williams, R. L., "Fast High-Sensitivity Silicon Photo-Diodes," Jour. Opt. Soc. Am. 52, No. 11, 1237 (November 1962).

11 Kron, G., "Developments in the Practical Use of Photocells for Measuring Faint Light," Astrophysical Jour., 115, No. 1,(January 1952).

12 Steinke, E., Zeits. fur Phys., 38, 378 (1936).

13 Low, F., "Low-Temperature Germanium Bolometer," Jour. Opt. Soc. Am., 51, No. 11 (November 1961).

14 Franzen, W., "Non-Isothermal Superconducting Bolometer: Theory of Operation," Jour. Opt. Soc. Am., 53, No. 5 (May 1963).

15 Saito, S., K. Kurokawa, Y. Fujii, T. Kimura, Y. Uno, "Detection and Amplification of the Microwave Signal in Laser Light by a Parametric Diode," Proc. IEEE 50, No. 11, p. 2369 (November 1962).

16 Garbrecht, K., W. Heinlein, "Noise Performance of Photo-Diodes in Parametric Amplifiers," Proc. IEEE 52, No. 2, p. 192 (February 1964).

17 Saito, S. and Y. Fujii, "On the Noise Performance of a Photo-Parametric Amplifier," Proc. IEEE 52, No. 8, p. 978 (August 1964).

18 Haitz, R. H., A. Goetzberger, R. M. Scarlett, and W. Shockley, "Avalanche Effects in Silicon p-n Junctions I. Localized Photomultiplication Studies on Microphasmas," Jour. Appl. Phys. 34, No. 6 1581 (June 1963).

19 Di Domenico, M., W. M. Sharpless, and J. J. McNicol, "High Speed Photo Detection in Germanium and Silicon Cartridge Type Point Contact Photo-Diodes," Appl. Optics 4, No. 6 677 (June 1965).

20 Levy, G., "Infra Red System Design," Electrical Design News, May 1958.

21 Lallemand, A., "Photomultipliers," in Astronomical Techniques, ed. by W. A. Hiltner, Vol. II of Stars and Stellar Systems, University of Chicago Press, 1960.

22 Ball, W. P., Unpublished Hughes Memorandum, "Simulated Space-Nuclear Radiation Effects Tests on Canopus Sensor."

23 McIlwain, C. E., "The Radiation Belts, Natural and Artificial," Science 142, 355-361, October 1963.

24 "Transistor Design Effects pm Radiation Resistance," Hughes Aircraft Company, Semiconductor Division, Final Report, DA-36-039-AMC-02352(E).

25 Jaffe, L. D. and J. B. Rittenhouse, "Evaporation Effects on Materials in Space," Materials for Missiles and Spacecraft, McGraw-Hill, Chapter 9, 1963.

26 Clauss, F. J., "Lubrication," Materials for Missiles and Spacecraft, McGraw-Hill, Chapter 10, 1963.

27 Beard, D. B., "Interplanetary Dust Distribution and Erosion Effects," in First Symposium Surface Effects on Spacecraft Materials, John Wiley, 1960.

28 Davidson, J. R. and P. E. Sandorff, Environmental Problems of Space Flight Structures, II. Meteoroid Hazard, NASA TN D-1993, January 1963.

29 Naumann, R. J., "Observed Torque-Producing Forces Acting on Satellites," NASA TR R-183, December 1963.

30 Bandeen, W. R. and W. P. Manger, "Angular Motion of the Spin Axis of Tiros I Meteorological Satellite Due to Magnetic and Gravitational Torque," Jour. Geophys. Res. 65, pp. 2992-2996, 1960.

31 Smith, G. Louis, "Effects of Magnetically Induced Eddy-Current Torques on Spin Motions of an Earth Satellite," NASA TND-2198, April 1964.

32 Goddard Space Flight Center and U. S. Weather Bureau, Final Report on the Tiros I Meteorological Satellite System, TR R-131.

33 Goldstein, H., Classical Mechanics, Addison Wesley Publishing Company, Reading, Massachusetts, 1959, pp. 124-127.

34 Harrington, D. C.,"Noise Error Analysis of an Optical Star and Planet Scanner," National Aerospace Electronics Conference, IEEE, May 1963.

35 Robinson, D. Z.,"Methods of Background Description and Their Utility," Proceedings IRE, Vol. 47, 1959, p. 1554.

36 Eldering, H. G.,"Method for Complete Description of Infrared Sky Backgrounds," Jour. Opt. Soc. Am., 51, 1424 (1961).

37 Jones, R. C., "Information Capacity of Radiation Detectors," Jour. Opt. Soc. Am., 50, 1166 (1960).

38 Jones, R. C.,"Information Capacity of a Beam of Light," Jour. Opt. Soc. Am., 52, 493 (1962).

39 Bharucha-Reid, Elements of the Theory of Markov Processes and Their Applications, McGraw-Hill Book Company, New York, 1960, Chapter 7.

40 Parzen, E., Stochastic Processes, Holden-Day, Inc., San Francisco, 1962, p. 143.

41 Wilks, S. S., Mathematical Statistics, John Wiley and Sons, New York, 1962, p. 402.

42 Cramer, H., Mathematical Methods of Statistics, Princeton University Press, Princeton, 1946, p. 477.

43 Rice, S. O.,"Mathematical Analysis of Random Noise," Bell System Tech. Jour., 23, 282-332 (1944), Bell System Tech. Jour., 24, 46-156 (1945).

44 Zimmerman, C. D.,"Comparison of Two Methods of Star Detection," Memorandum TM-141, Research Division, Control Data Corporation, Minneapolis, Minnesota, July 1964.

45 Levenbach, H., "The Zero-Crossing Problem," Research Report No. 63-4, Dept. of Elect. Eng., Queen's University, Kingston, Ontario, Canada, Sept. 1963.

46 Wilks, S. S., Mathematical Statistics, John Wiley and Sons, New York, 1962, p. 177.

47 Wainstein, L. A. and V. D. Zubalsov, Extraction of Signals from Noise, Prentice-Hall, Englewood Cliffs, New Jersey, 1962, Chapter 8.

48 Allen, C. W., Astrophysical Quantities, Athlone Press, London, 1955, pp. 213, 214.

49 Lowen, Irving B. and Marvin S. Maxwell, Scanning Celestial Attitude Determination System (SCADS). Presented at the Twelfth East Coast Conference on Aerospace and Navigational Electronics, October 27-29, 1965, Baltimore, Maryland.

APPENDIX A

FLOW CHARTS FOR COMPUTER SOLUTION

This appendix contains the flow charts for the computer solution to the problem of obtaining the celestial attitude of the Tiros and Nimbus spacecraft from the output of the SCADS sensor. The analysis is given in Section IV.

The chart given applies directly to Tiros. Precession is assumed. The Nimbus problem is simply a special case of the Tiros problem. For Nimbus, we assume $\theta \equiv \phi \equiv 0$.

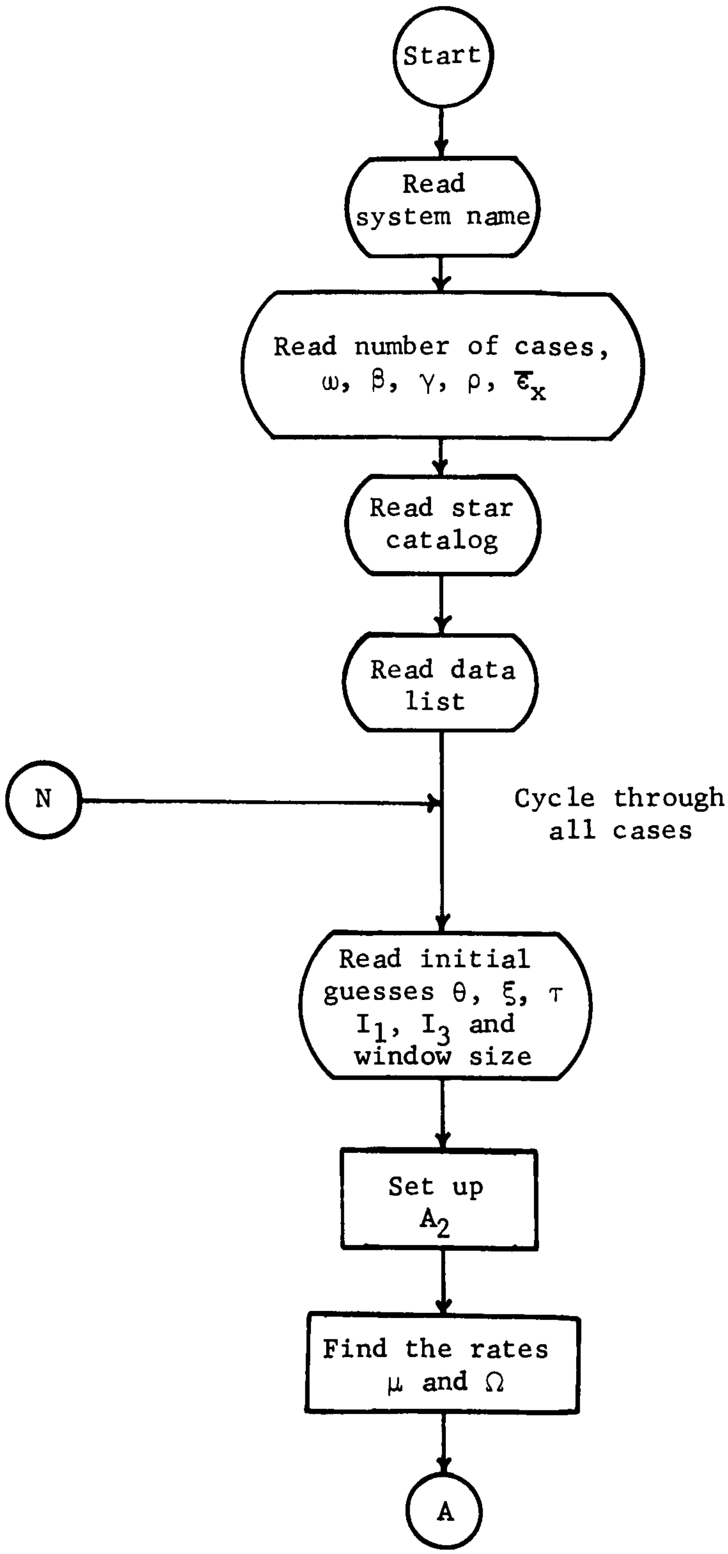
Start
Read system name
Read number of cases, ω, β, γ, ρ, $\bar{\varepsilon}_x$
Read star catalog
Read data list
N
Cycle through all cases
Read initial guesses θ, ξ, τ I_1, I_3 and window size
Set up A_2
Find the rates μ and Ω
A

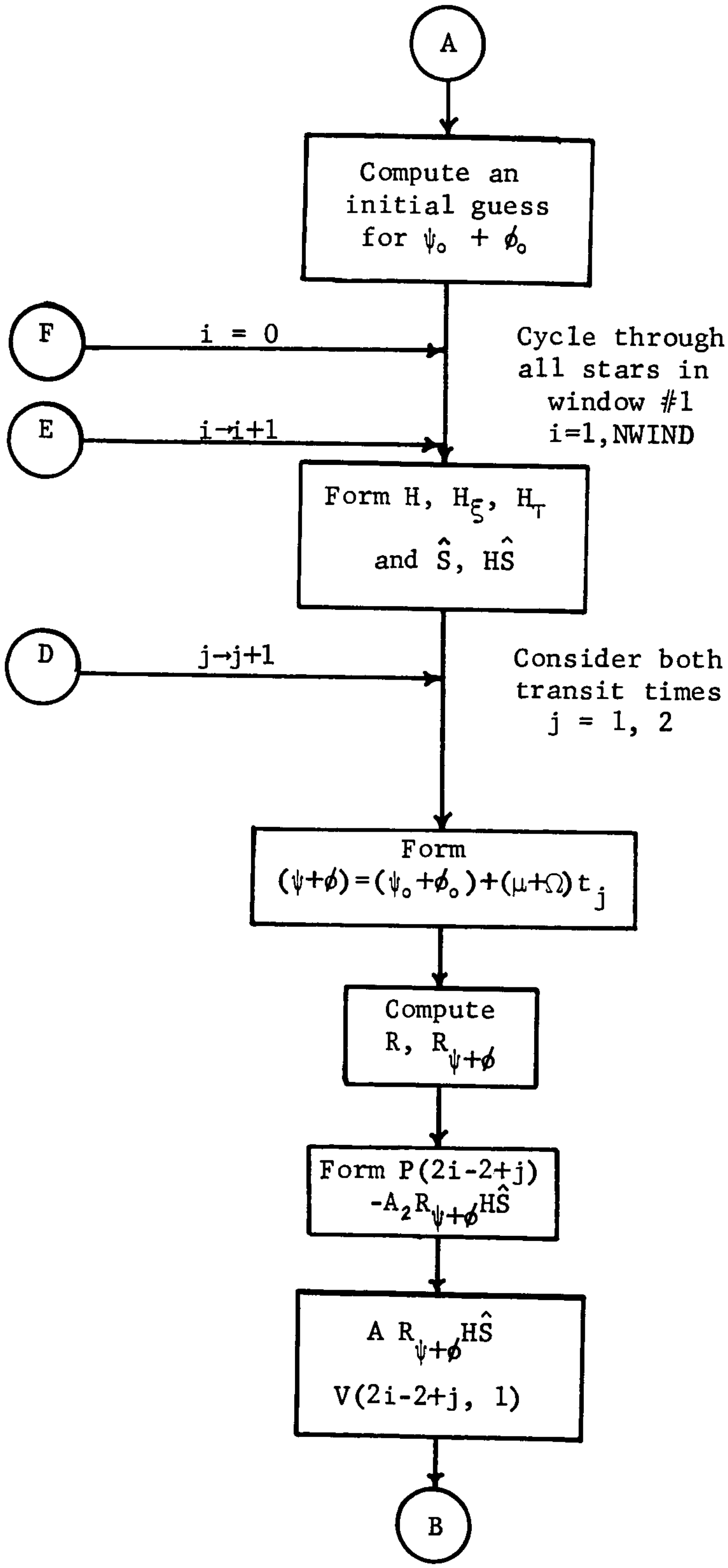
A
Compute an initial guess for $\psi_o + \phi_o$
F
$i = 0$
E
$i \rightarrow i+1$
Cycle through all stars in window #1 i=1,NWIND
Form H, H_ξ, H_T and $\hat{S}$, $H\hat{S}$
D
$j \rightarrow j+1$
Consider both transit times $j = 1, 2$
Form $(\psi+\phi) = (\psi_o+\phi_o)+(\mu+\Omega)t_j$
Compute R, $R_{\psi+\phi}$
Form $P(2i-2+j)$ $-A_2 R_{\psi+\phi} H\hat{S}$
$A\ R_{\psi+\phi} H\hat{S}$ $V(2i-2+j,\ 1)$
B

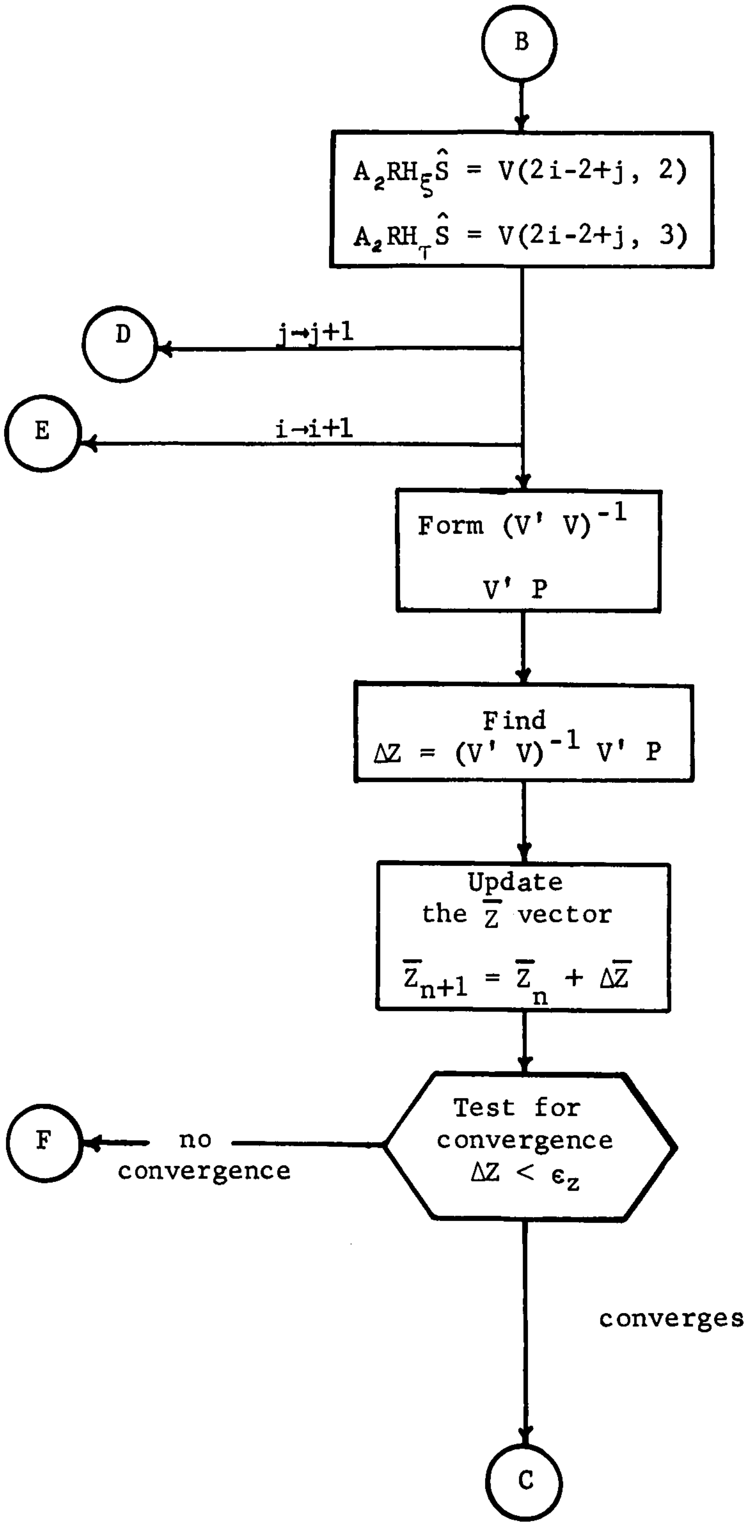
B
A₂RH_ξŜ = V(2i-2+j, 2)
A₂RH_TŜ = V(2i-2+j, 3)
j→j+1
D
i→i+1
E
Form (V' V)^-1
V' P
Find
ΔZ = (V' V)^-1 V' P
Update
the Z̄ vector
Z̄_n+1 = Z̄_n + ΔZ̄
Test for
convergence
ΔZ < ε_z
no
convergence
F
converges
C

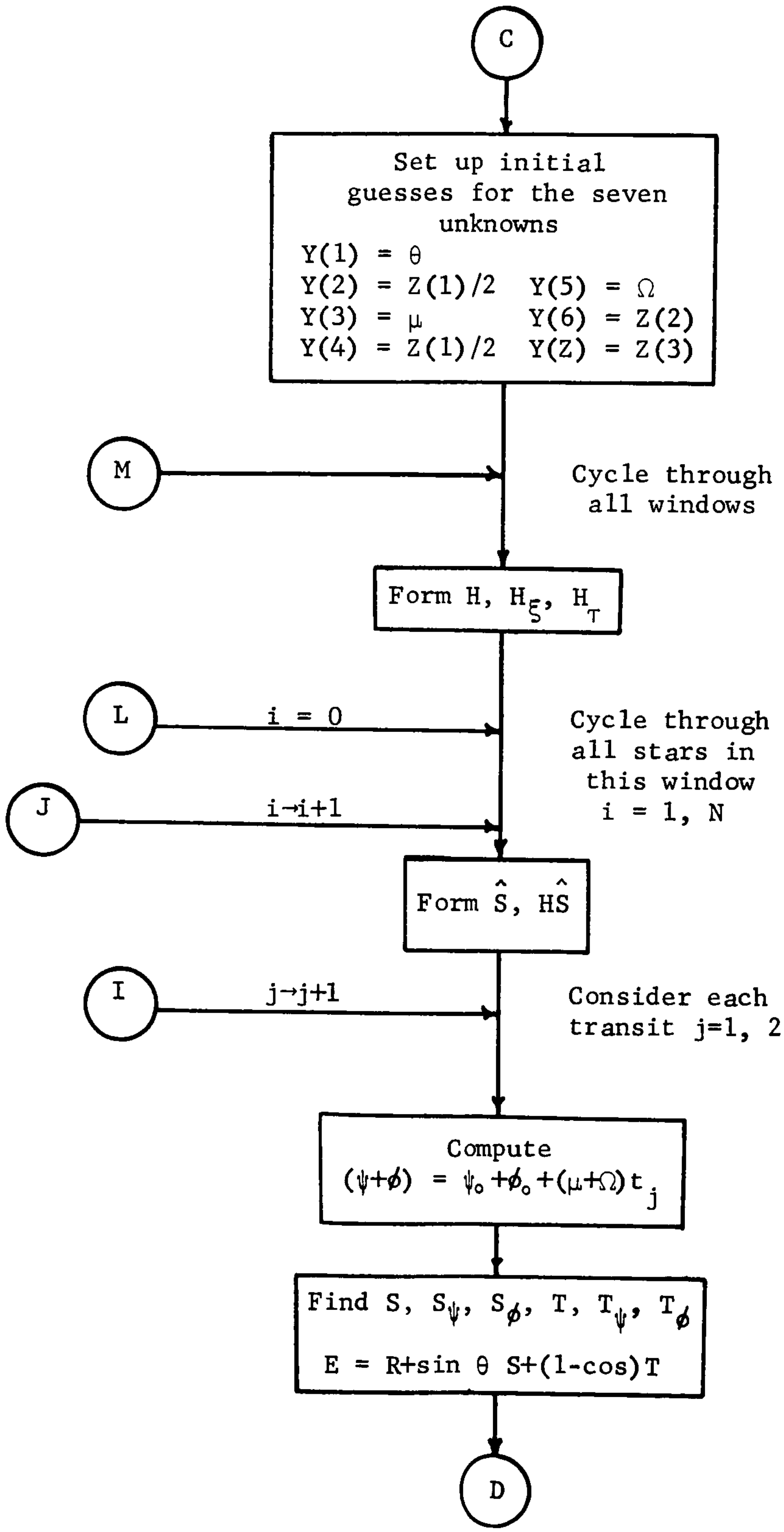
C
Set up initial guesses for the seven unknowns
Y(1) = θ
Y(2) = Z(1)/2
Y(3) = μ
Y(4) = Z(1)/2
Y(5) = Ω
Y(6) = Z(2)
Y(Z) = Z(3)
M
Cycle through all windows
Form H, H_ξ, H_T
L
i = 0
J
i→i+1
Cycle through all stars in this window i = 1, N
Form $\hat{S}$, $H\hat{S}$
I
j→j+1
Consider each transit j=1, 2
Compute
$(\psi+\phi) = \psi_o + \phi_o + (\mu+\Omega)t_j$
Find S, S_ψ, S_ϕ, T, T_ψ, T_ϕ
E = R+sin θ S+(1-cos)T
D

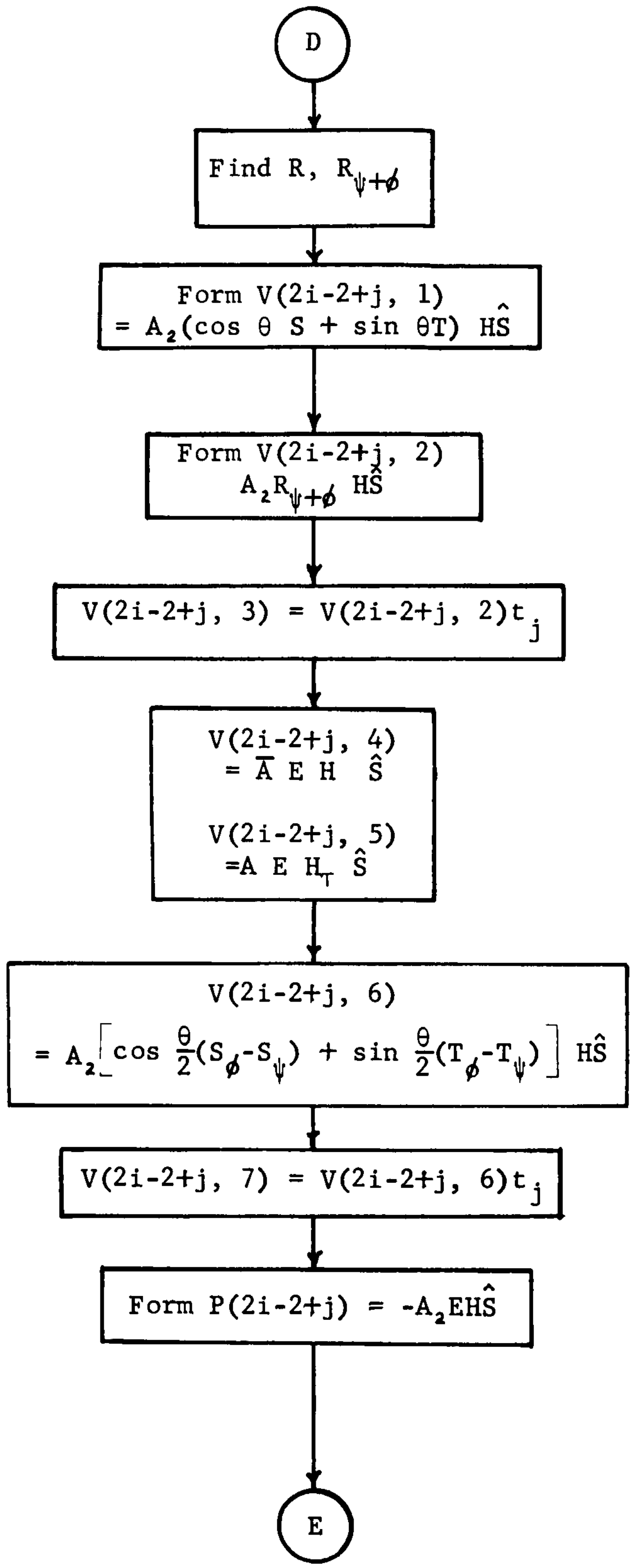
D
Find R, $R_{\psi+\phi}$
Form V(2i-2+j, 1)
$= A_2(\cos\theta\ S + \sin\theta T)\ H\hat{S}$
Form V(2i-2+j, 2)
$A_2 R_{\psi+\phi}\ H\hat{S}$
V(2i-2+j, 3) = V(2i-2+j, 2)t_j
V(2i-2+j, 4)
$= \overline{A}\ E\ H\ \hat{S}$
V(2i-2+j, 5)
$= A\ E\ H_T\ \hat{S}$
V(2i-2+j, 6)
$= A_2\left[\cos\frac{\theta}{2}(S_\phi - S_\psi) + \sin\frac{\theta}{2}(T_\phi - T_\psi)\right] H\hat{S}$
V(2i-2+j, 7) = V(2i-2+j, 6)t_j
Form P(2i-2+j) = $-A_2 EH\hat{S}$
E

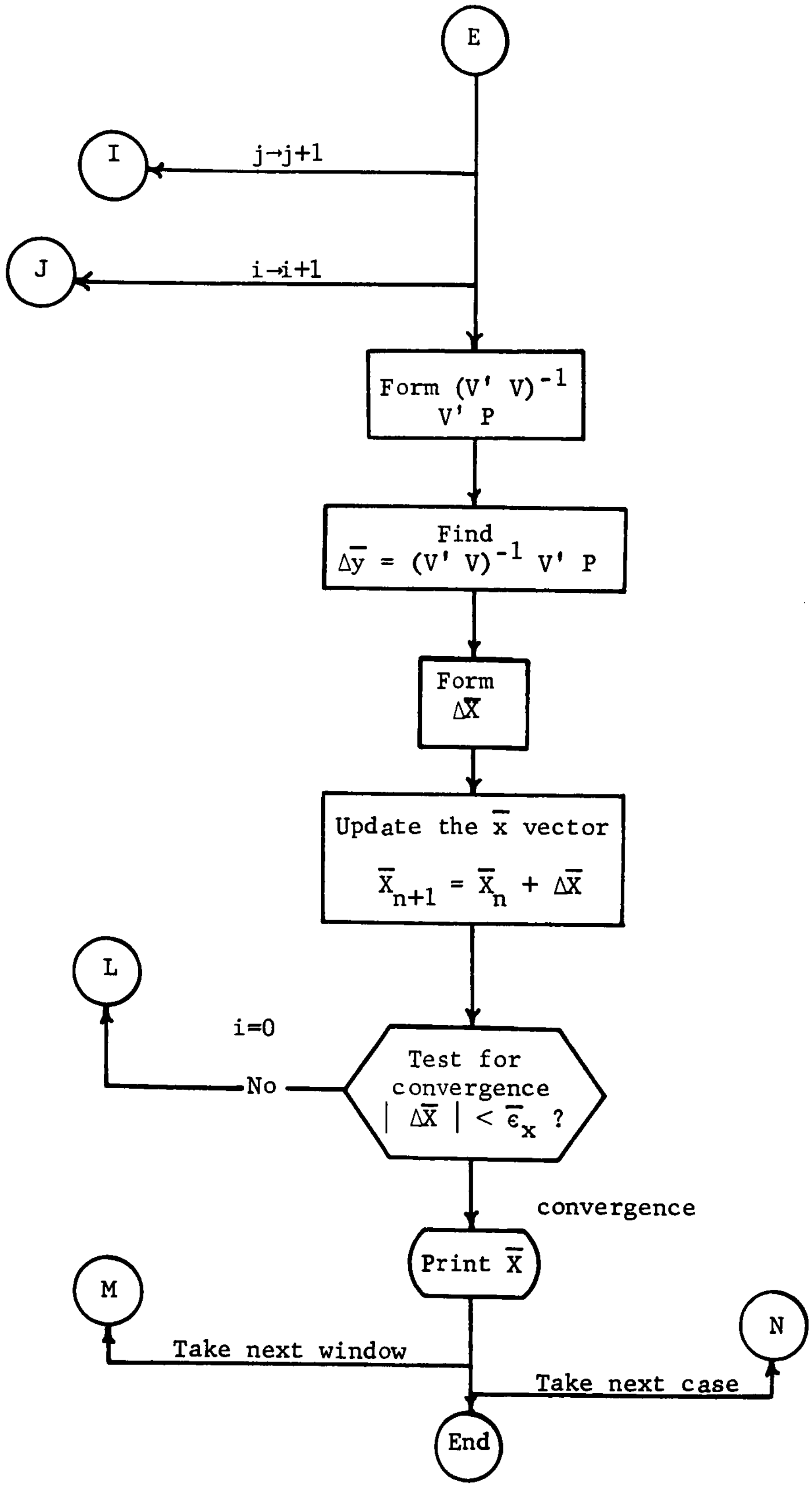
E
I
j→j+1
J
i→i+1
Form (V' V)^-1 V' P
Find Δȳ = (V' V)^-1 V' P
Form ΔX̄
Update the x̄ vector
X̄n+1 = X̄n + ΔX̄
L
i=0
No
Test for convergence | ΔX̄ | < ε̄x ?
convergence
Print X̄
M
Take next window
N
Take next case
End

APPENDIX B

TORQUE-FREE MOTION OF A NEARLY SYMMETRIC BODY

The following appendix shows to what extent the torque-free orientation motion of a rigid, nearly symmetric body may be approximated by the motion of a symmetric body. This work has been done by Control Data Corporation, under Contract No. NAS1-2902, and is included here in reference to the motion of Tiros.

The general problem of describing the orientation as a function of time of a torque-free rigid body with one point fixed is a classical problem of analytical dynamics. The solution may be written in terms of elliptic functions, and hence may be considered solved. However, the general solution is inconvenient for numerical computations and physical interpretation.

If the body has two equal moments of inertia the modulus of the elliptic functions, k, becomes zero and hence these functions degenerate into circular functions. If two moments are nearly equal, k is generally small in comparison to unity; and thus the elliptic functions may be written as a series of circular functions. (Reference [2]). Our purpose here is to develop such a series. We will rely on the general solution as presented by Whittaker (Reference [1], pages 144-152) and will retain his notation.

The orientation of the principle axes of the body with respect to a preferred inertial system can be specified by the three Euler angles θ, ϕ, ψ. Utilizing Whittaker's results we may write

$$\cos\theta = \frac{(\sinh\gamma - q^2\sinh 3\gamma + q^6\sinh 5\gamma + \ldots)}{(\cosh\gamma + q^2\cosh 3\gamma + q^6\cosh 5\gamma + \ldots)}$$

$$\times\frac{(1 + 2q\cos 2\mu t + 2q^4\cos 4\mu t + \ldots)}{(1 - 2q\cos 2\mu t + 2q^4\cos 4\mu t + \ldots)}$$

$$\tan(\psi - \psi_o) = \frac{(1 + 2q\cosh 2\gamma + 2q^4\cosh 4\gamma + \ldots)}{(1 - 2q\cosh 2\gamma + 2q^4\cosh 4\gamma + \ldots)}$$

$$\times\frac{(\sin\mu t - q^2\sin 3\mu t + q^6\sin 5\mu t \ldots..)}{(\cos\mu t + q^2\cos 3\mu t + q^6\cos 5\mu t \ldots..)}$$

$$\phi = \phi_o + \left(\frac{d}{A} + 4\mu\,\frac{q\sinh 2\gamma - 2q^4\sinh 4\gamma + \ldots}{1 - 2q\cosh 2\gamma + 2q^4\cosh 4\gamma - \ldots}\right)\cdot t$$

$$-\tan^{-1}\left(\frac{2q\sin 2\mu t\sinh 2\gamma - 2q^4\sin 4\mu t\sinh 4\gamma + \ldots}{1 - 2q\cos 2\mu t\cosh 2\gamma + 2q^4\cos 4\mu t\ \mathrm{cish}\ 4\gamma + \ldots}\right) \tag{b-1}$$

where either $A \geq B > C$, $Bc - d^2 > 0$ or $A \leq B < C$, $Bc - d^2 < 0$ and q is the parameter of the theta-functions (related to the original elliptic functions) and is small if the modulus k is small.

In order that approximations can be made in (b-1), we must attribute an order of smallness to the various terms. Let the three moments of inertia be given by

$$A = I_1\ (1 - \epsilon)$$
$$B = I_1\ (1 + \epsilon)$$
$$C = I_3 \qquad , A \geq B > C \text{ or } A \leq B < C \tag{b-2}$$

where $-1 \ll \epsilon \ll 1$, $\epsilon \geq 0$ if $I_3 > B$, $\epsilon \leq 0$ if $I_3 < B$. From page 146 of Reference [1],

$$k^2 = - \frac{2\epsilon\ (r + s)}{(1 - r\epsilon)\ (1 - s\epsilon)} \tag{b-3}$$

where

$$r = \frac{I_1}{I_3 - I_1}$$

$$s = \frac{I_1\ c}{I_1\ c - d^2} \qquad , \frac{1}{s} + \epsilon > 0 \text{ if } \epsilon < 0$$
$$\frac{1}{s} + \epsilon < 0 \text{ if } \epsilon > 0.$$

In order to make further approximations in Equation (b-3) we must be assured that $r\epsilon$ and $s\epsilon$ are both between -1 and 1.

This smallness can be expressed as

$$\epsilon r = 0(n)$$
$$\epsilon s = 0(n)$$

where terms of order n are between -1 and 1. Approximations may now be made in Equation (b-3) with the result that

$$k^2 = -2\epsilon(r + s)(1 + \epsilon\ (r + s) + \epsilon^2(r^2 + s^2 + rs)) + 0(n^4). \tag{b-4}$$

From page 147 of Reference [1] we have

$$q = \frac{k^2}{16} + \frac{k^4}{32} + \frac{21\,k^6}{1024} + 0(k^8).$$

So,

$$q = -\frac{\epsilon}{8}(r + s)\left[1 + \frac{\epsilon^2}{16}(7r^2 + 7s^2 - 2rs)\right] + 0(n^4). \qquad \text{(b-5)}$$

Now the parameter γ must be determined. Again Reference [1] gives the result

$$\frac{1 + 2q \cosh 2\gamma + 2q^4 \cosh 4\gamma + \ldots}{1 - 2q \cosh 2\gamma + 2q^4 \cosh 4\gamma - \ldots} = \left(\frac{B^2}{A^2} \cdot \frac{d^2 - cA}{d^2 - cB} \cdot \frac{A - C}{B - C}\right)^{\frac{1}{4}}$$

$$= \left[\left(\frac{1 + \epsilon}{1 - \epsilon}\right)^2 \cdot \frac{1 - \epsilon s}{1 + \epsilon s} \cdot \frac{1 + \epsilon r}{1 - \epsilon r}\right]^{\frac{1}{4}}$$

$$= 1 + \frac{\epsilon}{2}(r - s + 2) + \frac{\epsilon^2}{8}(r - s + 2)^2$$

$$+ 0(n^3).$$

Hence $2q \cosh 2\gamma = 0(n)$, and

$$q \cosh 2\gamma = \frac{\epsilon}{8}(r - s + 2) + 0(n^3). \qquad \text{(b-6)}$$

Since $q \cosh 2\gamma = 0(n)$, approximations can now be made in Equation (b-1) with the result

$$\cos\theta = \tanh\gamma[1 + 4q \cos 2\mu t + 4q^2(2\cos^2 2\mu t - \cosh 2\gamma)$$
$$- 4q^3 \cos 2\mu t \cosh 3\gamma] + 0(n^4) \qquad \text{(b-7)}$$

$$\tan(\psi - \psi_0) = \tan \mu t\left[1 + \frac{\varepsilon}{2}(r - s + 2) + \frac{\varepsilon^2}{8}\left((r - s + 2)^2 - \tfrac{1}{2}(r + s)^2\right) + 0(n^3)\right] \qquad \text{(b-8)}$$

$$\begin{aligned}\phi = \phi_0 &+ \left[\frac{d}{A} + 4\mu q \sinh 2\gamma(1 + 2q \cosh 2\gamma + 4q^2 \cosh^2 2\gamma) + 0(n^4)\right] t \\ &- 2q \sin 2\mu t \sinh 2\gamma(1 + 2q \cosh 2\gamma \cos 2\mu t \\ &+ 4q^2 \cosh^2 2\gamma \cos^2 2\mu t + \frac{4q^2}{3}\sinh^2 2\gamma \sin^2 2\mu t) + 0(n^4).\end{aligned} \qquad \text{(b-9)}$$

In Equation (b-8) we may take the arctangent of each side, and in Equation (b-7) we may set

$$\tanh \gamma \equiv \cos \theta_0$$

and then take the arc cosine of each side. Hence,

$$\begin{aligned}\theta = \theta_0 &- 4q \cot \theta_0 [\cos 2\mu t + q(2 \csc^2 \theta_0 \cos^2 2\mu t - \cosh 2\gamma)] \\ &+ 0(n^3)\end{aligned} \qquad \text{(b-10)}$$

$$\begin{aligned}\psi = \psi_0 &+ \mu t + \frac{\varepsilon \sin 2\mu t}{4}\left[(r - s + 2) + \frac{\varepsilon}{4}\left((r - s + 2)^2 \cos 2\mu t \right.\right. \\ &\left.\left. - \frac{(r + s)^2}{2}\right)\right] + 0(n^3).\end{aligned} \qquad \text{(b-11)}$$

Now, Equations (b-9), (b-10), and (b-11) are not useful as given since they involve the dependent parameters, θ_0, r, and s. We choose to eliminate s from the system in favor of the more physically meaningful parameters r and θ_0.

From Equations (b-5) and (b-6),

$$s = \frac{2 + r(1 + \cosh 2\gamma)}{1 - \cosh 2\gamma} + \frac{0(n^3)}{\epsilon} .$$

But,

$$\cosh 2\gamma \equiv \frac{1 + \tanh^2 \gamma}{1 - \tanh^2 \gamma} \equiv \frac{1 + \cos^2 \theta_o}{\sin^2 \theta_o} .$$

Thus,

$$s = - \frac{\sin^2 \theta_o + r}{\cos^2 \theta_o} + \frac{0(n^3)}{\epsilon} ,$$

$$q = \frac{\epsilon}{8} \tan^2 \theta_o \; (1 + r) + 0(n^3).$$

Hence, (b-9), (b-10), and (b-11) become

$$\theta = \theta_o - \frac{\epsilon}{2} \tan \theta_o \; (1 + r)[\cos 2\mu t + \frac{\epsilon}{8} \sec^2 \theta_o (1 + r)(\cos 4\mu t - \cos^2 \theta_o)] + 0(n^3) \qquad \text{(b-12)}$$

$$\psi = \psi_o + \mu t + \frac{\epsilon}{4} (1 + r)(2 + \tan^2 \theta_o) \sin 2\mu t \left[1 + \frac{\epsilon}{8}(1 + r)(2 + \tan^2 \theta_o) \times \left(2 \cos 2 \mu t - \left(\frac{\sin \theta_o}{1 + \cos^2 \theta_o}\right)^2\right)\right] + 0(n^3) \qquad \text{(b-13)}$$

$$\phi = \phi_\circ + \left[\frac{d}{A} + \frac{\mu\epsilon\ (1 + r)}{\cos\ \theta_\circ}\ \left(1 + \frac{\epsilon}{4}\ (1 + r)(2 + \tan^2\ \theta_\circ)\right)\right.$$

$$\left. + 0(n^3)\right]\ t - \frac{\epsilon(1 + r)}{2\ \cos\ \theta_\circ}\ \sin\ 2\mu t\ \left(1 + \frac{\epsilon}{4}(1 + r)(2 + \tan^2\ \theta_\circ)\cos\ 2\mu t\right)$$

$$+ 0(n^3) \tag{b-14}$$

where

$$1 + r = \frac{I_3}{I_3 - I_1}$$

$$\epsilon \leq 0 \quad \text{if } I_3 > I_1$$

$$\epsilon \geq 0 \quad \text{if } I_3 < I_1$$

$$\theta_\circ \neq \frac{\pi}{2}.$$

The only problem now remaining is to find the angular rate μ in terms of d, $\theta_\circ$, and r. Again from Whittaker,

$$\mu^2 = \frac{(B - C)(Ac - d^2)}{ABC(1 + 2q + 0(q^4))} = \frac{d^2(1 - \epsilon r)(1 - \epsilon S)\ \cos^2\ \theta_\circ}{I_1^{\ 2}(1 + r)^2\ (1 - \epsilon^2)\ (1 + 2q + 0(q^4))}.$$

$$\mu = -\frac{d}{(r + 1)\ I_1}\ \cos\ \theta_\circ\ \ (1 + \frac{\epsilon^2}{2}(1 + r)(1 - r\ \sec^2\ \theta_\circ$$

$$- \frac{3}{8}\ \tan^4\ \theta_\circ\ \ (1 + r))) + 0(n^3)$$

Hence, the coefficient of t in Equation (b-14) becomes

$$\frac{d}{I_1}\left[1 + \epsilon^2 (1 - \frac{1}{4}(1 + r)(2 + \tan^2 \theta_o)\right] + 0(n^3)$$

References

[1] Whittaker, E. T., Analytical Dynamics of Particles and Rigid Bodies, Cambridge University Press, 1959, pp. 144-152.

[2] Bateman, H., Higher Transcendental Functions, Volume II, McGraw-Hill, New York, 1953, p. 345.

APPENDIX C

PROJECTIONS FOR MANUAL SOLUTION

This appendix contains the mapping of stars onto a plane as described in Section IV-D. This projection may be used to obtain an approximate manual solution to the problem of obtaining the celestial attitude from the output of the SCADS sensor. All stars of visual magnitude four and brighter are shown.

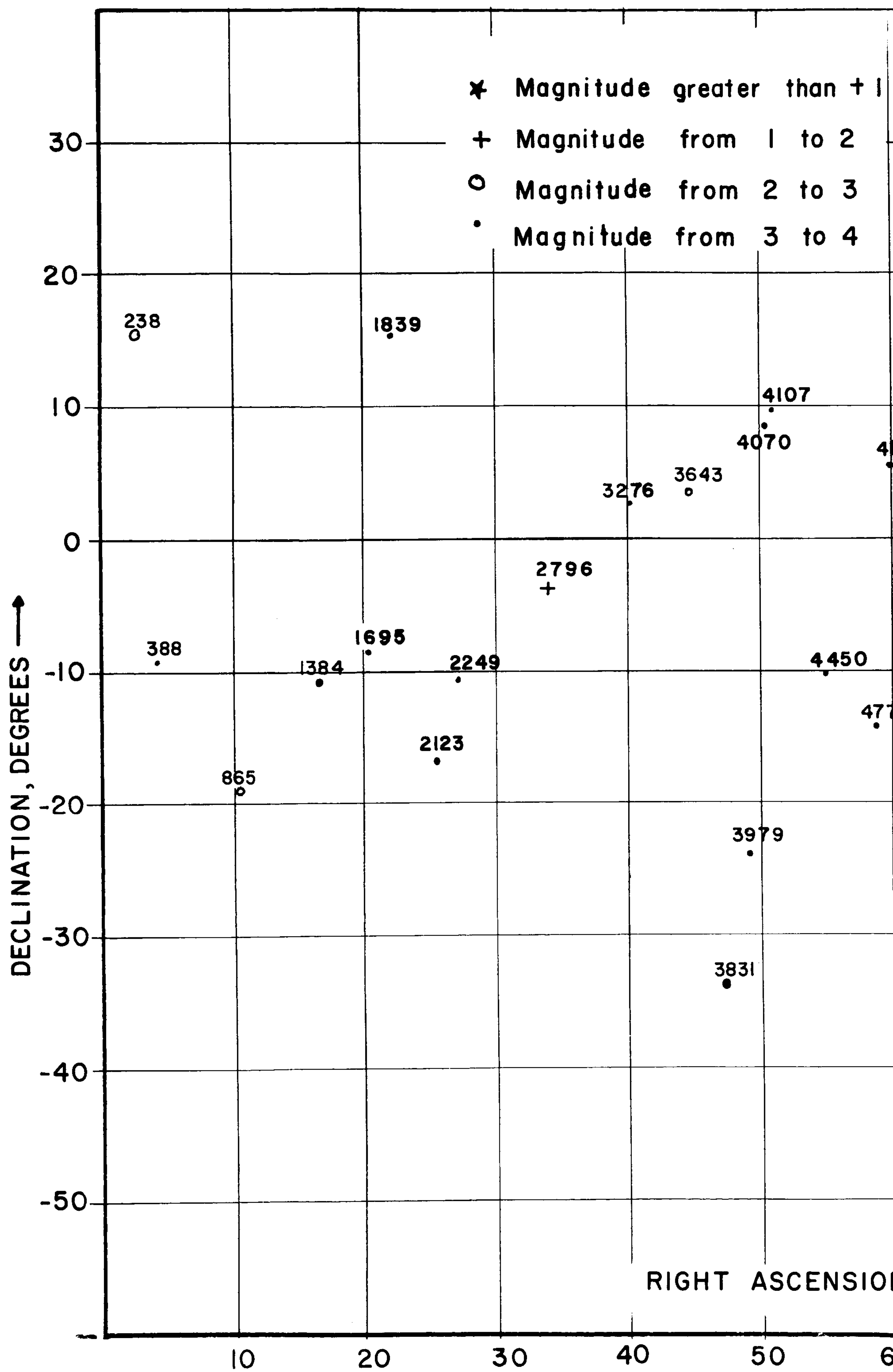
Magnitude greater than + 1
Magnitude from 1 to 2
Magnitude from 2 to 3
Magnitude from 3 to 4
DECLINATION, DEGREES
RIGHT
30
20
10
0
-10
-20
-30
-40
-50
10
20
30
40
50
238
1839
4107
4070
3643
3276
2796
388
1695
1384
2249
4450
2123
865
3979
3831

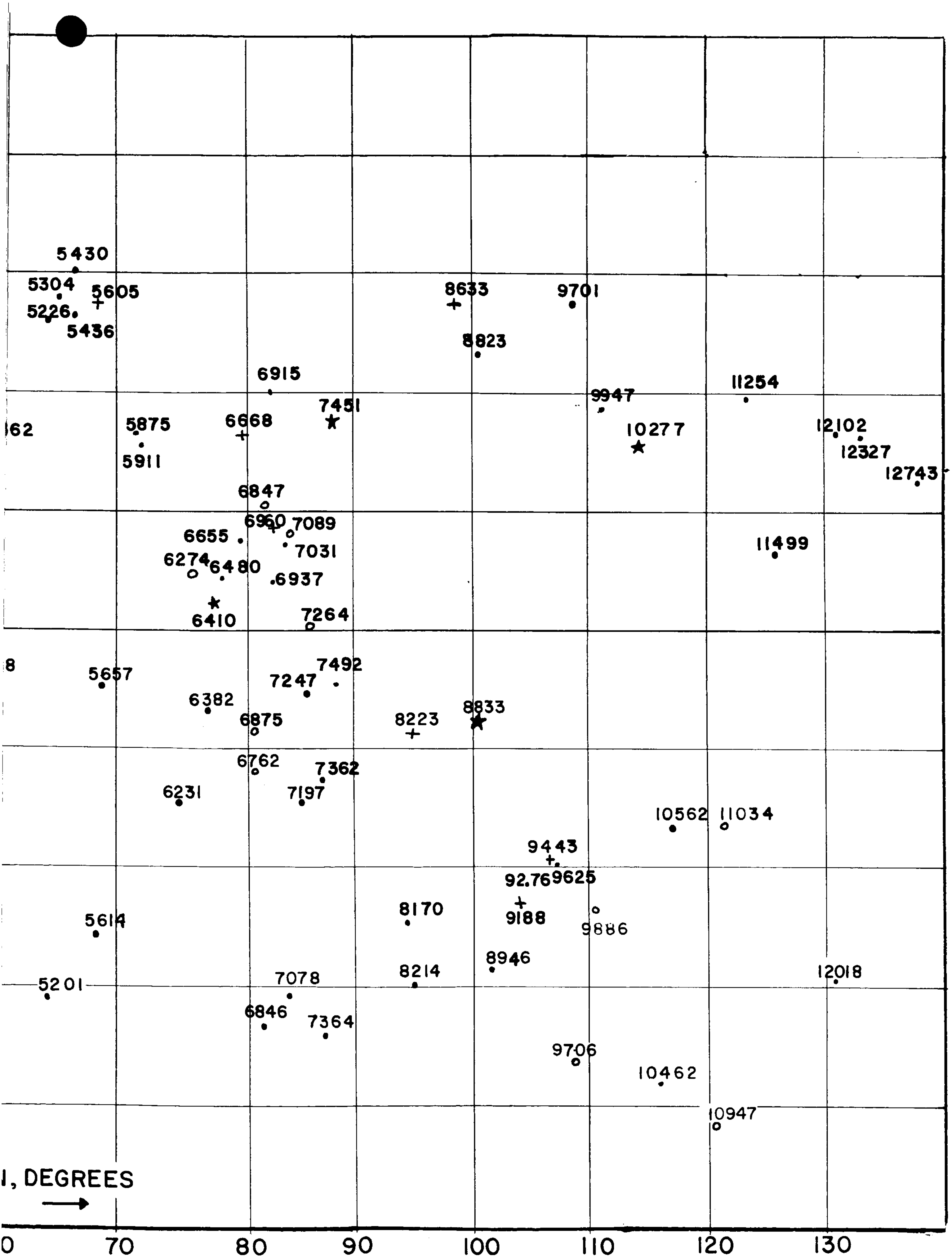
5430
5304
5605
5226
5436
8633
9701
8823
6915
11254
9947
7451
162
5875
6668
10277
12102
12327
5911
12743
6847
6960
7089
6655
7031
11499
6274
6480
6937
6410
7264
8
7492
5657
7247
6382
8833
6875
8223
6762
7362
6231
7197
10562
11034
9443
92.76
9625
8170
9188
9886
5614
8946
8214
12018
5201
7078
6846
7364
9706
10462
10947
, DEGREES
0
70
80
90
100
110
120
130

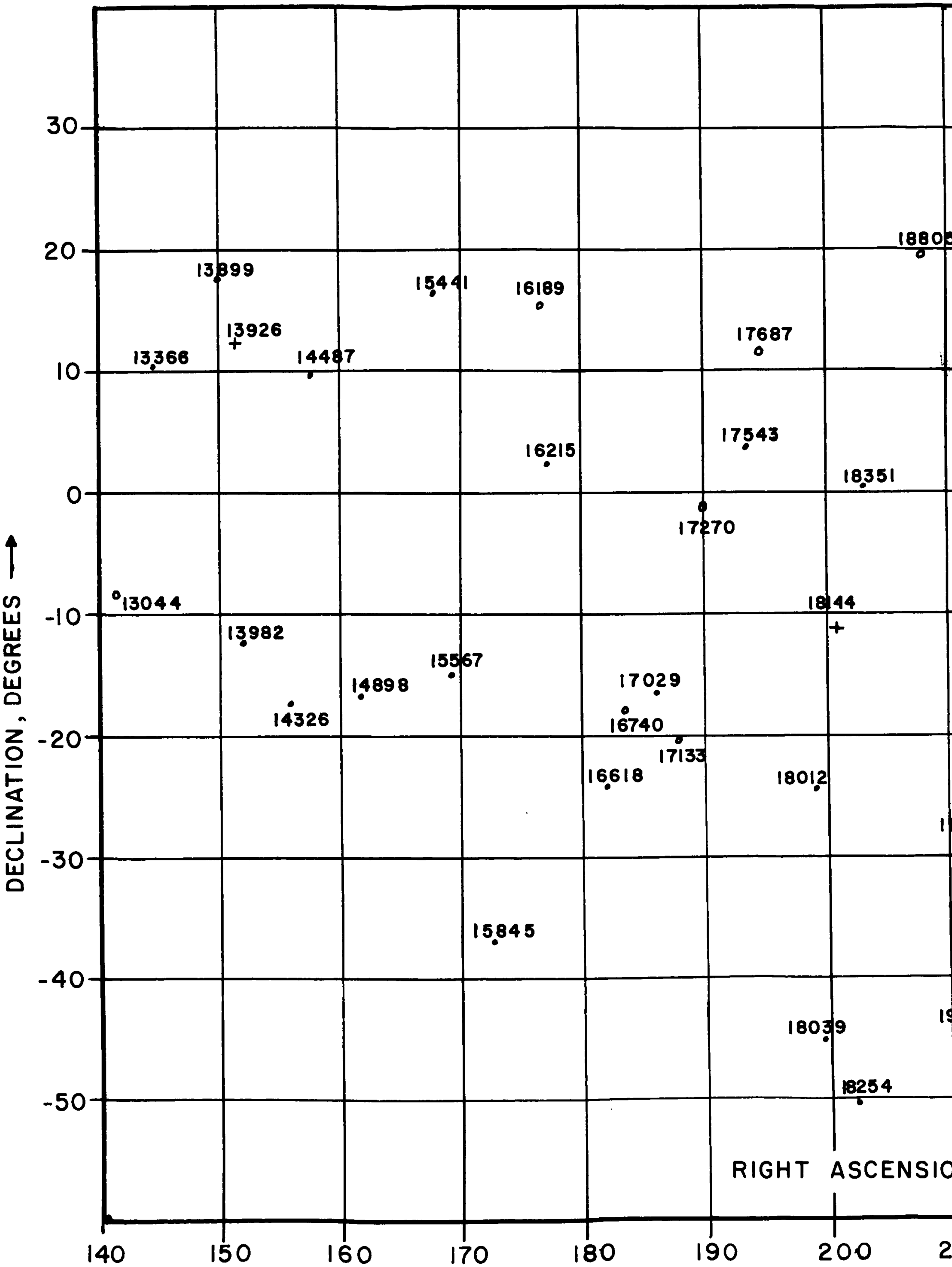
DECLINATION, DEGREES
RIGHT ASCENSIO
30
20
10
0
-10
-20
-30
-40
-50
140
150
160
170
180
190
200
13899
15441
16189
18805
13926
17687
13366
14487
17543
16215
18351
17270
13044
18144
13982
15567
17029
14898
14326
16740
17133
16618
18012
15845
18039
18254

c-4

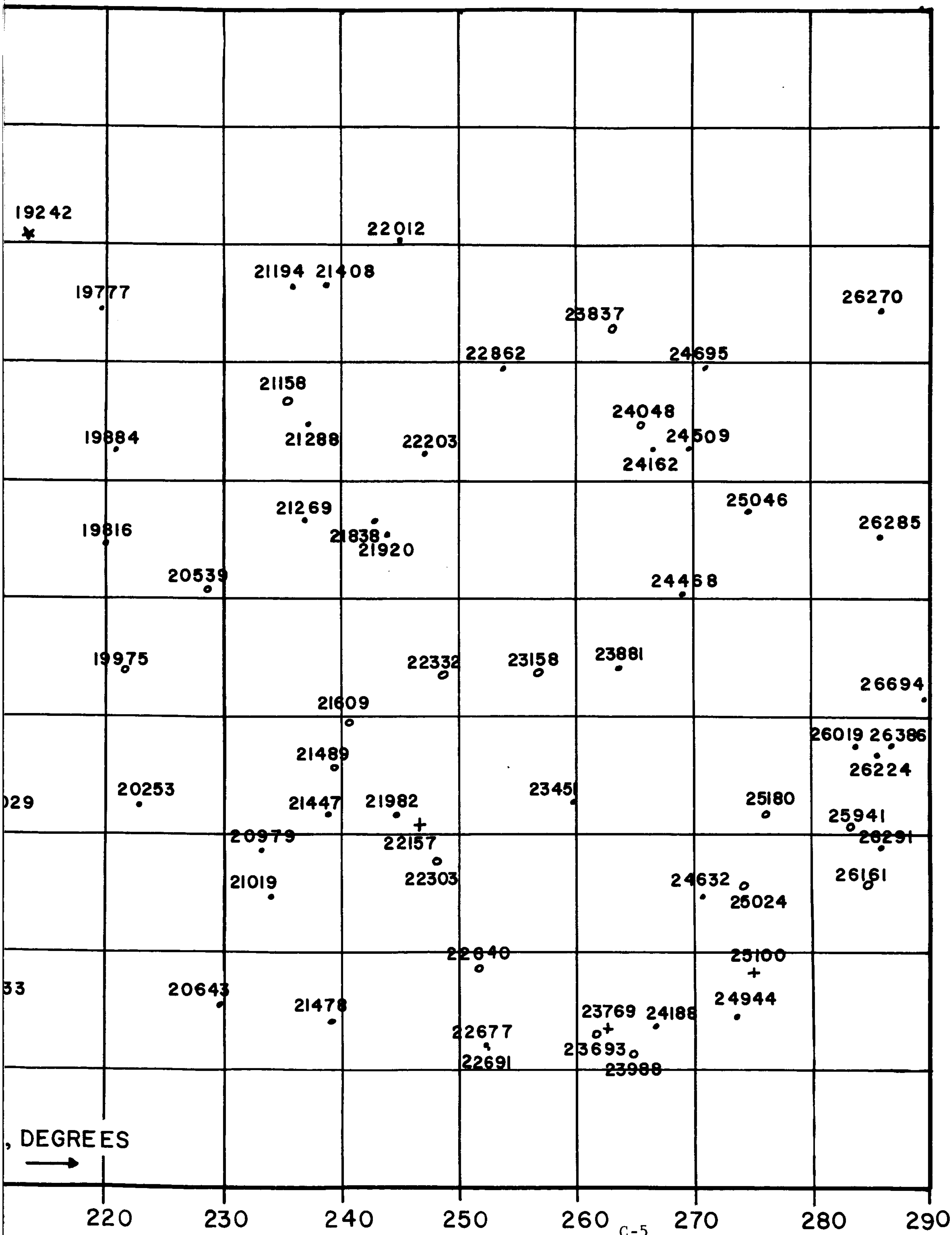

19242
22012
21194
21408
19777
26270
23837
22862
24695
21158
24048
19884
21288
22203
24509
24162
21269
25046
26285
19816
21838
21920
20539
24468
19975
22332
23158
23881
26694
21609
26019
26386
21489
26224
029
20253
23451
21447
21982
25180
25941
20979
22157
26291
22303
21019
24632
26161
25024
22640
25100
33
20643
21478
24944
23769
24188
22677
23693
22691
23988
, DEGREES
220
230
240
250
260
270
280
290

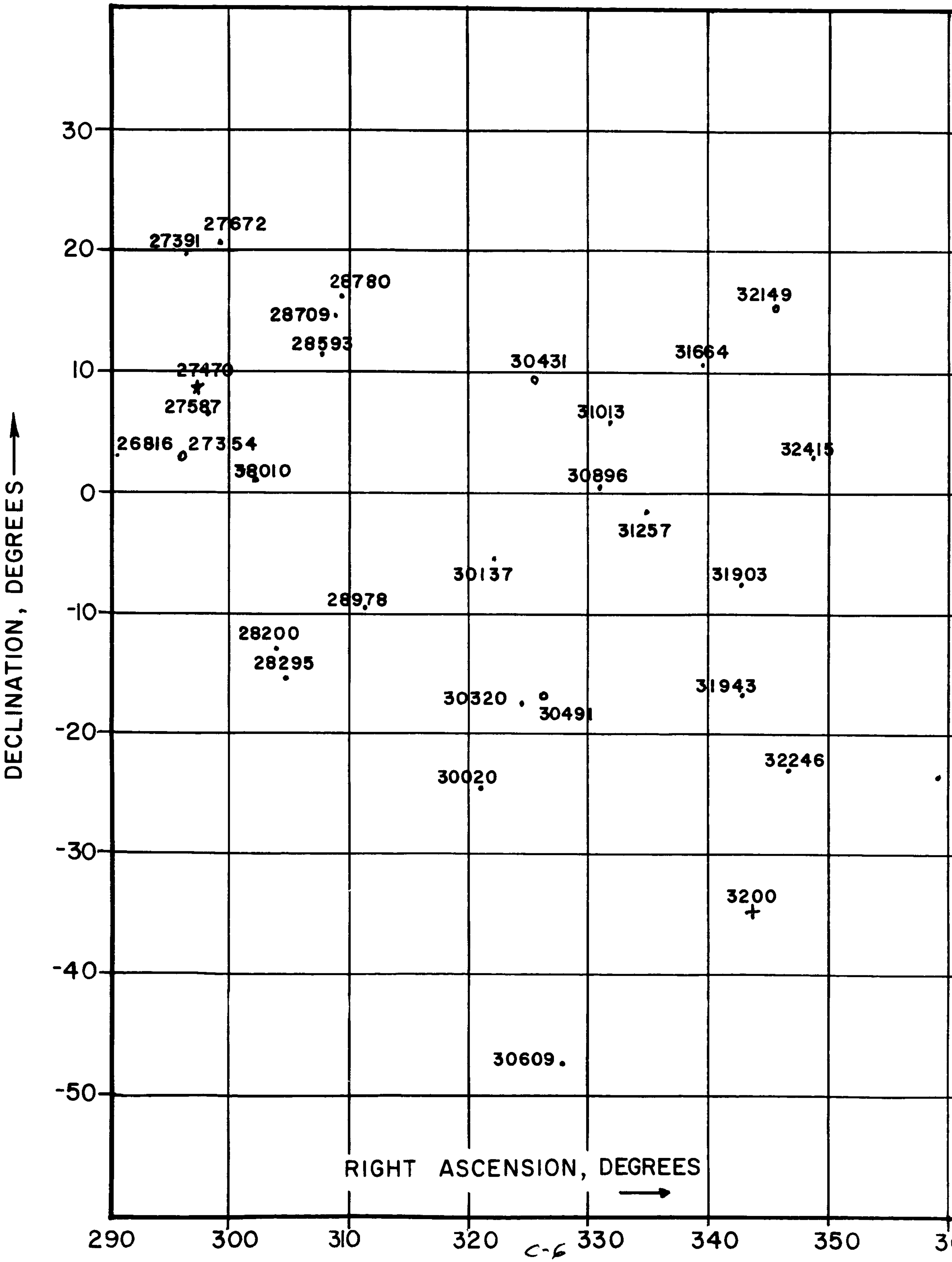

DECLINATION, DEGREES
RIGHT ASCENSION, DEGREES
30
20
10
0
-10
-20
-30
-40
-50
290
300
310
320
330
340
350
27672
27391
28780
28709
28593
27470
27587
26816
27354
38010
30431
31664
32149
31013
32415
30896
31257
30137
31903
28978
28200
28295
30320
30491
31943
32246
30020
3200
30609

C-6

APPENDIX D

EVALUATION OF H(t) AND ITS INTEGRAL

The function H(t) is defined as

$$\int_{t-T_f}^{t} G(x)\,dx \qquad \text{(d-1)}$$

where $G(x) = \Phi(X/\sigma + T_s/2\sigma) - \Phi(X/\sigma - T_s/2\sigma)$. For convenience, let $\alpha = t - T_f$ and $\beta = t$. Then

$$\int_{\alpha}^{\beta} \Phi(x/\sigma + T_s/2\sigma)dx = \int_{\alpha'}^{\beta'} \Phi(u)\,\sigma\,du \qquad \text{(d-2)}$$

with $\alpha' = \alpha/\sigma + T_s/2\sigma$ and $\beta' = \beta/\sigma + T_s/2\sigma$.

$$\sigma \int_{\alpha'}^{\beta'} \Phi(u)\,du = \sigma[u\,\Phi(u)]_{\alpha'}^{\beta'} - \sigma \int_{\alpha'}^{\beta'} u\phi(u)\,du \qquad \text{(d-3)}$$

$$= \sigma[\beta'\,\Phi(\beta') - \alpha'\Phi(\alpha')] + \sigma[\phi(\beta') - \phi(\alpha')]$$

where

$$\phi(u) = \frac{d}{du}\,\Phi(u)$$

Similarly

$$\int_{\alpha}^{\beta} \Phi(x/\sigma - T_s/2\sigma)dx = \int_{\alpha''}^{\beta''} \Phi(v)\,\sigma\,dv \qquad \text{(d-4)}$$

(equation continued)

$$= \sigma[\beta'' \, \Phi \, (\beta'') - \alpha'' \, \Phi \, (\alpha'')]$$

$$+ \sigma[\phi(\beta'') - \phi(\alpha'')]$$

with

$$\alpha'' = \alpha/\sigma - T_s/2\sigma \quad \text{and} \quad \beta'' = \beta/\sigma - T_s/2\sigma$$

Substituting α', β', α'', β'' one obtains

$$H(t) = (t + T_s/2) \; \Phi\left(\frac{t + T_s/2}{\sigma}\right) - (t - T_s/2)\, \Phi\left(\frac{t - T_s/2}{\sigma}\right) \qquad \text{(d-5)}$$

$$- \left[(t - T_f + T_s/2)\, \Phi\left(\frac{t-T_f+ T_s/2}{\sigma}\right) - (t - T_f - T_s/2)\, \Phi\left(\frac{t-T_f-T_s/2}{\sigma}\right)\right]$$

$$+ \sigma\left[\phi\left(\frac{t + T_s/2}{\sigma}\right) - \phi\left(\frac{t - T_s/2}{\sigma}\right)\right]$$

$$- \sigma\left[\phi\left(\frac{t - T_f + T_s/2}{\sigma}\right) - \phi\left(\frac{t - T_f - T_s/2}{\sigma}\right)\right]$$

The integral of H(t) can be evaluated directly.

$$\int_{-\infty}^{\infty} H(t)\, dt = \int_{-\infty}^{\infty} \int_{t-T_f}^{t} G(x)\, dx\, dt = \int_{-\infty}^{\infty} \int_{x}^{x+T_f} G(x)\, dt\, dx \qquad \text{(d-6)}$$

$$= T_f \int_{-\infty}^{\infty} G(x)\, dx$$

By direct integration, one can show that

$$\int_{-a}^{a} G(t)\,dt = (a + T_s/2)\,\Phi\left(\frac{a + T_s/2}{\sigma}\right) \tag{d-7}$$

$$- (-a + T_s/2)\,\Phi\left(\frac{-a + T_s/2}{\sigma}\right)$$

$$+ \sigma\,\phi\left(\frac{a + T_s/2}{\sigma}\right) - \sigma\,\phi\left(\frac{-a + T_s/2}{\sigma}\right)$$

$$- (a - T_s/2)\,\Phi\left(\frac{a - T_s/2}{\sigma}\right)$$

$$+ (-a - T_s/2)\,\Phi\left(\frac{-a - T_s/2}{\sigma}\right)$$

$$- \sigma\,\phi\left(\frac{a - T_s/2}{\sigma}\right) + \sigma\,\phi\left(\frac{-a - T_s/2}{\sigma}\right)$$

$$\int_{-\infty}^{\infty} G(t)\,dt = \lim_{a \to \infty} a\left[\Phi\left(\frac{a + T_s/2}{\sigma}\right) - \Phi\left(\frac{a - T_s/2}{\sigma}\right)\right] \tag{d-8}$$

$$+ \lim_{a \to \infty} a\left[\Phi\left(\frac{-a + T_s/2}{\sigma}\right) - \Phi\left(\frac{-a - T_s/2}{\sigma}\right)\right] + T_s$$

Since the first two terms vanish

$$\int_{-\infty}^{\infty} H(t)\, dt = T_s\, T_f \tag{d-9}$$

It is easily shown that

$$H(t) \leq H(T_f/2) < \lim_{\sigma \to 0} H(T_f/2) = T_f \tag{d-10}$$

Hence, $0 < \dfrac{H(t)}{T_f} < 1$ and

$$T_s = \int_{-\infty}^{\infty} \frac{H(t)}{T_f}\, dt > \int_{-\infty}^{\infty} \left[\frac{H(t)}{T_f}\right]^k dt \tag{d-11}$$

Further,

$$\int_{-\infty}^{\infty} \left[\frac{H(t)}{T_f}\right]^2 dt > \left[\int_{-\infty}^{\infty} \frac{H(t)}{T_f}\, dt\right]^2 = T_s^{\,2} \tag{d-12}$$

Therefore,

$$T_s\, T_f^{\,2} > \int_{-\infty}^{\infty} [H(t)]^2\, dt > T_s^{\,2}\, T_f^{\,2} \tag{d-13}$$

and

$$T_s \; T_f^{\;k} > \int_{-\infty}^{\infty} [H(t)]^k \, dt \tag{d-14}$$

APPENDIX E

EVALUATION OF INTENSITY MOMENTS

To estimate $\sum_{M_o+1}^{\infty} \nu(M)\ \lambda^k(M)$ we assume $\nu(M)$ is a continuous function which can be approximated by a Gaussian density. Hence

$$\sum_{M_o+1}^{\infty} \nu(M)\ \lambda^k(M) \approx \int_{M_o+\frac{1}{2}}^{\infty} \nu(M)\ \lambda^k(M)\ dM \qquad \text{(e-1)}$$

Because of the nature of available star data, we find constants a, b, c such that

$$N_M = a\ \Phi\ (bM + c) \qquad \text{(e-2)}$$

where N_M is the number of stars per square degree brighter than photographic magnitude M, and where

$$\Phi(z) = \frac{1}{\sqrt{2\pi}} \int_{-\infty}^{z} e^{-\frac{1}{2}t^2}\ dt \qquad \text{(e-3)}$$

Let T_γ be the number of square degrees scanned per second by the optical device. Then

$$\nu(M) = T_\gamma\ \frac{d}{dM}\ (N_M) \qquad \text{(e-4)}$$

Estimation of N_M

The basic problem is to determine a, b, c in (e-2) using three points (M_i, N_{M_i}) i = 1, 2, 3. The three points give three equations

$$N_{M_1} = a\,\Phi\,(bM_1 + c) \tag{e-5}$$

$$N_{M_2} = a\,\Phi\,(bM_2 + c) \tag{e-6}$$

$$N_{M_3} = a\,\Phi\,(bM_3 + c) \tag{e-7}$$

By taking ratios, we obtain

$$N_{M_1}\,\Phi\,(bM_2 + c) = N_{M_2}\,\Phi\,(bM_1 + c) \tag{e-8}$$

$$N_{M_2}\,\Phi\,(bM_3 + c) = N_{M_3}\,\Phi\,(bM_2 + c) \tag{e-9}$$

Taking derivatives with respect to c and natural logs of both sides, we find

$$\ln N_{M_1} - \tfrac{1}{2}(bM_2 + c)^2 = \ln N_{M_2} - \tfrac{1}{2}(bM_1 + c)^2 \tag{e-10}$$

$$\ln N_{M_2} - \tfrac{1}{2}(bM_3 + c)^2 = \ln N_{M_3} - \tfrac{1}{2}(bM_2 + c)^2 \tag{e-11}$$

or

$$b[b(M_2 + M_1) + 2c] = -2K_{21} \tag{e-12}$$

$$b[b(M_3 + M_2) + 2c] = -2K_{32} \tag{e-13}$$

where $K_{ij} = \ln(N_{M_i}/N_{M_j})/(M_i - M_j)$. Taking ratios gives

$$\frac{b(M_2 + M_1) + 2c}{b(M_3 + M_2) + 2c} = \frac{K_{21}}{K_{32}} \tag{e-14}$$

which implies $c = -\frac{1}{2}\beta b$ where

$$\beta = \frac{K_{21}(M_3 + M_2) - K_{32}(M_2 + M_1)}{K_{21} - K_{32}} \tag{e-15}$$

Substituting into (e-12) we obtain

$$b[b(M_2 + M_1) - \beta b] = -2K_{21} \tag{e-16}$$

or

$$b = \left[\frac{2K_{21}}{\beta - (M_2 + M_1)}\right]^{\frac{1}{2}} \tag{e-17}$$

Using $M_1 = 2$, $M_2 = 12$, $M_3 = 21$, and using astrophysical data given by Allen [18] ($N_2 = 9.12 \times 10^{-4}$, $N_{12} = 5.89 \times 10^1$, $N_{21} = 2.51 \times 10^4$), we find that $\beta = 83.3$, which gives $b = .173$ can $c = -7.21$. Thus $N_M = a\Phi(.173M - 7.21)$. Using $M = 12$, $a = \dfrac{28.8}{\Phi(-5.13)} = 1.99 \times 10^8$. Hence $N_M = (1.99\times10^8)\Phi(.173M-7.21)$

In Figure E-1 the percent deviation $100 \times [a\,\Phi(bM + c) - N_M]/N_M$ is graphed as a function of M using data given by C. W. Allen [48].

One of the uses for this formula is in estimating the starlight not accounted for by the stars of magnitude 21.5 or brighter. C. W. Allen lists this value as equivalent to 0.8 tenth magnitude stars. Using

$$\int_{21.5}^{\infty} \frac{d}{dM}(N_M)\,\lambda(M)\,dM \qquad \text{as an estimate of this residual}$$

starlight, we get a value of 2.07 tenth magnitude stars.

Evaluation of Intensity Moments

Now consider the calculation of

$$\int_{k}^{\infty} \frac{d}{dM}(N_M)\,\lambda^k(M)\,dM \tag{e-18}$$

where $\lambda(M) = a'e^{-b'M}$.

$$\int_{k}^{\infty} \frac{d}{dM}(N_M)\,\lambda^k(M)\,dM = \int_{k}^{\infty} \frac{d}{dM}\Big[a\,\Phi(bM + c)\Big]\quad a'^k\,e^{-kb'M}dM \tag{3-19}$$

$$= \frac{a\,ba'^k}{\sqrt{2\pi}} \int_{k}^{\infty} e^{-\frac{1}{2}(bM+c)^2 - kb'M}\,dM$$

 (equation continued)

M	$a\Phi(bM+c)$	Tabulated Values (N_m)
2	3.96×10^{-4}	9.12×10^{-4}
3	2.05×10^{-3}	2.51×10^{-3}
4	10.05×10^{-3}	7.76×10^{-3}
5	2.80×10^{-2}	2.34×10^{-2}
6	7.42×10^{-2}	7.24×10^{-2}
7	1.79×10^{-1}	2.04×10^{-1}
8	5.57×10^{-1}	5.62×10^{-1}
9	1.59	1.55
10	4.24	4.17
11	1.09×10^{1}	1.12×10^{1}
12	2.98×10^{1}	2.88×10^{1}
13	7.00×10^{1}	7.41×10^{1}
14	1.66×10^{2}	1.82×10^{2}
15	3.82×10^{2}	4.17×10^{2}
16	8.95×10^{2}	9.55×10^{2}
17	1.95×10^{3}	2.14×10^{3}
18	4.12×10^{3}	4.36×10^{3}
19	8.80×10^{3}	7.94×10^{3}
20	1.76×10^{4}	1.48×10^{4}
21	3.42×10^{4}	2.51×10^{4}

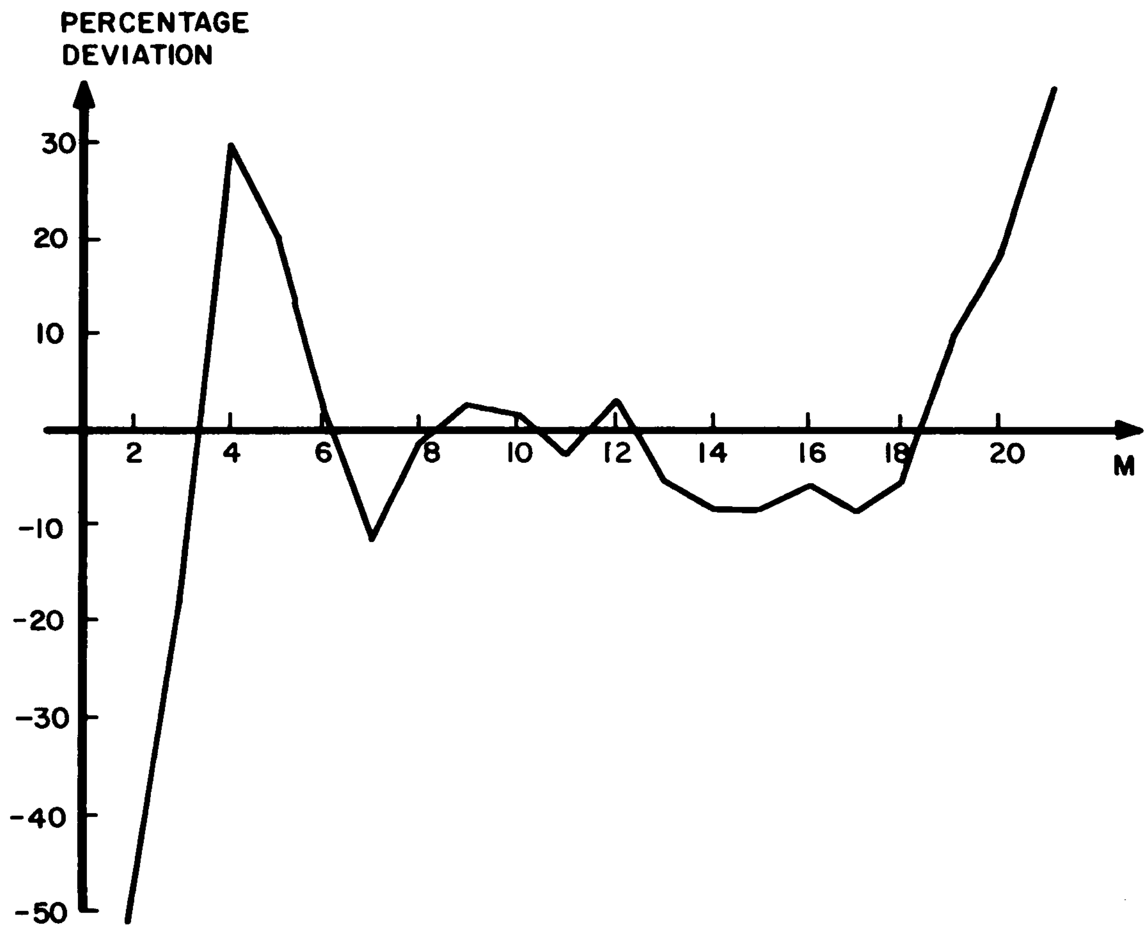

NOTE: The deviations are due to the accuracy of the available tables.

Figure E-1: Cumulative Star Density

$$= \frac{aba'^k}{\sqrt{2\pi}} \int_k^{\infty} \exp\left\{ -\tfrac{1}{2}b^2\left[M + \frac{bc + kb'}{b^2}\right]^2 + \tfrac{1}{2}\left[\left(\frac{bc + b'k}{b}\right)^2 - c^2\right]\right\} dM$$

Letting $u = b\left[M + \frac{bc + kb'}{b^2}\right]$ and $du = bdM$ we get

$$\frac{aba'^k}{\sqrt{2\pi}} \int_{b\left[k + \frac{bc+b'k}{b^2}\right]}^{\infty} e^{-\frac{1}{2}u^2} \; e^{\frac{1}{2}\left[\left(\frac{bc+b'k}{b}\right)^2 - c^2\right]} \; \frac{1}{b}\, du \qquad \text{(e-20)}$$

$$= aa'^k \, e^{\frac{1}{2}\left[\left(\frac{bc+b'k}{b}\right)^2 - c^2\right]} \left[1 - \Phi\left(bK + c + \frac{b'}{b}\; k\right)\right]$$

We assume $\lambda(M) = (5.06 \times 10^6)\, e^{-.921M}\; D^2$

= number of photons per second arriving from a star of M^{th} magnitude through an aperture of diamter D in inches.

Then

$$\left\{ \begin{array}{l} k = M_0 + \tfrac{1}{2} \\ \\ \nu(M) = T_\gamma \;\; \dfrac{d}{dM}\left[a\; \Phi\; (bM + c)\right] \\ \\ \lambda^k(M) = a'^k\, e^{-b'kM} \end{array} \right\} \qquad \text{(e-21)}$$

with $a = 1.99 \times 10^8$, $a' = D^2\;(5.06 \times 10^6)$, $b = .173$, $b' = .921$, and $c = -7.21$. Thus

$$\int_{M_o+\frac{1}{2}}^{\infty} \nu(M)\, \lambda^k(M)\, dM = \tag{e-22}$$

$$= D^{2k}\, T_\gamma (1.99)(5.06)^k \cdot 10^{8-10.67k+6.154k^2} [1-\Phi(.173M_o+5.32k-7.12)]$$

$$= \frac{D^{2k}}{T_{sp}} \sin(fov/2)(8.209)(5.06)^k \cdot 10^{12-10.67k+6.154k^2} [1-\Phi(.173M_o+5.32k-7.12)]$$

where fov is the field of view of the lens system in Figure I-2, and T_{sp} is the scan period in seconds.

APPENDIX F

FORTRAN PROGRAM CODE

```
      PROGRAM TI NI
      COMMON NUM,D,SW,FOL,SGA,SGI,AR,FOV,CP,EO,SW1,SP,DL,AI,TIRE,EQ,TS,
     1SOAP,FML,FMS,COP,FMR,FMD,TAU,BOR,SGA1,SGI1,PTC,NS,ADD,SEN,POPS,
     2RPHI,RPHI1,DPHI,DPHI1,PT,A,BL,SW2,TS1,D1,D2,NSL,AI1,N,DFOV,NF,
     1SEN1,FMS1,NCG,PMAGN,ENFSDS
      DIMENSION P(10), F(10), V(10), AR(78), CP(8), COP(20),
     1            BAK10(10),IBS(10,10),RPH (10),DPH (10),PRD(10),
     1FMSB(10),FMBT(10) ,ADDPT(10),
     1BR(1000), X(1000), Y(1000), Z(1000),IC(1000)
      CALL INPUT
      TIRE=50.
      READ 3610,TERP,FMSF,GAMM,FOV,SP,SGA,EO,A,PT,EFAL,NS,NPOINT
 3610 FORMAT(10(F5.2,1X),2(I5,1X))
      READ3630,(RPH (I),DPH (I),BAK10(I),ADDPT(I),I=1,NPOINT)
 3630 FORMAT(4(F6.2,1X))
      DTR=.01745329252O
      REWIND 3
      READ INPUT TAPE 3, 6, (IC(I), BR(I), X(I), Y(I), Z(I), I = 1,1000)
    6 FORMAT (3X, I5, F9.2, 3F13.8)
      REWIND 3
      DO 1040 NSP=1,2
      READ 3610,TERP,FMSF,GAMM,FOV,SP,SGA,EO,A,PT,EFAL,NS,NPOINT
      DO 1030 NP=1,10
      READ3620,(AR(I),I=34,41),DL,EQ,(AR(I),I=71,78)
 3620 FORMAT(8A6,1X,F9.2,1X,F6.2/8A6)
      RPHI=0
      RPHI1=360
      DPHI=-10
      DPHI1=-10
      SW=SGA*TERP
      DMAX=0
      AI=GAMM-FOV*.5
      AL=COSF(DTR*GAMM)
      AU=COSF(DTR*(GAMM-FOV))
      JUMPL=0
C  LOOP ON POINTING DIRECTIONS
      DO 900 L=1,NPOINT
  161 CONTINUE
C          DETERMINE LIMITING MAGNITUDE
      CALL DIRCOS(RPH (L),DPH (L),XPHI,YPHI,ZPHI)
      NN = 0
      DO 5 I = 1,1000
      FIP = X(I)*XPHI + Y(I)*YPHI + Z(I)*ZPHI
      IF (FIP-AU) 7, 7, 3
    7 IF (FIP-AL) 3, 8, 8
    8 NN = NN + 1
      IBS(L,NN)=I
      IF (NN-NS) 3, 9, 9
    3 IF (BR(I)-4.5) 5, 158, 158
  158 PRINT 159,NN,FOV
  159 FORMAT(//,2X,I3,25H  STARS PRESENT IN FOV OF  F8.3,2X,7HDEGREES)
      GO TO 900
    5 CONTINUE
    9 FML=BR(I)
      TSFACT=SP/(21600.*SINF(DTR*AI))
  850 TS=SW*TSFACT
```

```
      FMS=FMSF
      SGAC=-1
      FMD=DL*TS*A
      D = SQRTF (FMS/(A*EQ*EO*1.20E7*EXPF (-.92103404*FML)*TS))
      IF(D-DMAX) 910,920,920
  910 FMS=FMS*(DMAX/D)**2
      D=DMAX
      GO TO 930
  920 DMAX=D
  930 FMB=NSL*A*EQ*EO*TS*FOV*SW*BAK10(L)*D**2*20.
C        DETERMINE THRESHOLD TAU
      DO 700 I=1,NS
      INDO=IBS(L,I)
      FMSB(I)=FMS*EXPF(2.3025850930*.4*(FML-BR(INDO)))
      FMBT(I)=FMSB(I)+FMB+FMD
  700 CONTINUE
      ITAU=FMBT(NS)-SQRTF(FMBT(NS))*1.28
      INT=0
      JNT=0
  750 TPROB=1
      DO 710 I=1,NS
      CALL PRODEC(ITAU,FMBT(I),PRD(I))
  710 TPROB=TPROB*PRD(I)
      IF(TPROB-PT) 730,720,740
  730 ITAU=ITAU-1
      INT=1
      IF(INT-JNT) 721,721,750
  740 JNT=1
      IF(INT-JNT) 770,720,720
  770 ITAU=ITAU+1
      GO TO 750
  721 TPROB=1
      DO 711 I=1,NS
      CALL PRODEC(ITAU,FMBT(I),PRD(I))
  711 TPROB=TPROB*PRD(I)
  720 CONTINUE
      PTC=PRD(NS)
      TAU=ITAU
      ITC=ITAU
      FMNOS=FMB+FMD
      CALL PRODEC(ITC,FMNOS,PFSD)
      ENFSDS=PFSD*SP/TS
      IF(ENFSDS-EFAL) 810,810,800
  800 CONTINUE
      SW=.9*SW
      GO TO 850
  810 CONTINUE
  820 CONTINUE
      IF(JUMPL) 900,900,1000
  900 CONTINUE
  155 CALL PRINT(0)
      SGA1=SW/TERP
      L=0
      JUMPL=1
      GO TO 1010
 1000 ML = FML + 1.5
```

```
      ML2 = ML + 1
  116 SA = (AU - AL)/2.
      F(ML-1) = FMS
      SEN = 0.
      DO 130 I = ML, ML2
  130 F(I) = .398*F(I-1)
      DO 150 I = ML, ML2
      F(I) = F(I) + FMB + FMD
      CALL PRODEC (ITC, F(I), P(I))
      EN = SA*N(I)*P(I)
  150 SEN = EN + SEN
      FLN10=2.302585093n
      PMAGN=2.5*LOGF(FMS/(FMB+FMD))/FLN10+FML
      TSDSW=TS*D**2*SW
      SGI1=SQRTF(FMS+FMB+FMD)/FMS
      CALL PRINT(1)
 1010 L=L+1
      IF(L-NPOINT) 1020,1020,1030
 1020 CONTINUE
      ADD=ADDPT(L)
      RPHI=RPH(L)
      DPHI=DPH(L)
      INDO=IBS(L,NS)
      FML=BR(INDO)
      FMS=A*EQ*EO*TS*1.2E7*D**2*EXPF(-.921034n4*FML)
      GO TO 930
 1030 CONTINUE
 1040 CONTINUE
      END
C
```

```
      SUBROUTINE DIRCOS (RA, DEC, X, Y, Z)
      DTR=.017453292520
      RAD=RA*DTR
      DECD=DEC*DTR
      CDEC=COSF(DECD)
      XT=COSF(RAD)*CDEC
      YT=SINF(RAD)*CDEC
      ZT=SINF(DECD)
      X = -.20791169*XT + .97814760*YT
      Y = -.45921248*XT = .09750863*YT - .88294759*ZT
      Z = -.86365307*XT = .18357513*YT + .46947156*ZT
      RETURN
      END
C
```

```
      SUBROUTINE  CUMNOR(X,C,FM,FS,V)
C   V=C*PHI((X-FM)/FS)
C     C*(VALUE OF CUM. NORMAL WITH MEAN FM AND S.D. FS)
      PX=X
      PY=((PX-FM)/FS)*.70710678119
      Y=ABSF(PY)
      D=((((((.0000430638*Y+.0002765672)*Y+.0001520143)*Y+.0092705272)*Y
     1+.0422820123)*Y+.0705230784)*Y+1.)**16
      ERF=1.-1./D
      V=.5*(1.+ERF)*C
      IF(PY) 20,30,30
   20 V=C-V
   30 RETURN
      END
C
```

```
      SUBROUTINE PRODEC(NTAU,FMPT,VPT)
C FMPT=MEAN  NTAU=THRESHOLD        VPT=TAIL VALUE
C  SUMS THE TAIL STARTING AT NTAU+1
      IF(FMPT-50.) 30,30,40
   40 FTAU=NTAU
      SDV=SQRTF(FMPT)
      CALL CUMNOR(FTAU,1.,FMPT,SDV,VPTC)
      VPT=1.-VPTC
      RETURN
   30 CONTINUE
      TERM=1
      DO 10 J=1,NTAU
      DIV=NTAU-J+1
   10 TERM=TERM*FMPT/DIV+1.
      VPT=1.-EXPF(-FMPT)*TERM
      IF(VPT-.1E-5) 15,20,20
   15 VPT=0
   20 RETURN
      END
C
```

```
      SUBROUTINE INPUT
      COMMON NUM,D,SW,FOL,SGA,SGI,AR,FOV,CP,EO,SW1,SP,DL,AI,TIRE,EQ,TS,
     1SOAP,FML,FMS,COP,FMB,FMD,TAU,BOB,SGA1,SGI1,PTC,NS,ADD,SEN,POPS,
     2RPHI,RPHI1,DPHI,DPHI1,PT,A,BL,SW2,TS1,D1,D2,NSL,AI1,N,DFOV,NF,
     1SEN1,FMS1,NCG,PMAGN,ENFSDS
      DIMENSION P(10), F(10), V(10), AR(78), CP(8), COP(20)
      READ 10, NUM, FOV, FOL, FMB, FMD, RPHI, DPHI, SGI, SGA, BL, DL
   10 FORMAT (A4, 4(1X, F5.1), 2(1X, F10.8), 2(1X, F5.2), 2(1X, F7.1))
      READ 20, PT, A, EO, EQ, FMS1, SP, SW1, SW2, TS1, D1, D2, NS, NSL
   20 FORMAT (4(F4.2, 1X), 7(F6.2, 1X), 2(I3, 1X))
      READ 30, AI1, (N(I), I = 1,7), DFOV, NF, SEN1
   30 FORMAT (F5.1, 7(1X, I5), 1X, F5.1, 1X, I3, 1X, F5.1)
      READ 35, POPS, BOB, TIRE, SOAP, ADD
   35 FORMAT (5(F7.3, 1X))
      READ 40, (CP(I), I = 1,8), (AR(I), I = 65,67)
   40 FORMAT (8A6,1X,3A6)
      READ 50, (AR(I), I = 1,5), NCG, (AR(I), I = 11,15)
   50 FORMAT (5A6, 1X, A4, 1X, 5A6)
      READ 60, (AR(I), I = 7,10), (AR(I), I = 16,19), (AR(I), I = 25,28)
   60 FORMAT (8A6, 1X, 4A6)
      READ 70, (AR(I), I = 20,24), (AR(I), I = 29,33)
   70 FORMAT (10A6)
      READ 80, (AR(I), I = 34,45)
   80 FORMAT (8A6, 1X, 4A6)
      READ 90, (AR(I), I = 46,57)
   90 FORMAT (4A6, 1X, 8A6)
      READ 100, (COP(I), I = 1,12)
  100 FORMAT (12A6)
      READ 110, (AR(I), I = 58,64)
  110 FORMAT (6A6, 1X, A6)
      RETURN
      END
```

```
      SUBROUTINE PRINT(NOPT)
      COMMON NUM,D,SW,FOL,SGA,SGI,AR,FOV,CP,EO,SW1,SP,DL,AI,TIRE,EQ,TS,
     1SOAP,FML,FMS,COP,FMB,FMD,TAU,ROR,SGA1,SGI1,PTC,NS,ADD,SEN,POPS,
     2RPHI,RPHI1,DPHI,DPHI1,PT,A,BL,SW2,TS1,D1,D2,NSL,AI1,N,DFOV,NF,
     1SEN1,FMS1,NCG,PMAGN,ENFSDS
      DIMENSION P(10), F(10), V(10), AR(78), CP(8), COP(20)
      IF(NOPT) 100,100,200
  100 CONTINUE
      DIM=SW
      TSM=1.0E6*TS
      FOL=D
      DTR=.01745329252O
      FARG1=DTR*FOV*.5
      SLLN=2.*FOL*SINF(FARG1)/COSF(FARG1)
      FARG2=DTR*SW*.008333333333
      SWMLS=2000.*FOL*SINF(FARG2)/COSF(FARG2)
      PRINT 5, NUM
    5 FORMAT(1H1,     36X,38H* DESIGN FOR SCANNING OPTICAL SYSTEM *,15X,
     14HNO. A4, ///,2X,16H* OPTICAL SYSTEM,39X,23H* RETICLE CONFIGURATIO
     2N/)
      PRINT 10,  D,SW,SWMLS
   10 FORMAT(6X,17HAPERTURE DIAMETER,6X,F7.3,7H INCHES,18X,14HWIDTH OF S
     1LITS,7X,F7.3, 8H ARC MIN,2X,F9.3,5H MILS)
      PRINT 15, FOL,FOV,SLLN
   15 FORMAT(6X,19HFOCAL LENGTH (MIN.), 4X,F7.3,7H INCHES,18X,15HLENGTH
     1OF SLITS,6X,F7.3,8H DEGREES,2X,F9.3,4H IN.)
      PRINT 20, DIM,(AR(I),I=1,5)
   20 FORMAT(6X,21HIMAGE DIAMETER         ,2X,F7.3,12H ARC MINUTES,13X,
     110HSLIT SHAPE,12X,5A6)
      PRINT 25, FOV,(CP(I),I=1,4)
   25 FORMAT(6X,13HFIELD OF VIEW,10X,F7.3,8H DEGREES,17X,12HCODE PATTERN,
     110X,4A6)
      PRINT 30, (AR(I),I=65,67),(CP(I),I=5,8)
   30 FORMAT(6X,19HFIELD OF VIEW SHAPE,5X,3A6,35X,4A6)
      PRINT 35,  EO,NCG
   35 FORMAT(6X,18HOPTICAL EFFICIENCY,7X,F4.2,26X,22HNUMBER OF CODE GROU
     1PS ,A4)
      PRINT 40, (AR(I),I=7,24)
   40 FORMAT(6X,19HOPTICAL ARRANGEMENT,5X,4A6, 7X,10HCOLOR CODE,12X,5A6,
     1/30X,4A6, 7X,20HRELATIVE ORIENTATION,2X,5A6)
      PRINT 45, (AR(I),I=25,33)
   45 FORMAT(6X,15HSPECTRAL FILTER,9X,4A6, 9X,14HOF CODE GROUPS,6X,5A6//
     1//)
      PRINT 50,
   50 FORMAT(2X,10H* DETECTOR,45X,8H* MOTION,/)
      PRINT 55, (AR(I),I=34,37),SP
   55 FORMAT(6X,16HTYPE OF DETECTOR,6X,4A6,9X,11HSCAN PERIOD,12X,F7.2,8H
     1 SECONDS)
      PRINT 60, (AR(I),I=38,41),DL,AI
   60 FORMAT(28X,4A6,9X,18HANGLE BETWEEN SPIN/6X,12HDARK CURRENT4X,F12.2
     1,
     118H PULSES PER SECOND,11X,21HAXIS AND OPTICAL AXIS ,F7.2,8H DEGREE
     2S)
      PRINT 65, TIRE
   65 FORMAT(6X,13HTIME RESPONSE,8X,F7.2,13H NANOSECONDS ,14X,17HSTAR TR
     1ANSIT TIME)
```

```
      PRINT 70, EQ,TSM
   70 FORMAT(6X,18HQUANTUM EFFICIENCY,6X,F6.4,27X,13H(CENTRAL RAY),5X,F1
     10.2,13H MICROSECONDS)
      PRINT 75, (AR(I),I=42,45),RPHI,RPHI1,SOAP,DPHI,DPHI1
   75 FORMAT(6X,19HDETECTION TECHNIQUE,3X,4A6,9X,19HPOINTING DIRECTIONS
     1/6X,19HRMS SPREAD OF PULSE,38X,15HRIGHT ASCENSION,6X,F7.2,4H TO ,F
     27.2,2X,7HDEGREES/8X,19HAMPLITUDES TO MEAN ,F7.2,29X,11HDECLINATION
     3,10X,F7.2,4H TO ,F7.2,2X,7HDEGREES)
      PRINT 230,(AR(I),I=71,78)
  230 FORMAT (6X,12HCATHODE SIZE/8X,8A6)
      RETURN
  200 PRINT 210,RPHI,DPHI
  210 FORMAT(1H1,46X,21H* DESIGN EVALUATION *//54X,18HPOINTING DIRECTION
     1/56X,15HRIGHT ASCENSION F10.2,2X,7HDEGREES/56X,11HDECLINATION
     2F14.2,2X,7HDEGREES//)
      PRINT 80, FML
   80 FORMAT(2X,24H* TARGET CHARACTERISTICS,31X,34H* SIGNAL AND NOISE CH
     1ARACTERISTICS//6X,23HLIMITING STAR MAGNITUDE,1X,F6.2,13H PHOTOGRAP
     2HIC,12X,39HMEAN NUMBER OF PULSES FROM LIMITING MAG)
      PRINT 85, (AR(I),I=46,49),FMS
   85 FORMAT(6X,16HSPECTRAL CLASSES,8X,4A6,9X,24HSTAR DURING STAR TRANSI
     1T,15X,F8.2)
      PRINT 90,(COP(I),I=1,8),FMB,(COP(I),I=9,12)
   90 FORMAT(6X,22HPLANETS, SUN. OR EARTH,2X,4A6,7X,34HMEAN NUMBER OF PU
     1LSES FROM STELLAR,/8X,16HIN FIELD OF VIEW,6X,4A6,9X,30HBACKGROUND
     2DURING STAR TRANSIT11X,F8.4/30X,4A6,7X,31HMEAN NUMBER OF PULSES FR
     3OM DARK)
      PRINT 95, (AR(I),I=50,53),FMD
   95 FORMAT(6X,24HSIGNIFICANCE OF EARTHS  ,4A6,9X,27HCURRENT DURING STA
     1R TRANSIT14X,F8.4)
      PRINT 100, (AR(I),I=54,57),PMAGN,TAU
  100 FORMAT(8X,10HATMOSPHERE,12X,4A6,7X,26HPHOTOGRAPHIC MAG. OF NOISE,
     117X,F6.2/61X,19HDETECTION THRESHOLD,22X,F8.2)
      PRINT 105,BOB
  105 FORMAT(61X,30HMEAN VALUE OF OFF-PEAK MAXIMUM/63X,16HFOR CODE PATTE
     1RN,23X,F8.2////)
      PRINT 110,
  110 FORMAT(2X,34H* STAR TRANSIT CHARACTERISTICS FOR,21X,24H* SYSTEM CH
     1ARACTERISTICS/4X,23HLIMITING-MAGNITUDE STAR/)
      PRINT 115, SGA1
  115 FORMAT(6X,17HPOSITION ACCURACY,11X,F7.3,12H ARC MINUTES,7X,33H MIN
     2IMUM NUMBER OF STARS IN FIELD)
      PRINT 120, SGI1
  120 FORMAT(6X,27HRELATIVE INTENSITY ACCURACY,3X,F4.2,23X,31HOF VIEW WI
     1TH LIMITING MAGNITUDE)
      PRINT 125, PTC,NS
  125 FORMAT(6X,24HPROBABILITY OF DETECTION,6X,F4.2,23X,12HAND BRIGHTER,
     122X,I2)
      PRINT 130, ADD
  130 FORMAT(6X,23HEXPECTED NUMBER OF WEAK,32X,35HACCURACY OF ATTITUDE D
     1ETERMINATION ,F6.2,12H ARC MINUTES)
      PRINT 140, SEN, POPS
  140 FORMAT(8X,23HSTARS DETECTED PER SCAN,3X,F8.4,19X,35HPROBABILITY OF
     1 CORRECT STAR-PATTERN/6X,24HEXPECTED NUMBER OF FALSE,33X,
     211HRECOGNITION,24X,F3.1)
      PRINT 145, ENFSDS,(AR(I),I=58,64)
```

```
145 FORMAT(8X,26HSTAR DETECTIONS PER SCAN  ,F8.4,19X,29HPATTERN RECOGN
   1ITION TECHNIQUE,7X,3A6/97X,3A6/61X,32HMEAN NUMBER OF STEPS FOR PAT
   2TERN/63X,11HRECOGNITION,23X,A6)
    RETURN
    END
```

APPENDIX G

DETECTION AND FUNDAMENTAL ACCURACY LIMITATION CONSIDERATIONS

Notation

The following is a list of symbols that have a consistent meaning throughout this appendix.

λ_s = average number of photons received from a star per unit of time

ϵ_o = optical efficiency of lens system

σ = dispersion of diffraction pattern on the focal plane

T_s = time elapse for star to cross slit

$\lambda'_s(t)$ = average number of photons arriving at photomultiplier at time t

$$\Phi(t) = \frac{1}{\sqrt{2\pi}} \int_{-\infty}^{t} e^{-\frac{1}{2}x^2}\, dx$$

$$G(t) = \Phi\left(\frac{t}{\sigma} + \frac{T_s}{2\sigma}\right) - \Phi\left(\frac{t}{\sigma} - \frac{T_s}{2\sigma}\right)$$

M_L = limiting magnitude (photographic)

$\lambda(m)$ = photon arrival rate for a star of magnitude M

$\lambda'_b(t)$ = photon arrival rate at the photomultiplier for weak stars at time t

$\nu(M)$ = average density of stars of magnitude M

α = fraction of photoelectric pulses transmitted by threshold clamp

ϵ_q = quantum efficiency of photomultiplier

λ_d = number of noise pulses resulting from photomultiplier

η = average number of pulses received in the interval (-T, T)

ρ = ratio of star pulse rate to "noise" pulse rate

t_o = time at which star crosses the center of the slit

$\hat{t}_o$ = estimate of t_o

$\hat{\lambda}_s$ = estimate of λ_s

T_f = time duration of holding filter

$y(t)$ = number of pulses in holding filter at time t

$\mu(t)$ = average number of pulses in holding filter at time t

$$H(t) = \int_{t-T_f}^{t} G(x)\, dx$$

T_{sp} = scan period

β = average number of pulses in holding filter when a star of magnitude M is at the center of the slit

T' = time at which $y(t)$ exceeds τ

t'' = time at which $y(t)$ drops below τ

$t^* = \frac{1}{2}(t' + t'') - T_{f/2}$ = estimation of the time that the star crosses the slit

$t_{\tau+1}$ = arrival time of the $(\tau+1)$-th pulse

$t'_{\tau+1}$ = arrival time of the τ^{th} from last pulse

$p(n)$ = probability of receiving n pulses from a star

P_τ = probability of receiving more than τ pulses from a star

N_M = number of stars per square degree brighter than photographic magnitude M

T_γ = number of square degrees scanned by the optical device

A. Description of Statistical Problem*

It is natural to characterize the scanning system by four parameters:

i. probability of detection

ii. variance of the intensity estimate

iii. variance of the crossing time estimate (angle accuracy)

iv. expected number of "false star detections" per scan.

Explicit formulas are derived for these four parameters in terms of slit width, star intensity, spin rate, diameter of the diffraction circle, etc.

In this section certain statistical models are postulated for the stellar radiation, background and internal noise; see Table G-1**. The photon arrivals from the stars form a Poisson process. The background consists of "weak" stars with random spatial distributions***. Two sources of internal noise are considered, dark current and the random character of electron emission. Electronic noise is assumed to be negligible. The composite output of the photomultiplier is a sequence of pulses with random amplitudes and separation. Since the amplitude variations do not contain information about the stars, the output pulses of the multiplier are

---

* This work was sponsored in part by the Research Division, Control Data Corporation, Minneapolis, Minnesota.

** D. C. Harrington has also investigated noise errors. [34]

*** A similar problem has been studied for infrared detection by D. Z. Robinson [35] and H. G. Eldering. [36]

clamped to a fixed level when they exceed a threshold; see Figure G-3.

Also, the basic problems of detection and estimation are approached using statistical methods of hypothesis testing and estimation. A detection method is derived that maximizes the probability of detecting a star. Also absolute lower bounds are derived for the variance of the intensity estimate and crossing time estimate. These results represent the "information limits" that may be achievable using the output of the threshold clamp.*

TABLE G-1

Noise Sources

Source	Statistical Model	Relative Magnitude
Stellar Radiation	Intensity Fixed Photon Arrivals--Poisson	1 (Fourth Magnitude)
Background (Weak Stars)	Random Spatial Distribution Photon Arrivals--Poisson	1/10
Internal Noise Dark Current	Equivalent to Homogeneous Radiation	1/50
Electron Emission of Photomultiplier	Random-Model Based on Empirical Data	1/5 - 1/10
Thermal Electronic Noise	Neglected	0

In general, one must compromise between ease of implementation and the

* R. C. Jones has applied statistical information theory to the "detection problem". [37] and [38]

desirable properties of the methods. A reasonable compromise is based on counting and threshold crossings. Namely, a holding filter counts the number of pulses in a sliding interval of fixed length. If the count exceeds a fixed threshold, a star is said to be "present" at the average of the first and second threshold crossing; see Figure I-3.

In the next section, processing techniques are outlined for the threshold method of detection. The probability of detection for this method along with the expected number of false star detections per scan are evaluated. An intensity estimate and its variance are derived. The variance of the crossing time estimate is determined by assuming the background and dark current negligible compared to the star radiation and that the diffraction circle is small, compared to the slit width. An explicit formula is derived for the variance in terms of the system parameters.

1. Statistical Models

There are three sources of randomness or noise in a scanning system. The stellar radiation consists of photons whose arrival times are random. "Weak" stars appear as undesirable signals or noise; the stars are assumed to have random spatial distributions. The photomultiplier is the third noise source. Electronic noise is neglected.

a. Star Radiation

The photons from a star are assumed to form a Poisson process with parameter λ_s; i.e., on the average λ_s photons are received per unit of time.* The photons have equal energy relative to the photomultiplier. The optical system produces a diffraction pattern that is two-dimensional Gaussian; the energy density in the focal plane is given by

$$\frac{\epsilon_0 \lambda_s}{2\pi \sigma^2} e^{-\frac{1}{2}(x^2+y^2)/\sigma^2} \tag{g-1}$$

where ϵ_0 denotes the optical efficiency. Let T_s be the time it takes the center of the star image to cross the slit. For convenience, time will be measured from the event of the star crossing the center of the slit. Hence, the photon arrivals at the photomultiplier form a non-stationary Poisson process with parameter $\lambda_s'(t) = \epsilon_0 \lambda_s G(t)$, where

$$G(t) = \Phi(t/\sigma + T_s/2\sigma) - \Phi(t/\sigma - T_s/2\sigma) \tag{g-2}$$

and

$$\Phi(t) = \frac{1}{\sqrt{2\pi}} \int_{-\infty}^{t} e^{-\frac{1}{2}x^2} dx \tag{g-3}$$

Note that 80 per cent of the star radiation passes through the slit when $T_s/2 = 1.28\sigma$; i.e., $\lambda_s'(0) = .8\, \epsilon_0 \lambda_s$. The function G(t) is graphed in

* Note that λ_s depends on the star magnitude and the aperture of the optical system.

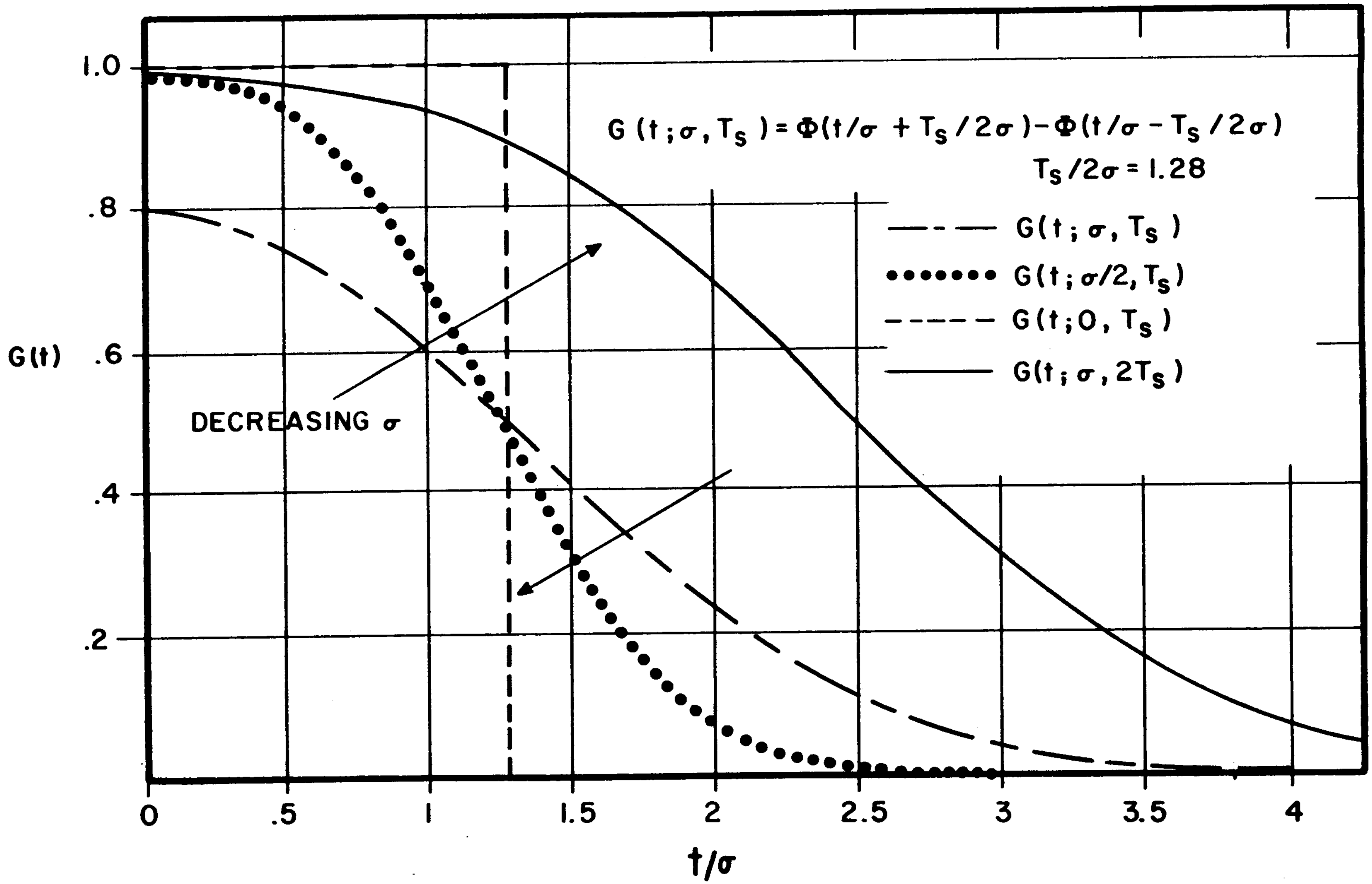

Figure G-1: Graph of G(t), Fraction of Radiation Passing Slit

Figure G-1. G(t) is a factor which represents the proportion of total radiation passing the slit as a function of time. The time scale is divided by the effective diameter of the diffraction circle, σ.

b. Weak Stars

Assume stars with magnitudes M_o and brighter are used for navigation and are included in the stored star map. One would like to obtain a detection method that discriminates against stars with magnitudes greater than M_o. If a weak star is detected, the system must recognize it as a weak star and delete it. This requires extra processing capability. Consequently, one would like a detection method that has a high probability (>.9) of detecting a star of magnitude M_o and that results in a few (two or three) weak-star detections in a scan period.

For a given scan direction, the photon arrivals at the photomultiplier (due to the background) form a non-stationary Poisson process with mean

$$\lambda_b'(t) = \epsilon_o \sum_{M=M_o+1}^{\infty} \lambda(M) \sum_j G(t) - t_j(M)) \qquad \text{(g-4)}$$

where $\lambda(M)$ is the photon arrival rate for a star of magnitude M (for the specified optical aperture), and $t_j(M)$ is the time when the j^{th} star of magnitude M is at the center of the slit. Since it is impractical to express $t_j(M)$ analytically as a function of the scan direction, they are assumed to be random variables. For each magnitude M, the $t_j(M)$'s are assumed to form a Poisson process with mean $\nu(M)$; parameter $\nu(M)$ is a measure of the average density of stars of magnitude M. The Poisson processes corresponding to different M's are assumed to be independent.

It is reasonable to assume the $t_j(M)$'s have a Poisson distribution. Let N be the total number of stars of magnitude M. Assuming the stars are uniformly distributed over the celestial sphere, the probability of n M^{th} magnitude stars in a specific solid angle γ is

$$\binom{N}{n} \left[\frac{\gamma}{4\pi}\right]^n \left[1 - \frac{\gamma}{4\pi}\right]^{N-n} \qquad \text{(g-5)}$$

Since N is large and $\gamma \ll 4\pi$, the probability distribution of n can be approximated by

$$\frac{1}{n!} \quad \frac{N\gamma}{4\pi}^{\;n} e^{-\gamma N/4\pi} \qquad \text{(g-6)}$$

with γ = (slit length) x (sweep rate) x (time) and

$$\nu(M) = \frac{N \text{ x (slit length) x (sweep rate)}}{4\pi} \; * \qquad \text{(g-7)}$$

Therefore, the $t_j(M)$'s form a Poisson process.

c. Internal Noise

There are three sources of noise generated by the photomultiplier:

---

* A similar approach has been used by Bharucha-Reid to describe the distribution of stars and galaxies [39].

(1) the random character of the electron emission which modulates the amplitude of the output pulses, (2) internally generated noise or dark current, (3) the random time spread of electrons in a cascade. These effects are reduced by using a threshold-clamp at the output of the photomultiplier. The output pulses below a fixed threshold are deleted; those above the threshold are clamped to a fixed level to form a "standard" pulse. This technique does not eliminate all of the dark current; high energy pulses will exceed the threshold. These residual noise pulses are assumed to form a Poisson process with parameter λ_d. Also, the lower energy output pulses resulting from incident photons will be deleted. Let $1-\alpha$ be the fraction of the pulses deleted.

The composite output of the threshold-clamp is a sequence of pulses of fixed amplitude and random spacing, see Figure I-3. For a fixed background and an overall quantum efficiency ϵ_q (pulses per photon), the output of the threshold-clamp forms a Poisson process with intensity

$$\alpha\, \epsilon_q[\lambda_s'(t) + \lambda_b(t)] + \lambda_d \qquad \text{(g-8)}$$

2. Information Limits

There are intrinsic limitations on the accuracy and reliability that can be achieved using the output of the threshold-clamp. These limitations represent the "information limits" of the scanning optical system.

The output of the threshold-clamp is observed for a period -T to T, with

2T much larger than the time required for the star to cross the slit, i.e., $T_s \ll 2T$. Assume one star crosses the slit in this period, at time t_o. Further, assume t_o is not "near" the edges of the period, i.e., $|t_o| + T_s < T$. Let $\tau_1 < \tau_2 < \tau_3 < \ldots$ represent the times at which pulses are observed in the period. The joint density function of $(\tau_1, \tau_2, \ldots, \tau_n)$, conditional on observing n pulses is*

$$f(\tau_1, \ldots, \tau_n | n, t_o, \lambda_s) = n! \prod_{j=1}^{n} \frac{\alpha\, \epsilon_q\, \epsilon_o\, \lambda_s\, G(\tau_j - t_o) + \alpha\, \epsilon_q\, \epsilon_o\, \lambda_b'(\tau_j) + \lambda_d}{\int_{-T}^{T} [\alpha\, \epsilon_q\, \epsilon_o\, \lambda_s\, G(t-t_o) + \alpha\, \epsilon_q\, \epsilon_o\, \lambda_b'(t) + \lambda_d] dt} \tag{g-9}$$

In the following discussion, $\lambda_b'(t)$ is assumed to be constant, say $\epsilon_o\, \lambda_b$. The probability of obtaining n pulses in the period (-T, T) is

$$P(n | t_o, \lambda_s) = \frac{\eta^n}{n!} e^{-\eta} \tag{g-10}$$

where

$$\eta = \int_{-T}^{T} [\alpha\, \epsilon_q\, \epsilon_o\, \lambda_s\, G(t - t_o) + \alpha\, \epsilon_q\, \epsilon_o\, \lambda_b + \lambda_d]\, dt \tag{g-11}$$

* E. Parzen [40] develops several basic relationships for Poisson processes.

In Appendix D, it is shown that

$$\int_{-\infty}^{\infty} G(t)\, dt = T_s \qquad \text{(g-12)}$$

Since t_o is not "near" the ends of the period

$$\eta = \alpha\, \epsilon_q\, \epsilon_o\, \lambda_s\, T_s + 2\alpha\, \epsilon_q\, \epsilon_o\, \lambda_b\, T + 2\lambda_d T \qquad \text{(g-13)}$$

and $P\,(n|t_o, \lambda_s)$ is independent of t_o. Further, the joint probability function of $(\tau_1, \ldots, \tau_n)$ and n is

$$f(\tau_1, \ldots, \tau_n | n, t_o, \lambda_s)\; P(n|\lambda_s) =$$

$$\prod_{j=1}^{n} \left\{ \alpha\, \epsilon_q\, \epsilon_o\, \lambda_s\, G(\tau_j - t_o) + \alpha\, \epsilon_q\, \epsilon_o\, \lambda_b + \lambda_d \right\} e^{-\eta} \qquad \text{(g-14)}$$

a. Detection

Detection is basically a statistical problem of testing the hypothesis that $\lambda_s = 0$ as opposed to $\lambda_s \geq \lambda(M_o)$. There are two types of errors: Type I - a star is "detected" when no star is present, Type II - a star is not detected when a star is present; see Figure G-2. In practice, most false star detections can be eliminated by comparison to stored star charts. On the other hand, if a star is missed, the system accuracy is reduced; and it may be impossible to obtain the required attitude and position estimates. Hence, the goal is to select a detection method that minimizes the probability of a Type II for a fixed probability of a Type I error. The detection method which is developed in the following paragraphs meets this goal.

Assume the star which may occur in the period (-T, T) has an intensity $\lambda_1 \geq \lambda(M_o)$. The optimum detection method is based on a likelihood ratio test statistic $\mathfrak{J}$, which depends on n and the τ_j's.* If $\mathfrak{J}$ is larger than a specified constant C_p, a star is said to be present. If $\mathfrak{J}$ is less than C_p, no star is detected. The constant C_p is selected so that the probability of a Type I error is P. The probability of a Type II error is minimized using this detection method for a star of intensity λ_1, as will be shown.

The test statistic is

$$\mathfrak{J}(\tau_1, \ldots \tau_n; n) = \frac{\sup\limits_{t_o} \left\{ f(\tau_1, \ldots, \tau_n | n, t_o, \lambda_1) \, P(n|\lambda_1) \right\}}{f(\tau_1, \ldots, \tau_n | n, t_o, 0) \, P(n|))}$$

$$= \sup_{t_o} \left\{ \prod_{j=1}^{n} \left[\frac{\alpha \, \epsilon_q \, \epsilon_o \, \lambda_1 \, G(\tau_j - t_o) + \alpha \, \epsilon_q \, \epsilon_o \, \lambda_b + \lambda_d}{\alpha \, \epsilon_q \, \epsilon_o \, \lambda_b + \lambda_d} \right] \right\} e^{-\alpha \, \epsilon_q \epsilon_o \lambda_1 T_s} \qquad \text{(g-15)}$$

Note that $\mathfrak{J}$ is independent of the duration of the observation, 2T. For convenience let

---

* S. Wilks [41] discusses likelihood ratio tests.

		STATE OF NATURE	
		NO STAR PRESENT	STAR PRESENT
DECISION	NO STAR PRESENT		TYPE II ERROR
	STAR PRESENT	TYPE I ERROR	

Figure G-2: Detection Errors

$$\rho = \frac{\alpha \epsilon_q \epsilon_o \lambda_1}{\alpha \epsilon_q \epsilon_o \lambda_b + \lambda_d} \qquad \text{(g-16)}$$

which is the ratio of the star pulse rate to the "noise" pulse rate. The parameter ρ is like a signal to noise ratio. The detection method can be based equivalently on

$$\mathcal{J}' (\tau_1, \ldots, \tau_n; n) = \sum_{j=1}^{n} \ln[\rho\, G(\tau_j - \hat{t}_o) + 1] \qquad \text{(g-17)}$$

where $\hat{t}_o$ is the value of t_o that maximized $f(\tau_1, \ldots, \tau_n | n, t_o, \lambda_1)$.

For many cases of interest, G(t) can be approximated by an exponential function of the form

$$G(t) \approx G(0)\, e^{-\frac{1}{2}(t/\sigma_1)^2} \qquad \text{(g-18)}$$

where σ_1 is a parameter selected to "minimize" the discrepancy between G(t) and the approximation for $-T_s \leq t \leq T_s$. In general, the integral of the approximation is not equal to the integral of G(t). From the mean value theorem,

$$G(t) = \Phi\left(\frac{t}{\sigma} + \frac{T_s}{2\sigma}\right) - \Phi\left(\frac{t}{\sigma} \quad \frac{T_s}{2\sigma}\right) = \phi(\xi)\frac{T_s}{\sigma} \qquad \text{(g-19)}$$

where $t/\sigma - T_s/2\sigma \leq \xi \leq t/\sigma + T_s/2\sigma$ and

$$\phi(t) = \frac{1}{\sqrt{2\pi}} e^{-t^2/2} \tag{g-20}$$

As $T_s/2\sigma$ approaches zero $G(t)T_s$ approaches $\sigma^{-1}\ \phi(t/\sigma)$ uniformly on the real line. Note that the variance corresponding to the probability density function $G(t)/T_s$ is

$$\sigma^2\left[1 + \frac{1}{3}\left(\frac{T_s}{2\sigma}\right)^2\right] \tag{g-21}$$

In Figure G-3, G(t) is graphed with an exponential approximation.

This figure depicts the relationship between G(t) and the exponential approximation for two values of σ, the effective diameter of the diffraction circle.

Using this approximation to G(t), one can determine $\hat{t}_o$. Setting the derivative of $\ln f(\tau_1, \ldots, \tau_n | n, t_o, \lambda_1)$ equal to zero, one obtains

$$\sum_{j=1}^{n} \frac{\tau_j - t_o}{1 + [\rho\ G(\tau_j - t_o)]^{-1}} = 0 \tag{g-22}$$

Assuming $\rho G(\tau_j - t_o) \ll 1$ for $j = 1, 2, \ldots n$,

$$\sum_{j=1}^{n} (\tau_j - t_o) \left\{1 - [\rho G(\tau_j - t_o)]^{-1} + [\rho G(\tau_j - t_o)]^{-2} - \ldots\right\} = 0^* \tag{g-23}$$

* The probability that $\rho G(\tau_j - t_o) > 1$ for all j approaches unity as ρ increases without bound.

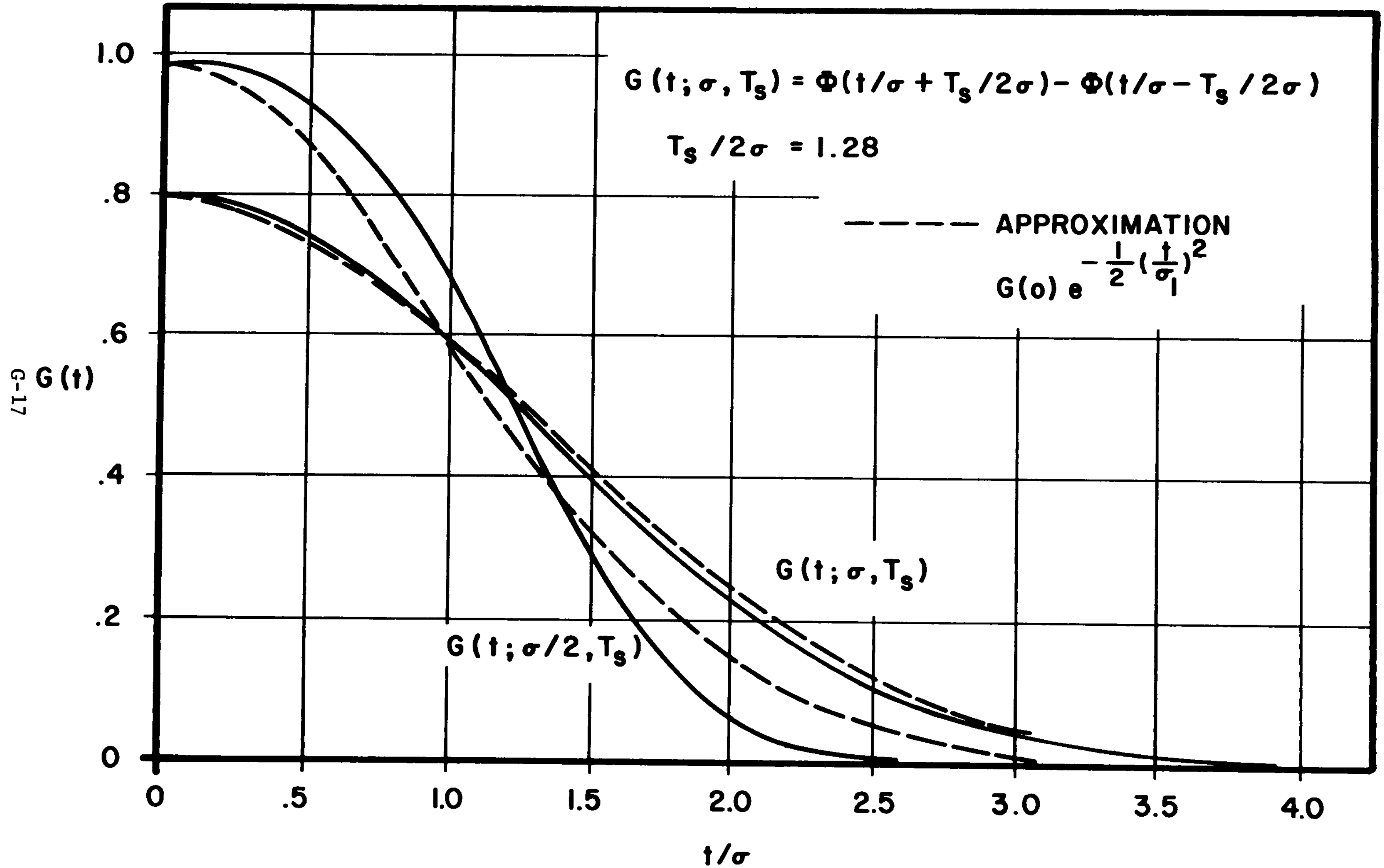

Figure G-3: Graph of G(t) and Gaussian Approximation

The first term is zero if

$$t_o = \bar{\tau} \equiv \frac{1}{n} \sum_{j=1}^{n} \tau_j \tag{g-24}$$

Since G(t) is an even function, and since the τ_j are distributed about their average $\bar{\tau}$, the higher order terms will be small when $t_o = \bar{\tau}$. Hence $\hat{t}_o$ can be approximated by $\bar{\tau}$. Note that $\bar{\tau}$ is an unbiased estimate of t_o. Also $\mathcal{J}'$ has a simple approximation when G(t) is approximated by an exponential function and when $\rho G(\tau_j - \bar{\tau}) \gg 1$. Namely,

$$\mathcal{J}'(\tau_1, \tau_2, \ldots, \tau_n; n) \approx n \ln[\rho G(0)] - \frac{1}{2\sigma_1^2} \sum_{j=1}^{n} (\tau_j - \bar{\tau})^2 \tag{g-25}$$

Hence the likelihood ratio test becomes:

$$\begin{cases} \text{if } nL - \dfrac{1}{2\sigma_1^2} \displaystyle\sum_{j=1}^{n} (\tau_j - \bar{\tau})^2 > C_P' & \text{a star is present} \\[2ex] \text{if } nL - \dfrac{1}{2\sigma_1^2} \displaystyle\sum_{j=1}^{n} (\tau_j - \bar{\tau})^2 < C_P' & \text{no star is present,} \end{cases}$$

where $L = \ln[\rho\, G(0)]$. In other words, a star is "present" if many closely spaced pulses are received. Using these approximations, one can estimate the probability of Type II and Type I errors.

First consider Type II errors. For $\rho \gg 1$, the unordered τ_j's have a density function $G(t - t_o)/T_s$. Further, if $T_s/2\sigma$ is "small", $G(t - t_o)/T_s$

can be approximated by a normal density function with mean t_o and variance $\sigma^2 \approx \sigma_1^2$. Hence

$$\frac{1}{\sigma_1^2} \sum_{j=1}^{n} (\tau_j - \bar{\tau})^2 \tag{g-26}$$

has a chi-square distribution with n - 1 degrees of freedom. For fixed n the probability of a Type II error is

$$P\left\{ \text{Type II error} \middle| n \right\} = P\left\{ \chi^2_{n-1} > 2(nL - C'_P) \right\} \tag{g-27}$$

Hence

$$P\left\{ \text{Type II error} \right\} = \sum_{n=2}^{n} P(n|\tau_1)\, P\left\{ \chi^2_{n-1} > 2(nL - C'_P) \right\} \tag{g-28}$$

The probability of a Type II error is independent of t_o.

Next consider Type I errors. In this case, the τ_j's have a uniform distribution over the interval (-T , T). Since

$$\sum_{j=1}^{n} (\tau_j - \bar{\tau})^2 \tag{g-29}$$

does not have a simple distribution it is convenient to approximate it by a chi-square random variable. The expected value of (g-29) is $(n - 1)T^2/3$. Hence it is natural to assume

$$\sum_{j=1}^{n} (\tau_j - \bar{\tau})^2 \Big/ (T^2/3) \qquad \text{(g-30)}$$

has a chi-square distribution with n - 1 degrees of freedom. Then

$$P\left\{\text{Type I error}\right\} = \sum_{n=2}^{\infty} P(n|0)\, P\left\{\chi^2_{n-1} < \frac{3\sigma_1{}^2}{T^2} (nL - C_P')\right\} \qquad \text{(g-31)}$$

The parameter C_P' is selected so that the probability of a Type I error is equal to P.

The detection method based on $\mathcal{J}'$ has a relatively simple analogy implementation. The random process defined by

$$X(t) = \sum_{j=1}^{n} \ln[\rho\ G(\tau_j - t) + 1] \qquad \text{(g-32)}$$

can be interpreted as "shot noise" corresponding to an impulse response function

$$W(t) = \ln[\rho\ G(t) + 1] \qquad \text{(g-33)}$$

The process X(t) can be generated by passing the output of the threshold-clamp through a filter with an impulse response that approximates

$$\ln[\rho\ G(t) + 1] \qquad \text{(g-34)}$$

The maximum value of X(t) is $\mathcal{J}'$. If output of the filter exceeds C_p', a star is said to be present. Also the time $\hat{t}_0$ at which X(t) achieves its maximum is a reasonable estimate of the time at which the star is in the center of the slit.

The impulse W(t) is a positive, even function which converges to zero as $|t|$ increases without bound. If $\rho \gg 1$, the impulse function can be approximated by

$$W(t) \approx \ln[\rho\ G(0)] - \tfrac{1}{2}\left(\frac{t}{\sigma_1}\right)^2 \tag{g-35}$$

"near" the origin.

For a fixed value of t, the characteristic function of the probability density of X(t) is given by

$$\log \phi_x(u) = \int_{-\infty}^{\infty}\left[e^{iuw(t)} - 1\right]\left[\frac{\alpha\ \epsilon_q\epsilon_0\lambda_s G(t) + \alpha\ \epsilon_q\epsilon_0\lambda_b + \lambda_d}{\alpha\ \epsilon_q\epsilon_0\lambda_s T_s + 2\alpha\ \epsilon_q\epsilon_0\lambda_b T + 2\lambda_d T}\right] dt \tag{g-36}$$

b. Estimation

There are intrinsic limitations on the accuracy to which the star position t_0 and intensity λ_s can be estimated. In the following paragraphs, lower bounds are derived for the variance of estimators of t_0 and λ_s. Also maximum likelihood estimators are derived, and their variances compared to the bounds.

First consider estimation of t_0. For fixed observed values of

$(\tau_1,\ldots,\tau_n)$ and n, the maximum likelihood estimate of t_o is that value of t_o which maximizes $f(\tau_1,\ldots,\tau_n|n,t_o,\lambda_s)\ P(n|\lambda_s)$, which is $\hat{t}_o$.

Previously we have shown that $\hat{t}_o$ is approximately

$$\tau \equiv \frac{1}{n} \sum_{j=1}^{n} \tau_j \tag{g-37}$$

Using this approximation, clearly

$$\hat{t}_o = \frac{1}{n} \sum_{j=1}^{n} t_j \tag{g-38}$$

where $(t_1,t_2,\ldots,t_n)$ is a random sample of size n with a density

$$\frac{1}{\eta}\left[\alpha\epsilon_q\epsilon_o\lambda_s G(t-t_o)+2\alpha\epsilon_q\epsilon_o\lambda_b T+2\lambda_d T\right] \tag{g-39}$$

The expected value of $\hat{t}_o$ given $n\geq 1$ can be shown to be

$$\epsilon(\hat{t}|n\geq 1) = t_o \tag{g-40}$$

The variance of $\hat{t}_o$ given $n\geq 1$ can be shown to be

$$\mathrm{Var}(\hat{t}_o|n\geq 1) = E(1/n|n\geq 1)\ \mathrm{Var}(t) \tag{g-41}$$

with

$$\epsilon(1/n|n\geq 1) = \left[e^{\eta} - 1\right]^{-1} \sum_{j=1}^{\infty} \frac{1}{k} \frac{\eta^k}{k!} \tag{g-42}$$

and

$$\mathrm{Var}(t) = \int_{-T}^{T} (x-t_o)^2 \frac{1}{\eta}\left[\alpha\epsilon_q\epsilon_o\lambda_s G(x - t_o) + 2\alpha\epsilon_q\epsilon_o\lambda_b T + 2\lambda_d T\right] dx \tag{g-43}$$

For $\quad G(t) \approx T_s/\sigma\ \varphi(t/\sigma)$ (g-44)

$$\lambda_b/\lambda_s \ll 1 \tag{g-45}$$

$$\lambda_d/(\alpha\epsilon_q\epsilon_o\lambda_s) \ll 1 \tag{g-46}$$

the variance of t is σ^2.

Using the Cramer-Rao bound in this problem, one can determine a lower bound on the variance of unbiased estimators of t_o. The bound is the reciprocal of

$$\varepsilon\left[\frac{\partial}{\partial t_\circ}\ln\left[f(t_1,\ \ldots,\ t_n|n,\ t_\circ,\ \lambda_s)\ P(n|\lambda_s)\right]\right]^2 \tag{g-47}$$

$$= \varepsilon\left[\sum_{j=1}^{n}\left(\frac{\alpha\varepsilon_q\varepsilon_\circ\lambda_s G'(t_j-t_\circ)}{\alpha\varepsilon_q\varepsilon_\circ\lambda_s G(t_j-t_\circ)+\alpha\varepsilon_q\varepsilon_\circ\lambda_b+\lambda_d}\right)^2\right]$$

$$= \eta\varepsilon_t\left[\frac{\alpha\varepsilon_q\varepsilon_\circ\lambda_s G'(t-t_\circ)}{\alpha\varepsilon_q\varepsilon_\circ\lambda_s G(t-t_\circ)+\alpha\varepsilon_q\varepsilon_\circ\lambda_b+\lambda_d}\right]^2$$

Using (g-44), (g-45), and (g-46), the bound becomes the reciprocal of

$$\frac{\alpha\varepsilon_q\varepsilon_\circ\lambda_s}{\sigma^2}\int_{-\infty}^{\infty}\frac{\left[\varphi\left(\frac{x}{\sigma}+\frac{T_s}{2\sigma}\right)-\varphi\left(\frac{x}{\sigma}-\frac{T_s}{2\sigma}\right)\right]^2}{\frac{T_s}{\sigma}\ \varphi\left(\frac{x}{\sigma}\right)}\,dx \tag{g-48}$$

$$= \frac{4\alpha\varepsilon_q\varepsilon_\circ\lambda_s}{T_s}\ \sinh\left(\frac{T_s}{2\sigma}\right)^2$$

Hence for any unbiased estimator $g(\tau_1,\ \ldots,\ \tau_n,\ n)$ of $t_\circ$,

$$\mathrm{Var}\left[\frac{g(\tau_1,\ \ldots,\ \tau_n,n)}{T_s}\right] \geqslant \frac{1}{2}\left[\alpha\varepsilon_q\varepsilon_\circ\lambda_s T_s\ \sinh\ (T_s/2\sigma)^2\right]^{-1} \tag{g-49}$$

This bound and the variance of $\hat{t}_\circ$ are compared in Figure G-4.

Examination of these two functions in Figure G-4 indicates that the variance of the estimator of t_o, i.e., $\hat{t}_o = \frac{1}{n}\sum_{j=1}^{n} t_j$, is very close to the lower bound for any unbiased estimator of t_o. Another interesting fact obtained from Figure G-4 is that interpolation of the diffraction circle to within one-tenth of the diameter is possible, given that the mean of the photoelectric output is greater than 18.

Next consider estimation of λ_s. The Cramer-Rao [42] bound for unbiased estimators of λ_s is the reciprocal of

$$-E\left\{\frac{\partial^2}{\partial\lambda_s^2} \ln\left[f(\tau_1, \ldots, \tau_n | n, t_o, \lambda_s)\; P(n|\lambda_s)\right]\right\} = \tag{g-50}$$
$$-E\left\{\frac{\partial^2}{\partial\lambda_s^2} \ln\left[f(\tau_1, \ldots, \tau_n | n, t_o, \lambda_s)\right]\right\} - E\left\{\frac{\partial^2}{\partial\lambda_s^2} \ln\left[P(n|\lambda_s)\right]\right\}$$

Using approximations (g-45) and (g-46), the first term on the right of Equation (g-50) can be neglected.

$$-E\left\{\frac{\partial^2}{\partial\lambda_s^2} \ln\left[f(\tau_1, \ldots, \tau_n | n, t_o, \lambda_s)\right]\right\}$$

$$= E\left\{\sum_{j=1}^{n}\left[\frac{\alpha\epsilon_q\epsilon_o G(\tau_j - t_o)}{\alpha\epsilon_q\epsilon_o\lambda_s G(\tau_j - t_o) + \alpha\epsilon_q\epsilon_o\lambda_b + \lambda_d}\right]^2\right.$$

$$\left. - n\left[\frac{\alpha\epsilon_q\epsilon_o T_s}{\alpha\epsilon_q\epsilon_o\lambda_s T_s + 2\alpha\epsilon_q\epsilon_o\lambda_b T + 2\lambda_d T}\right]^2\right\}$$

$$\approx E\left\{\sum_{j=1}^{n}\frac{1}{\lambda_s} - \frac{n}{\lambda_s}\right\} = 0 \tag{g-51}$$

The second term on the right of Equation (g-50) is

$$-E\left\{\frac{\partial^2}{\partial \lambda_s^2} \ln[P(n|\lambda_s)]\right\} = \frac{(\alpha \epsilon_q \epsilon_o T_s)^2}{\eta} \qquad \text{(g-52)}$$

Hence for any unbiased estimator $h(\tau_1, \ldots, \tau_n, n)$ of λ_s

$$\mathrm{Var}\left[\frac{h(\tau_1, \ldots, \tau_n, n)}{\lambda_s}\right] \geq \frac{\eta}{(\alpha \epsilon_q \epsilon_o T_s \lambda_s)^2} \qquad \text{(g-53)}$$

if the background and dark current are small compared to the star signal. A natural estimator of λ_s is

$$\hat{\lambda}_s = \frac{n - 2T(\alpha \epsilon_o \epsilon_q \lambda_b + \lambda_d)}{\alpha \epsilon_q \epsilon_o T_s} \qquad \text{(g-54)}$$

The expectation of $\hat{\lambda}_s$ is λ_s. Also the variance of $\hat{\lambda}_s$ equals the lower bound, Equation (g-53). Therefore, the estimator $\hat{\lambda}_s$ has minimum variance and is unbiased.

B. Processing Techniques

In general one must compromise between ease of implementation and the desirable properties of the methods. A reasonable digital implementation is based on counting and threshold crossings. Namely, a holding filter is used to count the number of pulses in a sliding interval of fixed length. If the count exceeds a fixed threshold, a star is said to be "present" at the average of the first and second crossing; see Figure I-3. Let T_f represent the duration of the holding filter. The output of the filter $y(t)$ is a random step function. If the diffraction circle is small

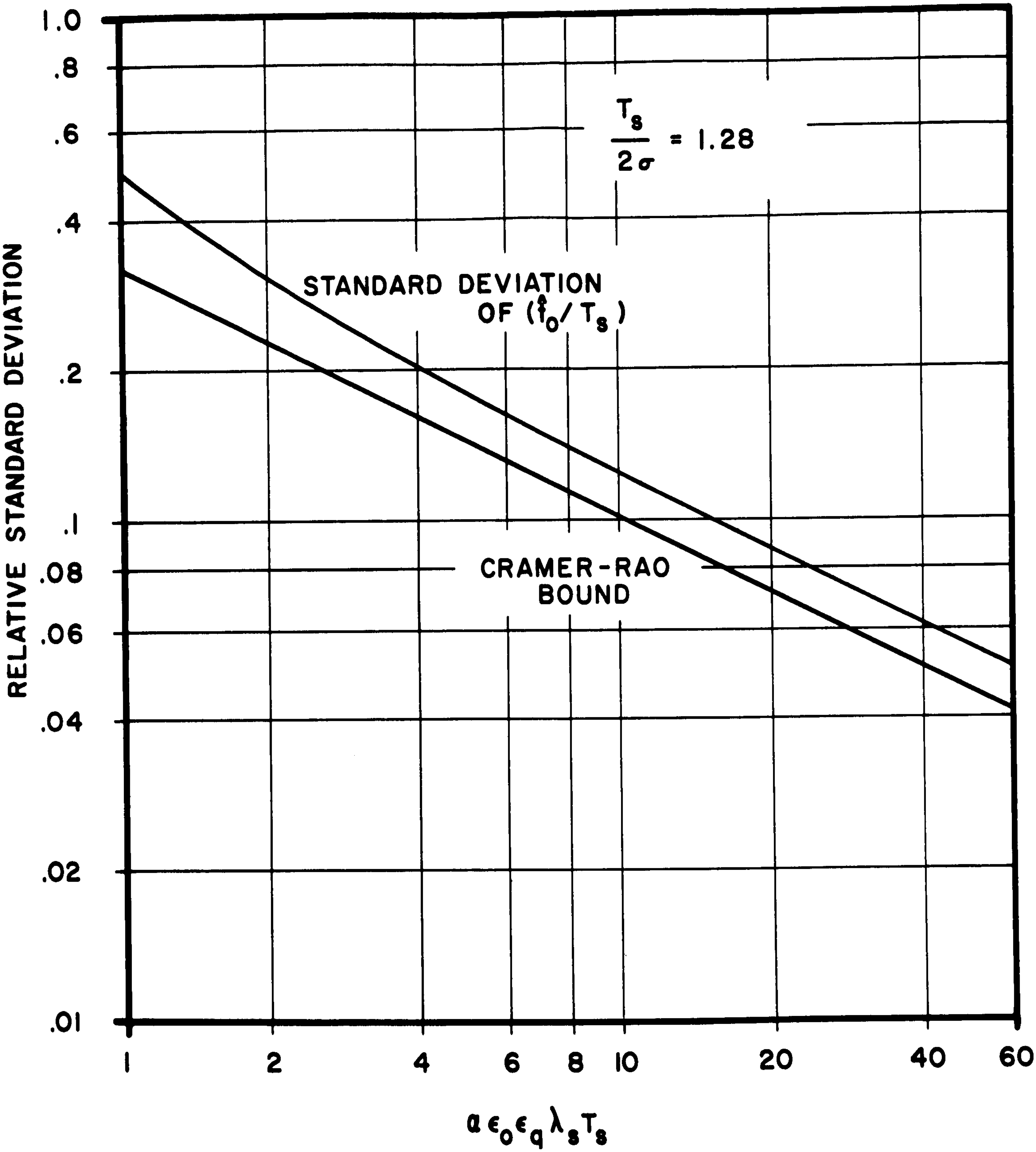

Figure G-4: Standard Deviation of t_0/T_s and Lower Bound compared to slit width and the star is bright, $y(t)$ approaches a triangular pulse whose peak occurs at time $T_f/2$.

The conditional distribution of $y(t)$, given the $t_j(M)$'s, is Poisson with mean

$$\mu(t) = \alpha\epsilon_q\epsilon_o\lambda_s H(t) + \alpha\epsilon_q\epsilon_o \sum_{M=M_o+1}^{\infty} \lambda(M) \sum_j H(t-t_j(M)) + T_f\lambda_d \tag{g-55}$$

where $H(t) = \int_{t-T_f}^{t} G(x)dx$. An explicit expression for $H(t)$ in terms of the standard normal distribution function is derived in Appendix D: vis.,

$$H(t) = (t + T_s/2)\,\Phi\left(\frac{t + T_s/2}{\sigma}\right) - (t - T_s/2)\,\Phi\left(\frac{t - T_s/2}{\sigma}\right)$$

$$- \left[(t - T_f + T_s/2)\,\Phi\left(\frac{t - T_f + T_s/2}{\sigma}\right) - (t - T_f - T_s/2)\,\Phi\left(\frac{t-T_f-T_s/2}{\sigma}\right)\right]$$

$$+\sigma\left[\varphi\left(\frac{t + T_s/2}{\sigma}\right) - \varphi\left(\frac{t - T_s/2}{\sigma}\right)\right]$$

$$-\sigma\left[\varphi\left(\frac{t - T_f + T_s/2}{\sigma}\right) - \varphi\left(\frac{t - T_f - T_s/2}{\sigma}\right)\right] \tag{g-56}$$

The function $H(t)$ is graphed in Figure G-5 for $T_s = T_f$. Hence,

$$P\left\{y(t) = k \,|\, t_j(M)\right\} = \left[\frac{\mu(t)}{k!}\right]^k e^{-\mu(t)}$$

It is represented for three values of σ given T_s, and two values of T_s given σ. Observing the variation of σ it is seen that $H(t)$ becomes triangular as σ approaches zero.

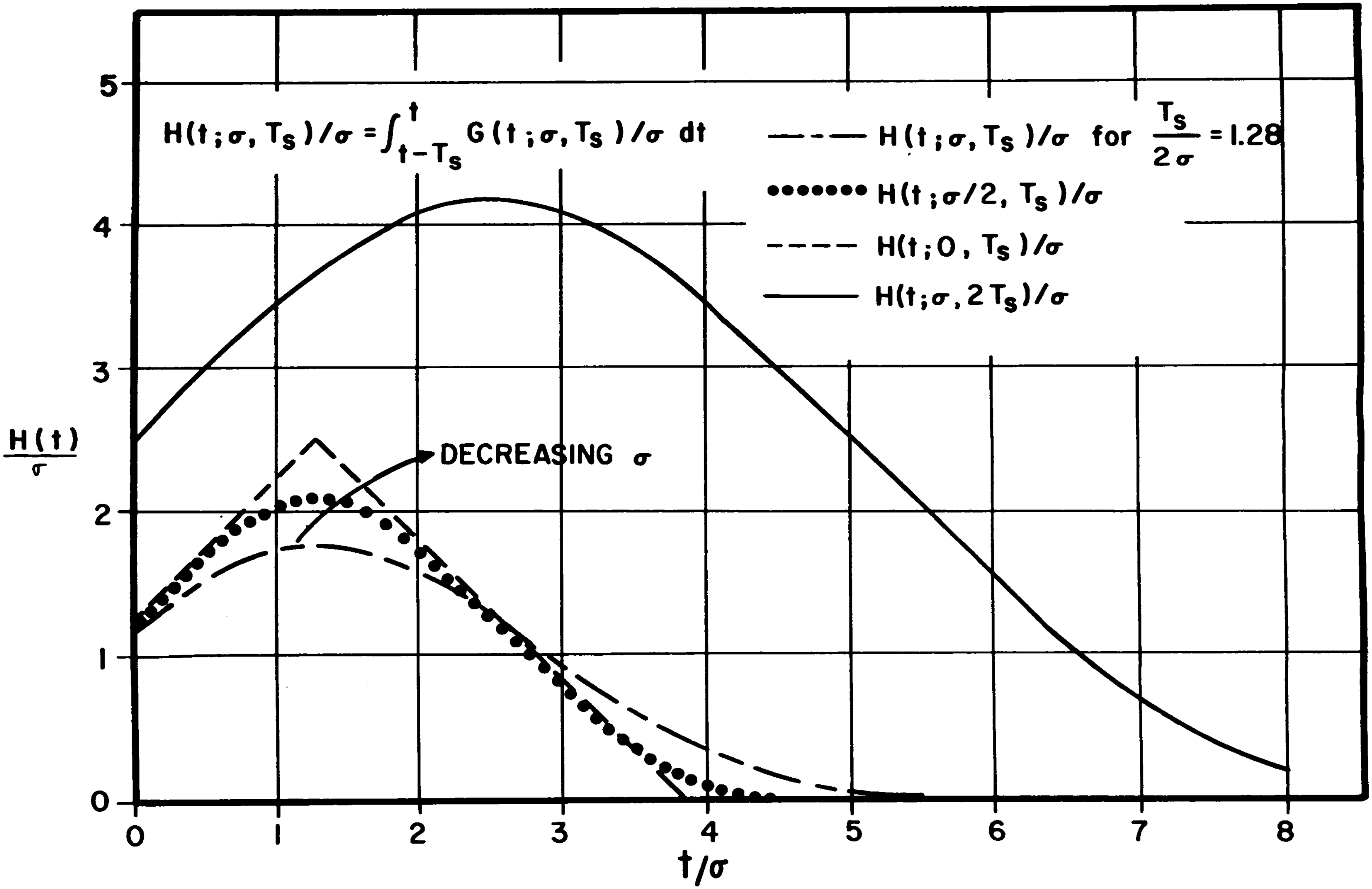

Figure G-5: Integral of G(t), Output of Holding Filter Divided by λ_s

Since the $t_j(M)$'s are random variables, $\mu(t)$ is a stochastic process. The unconditional probability distribution of $y(t)$ is

$$P\left\{y(t) = k\right\} = \int_0^\infty \frac{x^k}{k!} e^{-x} \psi_t(x)dx \qquad (g\text{-}57)$$

where $\psi_t(x)$ is the probability density function of $\mu(t)$. The summation

$$\alpha\epsilon_q\epsilon_o\lambda(M) \sum_j H(t - t_j(M)) \qquad (g\text{-}58)$$

has well known properties. Its mean and variance are

$$\alpha\epsilon_q\epsilon_o\nu(M)\int_{-\infty}^{\infty} H(t)dt \qquad (g\text{-}59)$$

and

$$\alpha^2\epsilon_q{}^2\epsilon_o{}^2\nu(M)\lambda^2(M)\int_{-\infty}^{\infty} H^2(t)dt^* \qquad (g\text{-}60)$$

Hence, the mean and variance of $\mu(t)$ are

$$\mathcal{E}\,\mu(t) = \alpha\epsilon_q\epsilon_o\lambda_s H(t) + \alpha\epsilon_q\epsilon_o\int_{-\infty}^{\infty} H(t)dt \sum_{M=M_o+1}^{\infty} \nu(M)\lambda(M) + T_f\,\lambda_d \qquad (g\text{-}61)$$

and

$$\text{Var}\ \ \mu(t) = \alpha^2\epsilon_q{}^2\epsilon_o{}^2\int_{-\infty}^{\infty} H^2(t)dt \sum_{M=M_o+1}^{\infty} \nu(M)\lambda^2(M) \qquad (g\text{-}62)$$

In Appendix D, it is shown that

$$\int_{-\infty}^{\infty} H(t)dt = T_f T_s \qquad (g\text{-}63)$$

$$T_f{}^2T_s{}^2 < \int_{-\infty}^{\infty} H^2(t)dt < T_f{}^2T_s \qquad (g\text{-}64)$$

$$\int_{-\infty}^{\infty} H^k(t)dt < T_f{}^kT_s \qquad (g\text{-}65)$$

In Appendix E, the summation

$$\sum_{M=M_o+1}^{\infty} \nu(M)\lambda^k(M) \qquad k=1,2,\ldots \qquad (g\text{-}66)$$

is shown to be approximately

* A proof is given by S. O. Rice [43].

$$\frac{D^{2k}}{T_{sp}} \sin\left(\frac{fov}{2}\right) (5.06)^k \; (2.54 \times 10^{6k+2}) \cdot \left[1-\Phi(.173M_o + 5.32k - 7.12)\right] \tag{g-67}$$

where

D = diameter of the optical aperture in inches

T_{sp} = scan period in seconds

fov = optical field of view.

This expression was developed for the optical system illustrated in Figure I-2.

The distribution of $\mu(t)$ is approximately normal for many cases of interest. The k-th semi-invariant of the summation

$$\alpha\epsilon_q\epsilon_o\lambda(M) \sum_j H(t - t_j(M)) \tag{g-68}$$

is

$$\varkappa_k = \sum_{M=M_o+1}^{\infty} \nu(M)\lambda^k(M) \; (\alpha\epsilon_q\epsilon_o)^k \int_{-\infty}^{\infty} H^k(t)dt \tag{g-69}$$

If $\varkappa_k$ is small compared to $\varkappa_2$, $\mu(t)$ is approximately normal. Using the above results one obtains

$$\frac{\varkappa_k}{\varkappa_2} < (\alpha\epsilon_q\epsilon_o)^{k-2} \frac{T_f{}^k T_s \sum\nu(M)\lambda^k(M)}{T_f{}^2 T_s{}^2 \sum\nu(M)\lambda^2(M)} \tag{g-70}$$

A typical case may produce values such as

$$\frac{\varkappa_3}{\varkappa_2} < 1.08 \times 10^{-10}, \quad \frac{\varkappa_4}{\varkappa_2} < 1.15 \times 10^{-34} \tag{g-71}$$

Assume $\psi_t(x)$ is a normal density with mean $m = \mathcal{E}\mu(t)$ and variance $v = \text{Var}\,\mu(t)$, and

$$P\left\{y(t) = k\right\} \approx \int_{-\infty}^{\infty} \frac{x^k}{k!} e^{-x} \psi_t(x)dx \tag{g-72}$$

Transform variables with

$$x = \sqrt{v}\, w - v + m \tag{g-73}$$

Then

$$P\left\{y(t) = k\right\} \approx \int_{-\infty}^{\infty} \sqrt{v}\left[\sqrt{v}\, w - v + m\right]^k \frac{1}{k!} e^{+\frac{1}{2}v-m} \varphi(w)dw \tag{g-74}$$

where φ is the standard normal density function. Further,

$$P\left\{y(t) = k\right\} \approx \frac{\sqrt{v}e^{\frac{1}{2}v-m}}{k!} \sum_{j=o}^{k} \binom{k}{j} v^{j/2} (-v+m)^{k-j} \int_{-\infty}^{\infty} w^j \varphi(w)dw \tag{g-75}$$

and

$$\int_{-\infty}^{\infty} w^{2j} \varphi(w)dw = \prod_{i=1}^{j} (2i - 1) \qquad j = 1,2,\ldots \tag{g-76}$$

$$\int_{-\infty}^{\infty} w^{2j+1} \varphi(w)dw = 0 \tag{g-77}$$

Note that $P\left\{y(t) = k\right\}$ is time dependent through $\mathcal{E}\,\mu(t)$.

1. Star Detection

Detection is based on a threshold τ. Given $y(t)$ exceeds τ at time t' and remains greater than τ until t'', a <u>star detection</u> has occurred if a star is in the center of the slit between $t' - T_f/2$ and $t'' - T_f/2$. Hence, the probability of detecting a star (centered in the slit at time $t = 0$) is the probability that $y(T_f/2) > \tau$, which is

$$1 - \sum_{k=o}^{\tau} P\left\{y(T_f/2) = k\right\} \tag{g-78}$$

This sum can be evaluated using the above results, assuming $\mu(t)$ is normally distributed. This detection method is similar to the optimum method (developed in the preceeding section) in that a star is "present" if many closely spaced pulses are received.

2. Weak Star Discrimination

A measure of the performance of a detection method is its ability to discriminate against undesirable signals, in this case weak stars. For example, if one is interested in fourth magnitude stars (and brighter), detection of fifth, sixth and seventh magnitude stars is undesirable. One can show that the expected number of star detections for magnitudes greater than seven is negligible, even though the star density $\nu(M)$ is high.* Hence, it is reasonable to assume that the pulses resulting from different "weak stars" are widely spaced, and that the detections of the "weak stars" are independent.

Let $q_\tau(M)$ be the probability of detecting a star of magnitude M with threshold τ:

$$q_\tau(M) = \sum_{j=\tau+1}^{\infty} \frac{\beta^j}{j!} e^{-\beta} \tag{g-79}$$

where $\beta = \alpha\epsilon_q\epsilon_o\lambda(M)H(T_f/2) + T_f\lambda_d$. Then the times of star detections (of magnitude M) form a Poisson process; and the number of M-th magnitude star detections in a scan period T_{sp} is a Poisson variable with mean $q_\tau(M)\nu(M)T_{sp}$. Hence, the number of weak star detections in a scan period is a Poisson random variable with mean

$$\sum_{M=M_o+1}^{\infty} q_\tau(M)\nu(M)T_{sp}^{**} \tag{g-80}$$

---

* D. Zimmerman demonstrates the relative sparsity of weak star detections [44].

** The problem of weak star detection is very similar to the classical zero crossing problem; see the paper prepared by H. Levenbach [45].

3. Angle Estimation

Given $y(t)$ exceeds τ at time t' and remains greater than τ until t'', a star is said to be at that center of the slit at time $t^* = (t' + t'')/2 - T_f/2$. Let $t_{\tau+1}$ be the arrival time of the $(\tau+1)$th pulse, and $t'_{\tau+1}$ be the arrival time of the pulse which is τth from last. Then $t'=t_{\tau+1}$, $t'' = t'_{\tau+1} + T_f$, and $t^* = (t_{\tau+1} + t'_{\tau+1})/2$.* In the following paragraphs, we will derive the distribution of $t_{\tau+1}$, the distribution of $(t_{\tau+1}, t'_{\tau+1})$, the distribution of t^*, and the variance of t^*. In these derivations, it is assumed that the diffraction circle is "small" compared to the slit in width, that the background and dark current are negligible, and that $T_f = T_s$. The diffraction circle can be assumed to be "small" when $T_s/\sigma \geqslant 1.28$; see Figure G-3. Hence,

$$\lambda'_s(t) = \begin{cases} \epsilon_o\lambda_s & \text{for } -T_s/2<t<T_s/2 \\ 0 & \text{otherwise} \end{cases} \qquad \text{(g-81)}$$

and

$$\mu(t) = \begin{cases} \alpha\epsilon_q\epsilon_o\lambda_s(t + T_s/2) & \text{for } -T_s/2<t<T_s/2 \\ \alpha\epsilon_q\epsilon_o\lambda_s(-t + 3T_s/2) & \text{for } T_s/2<t<3T_s/2 \\ 0 & \text{otherwise} \end{cases} \qquad \text{(g-82)}$$

Let $$p(n) = \frac{(\alpha\epsilon_q\epsilon_o\lambda_s T_s)^n}{n!} e^{-\alpha\epsilon_q\epsilon_o\lambda_s T_s} \qquad \text{(g-83)}$$

---

* The maximum likelihood estimate (g-37) is an average of all the arrival times, not just the $(\tau+1)$th and $(n-t)$th arrival times.

$$P_\tau = \sum_{j=\tau+1}^{\infty} p(j) \qquad \text{(g-84)}$$

Distribution of $t_{\tau+1}$. The probability density of $t_{\tau+1}$ conditional on $y(T_s/2) > \tau$ is

$$f_{\tau+1}(t) = \frac{\alpha\epsilon_q\epsilon_o\lambda_s[\alpha\epsilon_q\epsilon_o\lambda_s(t+T_s/2)]^\tau}{\tau!\ P_\tau} e^{-\alpha\epsilon_q\epsilon_o\lambda_s(t+T_s/2)} \qquad \text{(g-85)}$$

for $-T_s/2 < t < T_s/2$ and zero elsewhere. The expectation of $t_{\tau+1}$ is given by

$$\mathcal{E}\left[t_{\tau+1} + T_s/2\right] = \int_{-T_s/2}^{T_s/2} \frac{(t+T_s/2)\alpha\epsilon_q\epsilon_o\lambda_s\left[\alpha\epsilon_q\epsilon_o\lambda_s(t+T_s/2)\right]^\tau}{\tau\ P_\tau} \cdot \qquad \text{(g-86)}$$
$$\cdot e^{-\alpha\epsilon_q\epsilon_o\lambda_s(t+T_s/2)}\,dt$$

$$= \frac{\tau+1}{\alpha\epsilon_q\epsilon_o\lambda_s}\ \frac{P_{\tau+1}}{P_\tau}$$

Note that $\mathcal{E}[t_{\tau+1}/T_s]$ only depends on the product $\alpha\epsilon_q\epsilon_o\lambda_s T_s$ and τ.

The second moment is

$$\mathcal{E}\,(t_{\tau+1} + T_s/2)^2 = \int_{-T_s/2}^{T_s/2} \frac{\left[\alpha\epsilon_q\epsilon_o\lambda_s(t+T_s/2)\right]^{\tau+2}}{\alpha\epsilon_q\epsilon_o\lambda_s\ \tau!\,P_\tau} e^{-\alpha\epsilon_q\epsilon_o\lambda_s(t+T_s/2)}\,dt \qquad \text{(g-87)}$$

$$= \frac{(\tau+1)(\tau+2)}{(\alpha\epsilon_q\epsilon_o\lambda_s)^2}\ \frac{P_{\tau+2}}{P_\tau}$$

Hence, the variance of $t_{\tau+1}$ is

$$\mathrm{Var}\ t_{\tau+1} = \frac{(\tau+1)(\tau+2)}{(\alpha\epsilon_q\epsilon_o\lambda_s)^2}\ \frac{P_{\tau+2}}{P_\tau} - \frac{(\tau+1)^2}{(\alpha\epsilon_q\epsilon_o\lambda_s)^2}\left[\frac{P_{\tau+1}}{P_\tau}\right]^2 \qquad \text{(g-88)}$$

Note that $\mathrm{Var}(t_{\tau+1}/T_s)$ only depends on $(\alpha\epsilon_q\epsilon_o\lambda_s T_s)$ and τ, and is graphed in Figure G-6.

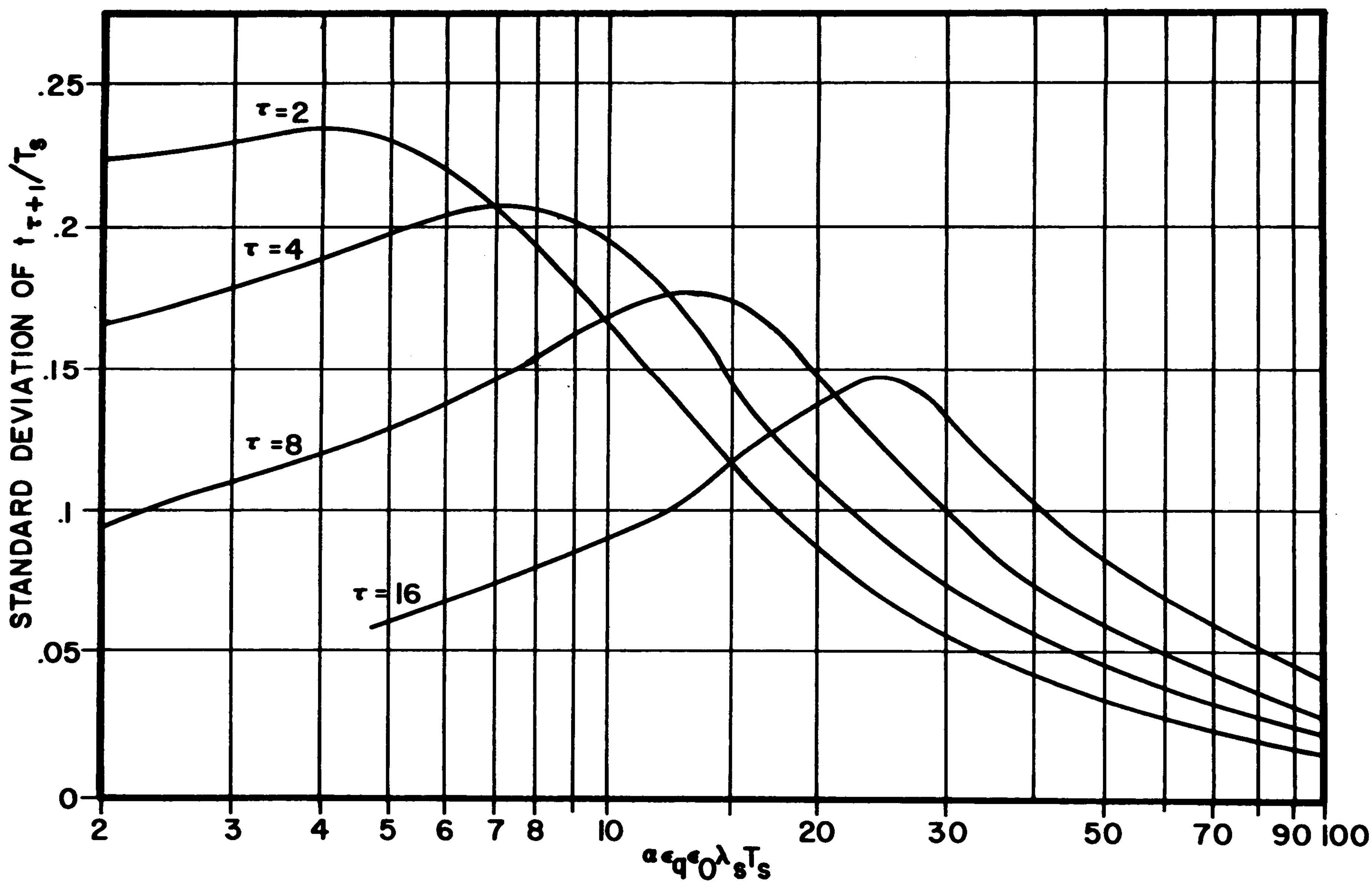

Figure G -6: Graph of the Standard Deviation of $(t_{\tau+1}/T_s)$ as a Function of the Expected Number of Pulses. $a\,\epsilon_q\,\epsilon_o\,\lambda_s\,T_s$, for Several Thresholds τ

This figure gives $[\mathrm{Var}\,(t_{\tau+1}/T_s)]^{\frac{1}{2}}$ as a function of $\alpha\epsilon_q\epsilon_\circ\lambda_s T_s$, the expected number of pulses. The different curves represent various values of the detection threshold, τ.

Distribution of $(t_{\tau+1}, t'_{\tau+1})$

Let n be the number of pulses received from time $-T_s/2$ to $T_s/2$; i.e., $n = y(T_s/2)$. If $n > \tau$, then y(t) crosses τ exactly twice (at t' and t"), and $-T_s/2 < t' \leq T_s/2 \leq t'' < 3/2\ T_s$ or $-T_s/2 < t_{\tau+1} < T_s/2$, $-T_s/2 < t'_{\tau+1} < T_s/2$.

Let $g_n(a, a')\,da\,da'$ be the probability that n pulses are received, and that $a < t_{\tau+1} < a + da$ and $a' < t'_{\tau+1} < a' + da'$, given $n > \tau$. If $n > 2\tau + 1$, $g_n(a, a') = 0$ for $a' < a$. If $\tau < n < 2\tau + 1$, $g_n(a, a') = 0$ for $a' > a$. If $n = 2\tau + 1$, the density $g_n(a, a')$ is not defined.

For $\tau < n < 2\tau + 1$,

$$g_n(a, a')\,da\,da' = \left[\frac{[\alpha\,\epsilon_q\epsilon_\circ\lambda_s(a' + T_s/2)]^{n-\tau-1}}{(n-\tau-1)!}\right] e^{-\alpha\epsilon_q\epsilon_\circ\lambda_s(a' + T_s/2)} \tag{g-89}$$

$$\cdot\ \alpha\epsilon_q\epsilon_\circ\lambda_s da' \left[\frac{[\alpha\epsilon_q\epsilon_\circ\lambda_s(a - a')]^{2\tau-n}}{(2\tau - n)!}\ e^{-\alpha\epsilon_q\epsilon_\circ\lambda_s(a-a')}\right]$$

$$\cdot\ \alpha\epsilon_q\epsilon_\circ\lambda_s da \left[\frac{\alpha\epsilon_q\epsilon_\circ\lambda_s(T_s/2 - a)^{n-\tau-1}}{(n-\tau-1)!}\ e^{-\alpha\epsilon_q\epsilon_\circ\lambda_s(T_s/2-a)}\right] \quad (P_\tau)^{-1}$$

$$= \frac{p(n)}{P_\tau} \quad \frac{n!}{(n - \tau - 1)!\ (2\tau - n)!\ (n - \tau - 1)!} \left[\frac{1}{2} + \frac{a'}{T_s}\right]^{n-\tau-1} \left[\frac{a-a'}{T_s}\right]^{2\tau-n}$$

$$\cdot \left[\frac{1}{2} - \frac{a}{T_s}\right]^{n-\tau-1} \quad \frac{1}{T_s^{\ 2}} \quad da\ da'$$

$$= \frac{p(n)}{P_\tau}\, D\left(\frac{1}{2} + \frac{a'}{T_s}, \frac{1}{2} - \frac{a}{T_s}; n - \tau, n - \tau, 2\tau - n + 1\right) \frac{1}{T_s^{\ 2}} \quad da\ da'$$

where D(-) represents the Dirichlet density function*

$$D(x_1, x_2; \nu_1, \nu_2, \nu_3) = \frac{\Gamma(\nu_1+\nu_2+\nu_3)}{\Gamma(\nu_1)\Gamma(\nu_2)\Gamma(\nu_3)}\, x_1^{\ \nu_1-1}\, x_2^{\ \nu_2-1}\, (1 - x_2 - x_1)^{\nu_3-1} \tag{g-90}$$

For $n = 2\tau + 1$

* The Dirichlet density is discussed by S. S. Wilks [46].

$$P\left\{t_{\tau+1}\le a,\ t'_{\tau+1}\le a',\ n = 2\tau+1 \mid n > \tau\right\}$$

$$= (P_\tau)^{-1}\sum_{k=\tau+1}^{2\tau+1} \frac{[\alpha\epsilon_q\epsilon_o\lambda_s T_s/2 + a^*)]^k}{k!}\ e^{-\alpha\epsilon_q\epsilon_o\lambda_s(T_s/2+a^*)} \qquad \text{(g-91)}$$

$$\cdot \frac{[\alpha\epsilon_q\epsilon_o\lambda_s(T_s/2 - a^*)]^{2\tau+1-k}}{(2\tau + 1 - k)!}\ e^{-\alpha\epsilon_q\epsilon_o\lambda_s(T_s/2-a^*)}$$

$$= \frac{p(2\tau +1)}{P_\tau}\sum_{k=\tau+1}^{2\tau+1}\binom{2\tau+1}{k}\left[\frac{1}{2} + \frac{a^*}{T_s}\right]^k\left[\frac{1}{2} - \frac{a^*}{T_s}\right]^{2\tau+1-k}$$

where $a^* = \min\ (a, a')$. Note that $t_{\tau+1} \equiv t'_{\tau+1}$ for $n = 2\tau + 1$. For $n > 2\tau + 1$

$$g_n(a, a')\ da\ da' = \left[\frac{[\alpha\epsilon_q\epsilon_o\lambda_s(a+T_s/2)]^\tau}{\tau!}\ e^{-\alpha\epsilon_q\epsilon_o\lambda_s(a+T_s/2)}\right] \qquad \text{(g-92)}$$

$$\cdot\alpha\epsilon_q\epsilon_o\lambda_s\left[\frac{[\alpha\epsilon_q\epsilon_o\lambda_s(a'-a)]^{n-2\tau-2}}{(n - 2\tau - 2)!}\ e^{-\alpha\epsilon_q\epsilon_o\lambda_s(a'-a)}\right]$$

$$\cdot\ \alpha\epsilon_q\epsilon_o\lambda_s da'\left[\frac{[\alpha\epsilon_q\epsilon_o\lambda_s(T_s/2 - a')]^\tau}{\tau!}\ e^{-\alpha\epsilon_q\epsilon_o\lambda_s(T_s/2-a')}\right](p_\tau)^{-1}$$

(equation continued)

$$= \frac{p(n)}{P_\tau} \frac{n!}{\tau!\ (n - 2\tau - 2)!\ \tau!} \left[\frac{1}{2} + \frac{a}{T_s}\right]^\tau \left[\frac{a' - a}{T_s}\right]^{n-2\tau-2} \left[\frac{1}{2} - \frac{a'}{T_s}\right]^\tau$$

$$\cdot \frac{1}{T_s^2}\ da\ da'$$

$$= \frac{p(n)}{P_\tau} D\left(\frac{1}{2} + \frac{a}{T_s}, \frac{1}{2} - \frac{a'}{T_s}\ ;\ \tau + 1, \tau + 1, n - 2\tau - 1\right) \frac{1}{T_s^2}\ da\ da'$$

Distribution of t^*. Since $t^* = (t_{\tau+1} + t'_{\tau+1})/2$, we will evaluate the distribution of $t_{\tau+1} + t'_{\tau+1}$. The probability density function of $t_{\tau+1} + t'_{\tau+1}$ can be derived from the following identity:

$$P\left\{b < t_{\tau+1} + t'_{\tau+1} \le b + db \mid n > \tau\right\} \tag{g-93}$$

$$= P\left\{b < t_{\tau+1} + t'_{\tau+1} \le b + db,\ \tau < n < 2\tau + 1 \mid n > \tau\right\}$$

$$+ P\left\{b < t_{\tau+1} + t'_{\tau+1} \le b + db,\ n = 2\tau + 1 \mid n > \tau\right\}$$

$$+ P\left\{b < t_{\tau+1} + t'_{\tau+1} \le b + db,\ n > 2\tau + 1 \mid n > \tau\right\}$$

Note that the density is symmetric in b about the origin. The first term is

$$\left[\sum_{n=\tau+1}^{2\tau} \int_{b/2}^{T_s/2} g_n(a, b - a)\ da\right] db \tag{g-94}$$

for b > 0.

The second term is

$$\left[\frac{[\alpha\epsilon_q\epsilon_\circ\lambda_s(b/2 + T_s/2)]^\tau}{\tau!} \quad e^{-\alpha\epsilon_q\epsilon_\circ\lambda_s(b/2 + T_s/2)}\right] \frac{\alpha\epsilon_q\epsilon_\circ\lambda_s}{2} \quad db \tag{g-95}$$

$$\cdot\left[\frac{[\alpha\epsilon_q\epsilon_\circ\lambda_s(T_s/2 - b/2)]^\tau}{\tau!} \quad e^{-\alpha\epsilon_q\epsilon_\circ\lambda_s(T_s/2 - b/2)}\right] \quad (P_\tau)^{-1}$$

$$= \frac{(2\tau + 1)!}{\tau!\ \tau!} \quad \left[\frac{1}{2} + \frac{b}{2T_s}\right]^\tau \left[\frac{1}{2} - \frac{b}{2T_s}\right]^\tau \quad \frac{(\alpha\epsilon_q\epsilon_\circ\lambda_s T_s)^{2\tau+1}}{(2\tau+1)!}$$

$$\cdot\ e^{-\alpha\epsilon_q\epsilon_\circ\lambda_s T_s} \quad (P_\tau)^{-1} \quad \frac{db}{2T_s}$$

$$= \frac{p(2\tau+1)}{P_\tau} \quad D\left(\frac{1}{2} + \frac{b}{2T_s}\ ,\ \tau + 1,\ \tau + 1\right) \quad \frac{db}{2T_s}$$

The third term is

$$\left[\sum_{n=2\tau+2}^{\infty} \int_{b/2}^{T_s/2} g_n(b - a',\ a)\ da'\right] \quad db \tag{g-96}$$

for b > 0.

Variance of t*. Since $t^* = (t_{\tau+1} + t'_{\tau+1})/2$ and the mean of t* is zero, the variance of t* is

$$\frac{1}{4}\mathcal{E}(t_{\tau+1} + t'_{\tau+1})^2 = \frac{1}{4}\mathcal{E}\left[(t_{\tau+1} + T_s/2) - (T_s/2 - t'_{\tau+1})\right]^2 \qquad (g\text{-}97)$$

$$= \frac{1}{4}\mathcal{E}(t_{\tau+1} + T_s/2)^2 + \frac{1}{4}\mathcal{E}(T_s/2 - t'_{\tau+1})^2$$

$$- \frac{1}{2}\mathcal{E}[(t_{\tau+1} + T_s/2)(T_s/2 - t'_{\tau+1})]$$

Since $t_{\tau+1} + T_s/2$ and $T_s/2 - t'_{\tau+1}$ have the same distribution,

$$\mathcal{E}(t_{\tau+1} + T_s/2)^2 = \mathcal{E}(T_s/2 - t'_{\tau+1})^2 = \frac{(\tau + 1)(\tau + 2)}{(\alpha\epsilon_q\epsilon_o\ \lambda_s)^2}\ \frac{P_{\tau+2}}{P_\tau} \qquad (g\text{-}98)$$

It is necessary to evaluate the last term in the variance with three steps: $\tau < n < 2\tau + 1$, $n = 2\tau + 1$, $n > 2\tau + 1$. For a fixed n between τ and $2\tau + 1$,

$$\mathcal{E}\left[(t_{\tau+1} + T_s/2)(T_s/2 - t'_{\tau+1})\right] \qquad (g\text{-}99)$$

$$= \mathcal{E}\left[(T_s/2 - t_{\tau+1} - T_s)(t'_{\tau+1} + T_s/2 - T_s)\right]$$

$$= \mathcal{E}\left[(T_s/2 - t_{\tau+1})(t'_{\tau+1} + T_s/2)\right] - T_s\mathcal{E}\left[t'_{\tau+1} + T_s/2\right]$$

(equation continued)

$$- T_s \mathcal{E}\left[T_s/2 - t_{\tau+1}\right] + T_s^{\,2}\,\frac{p(n)}{P_\tau} =$$

$$\mathcal{E}\left[(T_s/2 - t_{\tau+1})(t'_{\tau+1} + T_s/2)\right] + T_s\,\mathcal{E}(t_{\tau+1} - t'_{\tau+1})$$

Since $\mathcal{E}(t_{\tau+1} + T_s/2) = \mathcal{E}(T_s/2 - t'_{\tau+1})$,

$$T_s\,\mathcal{E}(t_{\tau+1} - t'_{\tau+1}) = 2T_s\,\mathcal{E}(t_{\tau+1} + T_s/2) - T_s^{\,2}\,\frac{p(n)}{P_\tau} \qquad \text{(g-100)}$$

$$= -\,2\,T_s\,\mathcal{E}(T_s/2 - t_{\tau+1}) + T_s^{\,2}\,\frac{p(n)}{P_\tau}$$

$$= -\,2\,T_s^{\,2}\,\frac{p(n)}{P_\tau}\,\frac{n-\tau}{n+1} + T_s^{\,2}\,\frac{p(n)}{P_\tau}$$

$$= T_s^{\,2}\left[-\,2\,\frac{p(n)}{P_\tau}\left(1 - \frac{\tau+1}{n+1}\right) + \frac{p(n)}{P_\tau}\right]$$

$$= T_s^{\,2}\left[-\,\frac{p(n)}{P_\tau} + 2\,\frac{\tau+1}{\alpha\epsilon_q\epsilon_o\lambda_s T_s}\,\frac{p(n+1)}{P_\tau}\right]$$

Similarly,

$$\mathcal{E}\left[(T_s/2 - t_{\tau+1})(t'_{\tau+1} + T_s/2)\right] = \tag{g-101}$$

$$\frac{p(n)}{P_\tau} T_s^2 \frac{(n-\tau)!\ (n-\tau)!\ n!}{(n+2)!\ (n-\tau-1)!\ (n-\tau-1)!} =$$

$$\frac{p(n)}{P_\tau} T_s^2 \frac{(n-\tau)^2}{(n+2)(n+1)} =$$

$$\frac{p(n)}{P_\tau} T_s^2 \frac{[(n+2) - (\tau+2)][(n+1) - (\tau+1)]}{(n+2)(n+1)} =$$

$$\frac{p(n)}{P_\tau} T_s^2 \left[1 - \frac{\tau+1}{n+1} + \frac{(\tau+2)(\tau+1)}{(n+2)(n+1)} - \frac{(\tau+2)(n+2-1)}{(n+2)(n+1)}\right] =$$

$$\frac{p(n)}{P_\tau} T_s^2 \left[1 - \frac{\tau+1}{n+1} + \frac{(\tau+2)(\tau+1)}{(n+2)(n+1)} - \frac{\tau+2}{n+1} + \frac{\tau+2}{(n+2)(n+1)}\right] =$$

$$\frac{p(n)}{P_\tau} T_s^2 \left[1 - \frac{2\tau+3}{n+1} + \frac{(\tau+2)^2}{(n+1)(n+2)}\right] =$$

$$\frac{T_s^2}{P_\tau}\left[p(n) - \frac{2\tau+3}{\alpha\epsilon_q\epsilon_o\lambda_s T_s}\ p(n+1) + \frac{(\tau+2)^2}{(\alpha\epsilon_q\epsilon_o\lambda_s T_s)^2}\ p(n+2)\right]$$

Hence,

$$\mathcal{E}\left[(t_{\tau+1} + T_s/2)(T_s/2 - t'_{\tau+1})\right] = \tag{g-102}$$

$$\frac{T_s^{\,2}}{P_\tau}\left[p(n) - \frac{2\tau + 3}{\alpha\epsilon_q\epsilon_o\lambda_s T_s}\;p(n+1) + \frac{(\tau + 2)^2}{(\alpha\epsilon_q\epsilon_o\lambda_s T_s)^2}\;p(n+2)\right.$$

$$\left. - p(n) + \frac{2(\tau + 1)}{\alpha\epsilon_q\epsilon_o\lambda_s T_s}\;p(n+1)\right] =$$

$$\frac{T_s^{\,2}}{P_\tau}\left[-\frac{p(n+1)}{\alpha\epsilon_q\epsilon_o\lambda_s T_s} + \frac{(\tau + 2)^2}{(\alpha\epsilon_q\epsilon_o\lambda_s T_s)^2}\;p(n+2)\right]$$

For a <u>fixed $n = 2\tau + 1$</u>, the density of $t_{\tau+1}$ is

$$\frac{p(2\tau+1)}{P_\tau}\;D\left(\frac{a}{T_s} + \frac{1}{2}\;;\;\tau + 1,\;\tau + 1\right)\frac{da}{T_s} \tag{g-103}$$

and

$$\mathcal{E}\left[(T_s/2 + t_{\tau+1})(T_s/2 - t_{\tau+1})\right] = \tag{g-104}$$

(equation continued)

$$\frac{p(2\tau+1)}{P_\tau} \quad T_s^{\,2} \quad \frac{(2\tau+1)!}{\tau!\,\tau!} \quad \frac{(\tau+1)!\,(\tau+1)!}{(2\tau+3)!} \quad =$$

$$\frac{(\tau+1)^2}{(n+1)(n+2)} \quad \frac{p(n)}{P_\tau} \quad T_s^{\,2} \quad = \quad \frac{(\tau+1)^2}{(\alpha\epsilon_q\epsilon_o\lambda_s)^2} \quad \frac{p(n+2)}{P_\tau}$$

For a fixed n greater than $2\tau + 1$,

$$\mathcal{E}\left[(T_s/2 + t_{\tau+1})(T_s/2 - t'_{\tau+1})\right] = T_s^{\,2} \quad \frac{p(n)}{P_\tau} \quad \frac{(\tau+1)!\,(\tau+1)!\,n!}{(n+2)!\,\tau!\,\tau!} \qquad \text{(g-105)}$$

$$= \frac{(\tau+1)^2}{(\alpha\epsilon_q\epsilon_o\lambda_s)^2} \quad \frac{p(n+2)}{P_\tau}$$

Therefore, twice the variance of t^* is

$$\frac{(\tau+1)(\tau+2)}{(\alpha\epsilon_q\epsilon_o\lambda_s)^2} \quad \frac{P_{\tau+2}}{P_\tau} - \frac{T_s^{\,2}}{P_\tau}\cdot\left[-\frac{1}{\alpha\epsilon_q\epsilon_o\lambda_s T_s} \sum_{n=\tau+1}^{2\tau} p(n+1)\right. \qquad \text{(g-106)}$$

$$\left. + \frac{(\tau+2)^2}{(\alpha\epsilon_q\epsilon_o\lambda_s T_s)^2} \sum_{n=\tau+1}^{2\tau} p(n+2)\right] - \frac{(\tau+1)^2}{(\alpha\epsilon_q\epsilon_o\lambda_s)^2} \quad \frac{p(2\tau+3)}{P_\tau}$$

$$- \frac{(\tau+1)^2}{(\alpha\epsilon_q\epsilon_o\lambda_s)^2} \sum_{n=2\tau+2}^{\infty} p(n+2)/P_\tau \quad =$$

(equation continued)

$$\frac{(\tau+1)(\tau+2)}{(\alpha\epsilon_q\epsilon_o\lambda_s)^2}\ \frac{P_{\tau+2}}{P_\tau}\ -\ \frac{T_s{}^2}{P_\tau}\left[-\ \frac{P_{\tau+1}\ -\ P_{2\tau+1}}{\alpha\epsilon_q\epsilon_o\lambda_s T_s}\right.$$

$$\left.+\ \frac{(\tau\ +\ 2)^2}{(\alpha\epsilon_q\epsilon_o\lambda_s T_s)^2}\ (P_{\tau+2}\ -\ P_{2\tau+2})\right]-\ \frac{(\tau\ +\ 1)^2}{(\alpha\epsilon_q\epsilon_o\lambda_s)^2}\ \frac{P_{2\tau+2}}{P_\tau}\ =$$

$$\frac{(\tau+2)^2\ -\ (\tau+1)^2}{(\alpha\epsilon_q\epsilon_o\lambda_s)^2}\ \frac{P_{2\tau+2}}{P_\tau}\ +\ \frac{(\tau+1)(\tau+2)-(\tau+2)^2}{(\alpha\epsilon_q\epsilon_o\lambda_s)^2}\ \frac{P_{\tau+2}}{P_\tau}$$

$$+\ \frac{T_s{}^2}{P_\tau}\ \frac{P_{\tau+1}\ -\ P_{2\tau+1}}{\alpha\epsilon_q\epsilon_o\lambda_s T_s}\ =$$

$$\frac{2\tau\ +\ 3}{(\alpha\epsilon_q\epsilon_o\lambda_s)^2}\ \frac{P_{2\tau+2}}{P_\tau}\ -\ \frac{\tau\ +\ 2}{(\alpha\epsilon_q\epsilon_o\lambda_s)^2}\ \frac{P_{\tau+2}}{P_\tau}\ +\ \frac{T_s{}^2}{P_\tau}\ \frac{P_{\tau+1}\ -\ P_{2\tau+1}}{\alpha\epsilon_q\epsilon_o\lambda_s T_s}$$

and

$$2\ \mathrm{Var}\ (t^*/T_s)\ =\ \frac{2\tau\ +\ 3}{(\alpha\epsilon_q\epsilon_o\lambda_s T_s)^2}\ \frac{P_{2\tau+2}}{P_\tau}\ -\ \frac{\tau\ +\ 2}{(\alpha\epsilon_q\epsilon_o\lambda_s T_s)^2}\ \frac{P_{\tau+2}}{P_\tau} \qquad \text{(g-107)}$$

$$+\ \frac{1}{\alpha\epsilon_q\epsilon_o\lambda_s T_s}\ \frac{P_{\tau+1}-P_{2\tau+1}}{P_\tau}$$

Note that $\mathrm{Var}(t^*/T_s) < 1/4$.

The above variance estimate is a lower bound on the actual variance since background and dark current were neglected. The standard deviation of t^*/T_s is graphed in Figure G-7.

A basic unsolved problem is to determine the variance of t^* when the diffraction circle is comparable to the slit in width. There are two approaches: (1) direct analytical approach, (2) indirect approach, using previous results. The analytical approach involves extending the above results; the basic difficulty is the non-stationary character of $\lambda_s'(t)$ in $(-T_s/2, T_s/2)$. Note that $y(t)$ can be viewed as birth-death process with birth rate $\mu(t)$ and death rate $\mu(t - T_f)$. The indirect approach is based on previous results from radar applications; i.e., range estimate. In such applications, one must estimate the position of a pulse and determine the variance of the estimate.* As yet, neither of these approaches has yielded a solution to the basic problem.

4. Intensity Estimation

It is natural to use $y(t^* + T_f/2)$ to estimate the intensity of the star. From Figure G-5, we note that the mean of $y(t)$ (and consequently, its distribution) is a slowly changing function of t near $t = T_f/2$. If the variance of t^* is small compared to the slit width, the distribution of $y(t^* + T_f/2)$ is approximately Poisson with mean

---

* This problem is discussed by Wainstein and Zubalsov [47].

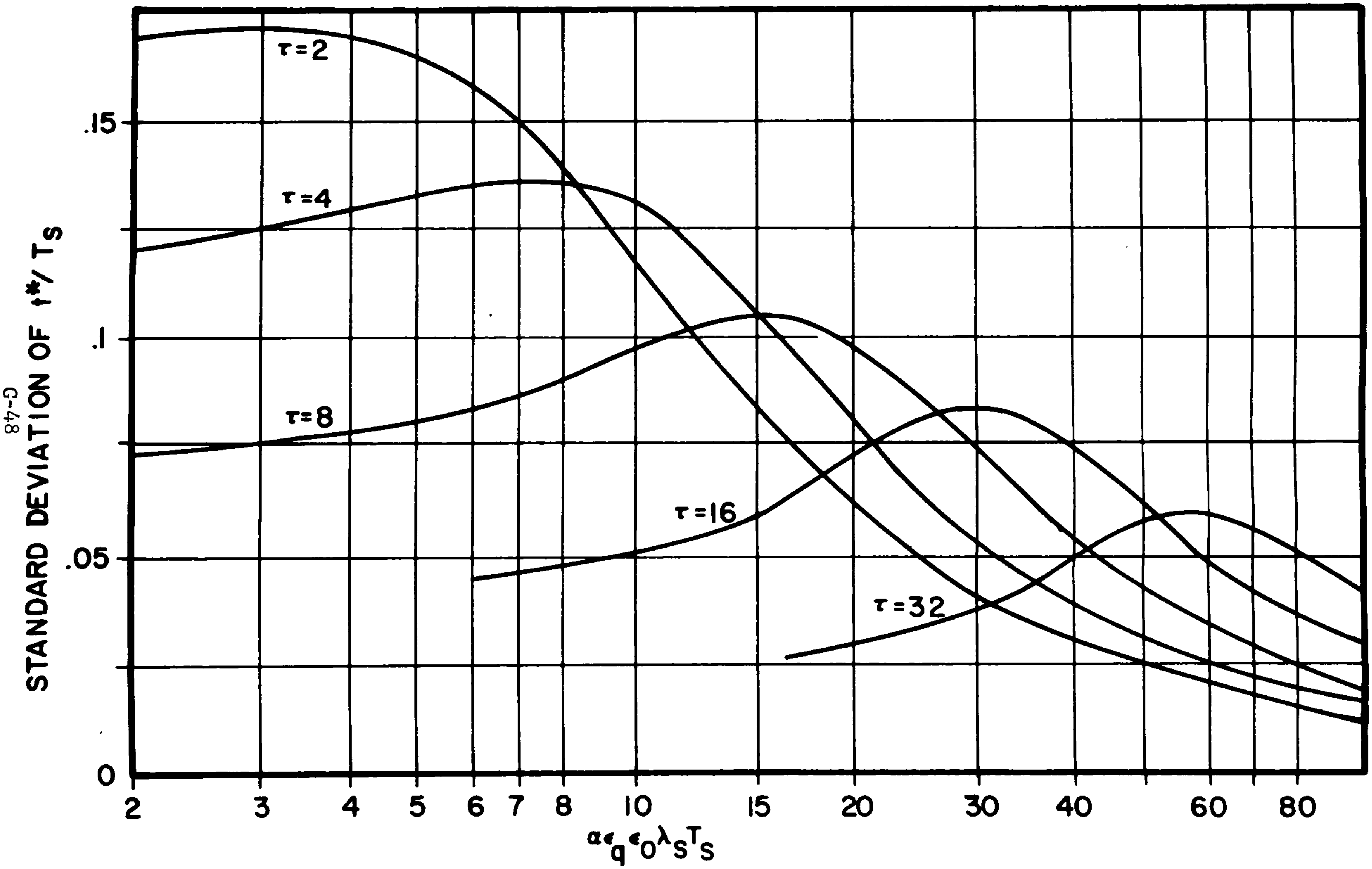

Figure G-7: Standard Deviation of t^*/T_s as Function of Expected Number of Pulses $\alpha\ \epsilon_q\ \epsilon_o\ \lambda_s\ T_s$

$$\alpha\epsilon_q\epsilon_o\lambda_s H(T_f/2) + \alpha\epsilon_q\epsilon_o T_f T_s \sum_{M=M_o+1}^{\infty} \nu(M)\,\lambda(M) + T_f\,\lambda_d \qquad \text{(g-108)}$$

A natural estimate of λ_s is

$$\hat{\lambda}_s = \frac{y(t^* + T_f/2) - \alpha\epsilon_q\epsilon_o T_f T_s \sum_{M=M_o+1}^{\infty} \nu(M)\,\lambda(M) - T_f\,\lambda_d}{\alpha\epsilon_q\epsilon_o\, H(T_f/2)} \; * \qquad \text{(g-109)}$$

which is unbiased. The standard deviation of $\hat{\lambda}_s/\lambda_s$ is

$$\frac{\left[\alpha\epsilon_q\epsilon_o\lambda_s H(T_f/2) + \alpha\epsilon_q\epsilon_o T_f T_s \sum_{M=M_o+1}^{\infty} \nu(M)\,\lambda(M) + T_f\,\lambda_d\right]^{1/2}}{\alpha\epsilon_q\epsilon_o\lambda_s H(T_f/2)} \qquad \text{(g-110)}$$

* This estimator has the same form as the minimum variance estimator (g-54).

APPENDIX H

SPECIAL APPLICATIONS OF A

SCANNING CELESTIAL ATTITUDE DETERMINATION SYSTEM (SCADS)

A. Effect on Accuracy and Star Availability of Eliminating 120 Degree Sector from Field of View

Several methods of on-board recording and preprocessing of the data gathered by the SCADS sensor have been discussed. One of these methods utilized the on-board tape recorder as a real time method of analog data storage. From the set of considered methods, this method requires a minimum of satellite power and hence is indeed an important method. However, the TV cameras on the Tiros satellite utilize the same tape recorder. Since the cloud coverage data takes precedance over the celestial attitude data, the SCADS sensor may not be able to receive inputs for a complete 360 degree rotation of the slit if the tape recorder is utilized by the SCADS sensor. The geometry of this effect is pictured in Figure H-1.

The angle, ϕ, through which the Tiros rotates so that the TV cameras pass from horizon to horizon is a function of the satellite's altitude, h. But, 500 nm $\leq$ h $\leq$ 1000 nm, and hence $116^{\circ} \leq \phi \leq 126^{\circ}$. In this supplement, we assume $\phi = 120^{\circ}$. Hence, we assume a 120° sector is eliminated from the effective field of view of the SCADS sensor.

In Figure H-2 we picture the instrument's effective field of view projected on the celestial sphere with a 120 degree sector removed. In this figure we indicate the removed sector to be centered about a northerly direction. However, the removed sector will be centered about the great

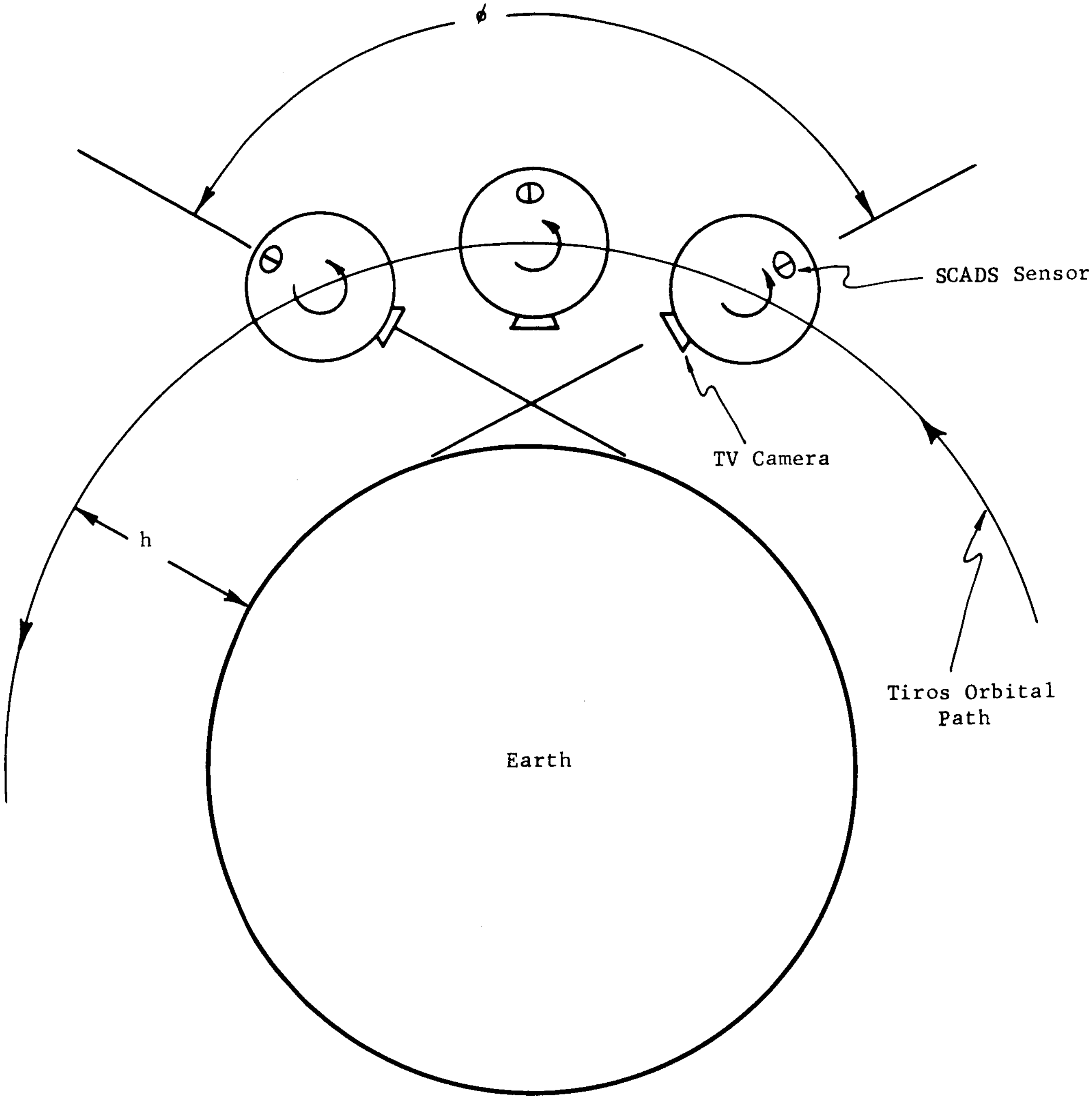

Figure H-1: Discontinuous Coverage of Earth by TV Camera

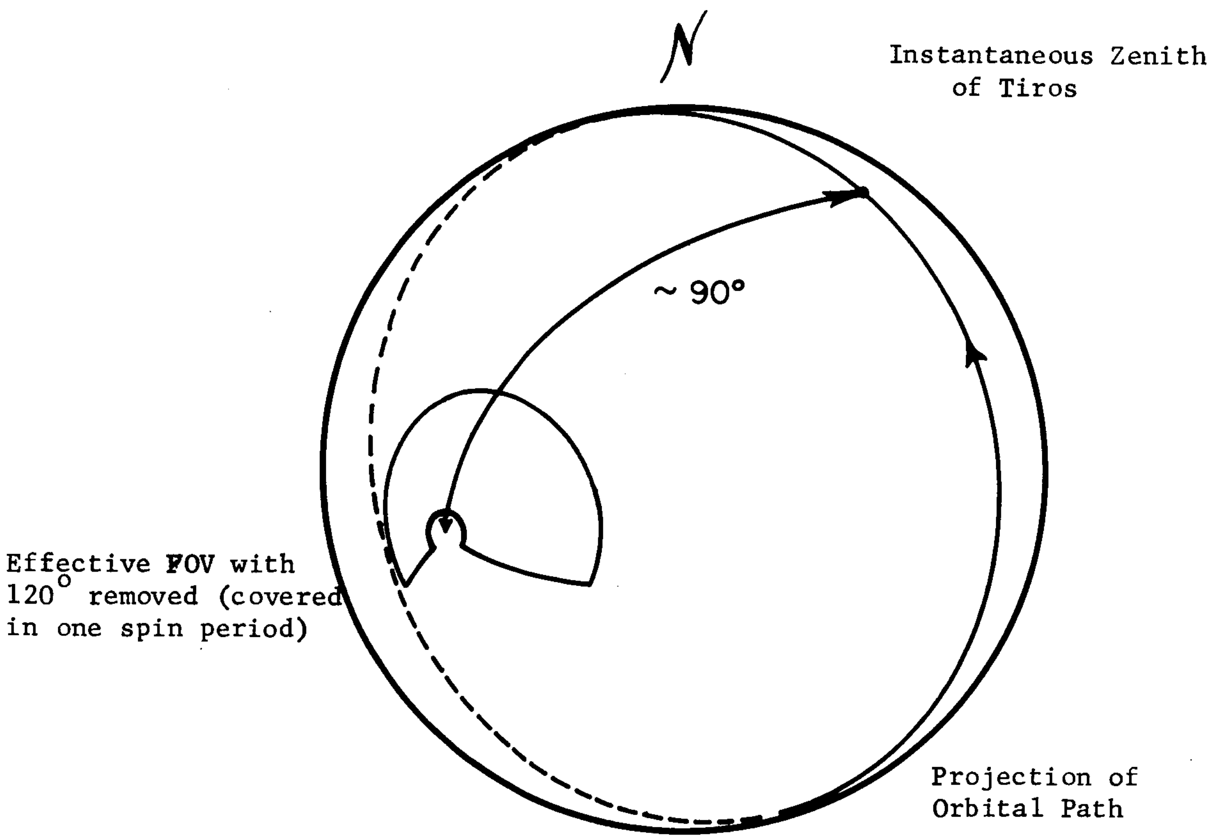

Figure H-2: Effective Field of View of SCADS Projected on Celestial Sphere (120° sector removed) circle arc joining the instantaneous nadir of the satellite and the spin axis. Hence, the removed sector will not lie in a fixed direction on the celestial sphere but will rotate as the satellite moves in its orbital path.

In Figures H-3, H-4, and H-5 we plot the magnitudes of the third, fourth, and fifth brightest stars in the effective field of view as a function of spin axis right ascension, α. These three figures correspond to three different removed sectors. The declination of the spin axis, δ, was set equal to -11 degrees. We may compare these figures with Figure III-6. In Figure III-6 no sector was removed from the instrument's field of view. In this case, the visual magnitude of the fifth brightest star in the field of view was always brighter than $M_V = 3.8$. However, in Figures H-3, H-4, and H-5 we note several right ascensions for the spin axis in which the visual magnitude of the fifth brightest star is dimmer than $M_V = 4$. In total, however, the results indicated in Figures H-3, H-4, and H-5 are not dramatically different from those given in Figure III-6.

In Figures H-6, H-7, and H-8 we plot the total celestial attitude error as a function of spin axis right ascension, α, for three, four, and five stars in the field of view. Three different sectors are blocked in these three figures. For these figures we fix the declination of the spin axis at $\delta = -11^{\circ}$ and the standard deviation of the error in the measurement of each azimuth at

$$\sigma(\mu_i) = 1 \text{ minute of arc, all } i \quad .$$

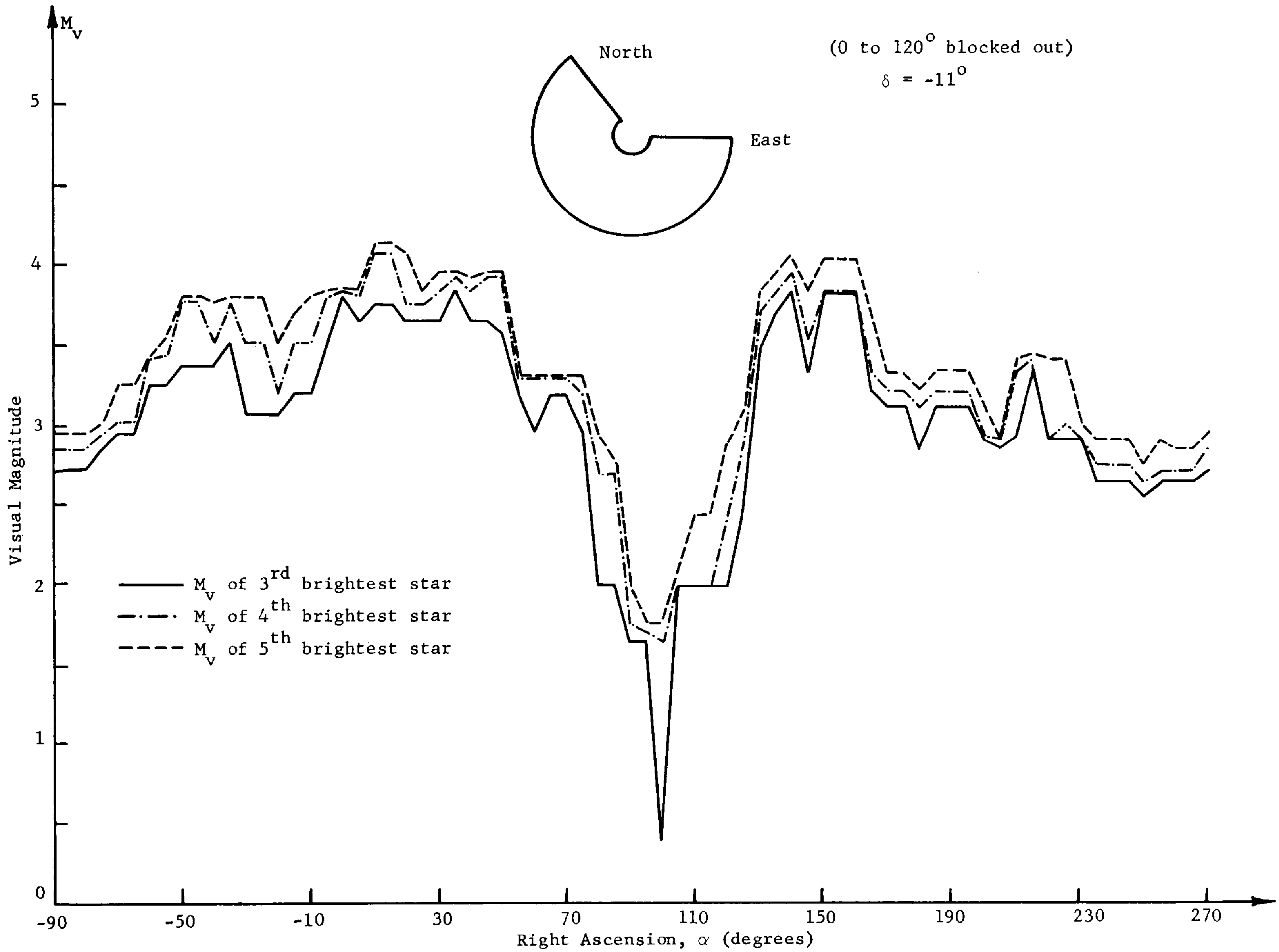

Figure H-3: Visual Magnitude of 3rd, fth, 5th Brightest Stars in Field of View as a Function of α

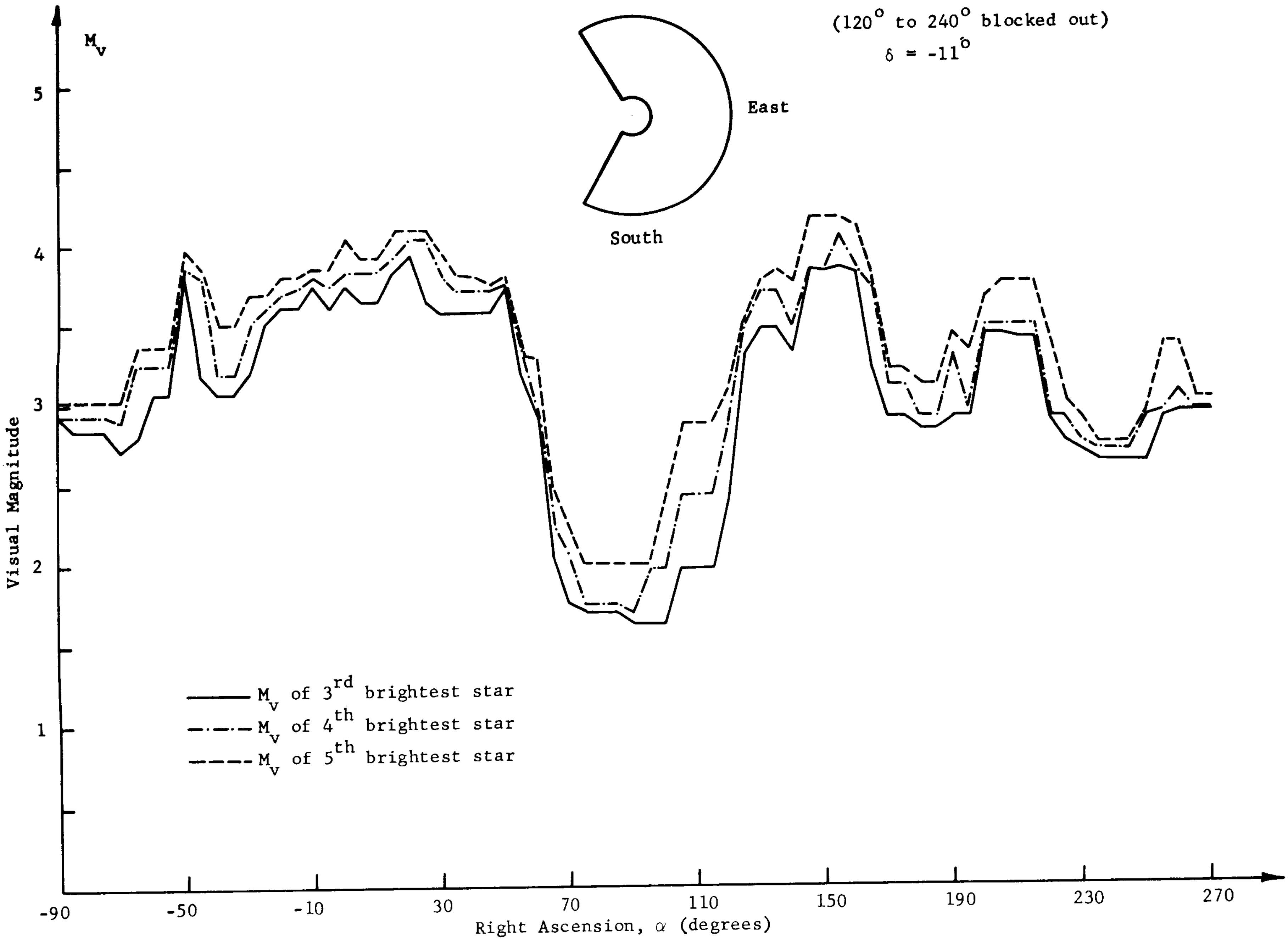

Figure H-4: Visual Magnitude of 3rd, 4th, 5th Brightest Stars in Field of View as a Function of α

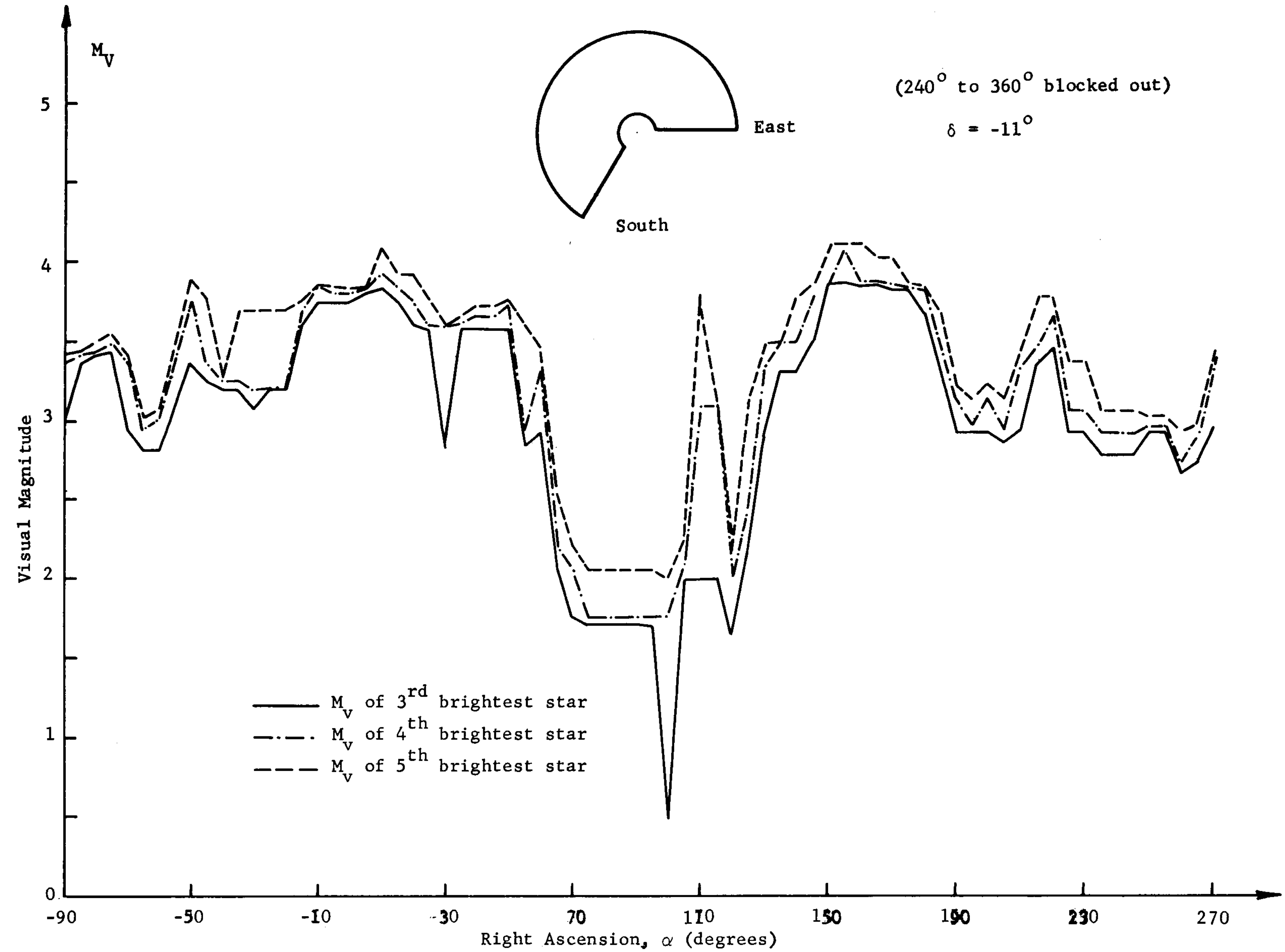

Figure H-5: Visual Magnitude of 3rd, 4th, 5th Brightest Stars in Field of View as a Function of α

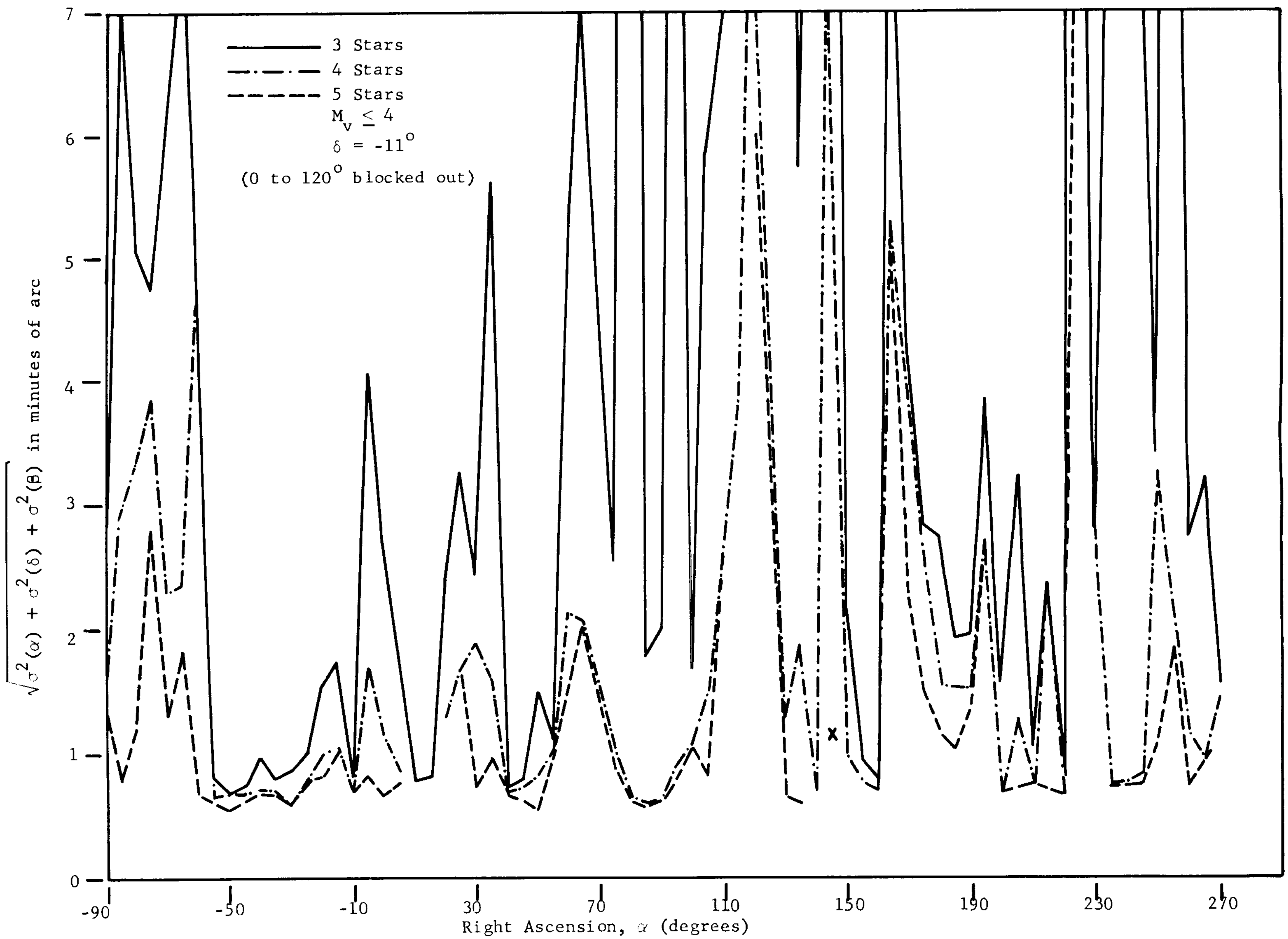

Figure H-6: Total Error as a Function of α for Three, Four, and Five Stars in Field of View

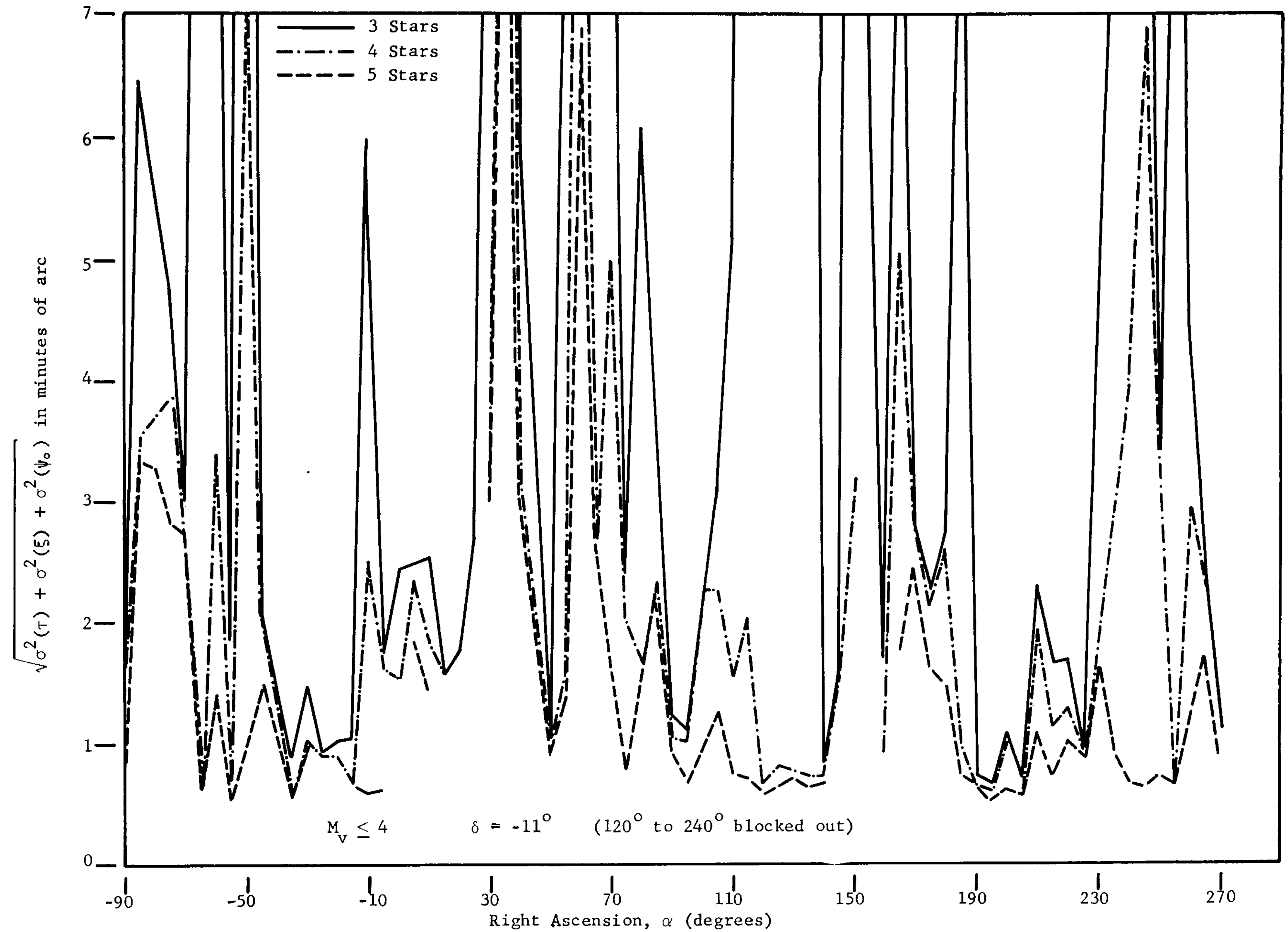

Figure H-7: Total Error as a Function of α for Three, Four, and Five Stars in Field of View

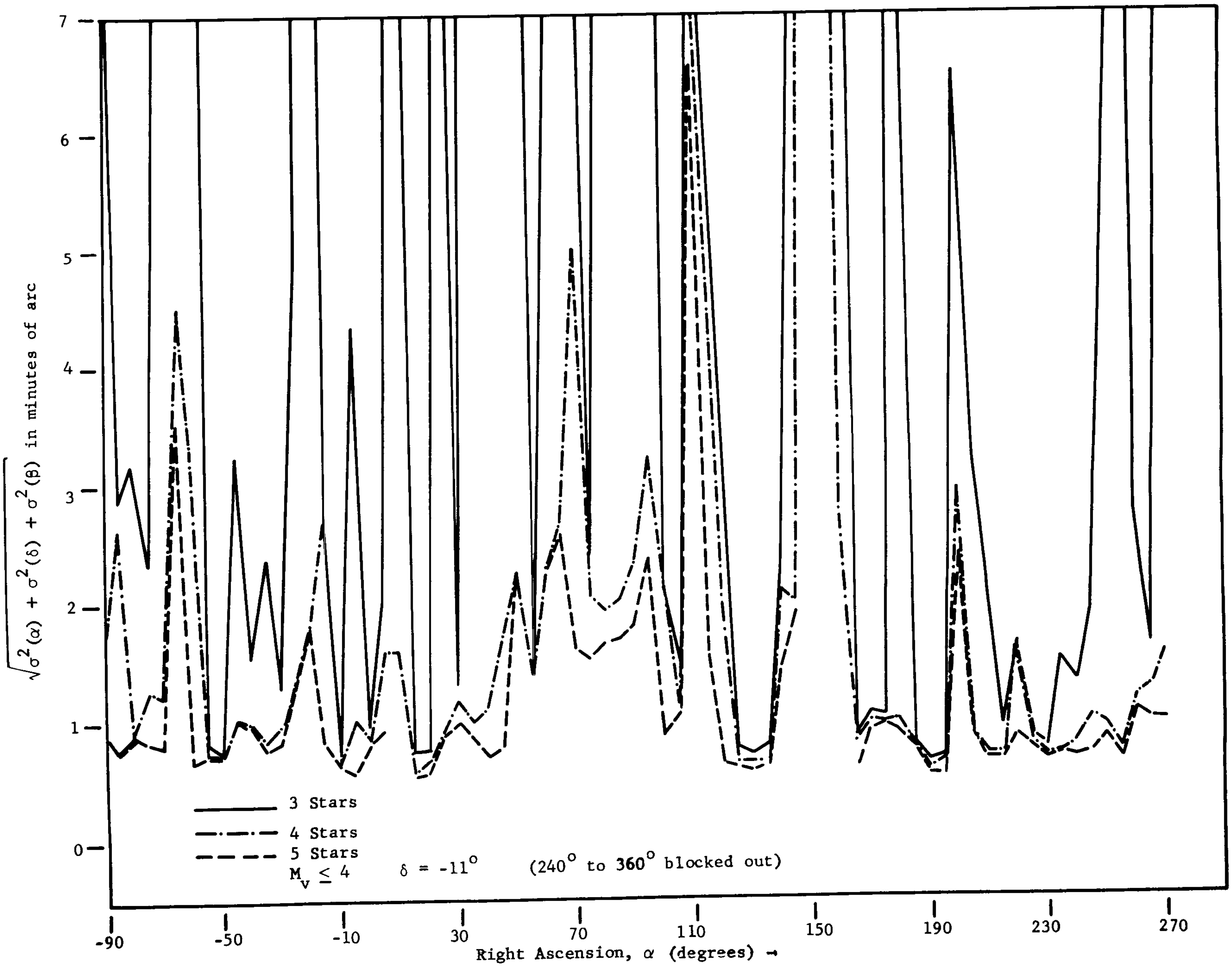

Figure H-8: Total Error as a Function of α for Third, Fourth, and Fifth Stars in Field of View

These errors in the measured quantities then cause errors in the Tiros attitude as indicated in the figures. By total celestial attitude error we mean $\sqrt{\sigma^2(\alpha) + \sigma^2(\beta) + \sigma^2(\delta)}$ where

$\sigma(\alpha)$ = standard deviation of right ascension of spin axis,

$\sigma(\delta)$ = standard deviation of declination of spin axis,

$\sigma(\beta)$ = standard deviation of angle between satellite zero azimuth direction and direction of local north (see Figure IV-10).

Let us compare the results of Figure H-6 with Figure V-7. Figure V-7 is plotted for the same parameters as those chosen for Figure H-6, except that a 120 degree sector was removed in Figure H-6. We see that if the variable bias level is set so that the brightest three stars in the field of view are utilized, then the total error is generally (but not always) smaller than if no sector were removed. For example, if no sector is removed (Figure V-7) then for α = 110 degrees the total error is 0.8 minute of arc (three stars), but for a 120 degree sector removed (Figure H-6) the same error is 6.8 arc minutes. This general result is to be expected, for removing a 120 degree sector generally forces a poorer geometry onto the problem.

In Figures H-6, H-7, and H-8 only stars equal to or brighter than visual magnitude 4.0 were utilized ($M_V \leq 4$). The probability of the sensor detecting a star of visual magnitude 4.0 is a function of the background and the threshold of the variable bias level, but this probability is generally less than 0.5 for a two to three inch optical system. Hence the elimination of these dimmer stars from consideration is realistic. This elimination causes the functions plotted in Figures H-6, H-7, and H-8 to be undefined at some points. For example, in Figure H-6 at α = 20 degrees we cannot obtain five stars ($M_V \leq 4$) nor even four stars in the truncated field of view. However, three stars are in this truncated field of view for all α.

The general conclusions from Figures H-6, H-7, and H-8 are as follows.

(1) With the truncated field of view (120 degree sector eliminated) it is not always possible to receive transits from five or even four stars of $M_V \leq 4$.

(2) If only three stars are utilized the errors are excessive (> .1 degree) for many values of α.

(3) However, if four stars are utilized (four stars are available for 98% of the cases examined) the error is seldom excessive.

(4) When the error which results if four stars are utilized is excessive, then five stars are generally available. Hence, the error is excessive for only 3% of the cases examined.

B. Effect of Truncated Field of View on Instrument Design

In Section A of this appendix we noted that eliminating a 120 degree sector from the field of view generally forces us to design the instrument to view dimmer stars. This fact necessitates a reevaluation of the instrument design parameters. Fortunately this reevaluation can be done via the automatic design program discussed and utilized in the main body of this report.

Table H-1 is the output of the automatic design program for various photomultipliers, pointing directions, and eliminated sectors. In Table H-2 we compare some results between cases with and without the elimination of the 120 degree sector.

For this table, we chose a pointing direction of δ = -10 degrees, α = 10 degrees. This point is near the Galactic South Pole, and hence represents an unfavorable location for the field of view. Note that the optical system requires a slightly larger lens system if a 120 degree sector is removed.

TABLE H-1

AUTOMATIC DESIGN OUTPUT FOR REMOVED SECTORS
(Pages H-15 through H-50)

* DESIGN FOR SCANNING OPTICAL SYSTEM * NO. SADS

* OPTICAL SYSTEM

APERTURE DIAMETER	1.700 INCHES
F NUMBER	0.209
FOCAL LENGTH (MAX.)	0.354 INCHES
IMAGE DIAMETER	0.563 ARC MINUTES
FIELD OF VIEW	20.000 DEGREES
FIELD OF VIEW SHAPE	CIRCULAR
OPTICAL EFFICIENCY	0.75
OPTICAL ARRANGEMENT	REFRACTING OPTICS
SPECTRAL FILTER	NONE

* RETICLE CONFIGURATION

WIDTH OF SLITS	0.563 ARC MIN		
	0.017	TO	0.098 MILS
LENGTH OF SLITS	20.000 DEGREES		0.125 IN.
SLIT SHAPE	TRUNCATED SECTOR		
CODE PATTERN	000100000000000000000000 000000000000000000000000		
NUMBER OF CODE GROUPS	1		
COLOR CODE	NONE		
RELATIVE ORIENTATION OF CODE GROUPS	ONE RADIAL SLIT		

* SENSOR AND DETECTION TECHNIQUE

TYPE OF DETECTOR	PHOTOMULTIPLIER RCA 1P21 RUGGEDIZED
DARK CURRENT	31200.00 PULSES PER SECOND
TIME RESPONSE	50.00 NANOSECONDS
QUANTUM EFFICIENCY	0.1000
DETECTION TECHNIQUE	HOLDING FILTER,THRESHOLD
RMS SPREAD OF PULSE AMPLITUDES TO MEAN	1.22
CATHODE SIZE RECTANGULAR	.375 BY .125 INCHES
NUMBER OF SCANS CORRELATED	1

* MOTION

SCAN PERIOD	6.00 SECONDS			
ANGLE BETWEEN SPIN AXIS AND OPTICAL AXIS	14.00 DEGREES			
STAR TRANSIT TIME (CENTRAL RAY)	645.91 MICROSECONDS			
POINTING DIRECTIONS				
RIGHT ASCENSION	110.00	TO	310.00	DEGREES
DECLINATION	-11.00	TO	-11.00	DEGREES

* DESIGN EVALUATION *

POINTING DIRECTION		
RIGHT ASCENSION	10.00	DEGREES
DECLINATION	-11.00	DEGREES

* TARGET CHARACTERISTICS

LIMITING STAR MAGNITUDE	4.37 PHOTOGRAPHIC
SPECTRAL CLASSES	ALL
PLANETS, SUN, OR EARTH IN FIELD OF VIEW	
SIGNIFICANCE OF EARTHS ATMOSPHERE	OUTSIDE ATMOSPHERE, HOWEVER, ANOTHER SCANNING CAMERA SCANS EARTH FOR 1/3 OF SCAN PERIOD AND IT HAS TELEMETRY PRIORITY OVER SADS SCANNER

* STAR TRANSIT CHARACTERISTICS FOR LIMITING-MAGNITUDE STAR

POSITION ACCURACY	0.094 ARC MINUTES
RELATIVE INTENSITY ACCURACY	0.24
PROBABILITY OF DETECTION	0.95
EXPECTED NUMBER OF WEAK STARS DETECTED PER SCAN	5.23n7
EXPECTED NUMBER OF FALSE STAR DETECTIONS PER SCAN	0.6791

Sector from 0^{o} to 120^{o} eliminated

0^{o} is North

90^{o} is West, etc.

* SIGNAL AND NOISE CHARACTERISTICS

MEAN NUMBER OF PULSES FROM LIMITING MAG STAR DURING STAR TRANSIT	30.00
MEAN NUMBER OF PULSES FROM STELLAR BACKGROUND DURING STAR TRANSIT	0.5639
MEAN NUMBER OF PULSES FROM DARK CURRENT DURING STAR TRANSIT	20.1524
PHOTOGRAPHIC MAG. OF NOISE	4.77
DETECTION THRESHOLD	39.00
MEAN VALUE OF OFF-PEAK MAXIMUM FOR CODE PATTERN	0.00

* SYSTEM CHARACTERISTICS

MINIMUM NUMBER OF STARS IN FIELD OF VIEW WITH LIMITING MAGNITUDE AND BRIGHTER	4
ACCURACY OF ATTITUDE DETERMINATION	0.65 ARC MINUTES
PROBABILITY OF CORRECT STAR-PATTERN RECOGNITION	0.9
PATTERN RECOGNITION TECHNIQUE	
MEAN NUMBER OF STEPS FOR PATTERN RECOGNITION	

* DESIGN EVALUATION *

POINTING DIRECTION

RIGHT ASCENSION	155.00	DEGREES
DECLINATION	-11.00	DEGREES

* TARGET CHARACTERISTICS

LIMITING STAR MAGNITUDE	4.10 PHOTOGRAPHIC
SPECTRAL CLASSES	ALL
PLANETS, SUN, OR EARTH IN FIELD OF VIEW	
SIGNIFICANCE OF EARTHS ATMOSPHERE	OUTSIDE ATMOSPHERE, HOWEVER, ANOTHER SCANNING CAMERA SCANS EARTH FOR 1/3 OF SCAN PERIOD AND IT HAS TELEMETRY PRIORITY OVER SADS SCANNER

* SIGNAL AND NOISE CHARACTERISTICS

MEAN NUMBER OF PULSES FROM LIMITING MAG STAR DURING STAR TRANSIT	38.47
MEAN NUMBER OF PULSES FROM STELLAR BACKGROUND DURING STAR TRANSIT	0.9399
MEAN NUMBER OF PULSES FROM DARK CURRENT DURING STAR TRANSIT	20.1524
PHOTOGRAPHIC MAG. OF NOISE	4.75
DETECTION THRESHOLD	48.00
MEAN VALUE OF OFF-PEAK MAXIMUM FOR CODE PATTERN	0.00

* STAR TRANSIT CHARACTERISTICS FOR LIMITING-MAGNITUDE STAR

POSITION ACCURACY	0.094 ARC MINUTES
RELATIVE INTENSITY ACCURACY	0.20
PROBABILITY OF DETECTION	0.93
EXPECTED NUMBER OF WEAK STARS DETECTED PER SCAN	1.0752
EXPECTED NUMBER OF FALSE STAR DETECTIONS PER SCAN	0.0000

* SYSTEM CHARACTERISTICS

MINIMUM NUMBER OF STARS IN FIELD OF VIEW WITH LIMITING MAGNITUDE AND BRIGHTER	4
ACCURACY OF ATTITUDE DETERMINATION	1.55 ARC MINUTES
PROBABILITY OF CORRECT STAR-PATTERN RECOGNITION	0.9
PATTERN RECOGNITION TECHNIQUE	
MEAN NUMBER OF STEPS FOR PATTERN RECOGNITION	

Sector from 120^{o} to 240^{o} eliminated

0^{o} is North

90^{o} is West, etc.

* DESIGN EVALUATION *

POINTING DIRECTION

RIGHT ASCENSION	155.00	DEGREES
DECLINATION	-11.00	DEGREES

* TARGET CHARACTERISTICS

LIMITING STAR MAGNITUDE	3.70 PHOTOGRAPHIC
SPECTRAL CLASSES	ALL
PLANETS, SUN, OR EARTH IN FIELD OF VIEW	
SIGNIFICANCE OF EARTHS ATMOSPHERE	OUTSIDE ATMOSPHERE, HOWEVER, ANOTHER SCANNING CAMERA SCANS EARTH FOR 1/3 OF SCAN PERIOD AND IT HAS TELEMETRY PRIORITY OVER SADS SCANNER

* SIGNAL AND NOISE CHARACTERISTICS

MEAN NUMBER OF PULSES FROM LIMITING MAG STAR DURING STAR TRANSIT	55.61
MEAN NUMBER OF PULSES FROM STELLAR BACKGROUND DURING STAR TRANSIT	0.9399
MEAN NUMBER OF PULSES FROM DARK CURRENT DURING STAR TRANSIT	20.1524
PHOTOGRAPHIC MAG. OF NOISE	4.75
DETECTION THRESHOLD	65.00
MEAN VALUE OF OFF-PEAK MAXIMUM FOR CODE PATTERN	0.00

* STAR TRANSIT CHARACTERISTICS FOR LIMITING-MAGNITUDE STAR

POSITION ACCURACY	0.094 ARC MINUTES
RELATIVE INTENSITY ACCURACY	0.16
PROBABILITY OF DETECTION	0.91
EXPECTED NUMBER OF WEAK STARS DETECTED PER SCAN	0.0305
EXPECTED NUMBER OF FALSE STAR DETECTIONS PER SCAN	0.0000

* SYSTEM CHARACTERISTICS

MINIMUM NUMBER OF STARS IN FIELD OF VIEW WITH LIMITING MAGNITUDE AND BRIGHTER	4
ACCURACY OF ATTITUDE DETERMINATION	1.50 ARC MINUTES
PROBABILITY OF CORRECT STAR-PATTERN RECOGNITION	0.9
PATTERN RECOGNITION TECHNIQUE	
MEAN NUMBER OF STEPS FOR PATTERN RECOGNITION	

Sector from 240° to 360° eliminated

* DESIGN FOR SCANNING OPTICAL SYSTEM * NO. SADS

* OPTICAL SYSTEM

APERTURE DIAMETER	3.419 INCHES
F NUMBER	1.028
FOCAL LENGTH (MAX.)	3.516 INCHES
IMAGE DIAMETER	0.116 ARC MINUTES
FIELD OF VIEW	20.000 DEGREES
FIELD OF VIEW SHAPE	CIRCULAR
OPTICAL EFFICIENCY	0.75
OPTICAL ARRANGEMENT	REFRACTING OPTICS
SPECTRAL FILTER	NONE

* RETICLE CONFIGURATION

WIDTH OF SLITS	0.116 ARC MIN	
	0.034 TO	0.199 MILS
LENGTH OF SLITS	20.000 DEGREES	1.240 IN.
SLIT SHAPE	TRUNCATED SECTOR	
CODE PATTERN	0001000000000000000000000 0000000000000000000000000	
NUMBER OF CODE GROUPS	1	
COLOR CODE	NONE	
RELATIVE ORIENTATION OF CODE GROUPS	ONE RADIAL SLIT	

* SENSOR AND DETECTION TECHNIQUE

TYPE OF DETECTOR	PHOTOMULTIPLIER RCA C70113A RUGGEDIZED
DARK CURRENT	128000.00 PULSES PER SECOND
TIME RESPONSE	50.00 NANOSECONDS
QUANTUM EFFICIENCY	0.1200
DETECTION TECHNIQUE	HOLDING FILTER,THRESHOLD
RMS SPREAD OF PULSE AMPLITUDES TO MEAN	1.22
CATHODE SIZE MIN WINDOW DIAMETER	1.24 IN.
NUMBER OF SCANS CORRELATED	1

* MOTION

SCAN PERIOD	6.00 SECONDS
ANGLE BETWEEN SPIN AXIS AND OPTICAL AXIS	14.00 DEGREES
STAR TRANSIT TIME (CENTRAL RAY)	132.99 MICROSECONDS
POINTING DIRECTIONS	
RIGHT ASCENSION	110.00 TO 310.00 DEGREES
DECLINATION	-11.00 TO -11.00 DEGREES

* DESIGN EVALUATION *

POINTING DIRECTION

RIGHT ASCENSION	10.00	DEGREES
DECLINATION	-11.00	DEGREES

* TARGET CHARACTERISTICS

LIMITING STAR MAGNITUDE	4.37 PHOTOGRAPHIC
SPECTRAL CLASSES	ALL
PLANETS, SUN, OR EARTH IN FIELD OF VIEW	
SIGNIFICANCE OF EARTHS ATMOSPHERE	OUTSIDE ATMOSPHERE, HOWEVER, ANOTHER SCANNING CAMERA SCANS EARTH FOR 1/3 OF SCAN PERIOD AND IT HAS TELEMETRY PRIORITY OVER SADS SCANNER

* STAR TRANSIT CHARACTERISTICS FOR LIMITING-MAGNITUDE STAR

POSITION ACCURACY	0.019 ARC MINUTES
RELATIVE INTENSITY ACCURACY	0.23
PROBABILITY OF DETECTION	0.94
EXPECTED NUMBER OF WEAK STARS DETECTED PER SCAN	3.7465
EXPECTED NUMBER OF FALSE STAR DETECTIONS PER SCAN	0.6412

Sector from 0° to 120° eliminated

* SIGNAL AND NOISE CHARACTERISTICS

MEAN NUMBER OF PULSES FROM LIMITING MAG STAR DURING STAR TRANSIT	30.00
MEAN NUMBER OF PULSES FROM STELLAR BACKGROUND DURING STAR TRANSIT	0.1161
MEAN NUMBER OF PULSES FROM DARK CURRENT DURING STAR TRANSIT	17.0223
PHOTOGRAPHIC MAG. OF NOISE	4.98
DETECTION THRESHOLD	36.00
MEAN VALUE OF OFF-PEAK MAXIMUM FOR CODE PATTERN	0.00

* SYSTEM CHARACTERISTICS

MINIMUM NUMBER OF STARS IN FIELD OF VIEW WITH LIMITING MAGNITUDE AND BRIGHTER	4
ACCURACY OF ATTITUDE DETERMINATION	0.65 ARC MINUTES
PROBABILITY OF CORRECT STAR-PATTERN RECOGNITION	0.9
PATTERN RECOGNITION TECHNIQUE	
MEAN NUMBER OF STEPS FOR PATTERN RECOGNITION	

* DESIGN EVALUATION *

POINTING DIRECTION

RIGHT ASCENSION	155.00	DEGREES
DECLINATION	-11.00	DEGREES

* TARGET CHARACTERISTICS

LIMITING STAR MAGNITUDE	4.10 PHOTOGRAPHIC
SPECTRAL CLASSES	ALL
PLANETS, SUN, OR EARTH IN FIELD OF VIEW	
SIGNIFICANCE OF EARTHS ATMOSPHERE	OUTSIDE ATMOSPHERE, HOWEVER, ANOTHER SCANNING CAMERA SCANS EARTH FOR 1/3 OF SCAN PERIOD AND IT HAS TELEMETRY PRIORITY OVER SADS SCANNER

* STAR TRANSIT CHARACTERISTICS FOR LIMITING-MAGNITUDE STAR

POSITION ACCURACY	0.019 ARC MINUTES
RELATIVE INTENSITY ACCURACY	0.19
PROBABILITY OF DETECTION	0.94
EXPECTED NUMBER OF WEAK STARS DETECTED PER SCAN	0.8827
EXPECTED NUMBER OF FALSE STAR DETECTIONS PER SCAN	0.0000

Sector from 120° to 240° eliminated

* SIGNAL AND NOISE CHARACTERISTICS

MEAN NUMBER OF PULSES FROM LIMITING MAG STAR DURING STAR TRANSIT	38.47
MEAN NUMBER OF PULSES FROM STELLAR BACKGROUND DURING STAR TRANSIT	0.1935
MEAN NUMBER OF PULSES FROM DARK CURRENT DURING STAR TRANSIT	17.0223
PHOTOGRAPHIC MAG. OF NOISE	4.97
DETECTION THRESHOLD	44.00
MEAN VALUE OF OFF-PEAK MAXIMUM FOR CODE PATTERN	0.00

* SYSTEM CHARACTERISTICS

MINIMUM NUMBER OF STARS IN FIELD OF VIEW WITH LIMITING MAGNITUDE AND BRIGHTER	4
ACCURACY OF ATTITUDE DETERMINATION	1.55 ARC MINUTES
PROBABILITY OF CORRECT STAR-PATTERN RECOGNITION	0.9
PATTERN RECOGNITION TECHNIQUE	
MEAN NUMBER OF STEPS FOR PATTERN RECOGNITION	

* DESIGN EVALUATION *

POINTING DIRECTION

RIGHT ASCENSION	155.00	DEGREES
DECLINATION	-11.00	DEGREES

* TARGET CHARACTERISTICS

LIMITING STAR MAGNITUDE	3.70 PHOTOGRAPHIC
SPECTRAL CLASSES	ALL
PLANETS, SUN, OR EARTH IN FIELD OF VIEW	
SIGNIFICANCE OF EARTHS ATMOSPHERE	OUTSIDE ATMOSPHERE, HOWEVER, ANOTHER SCANNING CAMERA SCANS EARTH FOR 1/3 OF SCAN PERIOD AND IT HAS TELEMETRY PRIORITY OVER SADS SCANNER

* STAR TRANSIT CHARACTERISTICS FOR LIMITING-MAGNITUDE STAR

POSITION ACCURACY	0.019 ARC MINUTES
RELATIVE INTENSITY ACCURACY	0.15
PROBABILITY OF DETECTION	0.92
EXPECTED NUMBER OF WEAK STARS DETECTED PER SCAN	0.0204
EXPECTED NUMBER OF FALSE STAR DETECTIONS PER SCAN	0.0000

Sector from 240° to 360° eliminated

* SIGNAL AND NOISE CHARACTERISTICS

MEAN NUMBER OF PULSES FROM LIMITING MAG STAR DURING STAR TRANSIT	55.61
MEAN NUMBER OF PULSES FROM STELLAR BACKGROUND DURING STAR TRANSIT	0.1935
MEAN NUMBER OF PULSES FROM DARK CURRENT DURING STAR TRANSIT	17.0223
PHOTOGRAPHIC MAG. OF NOISE	4.97
DETECTION THRESHOLD	61.00
MEAN VALUE OF OFF-PEAK MAXIMUM FOR CODE PATTERN	0.00

* SYSTEM CHARACTERISTICS

MINIMUM NUMBER OF STARS IN FIELD OF VIEW WITH LIMITING MAGNITUDE AND BRIGHTER	4
ACCURACY OF ATTITUDE DETERMINATION	1.50 ARC MINUTES
PROBABILITY OF CORRECT STAR-PATTERN RECOGNITION	0.9
PATTERN RECOGNITION TECHNIQUE	
MEAN NUMBER OF STEPS FOR PATTERN RECOGNITION	

* DESIGN FOR SCANNING OPTICAL SYSTEM * NO. SADS

* OPTICAL SYSTEM

APERTURE DIAMETER	1.999 INCHES
F NUMBER	1.418
FOCAL LENGTH (MAX.)	2.836 INCHES
IMAGE DIAMETER	1.452 ARC MINUTES
FIELD OF VIEW	20.000 DEGREES
FIELD OF VIEW SHAPE	CIRCULAR
OPTICAL EFFICIENCY	0.75
OPTICAL ARRANGEMENT	REFRACTING OPTICS
SPECTRAL FILTER	NONE

* RETICLE CONFIGURATION

WIDTH OF SLITS	1.452 ARC MIN		
	0.345	TO	2.014 MILS
LENGTH OF SLITS	20.000 DEGREES		1.000 IN.
SLIT SHAPE	TRUNCATED SECTOR		
CODE PATTERN	0001000000000000000000000		
	0000000000000000000000000		
NUMBER OF CODE GROUPS	1		
COLOR CODE	NONE		
RELATIVE ORIENTATION OF CODE GROUPS	ONE RADIAL SLIT		

* SENSOR AND DETECTION TECHNIQUE

TYPE OF DETECTOR	PHOTOMULTIPLIER EMR 541D-01-14 RUGGEDIZED
DARK CURRENT	35.60 PULSES PER SECOND
TIME RESPONSE	50.00 NANOSECONDS
QUANTUM EFFICIENCY	0.0280
DETECTION TECHNIQUE	HOLDING FILTER,THRESHOLD
RMS SPREAD OF PULSE AMPLITUDES TO MEAN	1.22
CATHODE SIZE	
USEFUL CATHODE DIA.	1 INCH
NUMBER OF SCANS CORRELATED	1

* MOTION

SCAN PERIOD	6.00 SECONDS			
ANGLE BETWEEN SPIN AXIS AND OPTICAL AXIS	14.00 DEGREES			
STAR TRANSIT TIME (CENTRAL RAY)	1667.20 MICROSECONDS			
POINTING DIRECTIONS				
RIGHT ASCENSION	110.00	TO	310.00	DEGREES
DECLINATION	-11.00	TO	-11.00	DEGREES

* DESIGN EVALUATION *

POINTING DIRECTION		
RIGHT ASCENSION	10.00	DEGREES
DECLINATION	-11.00	DEGREES

* TARGET CHARACTERISTICS

LIMITING STAR MAGNITUDE	4.37 PHOTOGRAPHIC
SPECTRAL CLASSES	ALL
PLANETS, SUN, OR EARTH IN FIELD OF VIEW	
SIGNIFICANCE OF EARTHS ATMOSPHERE	OUTSIDE ATMOSPHERE, HOWEVER, ANOTHER SCANNING CAMERA SCANS EARTH FOR 1/3 OF SCAN PERIOD AND IT HAS TELEMETRY PRIORITY OVER SADS SCANNER

* STAR TRANSIT CHARACTERISTICS FOR LIMITING-MAGNITUDE STAR

POSITION ACCURACY	0.242 ARC MINUTES
RELATIVE INTENSITY ACCURACY	0.19
PROBABILITY OF DETECTION	0.95
EXPECTED NUMBER OF WEAK STARS DETECTED PER SCAN	0.4420
EXPECTED NUMBER OF FALSE STAR DETECTIONS PER SCAN	0.0000

Sector from 0° to 120° eliminated

* SIGNAL AND NOISE CHARACTERISTICS

MEAN NUMBER OF PULSES FROM LIMITING MAG STAR DURING STAR TRANSIT	30.00
MEAN NUMBER OF PULSES FROM STELLAR BACKGROUND DURING STAR TRANSIT	1.4556
MEAN NUMBER OF PULSES FROM DARK CURRENT DURING STAR TRANSIT	0.0594
PHOTOGRAPHIC MAG. OF NOISE	7.61
DETECTION THRESHOLD	22.00
MEAN VALUE OF OFF-PEAK MAXIMUM FOR CODE PATTERN	0.00

* SYSTEM CHARACTERISTICS

MINIMUM NUMBER OF STARS IN FIELD OF VIEW WITH LIMITING MAGNITUDE AND BRIGHTER	4
ACCURACY OF ATTITUDE DETERMINATION	0.65 ARC MINUTES
PROBABILITY OF CORRECT STAR-PATTERN RECOGNITION	0.9
PATTERN RECOGNITION TECHNIQUE	
MEAN NUMBER OF STEPS FOR PATTERN RECOGNITION	

* DESIGN EVALUATION *

POINTING DIRECTION		
RIGHT ASCENSION	155.00	DEGREES
DECLINATION	-11.00	DEGREES

* TARGET CHARACTERISTICS

LIMITING STAR MAGNITUDE	4.10 PHOTOGRAPHIC
SPECTRAL CLASSES	ALL
PLANETS, SUN, OR EARTH IN FIELD OF VIEW	
SIGNIFICANCE OF EARTHS ATMOSPHERE	OUTSIDE ATMOSPHERE, HOWEVER, ANOTHER SCANNING CAMERA SCANS EARTH FOR 1/3 OF SCAN PERIOD AND IT HAS TELEMETRY PRIORITY OVER SADS SCANNER

* STAR TRANSIT CHARACTERISTICS FOR LIMITING-MAGNITUDE STAR

POSITION ACCURACY	0.242 ARC MINUTES
RELATIVE INTENSITY ACCURACY	0.17
PROBABILITY OF DETECTION	0.93
EXPECTED NUMBER OF WEAK STARS DETECTED PER SCAN	0.0610
EXPECTED NUMBER OF FALSE STAR DETECTIONS PER SCAN	0.0000

Sector from 120° to 240° eliminated

* SIGNAL AND NOISE CHARACTERISTICS

MEAN NUMBER CF PULSES FROM LIMITING MAG STAR DURING STAR TRANSIT	38.47
MEAN NUMBER OF PULSES FROM STELLAR BACKGROUND DURING STAR TRANSIT	2.4259
MEAN NUMBER OF PULSES FROM DARK CURRENT DURING STAR TRANSIT	0.0594
PHOTOGRAPHIC MAG. OF NOISE	7.07
DETECTION THRESHOLD	31.00
MEAN VALUE OF OFF-PEAK MAXIMUM FOR CODE PATTERN	0.00

* SYSTEM CHARACTERISTICS

MINIMUM NUMBER OF STARS IN FIELD OF VIEW WITH LIMITING MAGNITUDE AND BRIGHTER	4
ACCURACY OF ATTITUDE DETERMINATION	1.55 ARC MINUTES
PROBABILITY OF CORRECT STAR-PATTERN RECOGNITION	0.9
PATTERN RECOGNITION TECHNIQUE	
MEAN NUMBER OF STEPS FOR PATTERN RECOGNITION	

* DESIGN EVALUATION *

POINTING DIRECTION		
RIGHT ASCENSION	155.00	DEGREES
DECLINATION	-11.00	DEGREES

* TARGET CHARACTERISTICS

LIMITING STAR MAGNITUDE	3.70 PHOTOGRAPHIC
SPECTRAL CLASSES	ALL
PLANETS, SUN, OR EARTH IN FIELD OF VIEW	
SIGNIFICANCE OF EARTHS ATMOSPHERE	OUTSIDE ATMOSPHERE, HOWEVER, ANOTHER SCANNING CAMERA SCANS EARTH FOR 1/3 OF SCAN PERIOD AND IT HAS TELEMETRY PRIORITY OVER SADS SCANNER

* SIGNAL AND NOISE CHARACTERISTICS

MEAN NUMBER OF PULSES FROM LIMITING MAG STAR DURING STAR TRANSIT	55.61
MEAN NUMBER OF PULSES FROM STELLAR BACKGROUND DURING STAR TRANSIT	2.4259
MEAN NUMBER OF PULSES FROM DARK CURRENT DURING STAR TRANSIT	0.0594
PHOTOGRAPHIC MAG. OF NOISE	7.07
DETECTION THRESHOLD	48.00
MEAN VALUE OF OFF-PEAK MAXIMUM FOR CODE PATTERN	0.00

* STAR TRANSIT CHARACTERISTICS FOR LIMITING-MAGNITUDE STAR

POSITION ACCURACY	0.242 ARC MINUTES
RELATIVE INTENSITY ACCURACY	0.14
PROBABILITY OF DETECTION	0.91
EXPECTED NUMBER OF WEAK STARS DETECTED PER SCAN	0.0004
EXPECTED NUMBER OF FALSE STAR DETECTIONS PER SCAN	0.0000

* SYSTEM CHARACTERISTICS

MINIMUM NUMBER OF STARS IN FIELD OF VIEW WITH LIMITING MAGNITUDE AND BRIGHTER	4
ACCURACY OF ATTITUDE DETERMINATION	1.50 ARC MINUTES
PROBABILITY OF CORRECT STAR-PATTERN RECOGNITION	0.9
PATTERN RECOGNITION TECHNIQUE	
MEAN NUMBER OF STEPS FOR PATTERN RECOGNITION	

Sector from 240° to 360° eliminated

* DESIGN FOR SCANNING OPTICAL SYSTEM * NO. SADS

* OPTICAL SYSTEM

APERTURE DIAMETER	0.553 INCHES
F NUMBER	2.000
FOCAL LENGTH (MAX.)	1.106 INCHES
IMAGE DIAMETER	1.452 ARC MINUTES
FIELD OF VIEW	20.000 DEGREES
FIELD OF VIEW SHAPE	CIRCULAR
OPTICAL EFFICIENCY	0.75
OPTICAL ARRANGEMENT	REFRACTING OPTICS
SPECTRAL FILTER	NONE

* RETICLE CONFIGURATION

WIDTH OF SLITS	1.452 ARC MIN	
	0.135 TO	0.785 MILS
LENGTH OF SLITS	20.000 DEGREES	0.390 IN.
SLIT SHAPE	TRUNCATED SECTOR	
CODE PATTERN	000100000000000000000000	
	000000000000000000000000	
NUMBER OF CODE GROUPS	1	
COLOR CODE	NONE	
RELATIVE ORIENTATION OF CODE GROUPS	ONE RADIAL SLIT	

* SENSOR AND DETECTION TECHNIQUE

TYPE OF DETECTOR	PHOTOMULTIPLIER EMR 541B-03
DARK CURRENT	4870.00 PULSES PER SECOND
TIME RESPONSE	50.00 NANOSECONDS
QUANTUM EFFICIENCY	0.3660
DETECTION TECHNIQUE	HOLDING FILTER,THRESHOLD
RMS SPREAD OF PULSE AMPLITUDES TO MEAN	1.22
CATHODE SIZE ACTIVE CATHODE DIA.	.39 IN.
NUMBER OF SCANS CORRELATED	1

* MOTION

SCAN PERIOD	6.00 SECONDS	
ANGLE BETWEEN SPIN AXIS AND OPTICAL AXIS	14.00 DEGREES	
STAR TRANSIT TIME (CENTRAL RAY)	1667.20 MICROSECONDS	
POINTING DIRECTIONS		
RIGHT ASCENSION	110.00 TO 310.00	DEGREES
DECLINATION	-11.00 TO -11.00	DEGREES

* DESIGN EVALUATION *

POINTING DIRECTION		
RIGHT ASCENSION	10.00	DEGREES
DECLINATION	-11.00	DEGREES

* TARGET CHARACTERISTICS

LIMITING STAR MAGNITUDE	4.37 PHOTOGRAPHIC
SPECTRAL CLASSES	ALL
PLANETS, SUN, OR EARTH IN FIELD OF VIEW	
SIGNIFICANCE OF EARTHS ATMOSPHERE	OUTSIDE ATMOSPHERE, HOWEVER, ANOTHER SCANNING CAMERA SCANS EARTH FOR 1/3 OF SCAN PERIOD AND IT HAS TELEMETRY PRIORITY OVER SADS SCANNER

* STAR TRANSIT CHARACTERISTICS FOR LIMITING=MAGNITUDE STAR

POSITION ACCURACY	0.242 ARC MINUTES
RELATIVE INTENSITY ACCURACY	0.21
PROBABILITY OF DETECTION	0.95
EXPECTED NUMBER OF WEAK STARS DETECTED PER SCAN	1.9478
EXPECTED NUMBER OF FALSE STAR DETECTIONS PER SCAN	0.0000

Sector from 0° to 120° eliminated

* SIGNAL AND NOISE CHARACTERISTICS

MEAN NUMBER OF PULSES FROM LIMITING MAG STAR DURING STAR TRANSIT	30.00
MEAN NUMBER OF PULSES FROM STELLAR BACKGROUND DURING STAR TRANSIT	1.4556
MEAN NUMBER OF PULSES FROM DARK CURRENT DURING STAR TRANSIT	8.1193
PHOTOGRAPHIC MAG. OF NOISE	5.61
DETECTION THRESHOLD	29.00
MEAN VALUE OF OFF-PEAK MAXIMUM FOR CODE PATTERN	0.00

* SYSTEM CHARACTERISTICS

MINIMUM NUMBER OF STARS IN FIELD OF VIEW WITH LIMITING MAGNITUDE AND BRIGHTER	4
ACCURACY OF ATTITUDE DETERMINATION	0.65 ARC MINUTES
PROBABILITY OF CORRECT STAR-PATTERN RECOGNITION	0.9
PATTERN RECOGNITION TECHNIQUE	
MEAN NUMBER OF STEPS FOR PATTERN RECOGNITION	

* DESIGN EVALUATION *

POINTING DIRECTION		
RIGHT ASCENSION	155.00	DEGREES
DECLINATION	-11.00	DEGREES

* TARGET CHARACTERISTICS

LIMITING STAR MAGNITUDE	4.10 PHOTOGRAPHIC
SPECTRAL CLASSES	ALL
PLANETS, SUN, OR EARTH IN FIELD OF VIEW	
SIGNIFICANCE OF EARTHS ATMOSPHERE	OUTSIDE ATMOSPHERE, HOWEVER, ANOTHER SCANNING CAMERA SCANS EARTH FOR 1/3 OF SCAN PERIOD AND IT HAS TELEMETRY PRIORITY OVER SADS SCANNER

* STAR TRANSIT CHARACTERISTICS FOR LIMITING-MAGNITUDE STAR

POSITION ACCURACY	0.242 ARC MINUTES
RELATIVE INTENSITY ACCURACY	0.18
PROBABILITY OF DETECTION	0.94
EXPECTED NUMBER OF WEAK STARS DETECTED PER SCAN	0.3782
EXPECTED NUMBER OF FALSE STAR DETECTIONS PER SCAN	0.0000

Sector from 120° to 240° eliminated

* SIGNAL AND NOISE CHARACTERISTICS

MEAN NUMBER OF PULSES FROM LIMITING MAG STAR DURING STAR TRANSIT	38.47
MEAN NUMBER OF PULSES FROM STELLAR BACKGROUND DURING STAR TRANSIT	2.4259
MEAN NUMBER OF PULSES FROM DARK CURRENT DURING STAR TRANSIT	8.1193
PHOTOGRAPHIC MAG. OF NOISE	5.51
DETECTION THRESHOLD	38.00
MEAN VALUE OF OFF-PEAK MAXIMUM FOR CODE PATTERN	0.00

* SYSTEM CHARACTERISTICS

MINIMUM NUMBER OF STARS IN FIELD OF VIEW WITH LIMITING MAGNITUDE AND BRIGHTER	4
ACCURACY OF ATTITUDE DETERMINATION	1.55 ARC MINUTES
PROBABILITY OF CORRECT STAR-PATTERN RECOGNITION	0.9
PATTERN RECOGNITION TECHNIQUE	
MEAN NUMBER OF STEPS FOR PATTERN RECOGNITION	

* DESIGN EVALUATION *

POINTING DIRECTION		
RIGHT ASCENSION	155.00	DEGREES
DECLINATION	-11.00	DEGREES

* TARGET CHARACTERISTICS

LIMITING STAR MAGNITUDE	3.70 PHOTOGRAPHIC
SPECTRAL CLASSES	ALL
PLANETS, SUN, OR EARTH IN FIELD OF VIEW	
SIGNIFICANCE OF EARTHS ATMOSPHERE	OUTSIDE ATMOSPHERE, HOWEVER, ANOTHER SCANNING CAMERA SCANS EARTH FOR 1/3 OF SCAN PERIOD AND IT HAS TELEMETRY PRIORITY OVER SADS SCANNER

* STAR TRANSIT CHARACTERISTICS FOR LIMITING-MAGNITUDE STAR

POSITION ACCURACY	0.242 ARC MINUTES
RELATIVE INTENSITY ACCURACY	0.15
PROBABILITY OF DETECTION	0.91
EXPECTED NUMBER OF WEAK STARS DETECTED PER SCAN	0.0052
EXPECTED NUMBER OF FALSE STAR DETECTIONS PER SCAN	0.0000

* SIGNAL AND NOISE CHARACTERISTICS

MEAN NUMBER OF PULSES FROM LIMITING MAG STAR DURING STAR TRANSIT	55.61
MEAN NUMBER OF PULSES FROM STELLAR BACKGROUND DURING STAR TRANSIT	2.4259
MEAN NUMBER OF PULSES FROM DARK CURRENT DURING STAR TRANSIT	8.1193
PHOTOGRAPHIC MAG. OF NOISE	5.51
DETECTION THRESHOLD	55.00
MEAN VALUE OF OFF-PEAK MAXIMUM FOR CODE PATTERN	0.00

* SYSTEM CHARACTERISTICS

MINIMUM NUMBER OF STARS IN FIELD OF VIEW WITH LIMITING MAGNITUDE AND BRIGHTER	4
ACCURACY OF ATTITUDE DETERMINATION	1.50 ARC MINUTES
PROBABILITY OF CORRECT STAR-PATTERN RECOGNITION	0.9
PATTERN RECOGNITION TECHNIQUE	
MEAN NUMBER OF STEPS FOR PATTERN RECOGNITION	

Sector from 240° to 360° eliminated

* DESIGN FOR SCANNING OPTICAL SYSTEM * NO. SADS

* OPTICAL SYSTEM

APERTURE DIAMETER	0.864 INCHES
F NUMBER	3.283
FOCAL LENGTH (MAX.)	2.836 INCHES
IMAGE DIAMETER	1.452 ARC MINUTES
FIELD OF VIEW	20.000 DEGREES
FIELD OF VIEW SHAPE	CIRCULAR
OPTICAL EFFICIENCY	0.75
OPTICAL ARRANGEMENT	REFRACTING OPTICS
SPECTRAL FILTER	NONE

* RETICLE CONFIGURATION

WIDTH OF SLITS	1.452 ARC MIN	
	0.345 TO	2.014 MILS
LENGTH OF SLITS	20.000 DEGREES	1.000 IN.
SLIT SHAPE	TRUNCATED SECTOR	
CODE PATTERN	0001000000000000000000000	
	0000000000000000000000000	
NUMBER OF CODE GROUPS	1	
COLOR CODE	NONE	
RELATIVE ORIENTATION OF CODE GROUPS	ONE RADIAL SLIT	

* SENSOR AND DETECTION TECHNIQUE

TYPE OF DETECTOR	PHOTOMULTIPLIER EMR 541A-01-14 RUGGEDIZED
DARK CURRENT	2540.00 PULSES PER SECOND
TIME RESPONSE	50.00 NANOSECONDS
QUANTUM EFFICIENCY	0.1500
DETECTION TECHNIQUE	HOLDING FILTER,THRESHOLD
RMS SPREAD OF PULSE AMPLITUDES TO MEAN	1.22
CATHODE SIZE USEFUL CATHODE DIA.	1 INCH
NUMBER OF SCANS CORRELATED	1

* MOTION

SCAN PERIOD	6.00 SECONDS
ANGLE BETWEEN SPIN AXIS AND OPTICAL AXIS	14.00 DEGREES
STAR TRANSIT TIME (CENTRAL RAY)	1667.20 MICROSECONDS
POINTING DIRECTIONS	
RIGHT ASCENSION	110.00 TO 310.00 DEGREES
DECLINATION	-11.00 TO -11.00 DEGREES

* DESIGN EVALUATION *

POINTING DIRECTION

RIGHT ASCENSION	10.00	DEGREES
DECLINATION	-11.00	DEGREES

* TARGET CHARACTERISTICS

LIMITING STAR MAGNITUDE	4.37 PHOTOGRAPHIC
SPECTRAL CLASSES	ALL
PLANETS, SUN, OR EARTH IN FIELD OF VIEW	
SIGNIFICANCE OF EARTHS ATMOSPHERE	OUTSIDE ATMOSPHERE, HOWEVER, ANOTHER SCANNING CAMERA SCANS EARTH FOR 1/3 OF SCAN PERIOD AND IT HAS TELEMETRY PRIORITY OVER SADS SCANNER

* STAR TRANSIT CHARACTERISTICS FOR LIMITING-MAGNITUDE STAR

POSITION ACCURACY	0.242 ARC MINUTES
RELATIVE INTENSITY ACCURACY	0.20
PROBABILITY OF DETECTION	0.94
EXPECTED NUMBER OF WEAK STARS DETECTED PER SCAN	0.9072
EXPECTED NUMBER OF FALSE STAR DETECTIONS PER SCAN	0.0000

Sector from 0° to 120° eliminated

* SIGNAL AND NOISE CHARACTERISTICS

MEAN NUMBER OF PULSES FROM LIMITING MAG STAR DURING STAR TRANSIT	30.00
MEAN NUMBER OF PULSES FROM STELLAR BACKGROUND DURING STAR TRANSIT	1.4556
MEAN NUMBER OF PULSES FROM DARK CURRENT DURING STAR TRANSIT	4.2347
PHOTOGRAPHIC MAG. OF NOISE	6.17
DETECTION THRESHOLD	26.00
MEAN VALUE OF OFF-PEAK MAXIMUM FOR CODE PATTERN	0.00

* SYSTEM CHARACTERISTICS

MINIMUM NUMBER OF STARS IN FIELD OF VIEW WITH LIMITING MAGNITUDE AND BRIGHTER	4
ACCURACY OF ATTITUDE DETERMINATION	0.65 ARC MINUTES
PROBABILITY OF CORRECT STAR-PATTERN RECOGNITION	0.9
PATTERN RECOGNITION TECHNIQUE	
MEAN NUMBER OF STEPS FOR PATTERN RECOGNITION	

* DESIGN EVALUATION *

POINTING DIRECTION

RIGHT ASCENSION	155.00	DEGREES
DECLINATION	-11.00	DEGREES

* TARGET CHARACTERISTICS

LIMITING STAR MAGNITUDE	4.10 PHOTOGRAPHIC
SPECTRAL CLASSES	ALL
PLANETS, SUN, OR EARTH IN FIELD OF VIEW	
SIGNIFICANCE OF EARTHS ATMOSPHERE	OUTSIDE ATMOSPHERE, HOWEVER, ANOTHER SCANNING CAMERA SCANS EARTH FOR 1/3 OF SCAN PERIOD AND IT HAS TELEMETRY PRIORITY OVER SADS SCANNER

* STAR TRANSIT CHARACTERISTICS FOR LIMITING-MAGNITUDE STAR

POSITION ACCURACY	0.242 ARC MINUTES
RELATIVE INTENSITY ACCURACY	0.17
PROBABILITY OF DETECTION	0.93
EXPECTED NUMBER OF WEAK STARS DETECTED PER SCAN	0.1471
EXPECTED NUMBER OF FALSE STAR DETECTIONS PER SCAN	0.0000

Sector from 120^{o} to 240^{o} eliminated

* SIGNAL AND NOISE CHARACTERISTICS

MEAN NUMBER OF PULSES FROM LIMITING MAG STAR DURING STAR TRANSIT	38.47
MEAN NUMBER OF PULSES FROM STELLAR BACKGROUND DURING STAR TRANSIT	2.4259
MEAN NUMBER OF PULSES FROM DARK CURRENT DURING STAR TRANSIT	4.2347
PHOTOGRAPHIC MAG. OF NOISE	6.00
DETECTION THRESHOLD	35.00
MEAN VALUE OF OFF-PEAK MAXIMUM FOR CODE PATTERN	0.00

* SYSTEM CHARACTERISTICS

MINIMUM NUMBER OF STARS IN FIELD OF VIEW WITH LIMITING MAGNITUDE AND BRIGHTER	4
ACCURACY OF ATTITUDE DETERMINATION	1.55 ARC MINUTES
PROBABILITY OF CORRECT STAR-PATTERN RECOGNITION	0.9
PATTERN RECOGNITION TECHNIQUE	
MEAN NUMBER OF STEPS FOR PATTERN RECOGNITION	

* DESIGN EVALUATION *

POINTING DIRECTION
RIGHT ASCENSION 155.00 DEGREES
DECLINATION -11.00 DEGREES

* TARGET CHARACTERISTICS

LIMITING STAR MAGNITUDE	3.70 PHOTOGRAPHIC
SPECTRAL CLASSES	ALL
PLANETS, SUN, OR EARTH IN FIELD OF VIEW	
SIGNIFICANCE OF EARTHS ATMOSPHERE	OUTSIDE ATMOSPHERE, HOWEVER, ANOTHER SCANNING CAMERA SCANS EARTH FOR 1/3 OF SCAN PERIOD AND IT HAS TELEMETRY PRIORITY OVER SADS SCANNER

* STAR TRANSIT CHARACTERISTICS FOR LIMITING-MAGNITUDE STAR

POSITION ACCURACY	0.242 ARC MINUTES
RELATIVE INTENSITY ACCURACY	0.14
PROBABILITY OF DETECTION	0.92
EXPECTED NUMBER OF WEAK STARS DETECTED PER SCAN	0.0025
EXPECTED NUMBER OF FALSE STAR DETECTIONS PER SCAN	0.0000

* SIGNAL AND NOISE CHARACTERISTICS

MEAN NUMBER OF PULSES FROM LIMITING MAG STAR DURING STAR TRANSIT	55.61
MEAN NUMBER OF PULSES FROM STELLAR BACKGROUND DURING STAR TRANSIT	2.4259
MEAN NUMBER OF PULSES FROM DARK CURRENT DURING STAR TRANSIT	4.2347
PHOTOGRAPHIC MAG. OF NOISE	6.00
DETECTION THRESHOLD	51.00
MEAN VALUE OF OFF-PEAK MAXIMUM FOR CODE PATTERN	0.00

* SYSTEM CHARACTERISTICS

MINIMUM NUMBER OF STARS IN FIELD OF VIEW WITH LIMITING MAGNITUDE AND BRIGHTER	4
ACCURACY OF ATTITUDE DETERMINATION	1.50 ARC MINUTES
PROBABILITY OF CORRECT STAR-PATTERN RECOGNITION	0.9
PATTERN RECOGNITION TECHNIQUE	
MEAN NUMBER OF STEPS FOR PATTERN RECOGNITION	

Sector from 240° to 360° eliminated

NO. SADS

* DESIGN FOR SCANNING OPTICAL SYSTEM *

* OPTICAL SYSTEM

APERTURE DIAMETER	1.999 INCHES
F NUMBER	2.400
FOCAL LENGTH (MAX.)	4.798 INCHES
IMAGE DIAMETER	1.452 ARC MINUTES
FIELD OF VIEW	20.000 DEGREES
FIELD OF VIEW SHAPE	CIRCULAR
OPTICAL EFFICIENCY	0.75
OPTICAL ARRANGEMENT	REFRACTING OPTICS
SPECTRAL FILTER	NONE

* RETICLE CONFIGURATION

WIDTH OF SLITS	1.452 ARC MIN	
	0.584 TO	3.407 MILS
LENGTH OF SLITS	20.000 DEGREES	1.692 IN.
SLIT SHAPE	TRUNCATED SECTOR	
CODE PATTERN	000100000000000000000000	
	000000000000000000000000	
NUMBER OF CODE GROUPS	1	
COLOR CODE	NONE	
RELATIVE ORIENTATION OF CODE GROUPS	ONE RADIAL SLIT	

* SENSOR AND DETECTION TECHNIQUE

TYPE OF DETECTOR	PHOTOMULTIPLIER EMR 543D-01 RUGGEDIZED
DARK CURRENT	80.00 PULSES PER SECOND
TIME RESPONSE	50.00 NANOSECONDS
QUANTUM EFFICIENCY	0.0280
DETECTION TECHNIQUE	HOLDING FILTER,THRESHOLD
RMS SPREAD OF PULSE AMPLITUDES TO MEAN	1.22
CATHODE SIZE	
ACTIVE CATHODE DIA.	1.69 IN.
NUMBER OF SCANS CORRELATED	1

* MOTION

SCAN PERIOD	6.00 SECONDS
ANGLE BETWEEN SPIN AXIS AND OPTICAL AXIS	14.00 DEGREES
STAR TRANSIT TIME (CENTRAL RAY)	1667.20 MICROSECONDS
POINTING DIRECTIONS	
RIGHT ASCENSION	110.00 TO 310.00 DEGREES
DECLINATION	-11.00 TO -11.00 DEGREES

* DESIGN EVALUATION *

POINTING DIRECTION

RIGHT ASCENSION	10.00	DEGREES
DECLINATION	-11.00	DEGREES

* TARGET CHARACTERISTICS

LIMITING STAR MAGNITUDE	4.37 PHOTOGRAPHIC
SPECTRAL CLASSES	ALL
PLANETS, SUN, OR EARTH IN FIELD OF VIEW	
SIGNIFICANCE OF EARTHS ATMOSPHERE	OUTSIDE ATMOSPHERE, HOWEVER, ANOTHER SCANNING CAMERA SCANS EARTH FOR 1/3 OF SCAN PERIOD AND IT HAS TELEMETRY PRIORITY OVER SADS SCANNER

* STAR TRANSIT CHARACTERISTICS FOR LIMITING-MAGNITUDE STAR

POSITION ACCURACY	0.242 ARC MINUTES
RELATIVE INTENSITY ACCURACY	0.19
PROBABILITY OF DETECTION	0.95
EXPECTED NUMBER OF WEAK STARS DETECTED PER SCAN	0.4685
EXPECTED NUMBER OF FALSE STAR DETECTIONS PER SCAN	0.0000

Sector from 0° to 120° eliminated

* SIGNAL AND NOISE CHARACTERISTICS

MEAN NUMBER OF PULSES FROM LIMITING MAG STAR DURING STAR TRANSIT	30.00
MEAN NUMBER OF PULSES FROM STELLAR BACKGROUND DURING STAR TRANSIT	1.4556
MEAN NUMBER OF PULSES FROM DARK CURRENT DURING STAR TRANSIT	0.1334
PHOTOGRAPHIC MAG. OF NOISE	7.56
DETECTION THRESHOLD	22.00
MEAN VALUE OF OFF-PEAK MAXIMUM FOR CODE PATTERN	0.00

* SYSTEM CHARACTERISTICS

MINIMUM NUMBER OF STARS IN FIELD OF VIEW WITH LIMITING MAGNITUDE AND BRIGHTER	4
ACCURACY OF ATTITUDE DETERMINATION	0.65 ARC MINUTES
PROBABILITY OF CORRECT STAR-PATTERN RECOGNITION	0.9
PATTERN RECOGNITION TECHNIQUE	
MEAN NUMBER OF STEPS FOR PATTERN RECOGNITION	

* DESIGN EVALUATION *

POINTING DIRECTION

RIGHT ASCENSION	155.00	DEGREES
DECLINATION	-11.00	DEGREES

* TARGET CHARACTERISTICS

LIMITING STAR MAGNITUDE	4.10 PHOTOGRAPHIC
SPECTRAL CLASSES	ALL
PLANETS, SUN, OR EARTH IN FIELD OF VIEW	
SIGNIFICANCE OF EARTHS ATMOSPHERE	OUTSIDE ATMOSPHERE, HOWEVER, ANOTHER SCANNING CAMERA SCANS EARTH FOR 1/3 OF SCAN PERIOD AND IT HAS TELEMETRY PRIORITY OVER SADS SCANNER

* STAR TRANSIT CHARACTERISTICS FOR LIMITING-MAGNITUDE STAR

POSITION ACCURACY	0.242 ARC MINUTES
RELATIVE INTENSITY ACCURACY	0.17
PROBABILITY OF DETECTION	0.94
EXPECTED NUMBER OF WEAK STARS DETECTED PER SCAN	0.0650
EXPECTED NUMBER OF FALSE STAR DETECTIONS PER SCAN	0.0000

* SIGNAL AND NOISE CHARACTERISTICS

MEAN NUMBER OF PULSES FROM LIMITING MAG STAR DURING STAR TRANSIT	38.47
MEAN NUMBER OF PULSES FROM STELLAR BACKGROUND DURING STAR TRANSIT	2.4259
MEAN NUMBER OF PULSES FROM DARK CURRENT DURING STAR TRANSIT	0.1334
PHOTOGRAPHIC MAG. OF NOISE	7.04
DETECTION THRESHOLD	31.00
MEAN VALUE OF OFF-PEAK MAXIMUM FOR CODE PATTERN	0.00

* SYSTEM CHARACTERISTICS

MINIMUM NUMBER OF STARS IN FIELD OF VIEW WITH LIMITING MAGNITUDE AND BRIGHTER	4
ACCURACY OF ATTITUDE DETERMINATION	1.55 ARC MINUTES
PROBABILITY OF CORRECT STAR-PATTERN RECOGNITION	0.9
PATTERN RECOGNITION TECHNIQUE	
MEAN NUMBER OF STEPS FOR PATTERN RECOGNITION	

Sector from 120° to 240° eliminated

* DESIGN EVALUATION *

POINTING DIRECTION		
RIGHT ASCENSION	155.00	DEGREES
DECLINATION	-11.00	DEGREES

* TARGET CHARACTERISTICS

LIMITING STAR MAGNITUDE	3.70 PHOTOGRAPHIC
SPECTRAL CLASSES	ALL
PLANETS, SUN, OR EARTH IN FIELD OF VIEW	
SIGNIFICANCE OF EARTHS ATMOSPHERE	OUTSIDE ATMOSPHERE, HOWEVER, ANOTHER SCANNING CAMERA SCANS EARTH FOR 1/3 OF SCAN PERIOD AND IT HAS TELEMETRY PRIORITY OVER SADS SCANNER

* STAR TRANSIT CHARACTERISTICS FOR LIMITING-MAGNITUDE STAR

POSITION ACCURACY	0.242 ARC MINUTES
RELATIVE INTENSITY ACCURACY	0.14
PROBABILITY OF DETECTION	0.91
EXPECTED NUMBER OF WEAK STARS DETECTED PER SCAN	0.0004
EXPECTED NUMBER OF FALSE STAR DETECTIONS PER SCAN	0.0000

* SIGNAL AND NOISE CHARACTERISTICS

MEAN NUMBER OF PULSES FROM LIMITING MAG STAR DURING STAR TRANSIT	55.61
MEAN NUMBER OF PULSES FROM STELLAR BACKGROUND DURING STAR TRANSIT	2.4259
MEAN NUMBER OF PULSES FROM DARK CURRENT DURING STAR TRANSIT	0.1334
PHOTOGRAPHIC MAG. OF NOISE	7.04
DETECTION THRESHOLD	48.00
MEAN VALUE OF OFF-PEAK MAXIMUM FOR CODE PATTERN	0.00

* SYSTEM CHARACTERISTICS

MINIMUM NUMBER OF STARS IN FIELD OF VIEW WITH LIMITING MAGNITUDE AND BRIGHTER	4
ACCURACY OF ATTITUDE DETERMINATION	1.50 ARC MINUTES
PROBABILITY OF CORRECT STAR-PATTERN RECOGNITION	0.9
PATTERN RECOGNITION TECHNIQUE	
MEAN NUMBER OF STEPS FOR PATTERN RECOGNITION	

Sector from 240° to 360° eliminated

* DESIGN FOR SCANNING OPTICAL SYSTEM * NO. SADS

* OPTICAL SYSTEM

APERTURE DIAMETER	0.894 INCHES
F NUMBER	5.360
FOCAL LENGTH (MAX.)	4.792 INCHES
IMAGE DIAMETER	1.452 ARC MINUTES
FIELD OF VIEW	20.000 DEGREES
FIELD OF VIEW SHAPE	CIRCULAR
OPTICAL EFFICIENCY	0.75
OPTICAL ARRANGEMENT	REFRACTING OPTICS
SPECTRAL FILTER	NONE

* RETICLE CONFIGURATION

WIDTH OF SLITS	1.452 ARC MIN
	0.584 TO 3.403 MILS
LENGTH OF SLITS	20.000 DEGREES 1.690 IN.
SLIT SHAPE	TRUNCATED SECTOR
CODE PATTERN	000100000000000000000000
	000000000000000000000000
NUMBER OF CODE GROUPS	1
COLOR CODE	NONE
RELATIVE ORIENTATION OF CODE GROUPS	ONE RADIAL SLIT

* SENSOR AND DETECTION TECHNIQUE

TYPE OF DETECTOR	PHOTOMULTIPLIER EMR 543A-01 RUGGEDIZED
DARK CURRENT	5140.00 PULSES PER SECOND
TIME RESPONSE	50.00 NANOSECONDS
QUANTUM EFFICIENCY	0.1400
DETECTION TECHNIQUE	HOLDING FILTER,THRESHOLD
RMS SPREAD OF PULSE AMPLITUDES TO MEAN	1.22
CATHODE SIZE	
ACTIVE CATHODE DIA.	1.69 IN.
NUMBER OF SCANS CORRELATED	1

* MOTION

SCAN PERIOD	6.00 SECONDS
ANGLE BETWEEN SPIN AXIS AND OPTICAL AXIS	14.00 DEGREES
STAR TRANSIT TIME (CENTRAL RAY)	1667.20 MICROSECONDS
POINTING DIRECTIONS	
RIGHT ASCENSION	110.00 TO 310.00 DEGREES
DECLINATION	-11.00 TO -11.00 DEGREES

* DESIGN EVALUATION *

POINTING DIRECTION

RIGHT ASCENSION	10.00	DEGREES
DECLINATION	-11.00	DEGREES

* TARGET CHARACTERISTICS

LIMITING STAR MAGNITUDE	4.37 PHOTOGRAPHIC
SPECTRAL CLASSES	ALL
PLANETS, SUN, OR EARTH IN FIELD OF VIEW	
SIGNIFICANCE OF EARTHS ATMOSPHERE	OUTSIDE ATMOSPHERE, HOWEVER, ANOTHER SCANNING CAMERA SCANS EARTH FOR 1/3 OF SCAN PERIOD AND IT HAS TELEMETRY PRIORITY OVER SADS SCANNER

* SIGNAL AND NOISE CHARACTERISTICS

MEAN NUMBER OF PULSES FROM LIMITING MAG STAR DURING STAR TRANSIT	30.00
MEAN NUMBER OF PULSES FROM STELLAR BACKGROUND DURING STAR TRANSIT	1.4556
MEAN NUMBER OF PULSES FROM DARK CURRENT DURING STAR TRANSIT	8.5694
PHOTOGRAPHIC MAG. OF NOISE	5.56
DETECTION THRESHOLD	30.00
MEAN VALUE OF OFF-PEAK MAXIMUM FOR CODE PATTERN	0.00

* STAR TRANSIT CHARACTERISTICS FOR LIMITING-MAGNITUDE STAR

POSITION ACCURACY	0.242 ARC MINUTES
RELATIVE INTENSITY ACCURACY	0.21
PROBABILITY OF DETECTION	0.94
EXPECTED NUMBER OF WEAK STARS DETECTED PER SCAN	1.6093
EXPECTED NUMBER OF FALSE STAR DETECTIONS PER SCAN	0.0000

* SYSTEM CHARACTERISTICS

MINIMUM NUMBER OF STARS IN FIELD OF VIEW WITH LIMITING MAGNITUDE AND BRIGHTER	4
ACCURACY OF ATTITUDE DETERMINATION	0.65 ARC MINUTES
PROBABILITY OF CORRECT STAR-PATTERN RECOGNITION	0.9
PATTERN RECOGNITION TECHNIQUE	
MEAN NUMBER OF STEPS FOR PATTERN RECOGNITION	

Sector from 0° to 120° eliminated

* DESIGN EVALUATION *

POINTING DIRECTION

RIGHT ASCENSION	155.00	DEGREES
DECLINATION	-11.00	DEGREES

* TARGET CHARACTERISTICS

LIMITING STAR MAGNITUDE	4.10 PHOTOGRAPHIC
SPECTRAL CLASSES	ALL
PLANETS, SUN, OR EARTH IN FIELD OF VIEW	
SIGNIFICANCE OF EARTHS ATMOSPHERE	OUTSIDE ATMOSPHERE, HOWEVER, ANOTHER SCANNING CAMERA SCANS EARTH FOR 1/3 OF SCAN PERIOD AND IT HAS TELEMETRY PRIORITY OVER SADS SCANNER

* STAR TRANSIT CHARACTERISTICS FOR LIMITING-MAGNITUDE STAR

POSITION ACCURACY	0.242 ARC MINUTES
RELATIVE INTENSITY ACCURACY	0.18
PROBABILITY OF DETECTION	0.93
EXPECTED NUMBER OF WEAK STARS DETECTED PER SCAN	0.3077
EXPECTED NUMBER OF FALSE STAR DETECTIONS PER SCAN	0.0000

* SIGNAL AND NOISE CHARACTERISTICS

MEAN NUMBER OF PULSES FROM LIMITING MAG STAR DURING STAR TRANSIT	38.47
MEAN NUMBER OF PULSES FROM STELLAR BACKGROUND DURING STAR TRANSIT	2.4259
MEAN NUMBER OF PULSES FROM DARK CURRENT DURING STAR TRANSIT	8.5694
PHOTOGRAPHIC MAG. OF NOISE	5.46
DETECTION THRESHOLD	39.00
MEAN VALUE OF OFF-PEAK MAXIMUM FOR CODE PATTERN	0.00

* SYSTEM CHARACTERISTICS

MINIMUM NUMBER OF STARS IN FIELD OF VIEW WITH LIMITING MAGNITUDE AND BRIGHTER	4
ACCURACY OF ATTITUDE DETERMINATION	1.55 ARC MINUTES
PROBABILITY OF CORRECT STAR-PATTERN RECOGNITION	0.9
PATTERN RECOGNITION TECHNIQUE	
MEAN NUMBER OF STEPS FOR PATTERN RECOGNITION	

Sector from 120° to 240° eliminated

* DESIGN EVALUATION *

POINTING DIRECTION		
RIGHT ASCENSION	155.00	DEGREES
DECLINATION	-11.00	DEGREES

* TARGET CHARACTERISTICS

LIMITING STAR MAGNITUDE	3.70 PHOTOGRAPHIC
SPECTRAL CLASSES	ALL
PLANETS, SUN, OR EARTH IN FIELD OF VIEW	
SIGNIFICANCE OF EARTHS ATMOSPHERE	OUTSIDE ATMOSPHERE, HOWEVER, ANOTHER SCANNING CAMERA SCANS EARTH FOR 1/3 OF SCAN PERIOD AND IT HAS TELEMETRY PRIORITY OVER SADS SCANNER

* STAR TRANSIT CHARACTERISTICS FOR LIMITING-MAGNITUDE STAR

POSITION ACCURACY	0.242 ARC MINUTES
RELATIVE INTENSITY ACCURACY	0.15
PROBABILITY OF DETECTION	0.92
EXPECTED NUMBER OF WEAK STARS DETECTED PER SCAN	0.0072
EXPECTED NUMBER OF FALSE STAR DETECTIONS PER SCAN	0.0000

* SIGNAL AND NOISE CHARACTERISTICS

MEAN NUMBER OF PULSES FROM LIMITING MAG STAR DURING STAR TRANSIT	55.61
MEAN NUMBER OF PULSES FROM STELLAR BACKGROUND DURING STAR TRANSIT	2.4259
MEAN NUMBER OF PULSES FROM DARK CURRENT DURING STAR TRANSIT	8.5694
PHOTOGRAPHIC MAG. OF NOISE	5.46
DETECTION THRESHOLD	55.00
MEAN VALUE OF OFF-PEAK MAXIMUM FOR CODE PATTERN	0.00

* SYSTEM CHARACTERISTICS

MINIMUM NUMBER OF STARS IN FIELD OF VIEW WITH LIMITING MAGNITUDE AND BRIGHTER	4
ACCURACY OF ATTITUDE DETERMINATION	1.50 ARC MINUTES
PROBABILITY OF CORRECT STAR-PATTERN RECOGNITION	0.9
PATTERN RECOGNITION TECHNIQUE	
MEAN NUMBER OF STEPS FOR PATTERN RECOGNITION	

Sector from 240° to 360° eliminated

* DESIGN FOR SCANNING OPTICAL SYSTEM * NO. SADS

* OPTICAL SYSTEM

APERTURE DIAMETER	0.894 INCHES
F NUMBER	8.246
FOCAL LENGTH (MAX.)	7.373 INCHES
IMAGE DIAMETER	1.452 ARC MINUTES
FIELD OF VIEW	20.000 DEGREES
FIELD OF VIEW SHAPE	CIRCULAR
OPTICAL EFFICIENCY	0.75
OPTICAL ARRANGEMENT	REFRACTING OPTICS
SPECTRAL FILTER	NONE

* RETICLE CONFIGURATION

WIDTH OF SLITS	1.452 ARC MIN 0.898 TO 5.235 MILS
LENGTH OF SLITS	20.000 DEGREES 2.600 IN.
SLIT SHAPE	TRUNCATED SECTOR
CODE PATTERN	000100000000000000000000 000000000000000000000000
NUMBER OF CODE GROUPS	1
COLOR CODE	NONE
RELATIVE ORIENTATION OF CODE GROUPS	ONE RADIAL SLIT

* SENSOR AND DETECTION TECHNIQUE

TYPE OF DETECTOR	PHOTOMULTIPLIER EMR 544A-01 RUGGEDIZED
DARK CURRENT	8670.00 PULSES PER SECOND
TIME RESPONSE	50.00 NANOSECONDS
QUANTUM EFFICIENCY	0.1400
DETECTION TECHNIQUE	HOLDING FILTER,THRESHOLD
RMS SPREAD OF PULSE AMPLITUDES TO MEAN	1.22
CATHODE SIZE ACTIVE CATHODE DIA.	2.6 IN.
NUMBER OF SCANS CORRELATED	1

* MOTION

SCAN PERIOD	6.00 SECONDS
ANGLE BETWEEN SPIN AXIS AND OPTICAL AXIS	14.00 DEGREES
STAR TRANSIT TIME (CENTRAL RAY)	1667.20 MICROSECONDS
POINTING DIRECTIONS	
RIGHT ASCENSION	110.00 TO 310.00 DEGREES
DECLINATION	-11.00 TO -11.00 DEGREES

* DESIGN EVALUATION *

POINTING DIRECTION		
RIGHT ASCENSION	10.00	DEGREES
DECLINATION	-11.00	DEGREES

* TARGET CHARACTERISTICS

LIMITING STAR MAGNITUDE	4.37 PHOTOGRAPHIC
SPECTRAL CLASSES	ALL
PLANETS, SUN, OR EARTH IN FIELD OF VIEW	
SIGNIFICANCE OF EARTHS ATMOSPHERE	OUTSIDE ATMOSPHERE, HOWEVER, ANOTHER SCANNING CAMERA SCANS EARTH FOR 1/3 OF SCAN PERIOD AND IT HAS TELEMETRY PRIORITY OVER SADS SCANNER

* SIGNAL AND NOISE CHARACTERISTICS

MEAN NUMBER OF PULSES FROM LIMITING MAG STAR DURING STAR TRANSIT	30.00
MEAN NUMBER OF PULSES FROM STELLAR BACKGROUND DURING STAR TRANSIT	1.4556
MEAN NUMBER OF PULSES FROM DARK CURRENT DURING STAR TRANSIT	14.4547
PHOTOGRAPHIC MAG. OF NOISE	5.06
DETECTION THRESHOLD	35.00
MEAN VALUE OF OFF-PEAK MAXIMUM FOR CODE PATTERN	0.00

* STAR TRANSIT CHARACTERISTICS FOR LIMITING-MAGNITUDE STAR

POSITION ACCURACY	0.242 ARC MINUTES
RELATIVE INTENSITY ACCURACY	0.23
PROBABILITY OF DETECTION	0.94
EXPECTED NUMBER OF WEAK STARS DETECTED PER SCAN	3.2675
EXPECTED NUMBER OF FALSE STAR DETECTIONS PER SCAN	0.0250

* SYSTEM CHARACTERISTICS

MINIMUM NUMBER OF STARS IN FIELD OF VIEW WITH LIMITING MAGNITUDE AND BRIGHTER	4
ACCURACY OF ATTITUDE DETERMINATION	0.65 ARC MINUTES
PROBABILITY OF CORRECT STAR-PATTERN RECOGNITION	0.9
PATTERN RECOGNITION TECHNIQUE	
MEAN NUMBER OF STEPS FOR PATTERN RECOGNITION	

Sector from 0° to 120° eliminated

* DESIGN EVALUATION *

POINTING DIRECTION

RIGHT ASCENSION	155.00	DEGREES
DECLINATION	-11.00	DEGREES

* TARGET CHARACTERISTICS

LIMITING STAR MAGNITUDE	4.10 PHOTOGRAPHIC
SPECTRAL CLASSES	ALL
PLANETS, SUN, OR EARTH IN FIELD OF VIEW	
SIGNIFICANCE OF EARTHS ATMOSPHERE	OUTSIDE ATMOSPHERE, HOWEVER, ANOTHER SCANNING CAMERA SCANS EARTH FOR 1/3 OF SCAN PERIOD AND IT HAS TELEMETRY PRIORITY OVER SADS SCANNER

* STAR TRANSIT CHARACTERISTICS FOR LIMITING=MAGNITUDE STAR

POSITION ACCURACY	0.242 ARC MINUTES
RELATIVE INTENSITY ACCURACY	0.19
PROBABILITY OF DETECTION	0.94
EXPECTED NUMBER OF WEAK STARS DETECTED PER SCAN	0.7586
EXPECTED NUMBER OF FALSE STAR DETECTIONS PER SCAN	0.0000

* SIGNAL AND NOISE CHARACTERISTICS

MEAN NUMBER OF PULSES FROM LIMITING MAG STAR DURING STAR TRANSIT	38.47
MEAN NUMBER OF PULSES FROM STELLAR BACKGROUND DURING STAR TRANSIT	2.4259
MEAN NUMBER OF PULSES FROM DARK CURRENT DURING STAR TRANSIT	14.4547
PHOTOGRAPHIC MAG. OF NOISE	4.99
DETECTION THRESHOLD	44.00
MEAN VALUE OF OFF-PEAK MAXIMUM FOR CODE PATTERN	0.00

* SYSTEM CHARACTERISTICS

MINIMUM NUMBER OF STARS IN FIELD OF VIEW WITH LIMITING MAGNITUDE AND BRIGHTER	4
ACCURACY OF ATTITUDE DETERMINATION	1.55 ARC MINUTES
PROBABILITY OF CORRECT STAR-PATTERN RECOGNITION	0.9
PATTERN RECOGNITION TECHNIQUE	
MEAN NUMBER OF STEPS FOR PATTERN RECOGNITION	

Sector from 120° to 240° eliminated

* DESIGN EVALUATION *

POINTING DIRECTION

RIGHT ASCENSION	155.00	DEGREES
DECLINATION	-11.00	DEGREES

* TARGET CHARACTERISTICS

LIMITING STAR MAGNITUDE	3.70 PHOTOGRAPHIC
SPECTRAL CLASSES	ALL
PLANETS, SUN, OR EARTH IN FIELD OF VIEW	
SIGNIFICANCE OF EARTHS ATMOSPHERE	OUTSIDE ATMOSPHERE, HOWEVER, ANOTHER SCANNING CAMERA SCANS EARTH FOR 1/3 OF SCAN PERIOD AND IT HAS TELEMETRY PRIORITY OVER SADS SCANNER

* STAR TRANSIT CHARACTERISTICS FOR LIMITING-MAGNITUDE STAR

POSITION ACCURACY	0.242 ARC MINUTES
RELATIVE INTENSITY ACCURACY	0.15
PROBABILITY OF DETECTION	0.91
EXPECTED NUMBER OF WEAK STARS DETECTED PER SCAN	0.0166
EXPECTED NUMBER OF FALSE STAR DETECTIONS PER SCAN	0.0000

Sector from 240° to 360° eliminated

* SIGNAL AND NOISE CHARACTERISTICS

MEAN NUMBER OF PULSES FROM LIMITING MAG STAR DURING STAR TRANSIT	55.61
MEAN NUMBER OF PULSES FROM STELLAR BACKGROUND DURING STAR TRANSIT	2.4259
MEAN NUMBER OF PULSES FROM DARK CURRENT DURING STAR TRANSIT	14.4547
PHOTOGRAPHIC MAG. OF NOISE	4.99
DETECTION THRESHOLD	61.00
MEAN VALUE OF OFF-PEAK MAXIMUM FOR CODE PATTERN	0.00

* SYSTEM CHARACTERISTICS

MINIMUM NUMBER OF STARS IN FIELD OF VIEW WITH LIMITING MAGNITUDE AND BRIGHTER	4
ACCURACY OF ATTITUDE DETERMINATION	1.50 ARC MINUTES
PROBABILITY OF CORRECT STAR-PATTERN RECOGNITION	0.9
PATTERN RECOGNITION TECHNIQUE	
MEAN NUMBER OF STEPS FOR PATTERN RECOGNITION	

* DESIGN FOR SCANNING OPTICAL SYSTEM *   NO. SADS

* OPTICAL SYSTEM

APERTURE DIAMETER	0.669 INCHES
F NUMBER	4.238
FOCAL LENGTH (MAX.)	2.836 INCHES
IMAGE DIAMETER	1.452 ARC MINUTES
FIELD OF VIEW	20.000 DEGREES
FIELD OF VIEW SHAPE	CIRCULAR
OPTICAL EFFICIENCY	0.75
OPTICAL ARRANGEMENT	REFRACTING OPTICS
SPECTRAL FILTER	NONE

* RETICLE CONFIGURATION

WIDTH OF SLITS	1.452 ARC MIN
	0.345 TO 2.014 MILS
LENGTH OF SLITS	20.000 DEGREES 1.000 IN.
SLIT SHAPE	TRUNCATED SECTOR
CODE PATTERN	000100000000000000000000 000000000000000000000000
NUMBER OF CODE GROUPS	1
COLOR CODE	NONE
RELATIVE ORIENTATION OF CODE GROUPS	ONE RADIAL SLIT

* SENSOR AND DETECTION TECHNIQUE

TYPE OF DETECTOR	PHOTOMULTIPLIER EMR 541F-01-14 RUGGEDIZED
DARK CURRENT	13.48 PULSES PER SECOND
TIME RESPONSE	50.00 NANOSECONDS
QUANTUM EFFICIENCY	0.2500
DETECTION TECHNIQUE	HOLDING FILTER,THRESHOLD
RMS SPREAD OF PULSE AMPLITUDES TO MEAN	1.22
CATHODE SIZE ACTIVE CATHODE DIA.	1.0 IN.
NUMBER OF SCANS CORRELATED	1

* MOTION

SCAN PERIOD	6.00 SECONDS
ANGLE BETWEEN SPIN AXIS AND OPTICAL AXIS	14.00 DEGREES
STAR TRANSIT TIME (CENTRAL RAY)	1667.20 MICROSECONDS
POINTING DIRECTIONS	
RIGHT ASCENSION	110.00 TO 310.00 DEGREES
DECLINATION	-11.00 TO =11.00 DEGREES

* DESIGN EVALUATION *

POINTING DIRECTION		
RIGHT ASCENSION	10.00	DEGREES
DECLINATION	-11.00	DEGREES

* TARGET CHARACTERISTICS

LIMITING STAR MAGNITUDE	4.37 PHOTOGRAPHIC
SPECTRAL CLASSES	ALL
PLANETS, SUN, OR EARTH IN FIELD OF VIEW	
SIGNIFICANCE OF EARTHS ATMOSPHERE	OUTSIDE ATMOSPHERE, HOWEVER, ANOTHER SCANNING CAMERA SCANS EARTH FOR 1/3 OF SCAN PERIOD AND IT HAS TELEMETRY PRIORITY OVER SADS SCANNER

* STAR TRANSIT CHARACTERISTICS FOR LIMITING-MAGNITUDE STAR

POSITION ACCURACY	0.242 ARC MINUTES
RELATIVE INTENSITY ACCURACY	0.19
PROBABILITY OF DETECTION	0.95
EXPECTED NUMBER OF WEAK STARS DETECTED PER SCAN	0.4293
EXPECTED NUMBER OF FALSE STAR DETECTIONS PER SCAN	0.0000

* SIGNAL AND NOISE CHARACTERISTICS

MEAN NUMBER OF PULSES FROM LIMITING MAG STAR DURING STAR TRANSIT	30.00
MEAN NUMBER OF PULSES FROM STELLAR BACKGROUND DURING STAR TRANSIT	1.4556
MEAN NUMBER OF PULSES FROM DARK CURRENT DURING STAR TRANSIT	0.0225
PHOTOGRAPHIC MAG. OF NOISE	7.64
DETECTION THRESHOLD	22.00
MEAN VALUE OF OFF-PEAK MAXIMUM FOR CODE PATTERN	0.00

* SYSTEM CHARACTERISTICS

MINIMUM NUMBER OF STARS IN FIELD OF VIEW WITH LIMITING MAGNITUDE AND BRIGHTER	4
ACCURACY OF ATTITUDE DETERMINATION	0.65 ARC MINUTES
PROBABILITY OF CORRECT STAR-PATTERN RECOGNITION	0.9
PATTERN RECOGNITION TECHNIQUE	
MEAN NUMBER OF STEPS FOR PATTERN RECOGNITION	

Sector from 0° to 120° eliminated

* DESIGN EVALUATION *

POINTING DIRECTION

RIGHT ASCENSION	155.00	DEGREES
DECLINATION	-11.00	DEGREES

* TARGET CHARACTERISTICS

LIMITING STAR MAGNITUDE	4.10 PHOTOGRAPHIC
SPECTRAL CLASSES	ALL
PLANETS, SUN, OR EARTH IN FIELD OF VIEW	
SIGNIFICANCE OF EARTHS ATMOSPHERE	OUTSIDE ATMOSPHERE, HOWEVER, ANOTHER SCANNING CAMERA SCANS EARTH FOR 1/3 OF SCAN PERIOD AND IT HAS TELEMETRY PRIORITY OVER SADS SCANNER

* STAR TRANSIT CHARACTERISTICS FOR LIMITING-MAGNITUDE STAR

POSITION ACCURACY	0.242 ARC MINUTES
RELATIVE INTENSITY ACCURACY	0.17
PROBABILITY OF DETECTION	0.93
EXPECTED NUMBER OF WEAK STARS DETECTED PER SCAN	0.0591
EXPECTED NUMBER OF FALSE STAR DETECTIONS PER SCAN	0.0000

Sector from 120° to 240° eliminated

* SIGNAL AND NOISE CHARACTERISTICS

MEAN NUMBER OF PULSES FROM LIMITING MAG STAR DURING STAR TRANSIT	38.47
MEAN NUMBER OF PULSES FROM STELLAR BACKGROUND DURING STAR TRANSIT	2.4259
MEAN NUMBER OF PULSES FROM DARK CURRENT DURING STAR TRANSIT	0.0225
PHOTOGRAPHIC MAG. OF NOISE	7.09
DETECTION THRESHOLD	31.00
MEAN VALUE OF OFF-PEAK MAXIMUM FOR CODE PATTERN	0.00

* SYSTEM CHARACTERISTICS

MINIMUM NUMBER OF STARS IN FIELD OF VIEW WITH LIMITING MAGNITUDE AND BRIGHTER	4
ACCURACY OF ATTITUDE DETERMINATION	1.55 ARC MINUTES
PROBABILITY OF CORRECT STAR-PATTERN RECOGNITION	0.9
PATTERN RECOGNITION TECHNIQUE	
MEAN NUMBER OF STEPS FOR PATTERN RECOGNITION	

* DESIGN EVALUATION *

POINTING DIRECTION

RIGHT ASCENSION	155.00	DEGREES
DECLINATION	-11.00	DEGREES

* TARGET CHARACTERISTICS

LIMITING STAR MAGNITUDE	3.70 PHOTOGRAPHIC
SPECTRAL CLASSES	ALL
PLANETS, SUN, OR EARTH IN FIELD OF VIEW	
SIGNIFICANCE OF EARTHS ATMOSPHERE	OUTSIDE ATMOSPHERE, HOWEVER, ANOTHER SCANNING CAMERA SCANS EARTH FOR 1/3 OF SCAN PERIOD AND IT HAS TELEMETRY PRIORITY OVER SADS SCANNER

* STAR TRANSIT CHARACTERISTICS FOR LIMITING-MAGNITUDE STAR

POSITION ACCURACY	0.242 ARC MINUTES
RELATIVE INTENSITY ACCURACY	0.14
PROBABILITY OF DETECTION	0.91
EXPECTED NUMBER OF WEAK STARS DETECTED PER SCAN	0.0004
EXPECTED NUMBER OF FALSE STAR DETECTIONS PER SCAN	0.0000

Sector from 240° to 360° eliminated

* SIGNAL AND NOISE CHARACTERISTICS

MEAN NUMBER OF PULSES FROM LIMITING MAG STAR DURING STAR TRANSIT	55.61
MEAN NUMBER OF PULSES FROM STELLAR BACKGROUND DURING STAR TRANSIT	2.4259
MEAN NUMBER OF PULSES FROM DARK CURRENT DURING STAR TRANSIT	0.0225
PHOTOGRAPHIC MAG. OF NOISE	7.09
DETECTION THRESHOLD	48.00
MEAN VALUE OF OFF-PEAK MAXIMUM FOR CODE PATTERN	0.00

* SYSTEM CHARACTERISTICS

MINIMUM NUMBER OF STARS IN FIELD OF VIEW WITH LIMITING MAGNITUDE AND BRIGHTER	4
ACCURACY OF ATTITUDE DETERMINATION	1.50 ARC MINUTES
PROBABILITY OF CORRECT STAR-PATTERN RECOGNITION	0.9
PATTERN RECOGNITION TECHNIQUE	
MEAN NUMBER OF STEPS FOR PATTERN RECOGNITION	

TABLE H-2

COMPARISON OF SOME RESULTS BETWEEN CASES WITH AND WITHOUT SECTOR ELIMINATOR

Photo-multiplier	D		M_L		SW		E_f		E_w	
	Elim.	Present	Elim.	Present	Elim.	Present	Elim.	Present	Elim.	Present
EMR 541B-03	.553	.536	4.37	4.3	1.451	1.451	0	0	1.9	2.6
EMR 541D-01	1.999	1.936	4.37	4.3	1.451	1.451	0	0	.44	.55
EMR 541A-01	.864	.837	4.37	4.3	1.451	1.451	0	0	.15	1.91

D = diameter of optical system in inches

M_L = photographic magnitude of dimmest star detected

SW = optical slit width at optical axis in minutes of arc

E_f = expected number of false star detections per scan

E_w = expected number of weak star detections per scan

C. Use of SCADS Sensor for Attitude Determination of Deep Space Probes

Thus far the study is somewhat limited in that only the viewing geometry pertinent to the Tiros and Nimbus orbital paths were studied. We recommend that for any specific mission the viewing geometry be studied and then the optical system be designed. It may also be noted that for a spin stabilized satellite (if mounting considerations are no problem) the center of the SCADS field of view may be about the positive spin axis or about the negative spin axis. The direction which offers the most favorable geometry may then be chosen. For example, if the spin axis is the celestial North Pole-South Pole axis, then the SCADS field of view should be centered about the South Pole. Within fifty degrees of the North Pole are six stars brighter than visual magnitude 2, but there are thirteen such stars within fifty degrees of the South Pole.

It is true that the optical design is dependent upon the portion of the celestial sphere which is viewed. But, for a deep space probe and time duration as long as four years the spin axis of a spin stabilized satellite cannot be expected to remain fixed. Hence the instrument must be designed for the poorest case. This type of analysis was performed in the body of this report; other geometries will not produce reductions dramatically different from those already given.

1. Field of View Considerations

In order to determine attitude it is necessary that at least three celestial targets be detected for all pointing directions of the optical axis. The larger the field of view of the optical system, the fewer the total number of celestial targets needed. The fewer the number of celestial targets, the simple and more reliable is the target identification process. The instrument recommended employs a very wide field of view and thus requires only a limited number of targets.

A computer based simulation using a Control Data 1604 indicates that an optical system with a field of view of 180 degrees (hemispherical) provides a 99.99% probability of finding three or more stars for all pointing directions in the sky--provided the attitude sensor can detect the thirteen brightest stars in the sky. The distribution of positions of the thirteen brightest stars is shown in Figure H-9. Table H-3 shows the right ascension, declination, magnitudes, and general catalog numbers of these stars.*

TABLE H-3

STARS REQUIRED FOR HEMISPHERICAL SCAN TO PROVIDE AT LEAST THREE STARS IN ALL FIELDS OF VIEW

Magnitude	General Catalog No.	Right Ascension			Declination		
		h	m	s	°	'	"
-1.43	8833	6	42	56.7	-16	38	46
- .73	8302	6	22	50.5	-52	40	04
- .27	19728	14	36	11.2	-60	37	49
- .06	19242	14	13	22.8	19	26	31
+ .04	25466	18	35	14.7	38	44	09
+ .09	6427	5	12	59.5	45	56	58
+ .15	6410	5	12	08.0	- 8	15	29
+ .37	10277	7	36	41.1	5	21	16
+ .53	1979	1	35	51.2	-57	29	25
+ .66	18971	14	00	16.5	-60	07	58
+ .70	7451	5	52	27.8	7	23	58
+ .80	27470	19	48	20.6	8	44	05

* <u>Sky and Telescope</u>, August 1957, p. 470.

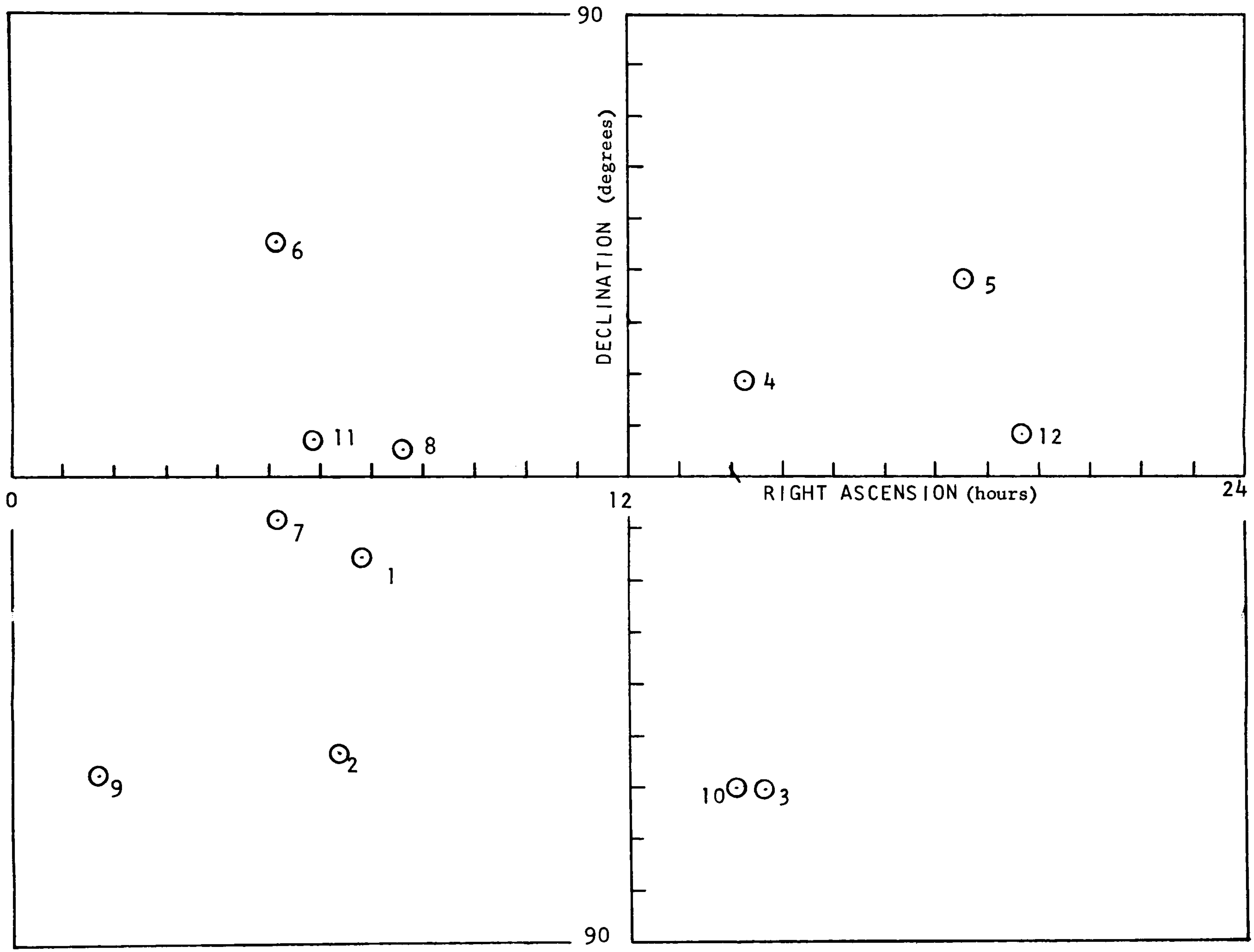

FIGURE H-9: POSITIONS OF BRIGHTEST 13 STARS that twelve stars give three or more stars in 99.6% of the cases. When these results are graphed, Figure H-10 is obtained. This shows, for example, that 91.6% of the time four or more stars will be in the field of view; 75% of the time five or more stars will be in the field of view. On the average there will be six stars in the field of view. This, of course, has important statistical ramifications in terms of the limitation of the effect of adverse stellar geometries on error propagation.

When the six solar system targets mentioned above are added to the basic star list of thirteen, an average of nine or ten celestial targets will be detected in a typical observing situation using a 180 degree scan of a 90 degree field of view.

2. Detector Lifetime

The most sensitive, readily available radiation detectors operate in or near the visible spectrum. These are the photomultiplier, cadmium sulfide photoconductor, and silicon photodiode. Of these, we discard cadmium sulfide at the outset. Though its response to steady light is comparable to the photomultiplier, its response time to weak light is of the order of seconds. Also, to be used at all, it requires a bias light to reduce a dark resistivity of thousands of megohms.

This leaves us the the photomultiplier and silicon diode. The probe must last for four years, under continuous operation. One anticipates no lifetime problems with the silicon diode, but it is necessary to examine the photomultiplier critically.

Because of their locations it is evident that certain of the brightest thirteen stars will be needed infrequently. An examination of the various possible cases has shown that for most pointing directions, star numbers 7, 8, 10, 11, and 12 will not be used. Thus, the majority of the time the system will function with only seven stars (1, 2, 3, 4, 5, 6, and 9).

Two factors conspire to complicate the above discussion:

(1) the scan field of the sensor may not be perfectly hemispherical, and

(2) there are at least six solar system bodies which will be detected from time to time.

The first of these factors tends to require the addition of several stars to the basic identification list; the second factor tends to reduce the number of stars needed in the list. The specific study of limiting magnitudes including these two factors is a function of specific launch dates and orbits and is rather complicated. When using an optical system canted off the axis of rotation, the occasional availability of 50% more targets (Jupiter, Saturn, Mars, Venus, Sun, and Moon) for attitude determination will more than compensate for the loss in scan field because of the obscuration at the center of the hemisphere.

We have stated above that a minimum of three stars will be present in all fields of view when using the thirteen brightest stars and a hemispherical scan. The question also arises as to the percentage of the time there will be four or more stars in the field of view, five or more, etc. For the 99% probability of successful identification required, several computer runs have been utilized to estimate the number of stars needed. The results show

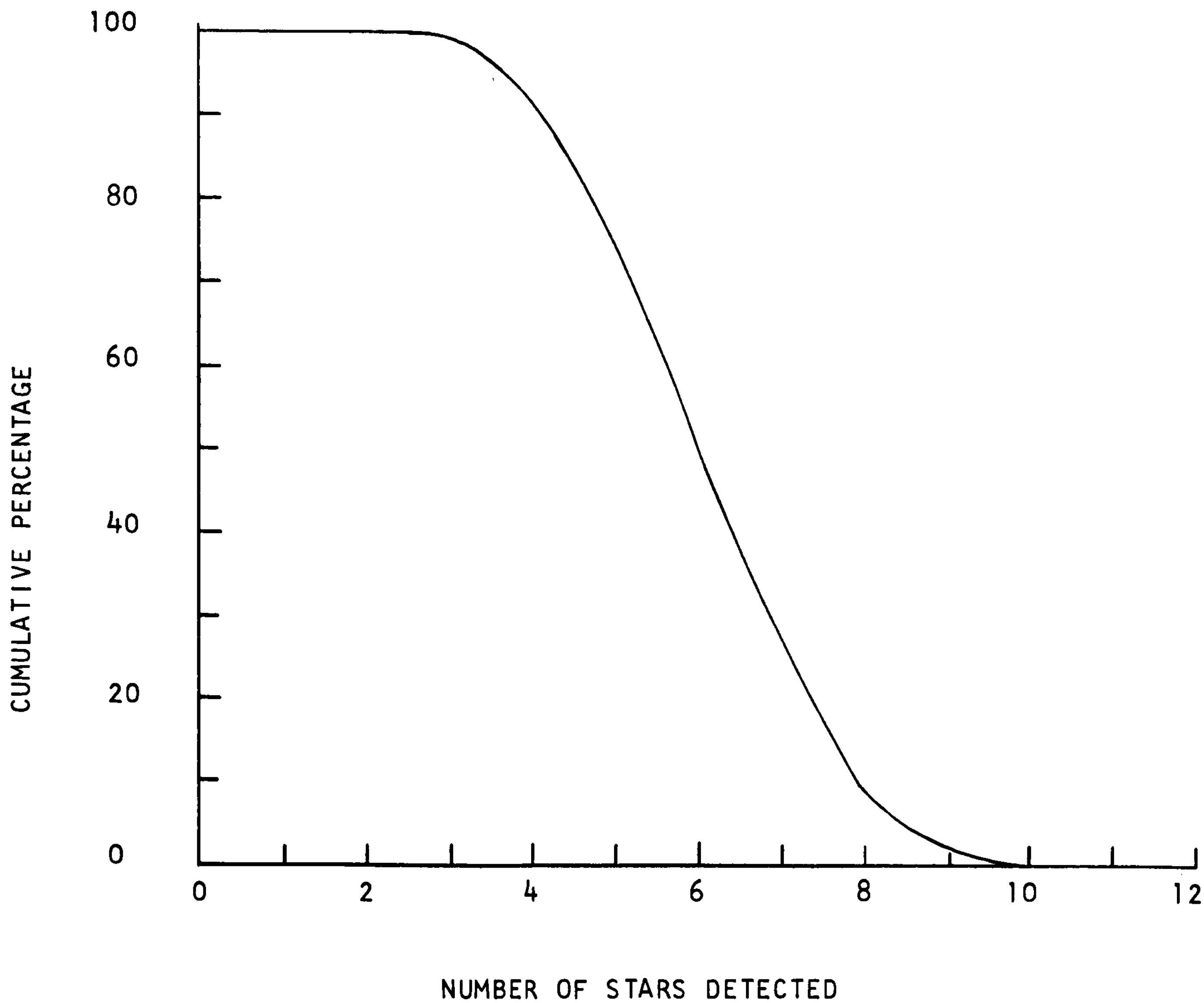

Figure H-10: Percentage of Cases in Which N or more Stars Will be Found in Hemispherical Field of View When Using 12 Brightest Stars

The principal factors limiting photomultiplier life are thought to be dynode failure in the last stages due to electron bombardment and electrolysis, photocathode fatigue due to ion bombardment, electrolytic action due to the photocurrent, and possibly poisoning of the photoemissive surface by the glass substrate [1, 2]. In addition, temperature dependent gain changes thought to be due to cesium migration in the tube commonly occur and vary among members of the same tube type. With low anode currents at room temperature or lower, these gain changes are small according to Cathey [1]. There appears to be little actual data on life tests as long as 1,000 hours, and this only on specially designed photocathodes [2].

Wargo, Haxby, and Shepherd [3] have studied fatigue effects on MgO secondary emitters due to electron bombardment. They found that the life of these secondary emitters varied inversely to the total charge drawn. Bombardment of the surface at 200 volts and 50 milli-amperes per square centimeter for eight hours reduced the secondary emission ratio by 20%.

With a 90 degree field of view using the thirteen brightest stars we have seen there are, on the average, six stars in the field of view. From Table H-3 we can find that the average intensity corresponds to visual magnitude .155. Using a .6 degree of arc rotational slit width which is 90 degrees in length, we find that these stars are in the slit for 1% of the time. If we use the energy flux from Vega (given in the following section), a one inch aperture (we leave out considerations of optical efficiency for convenience and compensate with an increase in aperture), a gain of 10^6, a quantum efficiency of 10%, and an S-4 response, we find the average current

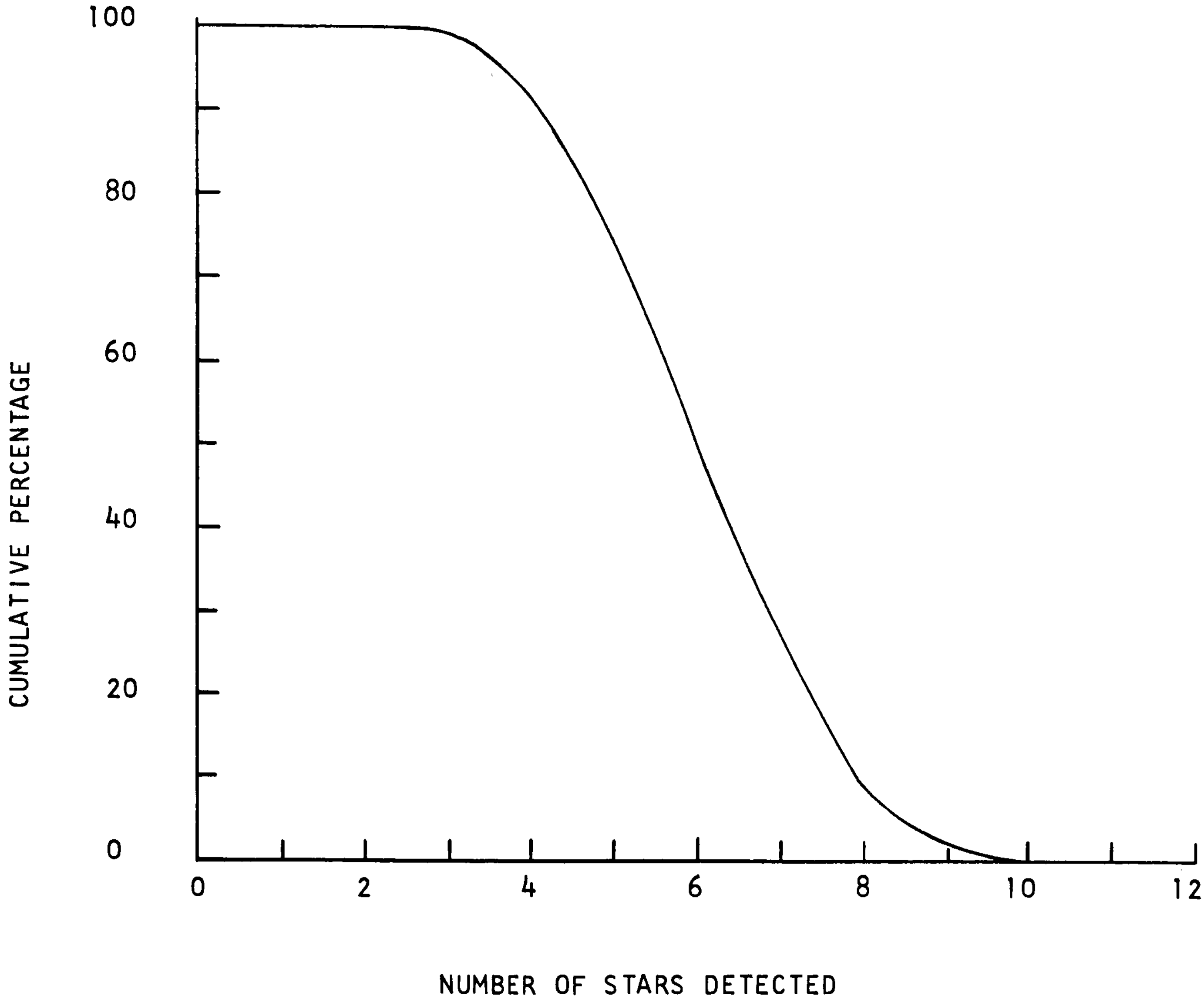

Figure H-10: Percentage of Cases in Which N or more Stars Will be Found in Hemispherical Field of View When Using 12 Brightest Stars

The principal factors limiting photomultiplier life are thought to be dynode failure in the last stages due to electron bombardment and electrolysis, photocathode fatigue due to ion bombardment, electrolytic action due to the photocurrent, and possibly poisoning of the photoemissive surface by the glass substrate [1, 2]. In addition, temperature dependent gain changes thought to be due to cesium migration in the tube commonly occur and vary among members of the same tube type. With low anode currents at room temperature or lower, these gain changes are small according to Cathey [1]. There appears to be little actual data on life tests as long as 1,000 hours, and this only on specially designed photocathodes [2].

Wargo, Haxby, and Shepherd [3] have studied fatigue effects on MgO secondary emitters due to electron bombardment. They found that the life of these secondary emitters varied inversely to the total charge drawn. Bombardment of the surface at 200 volts and 50 milli-amperes per square centimeter for eight hours reduced the secondary emission ratio by 20%.

With a 90 degree field of view using the thirteen brightest stars we have seen there are, on the average, six stars in the field of view. From Table H-3 we can find that the average intensity corresponds to visual magnitude .155. Using a .6 degree of arc rotational slit width which is 90 degrees in length, we find that these stars are in the slit for 1% of the time. If we use the energy flux from Vega (given in the following section), a one inch aperture (we leave out considerations of optical efficiency for convenience and compensate with an increase in aperture), a gain of 10^6, a quantum efficiency of 10%, and an S-4 response, we find the average current due to detected stars is 1.660×10^{-9} ampere. The average sky brightness due to all the stars averages 200 tenth magnitude stars per square degree on the galactic equator. This results in 7.490×10^{-10} ampere. The photomultiplier dark current plus leakage current may be taken as about 2×10^{-10} ampere. Thus, the average anode current will be about 3.61×10^{-9} ampere.

Since Wargo et al. [3] have found that 200 volts and 50 milli-amperes per square centimeter applied for eight hours cause the MgO to reduce to Mg and O_2 to such an extent that the tube is no longer functional, we may write

$$(50 \text{ M.A.})\ (8 \text{ hours}) = (3.61 \times 10^{-6} \text{ M.A.})\ Y \quad ,$$

where

Y = number of hours to reduce the MgO coating to Mg and O_2 to an extent that the tube is no longer functional. The average anode current being 3.61×10^{-9} ampere.

Hence, if we measure Y in years we have

$$Y = \frac{50 \times 8}{3.61 \times 10^{-6} \times 24 \times 365} \doteq 1.3 \times 10^{4} \text{ years.}$$

Hence, if one is careful not to expose the photomultiplier to intense light sources, no difficulty should be caused by the MgO dynode surfaces being reduced to Mg and O_2.

Cathey's results [1] have also indicated the importance of temperature on photomultiplier fatigue. At temperatures of 104° F and a current drain of 1 microampere, a tube with MgO dynodes deteriorated by 80% in 30 hours. However, at 72° F, the effects at 30 hours were minimal; no deterioration was observed. Cathey [1] also states categorically that "at anode currents below 0.1 microampere, fatigue effects are small on both MgO and CsSb dynodes" at room temperature. Tests were run on Dumont 6292 (MgO dynodes) and RCA 6655 and 5819 (CsSb dynodes). All these tubes have CsSb cathodes.

If dynode failure at the last stages due to electron bombardment and electrolytic action limits the photomultiplier life, it appears that a four year life under the conditions of the space probe can be attained. An unfocussed dynode structure such as the venetion blind type is desirable to avoid local high current density regions on the dynodes.

Next we consider photocathode life. It is known that a CsSb photosurface under intense illumination will last indefinitely without an applied field [4], indicating that ion bombardment and electrolysis cause fatigue in this case. No data on lifetime at low current levels seems to be available, but Schenkel [4] presents life data for a two inch diameter tri-alkali photoemitter taken under high illumination (3.62 milliwatts per square centimeter) wherein the photocurrent has fallen from 1500 microamperes to 1200 microamperes in about 0.4 hour. If we assume cathode fatigue is also proportional to charge evolved, we may estimate the life under an anode current of 3.61×10^{-9} with a tube gain of 10^6. Thus

$$\frac{1500 \times 10^{-6} \text{ ampere}}{2.54^2 \ \pi} \times .4 \text{ hour} = \left[\frac{(3.61 \times 10^{-9} \times 10^{-6}) \text{ ampere}}{1 \text{ cm}^2}\right] Y \quad ,$$

where

Y = number of hours for the anode current to drop to 80% of its original value (1500/1200 = .8) for a photocathode of 1 square centimeter.

Hence, if we measure Y in years we find

$$Y \doteq 90 \text{ years.}$$

Cesium antimonide photocathodes have even superior life characteristics. Cesium has a very low vapor pressure, hence it will migrate at elevated temperatures. However, below about 60°F, no measurable migration has been detected. Thus, if a photomultiplier is not exposed to intense light sources, the mission lifetime of four to five years continuous operation appears within the capabilities of ordinary photomultipliers.

3. Available Energy from the Limiting Magnitude Star

If we list the visual magnitudes of the faintest stars in Table H-3 and continue beyond those listed we obtain the sequence, starting with the tenth brightest star: 0.66, 0.70, 0.80, 0.85, 0.87, 0.98, 1.00.

The twelfth, thirteenth, and fourteenth brightst stars are closely grouped in visual magnitude differing by not more than .05 visual magnitude. From the fourteenth to the fifteenth star a jump of .11 in visual magnitude occurs suggesting we use fourteen stars in the list so that we can be more certain of detecting the weakest star in our list simultaneously discriminating against the next weakest.

Norton [5] gives the peak available energy flux from Vega (Type A0,

$11{,}000^{\circ}$ K, Visual Magnitude 0.04) as

$$f_{peak} = 6.16 \times 10^{-12} \text{ watt/cm}^2\text{/micron} .$$

For an S-4 photocathode response and a $11{,}000^{\circ}$ K temperature, we can derive an effective optical band pass, $\Delta\lambda$, of .1752 micron. We arrive at this from the equation

$$f_{bb\ peak}\ \Delta\lambda = \int_{\lambda_1}^{\lambda_2} f_{bb}(\lambda,\ T)\ d\lambda$$

where f_{bb} is the Planck function. For the silicon photodiodes described by Williams [6] the optical band pass derived in similar fashion is $\Delta\lambda = .1532$ micron. Assuming a two inch aperture of 100% optical efficiency, the respective energies incident on the detector effective in photoelectron production for the fourteenth brightest star are

$$f_{eff} \text{ photomultiplier} = 1.02 \times 10^{-11} \text{ watt,} \qquad \text{(h-1)}$$

$$f_{eff} \text{ silicon diode} = 8.92 \times 10^{-12} \text{ watt .} \qquad \text{(h-2)}$$

4. Signal-to-Noise Ratios

a. Photomultiplier

In general, if we assumed a body is radiating at a single frequency

$$n_{P.M.} = \epsilon_q \frac{f\lambda}{hc} \tag{h-3}$$

where $n_{P.M.}$ = number of photoelectrons per second utilized by the receiver

ϵ_q = quantum efficiency of receiver

f = energy flux (watts = 10^7 ergs/second)

λ = wave length (centimeters)

h = Planck's constant $\doteq 6.62 \times 10^{-27}$ erg second

c = speed of light $\doteq 3 \times 10^{10}$ cm./second;

hence, for

ϵ_q = .1 (photoelectrons/photon)

$f = 1.02 \times 10^{-11}$ watt $= 1.02 \times 10^{-4}$ erg/second

λ = .4 micron $= 4 \times 10^{-5}$ centimeter

$$n_{P.M.} = 2.06 \times 10^6 \text{ photoelectrons/second} . \tag{h-4}$$

Hence, 2.06×10^6 photoelectrons per second will be produced at the photocathode of a photomultiplier when viewing the fourteenth brightest star with a two inch aperture with 100% optical efficiency. If e is the electron charge 1.602×10^{-19} coulomb, this corresponds to a photocurrent of

$$i_c = e\, n_{P.M.} = 3.29 \times 10^{-13} \text{ ampere.}$$

With a gain of 10^6 an anode current,

$$i_a = .329 \text{ microampere} \tag{h-5}$$

The spin rate is six to thirty seconds. It is likely that the required pointing accuracy of .1 degree could be had with a .6 degree slit width, but then the average sky background of 200 tenth magnitude stars per square degree would be equivalent to the steady light from a -.08 visual magnitude star. With a slit of 1.38 minutes of arc slit width the background is down to that of a 2.87 visual magnitude star. Thus we choose a 1.5 minute of arc slit width. In this case the slit width is dictated by the star background rather than pointing accuracy requirements! Thus the time, T_s, in which a star transits the slit is such that

$$1.67 \times 10^{-3} \geq T_s \geq 4.17 \times 10^{-4} \text{ seconds.}$$

Choosing the six second rotation time (worst case) the required electrical band width of the detection electronics will be

$$\Delta f = \frac{2}{\pi T_s} = 1,527 \text{ cps} . \tag{h-6}$$

The dark current plus leakage will result in an A.C. noise current of

$$\sqrt{\overline{i_n}^2} = \sqrt{2e \; i_d \; \Delta f}$$

where

$\sqrt{\overline{i_n^2}}$ = A.C. noise current (amperes),

e = electron charge = 1.602×10^{-19} coulomb,

i_d = dark current plus leakage current (amperes),

Δf = electrical band width (cycles/second).

A typical value for i_d is

$$i_d = 2 \times 10^{-10} \text{ ampere,}$$

hence

$$\sqrt{\overline{i_n^2}} = 3.48 \times 10^{-13} \text{ ampere,}$$

an eminently satisfactory result.

b. Photodiode

To calculate the photodiode signal-to-noise we must first find an average wavelength in the photodiode response to 11,000° K black body radiation. We do this using tables of the photon energy distribution for "black" radiation, such as appear in Allen [7]. The result is

$$\lambda_{ave}(.4\ \mu - 1.0\ \mu) = .601 \text{ micron.}$$

A reasonable quantum efficiency for the silicon photodiode is 80%. Thus, by Equation (h-2) the number of excited photoelectrons per second will be

$$n_{Si} = \epsilon_q \frac{f\lambda}{hc} = \frac{8.92 \times 10^{-12} \times 6.01 \times 10^{-5} \times .8}{6.62 \times 10^{-27} \times 3 \times 10^{10}} \times 10^7$$

$$= 2.17 \times 10^7 \text{ photoelectrons/second,}$$

which in turn gives a signal current of

$$i_s = 3.47 \times 10^{-12} \text{ ampere.} \qquad \text{(h-7)}$$

From the analysis in Section III, pages 121-122, we may write

$$f_n^{\ 2} = 2 \left(\frac{hc}{\epsilon_q \lambda}\right)^2 n_{Si} \, \Delta f \qquad \text{(h-8)}$$

where

f_n = noise equivalent power (watts)

Δf = band width of detector (cycles/second);

therefore, the shot noise equation leads to

$$\sqrt{\overline{i_n}^2} = \sqrt{2e^2 \, n_c \, \Delta f} = e \, \frac{f_n \, \epsilon_q \, \lambda}{hc} \quad .$$

Williams [6] claims $f_n = 1.8 \times 10^{-13}$ watt for a good photodiode. Assuming our diode is as good we may compute the average noise current as

$$\sqrt{\overline{i_n}^2} = \frac{1.602 \times 10^{-19} \times 1.8 \times 10^{-13} \times .8 \times 6.01 \times 10^{-5}}{6.62 \times 10^{-27} \times 3 \times 10^{10}}$$

$$= 6.98 \times 10^{-13} \text{ ampere.} \qquad \text{(h-9)}$$

Thus the signal-to-noise ratio is

$$i_s / \sqrt{\overline{i_n}^2} = 4.96 \quad .$$

It can be easily increased by going to larger aperture, e.g. a three inch aperture would increase it by a factor 2.25.

c. Output Circuitry for Photodiode

If a photodiode is used with a 3.0 inch aperture we have seen that for a noise equivalent power of 1.8×10^{-13} watt the signal-to-noise ratio will be about 11. The diode load resistor must now be chosen large enough so that the thermal noise of the resistor will not limit the detector performance. Assume that this is to be one-tenth of the diode noise. The noise voltage on the resistor is,

$$\overline{v_n}^2 = 4k\ T\ R\ \Delta f \ ,$$

where k = Boltzmann's constant = 1.38×10^{-23} joule/$^{\circ}$K

T = diode temperature ($^{\circ}$K)

R = diode load resistance (ohms)

Δf = band width (cycles/second)

$\overline{v}_n^{\,2}$ = mean square voltage disturbance or Johnson noise across the load resistance, R (volts^2).

Due to the diode current, $\overline{i}_s$, a voltage, $\overline{v}_d$, where

$$\overline{i}_s^{\,2} R^2 = \overline{v}_d^{\,2}$$

appears at the load resistor R. In order that this voltage exceeds the Johnson noise (i.e. $\overline{v}_d^{\,2} \geq \overline{v}_n^{\,2}$) we must have

$$R \geq \frac{4\ k\ T\ \Delta f}{\overline{i}_s^{\,2}} \quad .$$

Using $\sqrt{\overline{i}_n^{\,2}}$ from Equation (h-9) and increasing the signal to noise ratio by a factor of 11 to account for the three inch aperture (T = 300° K),

$$R \geq \frac{4 \times 1.38 \times 10^{-23} \times 3 \times 10^2 \times 1.27 \times 10^2}{6.98^2 \times 10^{-26} \times 11^2}$$

$$= .0358 \text{ megohm.}$$

This indicates that Johnson noise will be no problem. Indeed, a much larger load resistor is desirable to increase the magnitude of the signal voltage. Commercial solid state amplifiers with input impedances of 10^4 megohms are available.

5. Statistics of Star Detection

Let us work with the fourteen brightest stars. To ease the star identification problem we would like to detect these fourteen stars with a high degree of certainty and to reject all other stars with a high degree of certainty. This would be done by setting some threshold below which the signal corresponding to a star transit would produce no output. Assume that the threshold is set so a .87 visual magnitude star is detected with probability .98 and a .98 visual magnitude star is detected with probability .02. The mean number of photoelectrons from the photocathode in 4.17×10^{-4} second (corresponds to six second spin period) will be (from Equation (h-4))

$$N_o = 885 \text{ photoelectrons (from the fourteenth brightest star).}$$

This mean is sufficiently large that the assumed Poisson distribution is almost normal, and the probability that the number, n, of photoelectrons exceeds the threshold, x, is

$$p(n \geq x \mid N_o) \doteq \frac{1}{2} \operatorname{erfc}\left(\frac{x - N_o}{\sqrt{2N_o}}\right) = p \qquad \text{(h-10)}$$

where

$$\operatorname{erfc} x \equiv \frac{2}{\sqrt{\pi}} \int_x^{\infty} e^{-\lambda^2} \, d\lambda$$

n = number of photoelectrons received,

x = number of photoelectrons set for the threshold

N_o = mean number of photoelectrons of the assumed Poisson distribution

$p(n \geq x \mid N_o)$ = probability that $n \geq x$ given the mean N_o (Poisson distribution assumed).

If N_o is the mean number of photoelectrons from a .87 visual magnitude star, the number from a .98 visual magnitude star, will be

$$N_o' = \beta N_o \tag{h-11}$$

where $\beta = \dfrac{N_o'}{N_o} = \dfrac{\text{mean number of photoelectrons from a .98 visual magnitude star}}{\text{mean number of photoelectrons from a .87 visual magnitude star}}$.

Hence,

$$\beta = 10^{-.4(.98-.87)} = 10^{-.044} \; .$$

The probability that the threshold is exceeded for a transit of a .98 visual magnitude star will then be,

$$p(n \geq x | \beta\, N_o) = \frac{1}{2} \operatorname{erfc} \frac{x - \beta N_o}{\sqrt{2\, \beta\, N_o}} \; . \tag{h-12}$$

Let us set

$$p(n \geq x | \beta N_o) = 1 - p(n \geq x | N_o) = 1 - p \; .$$

Hence,

$$x = \sqrt{\beta}\;\; N_o \tag{h-13}$$

and

$$\left(\frac{\mathrm{erf}^{-1}(2p - 1)}{1 - \sqrt{\beta}} \right)^2 = N_o \tag{h-14}$$

where erf^{-1} is the inverse of the error function.

Using $p = .98$ and $\sqrt{\beta} = .9506$, Equations (h-13) and (h-14) yield

$$N_o = 437 \text{ photoelectrons,}$$

and $x = 406$ photoelectrons. In other words, if 437 photoelectrons result, on the average, from the transit of a .87 visual magnitude star this star may be detected with probability .98, while .98 visual magnitude is rejected with probability .98 if the detection threshold is set at 406 photoelectrons. With 885 photoelectrons on the average, the statistics are even more favorable. With the 1.5 minute slit width the background, equivalent on the average to 2.87 visual magnitude, will contribute $69 \times 4.17 \times 10^{-4} \approx .02$ photoelectron and is neglected.

6. Azimuth Angle Accuracy

Though there is no question that .1 degree acuracy is possible with the 1.5 minute slit, it may be of interest to evaluate the attainable accuracy. In Appendix G, Equation (g-107) an expression was derived for azimuthal angle accuracy of star scanning optical systems. This result gives

$$2 \text{ var} \left(\frac{t^*}{T_s} \right) = \frac{1}{NP_x} \left(\frac{2x + 3}{N} P_{2x+2} - \frac{x + 2}{N} P_{x+2} - P_{2x+1} \right) \quad \text{(h-15)}$$

where

t^* = estimate of time of star crossing

T_s = average time of star in the slit

x = number of pulses set for the threshold

N = number of pulses transmitted by the filter, pulse being produced by the star

P_x = probability the threshold x is exceeded.

N is given by

$$N = \alpha \, \epsilon_o \, \epsilon_q \, \lambda_s \, T_s$$

where

α = fraction of pulses transmitted by the threshold clamp

ϵ_o = the optical efficiency

ϵ_q = quantum efficiency

λ_s = expected photon rate.

In our case, $N \approx N_o$. Dark current and background are neglected in Equation (h-15). Since x is large, Equation (h-15) becomes

$$2 \text{ var} \left(\frac{t^*}{T_s}\right) = \frac{1}{N_o} \left(1 - \frac{x + 2}{N_o}\right) . \qquad \text{(h-16)}$$

The ratio of azimuthal angle error, σ_θ, to rotational slit width, S_w, with $N_o = 437$, and $x = N_o\sqrt{\beta} = 406$ becomes

$$\frac{\sigma_\theta}{S_w} = \sqrt{\text{var } \frac{t^*}{T_s}} = .00862 \quad .$$

With 1.5 minute optical slit width this corresponds to an error in azimuth angle of $\sigma_\theta \approx 0.08$ arc second.

Similar considerations apply to the silicon photodiode. A .1 degree azimuth accuracy could be obtained in either case, with a slit as one degree of arc, were it not for sky background.

7. Attitude Determination Accuracy

In Figure H-11 we plot equal total error contours on a Mercator projection of the celestial sphere. As in the main body of the report we define the total error as

$$\sqrt{\sigma^2(\alpha) + \sigma^2(\delta) + \sigma^2(\beta)}$$

where

$\sigma(\alpha)$ = standard deviation of right ascension of spin axis,

$\sigma(\delta)$ = standard deviation of declination of spin axis,

$\sigma(\beta)$ = standard deviation of azimuth with respect to normal to reference direction.

In deriving the curves shown in Figure H-11 we assume that the measurement of the relative azimuth angles have independent distributions, come from distributions whose second moments exist, the mean of each distribution is the true value, and the standard deviation of each distribution is one minute of arc. Also the field of view was hemispherical and only the fourteen brightest stars were utilized.

Each curve in Figure H-11 has been assigned a number which is the total attitude error in minutes of arc if the spin axis were to lie along the locus of right ascension and declination indicated by the curve. For example, there are five closed curves in Figure H-11 dictated by one. If the axis were to have a right ascension and declination common to any point on one of these curves, then the total error in attitude would be one minute of arc. We note the complicated error contours and also several contours which indicate errors

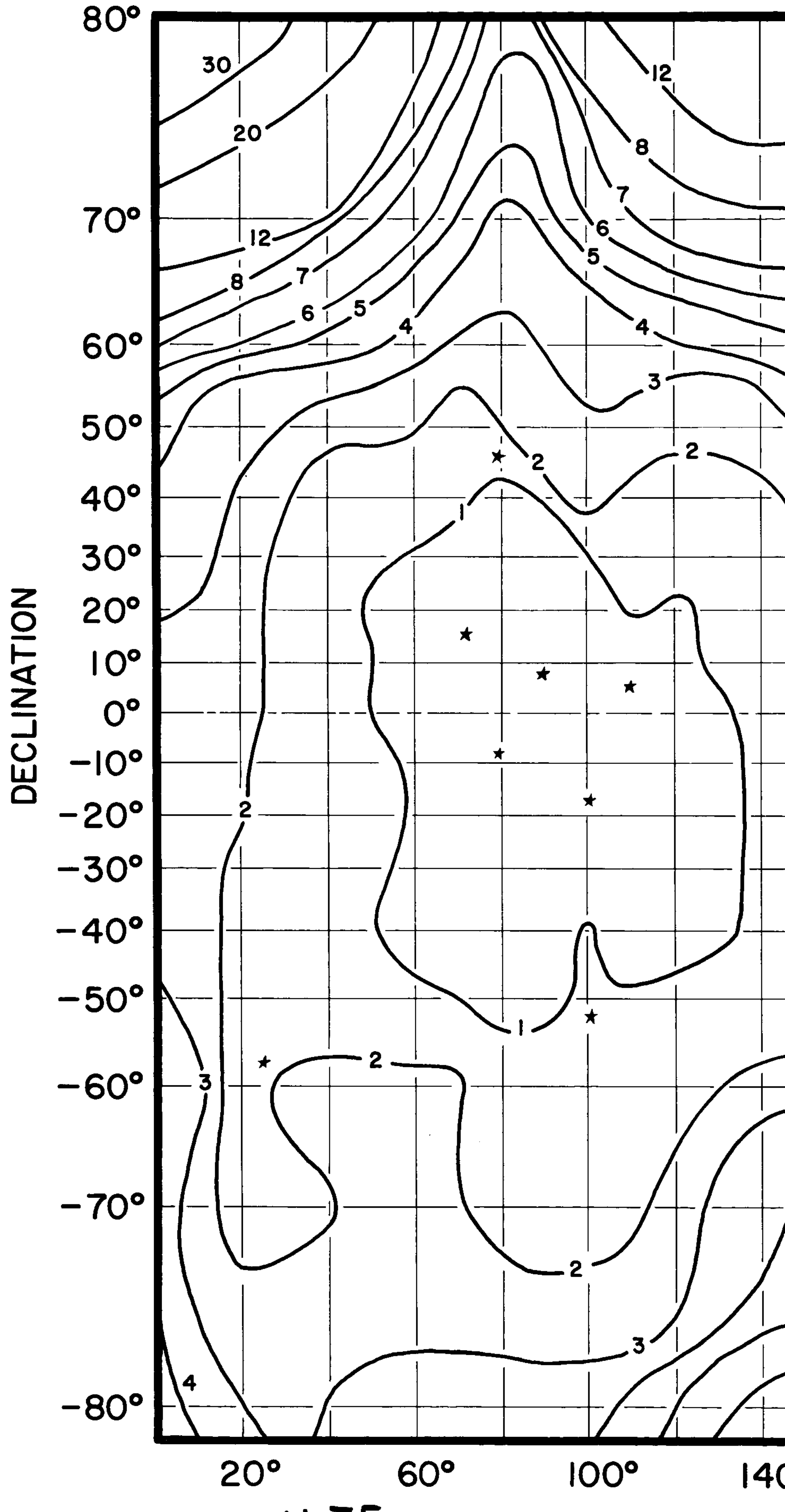

FIGURE H-11: TOTAL ATTITUDE ERROR

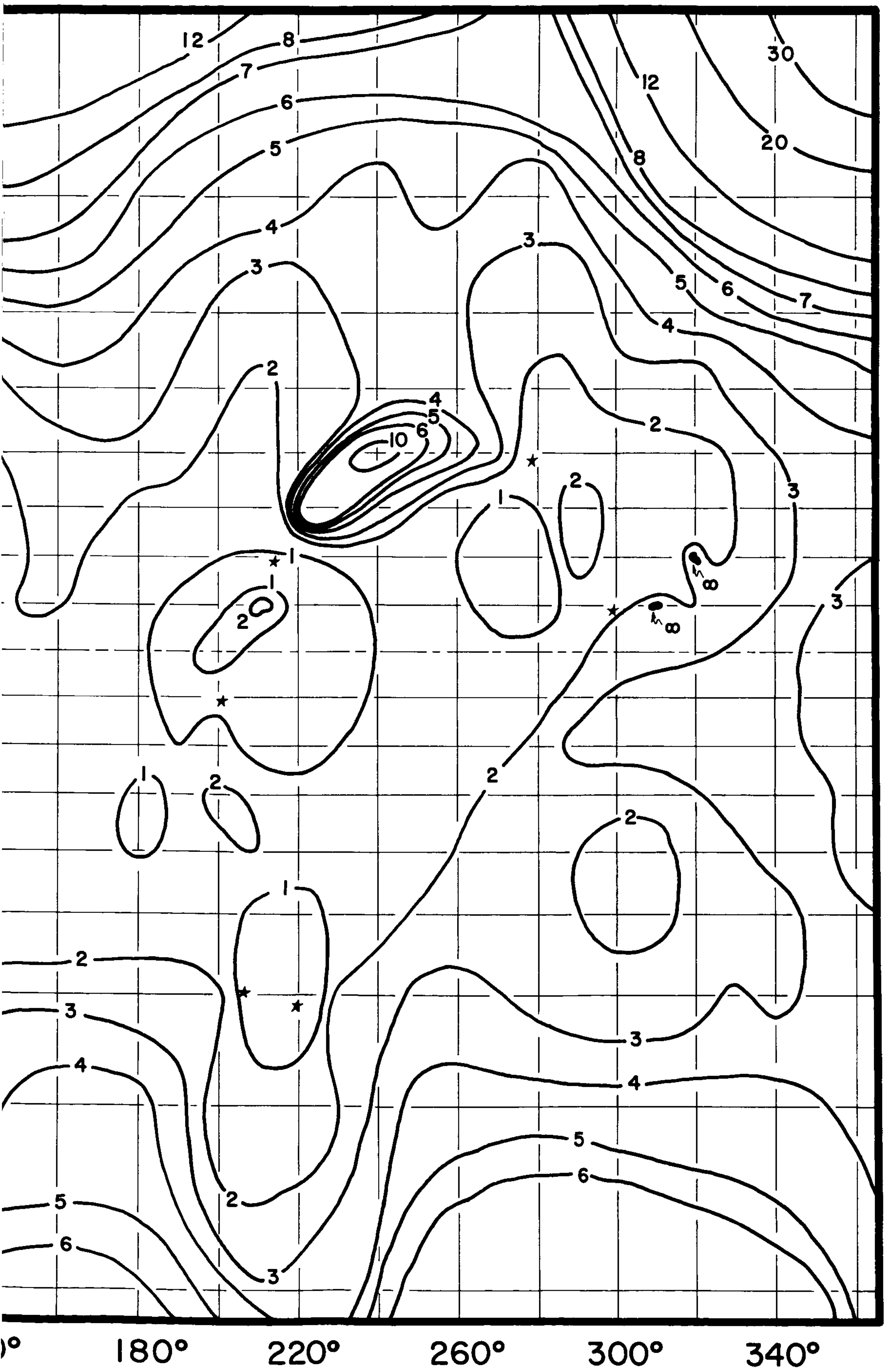

RIGHT ASCENSION
– MINUTES OF ARC

H-76

greater than .1 degree (= 6 minutes) at higher declinations. However, the Mercator projection gives an exaggerated view as to the extent of such regions. Actually, 84% of the celestial sphere is such that the total error is less than .1 degree (= 6 minutes).

Two small regions are such that only two of the fourteen brightest stars are in our hemispherical field of view. These regions are assigned an infinite error. The fourteen brightest stars are also shown on the figure.

8. Conclusions

Silicon diodes formed from ultra pure silicon can probably be used with a three inch aperture. These devices will require well designed high impedance circuitry.

Photomultipliers are likely to have lifetimes considerably in excess of the required four to five years, provided that the photomultiplier is kept below room temperature. These can be used with apertures as small as one-half inch.

With either sensor a pointing accuracy of .1 degree is readily obtained. Use of the fourteen brightest stars is recommended with a bias level set so as to detect the weakest in the list with probability .99 and the next weakest with probability .01.

Estimates of weight, size, and power may be made and are presented below.

	Photodiode		Photomultiplier	
	Spinning	Non-Spinning	Spinning	Non-Spinning
Weight	4.2 lbs.	5.8 lbs.	3.2 lbs.	4.8 lbs.
Volume	4" x 5" x 6"	4.5" x 5" x 8"	3" x 4" x 6"	3.5" x 4" x 8"
Power	6.2 watts	20.5 watts	5.7 watts	20 watts

If the spacecraft is spin stabilized, less weight, volume, and power will be required. Power must be supplied only when the sensor is in operation.

Presently, silicon diodes are manufactured with an active surface of less than 0.2 inch. It is not possible to produce a lens with a 90 degree field of view, 3.0 inch aperture, and an image size of 0.2 inch. Hence if a solid state detector were used special optical devices (e.g. fiber optics) must be utilized. If a photomultiplier were used, the characteristics of the lens system would be as follows:

field of view = 90°

image diameter = 1" (of total field of view)

focal length = 0.5"

aperture diameter = 0.5"

f number = 1.0 .

A lens with such parameters does not appear to be available commercially, but is well within the state-of-the art.

D. Some Considerations for the Use of the SCADS Sensor for Asteroid Detection

The capability of the SCADS sensor to detect many targets with near simultaneity makes the instrument an attractive one for the sighting and tracking of the minor planets or asteroids. As seen from Earth, the brightest asteroid has a visual magnitude of about 9.8, but for space probes two to three astronomical units from the sun the visual magnitude of asteroids would be considerably brighter.

In this section we give a discussion of the ability of the SCADS sensor to view asteroids from a space probe. First, however, we give a general discussion of some of the characteristics of the asteroids.

1. Characteristics of Asteroids

A belt of asteroids about 2.3 astronomical units wide exists between Mars and Jupiter. The direction of rotation of all is the same as that of the planets. Figure H-12 gives a pictorial description of this belt. Of the possible millions of asteroids present about 1600 have accurately cataloged orbits. The remaining ones are so small that it is not possible to perform accurate measurements so that their orbital characteristics may be computed. The total mass of the asteroids is not known but is estimated to be about 3×10^{-4} Earth mass.

The orbits of asteroids exhibit more variety than do those of the principal planets. Although the majority are not far from circular and are inclined at an average of nine degrees to the ecliptic plane, some differ greatly from this form. An extreme example is Hidalgo, whose orbit has an

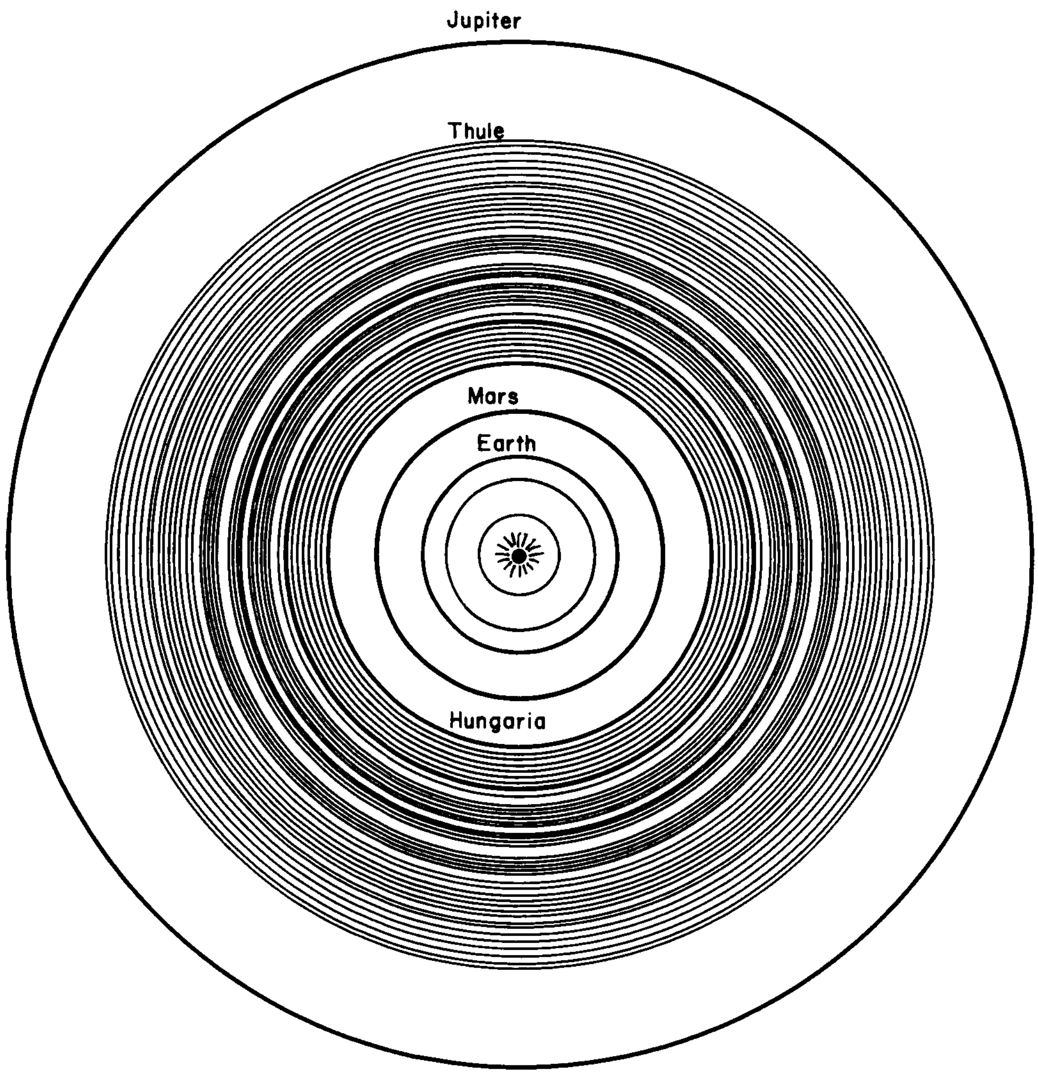

Figure H-12: Distribution of Minor Planets Between Mars and Jupiter From [9] eccentricity of 0.66 and is inclined 43 degrees to the ecliptic plane. Figure H-13 shows some of the more eccentric orbits of some asteroids. The distribution of orbital eccentricity of the charted asteroids is given in Figure H-14a which shows that the average eccentricity falls in the neighborhood of 0.15. Figure H-14b shows the distribution of orbital inclinations for these same asteroids, giving an average inclination of nine degrees to the ecliptic plane. Table H-4 gives some of the characteristics of four of the largest asteroids known. For additional information on these and other charted asteroids, one should consult a recent survey done by G. P. Kuiper and others.

TABLE H-4

CHARACTERISTICS OF SOME LARGER ASTEROIDS

Name	Diameter (km.)	Albedo	Avg. Vis. Mag. (Opposition)	Sidereal Period (Days)	a (AU)	e	i (Deg.)
Ceres	740	0.06	6.6	1681	2.767	0.079	10.6
Pallas	480	0.07	7.2	1684	2.767	0.235	34.8
Juno	200	0.12	8.2	1594	2.670	0.256	13.0
Vesta	380	0.26	5.8	1325	2.361	0.088	7.1

The periods of the asteroids are distributed in an irregular manner. According to Figure H-15, few asteroids take more than six or less than 3.5 years for one orbit about the sun. Also, in the distribution of periods there are several large gaps which are of great significance. These gaps are attributed to the control which the planet Jupiter exerts on the asteroids.

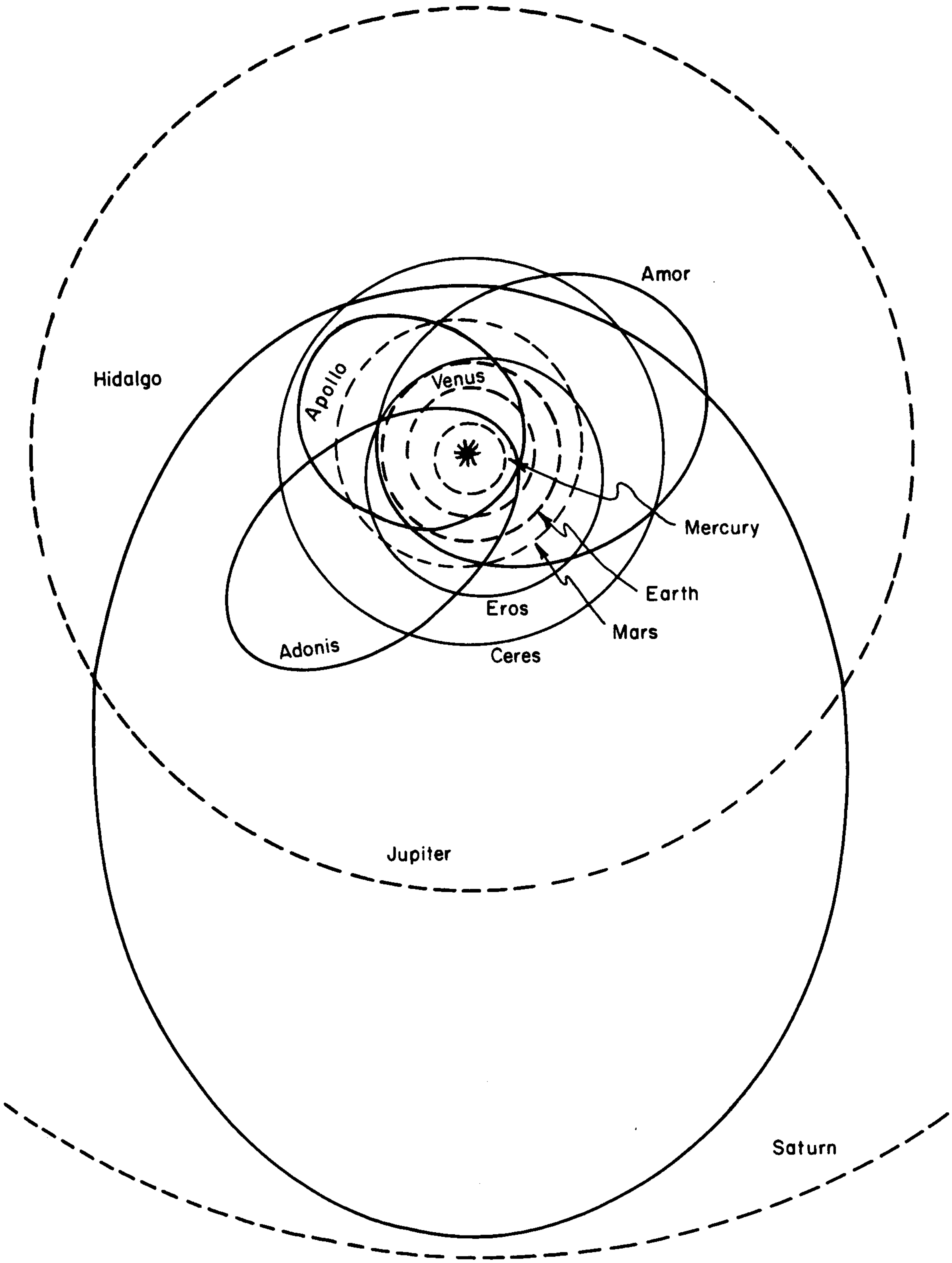

Figure H-13: Some Eccentric Asteroid Orbits From [9]

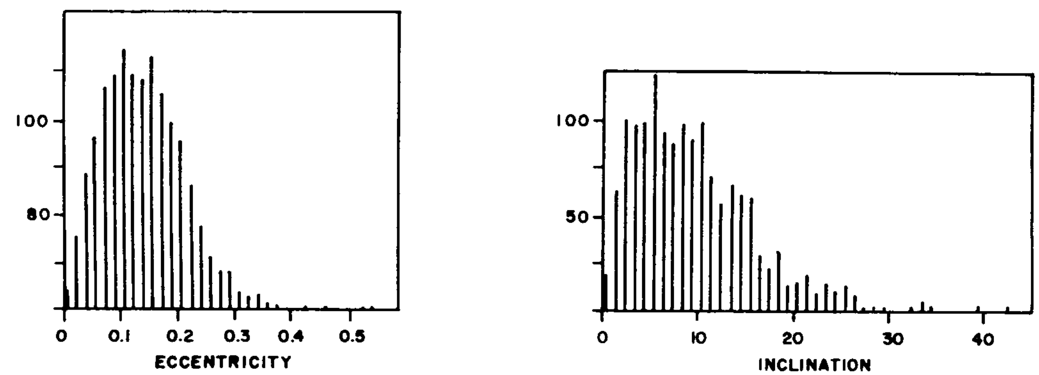

a) DISTRIBUTION OF ECCENTRICITY

b) DISTRIBUTION OF INCLINATION

Figure H-14: Distributions of Orbital Eccentricity and Inclination of the Charted Asteroids From [8]

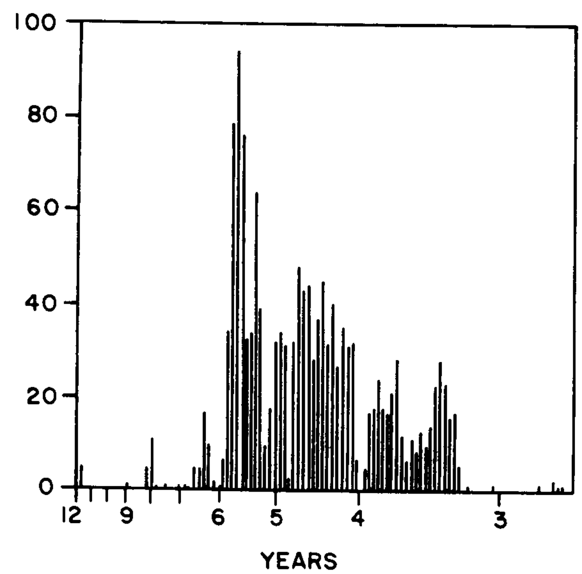

Figure H-15: Distribution of Periods of Cataloged Asteroids From [8]

The most conspicuous gaps are at 3.97, 4.76, and 5.95 years--exactly 1/3, 2/5, and 1/2 of Jupiter's 11.9 year period. Orbits whose periods are 1/4, 1/5, and 3/5 of Jupiter's also appear as depressions in Figure H-13. Those orbits, whose periods are rational multiples of some larger planet's orbital period, are called resonant orbits. The motions of these asteroids, in tune or in resonance with Jupiter, are peculiar. The steady pull of this large planet creates rhythmic changes in the asteroid motion eventually forcing them into different orbits as they approach a resonant orbit.

Those asteroids which have approximately the same period as Jupiter form an interesting group called the Trojans. Lagrange showed that if an asteroid moved about the sun in the same orbit as a planet and the asteroid were so located that the asteroid, the planet, and the sun were at the corners of an equilateral triangle, then the asteroid's position with respect to the planet would never change. Using this information astronomers set out to find such asteroids around Jupiter. These were found and thus called the Trojans. However, Lagrange neglected to consider the gravitational effect of other planets. Thus, even though an asteroid may not remain in this group permanently, it does remain for a considerable length of time.

The effect of harmonic orbital periods of the planet Jupiter are supported by facts about the distribution, eccentricity, and inclinations of the asteroids. Figure H-16 shows the percentage distribution of the cataloged asteroids as a function of their orbital radius where the radius r is related to the period by $p^2 = r^3$ (r measured in astronomical units and p in years). There is a distinct gap at 2.5 A.U. which corresponds to a period which

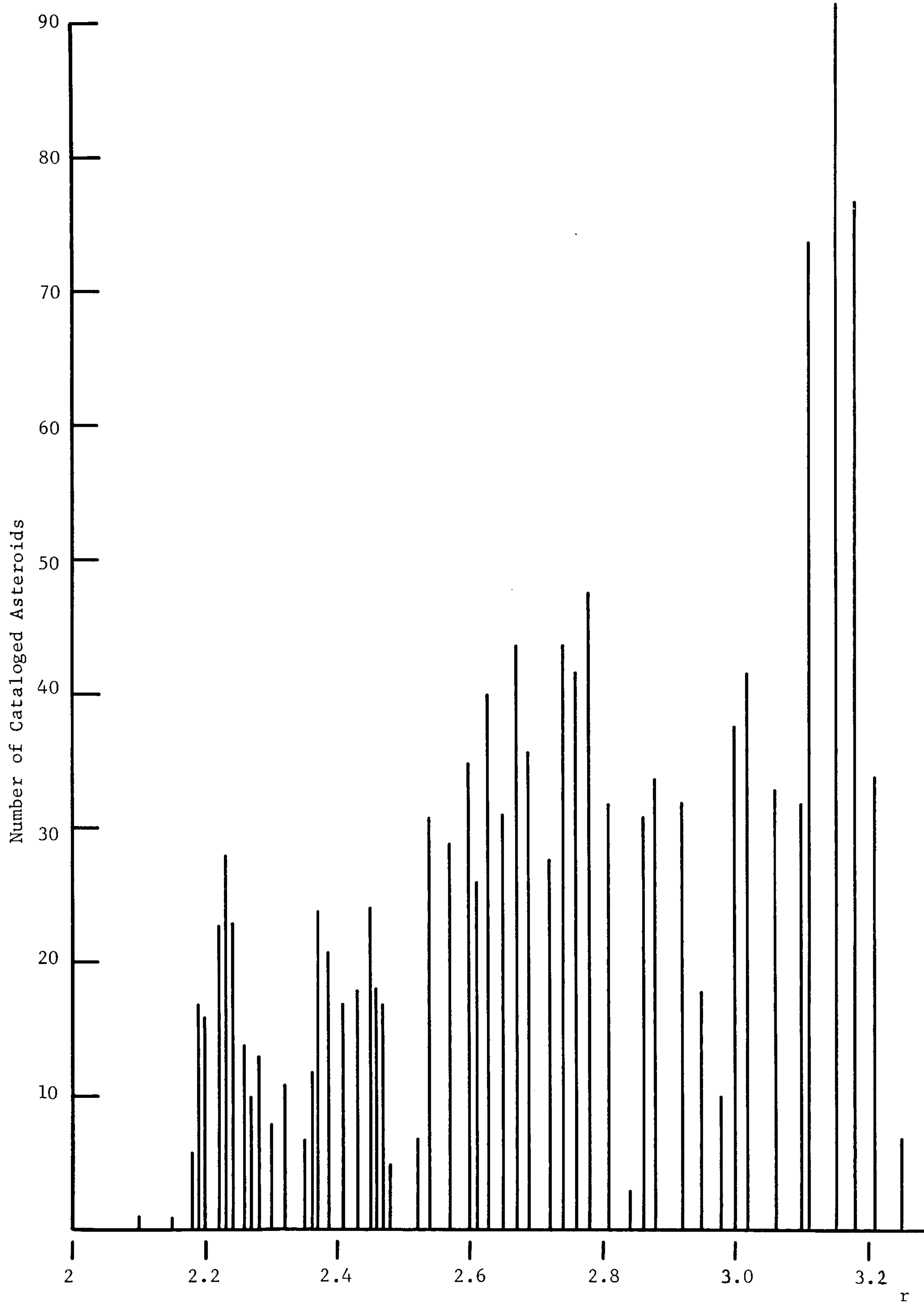
Number of Cataloged Asteroids
90
80
70
60
50
40
30
20
10
2
2.2
2.4
2.6
2.8
3.0
3.2
r

Fi

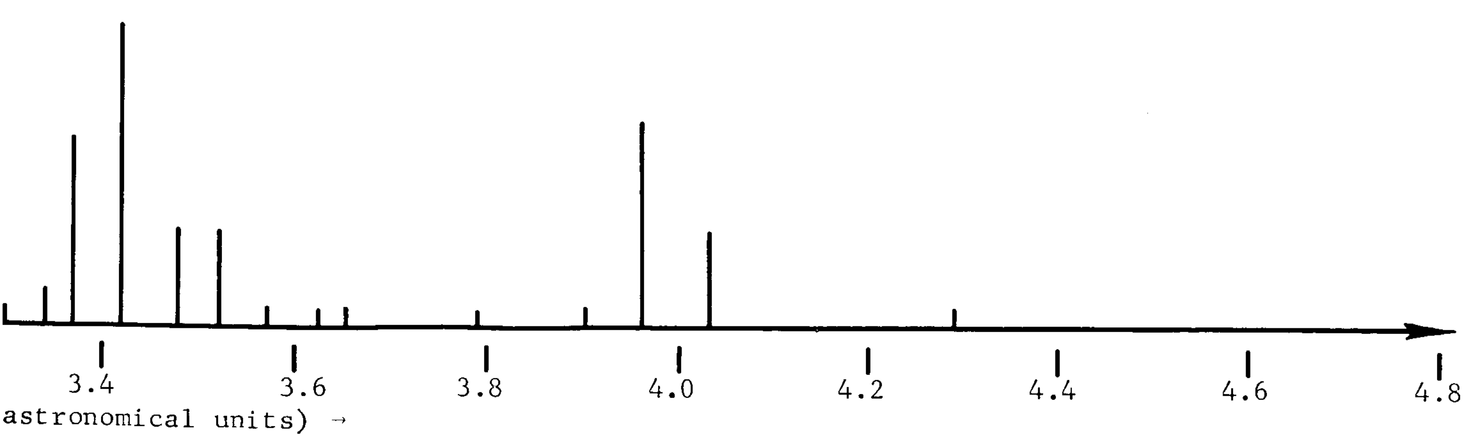

ure H-16: Distribution of Cataloged Asteroids as a Function of Orbital Radius is one-third of Jupiter's. Another gap occurs at 2.90 A.U.

Also, in an effort to create a mathematical model which would give a general description of the asteroids, their orbital elements were examined. Figure H-17 (which shows the average inclination as a function of orbital radius), Figure H-18 (which shows the average eccentricity as a function of orbital radius), and Figure H-19 (which shows the number of asteroids as a function of orbital radius) generally indicate that a truncated Gaussian distribution of the asteroids would be a good representation. Such a distribution is utilized in Section D-2. Beyond 3.2 A.U. it can be readily seen that there is an apparent lack of data. As seen from Earth, many of the asteroids in this region have a visual magnitude of +20 or dimmer. Hence, the probability of observation is very small due to limitations of Earth-bound equipment.

Finally, in Figure H-20 from Reference [8] is shown the visual magnitude as seen from Earth of the cataloged asteroids. Note that the brightest asteroid (Ceres) has a visual magnitude of 9.8.

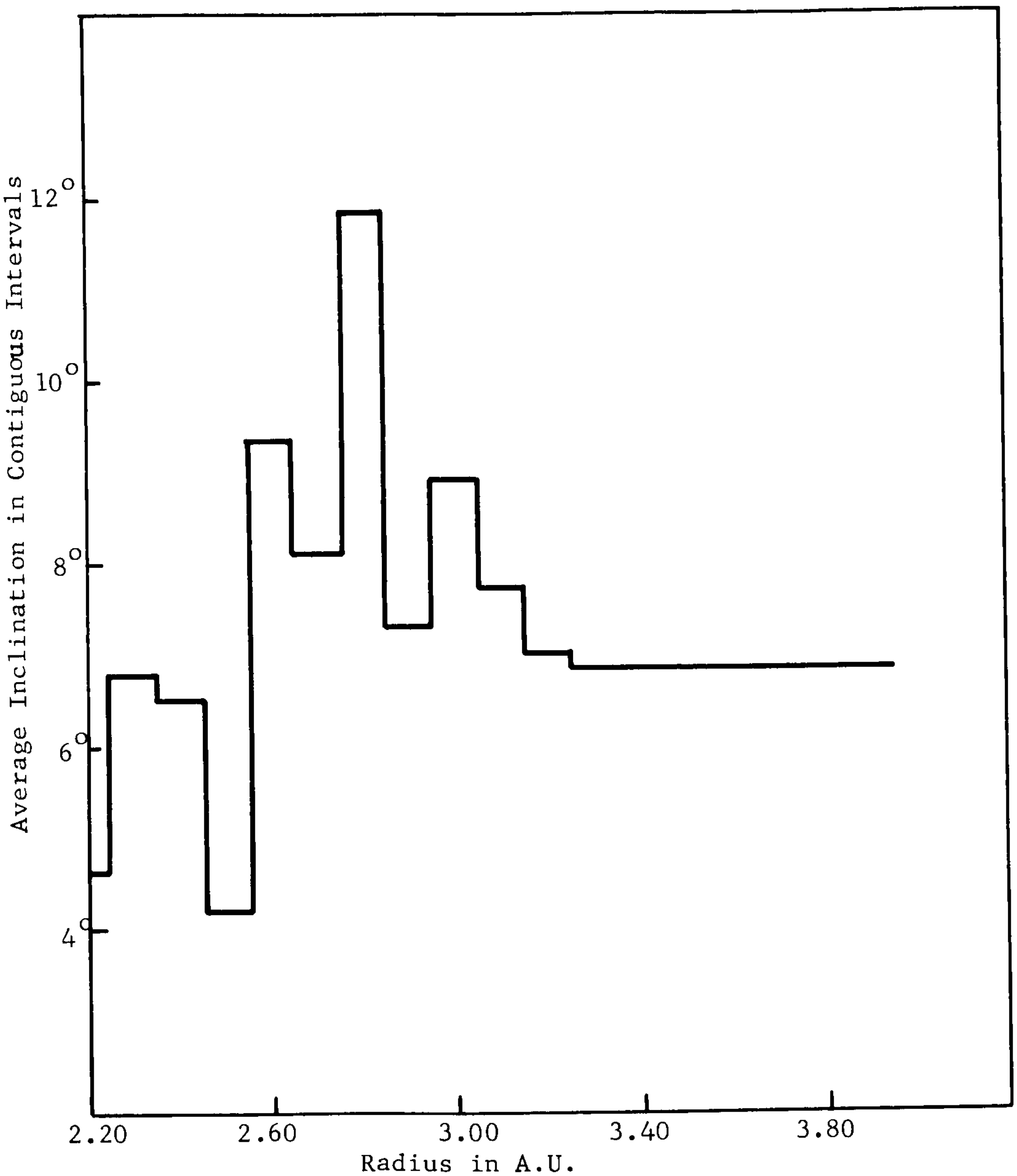

Figure H-17: Plot of the Average Inclination of the Cataloged Asteroids as a Function of the Radius of Their Orbits

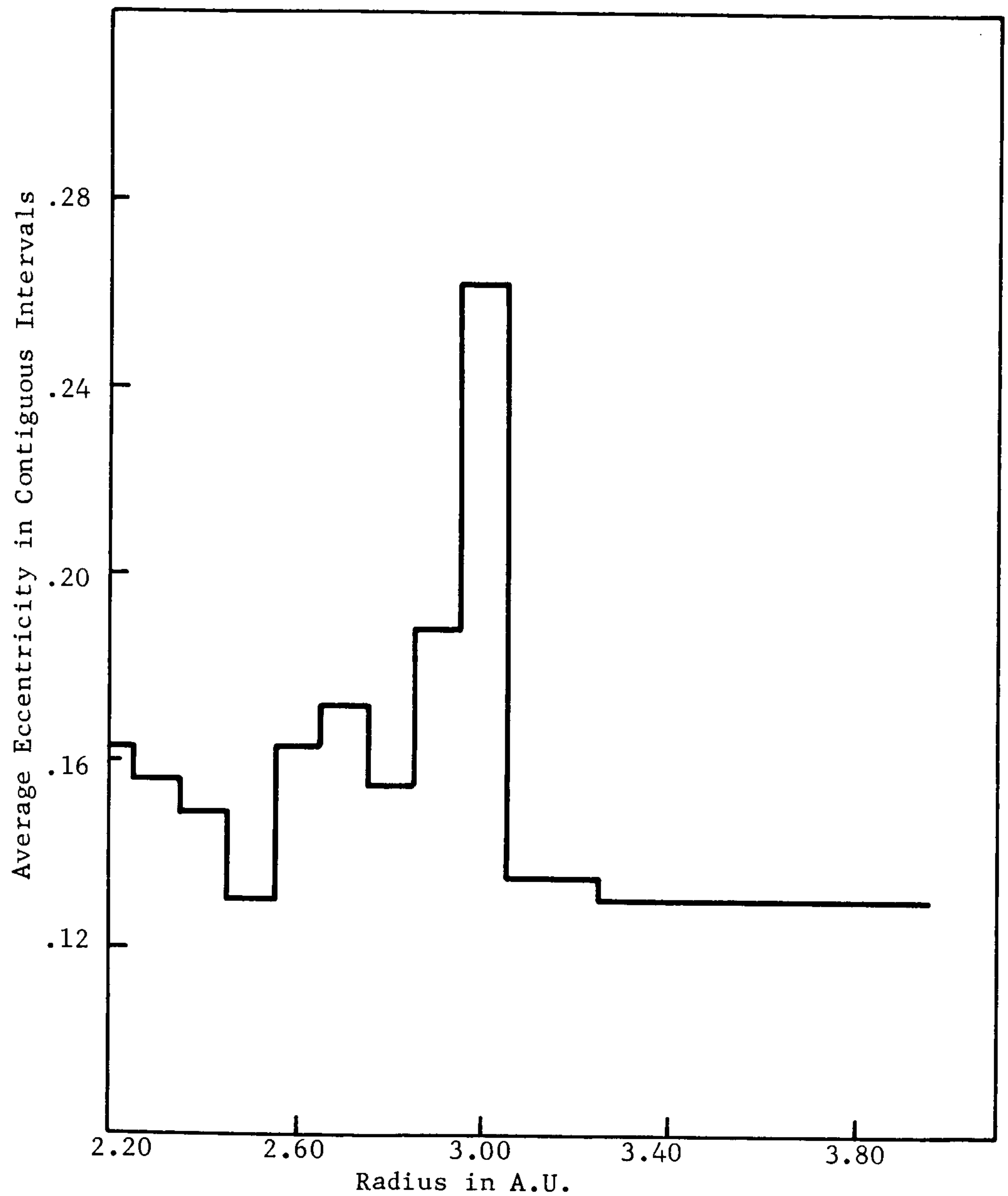

Figure H-18: Plot of the Eccentricity of Cataloged Asteroids as a Function of the Radius of Their Orbits

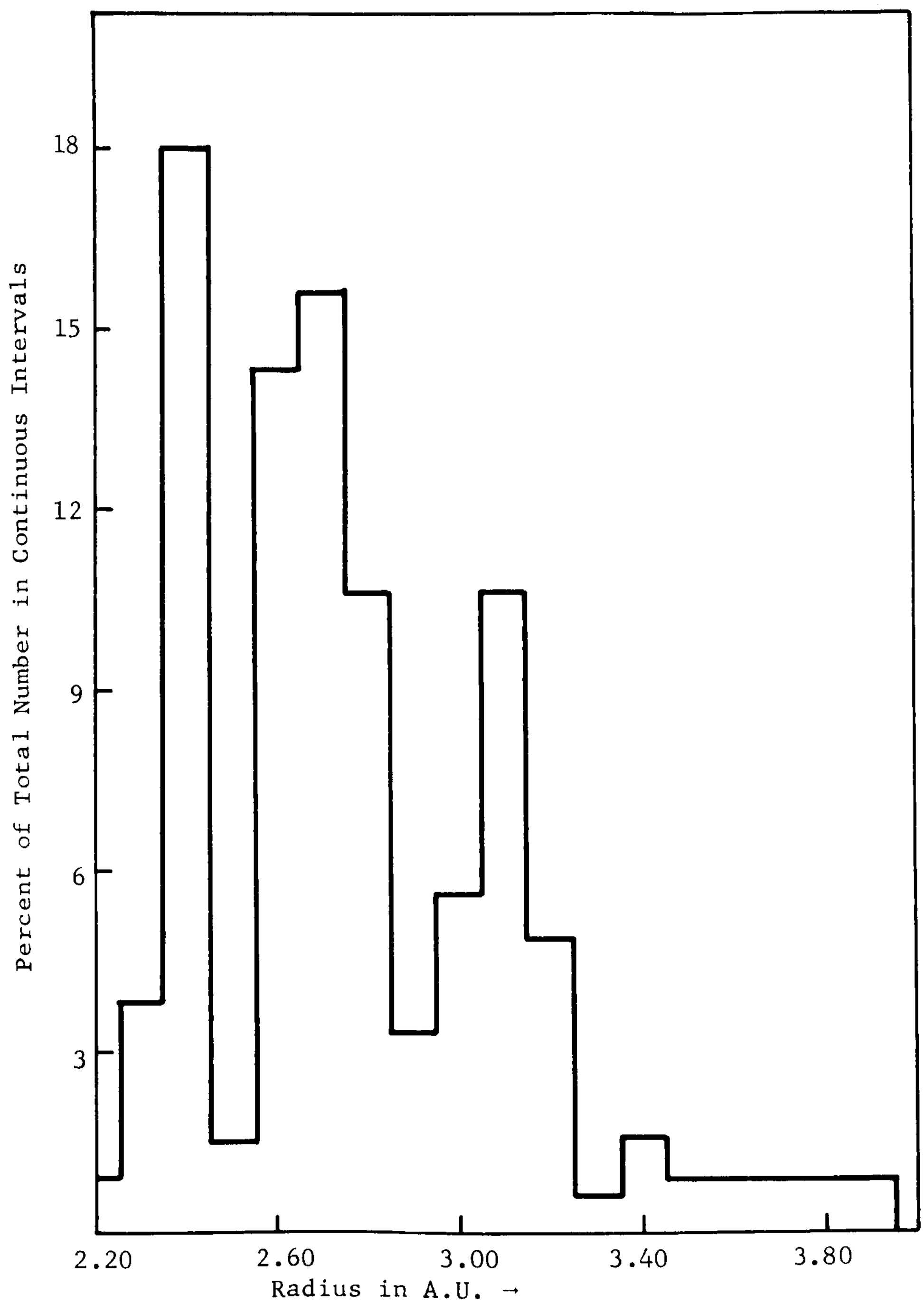

Figure H-19: Percent of Total Number of Asteroids in a Given Interval as a Function of r (in A.U.)

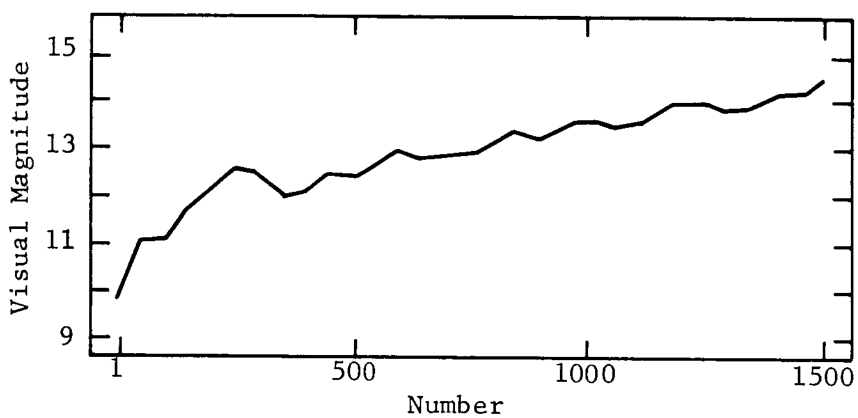

Figure H-20: Relation Between Average Brightness and Order of Discovery of Asteroids. The Order of Discovery of Asteroids is Indicated by the Number Assigned to Them

2. Viewability of Asteroids

The only clue to the constituent material of asteroids is the reflected light from their surfaces. From the subtle changes in the intensity and color of the reflected light some information can be derived about the nature of the asteroids. Since the size of asteroids cannot be measured directly some relations can be obtained by using their absolute magnitude. This relationship is shown in Table H-5. Even though the albedo varies, the average value is about .12. Since all the asteroids are viewed near full phase with no phase angle larger than 30 degrees, the change of phase angle is 0.030 magnitude per degree of 34 asteroids. Over the same angle range the coefficient is 0.028 for the moon and 0.032 for Mercury. On the other hand, Mars and Venus--planets with atmospheres--have lower albedos, near 0.015. This leads to the conclusion that the asteroids have no atmosphere.

From attempts to do a spectroscopic analysis of the light reflected from the asteroids it has been determined that asteroids are grayish or brownish like nearly all natural terrestrial materials.

While observing Eros in 1900 von Oppolzer found that its brightness changed greatly. It faded 1.5 magnitudes within 79 minutes and then returned to its original brightness in the next few hours. Within a period of five hours and sixteen minutes were two maximums and two minimums. However, several months later this variation was undetectable. After many models were proposed for this phenomena, the accepted one says that Eros is a long, thin, irregularly-shaped body something like a brick, which rotates about an axis which is nearly perpendicular to its greatest dimension. The irregularity of the brightness variations of Eros for different times of the year are explained by differences in the viewing aspects as both bodies rotate about the sun. From later observations, the length of Eros was found to be 22 kilometers and its diameter, 6 kilometers. Also, minor differences in the light variation between successive periods strongly implies that the surface is not smooth but quite irregular. In general Eros could be described as a whirling fragment. From later observations twenty-one asteroids have been found to vary in brightness with periods ranging from four hours nine minutes to eighteen hours. When present surveys are completed it is expected that many more variable brightness asteroids will be found.

Watson [8], in determining a distribution of the number of asteroids present in each step of absolute magnitude,* reports that for each step decrease in absolute magnitude the number of asteroids increases by a factor of $2.7 \approx e$. Moreover, there are three asteroids of absolute magnitude +4. Hence, we obtain the difference equation

$$N(m + 1) = 2.7\, N(m)$$
$$N(4) = 3$$

where $N(m)$ = number of asteroids of absolute magnitude m or brighter. Thus,

$$N(m) = 3 \times 2.7^{m-4} \quad \text{(h-17)}$$

* In dealing with asteroids we define absolute magnitude as the visual magnitude of an asteroid if that asteroid were placed 1 A.U. from the observer and the observer were near the sun.

Also, Watson has set forth a relationship between the absolute magnitude of an asteroid and its diameter as shown in Table H-5.

TABLE H-5

RELATION BETWEEN ABSOLUTE MAGNITUDE AND DIAMETER OF AN ASTEROID

Absolute Magnitude	5.0	10.0	15.0	20.0
Diameter (km.)	270.	27.	2.7	0.27

From this table we may write the difference equation,

$$D(m+5) = 0.1\ D(m)$$

$$D(5) = 270 \text{ kilometers},$$

where D(m) = diameter of asteroid in kilometers whose absolute magnitude is m. Hence,

$$D(m) = 2700 \times 10^{-\frac{m}{5}} \qquad \text{(h-18)}$$

So, from Equations (h-17) and (h-18) we may write

$$\log N = -5 \log 2.7 \log D + \log 3 + (5 \log 2700 - 4) \log 2.7$$

$$= 6.03351 - 2.15680 \log D \qquad \text{(h-19)}$$

Figure H-21 is a graph of Equation (h-19) which yields the number of asteroids of a given diameter or greater. This figure indicates approximately 10^6 asteroids of diameters of one kilometer or greater.

The magnitude of an asteroid is dependent on several factors: (1) diameter, (2) distance of observer from the observed asteroid, (3) solar illumination, and (4) the albedo. Assuming that the asteroid is a sphere, a specular reflector, and fully sun-illuminated, we may write the relationship

$$DR = d\sqrt{\rho}\; 10^{.2(26.7 + m_v)}$$

where
D = distance between asteroid and observer (see Figure H-19)
R = distance between asteroid and Sun (in A.U.)
d = diameter of asteroid (same units as D)
ρ = albedo of asteroid
m_v = visual magnitude of asteroid as seen by observed.

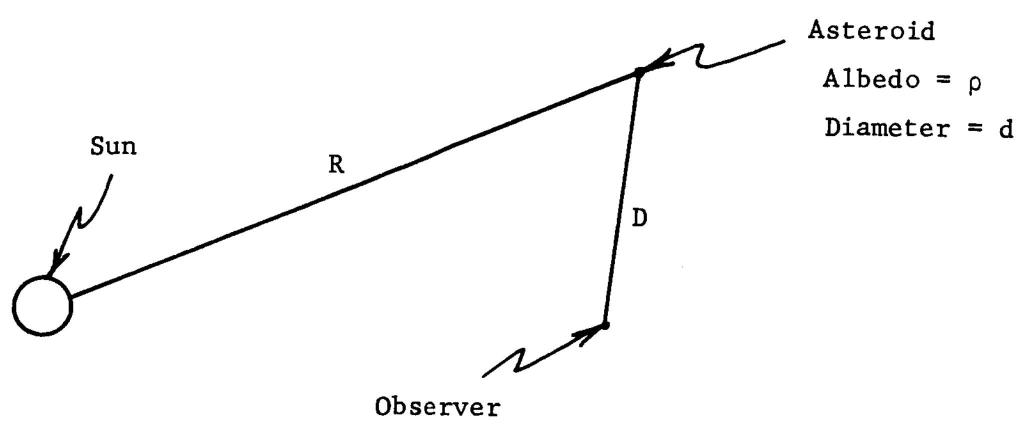

Figure H-22: Geometry of Asteroid Viewability

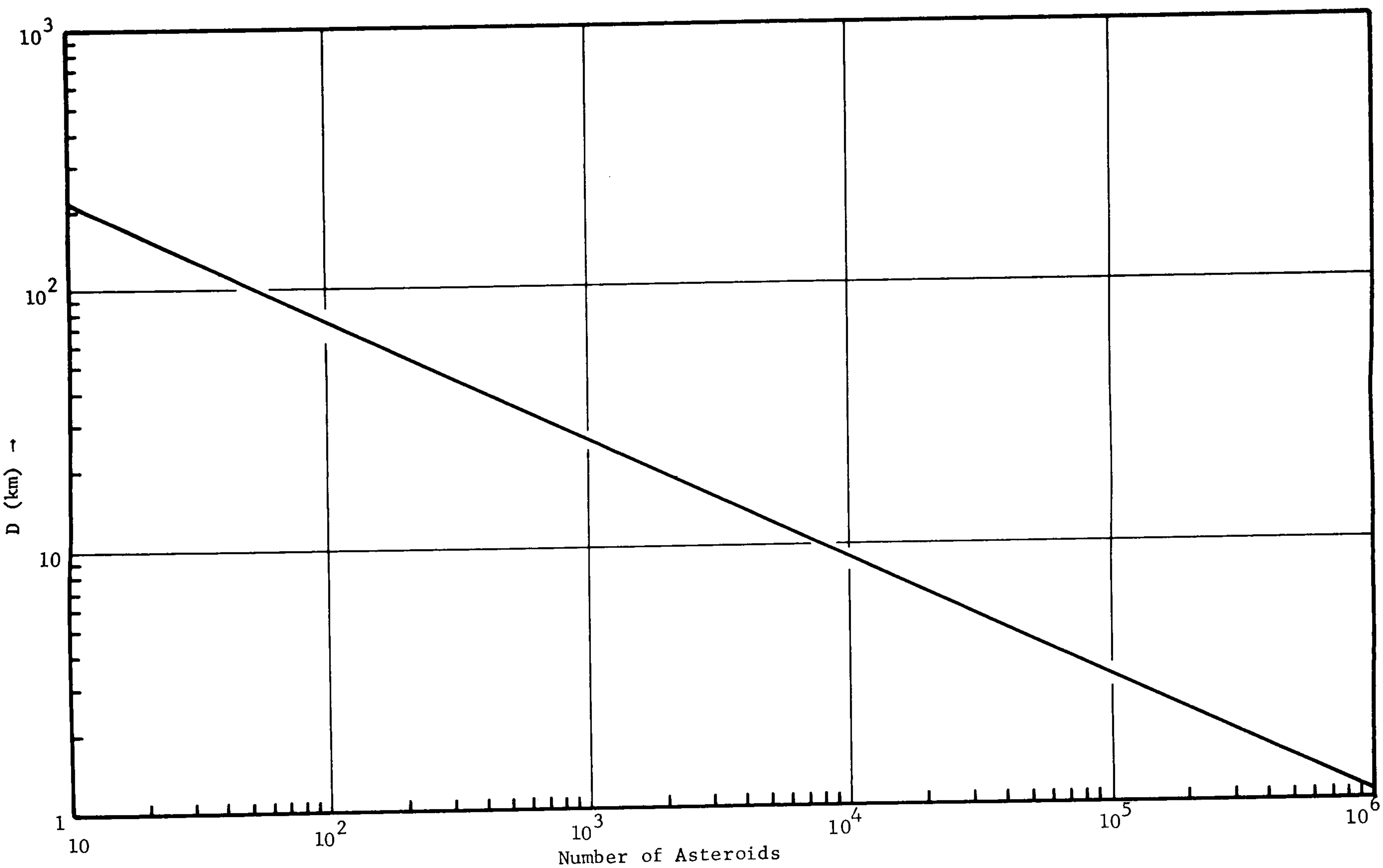

Figure H-21: Number of Asteroids Whose Diameter is Greater than D

In Figure H-23 we plot d as a function of D for $\rho = 0.1$, R = 3 A.U., and $m_v = 0, 2,$ and 4.

3. Expected Number and Detected Asteroids

a. Expected Number at a Given Distance from the Sun

From Figure H-23 we may note the larger asteroids can be detected at distances greater than the Earth-Moon distance. However, this graph yields no clue as to the number of asteroids which might be observed at a given visual magnitude and given observer's position. We now attack this problem. Since a catalog of all asteroids of diameter greater than one kilometer is not available, the method of attack must be statistical.

As a first approximation let us assume the asteroids are in a plane, then

$$n = \iint_R N(m)\ f(r, \phi)\ dr\ d\phi \qquad \text{(h-20)}$$

where $N(m)$ = total number of asteroids whose absolute magnitude is less than m

n = expected number of these asteroids that are in a region R

$f(r, \phi)$ = density function of asteroid distribution at distance r from the sun and azimuth angle ϕ from some fixed direction.

The relation between visual magnitude and absolute magnitude may be approximated as

$$m_v = m + 5 \log r\, d - 2.5 \log \left(\frac{1+\cos \psi}{2} \right) \qquad \text{(h-21)}$$

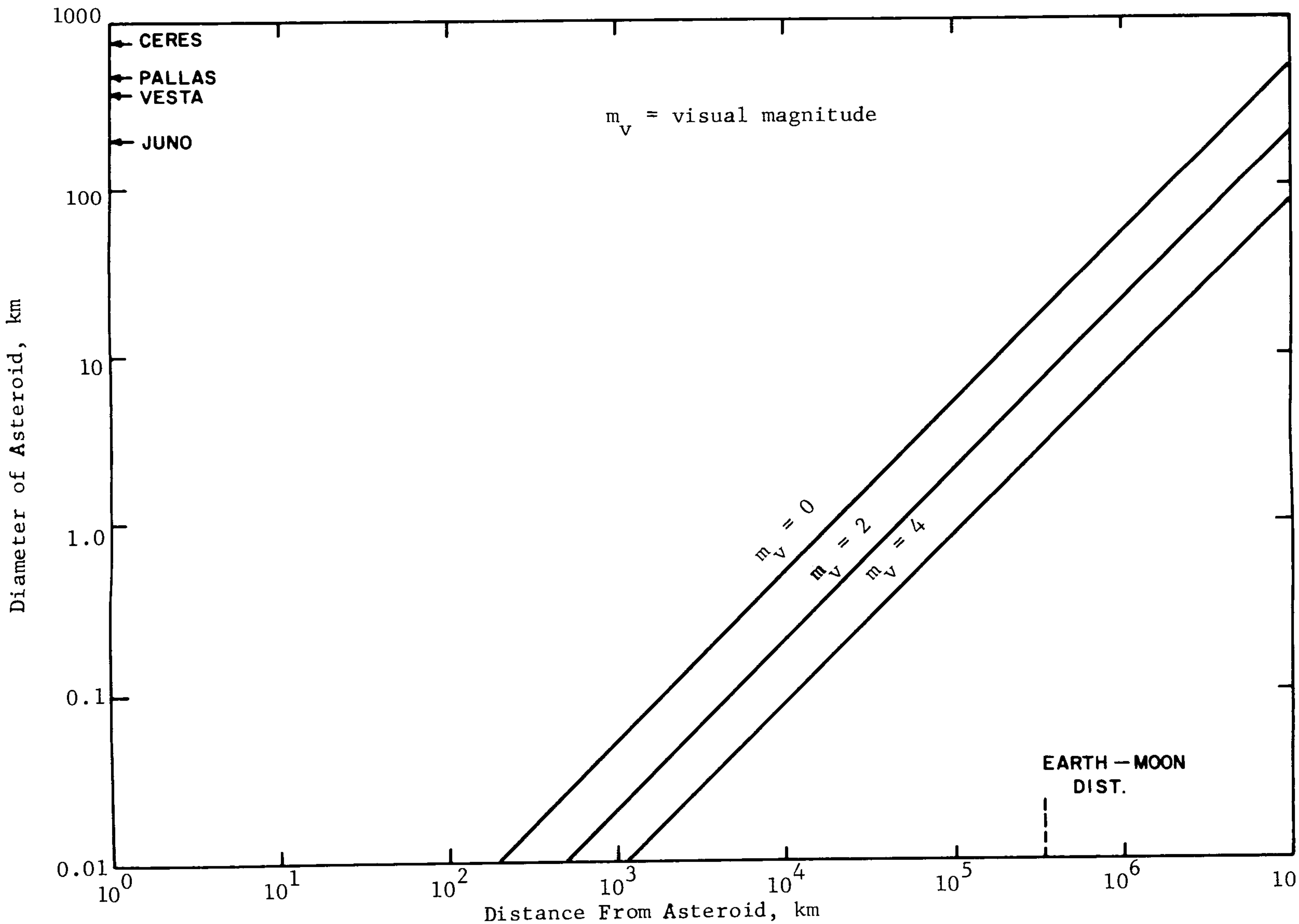

Figure 23: Diameter of Asteroids Visible From Various Ranges (Observer 3 A.U. From Sun, Asteroid Albedo = .1)

where m = absolute magnitude of the asteroid, i.e., the visual magnitude of the asteroid if the asteroid were 1 A.U. from the sun and the observer near the sun

r = distance of asteroid from the sun

d = distance between asteroid and observer

ψ = phase angle of the asteroid with respect to the observer (see Figure H-24).

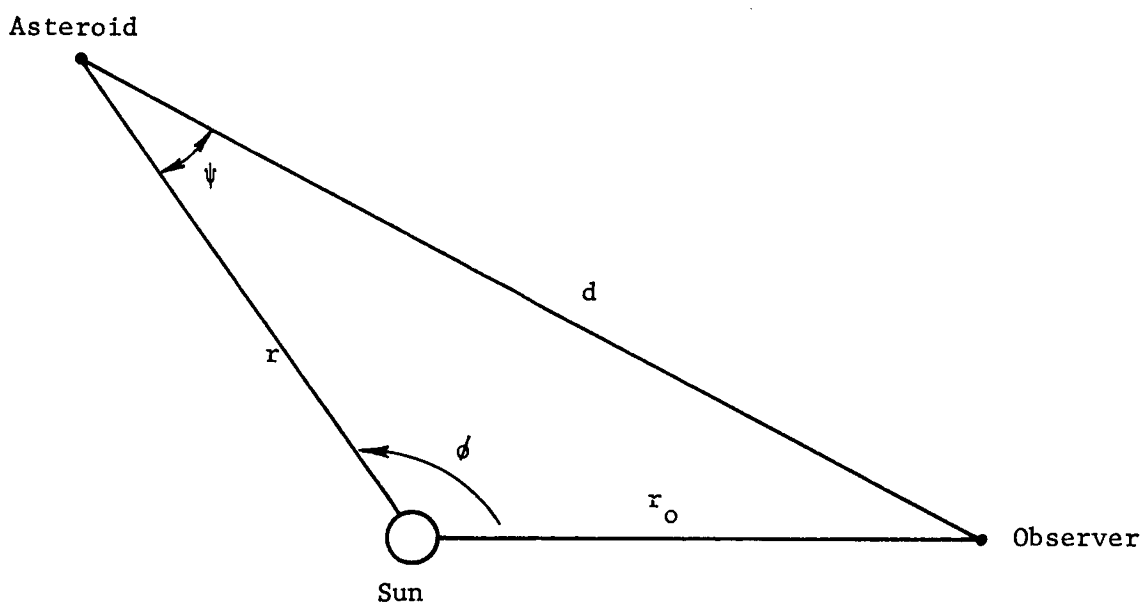

Figure H-24: Parameters Which Relate Visual and Absolute Magnitude

Substituting Equation (h-21) into (h-20) we obtain

$$n\,(r_o) = \iint_R N(m_v - g(r_o,\, r,\, \phi))\; f(r,\, \phi)\; dr\; d\,\phi \qquad \text{(h-22)}$$

where

$$g(r_o, r, \phi) = 5 \log (r\ d) - 2.5 \log \frac{1 + \cos \psi}{2}$$

$$d = \sqrt{r_o^2 + r^2 - 2r_o r \cos \phi}$$

$$\frac{1 + \cos \psi}{2} = \frac{r + d - r_o \cos \phi}{2d} \quad ,$$

r_o being the distance between the observer and the sun (we assume the observer is in the reference direction as in Figure H-24).

Now if we specify m_v in Equation (h-22) we may interpret $\eta\ (r_o)$ as the expected number of asteroids in R whose visual magnitude is less than m_v for an observer whose distance from the sun is r_o.

From our previous discussion we may take $N(m) = 3 \times (2.7)^{m-4}$. We will assume that these asteroids are distributed through space uniformly in azimuthal direction and truncated Gaussian in the radial direction. Hence,

$$f(r, \phi) = \frac{1.087}{2\pi \sqrt{2\pi}\ \sigma}\ e^{-\frac{1}{2}\left(\frac{r - \mu}{\sigma}\right)^2} , \quad 2.2 \leq r \leq 3.95$$

$$= 0, \quad \text{otherwise}$$

where μ = mean of the radial distribution

σ = standard deviation of the radial distribution.

A good approximation is

μ = 3.1 A.U.

σ = .5 A.U.

Hence, if we choose R to be the whole plane

$$n\,(r_o) \doteq \frac{1.5 \times 1.087 \times 2.7^{m_v - 4}}{\pi\sqrt{2\pi}} \int_{2.2}^{3.95} \int_{0}^{\pi} \frac{r + d - r_o \cos\phi}{r^2\, d^3}$$

$$\times \; e^{-2(r-3.1)^2}\, d\phi\, d\, r \;,$$

where we use the approximation $2.5 \log 2.7 \approx 1$. Now, the integration on ϕ may be reduced to complete elliptic integrals to yield

$$n\,(r_o) = .0207 \times 2.7^{m_v - 4} \int_{2.2}^{3.95} \frac{1}{r^2} \left[\frac{1}{r(r - r_o)}\, E(k) \right.$$

$$\left. + \frac{1}{r(r + r_o)}\; K(k) + \frac{\pi}{|r^2 - r_o^2|} \right] e^{-2(r-3.1)^2}\; dr \;,$$

where

$$K(k) = \int_0^{\pi/2} \frac{d\theta}{\sqrt{1 - k^2 \sin^2\theta}}$$

$$E(k) = \int_0^{\pi/2} \sqrt{1 - k^2 \sin^2\theta}\;\; d\theta$$

$$k = \frac{2\sqrt{r\, r_o}}{r + r_o} \quad .$$

The integration on r may be done by a numerical method. The result is indicated in Figure H-25.

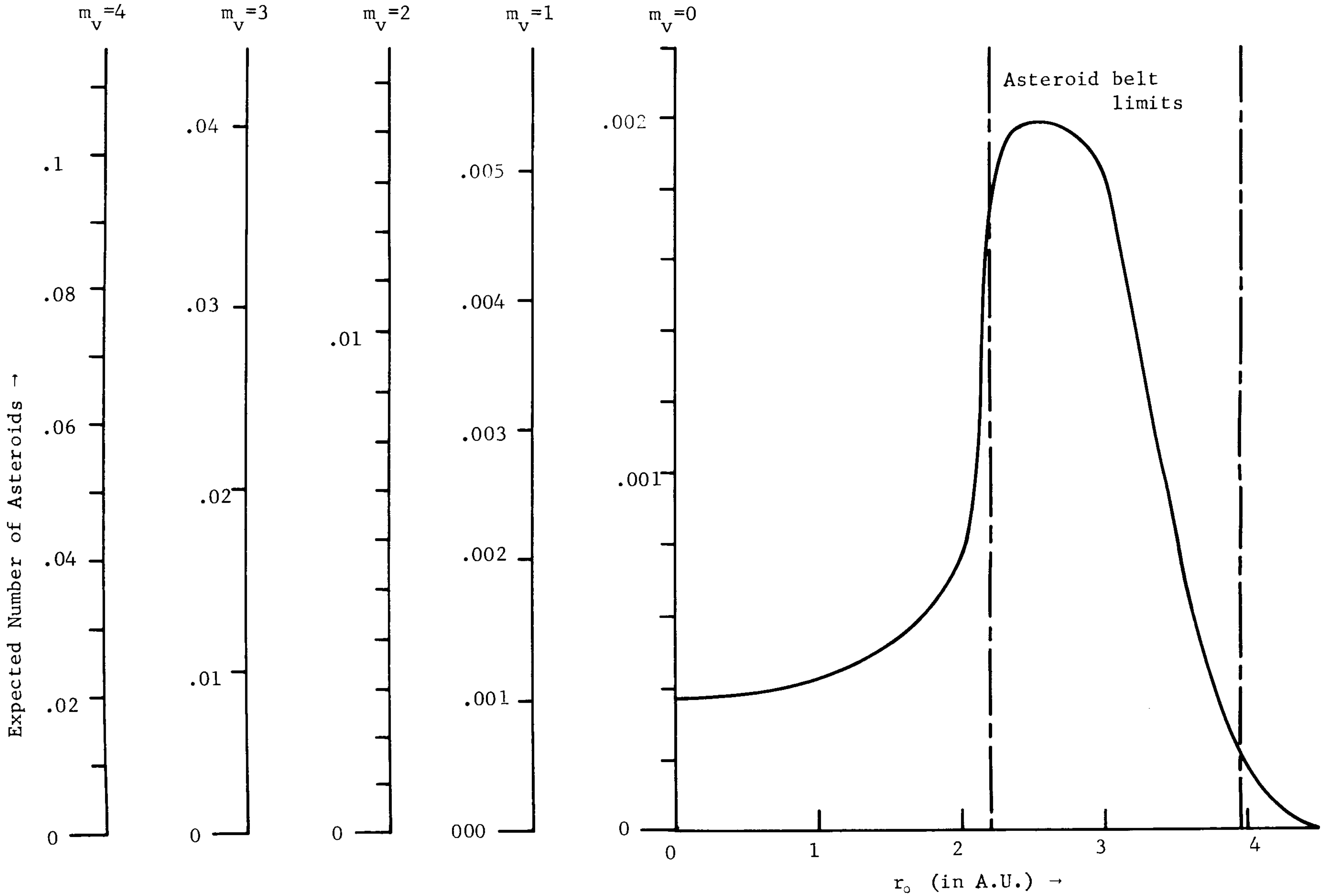

Figure H-25: Expected Number of Asteroids Seen at Various Magnitudes as a Function of Observer's Distance From Sun, r_o

Figure H-25 gives the expected number of asteroids as a function of the observer's distance from the sun, which are brighter than various visual magnitudes. This figure indicated that if an observer were randomly placed 2 A.U. from the sun, then at any instant the expected number of asteroids of visual magnitude 4 or brighter in 4π steradians is 0.041.

Note that the expected number of observable asteroids rapidly increases as the observer approaches the belt. This expected number then peaks before the belt's center and then rapidly decreases. Recall that this figure was derived on the assumption that all asteroids lie in a plane, with uniform distribution in azimuth, and a truncated Guassian distribution in radius. These assumptions are approximate as indicated by our previous work and by Narin [10].

b. Expected Number Detected by SCADS-Type Sensor

We would now like to answer the following question: How many asteroids would one expect to detect on a four-year journey along some given course by use of a SCADS-type sensor? Unfortunately, we have not given a definite answer to this question. The problem is not an elementary one. However, we can make some general comments.

From Figure H-25 we may note that one must be able to detect objects as dim as visual magnitude four to have a significant probability of asteroid detection. Objects that dim cannot be detected with any certainty with the hemispherical field of view, for the background is of the order of a first magnitude star. Thus, to detect asteroids the field of view must be limited to that approaching the sensor's field of view considered in the main body of this report. But this factor will reduce the probability of asteroid detection.

In total, the probability of asteroid detection by use of the sensor is not too good. In order to be assured of asteroid detection one could

(1) plan to journey to that point where the path would come close to the larger asteroids,

(2) obtain the circular trajectory whose radius is about 2.5 A.U. and in a rotational direction opposing that of the solar system, and

(3) design an instrument which operates at a slower spin period, i.e., from one to two minutes.

REFERENCES

[1] Cathey, L., "Fatigue in Photomultipliers," IRE Trans. on Nuc. Sci. NS-5, pp. 109-115 (December 1958).

[2] Cantarell, I., "Theoretical and Experimental Study of Fatigue in Photomultiplier Tubes," Nuc. Sci. and Engineering, 18, pp. 31-48 (1964).

[3] Wargo, P., B. V. Haxby, and W. G. Shephard, Jour. Appl. Phys., 27, No. 11, 1311 (November 1956).

[4] Schenkel, F. W., "New Developments in Photoemissive Tubes," IRE Trans. Nuc. Sci. NS-9, pp. 83-87 (June 1962).

[5] Norton, R. H., "The Absolute Spectral Energy Distribution of Canopus," JPL Tech. Rpt. No. 32-641, California Inst. of Technology, (August 16, 1964).

[6] Williams, R. L., "Fast High-Sensitivity Photodiode," Jour. Opt. Soc. Am. 52, No. 11, p. 1237 (November 1962).

[7] Allen, C. W., Astrophysical Quantities, Athlone Press, Second Edition, 1963.

[8] Watson, F. C., Between the Planets, Harvard University Press, 1956.

[9] DeVaucouleurs, G., and L. Radaus, Larousse Encyclopedia of Astronomy, Batchworth Press Limited, London, 1959.

[10] Narin, Francis, "Spatial Distribution and Motion of the Known Asteroids," AIAA Paper No. 66-149, January, 1966.